UNIVERSITÀ DEGLI STUDI DI MILANO

Scuola di Dottorato in Fisica, Astrofisica e Fisica Applicata

Dipartimento di Fisica

Ciclo XXXVIII

Probing the Higgs boson with the ATLAS detector:

precision measurement of the mass and search for rare decays to a low-mass dilepton system and a photon in proton-proton collisions at the LHC.

Supervisori: Prof. Leonardo Carminati
Dr. Ruggero Turra
Dr. Stefano Manzoni

Coordinatore: Prof. Aniello Mennella

Tesi di Dottorato di:
Laura Nasella
Matricola n. R13865
ORCID n. 0000-0002-4871-784X

Anno Accademico 2024/2025

Commission of the final examination:

Prof. Kerstin Tackmann
Prof. Hongtao Yang
Dr. Emanuele Di Marco

Referees:

Prof. Hongtao Yang
Dr. Emanuele Di Marco

Final examination:

25 March 2026
Università degli Studi di Milano, Dipartimento di Fisica, Milano, Italy

Settore Scientifico Disciplinare:
PHYS/01-A

PACS:
14.80.Bn, 13.85.Qk, 29.85.Fj

Keywords:
Particle physics; Higgs physics; Collider experiments; Particle detectors; Standard Model

Cover illustration:
The Higgs puzzle, idea by Laura Nasella, artwork by Mathis Dubau.

Abstract

This thesis presents three analyses based on proton–proton collision data recorded by the ATLAS detector at the Large Hadron Collider, using the full Run 2 dataset collected between 2015 and 2018 at a centre-of-mass energy of $\sqrt{s} = 13$ TeV, corresponding to an integrated luminosity of 140 fb^{-1}, and data recorded during the first part of Run 3 between 2022 and 2024 at $\sqrt{s} = 13.6$ TeV, corresponding to 165 fb^{-1}. The analyses focus on a detailed investigation of the Higgs boson within the Standard Model (SM), through the precision measurement of one of its fundamental parameters, the Higgs boson mass m_H, and the search for a rare SM decay mode not yet observed, namely the decay into a low-mass dilepton system and a photon.

The first analysis presents a precision measurement of the Higgs boson mass in the diphoton decay channel, $H \to \gamma\gamma$, using the full Run 2 dataset. The Higgs boson mass is measured to be $m_H = 125.17 \pm 0.11\,(\text{stat.}) \pm 0.09\,(\text{syst.})$ GeV $= 125.17 \pm 0.14$ GeV. The improved precision with respect to previous measurements is driven by the larger dataset and by significant advances in the calibration of the photon energy response, resulting in a measurement that is now statistically limited. A combination with the corresponding Run 1 measurement yields $m_H = 125.22 \pm 0.14$ GeV.

The second analysis furthermore combines the Higgs boson mass measurements obtained in the $H \to \gamma\gamma$ and $H \to ZZ^* \to 4\ell$ decay channels using ATLAS Run 1 and Run 2 data. The combined result, $m_H = 125.11 \pm 0.09\,(\text{stat.}) \pm 0.06\,(\text{syst.})$ GeV $= 125.11 \pm 0.11$ GeV, achieves a relative precision of 0.9 per mille and represents the most precise determination of the Higgs boson mass to date. All mass measurements are found to be consistent with each other and with previous ATLAS and CMS results.

The third analysis presents a search for the rare Higgs boson decay into a low-mass dilepton system with a photon, $H \to \ell\ell\gamma$ ($\ell = e, \mu$), using partial Run 3 data. The search targets the low dilepton mass region $m_{\ell\ell} < 30$ GeV, where the decay proceeds predominantly via an off-shell photon. The analysis is currently under ATLAS internal review, and preliminary expected results based on statistical uncertainties only are reported. The expected 95% confidence level upper limit on the production cross section times branching ratio is 1.65 (0.70) times the SM prediction under the signal-plus-background (background-only) hypothesis, and an expected significance of $Z = 2.53\,\sigma$ is obtained for a SM signal.

In addition, studies of the ATLAS detector performance relevant for these analyses are presented, including the optimisation of the multivariate Monte Carlo–based energy calibration for electrons and photons in Run 2 and Run 3, and dedicated studies of merged-electron identification, which are essential for the rare-decay $H \to \ell\ell\gamma$ search.

Contents

Introduction

The research presented in this PhD thesis is based on proton–proton collision data recorded by the ATLAS [1] detector at the Large Hadron Collider (LHC) [2]. The analyses exploit the full Run 2 dataset collected between 2015 and 2018 at a centre-of-mass energy of $\sqrt{s} = 13$ TeV, corresponding to an integrated luminosity of approximately 140 fb^{-1}, as well as proton–proton collision data recorded during the first part of Run 3 at an increased centre-of-mass energy of $\sqrt{s} = 13.6$ TeV. The Run 3 dataset considered in this thesis corresponds to data collected up to 2024, amounting to an integrated luminosity of about 165 fb^{-1}.

The LHC is the world's largest and most powerful particle accelerator. The ATLAS detector is one of the two general-purpose experiments at the LHC, together with CMS [3], and is designed to address a broad range of physics phenomena, from precision measurements of Standard Model (SM) processes to searches for physics beyond it. The SM provides a unified theoretical framework for the description of strong and electroweak interactions [4, 5] and encompasses all known elementary particles, including matter fields and force carriers.

A central component of the SM is the *Higgs mechanism*, independently proposed in 1964 by Higgs [6], by Englert and Brout [7], and by Guralnik, Hagen and Kibble [8] which accounts for the generation of particle masses while preserving electroweak gauge invariance. This mechanism postulates the existence of a scalar field, known as the *Higgs field*, whose quantum excitation manifests as the Higgs boson. The discovery of a Higgs-like particle by the ATLAS and CMS experiments in 2012 [9, 10] provided experimental confirmation of this mechanism and established the origin of mass for elementary particles through spontaneous *electroweak symmetry breaking*.

Following this discovery, a primary objective of the ATLAS physics programme has been the precise determination of the Higgs boson properties. In particular, the Higgs boson mass, m_H, plays a central role as a fundamental input parameter of the SM. Since Higgs production cross sections and decay branching ratios depend sensitively on m_H, a precise experimental determination of the mass is essential for testing the consistency of the Higgs couplings with SM predictions and for probing potential deviations associated with physics Beyond the Standard Model (BSM).

The measured value of m_H is a key input to global fits of electroweak observables [11] and plays an important role in testing the internal consistency of the SM, in particular through the interplay between the masses of the top quark and the W and Higgs bosons. Moreover, the stability of the electroweak vacuum depends sensitively on the Higgs

boson mass [12]. Its measurement therefore provides insight into whether the Universe resides in a stable global minimum of the Higgs potential or in a metastable state.

The Run 1 combined measurement of the Higgs boson mass in the $H \to ZZ^* \to 4\ell$ and $H \to \gamma\gamma$ channels by the ATLAS and CMS experiments yielded [13]

$$m_H = 125.09 \pm 0.24\,\text{GeV} = 125.09 \pm 0.21\,(\text{stat.}) \pm 0.11\,(\text{syst.})\,\text{GeV}, \tag{1}$$

which is since then considered the nominal value of m_H in the High Energy Physics (HEP) community.

Therefore, the first two analyses presented in this thesis focus on the precision measurement of the Higgs boson mass with the ATLAS detector. The first analysis presents the legacy measurement in the diphoton decay channel, $H \to \gamma\gamma$, using the full Run 2 dataset recorded at a centre-of-mass energy of $\sqrt{s} = 13$ TeV, corresponding to an integrated luminosity of 140 fb^{-1} [14].

Although the $H \to \gamma\gamma$ decay is rare, with a branching ratio of approximately 0.227%, this is compensated by the excellent photon trigger and reconstruction efficiencies of the ATLAS detector, together with the high resolution of the diphoton invariant mass, $m_{\gamma\gamma}$, of the order of 1–2 GeV. These features lead to a clear and well-resolved signal peak above a smoothly falling background, making this channel one of the two *golden channels* for the Higgs boson discovery, alongside $H \to ZZ^* \to 4\ell$.

The Higgs boson mass is determined from the position of the narrow resonant peak in the $m_{\gamma\gamma}$ distribution, superimposed on a large continuum background dominated by Quantum Chromodynamics (QCD) diphoton production, with additional contributions from γ+jet, dijet, and Drell–Yan processes. The invariant mass is reconstructed from the measured photon energies and directions with respect to the diphoton production vertex, and signal purity is enhanced by requiring two high-quality, isolated photons originating from the same primary vertex.

Compared to earlier ATLAS measurements based on Run 1 or partial Run 2 datasets (36 fb^{-1} collected between 2015 and 2016) [15], this full Run 2 $H \to \gamma\gamma$ analysis [14] benefits from the larger dataset, an new photon reconstruction algorithm with improved energy resolution [16] an enhanced determination of the photon energy scale with reduced systematic uncertainties [17], and an optimised event classification strategy. To further improve the precision on the Higgs boson mass, the Run 2 result is statistically combined with the previous ATLAS measurement in the $H \to \gamma\gamma$ channel based on 25 fb^{-1} of Run 1 data collected at $\sqrt{s} = 7$ and 8 TeV [13].

The second analysis presented in this thesis is the measurement of the Higgs boson mass obtained by combining the $H \to ZZ^* \to 4\ell$ [18] and $H \to \gamma\gamma$ [14] decay channels. The result [19] is based on 140 fb^{-1} of pp collision data collected by ATLAS during Run 2 at a centre-of-mass energy of $\sqrt{s} = 13$ TeV, and is subsequently combined with the corresponding Run 1 ATLAS measurements in both channels at $\sqrt{s} = 7$ and 8 TeV.

The combination is performed using a *profile likelihood ratio* approach, which allows for a consistent treatment of statistical and systematic uncertainties and their correlations between the two decay channels. A single value of the Higgs boson mass, m_H, is assumed and simultaneously fitted in both channels from the positions of the resonant peaks ob-

served in the $m_{4\ell}$ and $m_{\gamma\gamma}$ distributions. This full Run 2 result supersedes earlier measurements based on partial Run 2 datasets and benefits from the larger data sample, as well as from improved calibrations of the electron and photon energy [17] and of the muon momentum [20].

Despite the discovery of the Higgs boson more than a decade ago, several rare decay modes predicted by the SM have not yet been observed, owing to their small branching ratios and large backgrounds. Among these, the $H \to \mu\mu$ decay provides the most direct probe of the Higgs boson Yukawa coupling to second-generation fermions, while the loop-induced $H \to Z\gamma$ decay is particularly sensitive to potential BSM effects.

ATLAS has recently reported improved analyses of both channels using partial Run 3 data collected between 2022 and 2024, in combination with Run 2 results [21]. In the $H \to \mu\mu$ channel, an excess with a significance of 3.4σ (2.5σ expected) is observed, providing evidence for this decay mode [22]. The $H \to Z\gamma$ analysis yields an observed (expected) significance of 2.5σ (1.9σ) [23]. Previously, the ATLAS and CMS Run 2 combination reported the first evidence for the $H \to Z\gamma$ decay with a significance of 3.4σ [24].

In this context, the third analysis presented in this thesis is a Run 3 search for the rare SM Higgs boson decay into a photon (γ) and an off-shell photon (γ^*), $H \to \gamma\gamma^*$, where the virtual photon internally converts into a dilepton pair, $\gamma^* \to \ell\ell$ ($\ell = e, \mu$). Several processes contribute to the same $\ell\ell\gamma$ final state, including Dalitz decays mediated by an off-shell photon or a Z boson, as well as Higgs boson decays accompanied by photon radiation via final-state radiation (FSR). Their relative contributions depend on the invariant mass of the dilepton system, $m_{\ell\ell}$. The decay mediated by a virtual photon dominates the low dilepton mass region, $m_{\ell\ell} < 30$ GeV. Restricting the analysis to this region ensures statistical independence from the $H \to Z\gamma$ search, which targets events with an on-shell Z boson and requires $|m_{\ell\ell} - m_Z| < 10$ GeV, where $m_Z = 91.2$ GeV.

Beyond providing sensitivity to the Higgs boson decay rate, such $\ell\ell\gamma$ final states probe potential modifications of the Higgs boson couplings arising from extensions of the SM [25]. In addition, three-body Higgs boson decays offer a sensitive handle on possible CP-violation in the Higgs sector through the study of angular and kinematic observables, such as the forward–backward asymmetry [26, 27].

The CMS Collaboration performed a search in the $\mu\mu\gamma$ final state using 35.9 fb^{-1} of Run 2 data collected at $\sqrt{s} = 13$ TeV, setting a 95% Confidence Level (CL) upper limit on the Higgs boson production cross section times branching ratio of 4.0 times the SM expectation [28]. The ATLAS Collaboration subsequently extended this search using the full Run 2 dataset (139 fb^{-1}) [29], providing evidence for the $H \to \ell\ell\gamma$ process with an observed (expected) significance of 3.2σ (2.1σ) and a measured signal-strength parameter of $\mu = 1.5 \pm 0.5$.

The analysis presented in this thesis is based on pp collision data recorded at a centre-of-mass energy of $\sqrt{s} = 13.6$ TeV during the Run 3 data-taking period between 2022 and 2024, corresponding to an integrated luminosity of 165 fb^{-1}. It benefits from both the increased dataset and the higher centre-of-mass energy with respect to Run 2, which lead to an enhancement of the Higgs boson production cross sections that increased from approximately 55.83 pb at $\sqrt{s} = 13$ TeV to about 59.98 pb at $\sqrt{s} = 13.6$ TeV.

The analysis follows the strategy developed for the Run 2 search [29]. Events are se-

lected by requiring two leptons (electrons or muons) and a photon in the final state, and are subsequently categorised into mutually exclusive classes to maximise the signal sensitivity.
Due to the kinematics of the signal process, the energy deposits of the two electrons in the electromagnetic calorimeter are often reconstructed as a single cluster. Two types of electron candidates are therefore defined: *resolved electrons*, where a cluster is associated with a single inner-detector track, and *merged electrons*, where a single cluster is associated with two tracks and represents a merged electron pair. Events are accordingly divided into three channels: $\mu\mu$, resolved ee, and merged ee. Special care is required for the merged-electron channel, where a dedicated identification algorithm is employed to reconstruct two electrons within a single electromagnetic cluster. The energy calibration for merged electrons is derived from that used for converted photons, as their signatures closely resemble early photon conversions in the tracking detector.
The three-body invariant mass spectrum is fitted independently in each category using a Double-Sided Crystal Ball (DSCB) function to model the signal, while the background is described by an analytical function selected using the spurious signal method. The significance of a possible excess is evaluated through a simultaneous fit, and limits are set on the Higgs boson production cross section times branching ratio for the $H \to \ell\ell\gamma$ process. The expected results are presented in this thesis, while the observed results will be reported in an upcoming ATLAS publication.

Thesis summary and personal contribution

This thesis is composed of nine Chapters:

- Chapter 1 presents the theoretical framework relevant to this thesis, including the formulation of the SM of particle physics, spontaneous electroweak symmetry breaking, and the Higgs mechanism.
- Chapter 2 describes the LHC accelerator complex at CERN, providing an overview of its main components and performance during Run 2 and Run 3.
- Chapter 3 provides a detailed description of the ATLAS detector, with particular emphasis on the Liquid Argon electromagnetic calorimeter, which plays a central role in the measurements presented in this thesis, especially for photon reconstruction. During my doctorate I worked within the ATLAS Liquid Argon Calorimeter group, involved on both the day-to-day operation of the calorimeter and to the upgrade of the readout electronics foreseen for the High Luminosity Large Hadron Collider (HL-LHC) phase. For the former activity, I have been one of the on-call experts for the system that delivers the high voltage to the calorimeter electrodes, collecting more than 30 on-call weeks during Run 3. My duties ranged from solving hardware issues happening during the data-taking, as well as hardware and software maintenance during the periods without proton beams circulating in the LHC. For the latter activity within the HL-LHC upgrade, I worked on the Low Voltage Power Supply (LVPS) system of the calorimeter Front-End Crates. In particular, I tested different DC/DC conversion solutions for the Front-End Boards and evaluated the noise introduced into the readout chain.

- Chapter 4 reviews the Higgs boson phenomenology at hadron colliders, in particular at the LHC. It focuses on the Higgs boson production mechanisms and decay modes, the past Higgs boson mass measurements at the LHC, the width measurement, determination of the spin, parity, charge conjugation and the coupling measurements.
- Chapter 5 presents the software algorithms used for the offline reconstruction, identification, and calibration of physics objects in the ATLAS detector, with particular emphasis on photons and electrons, and also covering muons, jets, and missing transverse momentum.
- Chapter 6 details the photon and electron energy calibration steps in ATLAS during Run 2 and Run 3. My personal contribution focused on one of the first steps of the calibration chain: the training, maintenance, and optimisation of the multivariate Monte Carlo-based energy calibration described in Section 6.3. This calibration had not been updated since 2017; I revised and re-optimised it for the full Run 2 data-taking conditions and extended it to the Run 3 detector and simulation configuration.
- Chapter 7 presents the precision measurement of the Higgs boson mass in the $H \to \gamma\gamma$ decay channel using the full Run 2 dataset recorded by ATLAS at a centre-of-mass energy of $\sqrt{s} = 13$ TeV, corresponding to an integrated luminosity of 140 fb^{-1}, published in August 2023 [14]. I was the main analyzer, being involved in most aspects of the work, including event categorisation and optimisation, signal and background modelling, the evaluation of systematic uncertainties, the implementation of the statistical model, the extraction of the final results, the combination with the Run 1 measurement, and the validation of the analysis through extensive cross-checks.
- Chapter 8 describes the combined measurement of the Higgs boson mass [19] obtained by combining the $H \to \gamma\gamma$ results presented in Chapter 7 with the one from the $H \to ZZ^* \to 4\ell$ decay channel [18], using the full Run 2 dataset recorded by ATLAS at $\sqrt{s} = 13$ TeV, together with the corresponding Run 1 ATLAS measurements at $\sqrt{s} = 7$ and 8 TeV. I was one of the main contributors to this work, focusing on the $H \to \gamma\gamma$ input and the implementation of the statistical combination framework, including the treatment of systematic uncertainties and their correlations between the two decay channels and data-taking periods.
- Chapter 9 presents the Run 3 search for the rare SM Higgs boson decay into a photon and an off-shell photon, $H \to \gamma\gamma^*$, where the virtual photon internally converts into a low-mass dilepton pair, $\gamma^* \to \ell\ell$ ($\ell = e, \mu$), $m_{\ell\ell} < 30$ GeV. The analysis is based on proton–proton collision data recorded at a centre-of-mass energy of $\sqrt{s} = 13.6$ TeV during the Run 3 data-taking period between 2022 and 2024, corresponding to an integrated luminosity of 165 fb^{-1}. I am the primary contributor to this analysis and have been taking care of most aspects of the analysis, from data reduction, to signal and background modelling, to the statistical interpretation of the results. The analysis is currently under ATLAS approval stage and is expected to be made public in spring 2026.

1 The Standard Model and the Higgs boson

The theoretical foundation of my research doctorate is the Standard Model (SM) of particle physics.
The SM provides a unified framework for describing both strong and electroweak interactions and classifies all known elementary particles, including matter fields and force carriers. Developed between the 1950s and 1970s [30], it has proven extraordinarily successful, accurately predicting phenomena up to the highest energies currently probed and passing every experimental test to date.
In the SM, each particle is associated with a quantum field characterized by specific transformation properties under the Poincaré group, which determine its spin and parity. Their interactions arise from the principle of *local gauge invariance*, ensuring the *renormalizability* of the theory and its consistency at all energy scales. The SM combines the electroweak theory of Glashow [31], Weinberg [32], and Salam [33, 34] with Quantum Chromodynamics (QCD), the gauge theory of the strong interaction. A key element of the SM is the Higgs mechanism [6–8], which allows particles to acquire mass without violating electroweak gauge invariance. It predicts the existence of a scalar field—the Higgs field—whose excitations correspond to Higgs bosons. The observation of a Higgs-like particle by the A Toroidal LHC ApparatuS (ATLAS) and Compact Muon Solenoid (CMS) experiments [9, 10] in 2012 provided compelling confirmation of this mechanism and clarified the origin of elementary particle masses. Through spontaneous electroweak symmetry breaking, the Higgs field generates mass terms via its interactions with the SM particles.
Chapter 1 provides an overview of the topic: Section 1.1 introduces the SM, presenting its elementary particles in Section 1.1.1 and its fundamental interactions in Section 1.1.2. The Higgs mechanism is then discussed in Section 1.2.

1.1 The Standard Model

The SM is a gauge quantum field theory based on the internal symmetries of the Lie group $SU(2)_L \times U(1)_Y \times SU(3)_C$ [4, 5]. The subgroup $SU(2)_L \times U(1)_Y$ provides a unified description of Quantum Electrodynamics (QED) and the weak force, collectively referred to as the electroweak force. As explained later in Section 1.2.1, the electroweak symmetry is spontaneously broken via the Higgs mechanism to $U(1)_{EM}$, which governs electromagnetism. The subgroup $SU(3)_C$, on the other hand, describes the strong force,

as formulated by QCD. Therefore, the SM accounts for three of the four known fundamental forces—excluding only gravity, which at the subatomic scale is by far the weakest and can be safely neglected at HEP scales probed by hadron collider experiments.

1.1.1 Elementary particles

The SM classifies all the known elementary particles into two main categories: fermions and bosons.

Fermions Fermions are particles with half-integer spin that obey the Pauli exclusion principle. In the SM, there are 12 fundamental spin-$\frac{1}{2}$ fermionic fields, grouped into two subcategories of six particles each: *quarks* and *leptons*. Each subcategory is organized into three generations (or families) of doublets with identical electroweak *quantum numbers* (electric charge and weak isospin) but increasing mass. The first generation consists of the up and down quarks (u, d) and the electron with its neutrino (e, ν_e); the second generation comprises the charm and strange quarks (c, s) and the muon with its neutrino (μ, ν_μ); and the third generation includes the top and bottom quarks (t, b) and the tau with its neutrino (τ, ν_τ). Leptons interact only via the electroweak force, while quarks also experience the strong force. A key feature of the strong interaction is that quarks cannot be observed as free particles; they are always bound together to form colourless states called *hadrons* (see Section 1.1.2). Hadrons composed of three quarks have half-integer spin and are called *baryons*, whereas hadrons composed of a quark-antiquark pair have integer spin and are referred to as *mesons*. The SM also includes the anti-particles of all fermions, which have the same mass but opposite quantum numbers. The neutrino fields are considered massless, although experimental evidence from neutrino oscillations indicates that they possess a small but non-zero mass [35, 36].

Bosons The local gauge symmetry of the SM entails spin-1 gauge fields associated with the group generators; their quanta, the *gauge bosons*, mediate the fundamental interactions. The strong interaction is carried by eight massless gluons (g), which couple to the colour charge of quarks. The electroweak interaction is mediated by the $W^\pm$ and Z bosons, massive particles that couple to the weak isospin and weak hypercharge of fermions. The photon γ is massless and couples to the electric charge of fermions. The last particle of the SM is the Higgs boson H, hypothesized in 1964 [6–8] to explain the origin of mass for the massive gauge bosons and, more generally, for all elementary particles.

Figure 1.1 shows a schematic representation of the SM particles and their main properties.

1.1.2 Fundamental interactions

As previously discussed, the SM is formulated as a quantum field theory exhibiting local gauge invariance under the symmetry group $SU(2)_L \times U(1)_Y \times SU(3)_C$. An overview

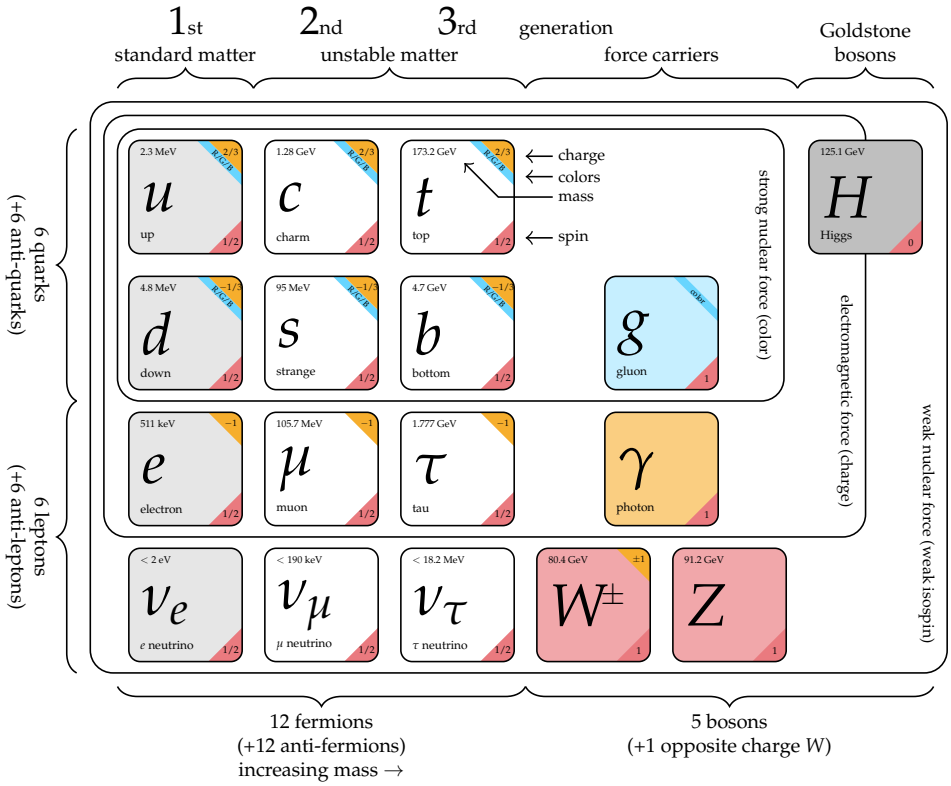

Figure 1.1 – Schematic overview of the SM elementary particles. Fermions, arranged into three generations, are shown on the left, while bosons appear on the right. Their masses and main quantum numbers are also indicated.

of its mathematical formulation is presented in the following paragraphs[1].

Quantum Electrodynamics

The QED describes the electromagnetic interaction between Dirac fermions and the photon vector field. It is based on the requirement of gauge invariance under the Abelian $U(1)$ symmetry group. Free (non-interacting) spinor fields $\psi(x)$, corresponding to spin-$\frac{1}{2}$ fermions of mass m and charge q, are described by the Dirac Lagrangian:

$$\mathcal{L}_{\text{Dirac}}^{\text{free}} = i\bar{\psi}\gamma^{\mu}\partial_{\mu}\psi - m\bar{\psi}\psi, \tag{1.1}$$

where $\bar{\psi} = \psi^{\dagger}\gamma^{0}$ denotes the Dirac adjoint, and the γ^{μ} are the Dirac matrices satisfying the Clifford algebra. The Dirac Lagrangian, $\mathcal{L}_{\text{Dirac}}^{\text{free}}$, is invariant under *global* $U(1)$ trans-

[1] Theoretical foundations and illustrative calculations are primarily adapted from the standard references by Peskin and Schroeder [37] and by Mandl and Shaw [38].

formations, implemented via the unitary operator $U = e^{i\alpha Q}$, where α is a constant phase, independent of the space-time coordinate x, and Q is the generator of the group, acting on the fermion field as $Q\psi = \psi$. The corresponding transformation laws for ψ and its Dirac adjoint are given in Equation (1.2):

$$\begin{aligned} \psi(x) &\longrightarrow \psi'(x) = e^{i\alpha Q}\psi(x) = e^{i\alpha}\psi(x), \\ \bar{\psi}(x) &\longrightarrow \bar{\psi}'(x) = e^{i\alpha Q}\bar{\psi}(x) = e^{-i\alpha}\bar{\psi}(x), \end{aligned} \tag{1.2}$$

which directly implies that the Dirac Lagrangian also remains invariant under a global $U(1)$ gauge transformation, $\mathcal{L}^{\text{free}\,\prime}_{\text{Dirac}} = \mathcal{L}^{\text{free}}_{\text{Dirac}}$. The *gauge principle* extends this invariance to *local* $U(1)$ gauge transformations, where the phase α now depends on the space-time coordinate, $\alpha(x)$. However, applying the same transformations as in Equation (1.2), one finds that the Dirac Lagrangian is no longer invariant under local $U(1)$ transformations. This is because the derivative term $\partial_\mu\psi(x)$ produces an additional term proportional to the derivative of the phase, $\partial_\mu\alpha(x)$, which does not cancel:

$$\partial_\mu\psi(x) \longrightarrow \partial_\mu\left[e^{i\alpha(x)}\psi(x)\right] = e^{i\alpha(x)}\left[\partial_\mu\psi(x) + i(\partial_\mu\alpha(x))\psi(x)\right]. \tag{1.3}$$

Local gauge invariance is restored by reformulating the theory from free to interacting. The partial derivative ∂_μ is replaced by the *covariant derivative* $D_\mu(x)$, acting on the fermion field as follows:

$$D_\mu(x)\psi(x) = [\partial_\mu + iqA_\mu(x)]\psi(x), \tag{1.4}$$

where a new vector field $A_\mu(x)$ (called *gauge field*) arises — associated with a spin-1 particle, the photon γ — which transforms under local $U(1)$ phase transformations as:

$$A_\mu(x) \longrightarrow A'_\mu(x) = A_\mu(x) - \frac{1}{q}\partial_\mu\alpha(x). \tag{1.5}$$

The transformation law of $A_\mu(x)$ cancels the additional term generated by the derivative in Equation (1.3). Introducing the covariant derivative restores the local gauge invariance of the Lagrangian. The resulting Lagrangian, obtained by replacing the partial derivative with the covariant derivative, also describes the interaction between the fermion field $\psi(x)$ and the gauge field $A_\mu(x)$. To complete the QED Lagrangian, a gauge-invariant kinetic term for the gauge field is added to describe the free propagation of the vector field $A_\mu(x)$—explicitly without any mass term: $\mathcal{L}^{\text{free}}_\gamma = -\frac{1}{4}F^{\mu\nu}F_{\mu\nu}$. This term is constructed from the field strength tensor $F_{\mu\nu}$, defined as:

$$F_{\mu\nu} = \partial_\mu A_\nu - \partial_\nu A_\mu, \tag{1.6}$$

which is invariant under the gauge transformation in Equation (1.5). The complete QED Lagrangian is therefore given by:

$$\begin{aligned}\mathcal{L}_{\text{QED}} &= i\bar{\psi}\gamma^{\mu}D_{\mu}\psi - m\bar{\psi}\psi - \frac{1}{4}F^{\mu\nu}F_{\mu\nu} \\ &= i\bar{\psi}\gamma^{\mu}\partial_{\mu}\psi - m\bar{\psi}\psi - q\bar{\psi}\gamma^{\mu}\psi A_{\mu} - \frac{1}{4}F^{\mu\nu}F_{\mu\nu} \\ &= \mathcal{L}_{\text{Dirac}}^{\text{free}} + \mathcal{L}_{\text{QED}}^{\text{int}} + \mathcal{L}_{\gamma}^{\text{free}},\end{aligned} \tag{1.7}$$

where the interaction term, $\mathcal{L}_{\text{QED}}^{\text{int}} = -q\bar{\psi}\gamma^{\mu}\psi A_{\mu}$, describes the coupling between the fermion field and the gauge field, i.e., the electron and the photon. Summing up, to obtain a locally gauge-invariant QED theory, it is necessary to introduce an interaction term between the Dirac fermion field and a new vector field A_{μ}, associated with a massless spin-1 particle, the photon. A mass term of the form $\frac{1}{2}m_{\gamma}^{2}A_{\mu}A^{\mu}$ is forbidden, as it would break gauge invariance. This principle holds in general: whenever a theory is promoted from global to local gauge invariance, it is necessary to introduce as many massless vector fields as there are generators of the symmetry group. Since $U(1)$ has a single generator, in QED we introduce only one gauge boson, the photon, which is massless and neutral. Consequently, photons do not interact with each other, as QED is an Abelian theory.

Quantum Chromodynamics

A stronger attractive force was postulated to explain how the atomic nucleus remains bound despite the protons' mutual electromagnetic repulsion. This hypothesized force was called the *strong force* because, as the name implies, it is the strongest of the four fundamental forces. At a distance of 1 femtometer (1 fm $= 10^{-15}$m), its strength is approximately 137 times that of the electromagnetic force, about 10^{6} times that of the weak force, and roughly 10^{38} times that of gravitation. Numerous observations over the last century led to the development of QCD:

- From the studies of the properties of the hadrons being discovered, the idea of multiplets appeared. This suggested a composite structure for hadrons, consisting of fundamental components called *quarks*. In the early 1960s, the static quark model proposed by Gell-Mann [39] and Zweig attempted to explain the hadron mass spectrum. However, it was clearly not the final theory of the strong interaction, as it was not a quantum field theory and did not describe the dynamics between quarks.
- Experiments at the Stanford Linear Accelerator Center (SLAC) National Accelerator Laboratory first showed in 1956 that the proton is not a point-like particle (Hofstadter [40] and collaborators, using elastic scattering between electrons and protons). About ten years later, deep inelastic scattering (DIS) measurements showed that at sufficiently large momentum transfer, electron–proton scattering can be described as scattering between electrons and the proton's constituents. However, it was found that these constituents account for only about half of the proton's total momentum. This provided clear evidence for the presence of additional components in nucleons beyond quarks: the neutral mediators of the strong interaction, called *gluons*.

- The Japan Deutschland England (JADE) experiment [41] at the e^+e^- collider at Deutsches Elektronen-Synchrotron (DESY) showed that quarks cannot be observed as isolated particles; instead, they produce hadronic jets, i.e., collimated sprays of hadrons.

All these complex phenomena can be explained by QCD, a non-Abelian gauge theory based on the $SU(3)_C$ symmetry group, where the subscript C denotes the *colour* charge carried by particles subject to the strong force. The colour charge in QCD plays the same role as the electric charge in QED. However, there is a fundamental difference between the electric charge and the colour charge: while there is a single electric charge, the phenomenology of the strong interaction suggests that quarks possess three types of colour, called *red*, *green*, and *blue*. Consequently, each quark field of a specific flavour ($f = u, d, c, s, t, b$) is a colour triplet, $\psi_f(x) = (\psi_f^{\mathrm{r}}(x), \psi_f^{\mathrm{g}}(x), \psi_f^{\mathrm{b}}(x))$, under the transformations of $SU(3)_C$. Quarks with different colour charges attract one another, and the particles that mediate this strong interaction are called gluons. Since the $SU(3)_C$ symmetry group has eight generators, the massless vector fields required by the theory, i.e. the gluons, are also eight in number. Unlike QED, QCD is a non-Abelian theory: gluons therefore carry colour charge themselves and exhibit self-interactions, unlike neutral photons, which do not interact with one another.
Similarly to QED, a theory that describes the strong interaction is obtained by requiring local gauge invariance under $SU(3)$:

$$\psi(x) \longrightarrow \psi'(x) = \exp\left[i\, g_S \sum_{a=1}^{8} \theta^a(x)\, t^a \right] \psi(x), \tag{1.8}$$

where g_S is the strong coupling constant typically expressed in terms of $\alpha_s = \frac{g_S^2}{4\pi}$, which defines the strong coupling constant, $\theta^a(x)$ are eight space-time dependent parameters, and t^a are the eight generators of the group. Imposing local gauge invariance requires the introduction, via the covariant derivative, of eight spin-1 boson fields — the colour fields or gluons $A_\mu^a(x)$ — analogous to the photon field $A_\mu(x)$ introduced in QED.
The QCD Lagrangian is therefore given by:

$$\mathcal{L}_{\mathrm{QCD}} = \sum_f \bar{\psi}_f^i(x) \left[i\gamma^\mu (D_\mu(x))_{ij} - m_f \delta_{ij} \right] \psi_f^j(x) - \frac{1}{4} \sum_{a=1}^{8} F^{\mu\nu\, a}(x) F_{\mu\nu}^a(x), \tag{1.9}$$

where:

- the subscript f denotes the quark flavour, $f = u, d, c, s, t, b$;
- the indices i and j run over the three colour quantum numbers (red, green, blue);
- $\psi_f(x)$ represents the quark fields, grouped in the colour triplet $\left(\psi_f^{\mathrm{r}}(x),\ \psi_f^{\mathrm{g}}(x),\ \psi_f^{\mathrm{b}}(x)\right)$;
- the first term includes both the free propagation of quarks and their interaction with the gluons through the covariant derivative, defined as

$$(D_\mu(x))_{ij} = \partial_\mu \delta_{ij} + i g_S \sum_{a=1}^{8} t_{ij}^a A_\mu^a(x), \tag{1.10}$$

where $t^a = \lambda^a/2$ are the generators of $SU(3)$, given in terms of the Gell-Mann matrices λ^a;

- the second term describes the free propagation of gluons and their self-interactions. $F^a_{\mu\nu}$ ($\mu, \nu = 0, 1, 2, 3$ are Lorentz indices, a runs over gluons types) is the gluon field strength tensor, defined as

$$F^a_{\mu\nu}(x) = \partial_\mu A^a_\nu(x) - \partial_\nu A^a_\mu(x) - g_S \sum_{b,c=1}^{8} f^{abc} A^b_\mu(x) A^c_\nu(x), \tag{1.11}$$

where f^{abc} are the structure constants of $SU(3)$. The term in the Lagrangian containing $F^a_{\mu\nu}$ gives rise to the kinetic energy of gluons and to cubic and quartic interaction terms, corresponding to three-gluon and four-gluon vertices.

Due to the non-Abelian nature of Quantum Chromodynamics, the strong coupling constant α_S is a *running* coupling. Its scale dependence arises from quantum corrections associated with gluon self-interactions, which lead to a negative β-function. As a consequence, α_S depends on the momentum transfer Q of the scattering process, i.e. $\alpha_S(Q^2)$. At large momentum transfer, the strong coupling is given by

$$\alpha_S(Q^2) \approx \frac{12\pi}{(33 - 2n_f) \ln\left(\frac{Q^2}{\lambda^2_{\text{QCD}}}\right)}. \tag{1.12}$$

where n_f is the number of quark flavours ($n_f = 6$ in the SM) and $\lambda_{\text{QCD}} \approx 200$ MeV sets the energy scale for perturbative QCD predictions. As a result of this dependence, QCD exhibits two salient properties: *asymptotic freedom* and *colour confinement*:

- *asymptotic freedom*: as the energy scale of the process $Q^2 \to \infty$, the strong coupling between quarks logarithmically approaches zero, meaning that at high energies the interaction becomes weaker and quarks behave almost as free particles;
- *colour confinement*: at low momentum transfer, of the order of λ_{QCD}, the coupling between quarks diverges. This implies that quarks cannot be isolated; although this behaviour has not yet been analytically proven, it underlies the phenomenon known as colour confinement, which states that coloured particles, such as quarks and gluons, cannot be observed in isolation, but only within colourless hadrons. At high energies, when attempting to extract a quark from a hadron, new $q\bar{q}$ pairs and gluons are produced. Since free coloured particles cannot exist, the quark and antiquark are bound into colourless hadrons via *hadronization*, resulting in the formation of a hadronic jet.

Electroweak interactions

The development of the electroweak theory was not straightforward, as it required several decades of theoretical and experimental progress. In the 1930s, a major step was the postulation of the neutrino by Pauli [42], proposed to explain the continuous energy

spectrum in β-decay ($n \to p + e^- + \bar{\nu}_e$). In the 1950s, further advancement came from the experimental discovery of parity violation in weak interactions.
A first theoretical framework for weak interactions was established in 1934 by Fermi [43], who formulated a four-fermion contact interaction to describe β-decay. However, this theory was non-renormalizable, leading to divergences in higher-order calculations and failing to provide a consistent description of weak interactions at high energies. Nevertheless, it highlighted key features of weak interactions, such as their short range, the Vector-Axial (V-A) structure of the charged weak current, and the fact that a conserved leptonic current between the electron and its neutrino hints at a conserved charge, the *weak isospin*.
In 1961, Glashow [44] proposed a unified description of electromagnetic and weak interactions based on the $SU(2)_L \times U(1)_Y$ gauge symmetry group. The subscript L indicates *left-handed* fermions: only the left-chiral components of quarks and leptons, defined as $\psi_L(x) = \frac{1}{2}(1-\gamma^5)\psi(x)$, interact with the three gauge fields associated with the $SU(2)_L$ group, $W^i_\mu(x)$, $i = 1,2,3$. Left-handed fermions transform as doublets under $SU(2)_L$ transformations, whereas the right-chiral components, $\psi_R(x) = \frac{1}{2}(1+\gamma^5)\psi(x)$, are singlets under $SU(2)_L$ and do not couple to the $W^i_\mu(x)$ gauge fields. The three generators of $SU(2)_L$, T_i with $i = 1,2,3$, are termed *weak isospin* operators. A summary of the left and right chiral components of leptons and quarks under the $SU(2)_L$ symmetry group is provided in Table 1.1.

	Isospin	**Leptons**	**Quarks**
Left-handed	$T_3 = \begin{pmatrix} +\frac{1}{2} \\ -\frac{1}{2} \end{pmatrix}$	$\begin{pmatrix} \nu_e \\ e \end{pmatrix}_L, \begin{pmatrix} \nu_\mu \\ \mu \end{pmatrix}_L, \begin{pmatrix} \nu_\tau \\ \tau \end{pmatrix}_L$	$\begin{pmatrix} u \\ d \end{pmatrix}_L, \begin{pmatrix} c \\ s \end{pmatrix}_L, \begin{pmatrix} t \\ b \end{pmatrix}_L$
Right-handed	$T_3 = 0$	e_R, μ_R, τ_R	$u_R, d_R, c_R, s_R, t_R, b_R$

Table 1.1 – Left and right chiral components of leptons and quarks under the $SU(2)_L$ symmetry group. Right-handed neutrinos do not exist in the original formulation of SM.

The $U(1)$ group in the electroweak theory is not the same as in QED: its charge is not the electric charge Q, but a new quantum number called the *weak hypercharge* Y, which affects the left-handed and right-handed components of fermions differently, whereas the electromagnetic current treats left- and right-handed components in the same way. The $U(1)_Y$ group has a single generator Y associated with the weak hypercharge, and consequently one gauge field, denoted by $B_\mu(x)$. In the context of the electroweak theory, the electric charge operator Q can be expressed in terms of the weak isospin and weak hypercharge operators through the Gell-Mann–Nishijima relation:

$$Q = T_3 + \frac{Y}{2}. \tag{1.13}$$

This relation illustrates in a simple way one of the key points of the construction of the electroweak theory: the correct combination of the weak isospin current and the weak

hypercharge current produces the electromagnetic current.

The electroweak Lagrangian is given by:

$$\mathcal{L}_{\mathrm{EW}} = i\bar{\psi}_L \gamma^\mu D_\mu \psi_L + i\bar{\psi}_R \gamma^\mu D_\mu \psi_R - \frac{1}{4}\sum_{i=1}^{3} W^{\mu\nu,i} W^i_{\mu\nu} - \frac{1}{4} B^{\mu\nu} B_{\mu\nu}, \tag{1.14}$$

summing over all the left-handed and right-handed fermions ψ_L and ψ_R. The first two terms describe the free propagation of fermions and their interaction with the gauge fields; the last two terms describe the free propagation of the gauge fields. The field strength tensors included in the Lagrangian of Equation (1.14) are defined as:

$$W^{\mu\nu,i} = \partial^\mu W^{\nu,i} - \partial^\nu W^{\mu,i} - g \sum_{j,k=1}^{3} \epsilon^{ijk} W^{\mu,j} W^{\nu,k} \tag{1.15}$$

and

$$B^{\mu\nu} = \partial^\mu B^\nu - \partial^\nu B^\mu, \tag{1.16}$$

where g and g' are the coupling constants associated with $SU(2)_L$ and $U(1)_Y$, respectively, and ϵ^{ijk} are the Levi-Civita tensor components.

As in QED and QCD, local gauge invariance is restored by introducing the covariant derivative D_μ. In the electroweak theory, D_μ acts differently on left-handed fermion doublets, which transform non-trivially under $SU(2)_L$, and on right-handed fermion singlets, which are singlets of $SU(2)_L$.

For a left-handed doublet ψ_L, the covariant derivative reads

$$\begin{aligned} D_\mu \psi_L(x) &= \left[\partial_\mu + ig \sum_{i=1}^{3} T_i W^i_\mu(x) + ig' Y B_\mu(x)\right] \psi_L(x) \\ &= \partial_\mu \psi_L(x) + \frac{ig}{2} \begin{pmatrix} W^3_\mu & W^1_\mu - iW^2_\mu \\ W^1_\mu + iW^2_\mu & -W^3_\mu \end{pmatrix} \psi_L(x) + i\frac{g' Y_L}{2} B_\mu \psi_L(x) \\ &= \partial_\mu \psi_L(x) + \frac{i}{2} \begin{pmatrix} gW^3_\mu + g' Y_L B_\mu & g(W^1_\mu - iW^2_\mu) \\ g(W^1_\mu + iW^2_\mu) & -gW^3_\mu + g' Y_L B_\mu \end{pmatrix} \psi_L(x), \end{aligned} \tag{1.17}$$

where $T_i = \sigma_i/2$ are the generators of $SU(2)_L$ and Y_L denotes the hypercharge of the left-handed doublet.

For right-handed fermion singlets ψ_R, which do not couple to the $SU(2)_L$ gauge fields, the covariant derivative reduces to

$$D_\mu \psi_R(x) = \left[\partial_\mu + ig \sum_{i=1}^{3} W^i_\mu(x) T_i + ig' Y B_\mu(x)\right] \psi_R(x) = \left[\partial_\mu + i\frac{g'}{2} Y_R B_\mu(x)\right] \psi_R(x). \tag{1.18}$$

Replacing the covariant derivative of Equations (1.17) and (1.18) into the Lagrangian of

Equation (1.14), one obtains the interaction terms between fermions and gauge bosons:

$$\mathcal{L}_{\text{EW}}^{\text{int}} = -\frac{1}{2}\bar{\psi}_L\gamma^\mu \begin{pmatrix} gW_\mu^3 + g'Y_L B_\mu & g(W_\mu^1 - iW_\mu^2) \\ g(W_\mu^1 + iW_\mu^2) & -gW_\mu^3 + g'Y_L B_\mu \end{pmatrix} \psi_L \; - \; \frac{g'}{2} Y_R \, \bar{\psi}_R \gamma^\mu B_\mu \psi_R, \quad (1.19)$$

where the sum runs over all the left-handed and right-handed fermions ψ_L and ψ_R. Already in Equation (1.19), one can identify the linear combinations of the gauge fields that correspond to the physical $W^\pm$ bosons, defined as

$$W_\mu^\pm = \frac{1}{\sqrt{2}}\left(W_\mu^1 \mp iW_\mu^2\right), \quad (1.20)$$

which mediate the charged weak current interactions between the up and down components of the weak isospin doublets. The electromagnetic interaction, mediated by the photon field A_μ as in QED, and the neutral weak current interaction, mediated by the Z boson field Z_μ, arise instead from a rotation of the W^3 and B fields by the Weinberg *weak mixing angle* θ_W:

$$\begin{pmatrix} A_\mu \\ Z_\mu \end{pmatrix} = \begin{pmatrix} \cos\theta_W & -\sin\theta_W \\ \sin\theta_W & \cos\theta_W \end{pmatrix} \begin{pmatrix} B_\mu \\ W_\mu^3 \end{pmatrix}. \quad (1.21)$$

To identify the gauge field A_μ with the photon field of electromagnetism, a further relation between the electric charge e, the coupling constants g and g', and the Weinberg angle must be satisfied: $e = g\sin\theta_W = g'\cos\theta_W$. Alongside the photon, another gauge boson enters the neutral sector of the electroweak interactions: the Z boson. The Z boson mediates weak neutral interactions between quarks and leptons of the same flavour, with different coupling strengths for left-handed and right-handed chiral components. Writing the Lagrangian of Equation (1.19) in terms of the physical fields $W^\pm$, Z, and A, it is possible to exhibit explicitly the three types of interactions — electromagnetic (EM), weak charged current (CC), and weak neutral current (NC) — in the Lagrangian:

$$\begin{aligned} \mathcal{L}_{\text{EW}}^{\text{int}} &= \underbrace{\mathcal{L}_{\text{EM}}}_{\text{Electromagnetic}} + \underbrace{\mathcal{L}_{\text{CC}}}_{\text{Charged Current}} + \underbrace{\mathcal{L}_{\text{NC}}}_{\text{Neutral Current}} \\ &= \underbrace{-eQ\bar{\psi}\gamma^\mu\psi A_\mu}_{\text{EM}} \underbrace{-\frac{g}{\sqrt{2}}\bar{\psi}\gamma^\mu\left[W_\mu^+(T_1 - iT_2) + W_\mu^-(T_1 + iT_2)\right]\psi}_{\text{CC}} \\ &\quad + \underbrace{\frac{e}{2\sin\theta_W\cos\theta_W}\bar{\psi}\gamma^\mu Z_\mu\left[T_3(1-\gamma^5) - Q\sin^2\theta_W\right]\psi}_{\text{NC}}. \end{aligned} \quad (1.22)$$

The described formulation of the electroweak theory is elegant, mathematically consistent, and predictive. However, it presents two major issues that need to be addressed:

- The boson fields $W_\mu^\pm$, Z_μ and A_μ must be massless to preserve the gauge invariance of the theory. While for the photon field A_μ this is indeed the case ($m_\gamma = 0$), the

other vector bosons have non-negligible masses [45, 46]:

$$m_W = 80360.2 \pm 9.9 \text{ MeV}, \quad m_Z = 91.1876 \pm 0.0021 \text{ GeV}. \tag{1.23}$$

Furthermore, mass terms of the form $m_W^2 W^{\pm,\mu} W_\mu^\mp$ and $m_Z^2 Z^\mu Z_\mu$ would explicitly violate the gauge invariance of the theory;

- The chiral nature of the electroweak gauge group forbids explicit mass terms for fermions as well, whereas they were allowed in QED. A mass-like term in the Lagrangian would be of the form $m_f \bar{\psi}\psi = m_f(\bar{\psi}_L \psi_R + \bar{\psi}_R \psi_L)$, but each term in this sum is not gauge-invariant, since $SU(2)_L$ acts differently on left-handed doublets and right-handed singlets. Nevertheless, experimental data confirm that all fermions are massive.

1.2 The Higgs boson

The problem of introducing the masses of the gauge bosons and fermions in the SM without spoiling the local gauge invariance of the theory was solved in 1964, when Higgs [6], Englert and Brout [7], and others proposed the Higgs mechanism and *spontaneous symmetry breaking*. These mechanisms allow the various particles to acquire mass *dynamically* through their interaction with a scalar field $\Phi(x)$, without losing the gauge invariance of the theory, which is necessary for its renormalizability.

1.2.1 The Higgs mechanism

The Higgs mechanism in QED

In this section, a simple illustrative example will be presented to show how the Higgs mechanism works, before introducing all the complications arising from the non-Abelian structure of the $SU(2)_L \times U(1)_Y$ group. This Abelian example demonstrates how a mass can be given to the QED photon. Consider a complex scalar field $\phi = \frac{1}{\sqrt{2}}(\phi_1 + i\phi_2)$ with a self-interaction potential of the form:

$$U(\phi) = \lambda(\phi^*\phi)^2 + \mu^2(\phi^*\phi). \tag{1.24}$$

The following Lagrangian describes the dynamics of the scalar field ϕ, its self-interaction, its coupling with the massless gauge field $A_\mu(x)$ and the free propagation of the gauge field:

$$\mathcal{L}_{\text{Higgs}} = (D^\mu\phi)^*(D_\mu\phi) - U(\phi) + \mathcal{L}_\gamma^{\text{free}} = (D^\mu\phi)^*(D_\mu\phi) - \lambda(\phi^*\phi)^2 - \mu^2(\phi^*\phi) - \frac{1}{4}F^{\mu\nu}F_{\mu\nu}, \tag{1.25}$$

where $D_\mu = \partial_\mu + ieA_\mu$ is the covariant derivative (same as in Equation (1.4)) and $F_{\mu\nu}$ is the field strength tensor of Equation (1.6). The Lagrangian in Equation (1.25) is invariant under local $U(1)$ phase transformations of the form:

$$\phi(x) \longrightarrow \phi'(x) = e^{i\alpha(x)}\phi(x), \qquad A_\mu(x) \longrightarrow A'_\mu(x) = A_\mu(x) - \frac{1}{e}\partial_\mu\alpha(x). \tag{1.26}$$

The scalar potential $U(\phi)$ of Equation (1.24) is the key ingredient of the Higgs mechanism. For $\lambda > 0$ and $\mu^2 > 0$, the potential has a unique minimum at $\phi_1 = \phi_2 = 0$. For $\lambda > 0$ and $\mu^2 < 0$, the potential acquires a "Mexican hat" shape, as shown in Figure 1.2, featuring a local maximum at $\phi_1 = \phi_2 = 0$ and a degenerate circle of minima given by

$$\phi_0 = \sqrt{\frac{-\mu^2}{2\lambda}}\, e^{i\theta}, \quad \text{with} \quad \theta \in [0, 2\pi). \tag{1.27}$$

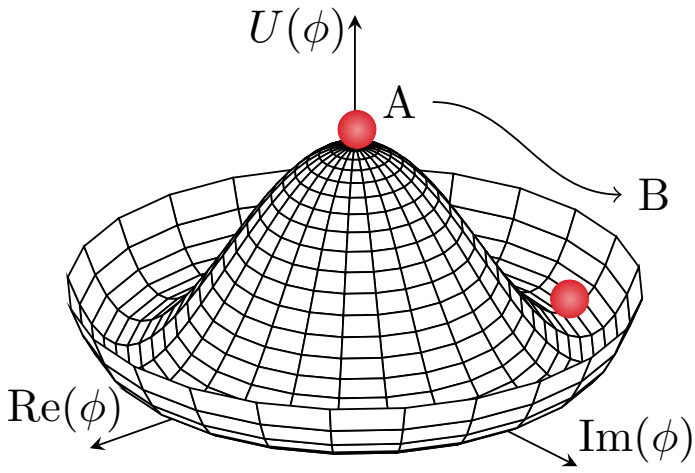

Figure 1.2 – Shape of the Higgs potential $U(\phi)$ in two dimensions, for $\lambda > 0$ and $\mu^2 < 0$, as a function of the real and imaginary components of the field (see Equation (1.24)).

Although all these states are equivalent, $\phi(x)$ adopts one of them as its ground state configuration. This choice gives rise to what is usually called *spontaneous symmetry breaking*, i.e., the symmetry is no longer manifest in the chosen ground state. Conventionally, the adopted ground state has $\theta = 0$, giving

$$\phi_0 = \sqrt{\frac{-\mu^2}{2\lambda}} \equiv \frac{v}{\sqrt{2}}, \tag{1.28}$$

where v is defined as the Vacuum Expectation Value (VEV) of the field ϕ. It is possible to redefine the field around its vacuum expectation value ϕ_0 by introducing two real fields, σ and η, which represent the radial and tangential excitations of the field about the minimum:

$$\phi = \frac{v}{\sqrt{2}} + \frac{1}{\sqrt{2}}(\sigma + i\eta). \tag{1.29}$$

Substituting Equation (1.29) into the Lagrangian of Equation (1.25), one obtains an ex-

panded Lagrangian with several interesting features:

$$\begin{aligned}\mathcal{L}_{\text{Higgs}} = & \underbrace{\frac{1}{2}e^2v^2A_\mu A^\mu}_{\text{Mass term for the gauge field}} \\ & + \underbrace{\frac{1}{2}(\partial_\mu\sigma)(\partial^\mu\sigma) - \mu^2\sigma^2 - \frac{\mu^2}{v}\sigma^3 - \frac{\mu^2}{4v^2}\sigma^4}_{\text{Higgs field } \sigma} \\ & + \underbrace{\frac{1}{2}(\partial_\mu\eta)(\partial^\mu\eta)}_{\text{Goldstone boson } \eta} \\ & + \underbrace{evA^\mu\partial_\mu\eta + eA^\mu(\sigma\partial_\mu\eta - \eta\partial_\mu\sigma) + \frac{1}{2}e^2A_\mu A^\mu(\sigma^2+\eta^2) - \frac{\mu^2}{2v^2}\sigma^2\eta^2}_{\text{Interaction terms between fields}} \\ & - \underbrace{\frac{1}{4}F^{\mu\nu}F_{\mu\nu}}_{\text{Gauge field kinetic term}} \quad . \end{aligned} \tag{1.30}$$

The first term underlined in red corresponds to the mass term for the gauge field A_μ, showing that the gauge boson acquires a mass $m_\gamma = ev$ through its interaction with the scalar field, without explicitly breaking gauge invariance. The second term in blue describes the dynamics of the scalar field σ, commonly referred to as the *Higgs field*, which acquires a mass $m_\sigma = \sqrt{-2\mu^2} = \sqrt{2\lambda}\,v$ and exhibits tri-linear and quartic self-interactions. The third term in green corresponds to a massless scalar boson, the *Goldstone boson* η and the remaining terms include interactions among the fields and the kinetic term of the gauge field. The Goldstone boson arises as a direct consequence of the spontaneous breaking of a continuous symmetry, in accordance with the Goldstone theorem [47]. The theorem states that if M out of N generators of a continuous symmetry are spontaneously broken, M spin-0 massless particles will appear in the theory. Although the Goldstone boson plays a key role in spontaneous symmetry breaking, it does not appear as a physical particle, since it can be *gauged away*. Specifically, if instead of the redefinition in Equation (1.29), one chooses the representation

$$\phi(x) = \frac{1}{\sqrt{2}}(v + \sigma(x))\,\exp\left[i\frac{\eta(x)}{v}\right],$$

it is possible to perform a local gauge transformation called the *unitary gauge*, which removes the imaginary part of ϕ and therefore the Goldstone boson η from the Lagrangian:

$$\begin{aligned}\phi(x) &\longrightarrow \phi'(x) = \exp\left[-i\frac{\eta(x)}{v}\right]\phi(x) = \frac{1}{\sqrt{2}}(v+\sigma(x)), \\ A_\mu(x) &\longrightarrow A'_\mu(x) = A_\mu(x) - \frac{1}{e}\partial_\mu\frac{\eta(x)}{v}.\end{aligned} \tag{1.31}$$

After this gauge transformation, all the terms that describe the massive vector boson A_μ and the massive scalar Higgs boson σ are still present in the Lagrangian.

The Higgs mechanism in the SM

The Higgs mechanism illustrated in the simpler QED case in the previous section can be extended to the $SU(2)_L \times U(1)_Y$ group in order to introduce mass terms for the gauge bosons of the electroweak sector, while keeping the photon massless, $m_A = 0$. This procedure is not applied to the $SU(3)_C$ group of QCD, since the gluons remain massless. Let us consider a weak isospin doublet of complex scalar fields,

$$\Phi(x) = \begin{pmatrix} \phi^+(x) \\ \phi^0(x) \end{pmatrix}, \tag{1.32}$$

which transforms under $SU(2)_L$ and $U(1)_Y$ gauge transformations as described in Section 1.1.2, with weak hypercharge $Y = +1$. The self-interaction potential of the scalar doublet is given in the same form as in Equation (1.24):

$$U(\Phi) = \lambda(\Phi^\dagger\Phi)^2 + \mu^2(\Phi^\dagger\Phi). \tag{1.33}$$

Considering also the covariant derivative D_μ to ensure local gauge invariance, the Lagrangian describing the dynamics of the scalar doublet Φ, its self-interaction, and its coupling to the massless gauge fields is

$$\mathcal{L}_{\text{Higgs}} = (D^\mu\Phi)^\dagger(D_\mu\Phi) - U(\Phi) = (D^\mu\Phi)^\dagger(D_\mu\Phi) - \lambda(\Phi^\dagger\Phi)^2 - \mu^2(\Phi^\dagger\Phi). \tag{1.34}$$

As in Section 1.2.1, for $\lambda > 0$ and $\mu^2 < 0$, the potential $U(\Phi)$ exhibits a degenerate circle of minima. The field $\Phi(x)$, however, will acquire one of these states as its ground state configuration, spontaneously breaking the $SU(2)_L \times U(1)_Y$ symmetry. Since the Higgs mechanism should preserve the $U(1)$ symmetry of QED, the Higgs boson must be neutral: for the down component, we have $Q = 0$ and $T_3 = -\frac{1}{2}$, so according to Equation (1.13), the weak hypercharge is $Y(\Phi) = +1$. Conventionally the adopted ground state is chosen to be

$$\Phi_0 = \frac{1}{\sqrt{2}}\begin{pmatrix} 0 \\ v \end{pmatrix}, \quad \text{with} \quad v = \sqrt{\frac{-\mu^2}{\lambda}}. \tag{1.35}$$

Expanding the field $\Phi(x)$ around its VEV, it can be written as

$$\Phi(x) = \frac{1}{\sqrt{2}}\begin{pmatrix} 0 \\ v + H + i\sum_{j=1}^{3}\eta_j \end{pmatrix}, \tag{1.36}$$

where the three Goldstone bosons η_j ($j = 1, 2, 3$) appear, corresponding to the three broken generators. As in the simpler QED case, these non-physical fields can be eliminated through a suitable gauge transformation, known as the unitary gauge. After performing

this transformation, the scalar doublet takes the form

$$\Phi(x) = \frac{1}{\sqrt{2}} \begin{pmatrix} 0 \\ v + H(x) \end{pmatrix}, \tag{1.37}$$

where $H(x)$ is the physical Higgs field, representing quantum excitations around the VEV v. Introducing this expression into the Lagrangian of Equation (1.34), one obtains:

$$\begin{aligned} \mathcal{L}_{\text{Higgs}} = & \underbrace{\frac{1}{2}(\partial_\mu H)(\partial^\mu H) + \mu^2 H^2 - \lambda v H^3 - \frac{\lambda}{4} H^4}_{\text{Higgs field } H \text{ dynamics}} \\ & + \underbrace{\frac{g^2 v^2}{4} W_\mu^- W^{+,\mu} + \frac{(g^2 + g'^2) v^2}{8} Z_\mu Z^\mu}_{\text{Mass terms for } W^\pm \text{ and } Z} \\ & + \underbrace{\frac{g^2}{4} W_\mu^- W^{+,\mu} H^2 + \frac{(g^2 + g'^2)}{8} Z_\mu Z^\mu H^2 + \frac{g^2 v}{2} W_\mu^- W^{+,\mu} H + \frac{(g^2 + g'^2) v}{4} Z_\mu Z^\mu H}_{\text{Interaction terms between fields}}. \end{aligned} \tag{1.38}$$

The term in the first row describes the dynamics of the Higgs field H, which acquires a mass

$$m_H = \sqrt{-2\mu^2} = \sqrt{2\lambda}\, v, \tag{1.39}$$

and exhibits trilinear and quartic self-interactions. While the VEV v can be determined experimentally from the Fermi coupling constant G_F [48],

$$v = \frac{1}{\sqrt{\sqrt{2} G_F}} \approx 246 \text{ GeV}, \tag{1.40}$$

the coupling λ remains a free parameter of the theory, leaving the Higgs boson mass m_H as an undetermined quantity before its experimental measurement. The second line describes the mass terms of the W and Z fields, related to the weak coupling constants g and g', the Weinberg angle θ_W and v:

$$m_W = \frac{g v}{2}, \quad m_Z = \frac{v\sqrt{g^2 + g'^2}}{2} = \frac{g v}{2\cos\theta_W} = \frac{m_W}{\cos\theta_W}, \tag{1.41}$$

in good agreement with the experimental values [45, 46]. The last line includes interaction terms between the Higgs field and the gauge bosons.

Mass generation for fermions

The chiral nature of the electroweak gauge group forbids explicit fermion mass terms as well. A Dirac mass term in the Lagrangian of the form

$$m_f \bar{\psi}\psi = m_f (\bar{\psi}_L \psi_R + \bar{\psi}_R \psi_L) \tag{1.42}$$

is not gauge-invariant, because the group $SU(2)_L \times U(1)_Y$ acts differently on the left-handed and right-handed components of the fermion field. However, experimental evidence confirms that all fermions are massive. Once again, the solution arises from the interaction with the Higgs doublet $\Phi(x)$ and its charge conjugate $\Phi^C(x) = -i\,T^2\,\Phi(x)$, together with spontaneous symmetry breaking.
Let us focus on a single quark family. Gauge-invariant Yukawa interaction terms involving the weak isospin doublet $\begin{pmatrix} u \\ d \end{pmatrix}_L$ and the right-handed singlets u_R and d_R are included in the SM Lagrangian:

$$\mathcal{L} = y_u\,(\bar{u}_L\,\bar{d}_L)\cdot\Phi^C\,u_R \;+\; y_d\,(\bar{u}_L\,\bar{d}_L)\cdot\Phi\,d_R \;+\; \text{h.c.}. \tag{1.43}$$

After spontaneous symmetry breaking, the Yukawa Lagrangian gives rise to mass terms for both up- and down-type quarks ($-m_u\bar{u}u$ and $-m_d\bar{d}d$), as well as interaction terms between the massive fermions and the Higgs field. By expanding the Higgs doublet Φ in terms of its VEV and the real scalar field H, as shown in Equation (1.37), the Yukawa Lagrangian becomes:

$$\mathcal{L}_{\text{Yukawa}} = -\frac{y_u v}{\sqrt{2}}\bar{u}u - \frac{y_d v}{\sqrt{2}}\bar{d}d - \frac{y_u}{\sqrt{2}}\bar{u}uH - \frac{y_d}{\sqrt{2}}\bar{d}dH. \tag{1.44}$$

The fermion masses $m_{u(d)} \equiv \frac{y_{u(d)}v}{\sqrt{2}}$ are directly proportional to the *Yukawa couplings* $y_{u(d)}$, which also determine the interaction strengths between the fermions and the Higgs boson, as shown in the second part of Equation (1.44).

2 | The Large Hadron Collider

This thesis presents results derived from proton-proton collision data provided by the Large Hadron Collider (LHC) [2].
The LHC is the world's largest and most powerful particle accelerator. It is located at the European Organization for Nuclear Research (CERN), near Geneva, Switzerland. The LHC is a circular collider for protons or heavy ions, with a circumference of 26.7 km, situated approximately 100 meters underground. It was constructed in a tunnel originally built between 1984 and 1989 for the Large Electron-Positron Collider (LEP), which operated from 1989 to 2000.
The LHC was designed to surpass the energy limitations of the LEP and to explore new frontiers in particle physics. Completed in 2008, it has been operational ever since, undergoing several upgrades and improvements over the years. The LHC was designed to collide protons at a maximum centre-of-mass energy of $\sqrt{s} = 14$ TeV and lead ions at a maximum centre-of-mass energy of $\sqrt{s} = 5.5$ TeV per nucleon pair.
The first data-taking period, known as Run 1, took place from 2010 to 2012, with pp collisions at $\sqrt{s} = 7$ TeV (2010-2011) and 8 TeV (2012). Following the Long Shutdown 1 (LS1) from 2013 to 2014, the accelerator was consolidated and finally delivered collisions for Run 2 (2015–2018) at a centre-of-mass energy of 13 TeV and an instantaneous luminosity of up to $\mathcal{L} = 2 \times 10^{34}$ cm^{-2}s^{-1} (for its definition, refer to Section 2.5). After another technical shutdown (Long Shutdown 2 (LS2), 2019–2021) for maintenance and upgrades, the LHC started its Run 3 in July 2022, colliding protons at a centre-of-mass energy of 13.6 TeV and reaching an instantaneous luminosity of up to $\mathcal{L} = 2.4 \times 10^{34}$ cm^{-2}s^{-1}.
Since this thesis is based on data collected during both Run 2 and Run 3, this Chapter provides a brief overview of the LHC conditions and its main operational parameters during both Runs.

2.1 From LEP to LHC

LEP was a circular electron–positron accelerator and collider. Although e^+e^- colliders offer several advantages over hadronic machines for precision measurements—primarily because electrons and positrons are elementary particles, unlike composite hadrons—this implies a well-defined initial state in terms of energy, momentum, and particle type, since the full center-of-mass energy is available in the hard interaction and no parton distribution functions are involved. As a consequence, the final states are typically cleaner and not dominated by underlying QCD activity or pileup. However, they also have a major drawback: energy loss due to *synchrotron radiation emission*.

In circular accelerators, charged particles emit synchrotron radiation when accelerated along a curved trajectory. The energy loss due to synchrotron radiation is inversely proportional to the fourth power of the particle's mass [49]:

$$P = \frac{dE}{dt} \propto \frac{E^4}{m^4}, \tag{2.1}$$

where E is the particle's energy and m its mass. Consequently, lighter particles, such as electrons, lose a substantial amount of energy in circular motion, which makes achieving high energies in circular colliders particularly challenging. In contrast, heavier particles, such as protons, radiate far less energy, allowing them to reach much higher energies in circular accelerators. To illustrate the magnitude of this effect, a proton is approximately 1836 times more massive than an electron [46], leading to a synchrotron radiation loss for electrons relative to protons of about

$$\frac{P_e}{P_p} \propto \left(\frac{m_p}{m_e}\right)^4 \sim 10^{13}, \tag{2.2}$$

assuming both particles have the same energy E.
Given this significant difference in behavior between electrons and protons in circular colliders, the LHC was designed as a proton-proton collider to achieve the highest possible collision energies. Since the LHC reuses the LEP tunnel, the radius of curvature R is essentially the same, allowing protons to reach energies several orders of magnitude higher than electrons in LEP. While LEP achieved a maximum centre-of-mass energy of $\sqrt{s} = 209$ GeV [50], the LHC was designed to reach a maximum centre-of-mass energy of $\sqrt{s} = 14$ TeV. This, of course, can only be achieved if higher magnetic fields are applied to keep the particles on the same orbit, according to the relation between the magnetic field B, the radius of curvature R, and the particle momentum p:

$$p[\text{GeV}] \approx 0.3 \cdot |q| \cdot B[\text{T}] \cdot R[\text{m}]. \tag{2.3}$$

2.2 Proton-proton interactions

As mentioned in Section 1.1, protons are not elementary particles but bound states of *partons*, namely quarks and gluons. Because of this composite nature, proton-proton collisions at the LHC can be classified into two main categories:

- *Soft collisions* are long-distance, low-momentum-transfer interactions between two protons in the colliding beams. Under these conditions, the protons effectively behave as point-like rather than composite particles. The final-state particles typically have low transverse momentum and are produced at small angles with respect to the beam axis. Although they do not usually mimic high-p_{T} hard-scattering signatures, soft interactions contribute to the underlying event and pileup, thereby affecting detector occupancies and the reconstruction performance;
- *Hard collisions* are short-distance, high-momentum-transfer interactions between

the constituent partons of the colliding protons. In these interactions, the internal structure of the protons becomes relevant, and the partons can be treated as quasi-free particles, approaching the regime of asymptotic freedom in QCD (see Section 1.1.2). The final-state particles produced in hard collisions typically have high transverse momentum and are emitted at larger angles with respect to the beam axis.

These hard collisions are of particular interest for studying fundamental interactions and for searches for new physics phenomena. However, the composite nature of protons introduces an additional layer of complexity in the analysis and interpretation of collision data. Each parton carries only a fraction x of the proton's total longitudinal momentum p:

$$p_{\text{parton}} = x\, p_{\text{proton}} \quad \text{with } 0 < x < 1, \tag{2.4}$$

where the value of x varies from event to event and from parton to parton within the same proton. The probability of finding a parton of type i carrying a momentum fraction x at a scale Q^2 is described by the Parton Distribution Function (PDF) $f_i(x, Q^2)$. The PDFs cannot be computed from first principles using perturbative QCD and must instead be determined from experimental data through global fits. However, once their behaviour at a given reference scale Q^2 is known, their energy-scale dependence is governed by the Dokshitzer-Gribov-Lipatov-Altarelli-Parisi (DGLAP) evolution equations [51–53], which describe how parton densities evolve with the probing scale.

At all momentum-transfer scales, the proton contains valence quarks, sea quarks, and gluons. As Q^2 increases, gluon radiation and quark-antiquark pair production enhance the gluon and sea-quark densities, particularly at small values of x, where they become dominant over the valence contribution.

An example of quark and gluon PDFs within the proton, extracted from the NNPDF3.1 NNLO set [54], is shown in Figure 2.1 at two different scales, $Q^2 = \mu^2 = 10\ \text{GeV}^2$ and $Q^2 = \mu^2 = 10^4\ \text{GeV}^2$.

These PDFs encode the non-perturbative structure of the proton and are essential for calculating the total cross section for a hard scattering process $pp \to X$:

$$\sigma_{pp\to X} = \sum_{i,j} \int_0^1 dx_1 \int_0^1 dx_2\, f_i(x_1, Q^2)\, f_j(x_2, Q^2)\, \hat{\sigma}_{ij\to X}(\hat{s}), \tag{2.5}$$

where $\hat{\sigma}_{ij\to X}(\hat{s})$ is the parton-level cross section for partons i and j and $\sqrt{\hat{s}} = \sqrt{x_1 x_2 s}$ is the parton-parton centre-of-mass energy, with $\sqrt{s}$ being the proton-proton centre-of-mass energy. Another consequence is that the exact parton-parton centre-of-mass energy $\sqrt{\hat{s}}$ is not known a priori, as it depends on the unknown momentum fractions x_1 and x_2.

To sum up, there are two main features characterising pp interactions. First, the actual parton-parton centre-of-mass energy is not exactly known and is lower than the nominal proton-proton centre-of-mass energy. This feature allows a broad range of centre-of-mass energies to be probed, even at fixed proton beam energy. Second, the interesting hard-scattering events (the most common being multi-jet final states) are hidden beneath the large QCD background arising from soft collisions, secondary interactions (pileup,

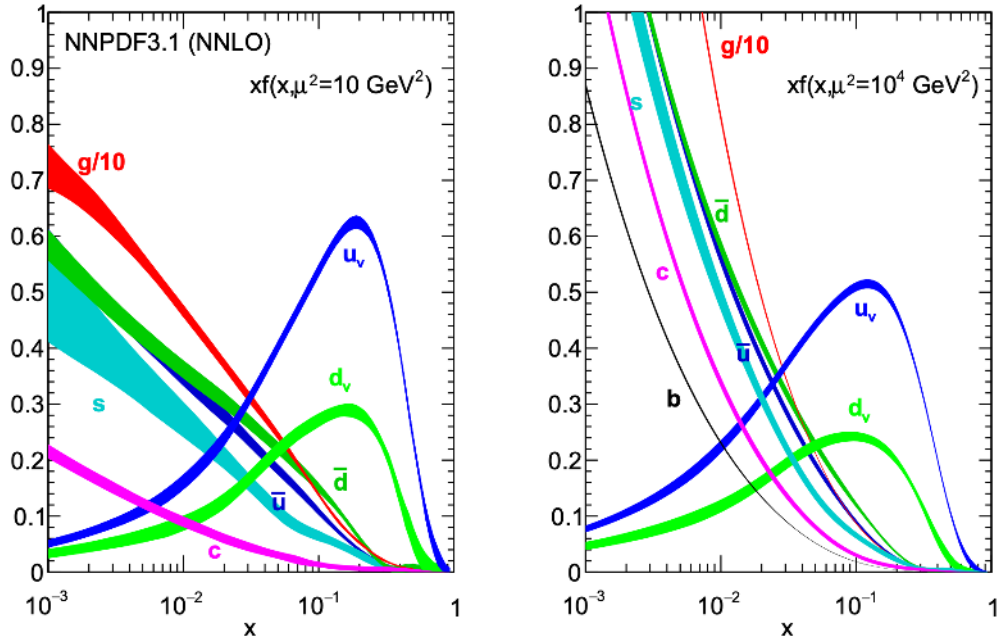

Figure 2.1 – Example of PDFs multiplied by the momentum fraction x, evaluated at two different scales: $Q^2 = \mu^2 = 10$ GeV^2 (left) and $Q^2 = \mu^2 = 10^4$ GeV^2 (right), for quarks and gluons within a proton. The PDFs are taken from the NNPDF3.1 NNLO set [54].

see Section 2.5), and the hadronisation of the remnants of the two hard-scattered protons (the so-called *underlying event*).

The exploration of rare processes therefore requires both high beam energies and high beam intensities: the former to enable the production of massive particles and to benefit from the typical increase of the cross section with energy (see Section 4.1 and Figure 4.1), and the latter to ensure a sufficiently large number of events for statistically significant measurements.

2.3 LHC operation and accelerator complex

The LHC [2, 55] is a synchrotron, namely a circular accelerator in which charged particles follow a closed orbit and are accelerated by time-synchronised electromagnetic fields. The increase in energy is provided by radio-frequency (RF) cavities, which generate an electric field parallel to the particle motion. If the circulating bunches remain in phase with the RF frequency (400 MHz), they receive an energy boost at each passage through a cavity. In particular at the LHC, acceleration up to the nominal beam energy of $\sqrt{s}/2$ is achieved using eight superconducting RF cavities. The synchronisation mechanism also stabilises the beam energy: protons that arrive slightly earlier or later than the ideal time, because they have, respectively, higher or lower energy than the nominal value, receive a corrective accelerating or decelerating kick, which gradually

brings them back toward the reference energy.
The curved trajectory of the beams is maintained by dipole magnets, which generate a magnetic field perpendicular to the direction of motion. This field provides the Lorentz force required to bend the particles along the circular path. As the beam energy increases, the dipole field must be ramped up accordingly to keep the particles on the same orbit, as expressed in Equation (2.3). The LHC employs 1232 niobium-titanium superconducting dipole magnets, each about 15 m long, operating at a temperature of 1.9 K and generating a magnetic field of up to 8.33 T to bend the beams along the 26.7 km tunnel. A photo and scheme of the LHC and its dipole magnets are shown in Figure 2.2.

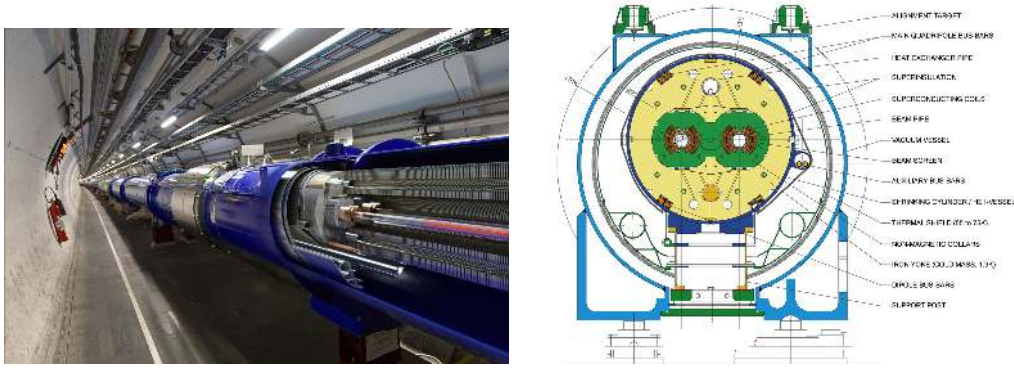

(a) **(b)**

Figure 2.2 – (a) Photo [55] of the LHC tunnel showing a 3D view of the dipole magnets. (b) Cross-section of an LHC dipole magnet, showing the cold mass and vacuum chamber [56]. The two proton beams travel within the two adjacent beam pipes, which can be seen at the centre of the ring's cross-section.

In addition to dipoles, the accelerator employs other types of magnets to ensure beam stability and focusing. Quadrupole magnets generate a field that focuses the beam in one transverse plane while defocusing it in the orthogonal plane; by arranging them in alternating sequences, a net focusing effect is achieved. The LHC uses 392 superconducting quadrupole magnets, each 5-7 m long. Higher-order multipole magnets, such as sextupoles, octupoles and decapoles, are employed to correct chromatic and nonlinear aberrations in the beam optics, compensate for imperfections, and maintain the required beam emittance over many turns.
The coordinated action of RF cavities and magnetic elements allows the beam to be accelerated up to the design energy while keeping it focused and confined along the reference orbit.
The LHC is not the first stage of proton (or ion) acceleration. Protons are injected into the LHC already accelerated to high energies in four steps by a chain of linear and circular accelerators [57]:

- From 2020, the first step is Liner accelerator 4 (Linac4), a linear accelerator designed to boost negative hydrogen ions (H^-) to an energy of 160 MeV. The ions are stripped of their two electrons to produce protons just before being injected into the next accelerator in the chain. Linac4 is 86 m long and located 12 m below ground.

During LS2, it replaced Liner accelerator 2 (Linac2), which had previously accelerated protons to 50 MeV for Run 2.

- Protons from Linac4 are injected into the Proton Synchrotron Booster (PSB), which consists of four stacked synchrotron rings with a circumference of 157 m. Here they are accelerated to 2 GeV.
- The protons are then transferred to the Proton Synchrotron (PS), a single-ring synchrotron with a circumference of 628 m, equipped with 277 magnets, including 100 dipoles to bend the beams. They are accelerated up to 26 GeV in this stage.
- The final step before injection into the LHC ring is the Super Proton Synchrotron (SPS), the second-largest machine in CERN's accelerator complex, with a circumference of nearly 7 km. The SPS can accelerate protons up to 450 GeV, at which point they are injected into the LHC. It contains 1317 electromagnets, including 744 dipoles to bend the beams around the ring.

The entire CERN accelerator complex is illustrated in Figure 2.3.

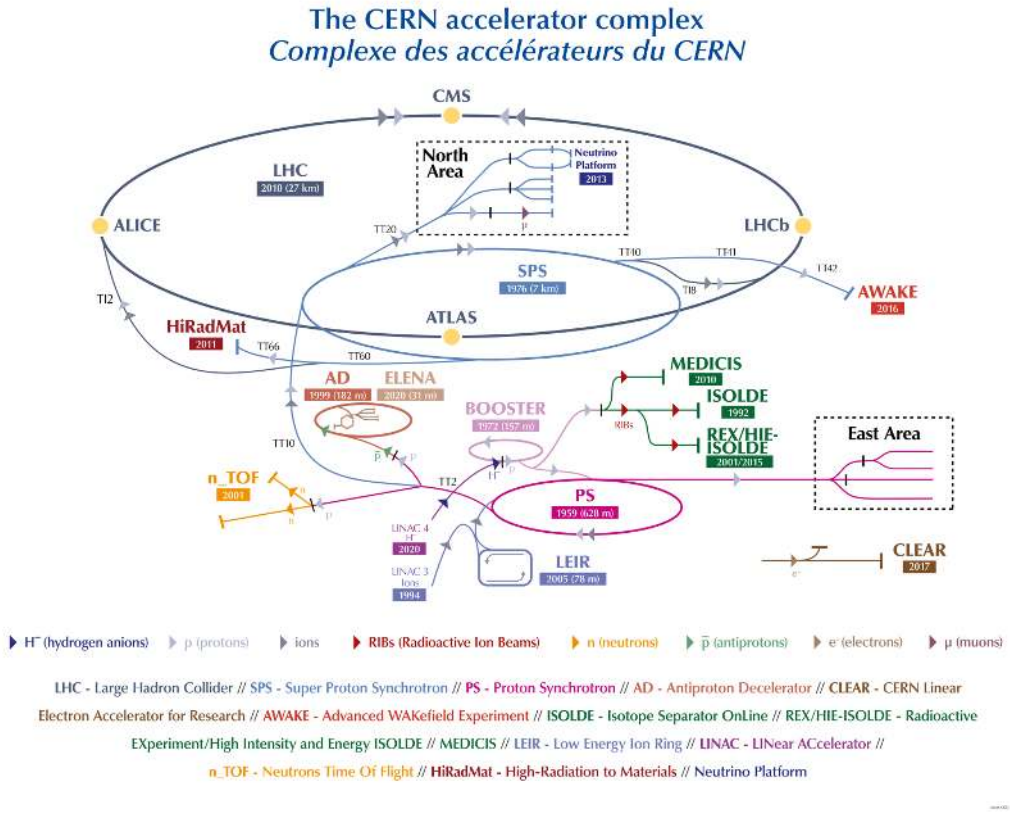

Figure 2.3 – Schematic layout of the CERN accelerator complex [58]. The main accelerator chain starts from Linac4 and proceeds through the PSB, PS, SPS, and finally to the LHC.

Eventually, the protons are injected into the LHC at an energy of 450 GeV and acceler-

ated to the final energy of 6.5 TeV (6.8 TeV) per beam for Run 2 (Run 3), resulting in a total centre-of-mass energy of 13 TeV in Run 2 and 13.6 TeV in Run 3.

2.4 Main experiments at the LHC

The two proton beams circulating in the LHC travel in opposite directions within two adjacent beam pipes, which are maintained at ultrahigh vacuum, as shown in the scheme of Figure 2.2b. Along the LHC tunnel, there are four main collision points corresponding to the locations of the four principal experiments, also visible in Figure 2.3:

- ATLAS [1] and CMS [3] are general-purpose detectors designed to cover a broad range of physics measurements in pp and heavy-ion collisions. They are used to study the SM, including the Higgs boson, and to search for new physics. The CMS detector is built around a large superconducting solenoid magnet generating a 4 T magnetic field; the complete detector measures 21 m in length, 15 m in width, and 15 m in height. The ATLAS detector will be described in greater detail in Chapter 3.

- Large Hadron Collider beauty (LHCb) [59] is a forward spectrometer optimised for studying particles containing b or c quarks. It focuses on flavour physics and precision measurements of CP-violating processes. Unlike ATLAS and CMS, which surround the collision point with a full 4π detector, LHCb uses a series of subdetectors arranged along the forward direction, covering a distance of 21 m from the interaction point (IP) on one side only.

- A Large Ion Collider Experiment (ALICE) [60] is a heavy-ion detector dedicated to studying the quark-gluon plasma and the properties of strongly interacting matter at extreme energy densities. The 10k-tonne ALICE detector measures 26 m in length, 16 m in height, and 16 m in width.

Additionally, there are five smaller experiments on the LHC dedicated to specialised researches. The smallest experiments are the TOTal cross section, Elastic scattering and diffraction dissociation Measurement (TOTEM) [61] and the Large Hadron Collider forward (LHCf) [62], which focus on "forward particles", protons or heavy ions that brush past each other rather than meeting head on when the beams collide. TOTEM uses detectors positioned on either side of the CMS IP, while LHCf is made up of two detectors which sit along the LHC beamline, at 140 m either side of the ATLAS collision point. The Monopole and Exotics Detector at the LHC - MoEDAL Apparatus for Penetrating Particles (MoEDAL-MAPP) [63] uses detectors deployed near LHCb to search for a hypothetical particle called the magnetic monopole. The ForwArd Search ExpeRiment (FASER) [64] and the Scattering and Neutrino Detector at the LHC (SND@LHC) [65], the two newest LHC experiments, are situated close to the ATLAS collision point in order to search for light new particles and to study neutrinos.

2.5 Luminosity and pileup

In a particle collider such as the LHC, the rate, i.e. the number of events per unit time, of a given process p is proportional to its cross section σ_p:

$$\frac{dN_p}{dt} = \mathcal{L} \cdot \sigma_p, \tag{2.6}$$

where the proportionality factor $\mathcal{L}$ is called the *instantaneous luminosity* and measures the collision rate per unit cross section. The instantaneous luminosity can be expressed in terms of key machine and beam parameters, under the assumption of ideal bunch collisions with Gaussian densities [2]:

$$\mathcal{L} = \frac{N_b^2 n_b f_{\text{rev}} \gamma_r}{4\pi\epsilon_n \beta^*} F, \tag{2.7}$$

where:

- N_b is the number of particles per bunch;
- n_b is the number of bunches per beam;
- f_{rev} is the revolution frequency;
- γ_r is the relativistic gamma factor;
- ϵ_n is the normalized transverse beam emittance, representing the spread of the protons' positions and momenta in the transverse plane;
- β^* is the value of the beta function at the IP, related to the transverse size of the beam at the collision point;
- F is a geometric factor accounting for the reduction in luminosity due to the crossing angle of the beams at the IP. It is always less than 1.

The value of these quantities changed over the years, as the LHC underwent several upgrades and improvements to reach its design performance. The main parameters during Run 2 and Run 3 are summarised in Tables 2.1 and 2.2.

Parameter	Design	2015	2016	2017	2018
Beam energy [TeV]	7.0	6.5	6.5	6.5	6.5
N_b protons per bunch [10^{11} p]	1.15	1.2	1.25	1.25	1.1
n_b bunches per beam	2808	2244	2220	1868-2556	2556
f_{rev} [kHz]	11.2	11.2	11.2	11.2	11.2
γ	7462	6929	6929	6929	6929
ϵ_n [µm rad]	3.75	2.6 - 3.5	1.8 - 2.2	1.8 - 2.2	1.8 - 2.2 2
β^* [cm]	55	80	40	40 $\rightarrow$ 30	30 $\rightarrow$ 27 $\rightarrow$ 25
Geometric luminosity loss F [%]	84	84	65	72	61
Crossing angle θ_c [µrad]	285	370	370 $\rightarrow$ 280	300 $\rightarrow$ 240	320 $\rightarrow$ 260
RMS bunch length σ_z [cm]	7.55	9	9	8	8
Peak luminosity [10^{34} cm^{-2} s^{-1}]	1.0	< 0.6	1.4	2.1	2.1

Table 2.1 – Summary of beam and machine parameters during the four years of Run 2, compared to the design values [66–68].

Parameter	Design	2022	2023	2024
Beam energy [TeV]	7.0	6.8	6.8	6.8
N_b protons per bunch [10^{11} p]	1.15	1.4	1.5	1.6
n_b bunches per beam	2808	2464	2464	2464
f_{rev} [kHz]	11.2	11.2	11.2	11.2
γ	7462	7250	7250	7250
ϵ_n [µm rad]	3.75	1.8 - 2.2	2.1 - 2.3	1.8-2.5
β^* [cm]	55	$60 \rightarrow 30$	$120 \rightarrow 30$	$120 \rightarrow 30$
Peak luminosity [10^{34} cm^{-2} s^{-1}]	1.0	2.4	2.2	2.3

Table 2.2 – Summary of beam and machine parameters during the first three years of Run 3, compared to the design values [69, 70].

Figure 2.4 and Figure 2.5 show the peak instantaneous luminosity achieved in each fill for each year of Run 2 and Run 3, respectively. Since 2016 and throughout Run 3, the LHC has consistently exceeded its design peak luminosity of 1×10^{34} cm^{-2}s^{-1}, reaching a peak value of 2.4×10^{34} cm^{-2}s^{-1} in 2022.

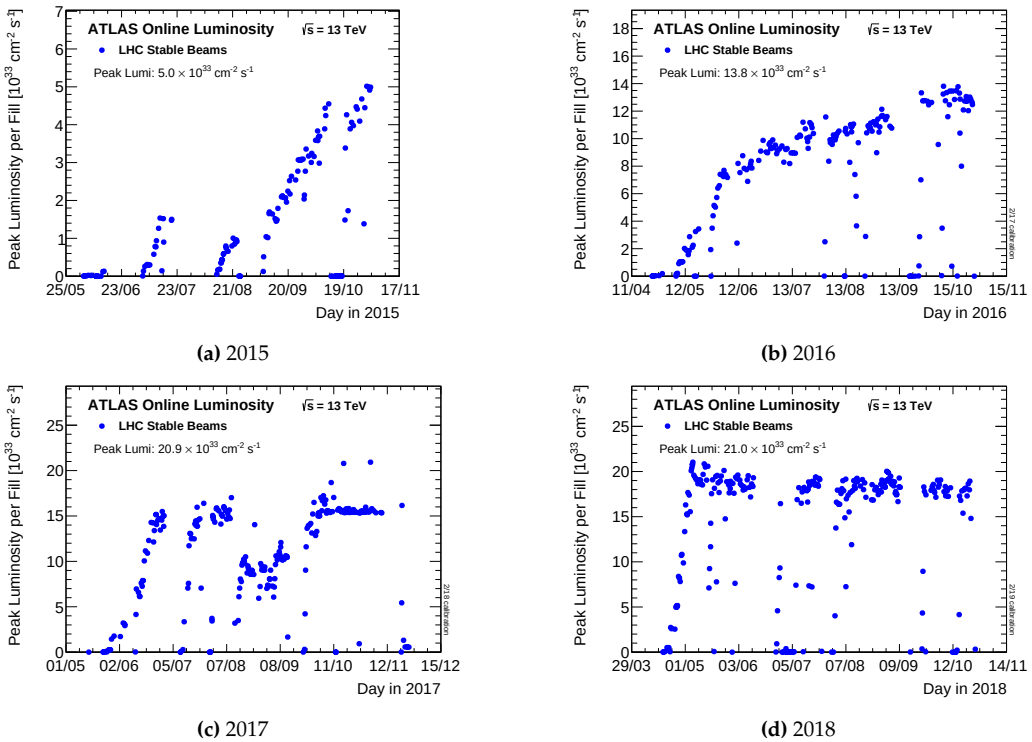

(a) 2015 **(b)** 2016 **(c)** 2017 **(d)** 2018

Figure 2.4 – Peak instantaneous luminosity delivered by the LHC during stable beams for each fill in the four data-taking years of Run 2: 2015 (a), 2016 (b), 2017 (c), and 2018 (d) [71].

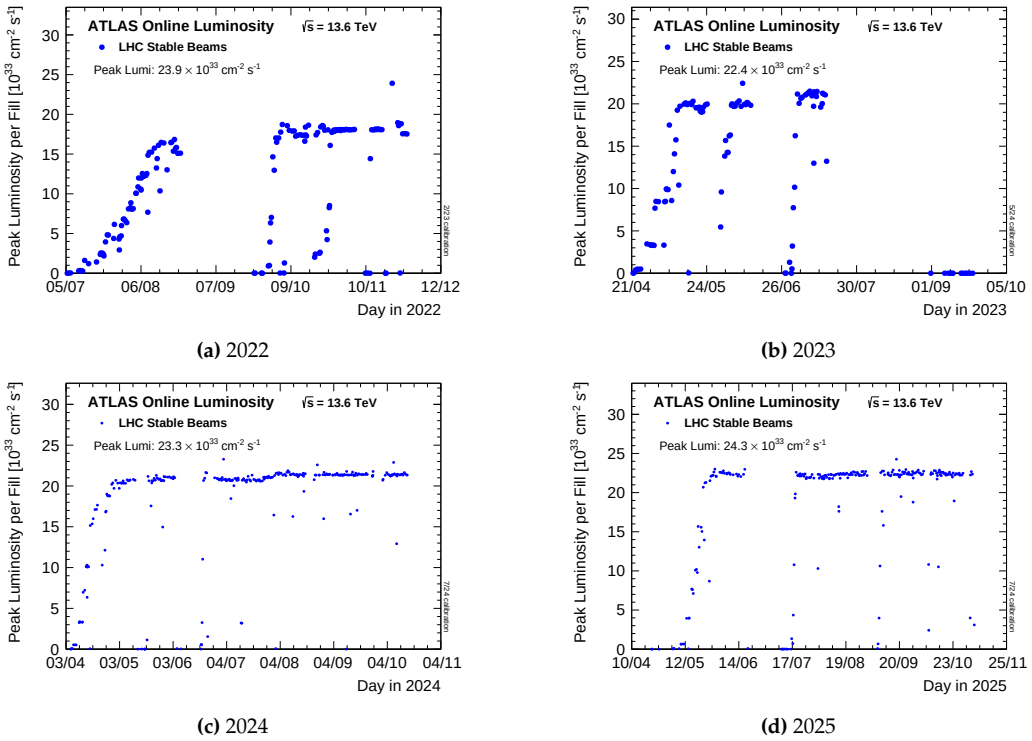

Figure 2.5 – Peak instantaneous luminosity delivered by the LHC during stable beams for each fill in the four data-taking years of Run 3: 2022 (a), 2023 (b), 2024 (c), and 2025 (d) [72].

The time integral of the instantaneous luminosity defines the integrated luminosity, $L = \int \mathcal{L}\, dt$, which is an important measure of an accelerator's performance. Integrating Equation (2.6) over time yields $N_p = L\sigma_p$, highlighting that L is proportional to the number of events of a given type occurring over a specified period. Since the cross section has the units of an area, the instantaneous luminosity has the dimensions of $\mathrm{cm}^{-2}\mathrm{s}^{-1}$, the integrated luminosity is usually expressed in terms of fractions of inverse barns, where $1\,\mathrm{b} = 10^{-24}\,\mathrm{cm}^2$.

At the LHC, the luminosity is measured by each of the main experiments. In particular, for ATLAS the luminosity measurement is derived primarily from the LUminosity Cherenkov Integrating Detector 2 (LUCID-2) [73], but other measurements are also provided by the Inner Detector (ID), the Tile Calorimeter, and the ElectroMagnetic EndCap (EMEC) Calorimeter and Forward Calorimeter (FCal), all in good agreement with each other (for the detectors description see Chapter 3). Figure 2.6 and Figure 2.7 show the total integrated luminosity as a function of time delivered by the LHC and recorded by ATLAS during stable beams for each year of Run 2 and Run 3, respectively. Figure 2.8 shows the total integrated luminosity for the full Run 2 and Run 3 periods.

In particle colliders, the instantaneous luminosity is not constant; for each fill, it decreases over time due to the degradation of both the beam intensity (i.e. a reduced num-

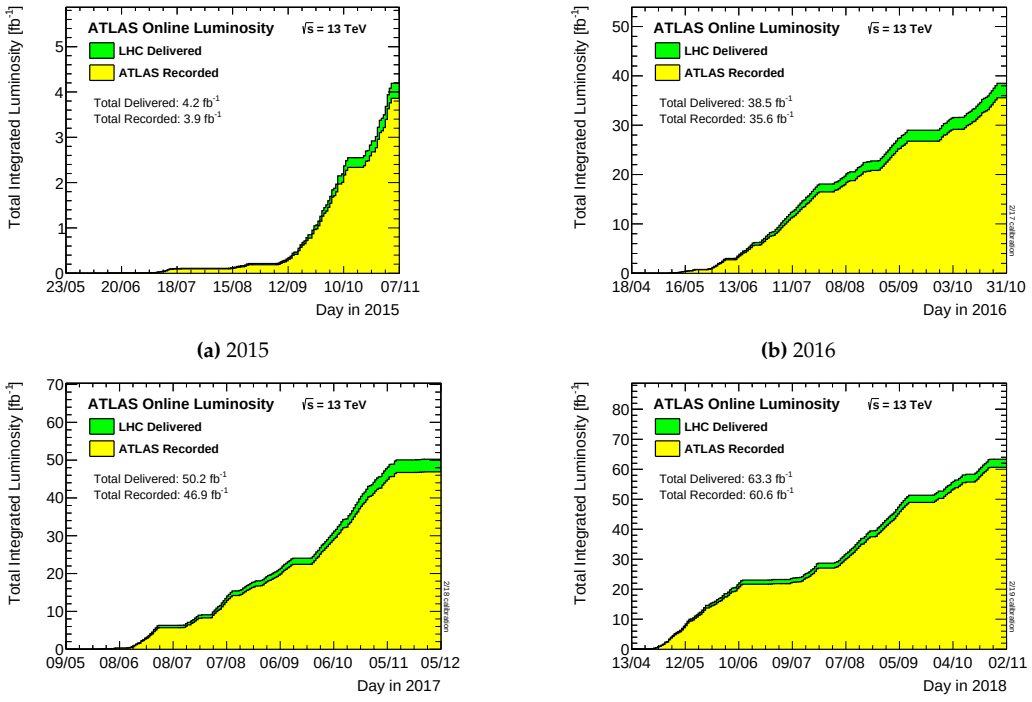

(a) 2015 **(b)** 2016

(c) 2017 **(d)** 2018

Figure 2.6 – Total integrated luminosity as a function of time delivered by the LHC (green) and recorded by ATLAS (yellow) during stable beams for each year of Run 2: 2015 (a), 2016 (b), 2017 (c), and 2018 (d) [71].

ber of protons in the bunches) and the emittance (a larger spread of momenta and positions of the protons within the bunches). The available time for stable-beam data-taking is optimised by taking into account this luminosity decrease and the duration required for the accelerator chain to deliver a new beam. The primary factor contributing to the luminosity decay is the pp collisions occurring at the LHC interaction points.

The LHC delivers such a high instantaneous luminosity that multiple pp interactions typically occur simultaneously at each bunch crossing within the interaction points. This is quantified by the average number of inelastic interactions per bunch crossing, known as the pileup, μ. Pileup events, which primarily result from soft collisions, overlap with the hard interactions of interest and are generally treated as background in physics analyses. Pileup adversely affects the reconstruction of the event of interest, degrading the energy resolution of physics objects such as jets, leptons, photons, and missing transverse energy ($E_{\mathrm{T}}^{\mathrm{miss}}$). Additionally, it complicates the reconstruction of tracks and vertices by creating a denser environment within the particle detector's tracker. The pileup is directly proportional to the instantaneous luminosity:

$$\mu = \frac{\mathcal{L} \cdot \sigma_{\mathrm{inel}}}{f_{\mathrm{rev}} \cdot n_b}, \tag{2.8}$$

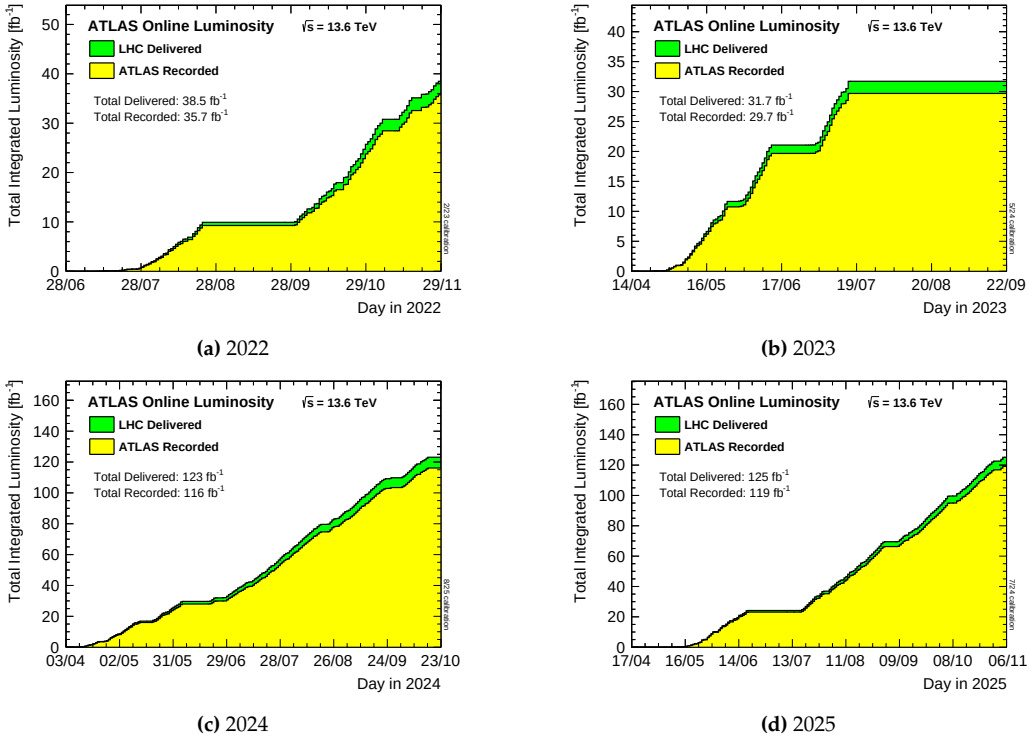

Figure 2.7 – Total integrated luminosity as a function of time delivered by the LHC (green) and recorded by ATLAS (yellow) during stable beams for each year of Run 3: 2022 (a), 2023 (b), 2024 (c), and 2025 (d) [72].

where σ_{inel} is the cross section for pp inelastic collisions. Figure 2.9a and Figure 2.9b show the mean number of interactions per bunch crossing during Run 2 and Run 3, year by year, respectively. From Figure 2.9c, which provides a comparison between the two runs, it is possible to observe that the pileup conditions have become more challenging in Run 3, with an average pileup of about $\langle\mu\rangle_{\text{Run 3}} = 55$ interactions per bunch crossing in Run 3, compared to about $\langle\mu\rangle_{\text{Run 2}} = 35$ in Run 2. Hence, it is important to find a good compromise between pushing for higher (integrated) luminosities that correspond to higher data statistics, and worsening of pileup conditions that can degrade the quality of the data.

In Run 3, the β^* luminosity-levelling technique [74] was adopted by the LHC to manage the pileup at the pp interaction points for the ATLAS and CMS experiments. This technique involves adjusting the beam squeezing to regulate the peak instantaneous luminosity, maintaining it at a roughly constant level over several hours. By controlling the instantaneous luminosity via the β^* parameter, the LHC ensures a stable target pileup for a longer duration during each fill, thereby optimising the data-taking conditions for the experiments and maximising the integrated luminosity.

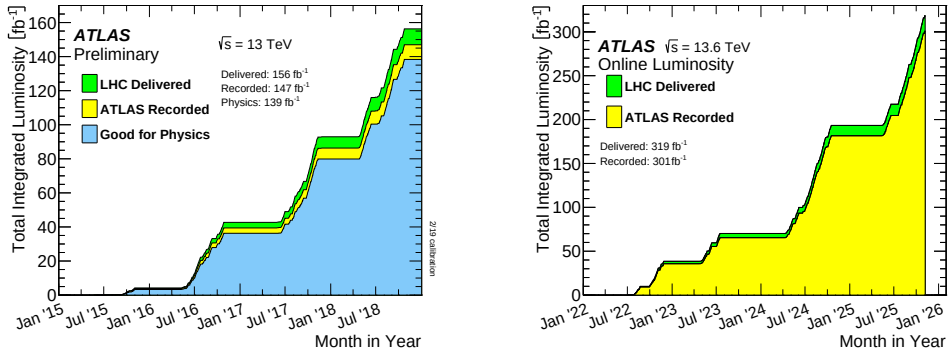

(a) Run 2 **(b)** Run 3

Figure 2.8 – Total integrated luminosity as a function of time delivered by the LHC (green) and recorded by ATLAS (yellow) during stable beams for Run 2 (a) [71] and Run 3 (b) [72]. The left-hand plot, also indicates the "Good for Physics" events (light-blue), i.e. events that satisfy the data quality criteria for physics analyses.

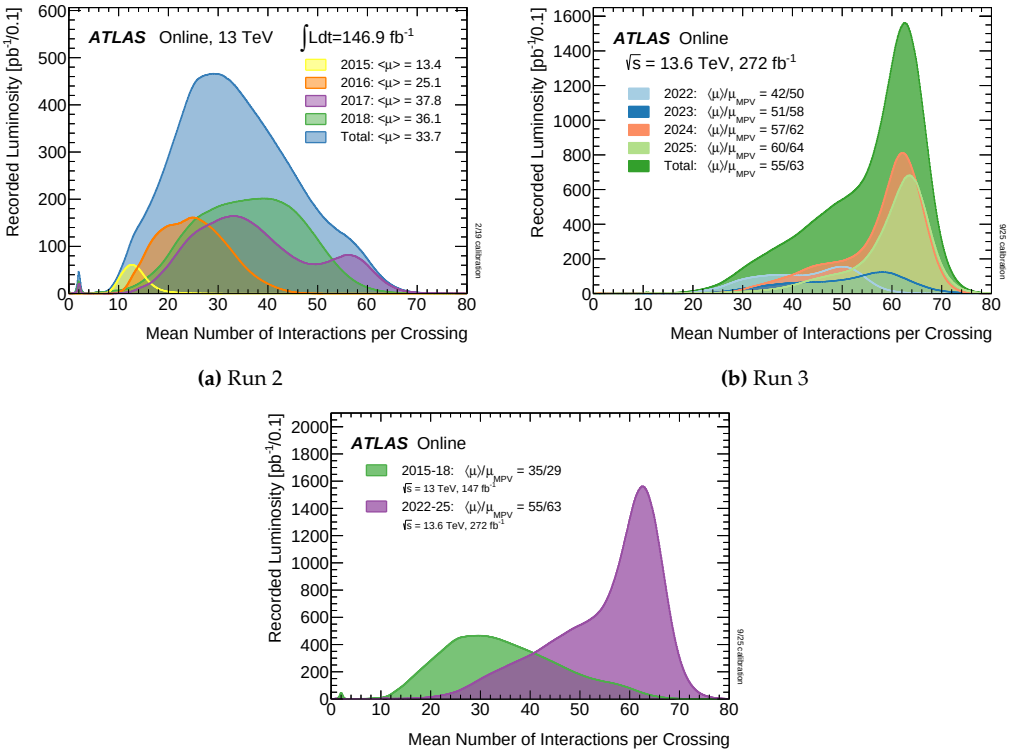

(a) Run 2

(b) Run 3

(c) Comparison

Figure 2.9 – The luminosity-weighted distribution of the mean number of interactions per crossing for the Run 2 (a) and Run 3 (b) pp collision data at 13 TeV (a) and 13.6 TeV (b) centre-of-mass energy. All data recorded by ATLAS during stable beams are shown, with the integrated luminosity and the mean $\langle\mu\rangle$ values provided by year in the figure [71, 72]. Figure (c) compares the distributions from Run 2 and Run 3.

3 The ATLAS experiment

The A Toroidal LHC ApparatuS (ATLAS) experiment [1], along with CMS [3], is one of the two general-purpose detectors at the LHC. It has a forward-backward symmetric cylindrical geometry with respect to the IP, with nearly 4π coverage in solid angle. It weighs almost 7000 tonnes, measures 46 m in length and 25 m in diameter, and is located approximately 100 m underground.
The detector consists of several nested sub-detectors which, moving outward from the beam pipe in the radial direction, are:

- the Inner Detector (ID), described in Section 3.3, a high-granularity tracker for the reconstruction of charged-particle trajectories and the identification of primary and secondary interaction vertices;
- the calorimeters, characterised in Section 3.4, which measure the energy of electrons, photons, and charged and neutral hadrons;
- the Muon Spectrometer (MS), presented in Section 3.5, which reconstructs and identifies muon tracks.

The detector also includes a magnet system (Section 3.2), which provides the magnetic fields required for the measurement of charged-particle momenta in the ID and in the MS, and the Trigger and Data Acquisition (TDAQ) system (Section 3.6), which analyses collision events in real time to select the most interesting ones for storage and further analysis.
The original configuration of the detector, as built for the start of the LHC and for Run 1 data-taking, is described in Reference [1]. As the LHC operating conditions evolved over the years, as described in Chapter 2, the ATLAS detector underwent substantial upgrades to maintain excellent performance under increasingly demanding conditions. The major upgrade between Run 2 and Run 3, which mainly involved the Electromagnetic (EM) calorimeter, the TDAQ system and the MS, is known as the *Phase-I Upgrade*. This upgrade, which moves towards the requirements foreseen for the HL-LHC running conditions, is documented in Reference [75].
The analyses presented in this thesis use data collected by ATLAS in both Run 2 and Run 3. Since Run 3 is still ongoing, the results shown here are among the first based on its (partial) dataset. This section therefore focuses on the Run 3 configuration of the detector [75], highlighting the main upgrades with respect to Run 2 and their impact on performance. The current ATLAS configuration is shown in Figure 3.1.

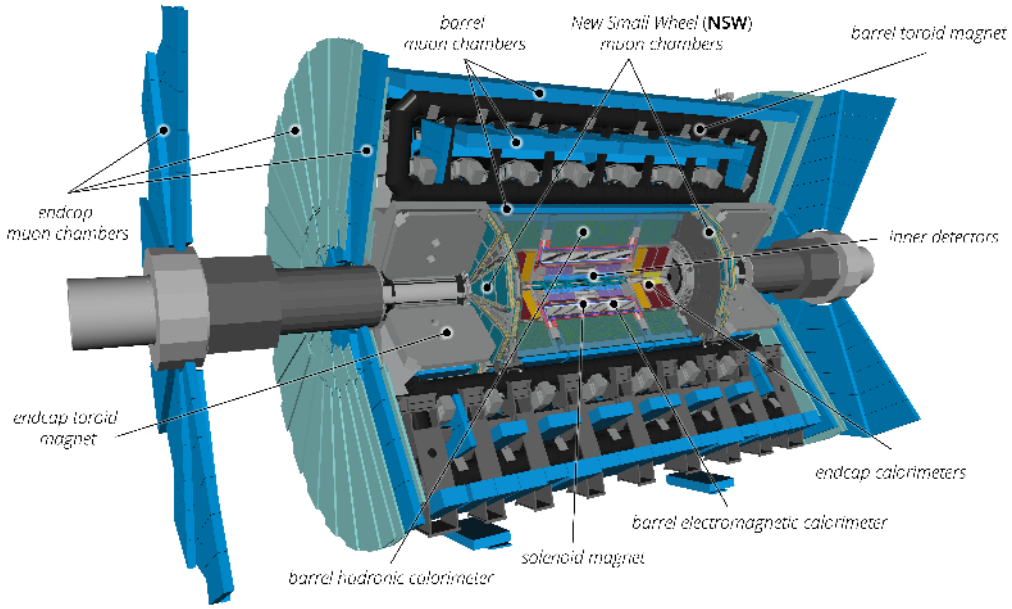

Figure 3.1 – Cut-away view of the Run 3 configuration of the ATLAS detector indicating the locations of the larger detector sub-systems [75].

3.1 Coordinate system

A right-handed coordinate system (x, y, z) is defined to describe the position and direction of particles inside the ATLAS detector. The origin is located at the nominal IP. The beam direction defines the z-axis, while the x-y plane is transverse to it, with the positive x-axis pointing from the IP toward the centre of the LHC ring, and the positive y-axis pointing upward (out of the xz-plane). Since the momentum of the colliding partons along the beam axis is unknown (see Section 2.2), boost-invariant transverse quantities are used, defined via the projection onto the xy-plane. Several key quantities are defined in the transverse plane, such as p_{T} (transverse momentum) and $E_{\mathrm{T}}^{\mathrm{miss}}$ (missing transverse momentum). The azimuthal angle ϕ is measured around the z-axis in the xy-plane, with $\phi = 0$ along the positive x-axis, while the polar angle θ is defined with respect to the z-axis, with $\theta = 0$ along the positive z-axis and $\theta = \pi/2$ in the xy-plane. The coordinate system is illustrated in Figure 3.2a.

The polar coordinates (η, ϕ) are used to have a Lorentz invariant angular coordinate system, where the *pseudorapidity* η is defined in terms of the polar angle θ as:

$$\eta = -\ln\left[\tan\left(\frac{\theta}{2}\right)\right]. \tag{3.1}$$

Positive and negative values of η correspond to the positive and negative directions along the z axis, with $\eta = 0$ representing the transverse plane at the IP, as illustrated in Figure 3.2b. For ultra-relativistic particles ($E \approx |\vec{p}|$), the pseudorapidity is approximately

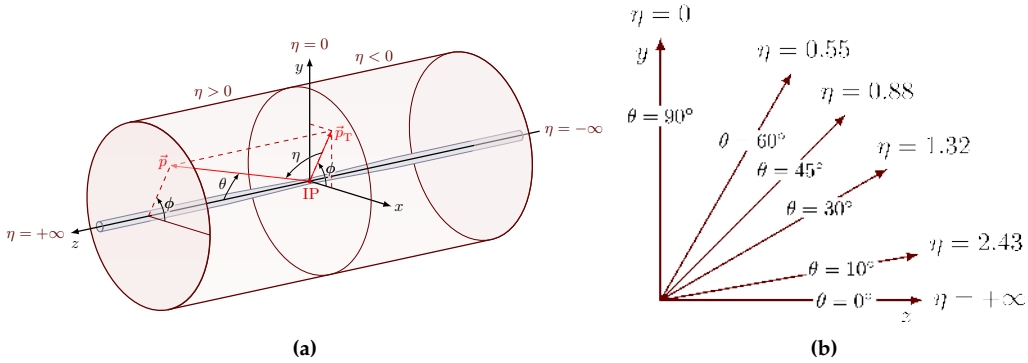

(a) **(b)**

Figure 3.2 – (a) The ATLAS detector coordinate system. (b) A sketch to show the relation, defined in Equation (3.1), between the pseudorapidity η and the polar angle θ.

equal to the *rapidity* y, defined as:

$$y = \frac{1}{2} \ln \left(\frac{E + p_z}{E - p_z} \right). \tag{3.2}$$

Rapidity has the useful property that differences in rapidity are invariant under Lorentz boosts along the beam axis. This makes it particularly convenient for describing particle production in colliders, where the centre-of-mass frame may differ from the laboratory frame. The advantage of using pseudorapidity over the standard polar angle is that differences in pseudorapidity between two points are also invariant under Lorentz boosts along the z-axis. This property is particularly useful when analysing events from pp collisions, as the hard interactions between partons can be asymmetric, producing boosted final states. The angular distance ΔR between two points in the transverse plane is given by:

$$\Delta R = \sqrt{(\Delta\eta)^2 + (\Delta\phi)^2}. \tag{3.3}$$

3.2 Magnet system

A well-defined magnetic field is necessary to bend the trajectories of charged particles produced in collisions, allowing their momenta to be measured. A charged particle moving in a magnetic field follows a curved trajectory, with the radius of curvature depending on both the particle's momentum and the strength of the magnetic field, as already described by Equation (2.3). Therefore, by measuring the radius of curvature and knowing the magnetic field strength, it is possible to reconstruct the particle's momentum. To generate the magnetic field, ATLAS uses a superconducting magnet system, that produces a magnetic field over a volume of approximately 12000 m^3, ensuring an almost complete geometric coverage of both the ID and the MS. The ATLAS magnet system, visible in Figure 3.3, consists of two parts:

- a central *solenoid magnet* [76], which surrounds the ID within the EM calorimeter and provides a magnetic field of 2 T along the beam axis. The solenoid is 5.8 m

long, with an inner radius of 1.23 m and an outer radius of 1.28 m. It is cooled to 4.5 K, and the magnetic field is generated by an electric current of 8 kA.

- a *toroidal magnet system*, composed of one barrel [77] and two endcap toroids [78]. The barrel toroid consists of eight separate superconducting coils, has an inner diameter of 9.4 m, an outer diameter of 20.1 m, and is 25.3 m long. Each of the two endcap toroids consists of eight superconducting coils located inside an insulating vacuum vessel, with a diameter of 10.7 m and a width of 5 m. The endcap toroids generate a magnetic field near the beam axis to deflect particles with small polar angles. The toroids are installed outside the calorimeters and produce a toroidal magnetic field of 0.5 T in the central region and 1 T in the endcap region, covering the MS volume. The toroidal magnetic field is generated by an electric current of 20 kA.

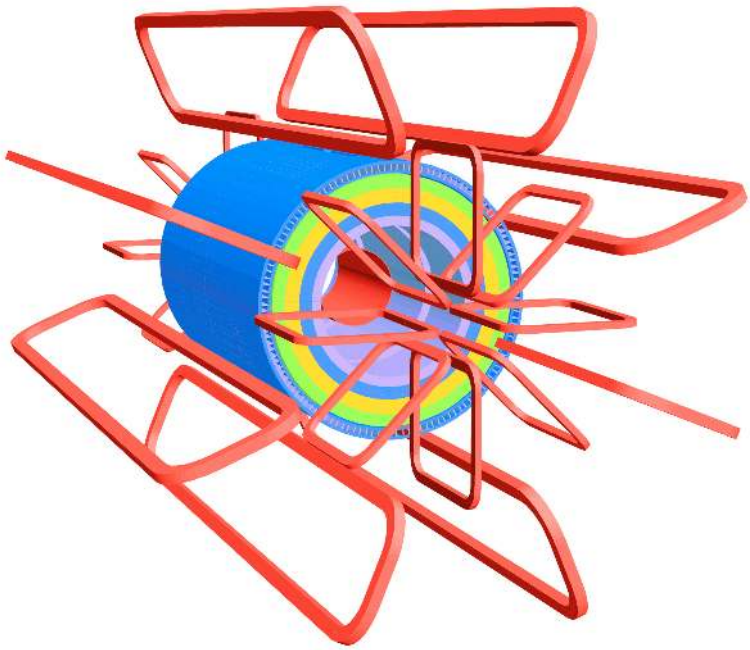

Figure 3.3 – Scheme of the ATLAS magnet system in red [79]. The solenoid magnet surrounds the ID and is located inside the EM calorimeter and it is the small red cylinder in the centre. The tile calorimeter is modelled by four layers with different magnetic properties, plus an outside return yoke. The eight barrel and endcap toroids coils are located outside the calorimeters and are the large red structures.

3.3 Inner Detector

The Inner Detector (ID) [80, 81] is the innermost detector of ATLAS, and therefore the closest to the IP. It has a cylindrical geometry, 6.2 m in length and 2.1 m in diameter, and is composed of a barrel and two end-cap regions, extending the coverage to $|\eta| < 2.5$.

The ID is designed to measure charged particle tracks with excellent resolution, providing their direction, impact parameters and momentum; it also reconstructs primary and secondary vertices and has electron identification capabilities. The momentum measurement is performed by evaluating the curvature of charged particle tracks in the 2 T magnetic field provided by the solenoid magnet.
It must withstand the radiation produced by the large number of highly energetic particles emerging from primary and secondary collisions. Its total material budget must be kept low to minimise the probability that electrons or photons initiate an electromagnetic shower (or hadrons a hadronic one) before reaching the calorimeter.
The ID is composed of three sub-detectors with different resolution and granularity: the Pixel detector, the SemiConductor Tracker (SCT) and the Transition Radiation Tracker (TRT). These systems will be described in the following paragraphs, and their full structure is shown in Figure 3.4.

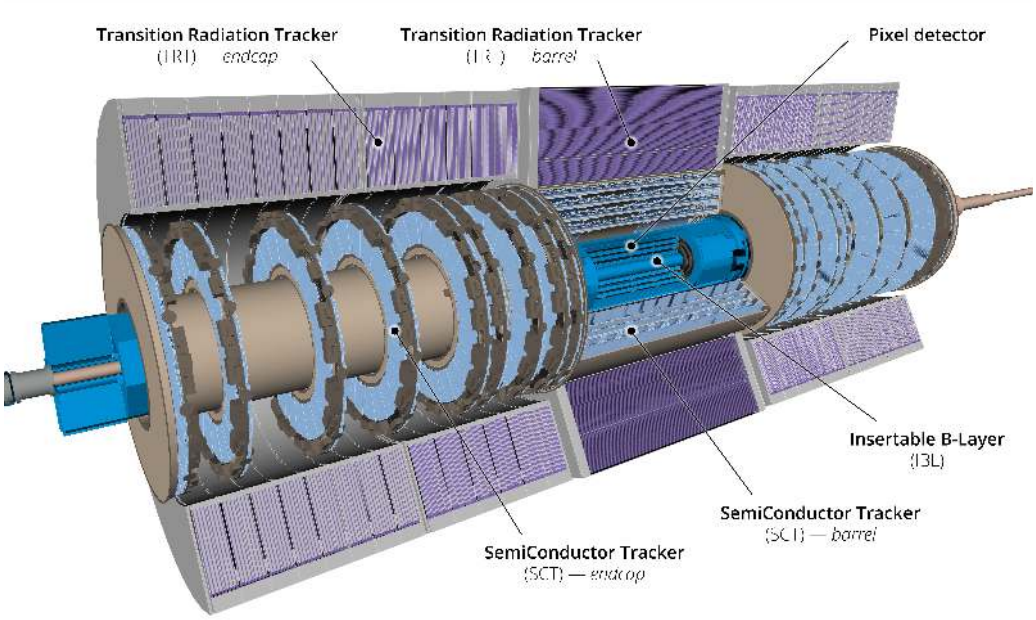

Figure 3.4 – Cut-away view of the ATLAS ID [75].

3.3.1 Pixel Detector

The Pixel Detector [82] is the first system encountered by particles emerging from the pp interaction.
In the barrel region, it comprises 1736 silicon pixel modules arranged in four concentric layers at radii of 3.3 cm, 5.1 cm, 8.9 cm, and 12.3 cm from the beamline. The innermost of these layers, known as the Insertable B-Layer (IBL) [83], was added for Run 2 to improve tracking performance by reducing the distance between the IP and the first detector layer. The addition of the IBL significantly enhanced the resolution of both the

longitudinal and transverse impact parameters of tracks, with improvements of up to a factor of two from Run 1 to Run 2.
Each of the two end-caps contains 288 modules, arranged in three disks. The pixel modules are segmented both in the R–ϕ plane and along the z axis, with a minimum pixel size of 50×250 μm^2 in the IBL and 50×400 μm^2 in the outer layers (with the longer side along the z direction).
The detector achieves an intrinsic spatial resolution of 8 μm in the R–ϕ plane within the IBL, which slightly degrades to 10 μm in both the outer barrel and end-cap regions. Along the z axis, the resolution is 40 μm in the IBL, degrading to 115 μm in the z (R) direction for the outer barrel (end-cap) layers. Typically, the Pixel Detector provides between three and four measurement points (*hits*) for track reconstruction.

3.3.2 SemiConductor Tracker

Following the Pixel Detector, the SCT [84] provides between four and nine additional hit measurements per track at intermediate radii (from 30 to 51 cm) within the ID volume. It is composed of eight concentric barrel layers of silicon microstrips arranged into four cylinders, while the end-cap regions each consist of nine disks, covering a pseudorapidity range of $|\eta| < 2.5$. In total, the SCT contains 4088 modules.
The barrel modules are rectangular, measuring 64.0×63.6 mm^2 with a strip pitch of 80 μm, whereas the end-cap modules are trapezoidal, with strip pitches varying from 56.9 μm to 94.2 μm. In the barrel, the strips are oriented parallel to the z axis, while in the end-caps they are arranged radially. To extract information on the z coordinate in the barrel, a stereo angle of 40 mrad is set between the two layers in each cylinder; a similar strategy is adopted in the end-caps to measure the R coordinate.
The silicon microstrips in the barrel (end-cap) regions provide single-hit spatial resolutions of 17 μm in the R–ϕ plane and 580 μm along the z (R) direction.

3.3.3 Transition Radiation Tracker

The outermost layer of the ID is the TRT [85], which covers a radial range between 55 cm and 108 cm from the beam line. It is composed of approximately 300,000 thin-walled drift tubes (or "straws") interleaved with polyester fibres and foils. In the barrel region, 50,000 straws, each 144 cm long, are oriented parallel to the beam axis, while the end-cap regions contain 250,000 straws, 39 cm long, arranged radially. Each straw has a diameter of just 4 mm and contains a 30 μm gold-plated tungsten wire at its centre. The straws are filled with a mixture of Xenon and Argon gas.
The TRT provides both tracking and particle identification information:

- when charged particles traverse the straws, they ionise the gas; the drift of the ionisation electrons generates a detectable signal. This allows the reconstruction of up to 36 additional tracking points per track, with a spatial resolution of about 170 μm in the R–ϕ plane;
- the TRT also functions as a transition radiation detector: when a relativistic particle crosses the interface between two materials with different refractive indices, it emits

transition radiation. The emitted energy scales with the Lorentz factor γ of the particle, allowing discrimination between electrons and pions in the energy range between 1 and 200 GeV, exploiting their mass difference ($m_e \approx 0.51$ MeV while $m_{\pi^\pm} \approx 139.57$ MeV [46]).

The transverse momentum resolution of the ATLAS ID, as measured during Run 1 prior to the insertion of the IBL, can be parametrised as

$$\frac{\sigma(p_T)}{p_T} = (4.83 \pm 0.16) \times 10^{-4}\,\text{GeV}^{-1} \cdot p_T, \tag{3.4}$$

as reported in Ref. [81].

3.4 Calorimeters

As explained in the previous paragraph, the ID measures charged particle tracks and momenta (with the exception of muons). At this stage, no information is yet available on neutral particles or on the particle energy. These measurements are provided by the calorimetric system.

Calorimeters [86] are instrumented blocks of dense material in which particles interact through electromagnetic or strong processes. These interactions produce a cascade of secondary particles, called a *shower*, with progressively lower energies. The incident particle's energy is fully absorbed by the calorimeter material, and the energy deposited in its active components is converted into measurable signals, such as scintillation light or ionisation charge, which can be related to the initial particle energy.

Calorimeters can be classified according to their construction into *homogeneous* and *sampling* calorimeters:

- Homogeneous calorimeters are made of a single material that is dense enough to absorb the energy of incident particles while also producing a detectable signal. The CMS electromagnetic calorimeter [87] is an example of this type, being composed of $PbWO_4$ crystals, an inorganic scintillator;
- Sampling calorimeters consist of alternating layers of different materials: the *passive* layers of dense absorber degrade the particle energy, while the *active* layers produce a measurable signal. All ATLAS calorimeters described in the following sections are sampling calorimeters, with different combinations of active and passive materials depending on the type of shower they are designed to measure.

Homogeneous calorimeters are sensitive to the full energy of the incident particle and therefore generally provide better energy resolution. In sampling calorimeters, part of the energy is lost in the passive layers, degrading the resolution; however, they are typically cheaper and more resistant to radiation.

Calorimeters are further classified into *electromagnetic* calorimeters, which are designed to contain electrons and photons through processes such as bremsstrahlung and pair production, and *hadronic* calorimeters, which measure hadrons via strong and electromagnetic interactions. The ATLAS calorimetric system, shown in Figure 3.5, includes

both electromagnetic (Liquid Argon (LAr), described in Section 3.4.2) and hadronic (LAr and Tile, described in Section 3.4.3) calorimeters, each covering different pseudorapidity ranges.

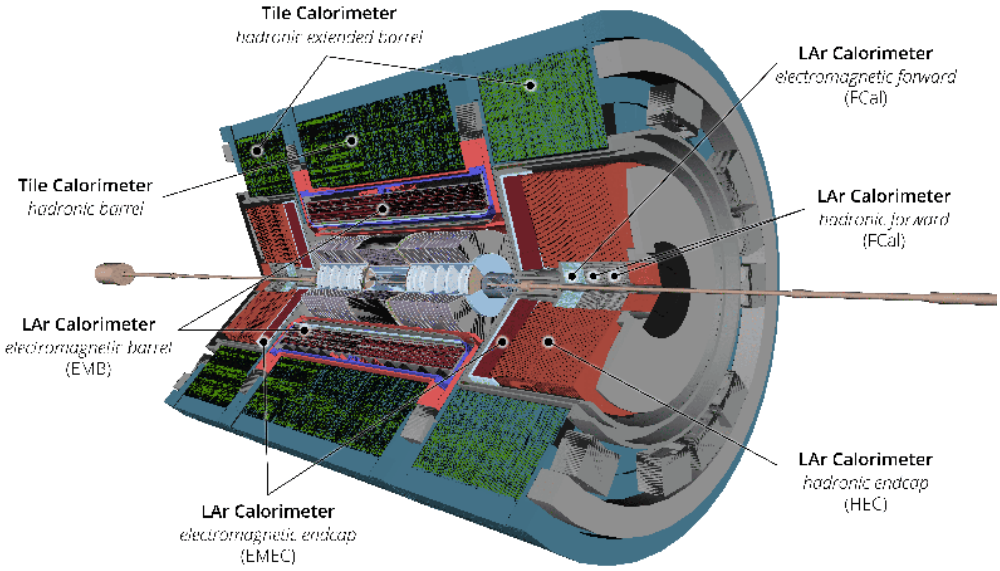

Figure 3.5 – Cut-away view of the ATLAS calorimeter system that measures the energies and positions of charged and neutral particles through interleaved absorber and active layers up to $|\eta| < 4.9$. LAr is used as the active medium for the electromagnetic calorimeters and all of the endcap and forward calorimeters; scintillating Tiles are used for hadron calorimetry in the central region [75].

3.4.1 Principles of calorimetry

As the EM shower develops in the calorimeter material, it proceeds through successive bremsstrahlung emission by electrons and positrons and pair production by photons. As a result, the number of secondary particles increases until their average energy drops below the *critical energy* ϵ_c. Below this threshold, ionisation dominates the energy loss for electrons, while the photoelectric effect dominates for photons. The shower reaches its maximum at a depth t_{max}, which depends on the initial energy E_0 of the incident particle and on the critical energy ϵ_c.
The critical energy depends on the properties of the absorber material, in particular on its atomic number Z, and can be parameterised as:

$$\epsilon_c = \frac{610\ \text{MeV}}{Z + 1.24}. \tag{3.5}$$

The shower depth t_{max}, at which the average energy of secondary particles reaches ϵ_c, is

referred to as the *depth at the maximum* of the electromagnetic shower, and is given by:

$$t_{\max} = \ln\left(\frac{E_0}{\epsilon_c}\right) + C_j, \tag{3.6}$$

where C_j is a constant depending on the type of incident particle: $C_e = -0.5$ for electrons and $C_\gamma = +0.5$ for photons.
At this stage, the showering process ceases, and the remaining particles are fully absorbed by the material. The longitudinal development of an electromagnetic shower is characterised by the *radiation length*, X_0, which represents the average distance an electron travels through the material before its energy is reduced by a factor of e^{-1}, i.e. $\langle E(x)\rangle = E_0 e^{-x/X_0}$. The radiation length depends on the absorber material and is given by:

$$X_0\ [\text{cm}] = \frac{716.4\,A}{Z\,(Z+1)\,\ln\left(287/\sqrt{Z}\right)} \cdot \frac{1}{\rho}, \tag{3.7}$$

where A is the atomic mass of the absorber and ρ is the density of the material. The depth required to contain 95% of the shower, expressed in units of X_0, can be approximated as:

$$t_{95\%}\ [\mathrm{X}_0] \approx t_{\max} + 0.08Z + 9.6. \tag{3.8}$$

For example, for LAr and lead (Pb), which are used in the ATLAS electromagnetic calorimeter as the active medium and absorber material, respectively, the critical energy and radiation length are [46]:

- LAr ($Z = 18$): $\epsilon_c \approx 32.84$ MeV, $X_0 \approx 14.00$ cm;
- Pb ($Z = 82$): $\epsilon_c \approx 7.43$ MeV, $X_0 \approx 0.5612$ cm.

Therefore, for a primary electron with an initial energy of $E = 100$ GeV, about 20–25 radiation lengths are required to contain 95% of the electromagnetic shower longitudinally, corresponding to approximately 260 cm of LAr or about 10 cm of lead.
The characteristic transverse size of an electromagnetic shower is described by the Molière radius, ρ_M, which represents the lateral spread of an electron from the shower axis after traversing a distance equal to X_0. Approximately 95% of the shower energy is contained within a distance of twice the Molière radius. The Molière radius depends only on the absorber material and it is independent of the incident particle energy. It can be calculated as:

$$\rho_M\ [\text{cm}] = \frac{21.2\ [\text{MeV}]}{\epsilon_c\ [\text{MeV}]} \times X_0. \tag{3.9}$$

For LAr and lead, the Molière radii are [46]:

- LAr: $\rho_M \approx 9.043$ cm;
- Pb: $\rho_M \approx 1.602$ cm.

Electromagnetic showers, initiated by incoming electrons or photons, consist exclusively of secondary electrons and photons. In contrast, hadronic showers—initiated by incoming hadrons—produce a variety of particles (e.g., protons, pions, neutrons) through nuclear interactions with the absorber nuclei. A key process within hadronic showers is the

decay of neutral hadrons (π^0, η, ...), primarily via the $\gamma\gamma$ channel, where the resulting secondary photons generate additional electromagnetic showers within the detector.

The energy deposited by this electromagnetic component is known as the *electromagnetic fraction*, f_{em}, which depends on the initial hadron energy and typically accounts for 30% to 60% of the total energy of the hadronic shower. The remaining energy corresponds to the *hadronic component*, f_{had}, which includes processes such as slow neutron production and spallation protons. Unlike the electromagnetic component, a fraction of the hadronic energy does not contribute to the detector signals, due to the loss of *invisible energy*, arising primarily from the binding energy of nucleons released during nuclear reactions. This invisible energy can account for up to 40% of the total non-electromagnetic energy. Consequently, the signal produced in a hadronic calorimeter by an incoming hadron is smaller than that produced by an electron or photon of the same energy. This difference in response between electromagnetic and hadronic showers is referred to as *non-compensation*.

The longitudinal development of a hadronic shower is governed by the *interaction length*, λ_{int}, which represents the average distance a particle travels within the absorber material before undergoing a nuclear interaction. An empirical approximation for the interaction length, expressed in cm, is given by:

$$\lambda_{\text{int}}\ [\text{cm}] \approx \frac{35\, A^{1/3}}{\rho}, \tag{3.10}$$

where A is the atomic mass of the absorber and ρ its density in g/cm^3. This formula provides a rough estimate and is valid for order-of-magnitude considerations; more accurate values of λ_{int} for specific materials are typically obtained from experimental measurements of hadronic cross sections. For a given material, the nuclear interaction length λ_{int} is significantly larger than the radiation length X_0, although the exact ratio depends on the absorber material. For example, for steel (iron), which is commonly used as an absorber in hadronic calorimeters, $\lambda_{\text{int}}^{\text{Fe}} \simeq 16.8$ cm [46], more than an order of magnitude larger than the corresponding radiation length $X_0^{\text{Fe}} \simeq 1.76$ cm. In contrast, for LAr, which is typically employed as an active medium, $\lambda_{\text{int}}^{\text{LAr}} = 85.77$ cm, approximately six times larger than $X_0^{\text{LAr}} = 14.00$ cm.

The longitudinal containment of 95% of a hadronic shower depends on the initial energy E of the primary hadron (in GeV) and can be expressed in units of the interaction length λ_{int} as

$$t_{95\%}\ [\lambda_{\text{int}}] = t_{\text{max}}\ [\lambda_{\text{int}}] + 2\, E^{0.13}, \tag{3.11}$$

where the depth of maximum shower development is given by

$$t_{\text{max}}\ [\lambda_{\text{int}}] = 0.2 \ln E + 0.7. \tag{3.12}$$

These expressions are empirical approximations, valid for order-of-magnitude estimates of the longitudinal development of hadronic showers.

For instance, the 95% longitudinal containment of a hadronic shower initiated by 100 GeV pions requires several interaction lengths, corresponding to approximately 450 cm of

LAr or about 120–170 cm of steel. Consequently, hadronic calorimeters, which are typically designed to have a depth of about 7–10 λ_{int}, are substantially larger than electromagnetic calorimeters.

In collider experiments, hadronic calorimeters are therefore realised as sampling calorimeters, employing dense materials such as steel or iron as absorbers and active media such as scintillators or liquid argon for signal readout.

Event-by-event fluctuations in the calorimeter response affect the resolution of energy measurements. The energy resolution of a calorimeter depends on the initial energy of the incoming particle and can be expressed as:

$$\frac{\sigma(E)}{E} = \frac{a}{\sqrt{E}} \oplus \frac{b}{E} \oplus c, \tag{3.13}$$

where $\sigma(E)$ is the standard deviation of the energy measurement, a is the stochastic term, b the noise term, and c the constant term. The symbol $\oplus$ indicates that the terms are combined in quadrature.

The *stochastic term* arises from the intrinsic statistical fluctuations in the shower development and in the sampling process, and decreases with increasing energy. In a homogeneous calorimeter, it is primarily influenced by fluctuations in the number of signal quanta contributing to the calorimeter response. For instance, when the active medium produces an ionisation signal, this corresponds to the number of ionisation tracks created by secondary electrons in the shower. Since this number is typically very large, the statistical fluctuations have a minimal impact on the energy resolution. By contrast, in calorimeters that rely on a Cherenkov signal, where the light yield is approximately 30 photoelectrons per GeV of deposited energy, such fluctuations can significantly affect the resolution. For a homogeneous calorimeter using ionisation signals, the stochastic term is usually of the order of a few $\%/\sqrt{E}$.

In electromagnetic sampling calorimeters, the main contribution to the stochastic term comes from sampling fluctuations, which arise due to event-by-event variations in the total energy deposited by shower particles in the active material. These fluctuations are influenced by the sampling fraction (i.e., the proportion of active material relative to the absorber layers) and the sampling frequency, defined as the number of active layers traversed by the shower along its longitudinal development. For such calorimeters, the stochastic term typically ranges from 5% to $20\%/\sqrt{E}$.

Hadronic calorimeters present a more complex scenario. In addition to the fluctuations described above, event-by-event variations in the electromagnetic fraction and in the invisible energy component of hadronic showers introduce further contributions to the energy resolution. These fluctuations typically exhibit a non-Gaussian distribution, causing their impact on the resolution to deviate from the standard $\propto 1/\sqrt{E}$ dependence. In non-compensating hadronic calorimeters, the stochastic term can range from 50% to $100\%/\sqrt{E}$.

The *noise term*, b, in Equation (3.13) accounts for contributions from electronic noise in the readout circuits, which is generally negligible within the energy range relevant for the ATLAS detector.

The *constant term*, c, represents energy-independent contributions to the resolution, such as non-uniformities in the calorimeter response, calibration uncertainties, and energy leakage from the rear of the calorimeter. This term becomes dominant at high energies, where the stochastic term is reduced.

3.4.2 The Electromagnetic Calorimeter

After the ID, the next detector system encountered by particles emerging from the IP is the Electromagnetic (EM) calorimeter [88–90], a sampling calorimeter that uses lead as the absorber material and LAr as the active medium. It consists of two main components:

- the central LAr Electromagnetic Barrel (EMB), which is 6.4 m long, 53 cm thick, and has an outer radius of 2.25 m. It covers the pseudorapidity range $|\eta| < 1.475$. The LAr layers are 2 mm thick, while the lead thickness varies between 1.1 mm and 1.5 mm;
- the LAr ElectroMagnetic EndCap (EMEC), which covers the two end-cap regions in the range $1.375 < |\eta| < 3.2$. Each end-cap is 2.7 m long and has an inner radius of 0.28 m and an outer radius of 2.05 m. The LAr layers are 2 mm thick, while the lead thickness varies between 1.7 mm and 2.2 mm. The transition areas between the barrel and end-caps are known as *crack regions* ($1.37 < |\eta| < 1.52$).

Each section of the EM Calorimeter is housed in its own cryostat to maintain the LAr at its operational temperature of 89 K.
The particles in the shower ionise the LAr, and the resulting charge is collected by copper electrodes positioned between the 2 mm LAr gaps. The lead absorbers and copper electrodes are arranged in an accordion geometry, which ensures full coverage in the azimuthal angle without dead regions. The sequence of LAr gaps, lead layers and copper electrodes is illustrated in Figure 3.6a. This design provides an effective depth of 22 X_0 in the EMB and 24 X_0 in the EMEC, ensuring almost full containment of electromagnetic showers with an energy of up to $1 \sim$ TeV.
The EM calorimeter comprises 182,468 cells along the η and ϕ coordinates and is segmented into four longitudinal layers, designed to accurately sample the longitudinal development of electromagnetic showers. The first layer is a presampler, located in front of the solenoid magnet, while the remaining three layers are arranged in the accordion geometry, forming the so-called accordion calorimeter. The cell granularity in both η and ϕ varies across the layers and detector regions, as detailed below and illustrated in Figure 3.6b for the EMB. The four layers, from the innermost to the outermost, are:

- *Layer 0* or *Presampler* (L0, PS): covering $|\eta| < 1.8$, it corrects for energy losses occurring upstream of the calorimeter, mainly in the cryostat walls and solenoid. It consists of a single LAr layer with a thickness of 11 mm, used to correct for energy losses in the material upstream of the calorimeter corresponding to approximately 2 X_0 at $\eta = 0$ and 4 X_0 at $\eta = 1.4$ (see Figure 6.1). The Presampler has a granularity of $\Delta\eta \times \Delta\phi = 0.025 \times 0.1$.

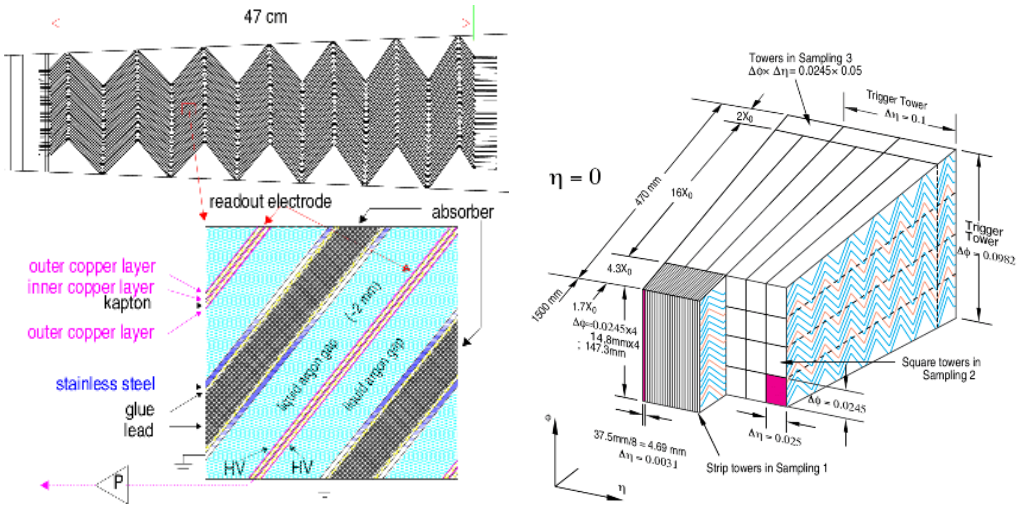

Figure 3.6 – (a) Accordion structure of the EMB calorimeter. The figure shows a view of a small sector of the barrel calorimeter in a plane transverse to the LHC beams. Honeycomb spacers in the LAr gap position the electrodes between the lead absorber plates. (b) Granularity of the EMB calorimeter layers in the $\eta \times \phi$ directions.

- *Layer 1* (L1, Strips): approximately $3-6\ X_0$ thick, it is segmented into narrow strips along η to provide precise measurements of the shower shape, crucial for discriminating single photons from overlapping photon pairs, for example from $\pi^0 \to \gamma\gamma$. In the EMB, the cell granularity varies from $\Delta\eta \times \Delta\phi = 0.0031 \times 0.1$ at $\eta = 0$ to 0.0063×0.1 at $\eta = 1.4$, while in the EMEC it ranges from 0.0031×0.1 at $\eta = 1.5$ to 0.01×0.1 at $\eta = 2.5$.
- *Layer 2* (L2, Middle): the thickest layer at about 16 X_0, responsible for absorbing most of the shower energy. The cell granularity is $\Delta\eta \times \Delta\phi = 0.025 \times 0.025$ in the EMB and varies from 0.025×0.025 at $\eta = 1.5$ to 0.05×0.025 at $\eta = 2.5$ in the EMEC.
- *Layer 3* (L3, Back): around 2 X_0 thick, designed to capture any remaining energy from high-energy showers and allows to estimate the energy leakage in the back of the calorimeter. The granularity is $\Delta\eta \times \Delta\phi = 0.05 \times 0.025$ in both the EMB and EMEC.

A summary of the thickness and granularity of the calorimeter layers is illustrated in Table 3.1.
The energy resolution of the LAr EM calorimeter has been measured [88]:

$$\frac{\sigma(E)}{E} \approx \frac{10\%}{\sqrt{E\ [\text{GeV}]}} \oplus 0.7\%, \tag{3.14}$$

which is consistent with the typical performance of sampling electromagnetic calorimeters. The sampling term varies with pseudorapidity $|\eta|$, while the noise term is negligible

Layer	Thickness [X_0]	$\Delta\eta \times \Delta\phi$ of **EMB** at $\eta = 0$	$\Delta\eta \times \Delta\phi$ of **EMEC** at $\eta = 1.5$
Presampler	up to 2 X_0	0.025×0.1	–
Layer 1	up to 6 X_0	0.0031×0.1	0.0031×0.1
Layer 2	up to 16 X_0	0.025×0.025	0.025×0.025
Layer 3	up to 2 X_0	0.05×0.025	0.05×0.025

Table 3.1 – A summary of the ATLAS LAr EM Calorimeter layers granularity. Thickness is given in radiation length (X_0) units. Granularity is given as $\Delta\eta \times \Delta\phi$. It is just reported for the EMB at $\eta = 0$ and for the EMEC at $\eta = 1.5$ as examples.

for energies above 0.5 GeV.

LAr Phase-I Upgrade

The main upgrade of the Run 3 system compared to Run 2 is the implementation of the new Digital Trigger (DT) readout [91], which provides finer-granularity inputs to the upgraded trigger system (see Section 3.6). During Run 1 and Run 2, the calorimeter signals sent to the trigger system consisted of $\Delta\eta \times \Delta\phi = 0.1 \times 0.1$ Trigger Towers (TT), formed by the analog summation of the E_{T} from the calorimeter cells across the longitudinal layers of the calorimeter. The new digital trigger readout path implemented for Run 3 is based on smaller clusters called *Super Cells*, obtained by introducing additional lateral and longitudinal segmentation, splitting the TTs longitudinally into four layers, with the middle ones further divided laterally along η into four strips each. A Super Cell can thus cover an area as small as $\Delta\eta \times \Delta\phi = 0.025 \times 0.1$, depending on the longitudinal layer in which it is located, with finer granularity in the Strips and Middle layers ($|\eta| < 2.5$), as shown in Figure 3.7. In this way, the granularity of the signals is increased by up to a factor of ten, significantly improving both the trigger selection efficiency for events with interesting signatures and its discrimination power against background events.
This increased granularity enables the use of shower-shape variables already at the Level-1 trigger, allowing a more accurate identification of electromagnetic objects and an improved rejection of hadronic backgrounds. In particular, the digital Super Cell information significantly enhances the trigger performance under the high pileup conditions expected in Run 3 ($\langle\mu\rangle \sim 50$–$60$), enabling lower transverse energy thresholds or reduced trigger rates for electron and photon signatures at a fixed efficiency.

3.4.3 The Hadronic Calorimeters

To cope with the higher particle flux and radiation levels at increasing $|\eta|$, the ATLAS detector is equipped with multiple hadronic calorimeters located outside the EM calorimeter, covering different pseudorapidity regions:

- The Tile Hadronic Calorimeter [93, 94] covers the central and extended barrel regions, up to $|\eta| < 1.7$. It is a 8.2 m long cylinder and has an outer radius of 4.25 m. The Tile Calorimeter is a sampling calorimeter that uses steel plates as

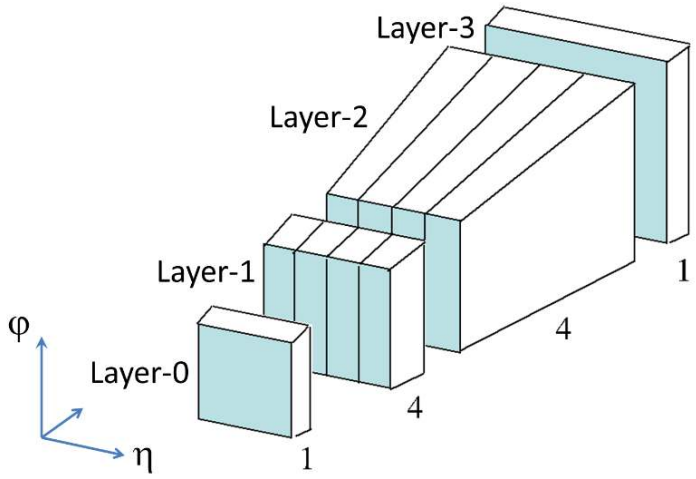

Figure 3.7 – Trigger granularity from each $\Delta\eta \times \Delta\phi = 0.1 \times 0.1$ TT after the Phase-I upgrade of the LAr calorimeter electronics [92]. Ten E_{T} values are provided from $1-4-4-1$ longitudinal/transverse samples, each forming a Super Cell.

absorber material and plastic scintillating tiles as the active medium, divided into three main longitudinal sections. When hadrons interact with the calorimeter, they produce hadronic showers of secondary particles. The plastic scintillators are excited by the energy deposited by the shower particles and then emit light, which is converted into an electrical signal with amplitude proportional to the deposited energy. The total thickness of the calorimeter corresponds to approximately 11 λ_{int} at $|\eta| = 0$, ensuring full containment of hadronic showers. The cell granularity is $\Delta\eta \times \Delta\phi = 0.1 \times 0.1$.

- The two wheels of the LAr Hadronic EndCap (HEC) [95, 96], covering the pseudorapidity range $1.5 < |\eta| < 3.2$, are also sampling calorimeters that use copper or tungsten plates as absorber material and LAr as the active medium. Each wheel is approximately 1 m thick and has an outer radius of 2.1 m. The total thickness of the calorimeter is $\sim 103\ X_0$ or $\sim 9.7\ \lambda_{\mathrm{int}}$ [95]. The cell granularity is $\Delta\eta \times \Delta\phi = 0.1 \times 0.1$ or $\Delta\eta \times \Delta\phi = 0.2 \times 0.2$, depending on η. The HEC overlaps with the Tile Calorimeter in the transition region $1.5 < |\eta| < 1.7$ and with the FCal in the forward region $3.1 < |\eta| < 3.2$.

The combined performance of the EM and HAD Calorimeters results in a global energy resolution of [88]

$$\frac{\sigma(E)}{E} \approx \frac{50\%}{\sqrt{E\ [\mathrm{GeV}]}} \oplus 3\%, \tag{3.15}$$

for hadrons in the central region ($|\eta| < 3.2$), which is typical for non-compensating hadronic calorimeters.

3.4.4 Forward Calorimeter

The ATLAS Forward Calorimeter (FCal) [97] is designed to measure the energy of both electromagnetic and hadronic showers in the forward regions, extending the pseudo-rapidity coverage of the ATLAS calorimetric system to $3.1 < |\eta| < 4.9$. Tolerance to radiation is fundamental in the forward region: therefore, LAr is used as an active material, with copper or tungsten rods acting as absorbers.
The typical energy resolution achieved by the FCal for incoming pions is given by [97]:

$$\frac{\sigma(E)}{E} \approx \frac{(94.2 \pm 1.6)\%}{\sqrt{E\ [\text{GeV}]}} \oplus (7.5 \pm 0.4)\%, \tag{3.16}$$

while for electrons it is:

$$\frac{\sigma(E)}{E} \approx \frac{(28.5 \pm 1.0)\%}{\sqrt{E\ [\text{GeV}]}} \oplus (3.5 \pm 0.1)\%. \tag{3.17}$$

3.5 Muon Spectrometer

Muons, together with weakly interacting neutrinos, are the only particles capable of traversing the ATLAS ID and calorimetric systems without being absorbed. Owing to their much larger mass compared to electrons, muons undergo a substantially reduced energy loss via bremsstrahlung – by a factor of approximately $(m_e/m_\mu)^2 \approx 2 \times 10^{-5}$ [46] – which strongly suppresses the probability of initiating electromagnetic showers in the calorimeters. Furthermore, muons do not participate in strong interactions with the detector material, allowing them to escape the ID and calorimeters with minimal energy loss.
The Muon Spectrometer (MS) [98], the outermost component of the ATLAS detector, tracks muon trajectories and measures their momenta within $|\eta| < 2.7$, providing triggering capabilities up to $|\eta| < 2.4$. Its design follows the geometry of the air-core toroidal magnet system (see Section 3.2), which divides the sub-detector into octants and curves muon trajectories in the (R, z) plane, enabling momentum determination. A cut-away view of the MS in Run 3 is shown in Figure 3.8.
The ATLAS MS is divided into a central barrel region and two endcaps, each composed of three stations: inner (closest to the calorimeters), middle (located within the toroidal magnetic field), and outer (outside the field). In the barrel, these stations form three concentric cylindrical layers around the beam axis, while in the endcaps they are arranged as disks perpendicular to the beam axis, referred to as Wheels.
Due to the large detector volume, continuous tracking is not feasible. Instead, muon trajectories are reconstructed from straight track segments measured independently in each station. Multilayered detectors provide several spatial measurements per muon, which are combined to form local segments and subsequently fitted across stations to reconstruct full curved muon tracks, matched to tracks reconstructed in the ID.
Precision measurements of the bending plane are provided by Monitored Drift Tubes (MDT) chambers over most of the detector acceptance ($|\eta| < 2.7$), supplemented by

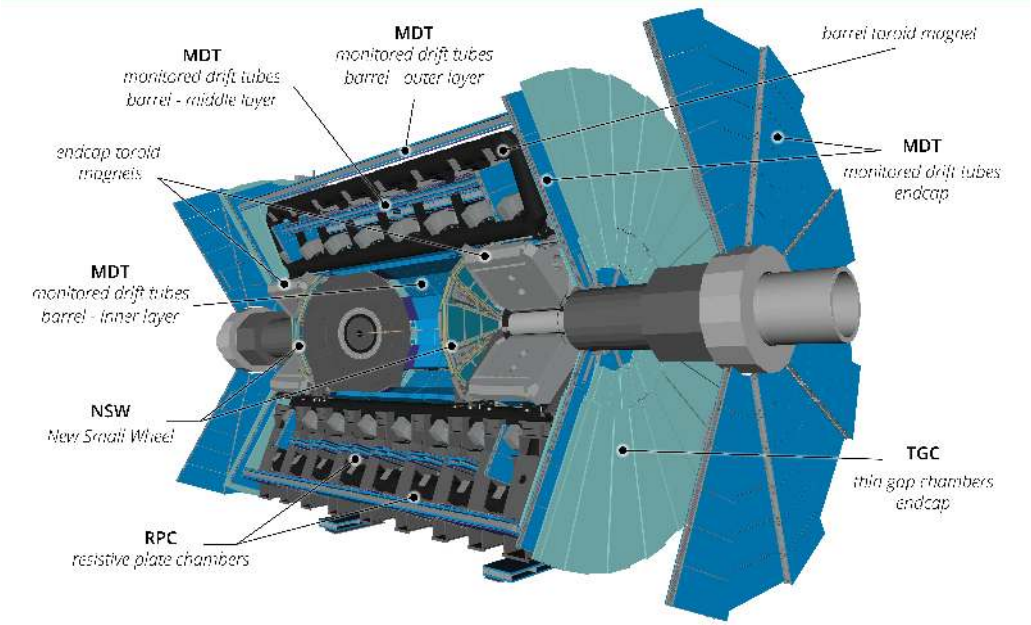

Figure 3.8 – Cut-away view of the ATLAS muon system, which detects charged particles exiting the barrel and endcap calorimeters and measures their momenta within $|\eta| < 2.7$. The system is built around an air-core toroidal magnet, and the main components upgraded for Run 3 (e.g., the New Small Wheels (NSW)) are visible [75].

Cathode Strip Chambers (CSC) chambers in the forward region ($2 < |\eta| < 2.7$). Each MDT chamber consists of 3–8 layers of aluminium drift tubes filled with a high-pressure Ar/CO_2 gas mixture, with a 50 μm central wire, achieving a spatial resolution of approximately 35 μm per chamber in the bending plane. CSC chambers are multiwire proportional chambers providing a resolution of about 40 μm in the bending plane and 5 mm in the azimuthal direction.

Muon triggering is performed by fast gaseous detectors: Resistive Plate Chambers (RPC) chambers in the barrel region and Thin Gap Chambers (TGC) chambers in the endcaps. These detectors provide bunch-crossing identification and coarse position measurements in the azimuthal direction, enabling fast muon trigger decisions.

During Phase-I, corresponding to the transition to Run 3, the innermost endcap stations were upgraded with the installation of the NSW, replacing the Run 2 Small Wheels (SW). The NSW system employs small-strip TGC and Micro-Mesh Gaseous Structure (MicroMegas) detectors, which provide both precision tracking and triggering capabilities. This upgrade significantly improves the spatial resolution in both the bending and azimuthal coordinates in the forward region, leading to a substantial reduction of fake muon triggers from hadronic backgrounds. Furthermore, the enhanced trigger performance allows efficient triggering on lower-p_T muons under the high pileup conditions of Run 3, while preparing the muon system for operation at the HL-LHC.

Fast muon triggering is provided by RPC chambers in the barrel region ($|\eta| < 1.05$)

and by TGC chambers in the endcaps ($1.05 < |\eta| < 2.4$), which deliver bunch-crossing identification and trigger signals with a time resolution of approximately 15–25 ns. With this configuration, the ATLAS muon spectrometer achieves a momentum resolution of about 2–3% at $p_{\mathrm{T}} \sim 10$ GeV, degrading to approximately 10% at $p_{\mathrm{T}} \sim 1$ TeV.

3.6 Trigger and Data Acquisition system

The LHC beams collide at the IP with a frequency of up to 40 MHz. Given a typical raw event size of the order of a few megabytes, this would correspond to a data throughput of $\mathcal{O}$(10–100 TB/s), far exceeding the available storage and processing capabilities of the ATLAS experiment [99]. Moreover, the vast majority of pp collisions at LHC energies involve only soft interactions, lacking the distinctive signatures of processes targeted by the ATLAS physics programme. Therefore, a key component of the ATLAS experiment is the TDAQ system, which efficiently selects and records only potentially interesting events, reducing the data output rate to a manageable level. It is a two-level system comprising a hardware-based Level-1 (L1) trigger [100] and a software-based High-Level Trigger (HLT) [101].

The L1 trigger is primarily based on two independent subsystems that use custom electronics to process reduced-granularity information from the calorimeters (**L1Calo**) and the muon detectors (**L1Muon**). These systems identify events containing high-p_{T} leptons, jets, or large missing or total transverse energy, which may indicate the presence of interesting physics processes. The L1 topological processor (**L1Topo**) receives Trigger OBjects (TOB) containing kinematic information from the L1Calo and L1Muon systems and applies additional topological selections. The final L1 trigger decision is produced by the Central Trigger Processor (CTP), which combines the inputs from L1Calo, L1Muon, and L1Topo.

The CTP also incorporates information on the LHC bunch pattern, externally configured to define which bunch crossings are eligible for triggering. This information is logically combined with other trigger conditions before generating the L1 decision. Most triggers are active only during bunch crossings where proton bunches collide (at a rate of about 30 MHz), although dedicated triggers for background studies can also be enabled in empty or unpaired bunch crossings.

Up to 512 distinct L1 trigger items can be configured in the CTP. To respect detector readout latency constraints, the CTP applies preventive dead time to limit the frequency of consecutive L1 accepts. A simple dead-time constraint ensures a minimum time between two accepts to avoid overlapping readout windows, while a complex dead-time constraint limits the number of accepts allowed within a defined number of bunch crossings to prevent front-end buffer overflows. The maximum L1 accept rate is 100 kHz with a fixed latency below 2.5 μs. Upon receiving an L1 accept signal, the corresponding events are forwarded to the HLT for further processing.

The HLT operates on a computing farm comprising about 60,000 CPU cores (up from approximately 40,000 in Run 2) and selects up to 3 kHz of events recorded with complete detector readout for permanent storage (compared to 1 kHz in Run 2), with additional bandwidth allocated for partial event readout. The average event processing time is

approximately 600 ms per event per core.
HLT algorithms reconstruct events with progressively higher levels of detail, either over the full detector or within specific Regions-of-Interests (RoIs) identified by the L1 trigger as containing candidate objects. Unlike the hardware-based L1 system, the HLT uses full-granularity information from all sub-detectors, achieving improved energy and momentum resolution and enabling precision tracking for particle identification.

3.6.1 Phase-I Upgrade

Before the start of Run 3, the trigger system underwent a major upgrade [92] to optimise its performance under the new LHC running conditions. The upgraded design was developed to cope with higher pileup levels while maintaining the same selection efficiency and reducing the overall L1 trigger rate.
The L1Calo system was significantly enhanced to perform on-detector digitisation of signals from the LAr calorimeters, enabling electromagnetic cluster reconstruction with up to ten times finer granularity and jet reconstruction with four times finer granularity. The LAr TTs are distributed to upgraded Feature Extraction (FEX) processors, which include electromagnetic Feature Extraction (eFEX), jet Feature Extraction (jFEX), and global Feature Extraction (gFEX). The eFEX exploits full Super Cell granularity for precise reconstruction of EM objects and hadronically decaying τ leptons. In the region $|\eta| < 2.5$, the jFEX receives TTs with twice the granularity of the legacy system, achieving performance comparable to the Run 2 L1Calo for single-jet triggers and improved efficiency for nearby jets in multi-jet triggers. The gFEX, designed with coarser granularity similar to the Run 2 system, processes data from the calorimeter on a single module, enabling the identification of boosted objects and global observables such as $E_{\mathrm{T}}^{\mathrm{miss}}$, crucial for BSM physics searches.
The L1 and HLT decisions are governed by *trigger menus* [102], which define the event types considered valuable for offline analysis and allocate a target rate to each of them. Figure 3.9a shows the total L1 trigger rate for a representative LHC fill during Run 3. Figure 3.9b illustrates the total HLT output rate, broken down by reconstructed streams such as main physics stream, containing triggers for general physics analyses or specific signatures, and calibration streams, used for detector performance studies and calibrations.
To end the Chapter, two photos of the ATLAS detector during the LS2 and the installation of the new NSW are shown in Figure 3.10.

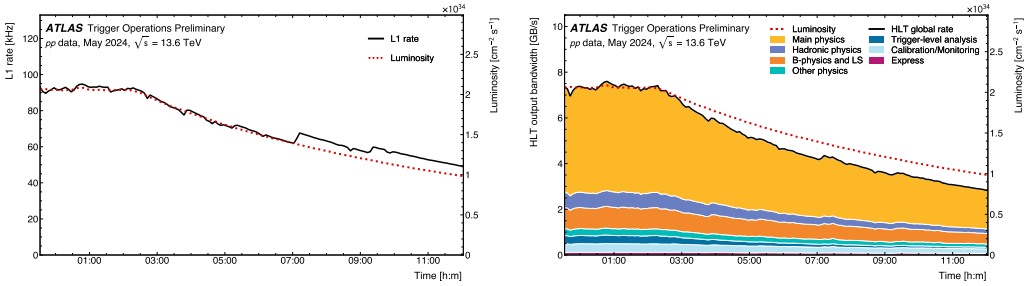

(a) L1 trigger rates. **(b)** HLT trigger rates.

Figure 3.9 – Total L1 (a) and HLT (b) physics trigger rates versus time for a fill in May 2024, with peak luminosity $L = 2.1 \times 10^{34}$ cm^{-2}s^{-1} and average pileup $\langle\mu\rangle = 63$ [103]. For L1, the luminosity is levelled for a period at the beginning of the fill; after that, the rate decreases with the decaying luminosity. Periodic increases in the L1 rate with respect to luminosity at the end of the fill are caused by prescale changes, as the luminosity and corresponding overall resource usage decline. For HLT, the streams presented in the plots are: the main physics stream, containing triggers for general physics analyses; the B-physics and light states (LS) stream, containing triggers specific to B-physics analyses; the hadronic physics stream, containing specialised hadronic triggers including selections for Vector Boson Fusion and di-Higgs; the express stream, recording events at a low rate for data quality monitoring; other streams with physics applications, such as zero-bias and background events; the trigger-level analysis (TLA) stream, recording a limited number of trigger objects; and the detector calibration and monitoring streams.

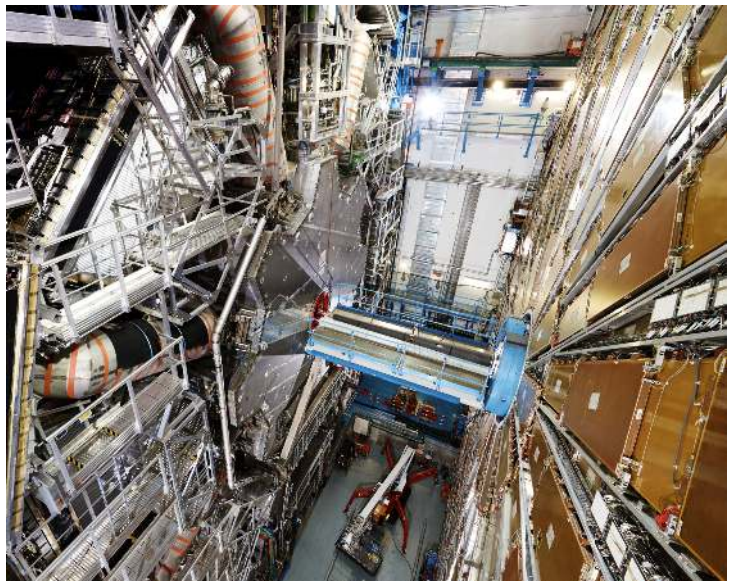

(a)

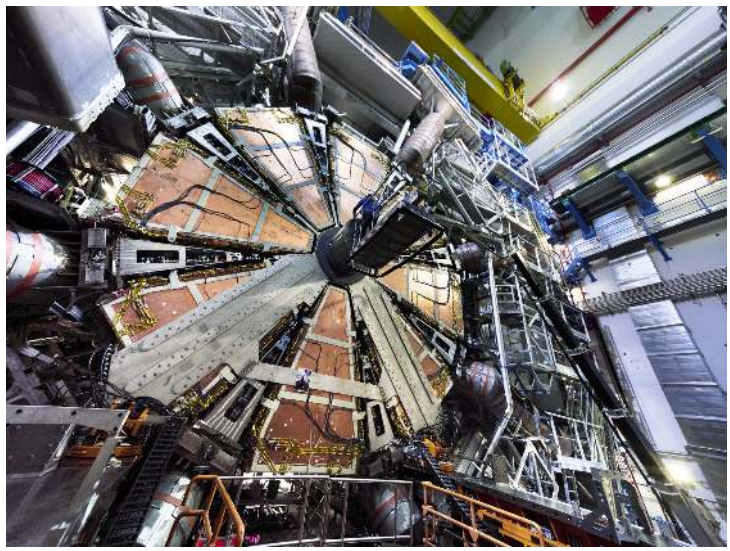

(b)

Figure 3.10 – (a) Cut-away view of the ATLAS detector during an open-detector maintenance period. The large barrel toroid magnet is visible on the left, while the muon chambers and calorimeter structures can be seen on the right. This image highlights the sheer scale and complexity of ATLAS, which measures 46 m in length and 25 m in diameter, and weighs about 7,000 tons. (b) The 100 tonnes NSW is lowered 80 metres underground in the ATLAS cavern at the LHC level. The NSW consists in a set of new precision tracking detectors based on the MicroMegas technology and new trigger detectors Small Strip TGC [104].

4 | Higgs boson phenomenology at the LHC

As discussed in Section 1.2, fermions and weak gauge bosons acquire their masses dynamically through interactions with the Higgs field. Consequently, the strength of the interaction between the Higgs boson and other SM particles is determined by their mass: for a fermion (weak boson) with mass m, the corresponding Higgs coupling is proportional to m (m^2). The SM therefore predicts the strongest interactions between the Higgs boson and the heaviest particles — namely, the top quark and the weak gauge bosons — while the couplings to lighter particles (such as leptons and light quarks) are highly suppressed.
In addition, the Higgs boson does not couple directly to either gluon or photon fields. This is a direct consequence of the gauge invariance of the SM under the unbroken $SU(3)_C \times U(1)_{\text{EM}}$ symmetry, as both the color and electromagnetic gauge fields remain massless.
Consequently, while Higgs boson production and decay processes are predominantly governed by its couplings to the top quark and the weak gauge bosons, the fact that most SM particles possess mass leads to a rich and diverse Higgs phenomenology. Furthermore, both the production cross sections and branching fractions depend on the Higgs boson mass, m_H, whose value is not predicted by the theory. A precise measurement of m_H is therefore essential to validate the SM description of the Higgs boson interactions. The following sections provide an overview of the main Higgs boson production (Section 4.1) and decay processes (Section 4.2) at the LHC, along with a summary of the key measurements performed since its discovery (Section 4.3) in 2012, with a particular focus on the mass measurement (Section 4.4) given the topic of this thesis. Subsequent sections discuss the measurements of the Higgs boson signal strengths and couplings (Section 4.7), as well as its width (Section 4.5), spin, and CP properties (Section 4.6).

4.1 Higgs boson production modes

At hadron colliders such as LHC, pp collisions occur with a centre-of-mass energy $\sqrt{s}$, as described in Chapter 2. In these conditions the SM Higgs boson can be produced through various mechanisms, each characterized by different initial states and final state topologies:

- **ggF**: the *gluon-gluon fusion* is the dominant Higgs boson production mechanism at the LHC, accounting for about 87% of the total cross section. Its SM cross section σ_{ggF} [105] (for $m_H = 125.09$ GeV at $\sqrt{s} = 13.6$ TeV, from QCD and electroweak

calculations at N^3LO and NLO accuracy, respectively) is more than an order of magnitude larger than that of any other production mode:

$$\sigma_{ggF} = 52.17^{+4.6\%}_{-6.7\%}\ (\text{QCD scale})\ \pm\ 3.2\%\ (\text{PDF} + \alpha_s)\ \text{pb}. \tag{4.1}$$

This process proceeds through a loop diagram in which two gluons from the colliding protons interact primarily via a top-quark loop to produce a Higgs boson. The leading-order Feynman diagram is shown in Figure 4.2a. The SM Higgs boson production cross sections at both $\sqrt{s} = 13$ TeV and $\sqrt{s} = 13.6$ TeV are summarised in Table 4.1.

- **VBF**: the *Vector Boson Fusion* process is the second most important Higgs boson production mode at the LHC. In this mechanism, two quarks from the colliding protons radiate virtual weak gauge bosons ($W^{\pm}$ or Z, collectively denoted as V), which subsequently *fuse* to produce a Higgs boson. The final state is characterised by two energetic jets originating from the scattered quarks, typically located in the forward regions of the detector, providing a distinctive signature for this process. The leading-order Feynman diagram is shown in Figure 4.2b, and the corresponding cross sections at $\sqrt{s} = 13$ TeV and $\sqrt{s} = 13.6$ TeV are summarised in Table 4.1.
- **WH** and **ZH**: in the *associated production with a vector boson* mode (VH), a Higgs boson is produced in association with a $W^{\pm}$ or a Z boson. In this process, two quarks annihilate into an off-shell vector boson V, which subsequently radiates a Higgs boson — a mechanism known as *Higgsstrahlung*. This production mode provides a particularly clean experimental signature thanks to the presence of the accompanying vector boson, which can decay leptonically, enabling efficient triggering and strong background suppression. The leading-order Feynman diagrams for these processes are similar to the one shown in Figure 4.2c, with the Higgs boson emitted from the vector boson line. The corresponding production cross sections at $\sqrt{s} = 13$ TeV and $\sqrt{s} = 13.6$ TeV are summarised in Table 4.1.
- **ggZH**: two gluons produce a Higgs boson in association with a Z boson via a heavy quark loop. This process is similar to ggF, but with an additional Z boson in the final state. The cross section is smaller than that of the WH and ZH processes, but it contributes to the overall VH production rate. An example leading-order Feynman diagram is shown in Figure 4.2d.
- **$t\bar{t}H$** and **$b\bar{b}H$**: in the *top-antitop (bottom-antibottom) associated production* mode, a Higgs boson is produced in association with a top (bottom) quark-antiquark pair. This process directly probes the Yukawa coupling between the Higgs boson and the top (bottom) quark, offering a unique opportunity to study the Higgs-fermion interaction. The leading-order Feynman diagram for the $t\bar{t}H$ ($b\bar{b}H$) process is shown in Figure 4.2e. These processes are tagged by the presence of multiple jets in the final state, and, in particular, the presence of jets from the hadronization of bottom quarks (termed *b*-jets).
- **tWH** and **tqH**: subdominant production modes where a Higgs boson is produced in association with a single top quark. These processes are sensitive to the relative

sign of the top-Higgs coupling and the Higgs coupling to weak bosons, providing complementary information to the $t\bar{t}H$ process. Some example leading-order Feynman diagrams are shown in Figures 4.2f to 4.2h.

Figure 4.1 shows the behaviour of the Higgs boson production cross sections for all the different production mechanisms available at hadron colliders, as a function of the LHC centre-of-mass energy, fixing $m_H = 125$ GeV. The characteristic increase of the cross section with energy is clearly visible. In particular, the increase in energy from $\sqrt{s} = 13$ TeV to $\sqrt{s} = 13.6$ TeV leads to an enhancement of about 7.4% in the ggF production cross section, with similar increases observed for the other production modes. These trends are more clearly illustrated in Table 4.1, which compares the SM Higgs production cross sections at the two energies.

		$\sqrt{s} = 13$ TeV			$\sqrt{s} = 13.6$ TeV		
Process	Accuracy	σ [pb]	QCD Scale [%]	PDF + α_S [%]	σ [pb]	QCD Scale [%]	PDF + α_S [%]
ggF	N3LO + NLO	48.58	$^{+4.56}_{-6.72}$	3.2	52.17	$^{+4.6}_{-6.7}$	3.2
VBF	NNLO + NLO	3.782	$^{+0.43}_{-0.33}$	2.1	4.075	$^{+0.5}_{-0.3}$	2.1
WH	NNLO + NLO	1.373	$^{+0.5}_{-0.7}$	1.8	1.453	$^{+0.4}_{-0.7}$	1.8
ZH	NNLO + NLO	0.8839	$^{+3.8}_{-3.2}$	1.6	0.9422	$^{+3.8}_{-3.2}$	1.6
ggZH	NLO + NLO	0.1227	$^{+3.9}_{-3.0}$	1.6	0.1359	$^{+3.9}_{-3.0}$	1.6
$t\bar{t}H$	NLO + NLO	0.5071	$^{+5.8}_{-9.2}$	3.6	0.5688	$^{+6.0}_{-9.3}$	3.5
$b\bar{b}H$	NLO	0.4880	$^{+20.2}_{-23.9}$		0.5257	$^{+20.3}_{-24.0}$	
tWH	NLO	0.015 17	$^{+4.9}_{-6.7}$	6.3	0.017 20	$^{+5.0}_{-6.8}$	6.3
tH (t-channel)	NLO	0.074 25	$^{+6.5}_{-14.9}$	3.7	0.083 53	$^{+6.5}_{-14.8}$	3.7
tH (s-channel)	NLO	0.002 88	$^{+2.4}_{-1.8}$	2.2	0.003 06	$^{+2.4}_{-1.7}$	2.2

Table 4.1 – Comparison of SM Higgs production cross sections at $\sqrt{s} = 13$ TeV [106] and 13.6 TeV [105] for $m_H = 125.09$ GeV in pp collisions. The accuracy reported in the table refers to QCD and electroweak (EW) calculations: when two entries are given, the first corresponds to the QCD accuracy and the second to the EW accuracy; when a single entry is reported, it refers to the QCD accuracy only.

Figure 4.3 displays the dependence of the SM Higgs boson production cross sections on the Higgs boson mass.

4.2 Higgs boson decay processes

After being produced in pp collisions, the Higgs boson has an extremely short lifetime (approximately 1.6×10^{-22} s according to the SM [106]) before decaying into other particles. The Higgs boson can decay into many different final states. The *branching ratio* ($\mathcal{BR}$) of a single possible final state X_i is defined as the ratio between the corresponding partial decay width and the total Higgs boson decay width, summed over all possible decay modes:

$$\mathcal{BR}(\mathrm{H} \to X_i) = \frac{\Gamma(\mathrm{H} \to X_i)}{\sum_i \Gamma(\mathrm{H} \to X_i)} \,. \tag{4.2}$$

The SM Higgs boson decay branching ratio for each decay mode can be evaluated as a function of m_H. Figure 4.4 shows the branching ratios as a function of the Higgs boson mass in the range containing the measured value, $m_H \in [120, 130]$ GeV. The main SM

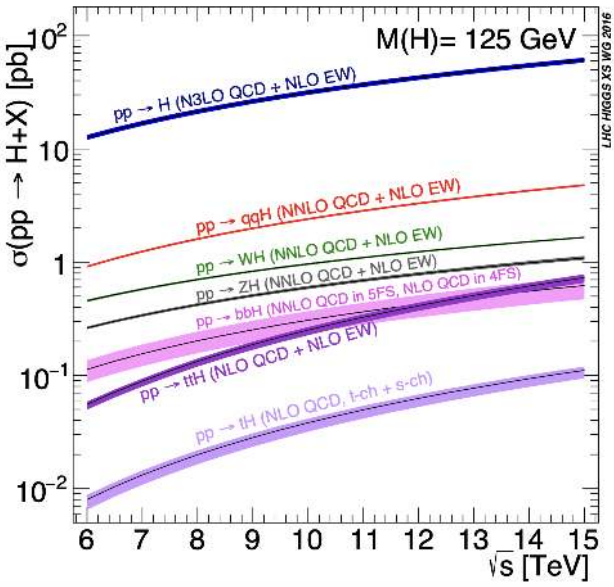

Figure 4.1 – The SM Higgs boson production cross sections as a function of the LHC centre-of-mass energy [106].

Higgs decay channels in this mass range, along with their characteristic features, are summarised below:

- $\boldsymbol{H \to b\bar{b}}$: the decay into a bottom quark–antiquark pair is the most probable Higgs boson decay mode for a mass around 125 GeV, with a branching ratio of approximately 58% [106]. This channel is experimentally challenging due to the large QCD background producing $b\bar{b}$ pairs. For this reason, it is typically studied in association with other particles, such as in VH production, where the leptonic decays of the vector boson provide clean experimental signatures and efficient background suppression [107]. Additionally, dedicated searches have been developed for boosted Higgs bosons decaying to $b\bar{b}$, where the two bottom quarks are collimated and reconstructed as a single large-radius jet with substructure and b-tagging techniques [108]. These approaches extend sensitivity to high transverse momentum regimes and provide complementary probes of the Higgs–bottom coupling.
- $\boldsymbol{H \to WW^*}$, $\boldsymbol{H \to ZZ^*}$: the Higgs boson can decay into a pair of massive vector bosons, with one of them off-shell. The $H \to WW^*$ decay has the second-highest branching ratio, approximately 21.5% at $m_H = 125$ GeV [106], while $H \to ZZ^*$ has a branching ratio of about 2.6%. These channels are experimentally clean due to the presence of charged leptons (electrons and muons) in the final state, making them crucial for Higgs boson studies. The most studied final states include leptonic decays of the vector bosons, such as $H \to WW^* \to \ell\nu\ell\nu$ ($\ell = e, \mu$) and $H \to ZZ^* \to 4\ell$ ($\ell = e, \mu$). Although requiring fully leptonic decays reduces the branching fraction, these channels were central in the early Higgs boson searches at the LHC. In partic-

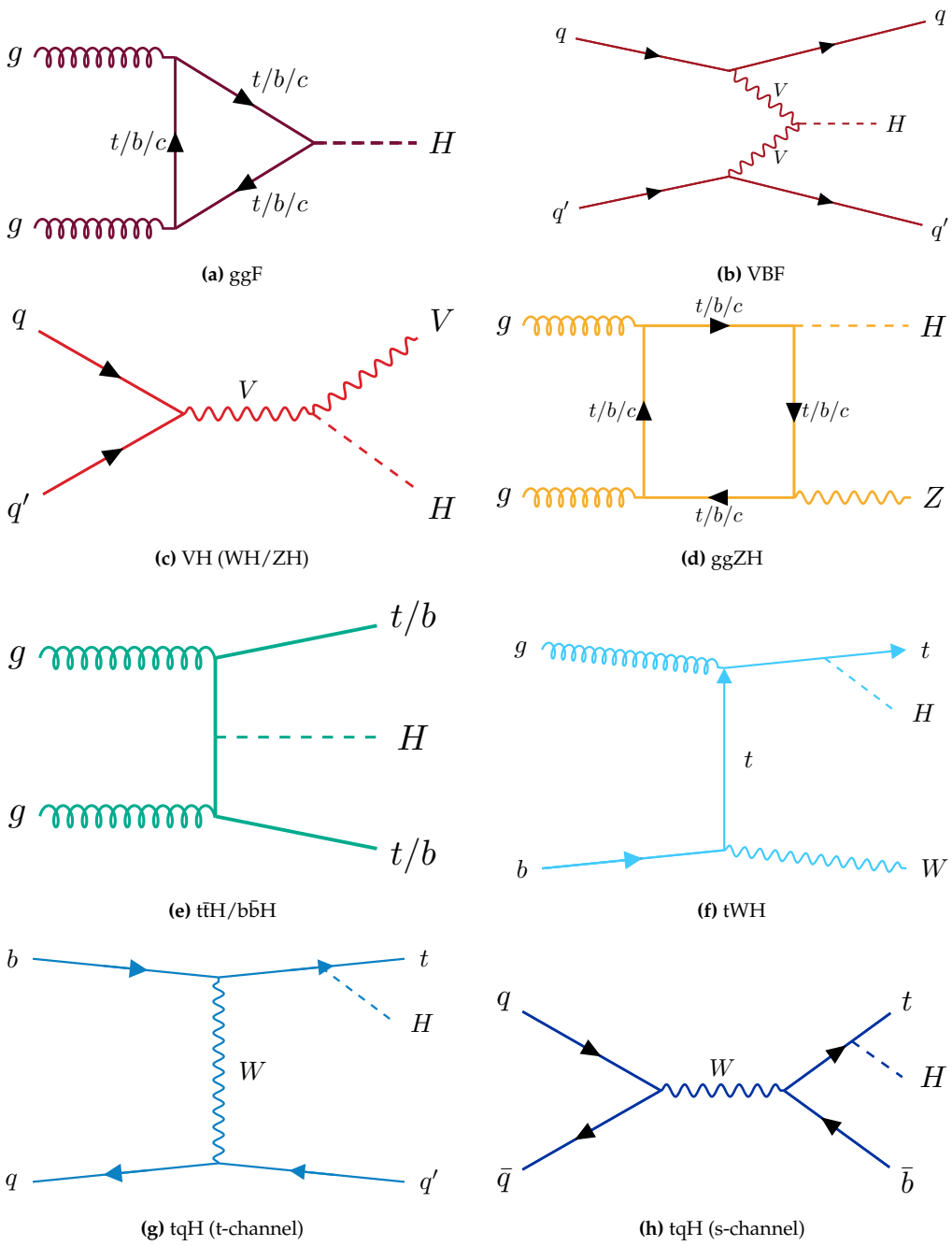

Figure 4.2 – Examples of leading-order Feynman diagrams for the main Higgs boson production processes at the LHC: (a) gluon-gluon fusion (ggF), (b) Vector Boson Fusion (VBF), (c) associated production with a vector boson (WH/ZH), (d) ggZH, (e) top-antitop (bottom-antibottom) associated production (tt̄H/bb̄H), (f) single top associated production (tWH), single top associated production in t-channel (g), and single top associated production in s-channel (h).

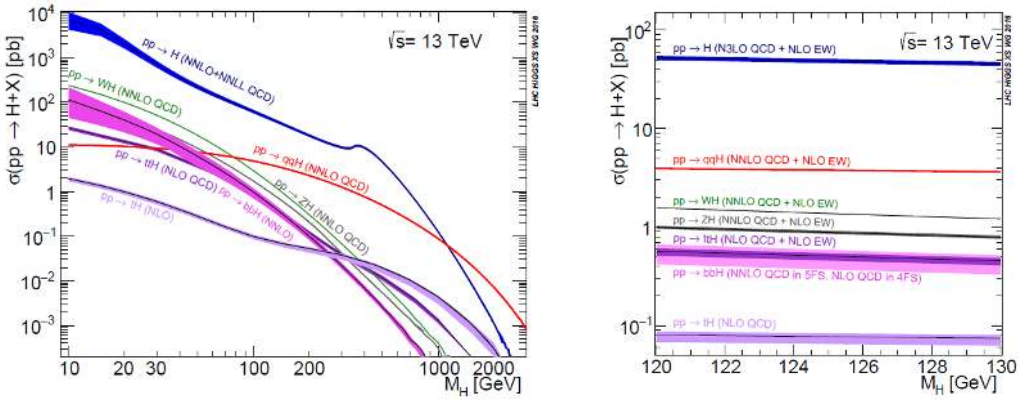

(a) $m_H \in [10, 2000]$ GeV **(b)** $m_H \in [120, 130]$ GeV

Figure 4.3 – The SM Higg boson production cross sections as a function of m_H at $\sqrt{s} = 13$ TeV for the mass ranges $m_H \in [10, 2000]$ GeV (a) and $m_H \in [120, 130]$ GeV (b) [106]. The uncertainties are represented by the width of the coloured line for each production mode.

ular, the $H \to ZZ^* \to 4\ell$ channel with $\ell = e, \mu$, known as one of the *golden channels* for Higgs boson discovery (see Section 4.3), provides an exceptionally clean signature with excellent mass resolution, enabling precise measurements of Higgs boson properties.

- $\boldsymbol{H \to \tau^+\tau^-}$, $\boldsymbol{H \to c\bar{c}}$, $\boldsymbol{H \to \mu^+\mu^-}$: the decay into a tau lepton pair is the second most probable fermionic decay mode of the Higgs boson, with a branching ratio of approximately 6.3% [106]. The decay into a charm quark-antiquark pair has a branching ratio of around 2.9% and is a key probe of the Higgs-charm Yukawa coupling, though it is very challenging to observe directly due to large backgrounds. Dedicated searches for $H \to c\bar{c}$ decays have been performed by the ATLAS and CMS collaborations, setting upper limits on the production rate that are several times larger than the SM expectation and constraining the Higgs-charm coupling modifier [109, 110]. The decay into a muon pair is much rarer, with a branching ratio of about 0.022%, and both collaborations have reported evidence for this mode [22, 111]. These channels provide important tests of the Yukawa couplings to second- and third-generation fermions.

- $\boldsymbol{H \to gg}$, $\boldsymbol{H \to \gamma\gamma}$: although the Higgs boson does not couple directly to the massless gluons and photons, it can decay into these particles via loop processes involving heavy charged particles, such as the top quark and W boson. The $H \to gg$ decay has a branching ratio of about 8.6% at $m_H = 125$ GeV [106], but is indistinguishable from the huge QCD background at hadron colliders. Conversely, while the $H \to \gamma\gamma$ decay is much rarer, with a branching ratio of approximately 0.227%, it provides a clean experimental signature due to the excellent photon energy resolution of the detectors. For these reasons, the $H \to \gamma\gamma$ decay mode was the second golden channel for the Higgs boson discovery. Examples of leading-order Feynman diagrams for this process are shown in Figure 4.5.

- $H \to Z\gamma$: this decay mode involves the Higgs boson decaying into a Z boson and a photon via loop processes and can be sensitive to potential BSM effects. However, it has a very small branching ratio of about 0.15% at $m_H = 125$ GeV [106], making it challenging to observe it experimentally. The ATLAS collaboration recently reported an observed (expected) significance of 2.5 (1.9) standard deviations [112], while, in the previous round of Run 2 analyses, the ATLAS and CMS Collaborations combined their results and reported the first evidence for the Higgs boson decay into a Z boson and a photon, with a statistical significance of 3.4σ [24].

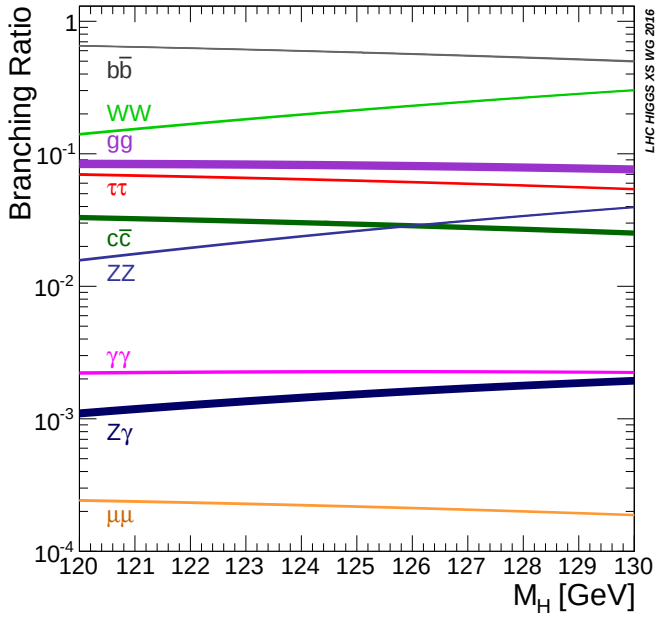

Figure 4.4 – The SM Higg boson decay branching ratios as a function of m_H in the mass range $m_H \in [120, 130]$ GeV. The uncertainties are represented by the width of the coloured line for each decay mode [106].

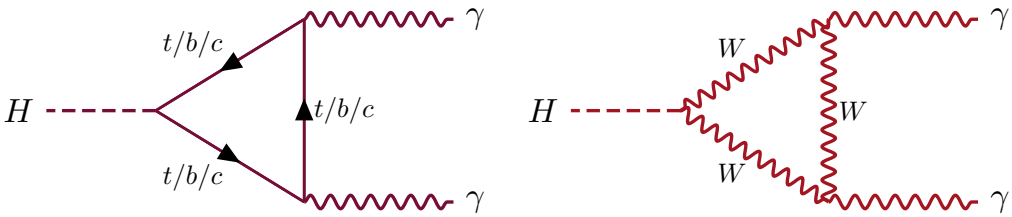

(a) fermion loop **(b)** W loop

Figure 4.5 – Leading-order Feynman diagrams for the $H \to \gamma\gamma$ decay process: (a) via a fermion loop (primarily top quark), and (b) via a W boson loop.

4.3 Higgs boson discovery at the LHC

On 4 July 2012, the ATLAS [113] and CMS [114] collaborations announced the observation of a new particle with a mass of about 125 GeV, consistent with the SM Higgs boson. The two experiments used partial Run 1 datasets corresponding to integrated luminosities of approximately 4.8 fb^{-1} (5.1 fb^{-1}) collected at $\sqrt{s} = 7$ TeV in 2011 and 5.8 fb^{-1} (5.3 fb^{-1}) at $\sqrt{s} = 8$ TeV in 2012 by the ATLAS (CMS) detector. Both collaborations combined the results of their searches in the most sensitive decay channels: $H \to \gamma\gamma$ and $H \to ZZ^* \to 4\ell$ (with $\ell = e, \mu$), $H \to WW^*$, $H \to \tau^+\tau^-$, and $H \to b\bar{b}$. The most significant excesses of events above the expected background were observed in the $H \to \gamma\gamma$ and $H \to ZZ^* \to 4\ell$ channels. Figures 4.6a and 4.6b show the observed local significance (p-value) for the background-only hypothesis for the two experiments: for mass hypotheses around 125 GeV, the data are inconsistent with the background-only assumption, with p-values of $\sim 10^{-9}$ (6σ) and $\sim 10^{-7}$ (5σ) for ATLAS and CMS, respectively.
This discovery marked a milestone in particle physics and opened a new era of precision studies of the Higgs boson's properties, which remain a central objective of the LHC physics programme.

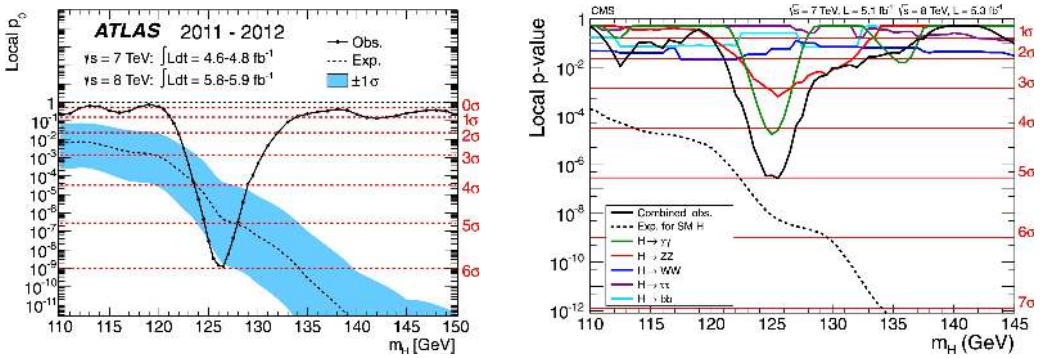

(a) ATLAS p-value

(b) CMS p-value

Figure 4.6 – Local p_0 values measured by ATLAS [113] (a) and CMS [114] (b), representing the probability for the background-only hypothesis to fluctuate to a signal-like excess at least as large as that observed, shown for the individual channels (coloured lines for CMS) and their combination (black line). The dashed curves indicate the median expected significance for a SM Higgs boson at each mass hypothesis. Horizontal lines correspond to p_0 values equivalent to significances from 0 to 6σ (a) and from 1 to 7σ (b).

4.4 Higgs boson mass measurement

After the discovery of the Higgs boson, a precise determination of its mass, m_H, became a key objective for both the ATLAS and CMS collaborations. The Higgs boson mass is a free parameter of the SM. Although not predicted by the theory, its measured value directly influences its couplings to other particles. Consequently, the production cross sections and decay branching ratios of the Higgs boson depend sensitively on its

mass, as discussed in Sections 4.1 and 4.2 and illustrated in Figures 4.3 and 4.4. In addition, the precise value of m_H has important implications for electroweak vacuum stability. The measured mass of approximately 125 GeV lies in a region suggesting that the electroweak vacuum may be meta-stable, as shown in Figure 4.7, a scenario with far-reaching consequences for cosmology and fundamental physics. By measuring m_H, one can infer whether the universe is in a global, and thus stable, minimum-energy state of the Higgs field potential, or in a local metastable one, from which it could decay to the ground state in the future. Furthermore, its precise determination is a crucial input to global electroweak SM fits [11], which test the internal consistency of the SM.

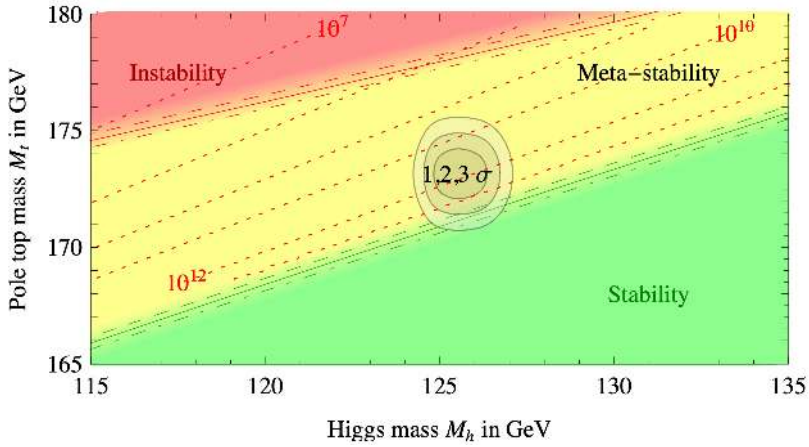

Figure 4.7 – Regions of absolute stability, meta-stability and instability of the SM vacuum in the m_t-m_H plane, in terms of parameter renormalized at the Planck scale [12].

The measurement of the Higgs boson mass using the full Run 2 dataset in the $H \to \gamma\gamma$ channel by ATLAS [14] is one of the main focuses of this thesis and will be described in great detail in Chapter 7. In Chapter 8, the combination of this result with the $H \to ZZ^* \to 4\ell$ measurement using the same dataset will also be presented, leading to the most precise determination of the Higgs boson mass from a single experiment to date [19].

This section provides an overview of the Higgs boson mass measurements performed during Run 1 of the LHC, focusing on the two channels that provided the most precise determinations. The mass measurement is primarily based on the $H \to \gamma\gamma$ and $H \to ZZ^* \to 4\ell$ channels, as they allow a full kinematic reconstruction of the final state with the best invariant mass resolution on the Higgs signal (1–2%):

- $\boldsymbol{H \to ZZ^* \to 4\ell}$: this channel provides an exceptionally clean signature with four isolated leptons (electrons or muons) in the final state, forming two pairs of opposite-sign, same-flavour leptons. The invariant mass of the four-lepton system can be reconstructed with high precision, enabling an accurate determination of the Higgs boson mass. The dominant background arises from continuum ZZ^* production; at lower masses, significant contributions also originate from Z+jets and $t\bar{t}$ production, where reconstructed lepton candidates either result from heavy-

flavour hadron decays or from jet mis-identification. Figure 4.8a shows the invariant mass distribution obtained with the full Run 1 dataset of the ATLAS experiment [115]. The combined measurement of the Higgs boson mass in this channel using the individual ATLAS [115] and CMS [116] Run 1 results yielded [13]:

$$m_{H\to 4\ell} = 125.15 \pm 0.40 \text{ GeV} = 125.15 \pm 0.37 \text{ (stat)} \pm 0.15 \text{ (syst) GeV}. \tag{4.3}$$

The more recent measurement of the Higgs boson mass using the full Run 2 dataset in the $H \to ZZ^* \to 4\ell$ channel by ATLAS [18] achieves a significantly improved precision, with an uncertainty reduced by approximately a factor of two compared to the Run 1 combined ATLAS and CMS result of Equation (4.3). This updated measurement and the analysis strategy will be discussed in more detail in Section 8.1.

- $\boldsymbol{H \to \gamma\gamma}$: the Higgs boson mass is extracted from the position of the narrow resonant peak in the diphoton invariant mass distribution, observed over a large, smoothly falling continuum background. The dominant irreducible background arises from QCD diphoton production, while reducible contributions originate from γ+jet and dijet events in which jets are misidentified as photons, as well as from Drell–Yan processes. The diphoton invariant mass is computed from the measured photon energies and directions with respect to the diphoton production vertex. To enhance the signal purity (with a signal-to-background ratio of $S/B \sim 1/50$ even after selection), events are required to contain two high-quality, isolated photons originating from the same primary vertex, with a reconstructed invariant mass in the range $m_{\gamma\gamma} \in [105, 160]$ GeV. *Identification* and *isolation* criteria (see Sections 5.1.5 to 5.1.8 for their definitions) based on calorimeter and tracking information are applied to suppress jet contamination. Figure 4.8b shows the invariant mass distribution obtained with the full Run 1 dataset of the ATLAS experiment [117]. The combined measurement of the Higgs boson mass in this channel using the individual ATLAS [117] and CMS [118] Run 1 results yielded [13]:

$$m_{H\to\gamma\gamma} = 125.07 \pm 0.29 \text{ GeV} = 125.07 \pm 0.25 \text{ (stat)} \pm 0.14 \text{ (syst) GeV}. \tag{4.4}$$

The Run 1 combined measurement of the Higgs boson mass in the $H \to \gamma\gamma$ and $H \to ZZ^* \to 4\ell$ channels with the ATLAS and CMS experiments gave as result [13]:

$$m_H = 125.09 \pm 0.24 \text{ GeV} = 125.09 \pm 0.21 \text{ (stat)} \pm 0.11 \text{ (syst) GeV}, \tag{4.5}$$

since then considered the nominal m_H value in the HEP community. The results obtained from the two individual channels and experiments and from their combination are summarised in Figure 4.9.

4.5 Higgs boson width

The SM predicts a very narrow natural decay width, Γ_H, for the Higgs boson of approximately 4.1 MeV [106] at $m_H = 125$ GeV, which is far too small to be measured directly

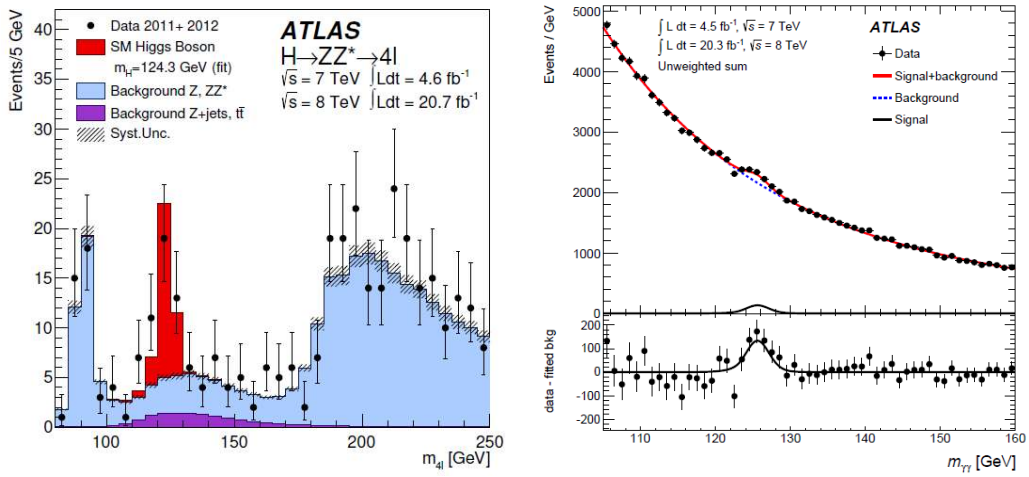

(a) $H \to ZZ^* \to 4\ell$ **(b)** $H \to \gamma\gamma$

Figure 4.8 – (a) Invariant mass distribution of the four-lepton system in the $H \to ZZ^* \to 4\ell$ channel observed by ATLAS using the full Run 1 dataset [115]. The black points correspond to the data, while the filled histograms show the expected SM signal (red) and background (blue and violet) contributions. (b) Invariant mass distribution of the diphoton system in the $H \to \gamma\gamma$ channel observed by ATLAS using the full Run 1 dataset [117]. The black points correspond to data; the fitted signal-plus-background model is shown in red, together with the background-only component (dashed blue line). The lower panel displays the residuals of the data with respect to the fitted background-only component.

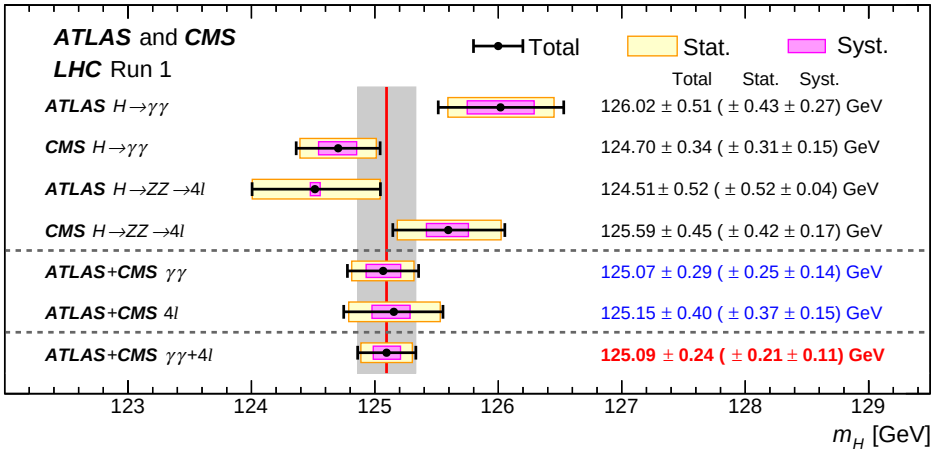

Figure 4.9 – Summary of the Higgs boson mass measurements from the $H \to \gamma\gamma$ and $H \to ZZ^* \to 4\ell$ channels by ATLAS and CMS using the full Run 1 dataset, and their combination [13]. The statistical component to the total uncertainty (black error bar) is highlighted in yellow, while the systematic contribution in pink.

on-shell at the LHC. However, the width can be indirectly constrained through studies of off-shell Higgs boson production in the $H \to ZZ^*$ channel. While Γ_H affects only the production cross section of an on-shell Higgs boson, the off-shell Higgs production rate is independent of Γ_H. Assuming that both on-shell and off-shell Higgs production follow the SM prediction (i.e. in the absence of contributions from new physics), Γ_H can be extracted by measuring the ratio of off-shell to on-shell cross sections. Using Run 2 data, both the ATLAS and CMS experiments successfully measured the total Higgs boson decay width for the first time: ATLAS obtained $\Gamma_H = 4.5^{+3.3}_{-2.5}$ MeV [119], while CMS measured $\Gamma_H = 3.2^{+2.4}_{-1.7}$ MeV [120], both results being consistent with the SM prediction. In addition to off-shell constraints in the $H \to ZZ$ channel, both experiments have also studied off-shell Higgs boson production in the $H \to WW \to \ell\nu\ell\nu$ final state. The ATLAS Collaboration reported constraints on off-shell production and the total Higgs boson width (observed (expected) upper bound at 95% confidence level of 13.1 (17.3) MeV) using the full Run 2 dataset in the WW channel [121], while the CMS Collaboration performed a direct extraction of Γ_H from off-shell measurements in $H \to WW \to e\nu\mu\nu$, obtaining $\Gamma_H = 3.9^{+2.7}_{-2.2}$ MeV [122]. These results provide complementary sensitivity to the $H \to ZZ$ channel and are consistent with the SM prediction. More recently, the ATLAS Collaboration reported updated constraints from a second-wave analysis of off-shell $H \to ZZ^*$ production, improving the sensitivity with refined analysis techniques [123]. Complementary constraints have also been derived by combining on-shell Higgs measurements with four top quarks production, which provides indirect sensitivity to Γ_H through the top Yukawa coupling [124]. These results further strengthen the overall consistency of the measured Higgs boson width with the SM.

4.6 Higgs boson spin, parity and charge conjugation

The determination of the *spin* (J) and the *charge conjugation* and *parity* (*CP*) quantum numbers of the Higgs boson is essential to confirm its identity as the SM scalar boson. In the SM, the Higgs boson is predicted to be a *CP*-even scalar particle with $J^{PC} = 0^{++}$. The charge conjugation quantum number can be constrained in a straightforward way. Photons are C-odd eigenstates ($C = -1$), and since charge conjugation is multiplicative, any particle decaying into a pair of photons must have $C = +1$. As the $H \to \gamma\gamma$ decay has been observed, the Higgs boson must therefore be a $C = +1$ state.

The Landau–Yang theorem [125] states that a massive spin-1 particle cannot decay into a pair of photons. Consequently, according to angular momentum conservation, a particle decaying into two photons must be either a spin-0 or a spin-2 boson. To discriminate between these possibilities, the angular distributions of the decay products in the $H \to \gamma\gamma$, $H \to ZZ^* \to 4\ell$ [126] and $H \to WW^* \to e\nu\mu\nu$ [127] channels have been studied. In particular, differential measurements of angular observables, such as $\cos\theta^*$ and related kinematic variables, provide strong sensitivity to the spin hypothesis. The diphoton channel played a key role in excluding spin-2 hypotheses, while the four-lepton channel provides the strongest sensitivity to the CP structure of the Higgs boson couplings. Results from both the ATLAS [126, 127] and CMS [128] experiments exclude several non-SM spin–parity configurations of the Higgs boson with a confidence level exceed-

ing 99.9% already using Run 1 data, firmly establishing the Higgs boson as a spin-0 particle, consistent with the SM prediction.
Concerning the CP quantum number, analyses of angular correlations in the $H \to ZZ^* \to 4\ell$ and $H \to WW^*$ channels exclude a pure CP-odd ($J^P = 0^-$) hypothesis at high confidence level. However, a scenario involving CP-mixing between CP-even and CP-odd components is not yet excluded and is the subject of ongoing precision studies. Overall, current measurements strongly favour the $J^P = 0^+$ assignment, consistent with the SM prediction.

4.7 Higgs boson signal strengths

The agreement between the cross sections and branching ratios predicted by the SM and those measured experimentally is often quantified using the *signal strength* μ. For a specific production process and decay mode $i \to H \to f$, the signal strengths for the production, μ_i, and for the decay, μ^f, are defined as

$$\mu_i = \frac{\sigma_i}{\sigma_i^{\text{SM}}}, \quad \mu^f = \frac{\mathcal{BR}^f}{\mathcal{BR}^f_{\text{SM}}}. \tag{4.6}$$

Here, σ_i denotes the measured production cross section for the process i (e.g. $i = \text{ggF}$, VBF, WH, ..., see Section 4.1), and $\mathcal{BR}^f$ is the measured branching ratio for the decay mode f (e.g. $f = b\bar{b}$, $\tau^+\tau^-$, $\gamma\gamma$, ..., see Section 4.2). The quantities σ_i^{SM} and $\mathcal{BR}^f_{\text{SM}}$ denote the corresponding SM predictions. A signal strength value of $\mu = 1$ indicates perfect agreement with the SM, while deviations from this value may point to new physics contributions affecting the Higgs boson production or decay rates.
Since σ_i and $\mathcal{BR}^f$ cannot be disentangled experimentally without additional assumptions, only the product of μ_i and μ^f can be directly measured, leading to a combined production-decay signal strength μ_i^f:

$$\mu_i^f = \mu_i \cdot \mu^f = \frac{\sigma_i \cdot \mathcal{BR}^f}{\sigma_i^{\text{SM}} \cdot \mathcal{BR}^f_{\text{SM}}}. \tag{4.7}$$

The simplest measurement that can be performed is to assume that all μ_i^f values are identical across the different production-decay combinations, so that the SM predictions in each bin are scaled by a single global signal strength μ (i.e. $\mu_i^f = \mu$). This parametrisation provides the most basic test of compatibility between the data and the SM expectations. The best-fit value obtained by ATLAS [129] using Run 2 data is

$$\mu = 1.05 \pm 0.06 = 1.05 \pm 0.03\,(\text{stat.}) \pm 0.03\,(\text{exp.}) \pm 0.04\,(\text{sig. th.}) \pm 0.02\,(\text{bkg. th.}), \tag{4.8}$$

where the total uncertainty is decomposed into contributions from statistical uncertainties (stat.), experimental systematic uncertainties (exp.), and theoretical uncertainties in the signal and background modelling. This result is compatible with the SM hypothesis

$\mu = 1$ within 1σ. For CMS [130], the best-fit value obtained using Run 2 data is

$$\mu = 1.002 \pm 0.057 = 1.002 \pm 0.029\,(\text{stat.}) \pm 0.036\,(\text{sig. th.}) \pm 0.033\,(\text{syst.}), \tag{4.9}$$

where the total uncertainty is decomposed into statistical, theoretical uncertainties in the signal prediction, and systematic uncertainties contributions. This result is also in excellent agreement with the SM prediction.
A more detailed approach consists of extracting the signal strength of each individual production process (or decay mode) by imposing $\forall f\ \mu^f = 1$ ($\forall i\ \mu_i = 1$), i.e. assuming that all decay branching ratios (production cross sections) are equal to their SM predictions while simultaneously fitting the μ_i (or μ^f) parameters. Figure 4.10 shows the individual signal strengths for the various Higgs boson production processes and decay modes measured by CMS using Run 2 data. Conversely, Figure 4.11 summarises the signal strengths for the different combinations of production and decay modes extracted from ATLAS Run 2 data. All these measurements exhibit excellent agreement with the SM predictions over several orders of magnitude.

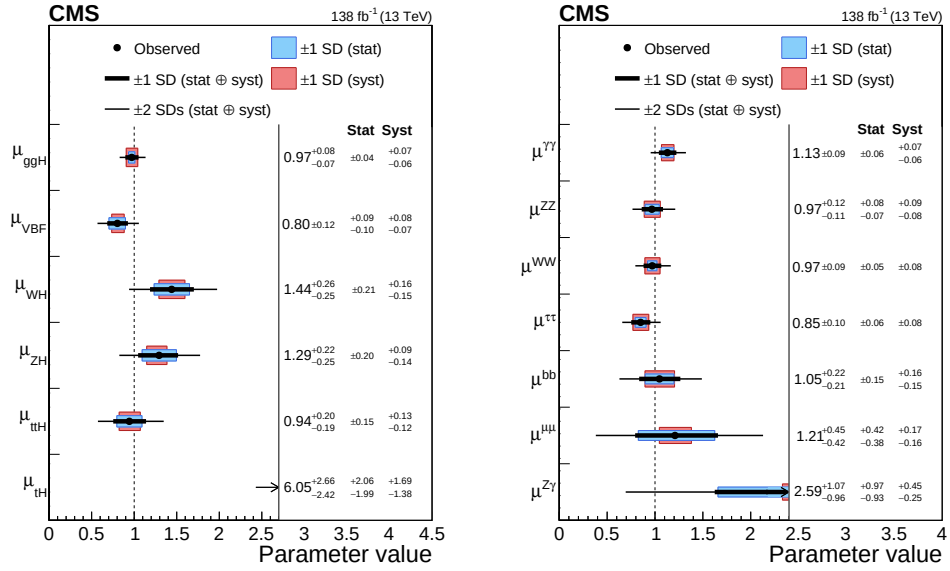

Figure 4.10 – Summary of signal strengths for various Higgs boson production modes (left) and decay processes (right), measured by CMS using Run 2 data [130]. The production signal strengths μ_i are determined assuming SM branching fractions, and vice versa. The uncertainties are shown as $1(2)\,\sigma$ confidence intervals, represented by the thick (thin) black lines. The statistical and systematic contributions to the total uncertainty are indicated by the blue and red bands, respectively.

While the signal strength provides a largely model-independent test of consistency with the SM, a more direct interpretation of the Higgs boson properties is obtained by expressing the measurements in terms of its fundamental couplings. In the κ framework, possible deviations from the SM expectations are parametrised through coupling modifiers (κ_i) that rescale the Higgs boson interactions with fermions and vector bosons.

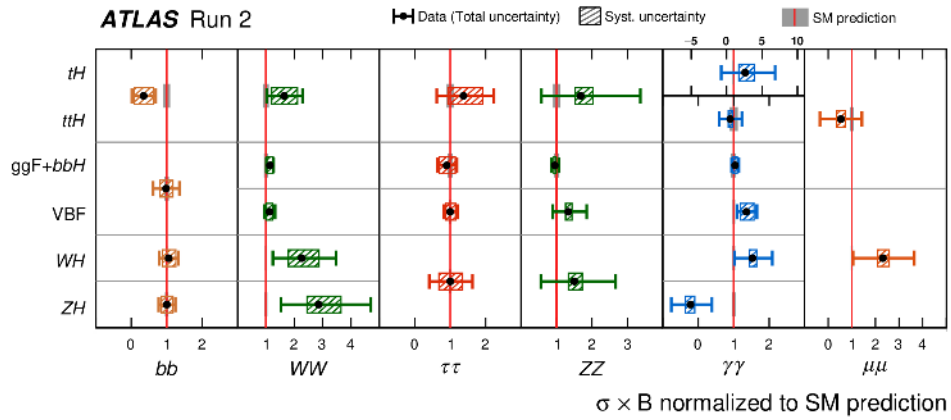

Figure 4.11 – Signal strengths for different combinations of Higgs boson production and decay modes measured by ATLAS using Run 2 data [129]. The central values are displayed together with the total uncertainty and its systematic component, highlighted by the coloured band.

A global combination of production and decay measurements allows the extraction of these modifiers and tests the mass-coupling relation predicted by the Higgs mechanism. Figure 4.12 shows the absolute coupling strengths as a function of the particle mass, as measured by the ATLAS and CMS collaborations using Run 2 data [129, 130]. The observed proportionality between coupling strength and particle mass over several orders of magnitude demonstrates a striking agreement with the SM prediction.

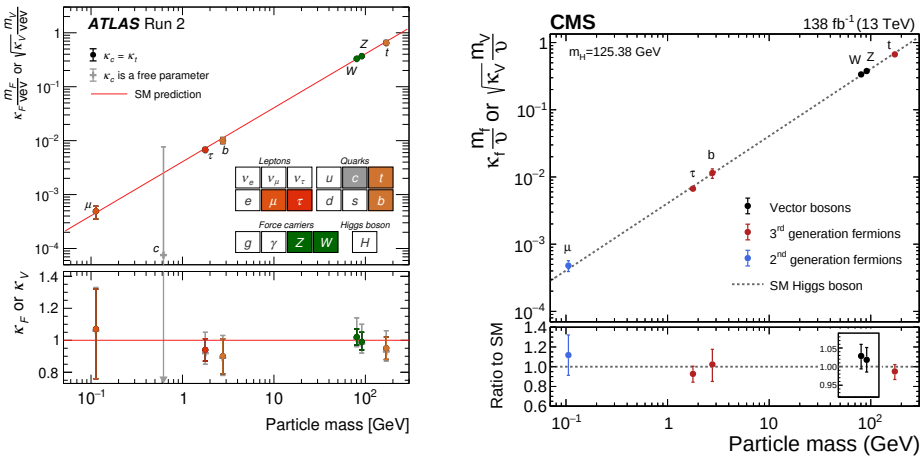

(a) **(b)**

Figure 4.12 – Summary of the coupling strength modifiers for the Higgs boson to different particles measured by ATLAS (4.12a) and (4.12b) using Run 2 data. In both cases, the absolute coupling strength modifiers are shown as a function of the mass of the probed particles, and the SM prediction is represented by the diagonal line.

5 Physics objects reconstruction with the ATLAS detector

The electrical signals generated by particles produced in the pp collisions and recorded by the ATLAS sub-detectors are digitised and stored for offline processing. The offline reconstruction of these events is performed by dedicated software algorithms, which transform the raw detector information into high-level physics objects such as photons, electrons, muons, and hadronic jets, to be used in physics analyses.

For instance, hits in the different layers of the ID (described in Section 3.3) or the MS (Section 3.5) are combined to form *tracks*. Conversely, energy deposits in the Calorimeters cells (Section 3.4), arising from electromagnetic and hadronic showers produced by incoming electrons, photons, and hadrons, are used to create *calorimetric clusters*. These low-level objects are then combined to reconstruct the final physics objects used in physics analyses. A schematic illustration of how information from the various sub-detectors is used to identify particles emerging from the pp collisions is shown in Figure 5.1.

Given that the analyses discussed in this thesis involve final states containing photons, electrons, and muons, particular attention will be devoted to the reconstruction of these objects. Nevertheless, a brief overview of the reconstruction of jets and missing transverse momentum will also be provided, as these objects are commonly used in many physics analyses. The reconstruction of electrons and photons is described in Section 5.1, that of muons in Section 5.2, jets in Section 5.3, and the reconstruction of the missing transverse momentum $E_{\mathrm{T}}^{\mathrm{miss}}$ in Section 5.4.

5.1 Electron and photon reconstruction

Electron and photon reconstruction in ATLAS is based on energy deposits almost fully contained within the EM Calorimeter, together with tracks and secondary vertices reconstructed in the ID. The procedure begins by forming clusters from energy deposits in topologically connected calorimeter cells (*topo-clusters*). Subsequent steps in the algorithm distinguish between electrons and photons, which may or may not have converted into an electron-positron pair in the ID material. Photons are classified as converted or unconverted depending on whether a conversion vertex is reconstructed. An overview of the electron and photon reconstruction workflow is shown in Figure 5.2.

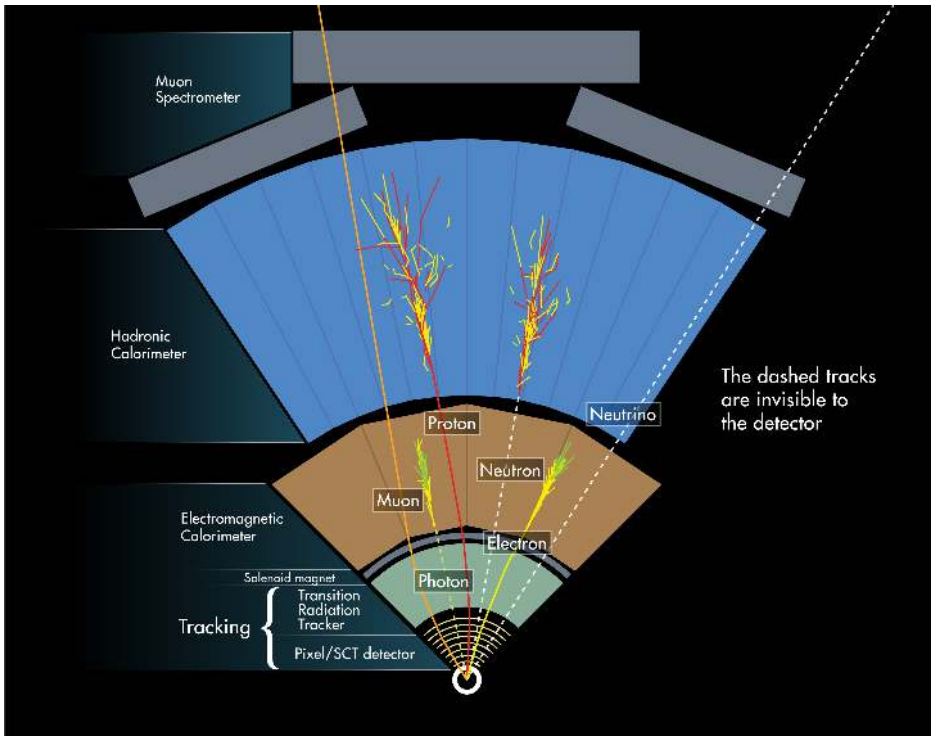

Figure 5.1 – Example signatures left in the ATLAS detector by different types of particles, shown in a cross sectional slice of the barrel region. The different sub-detectors are indicated, along with the reconstructed physics objects [131].

In the reconstruction process, tracks and candidate conversion vertices identified in the ID are matched to topo-clusters in the EM Calorimeter. Topo-clusters without associated tracks or conversion vertices are reconstructed as unconverted photons, while those matched to one or more conversion vertices give rise to converted photon candidates. Topo-clusters associated with at least one good quality track are identified as electron candidates.

The reconstruction of electron and photon candidates proceeds by forming *superclusters* from the matched topo-clusters. Superclusters are dynamic, variable-size clusters designed to collect energy from bremsstrahlung photons emitted by electrons and to merge the energy deposits from electron-positron pairs produced in photon conversions. Once superclusters are created, tracks are matched to electron superclusters and conversion vertices to photon superclusters. Because the superclustering procedure is run independently for electrons and photons, a single topo-cluster may seed both an electron and a photon supercluster. In such cases, both objects are reconstructed and flagged as ambiguous.

Finally, the physics objects used in analysis are built by resolving ambiguities, calibrating the electron and photon energies, and computing all quantities required for identification and isolation. A comprehensive description of the reconstruction algorithms is

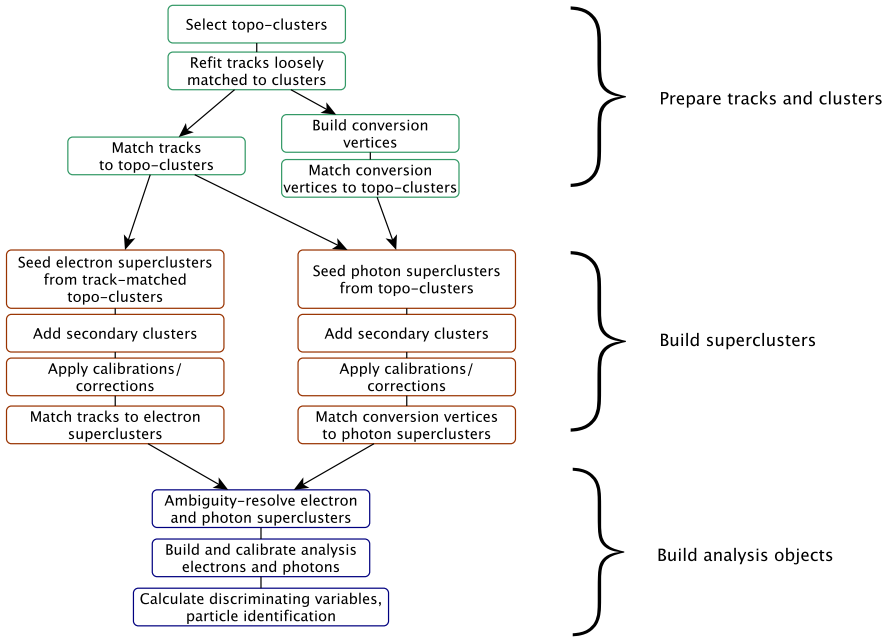

Figure 5.2 – Algorithm flow diagram for the electron and photon reconstruction [16].

provided in [16].

5.1.1 Energy clusters in the Electromagnetic Calorimeter

The lateral and longitudinal segmentation of the Calorimeters enables a three-dimensional reconstruction of particle showers, realised through the *topological clustering algorithm*, which forms variable-size energy clusters (*topo-clusters*) from topologically connected cells in the EM Calorimeter and constitutes the basis of electron and photon reconstruction [132].
The key quantity governing the formation of topo-clusters is the *significance* of a calorimeter cell, defined as

$$\zeta_{\text{cell}}^{\text{EM}} = \left| \frac{E_{\text{cell}}^{\text{EM}}}{\sigma_{\text{noise}}^{\text{EM}}} \right|, \tag{5.1}$$

where $E_{\text{cell}}^{\text{EM}}$ is the energy deposited in the cell and $\sigma_{\text{noise}}^{\text{EM}}$ is the expected noise, which accounts for both electronic read-out noise and contributions from pileup. The clustering algorithm scans the calorimeter map, selects seed cells, and grows clusters around them following the "4-2-0" scheme:

- Seed cells with $\zeta_{\text{cell}}^{\text{EM}} \geq 4$ are identified, excluding those in the Presampler and in Layer 1 of the EM Calorimeter;
- Neighbouring cells with $\zeta_{\text{cell}}^{\text{EM}} \geq 2$ are then collected around the seeds. If such a cell

is shared between two proto-clusters, the proto-clusters are merged into a single one;

- A surrounding "crown" of all nearest-neighbour cells with $\zeta_{\text{cell}}^{\text{EM}} \geq 0$ is added to the topo-cluster;
- Finally, topo-clusters containing two or more local maxima (cells with $E_{\text{cell}}^{\text{EM}} > 500\,\text{MeV}$ and at least four neighbours, none of which have a larger signal) are split into separate topo-clusters.

The energy of a topo-cluster is computed as the sum of the energies of its constituent cells, calibrated at the EM scale. Since the same clustering algorithm is used by ATLAS for the reconstruction of several physics objects (τ leptons, jets, etc.), topo-clusters may contain cells from both the EM and hadronic Calorimeters. To identify electromagnetic showers initiated by incoming photons or electrons, the EM component of the cluster is quantified as

$$f_{\text{EM}} = \frac{E_{\text{L1}} + E_{\text{L2}} + E_{\text{L3}}}{E_{\text{cluster}}}, \tag{5.2}$$

where E_{L1}, E_{L2}, and E_{L3} are the energies deposited in the three layers of the EM Calorimeter, and E_{cluster} is the total cluster energy. Clusters with $f_{\text{EM}} > 0.5$ are considered to originate from an electromagnetic shower, and cells from the hadronic Calorimeter are discarded. After removing the hadronic component, only topo-clusters with EM energy above 400 MeV are retained.

5.1.2 Track reconstruction and track-cluster matching

The next step in the reconstruction process is to select reconstructed tracks and photon-conversion vertices in the ID and to match them to topo-clusters in the EM Calorimeter. This track–cluster association provides the first discrimination between electrons, unconverted photons, and converted photons.

Track reconstruction is performed throughout the entire ID as part of the full event-reconstruction chain [133]. Charged particles traversing the detector deposit a small fraction of their energy through ionisation, producing electrical signals (*hits*) in the various detector layers. These hits are used to reconstruct the trajectories of charged particles, which follow helicoidal paths with radii inversely proportional to their momentum in the magnetic field in the ID (see Equation (2.3)).

The reconstruction of primary tracks produced by charged particles with lifetimes greater than 3×10^{-11} s and originating from the hard-scatter vertex is performed using an *inside-out* approach [134]. The process begins with the identification of track seeds, defined as groups of three hits in the Pixel detector and the SCT. Seeded track candidates are then extended by adding compatible hits from other ID layers using a Kalman filter algorithm [135]. A dedicated ambiguity-resolution procedure suppresses combinations of hits that do not correspond to a single particle (i.e. *fake tracks*) and resolves overlaps between candidates.

Tracks surviving the ambiguity-resolution step are refitted using a global χ^2 algorithm to obtain the final impact parameters. An attempt is then made to extend these silicon

tracks into the TRT: hits compatible with the extrapolated trajectory are added without modifying the original silicon segment.
A complementary *outside-in* procedure enhances the reconstruction efficiency for displaced tracks, such as those from photon conversions. Regions of interest in the EM Calorimeter are first identified, and hit segments reconstructed in the TRT are matched to them. These TRT segments are subsequently combined with short silicon seeds (two hits), forming track candidates through a procedure analogous to the inside-out reconstruction. A separate ambiguity-resolution step is applied to these candidates, followed by a global χ^2 refit to obtain the final track parameters.
The resulting track collection serves as the input to the vertex-finding algorithm [136], which identifies candidate primary and secondary vertices. Vertex positions are obtained by refitting the associated tracks with the constraint that they originate from the reconstructed vertex. Among the reconstructed primary vertices, the one with the highest sum of squared transverse momenta of its associated tracks is selected as the *hard-scatter vertex*. In $H \to \gamma\gamma$ analyses, however, the primary vertex is redefined according to the procedure described in Section 7.2.2.
Within the electron and photon reconstruction process, the standard tracking procedure is further refined to account for the substantial bremsstrahlung energy loss of electrons and to improve the identification of photon conversions. Fixed-size clusters in the EM Calorimeter compatible with electromagnetic showers define regions of interest. If track seeds without a matched primary track are found within these regions, a modified pattern-recognition algorithm—still based on the Kalman filter but allowing for up to 30% energy loss at each material intersection—is applied. Finally, all tracks are refitted using a global χ^2 algorithm, which permits additional energy loss where the standard fit fails.

Track-cluster matching

The next step in the reconstruction process involves matching the selected tracks to topo-clusters in the EM Calorimeter.
A preliminary *loose match* is performed between fixed-size EM clusters and reconstructed silicon tracks, based on spatial compatibility between the cluster barycentre and the track extrapolated to Layer 2 of the EM Calorimeter. A cluster is considered loosely matched to a track with reconstructed charge q if the following conditions are satisfied: $|\Delta\eta| < 0.05$ and $-0.20 < q \cdot (\phi_{\text{track}} - \phi_{\text{cluster}}) < 0.05$ when the track energy is used for the extrapolation from the last ID hit, or $-0.10 < q \cdot (\phi_{\text{track}} - \phi_{\text{cluster}}) < 0.05$ when the cluster energy is used for the extrapolation from the track perigee. The asymmetric requirement in $\Delta\phi$ accounts for bremsstrahlung photons that contribute to the calorimetric cluster but are not accounted for in the track reconstruction.
Silicon tracks satisfying the loose-match criteria are subsequently refitted using the Gaussian Sum Filter (GSF) algorithm [137], which provides improved track-parameter estimates. This refinement is particularly beneficial for low-p_{T} electrons and for electrons undergoing substantial bremsstrahlung energy loss.
The refitted tracks are then used for the final matching to the topo-clusters. A track with

reconstructed charge q is considered matched to a topo-cluster if, when extrapolated from its perigee to Layer 2 of the EM Calorimeter, it satisfies $|\Delta\eta| < 0.05$ and $-0.10 < q \cdot (\phi_{\text{track}} - \phi_{\text{cluster}}) < 0.05$. If multiple tracks satisfy these requirements for the same topo-cluster, a preferred track is selected based on the presence of pixel hits and on the smallest ΔR between the topo-cluster barycentre and the extrapolated track position at Layer 2. The properties of the electron candidate are then determined from this highest-ranking track.

Reconstruction of photon conversions

Tracks that are loosely matched to fixed-size EM clusters are used as input for the reconstruction of photon-conversion vertices in the ID. Two types of photon conversions are considered: *double-track* and *single-track* conversions.

- A *double-track* conversion vertex is formed from two oppositely charged tracks originating from a common point. Geometric criteria—such as the opening angle between the tracks, their separation at the point of closest approach, and their distance at the reconstructed vertex—ensure compatibility with the decay of a massless particle. Based on the presence of silicon hits, double-track conversions are classified as double silicon, silicon– TRT, or TRT– TRT, depending on whether both, one, or neither of the tracks has associated silicon information.

- *Single-track* conversions account for asymmetric conversions, in which one electron carries most of the original photon energy, or for conversions of highly energetic photons where the two tracks are too collimated to be resolved. These conversions typically occur at larger radii, where the TRT spatial resolution makes it more likely to miss one of the tracks. To reduce the misidentification of prompt electrons as single-track conversions, such vertices are reconstructed only when no hits are present in the innermost ID layer. In these cases, the innermost hit on the track is taken as the conversion vertex.

Conversion vertices are then matched to topo-clusters by extrapolating their associated tracks to Layer 2 of the EM Calorimeter and comparing their positions with the topo-cluster barycentre in η and ϕ. For conversions with at least one silicon track, a match is considered valid if $|\Delta\eta| < 0.05$ and $|\Delta\phi| < 0.05$. For conversions reconstructed exclusively from TRT tracks, the matching requirements depend on whether the first track lies in the barrel or in the endcaps. In the barrel, a match requires $|\Delta\eta| < 0.35$ and $|\Delta\phi| < 0.02$, while in the endcaps the corresponding criteria are $|\Delta\eta| < 0.20$ and $|\Delta\phi| < 0.02$.

If multiple conversion vertices are associated with a single topo-cluster, preference is given to double-track conversions with silicon hits, followed by other double-track candidates and finally single-track conversions. Within each category, the vertex with the smallest reconstructed conversion radius is selected as the most likely candidate.

5.1.3 Supercluster formation

The loosely matched topo-clusters and tracks serve as inputs to the *superclustering algorithm* [138], which operates in two distinct stages, described below.

Supercluster seeding The first stage scans the reconstructed topo-clusters to identify those suitable for initiating supercluster growth. Since the electron and photon reconstruction chains proceed independently, the seeding criteria differ for the two object types. Electron superclusters are seeded from topo-clusters with $E_{\mathrm{T}} > 1$ GeV that are matched to a track with at least four silicon hits in the ID. Conversely, photon superclusters are seeded from topo-clusters with no matched track and $E_{\mathrm{T}} > 1.5$ GeV.

Adding satellite topo-clusters In the second stage, the algorithm searches for satellite topo-clusters within a window of $\Delta\eta \times \Delta\phi = 0.075 \times 0.125$ centred on the seed topo-cluster barycentre. Only topo-clusters with lower E_{T} than the seed are considered as satellites. For electrons, additional satellite clusters may also be included within a larger window of $\Delta\eta \times \Delta\phi = 0.125 \times 0.3$, provided they have at least one matched track with silicon hits and are associated with the same best-matched track as the seed. For converted photons, satellite clusters are accepted if they are matched to the same conversion vertex as the seed or to one of the tracks associated with that vertex.
Figure 5.3 illustrates the satellite-cluster selection criteria for candidate electron and photon superclusters.

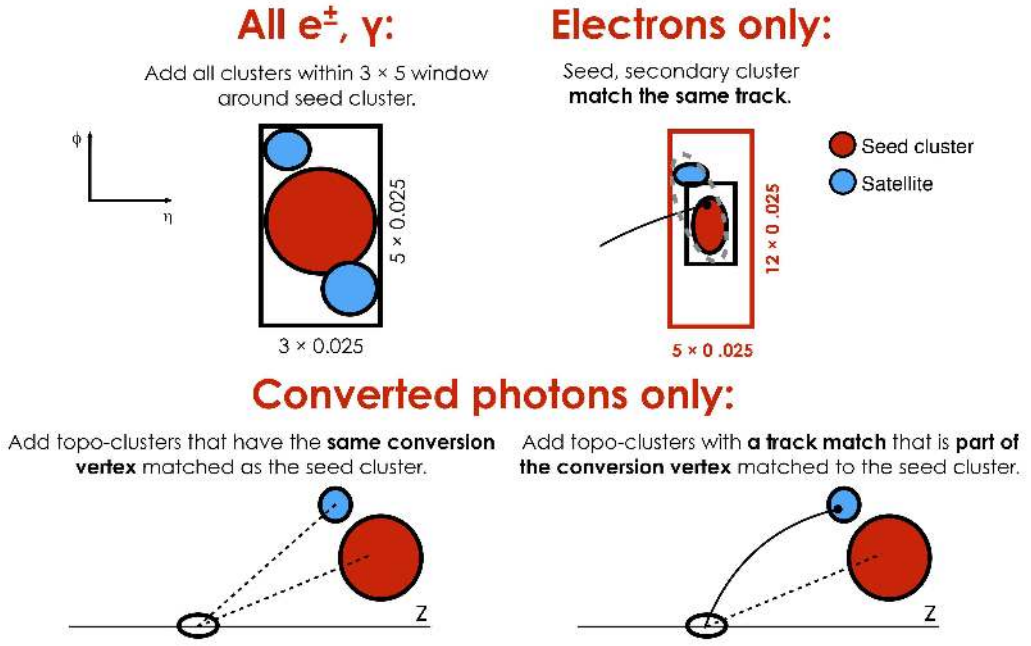

Figure 5.3 – Diagram of the superclustering algorithm for electrons and photons. Seed clusters are shown in red, satellite clusters in blue [16].

Supercluster formation Finally, the candidate electron and photon superclusters are formed by merging all the calorimeter cells from the seed topo-clusters and their associated satellites. The size of each constituent topo-cluster is constrained to a maximum width of 0.075 in the direction around its barycentre in the barrel (0.125 in the endcaps) of the EM Calorimeter. This constraint improves the estimation of systematic uncertainties related to the linearity of the energy response.

5.1.4 Preparation of electron and photon candidates for physics analysis

After the supercluster growth process is completed, tracks and conversion vertices are matched to electron and photon superclusters using the same procedures as for topo-clusters.

Since electron and photon superclusters are constructed independently, a single topo-cluster might serve as the seed for both an electron and a photon supercluster. To address this, an ambiguity resolution algorithm is applied to finalise the classification of the candidates, ensuring that each particle is correctly identified as an electron, a photon, or both. The simplest scenario involves a photon supercluster whose seed is not also matched to an electron supercluster: in this case, only a photon is reconstructed. Similarly, only an electron is reconstructed when an input electron supercluster does not share its seed with a photon. Otherwise, the following ambiguity resolution process (also summarised in Figure 5.4) is used to address the ambiguous cases:

- A given initially ambiguous object is classified only as a photon if its associated electron track has no hits in the silicon trackers, or, if that is the case, if it has no hits in the Pixel detector and is part of a matched double silicon conversion vertex.
- The object is flagged only as an electron if its track has four hits in the silicon trackers and is not part of a conversion vertex. Conversely, if a conversion vertex is found, the candidate particle is still reconstructed as an electron if the electron track has an innermost hit and the matched conversion vertex is not a double silicon vertex or, if that is the case, if at least one of its conversion tracks does not have an innermost hit. Finally, if the latter condition fails, an electron is reconstructed if its track is part of a silicon- TRT or a TRT- TRT conversion vertex whose radial distance with the innermost hit of the track is above 40 mm.
- Both an electron and a photon are reconstructed from the same initially ambiguous object if none of the previously described requirements are fulfilled or if the track p_{T} is smaller than 2 GeV or if $E^{\mathrm{cluster}}/p^{\mathrm{track}} > 10$. In such cases, the procedure still marks the initial candidate particle as ambiguous and each analysis is responsible for the final classification of such objects, depending on their specific requirements.

The construction of the final analysis objects is completed after their energy calibration, described in detail in Chapter 6 and the calculation of the discriminating variables for particle identification and isolation, discussed in the following Sections 5.1.5 to 5.1.8.

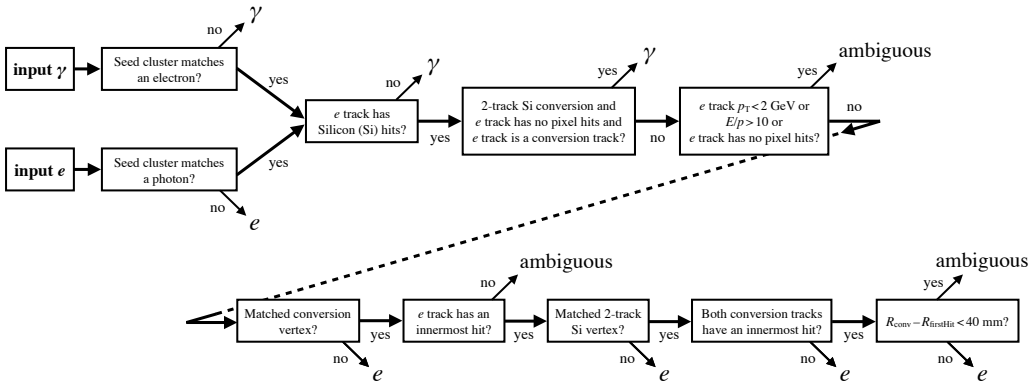

Figure 5.4 – Flowchart showing the logic of the ambiguity resolution for particles initially reconstructed both as electrons and photons. An *innermost hit* is a hit in the functioning pixel nearest to the beam-line along the track trajectory, E/p is the ratio of the supercluster energy to the measured momentum of the matched track, R_{conv} is the radial position of the conversion vertex, and R_{firstHit} is the smallest radial position of a hit in the track or tracks that make a conversion vertex [16].

5.1.5 Photon identification

The photon identification criteria are designed to efficiently distinguish *prompt photons* from *background photons* originating from hadron decays, typically within jets. Prompt photons are mainly produced in processes such as qg, $q\bar{q} \to \gamma + X$ in association with jets or qg, $q\bar{q} \to \gamma\gamma$, and more rarely through Higgs boson decays to photon pairs. Compared to hadronic jets, prompt photons produce narrow electromagnetic showers in the EM Calorimeter with limited energy leakage into the Hadronic Calorimeter.

The dominant background arises from energetic π^0 mesons within jets, which decay into two photons, $\pi^0 \to \gamma\gamma$. Thanks to the fine segmentation of the first layer of the EM Calorimeter, these decays can often be identified through the presence of two distinct local energy maxima, allowing for an efficient separation between such collimated photon pairs and genuine prompt photons.

Three photon identification Working Points (WP) — *Tight*, *Medium*, and *Loose* [16] — are defined through independent requirements on a set of discriminating calorimetric variables, known as *shower shapes*, shown in Table 5.1 for photons and for electrons. For electrons also discriminating variables related to track requirements are employed, as explained in Section 5.1.6. These variables exploit the characteristic differences between prompt-photon and jet-induced showers: prompt photons produce compact, well-contained energy deposits, whereas jet-induced showers tend to be wider, deeper, and more irregular. Consequently, observables sensitive to the lateral shower width in η and ϕ, to the hadronic leakage, and to the detailed structure of the shower in the finely segmented EM Layer 1 provide strong discriminating power in photon identification.

The *Loose* identification WP exploits variables such as R_{had}, R_{had_1}, R_η, and w_{η_2}, defined in the Table 5.1, and was used for photon triggers during the 2015 and 2016 data-taking periods of Run 2. The *Medium* working point adds a loose requirement on E_{ratio} and be-

Category	Description	Name	Usage
Hadronic leakage	Ratio of E_T in the first layer of the hadronic calorimeter to E_T of the EM cluster (used for $\|\eta\| < 0.8$ and $\|\eta\| > 1.37$)	R_{had1}	e/γ
	Ratio of E_T in the hadronic calorimeter to E_T of the EM cluster (used for $0.8 < \|\eta\| < 1.37$)	R_{had}	e/γ
EM third layer	Ratio of the energy in the third layer to the total energy in the EM calorimeter	f_3	e
EM second layer	Ratio of the sum of the energies of the cells contained in a 3×7 $\eta \times \phi$ rectangle to that in a 7×7 rectangle, both centred on the most energetic cell	R_η	e/γ
	Lateral shower width, $\frac{\sum E_i \eta_i^2}{\sum E_i} - \left(\frac{\sum E_i \eta_i}{\sum E_i}\right)^2$, computed in a 3×5 cell window	$w_{\eta 2}$	e/γ
	Ratio of the sum of the energies of the cells in a 3×3 rectangle to that in a 3×7 rectangle	R_ϕ	e/γ
EM first layer	Total lateral shower width, $\frac{\sum E_i (i - i_{max})^2}{\sum E_i}$, computed in a window of $\Delta\eta \simeq 0.0625$	$w_{s,tot}$	e/γ
	Lateral shower width in a 3-cell window around the highest-energy cell	$w_{s,3}$	γ
	Energy fraction outside the core of three central cells, within seven cells	f_{side}	γ
	Difference between the energy of the second maximum and the minimum between the first and second maxima	ΔE_s	γ
	Ratio of the energy difference between the first and second maxima to their sum	E_{ratio}	e/γ
	Ratio of the energy measured in the first layer to the total EM cluster energy	f_1	e/γ
Track conditions	Number of hits in the innermost pixel layer	$n_{innermost}$	e
	Number of hits in the pixel detector	n_{Pixel}	e
	Total number of hits in the pixel and SCT detectors	n_{Si}	e
	Transverse impact parameter relative to the beam line	d_0	e
	Significance of the transverse impact parameter	$\|d_0/\sigma(d_0)\|$	e
	Relative momentum loss between the perigee and the last measurement point	$\Delta p/p$	e
	Likelihood probability based on transition radiation in the TRT	eProbabilityHT	e
Track–cluster matching	$\Delta\eta$ between the EM first-layer cluster position and the extrapolated track	$\Delta\eta_1$	e
	Charge-weighted $\Delta\phi$ between the EM second-layer cluster and the extrapolated track	$\Delta\phi_{res}$	e
	Ratio of cluster energy to track momentum	E/p	e

Table 5.1 – Discriminating variables used for electron and photon identification. The usage column indicates if the variables are used for the identification of electrons, photons, or both [16].

came the main photon-trigger selection in early 2017 in order to maintain an acceptable trigger rate. The *Tight* WP is applied to a subset of photons passing the *Medium* selection and introduces additional requirements on R_η and R_ϕ (which describe the shower spread in the η and ϕ directions in Layer 2), on $w_{s,3}$ and $w_{s\ \mathrm{tot}}$ (characterising the lateral shower width in Layer 1), on f_{side} (the fraction of energy in the strip "crown" relative to its core), on ΔE_s (sensitive to the presence of double maxima within a single shower), and on f_1 (the fraction of the photon energy deposited in Layer 1).
Examples of trigger efficiencies for the primary diphoton triggers in Run 2 are shown in Figure 5.5 as a function of E_{T}, η, and $\langle\mu\rangle$.

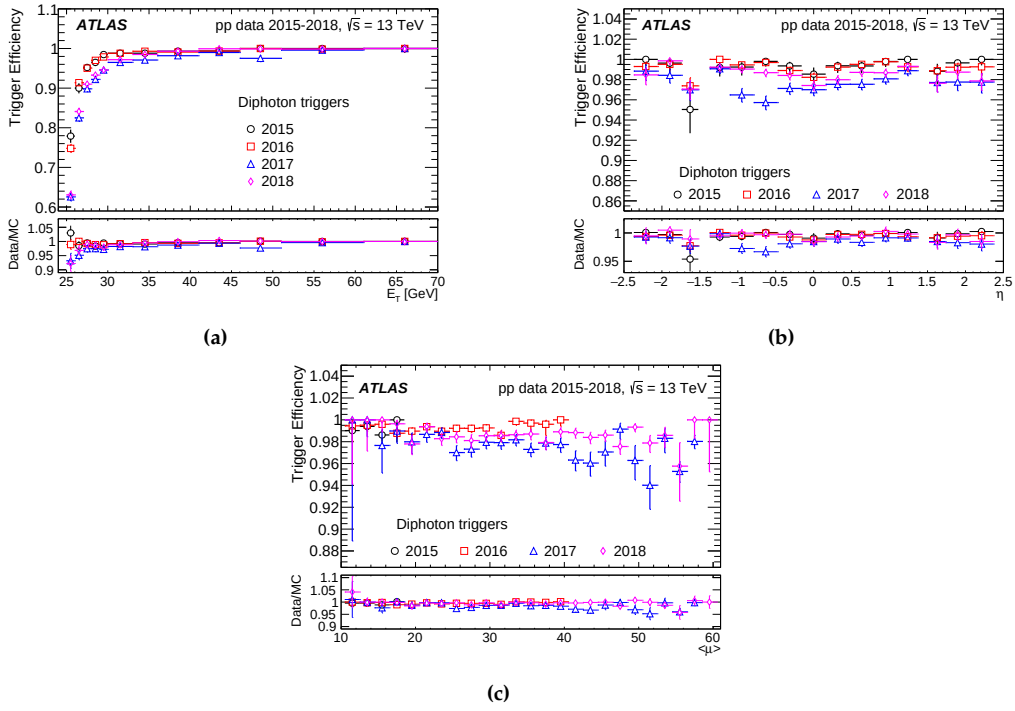

Figure 5.5 – Efficiencies of the 25 GeV leg of primary diphoton triggers in 2015-2018 as a function of the offline photon (a) E_{T}, (b) η and (c) $\langle\mu\rangle$ The ratios of data to Monte Carlo (MC) simulation efficiencies are also shown. The efficiency is computed with respect to offline photons satisfying *Tight* identification criteria and a 'calorimeter-only *Tight*' isolation requirement. Offline photon candidates in the calorimeter transition region $1.37 < |\eta| < 1.52$ are not considered. For (b) and (c), only offline candidates with $E_{\mathrm{T}} > 30$ GeV are used. The error bars indicate statistical and systematic uncertainties combined in quadrature [139].

The selection criteria for the three WPs are optimised separately in different pseudorapidity intervals to account for variations in calorimeter geometry and upstream material with $|\eta|$, which affect the shower-shape observables. In addition, the optimisation of the *Tight* working point is performed as a function of photon E_{T}. Compared to the previous E_{T}-independent strategy, this approach increases the *Tight* selection efficiency by up to 20% for photons with $E_{\mathrm{T}} < 30$ GeV while simultaneously improving the background

rejection at high E_T [16].
The 2 T solenoidal magnetic field bends the trajectories of the electron-positron pairs produced in photon conversions within the ID, resulting in wider electromagnetic showers along the ϕ direction compared to those of unconverted photons. For this reason, the *Tight* identification criteria applies dedicated requirements for converted and unconverted photons.
The *Loose* photon identification is optimised to achieve a $\sim$ 99% efficiency for photons with $E_T > 40$ GeV, with a corresponding background-rejection factor of about 1000 [16, 140, 141]. In contrast, the *Tight* selection achieves an efficiency of about 85% for photons with $E_T > 40$ GeV, increasing to approximately 92% for unconverted photons and 95% for converted photons when $E_T > 100$ GeV, as shown in Figures 5.6 and 5.7. The background-rejection factor for the *Tight* working point is around 5000 [16, 140, 141].
The photon-identification efficiency in data is measured using three complementary methods. The first relies on isolated photons collected with prescaled single-photon triggers, with the jet background estimated through control regions (matrix method). The second uses photons radiated from leptons in $Z \to \ell\ell\gamma$ decays, with ℓ being an electron or a muon (radiative Z method). The third employs electrons from $Z \to ee$ decays, whose shower shapes are transformed to resemble those of photons (electron extrapolation method). The resulting efficiency measurements for the *Tight* identification requirement are shown in Figures 5.6 and 5.7, based on Run 2 data [142]. These methods cover complementary E_T ranges: up to $\sim$ 100 GeV for the radiative-Z method, from 25 to 200 GeV for the electron-extrapolation method (reflecting the E_T spectrum of electrons from Z decays), and up to the TeV scale for the matrix method.
Data-to- MC scale factors are derived from these methods, and their uncertainties are propagated as systematic uncertainties in photon identification. As shown in the bottom panels of Figures 5.6 and 5.7, the scale factors differ from unity by up to 3-4% at $E_T = 10$ GeV and by at most 1-2% for $E_T > 40$ GeV, with the uncertainty decreasing from about 10% at $E_T = 10$ GeV to below 1-2% at higher E_T. To correct the photon-identification efficiency in simulation, the scale factors obtained from the three methods are combined using a weighted average in each $(|\eta|, E_T)$ bin of the photon.

5.1.6 Electron identification

As for photons, the identification procedure for electrons is required to discriminate *prompt electrons* from energy deposits originating from hadronic jets, converted photons, or real electrons produced in hadron decays. The discriminating variables, illustrated in Table 5.1, include the same shower-shape observables used for photon identification, together with additional quantities derived from the ID. The primary electron track must satisfy specific requirements on the number of hits in the innermost tracking layers and in the SCT. The track transverse impact parameter and its significance contribute to the discrimination, together with the track momentum resolution ($\Delta p/p$) and particle-identification information from the TRT.
The Run 2 electron identification algorithm is based on a multivariate likelihood discriminant, constructed from the likelihoods that a reconstructed electron originates from

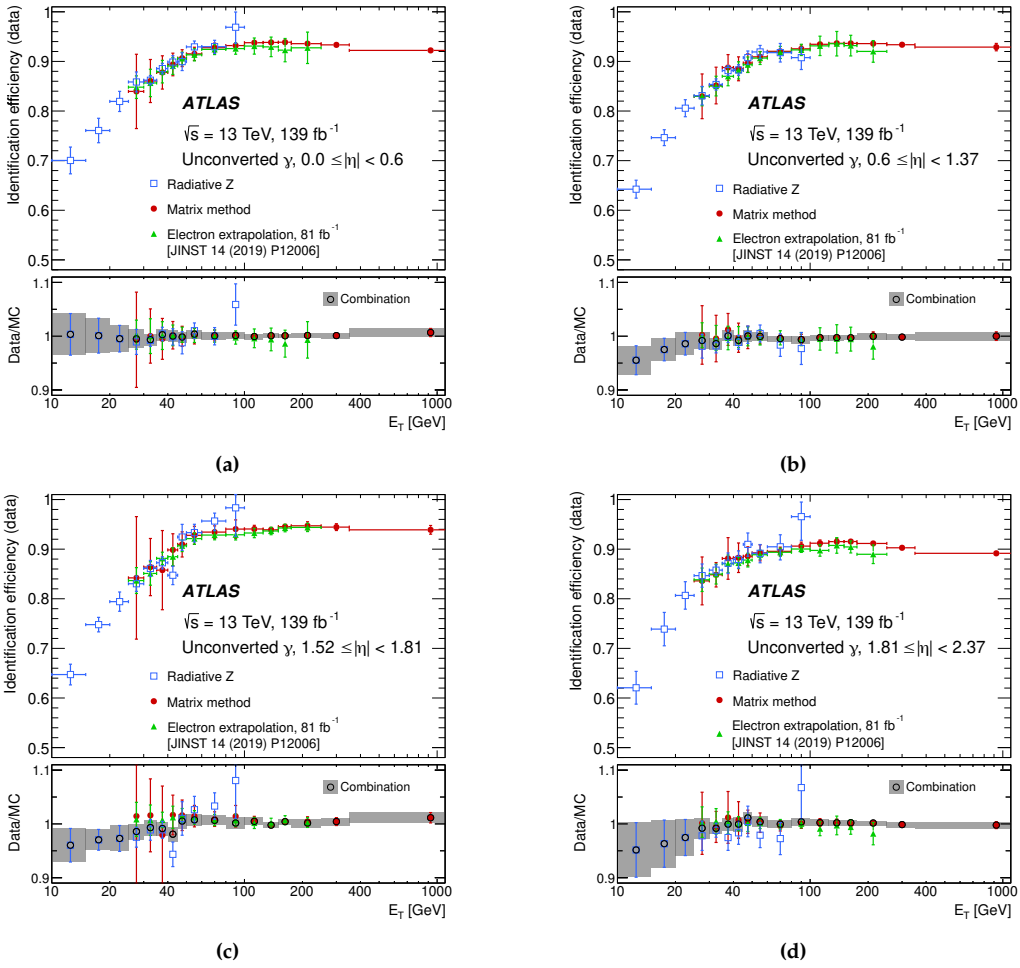

Figure 5.6 – The *Tight* photon identification efficiency measured in data, and the ratio of data-to- MC simulation efficiencies, for unconverted photons with a *Loose* isolation requirement applied as preselection, as a function of E_{T} in four different $|\eta|$ regions. Efficiencies are derived using three different measurement methods. The bottom panels also provide the combined scale factor, calculated as a weighted average of the individual scale factors, together with its total uncertainty, represented by the shaded area [142].

signal, L_s, or from background, L_b. These likelihoods are obtained from probability density functions P, built by smoothing histograms of the n discriminating variables with an adaptive kernel density estimator, separately for signal and background and in several $|\eta|$ and E_{T} bins:

$$L_{s(b)}(\mathbf{x}) = \prod_{i=1}^{n} P_{s(b),i}(x_i), \tag{5.3}$$

where $\mathbf{x}$ is the vector of discriminating variables and $P_{s(b),i}(x_i)$ are the corresponding signal or background probability densities. The likelihood discriminant is then defined

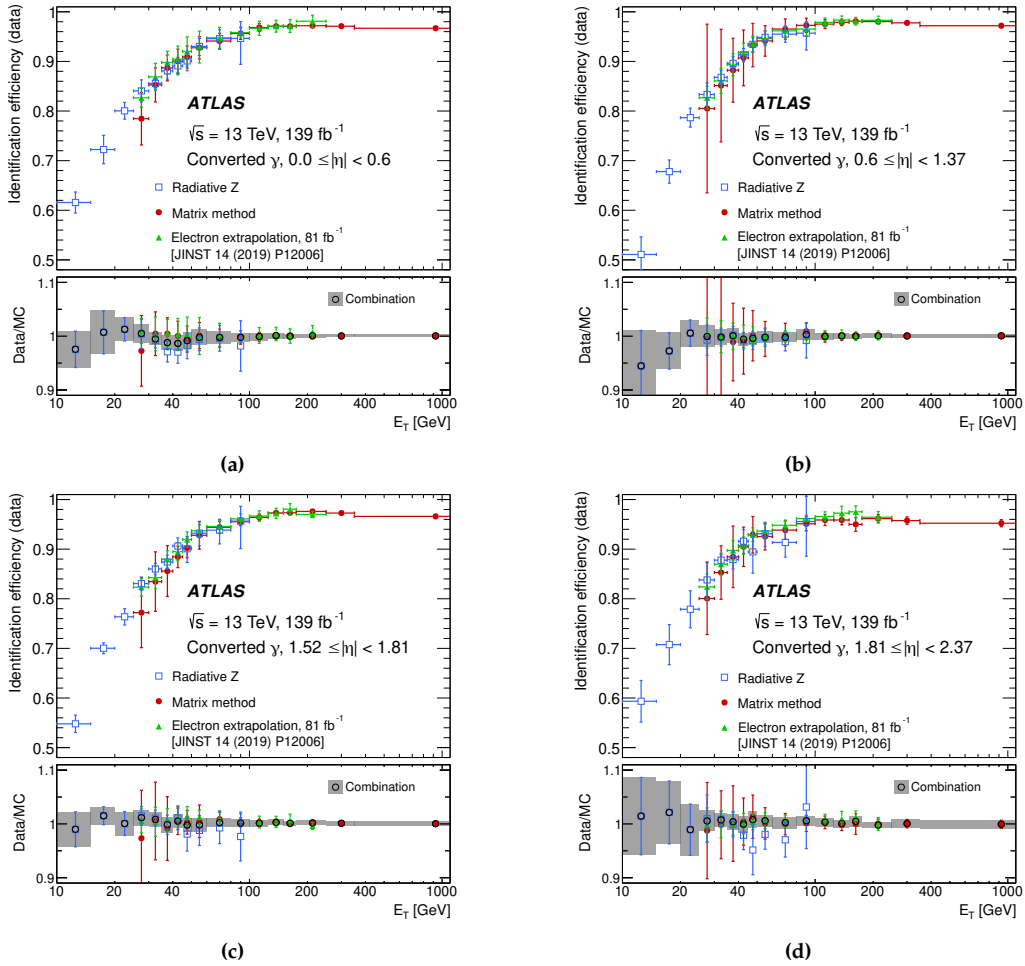

Figure 5.7 – The *Tight* photon identification efficiency measured in data, and the ratio of data-to- MC simulation efficiencies, for converted photons with a *Loose* isolation requirement applied as preselection, as a function of E_{T} in four different $|\eta|$ regions. Efficiencies are derived using three different measurement methods. The bottom panels also provide the combined scale factor, calculated as a weighted average of the individual scale factors, together with its total uncertainty, represented by the shaded area [142].

as the ratio of the two likelihoods:

$$d_L = \frac{L_s}{L_b}. \tag{5.4}$$

The probability density functions are derived with a data-driven method, using $Z \to ee$ and $J/\psi \to ee$ events for the signal component and dijet events for the background. Electron likelihood identification imposes a requirement on d_L. Three WPs with increasing background-rejection power and decreasing signal efficiency are defined: *Loose*, *Medium*, and *Tight*. The resulting identification efficiencies as a function of E_{T} and η are shown in Figure 5.8 for Run 2 and in Figure 5.9 for a partial Run 3 dataset.

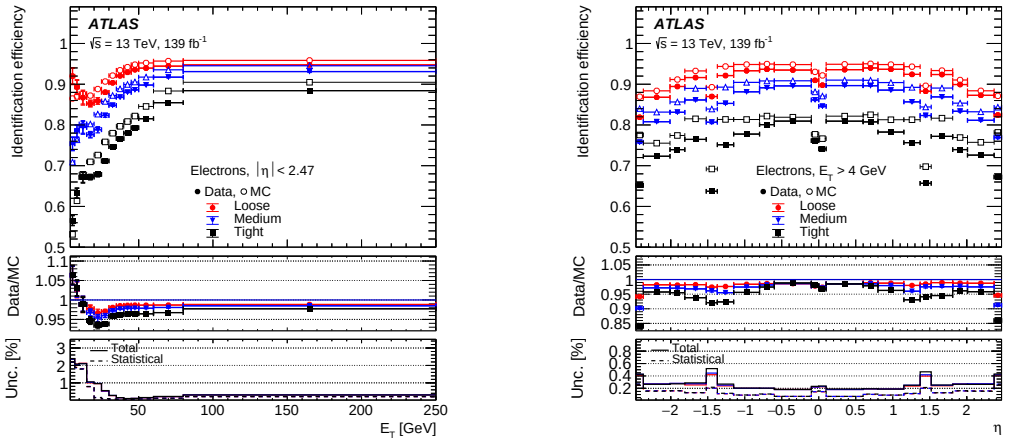

(a) **(b)**

Figure 5.8 – Identification efficiencies of electrons from $Z \to ee$ decays in Run 2 (2015-2018 data at 13 TeV corresponding to an integrated luminosity of $L = 139$ fb^{-1}) as a function of the electron's (a) transverse momentum and (b) pseudorapidity for the different identification working points. The top panels show the efficiencies obtained in data and simulation with their statistical and total uncertainties displayed as inner and outer error bars. The middle panels show their ratio that is applied as correction factor in analyses. The bottom panels show the statistical and the total uncertainties in the data/ MC ratio [142].

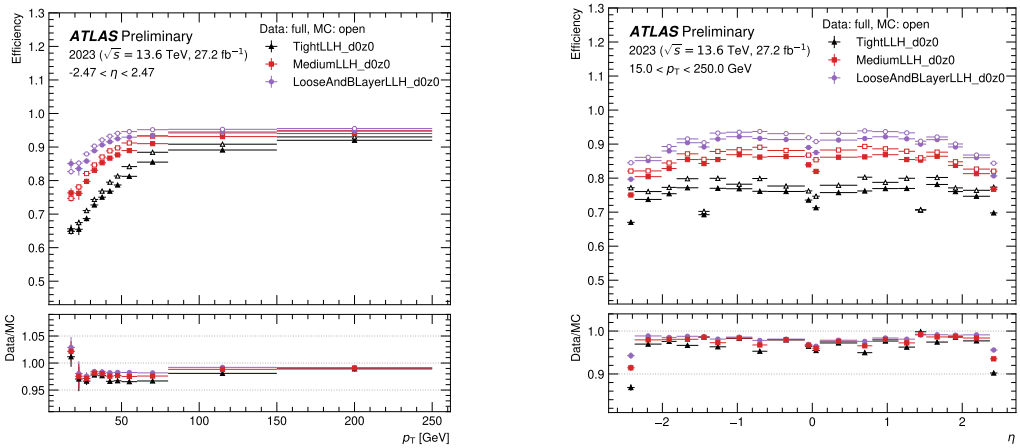

(a) **(b)**

Figure 5.9 – Identification efficiencies of electrons from $Z \to ee$ decays in Run 3 (2023 data at 13.6 TeV corresponding to an integrated luminosity of $L = 27.2$ fb^{-1}) as a function of the electron's (a) transverse momentum and (b) pseudorapidity for the different identification working points. The top panels show the efficiencies obtained in data and simulation with their statistical and total uncertainties displayed as inner and outer error bars. The bottom panels show the Data-to- MC ratio that is applied as correction factor in analyses [143].

5.1.7 Photon isolation

A typical photon from a $H \to \gamma\gamma$ decay is expected to be surrounded by minimal hadronic activity; isolation requirements on candidate photons are therefore used to further suppress the background from fake photons. The hadronic activity around a photon candidate is quantified using nearby energy deposits in the calorimeters or close-by tracks reconstructed in the ID. The idea is to measure the detector signals within a fixed distance of the photon direction and require that the surrounding activity remains small compared to the photon's own energy. Two classes of variables are used to evaluate photon isolation:

- *Calorimeter isolation*: $E_{\mathrm{T}}^{\mathrm{cone0.2}}$ is defined as the scalar sum of the transverse energy of all topo-clusters whose barycentre lies within a cone of radius $\Delta R = 0.2$ around the photon supercluster barycentre. The photon's own contribution is removed by subtracting the energy stored in a core window of size $\Delta\eta \times \Delta\phi = 0.125 \times 0.175$. Additional corrections account for photon energy leakage outside the core region, as well as for pileup and underlying-event contributions. Other calorimetric isolation variables follow the same definition but with larger cone sizes, such as $E_{\mathrm{T}}^{\mathrm{cone0.4}}$.
- *Track isolation*: The track-based isolation variable $p_{\mathrm{T}}^{\mathrm{cone0.2}}$ is computed as the scalar sum of the transverse momenta of all selected tracks within a cone of radius $\Delta R = 0.2$ around the photon direction. Tracks matched to a photon conversion are excluded for converted candidates. Selected tracks must satisfy $p_{\mathrm{T}} > 1\,\mathrm{GeV}$, $|\eta| < 2.5$, and be consistent with originating from the primary vertex.

Three photon-isolation working points are defined from specific requirements on calorimeter and track isolation, as summarised in Table 5.2 for Run 2. The photon isolation efficiency is measured using two complementary methods: radiative $Z \to \ell\ell\gamma$ decays and inclusive-photon data, following an approach analogous to that used for photon identification. Results from both methods are combined to produce a single set of scale factors for each WP, data-taking year, and photon-conversion category. Figure 5.10 shows the isolation efficiency from the $Z \to \ell\ell\gamma$ measurement as a function of E_{T}, η, and conversion status, together with the corresponding data-to- MC efficiency ratios.

Working point	Calorimeter isolation	Track isolation
Loose	$E_{\mathrm{T}}^{\mathrm{cone20}} < 0.065 \times E_{\mathrm{T}}$	$p_{\mathrm{T}}^{\mathrm{cone20}} / E_{\mathrm{T}} < 0.05$
Tight	$E_{\mathrm{T}}^{\mathrm{cone40}} < 0.022 \times E_{\mathrm{T}} + 2.45\,\mathrm{GeV}$	$p_{\mathrm{T}}^{\mathrm{cone20}} / E_{\mathrm{T}} < 0.05$
TightCaloOnly	$E_{\mathrm{T}}^{\mathrm{cone40}} < 0.022 \times E_{\mathrm{T}} + 2.45\,\mathrm{GeV}$	–

Table 5.2 – Definition of the photon isolation working points [16] in Run 2.

5.1.8 Electron isolation

To further distinguish signal electrons from background, electrons are required to be well isolated from surrounding hadronic activity. Electron isolation is quantified using both

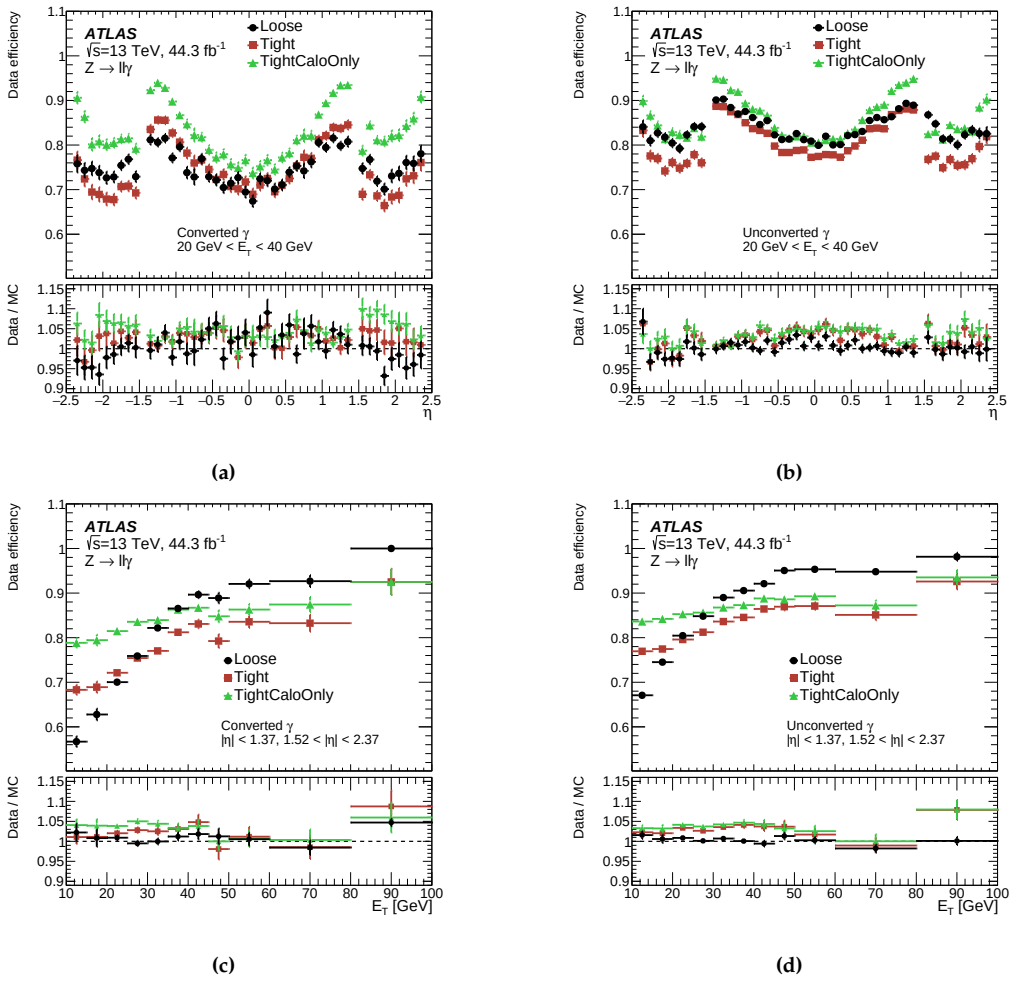

Figure 5.10 – Efficiency of the isolation working points defined in Table 5.2, using $Z \to \ell\ell\gamma$ events, for converted (left) and unconverted (right) photons as a function of photon η (top) and E_{T} (bottom). The lower panel shows the ratio of the efficiencies measured in data and in simulation. The total uncertainty is shown, including the statistical and systematic components [16].

calorimetric and track-based variables, for instance, $E_{\mathrm{T}}^{\mathrm{cone0.2}}$ and $p_T^{\mathrm{varcone0.2}}$. The calorimetric isolation, $E_T^{\mathrm{cone0.2}}$, is calculated, as for photons, as the scalar sum of the energy from all topo-clusters within a cone of radius $\Delta R = 0.2$ around the electron supercluster barycentre, corrected for the electron's own energy leakage and pileup contributions. The track isolation, $p_T^{\mathrm{varcone0.2}}$, sums the transverse momenta of all nearby tracks originating from the primary vertex, excluding the electron's track. A variable-sized cone, dependent on the electron's transverse momentum, is used to calculate $p_T^{\mathrm{varcone0.2}}$: this allows to take into account decays of heavy particles (such as the top quark), where high-p_{T} electrons are produced in close proximity to other decay products.

Further details on electron isolation algorithms are provided in Refs. [16, 142].

5.2 Muon reconstruction

The muon reconstruction [144] is based primarily on information from the ID and MS tracking detectors, with additional input from the Calorimeters. The reconstruction of charged particles in the ID is already described in Section 5.1.2 and in [134].
The first step of muon reconstruction involves the identification of local track segments in the MS, built from hits in the various muon chambers. These segments are then combined into preliminary MS track candidates using a global χ^2 fit, with loose pointing constraints to the IP and a parabolic approximation of the muon trajectory in the magnetic field. During this process, outlier hits are removed and additional compatible hits along the trajectory are included if they were not part of the initial candidate. The resulting tracks are subsequently refitted with a loose IP constraint, accounting for energy loss in the Calorimeters, and then back-extrapolated to the beam line. The transverse momentum of the extrapolated track is finally expressed at the IP.
The next step involves combining MS tracks with silicon tracks reconstructed in the ID to form muon candidates. Muon reconstruction follows five main strategies, corresponding to different muon *types*:

- *Combined (CB) muons* are built by matching MS tracks to ID tracks and performing a combined fit using hits from both detectors, while accounting for the energy loss in the Calorimeters. Based on the trajectory obtained from this fit, the association of MS hits may be updated and the fit repeated to refine the track parameters;
- *Inside-out (IO) combined muons* are reconstructed with a complementary inside-out algorithm that extrapolates ID tracks to the MS and requires at least three loosely aligned MS hits. The ID track, the Calorimeter energy loss, and the matched MS hits are then used in a combined track fit. Since this method does not rely on an independently reconstructed MS track, it recovers efficiency in regions with limited MS coverage and for low-p_{T} muons that may not reach the middle MS station.
- *Muon-spectrometer extrapolated (ME) muons* are formed by extrapolating MS tracks to the beamline when it cannot be matched to any ID track. Such muons are used to extend the acceptance outside that of the ID, thus fully exploiting the full MS coverage up to $|\eta| < 2.7$.
- *Segment-tagged (ST) muons* are reconstructed by requiring that an ID track extrapolated to the MS satisfies tight angular matching requirements to at least one reconstructed MS segment. This method recovers efficiency for low-p_{T} muons that may not reach the outer MS stations or for muons traversing regions with limited MS coverage.
- *Calorimeter-tagged (CT) muons* are built by associating ID tracks with minimum-ionising particle signatures in the Calorimeters. While the other muon reconstruction algorithms make use of ID tracks with p_{T} down to 2 GeV, a p_{T} threshold of 5 GeV is applied for CT muon reconstruction due to the large background contamination at low-p_{T}.

These different strategies ensure efficient muon reconstruction across a wide range of kinematic regions, maximising the muon reconstruction acceptance. While CB muons offer the highest purity, other types such as ST or CT muons help recover efficiency in regions with limited detector coverage or for low-p_{T} muons, even if with lower purity.

5.2.1 Muon momentum calibration

The muon momentum scale and resolution are studied using $J/\psi \to \mu\mu$ and $Z \to \mu\mu$ decays, by comparing the reconstructed invariant mass distributions in data and MC simulations [20].

The first step is the correction of the charge-dependent momentum scale in data. Even after dedicated alignment procedures, small residual misalignments in the ID and MS can introduce differences in the measured momentum of positively and negatively charged muons. This charge-dependent bias can be approximated as

$$\frac{q}{\hat{p}} = \frac{q}{p} + q \cdot \delta_s, \tag{5.5}$$

where $q = \pm 1$ is the muon charge, p and $\hat{p}$ are the corrected and uncorrected muon momenta, and δ_s denotes the sagitta bias. By comparing the invariant-mass distribution of muon pairs from Z-boson decays in data and simulation, a non-zero δ_s manifests as an additional broadening of the $m_{\mu\mu}$ resolution in data. Fitting the $m_{\mu\mu}$ spectrum in bins of muon η and ϕ allows the extraction of δ_s as a function of these variables, which is then used to correct the muon momentum in data. Before the corrections, the biases are up to 0.4 TeV^{-1} in certain detector regions. With this method, the biases are reduced to less than $2 \cdot 10^{-4}$ TeV^{-1} in all regions of the detector.

After the charge-dependent correction, the muon momentum calibration procedure addresses residual differences in the momentum scale and resolution between data and simulation.

A set of correction factors is derived in bins of muon η and ϕ by comparing the invariant-mass distributions of muon pairs from J/ψ and Z decays in data and simulation. The momentum scales corrects for inaccuracy in the description of the magnetic field integral and the dimension of the detector in the direction perpendicular to the magnetic field. They also model the effect from the inaccuracy in the simulation of the energy loss in the Calorimeter and other materials between the IP and the exit of the MS.

The muon resolution corrections account for the various effects that degrade the momentum resolution in data. They include fluctuations in the energy loss of muons traversing the detector material, the impact of multiple scattering and imperfections in the magnetic-field modelling, and the intrinsic limitations arising from the spatial resolution of the tracking detectors and residual misalignments. These contributions are parametrised and applied as additional smearing terms to bring the simulated muon momentum resolution into agreement with that observed in data.

The samples of $J/\psi \to \mu\mu$, $\Upsilon \to \mu\mu$ (statistically fully independent, not used in the correction factors derivation) and $Z \to \mu\mu$ decays are used to validate the momentum corrections and measure the muon momentum reconstruction performance. The invari-

ant mass distributions for the $J/\psi \to \mu\mu$, $Z \to \mu\mu$ and $\Upsilon \to \mu\mu$ candidates are shown in Figure 5.11 and compared with corrected simulation. The lineshapes of the resonances in simulation agree with the data within the systematic uncertainties, demonstrating the overall effectiveness of the p_{T} calibration. For $Z \to \mu\mu$ decays, the uncertainty in the momentum scale varies from a minimum of 0.05% for $|\eta| < 1$ to a maximum of 0.15% for $|\eta| \sim 2.5$. The dimuon mass resolution is about 1.3% (1.6%) at small values of pseudorapidity for J/ψ (Z) decays, and increases up to 2.1% (2.4%) in the endcaps. This corresponds to a relative muon p_{T} resolution of 1.8% (2.3%) at small values of pseudorapidity and 3.0% (3.4%) in the endcaps for J/ψ (Z) decays [20].

5.3 Jet reconstruction

Quarks and gluons are produced abundantly in pp collisions at the LHC, either through underlying-event activity or directly from the hard-scattering process. However, because of colour confinement (see Section 1.1.2), these particles cannot be observed individually in the final state. Instead, the fragmentation and hadronization of a colored parton give rise to a collimated spray of hadrons traveling in the direction of the original parton, commonly referred to as a jet.

5.3.1 Particle flow jets

Jets are collimated sprays of hadrons produced by the fragmentation and hadronization of energetic quarks and gluons. Since charged particles leave tracks in the ID and both charged and neutral hadrons deposit energy in the Calorimeters, jet reconstruction benefits from combining information from multiple sub-detectors.

ATLAS adopts a particle-flow (PFlow) strategy [145, 146], which aims to reconstruct all stable particles in the event by matching tracks to calorimeter energy clusters. Low-momentum charged particles are measured with the superior momentum resolution of the ID, while the Calorimeters provide accurate energy measurements at higher energies, a wider pseudorapidity coverage, and the ability to detect neutral particles. The ID also offers excellent angular resolution and allows matching tracks to the primary vertex, which is essential for pileup mitigation. After individual particle-flow objects are built—ideally representing the set of hadrons originating from a single parton—they serve as inputs for jet clustering. This results in improved jet energy and angular resolution relative to calorimeter-only reconstruction.

A practical challenge of the particle-flow approach is avoiding energy double-counting. Calorimeter deposits associated with charged particles already reconstructed via tracking must be subtracted without affecting nearby energy clusters. Achieving robust and accurate subtraction is a central aspect of the PFlow algorithm and critical for maintaining reliable jet energy measurements in high pileup environments.

Particle flow algorithm Topo-clusters, built from energy deposits in the ATLAS Calorimeters using the "4-2-0" scheme described in Section 5.1.1, together with tracks reconstructed in the ID, serve as inputs to the particle-flow algorithm. The algorithm proceeds

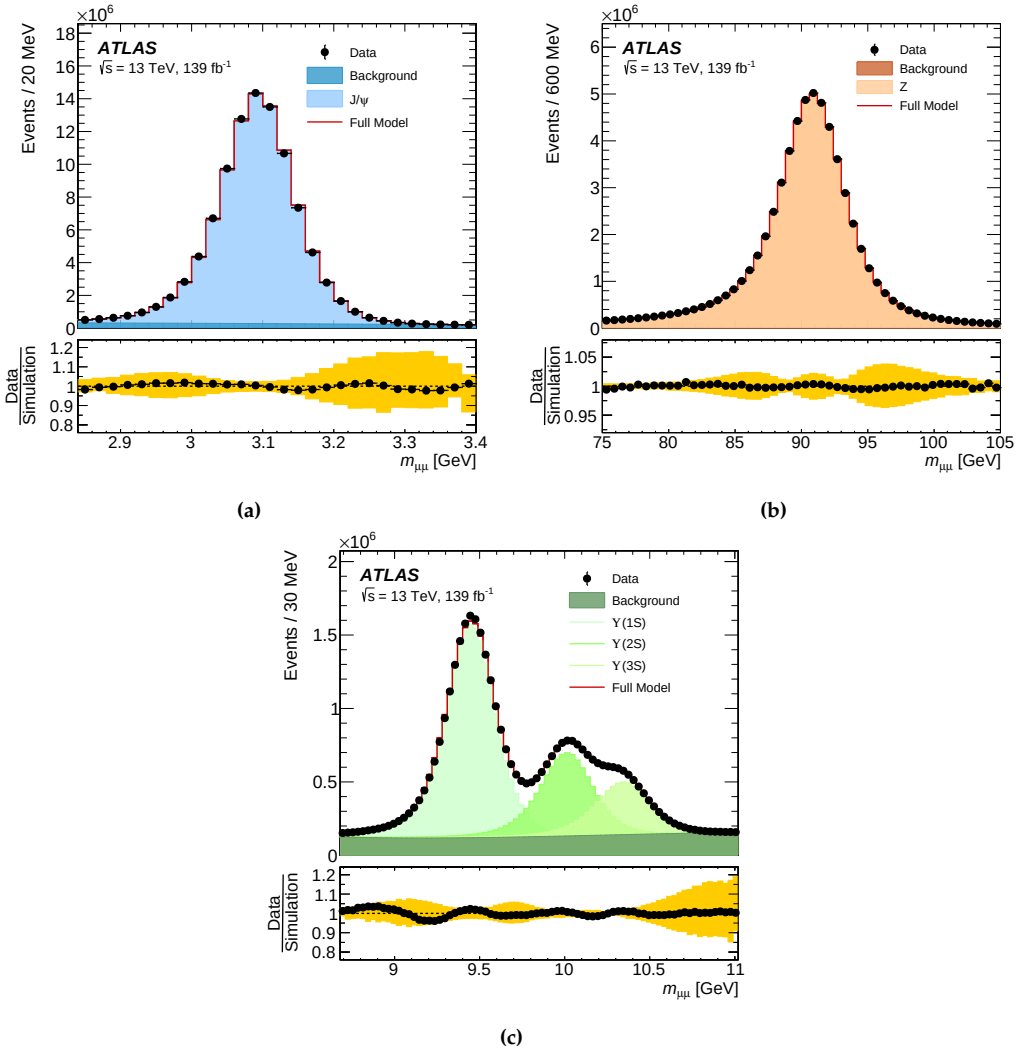

Figure 5.11 – Dimuon invariant mass distribution of (a) $J/\psi \to \mu\mu$, (b) $Z \to \mu\mu$ and (c) $\Upsilon \to \mu\mu$ candidate events reconstructed with CB muons. The upper panels show the invariant mass distribution for data and for the signal simulation plus the background estimate. The points show the data. The continuous line corresponds to the simulation with the MC momentum corrections applied. Background estimates are added to the signal simulation. The bands represent the effect of the systematic uncertainties in the MC momentum corrections. The lower panels show the ratios of the data to the MC simulation. In the Z sample, the MC background samples are added to the signal sample according to their expected cross-sections. The sum of background and signal MC distributions is normalised to the data [20].

through the following steps:

- **Track selection:** Tracks are required to meet strict quality criteria: at least nine silicon hits with no missing Pixel hits where expected, $0.5 < p_{\mathrm{T}} < 40$ GeV, and

$|\eta| < 2.5$. Very high-p_{T} tracks are excluded because they are often not sufficiently isolated, making an accurate subtraction of the associated calorimeter energy more difficult. Tracks matched to electron or muon candidates are also removed, as the algorithm is optimised for handling hadronic energy deposits.

- **Track–topo-cluster matching:** Each selected track is matched to a single topo-cluster. Candidate clusters must satisfy $E_{\mathrm{cluster}}/p_{\mathrm{track}} > 0.1$, where E_{cluster} is the topo-cluster energy and p_{track} the track momentum. Among these, the best match is chosen as the cluster with the smallest $\Delta R' = \sqrt{(\Delta\eta/\sigma_\eta)^2 + (\Delta\phi/\sigma_\phi)^2}$, where σ_η and σ_ϕ are the expected topo-cluster resolutions in η and ϕ, respectively.
- **Expected energy deposit:** The expected calorimeter energy deposit of a charged particle with momentum p_{track} is estimated as $\langle E_{\mathrm{dep}} \rangle = p_{\mathrm{track}} \cdot \langle E^{\mathrm{ref}}_{\mathrm{clus}}/p^{\mathrm{ref}}_{\mathrm{track}} \rangle$, where the reference energy-to-momentum ratios are derived from single-pion simulation samples.
- **Recovering split showers:** Since a particle may leave energy in multiple topo-clusters, the algorithm checks whether additional clusters should be associated with the track. This is done by comparing the matched topo-cluster energy with the expected energy deposit and evaluating the significance of their difference.
- **Cell-by-cell subtraction:** The estimated calorimeter energy associated with the particle is subtracted from the matched topo-clusters on a cell-by-cell basis.
- **Remnant removal:** If the remaining energy is consistent with expected shower fluctuations for a single particle, any residual topo-cluster energy is removed. This procedure is applied to tracks ordered by decreasing p_{T}, starting from those matched to a single cluster.

After these steps, summarised in Figure 5.12, the selected ID tracks and the surviving topo-clusters ideally represent the reconstructed event, with no double-counting of energy between the sub-detectors.

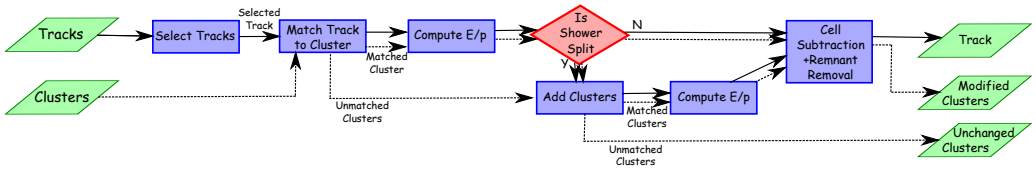

Figure 5.12 – A flow chart of how the particle flow algorithm proceeds, starting with track selection and continuing until the energy associated with the selected tracks has been removed from the calorimeter. At the end, charged particles, topo-clusters which have not been modified by the algorithm, and remnants of topo-clusters which have had part of their energy removed remain, in addition to clusters unchanged by the particle flow algorithm [145].

Jet clustering and reconstruction Particle-flow objects, defined from the topo-clusters that survive the subtraction procedure together with tracks associated to the hard-scattering vertex, are used as inputs for jet reconstruction.

ATLAS employs the anti-k_t algorithm [147] for jet clustering. This algorithm is infrared- and collinear-safe, meaning that the number and structure of reconstructed jets remain stable against the emission of soft or collinear particles, thus ensuring finite cross-section predictions at all perturbative orders.
The clustering of particle-flow objects into jets is governed by two distance measures, d_i and d_{ij}, defined as:

$$d_i = \frac{1}{p_{\mathrm{T},i}^2}, \qquad d_{ij} = \min\left(\frac{1}{p_{\mathrm{T},i}^2}, \frac{1}{p_{\mathrm{T},j}^2}\right)\frac{\Delta R_{ij}^2}{R^2}, \tag{5.6}$$

where $p_{\mathrm{T},i}$ and $p_{\mathrm{T},j}$ are the transverse momenta of particle-flow objects i and j, ΔR_{ij} is their separation in the η–ϕ plane, and R is a radius parameter that sets the characteristic jet size.
The algorithm computes all pairwise distances and compares them to the individual distances d_i. If $d_{ij} < d_i$, objects i and j are merged into a new object, which replaces them in the input set. If instead $d_{ij} > d_i$, object i is identified as a jet and removed from the list of clustering inputs. After each step, all relevant distances are recalculated. The procedure iterates until no further merging is possible.

5.3.2 Jet energy calibration

The calibration of jets in ATLAS is performed in several consecutive steps to correct for detector effects and to ensure that the reconstructed jet energy accurately reflects the energy of the corresponding particle-level jet. The first correction removes contributions from pileup and underlying-event activity, providing an estimate of the jet energy that originates only from the hard-scattering process. A simulation-based calibration is then applied to account for the non-compensating calorimeter response, dead material, and the dependence of the jet energy scale on η and p_{T}. Additional jet-by-jet corrections, known as the Global Sequential Calibration (GSC), exploit the internal structure of the jet—such as its energy distribution or the number of associated tracks—to further improve the energy resolution. Finally, data-driven *in situ* techniques are used to correct residual differences between data and simulation. These methods rely on momentum balance in γ+jet, Z+jet, and di-jet events, where the companion object is well calibrated. After applying all calibration steps, the jet energy scale and resolution achieve high accuracy across the full detector acceptance, ensuring reliable use of jets in physics analyses. After the full calibration procedure, the jet energy scale is known to the level of a few percent over a wide range of p_{T} and η, with a typical jet energy resolution of about 10–15% at $p_{\mathrm{T}} \sim 30$ GeV, improving to a few percent at high transverse momentum.

5.4 Missing transverse momentum reconstruction

The presence of neutrinos or potential new BSM particles that interact weakly with detector material can only be inferred through momentum imbalance in the transverse plane. Since the total transverse momentum in a pp collision is expected to be zero, any

undetectable particles produced would result in a missing transverse momentum, $E_{\mathrm{T}}^{\mathrm{miss}}$, measured within the ATLAS detector.
The $E_{\mathrm{T}}^{\mathrm{miss}}$ is an event-level quantity, calculated as the negative vector sum of the transverse momenta of all reconstructed objects in an event [148]. The $E_{\mathrm{T}}^{\mathrm{miss}}$ components along the x and y axes are defined as:

$$E_{x(y)}^{\mathrm{miss}} = -\sum_{\text{electrons}} E_{x(y)}^{e} - \sum_{\text{photons}} E_{x(y)}^{\gamma} - \sum_{\text{muons}} E_{x(y)}^{\mu} - \sum_{\text{jets}} E_{x(y)}^{\text{jet}} - \sum_{\text{taus}} E_{x(y)}^{\tau} - E_{x(y)}^{\text{soft}}, \quad (5.7)$$

where $E_{x(y)}^{i}$ represents the $x(y)$ component of the calibrated energy of physics object type i, and $E_{x(y)}^{\text{soft}}$ refers to contributions from tracks with $p_{\mathrm{T}} > 0.5$ GeV and $|\eta| < 2.5$, originating from the primary vertex but not associated with any reconstructed object. The magnitude of the missing transverse momentum and its azimuthal angle are given by:

$$E_{\mathrm{T}}^{\mathrm{miss}} = \sqrt{(E_x^{\mathrm{miss}})^2 + (E_y^{\mathrm{miss}})^2}, \quad \phi^{\mathrm{miss}} = \arctan\left(\frac{E_y^{\mathrm{miss}}}{E_x^{\mathrm{miss}}}\right). \quad (5.8)$$

6 Electron and photon energy calibration

Optimal energy reconstruction and calibration of the EM Calorimeter are essential for all analyses involving electrons and photons, and particularly for precise measurements of the masses and properties of the Higgs, W, and Z bosons. This applies, for instance, to the Higgs boson mass measurement in the $H \to \gamma\gamma$ channel described in Chapter 7, where the achievable mass accuracy is directly driven by the photon energy calibration, and to the search for Higgs boson decays into a low-mass dilepton pair and a photon (Chapter 9), where the energy resolution strongly influences the overall analysis sensitivity.

The measurement of photon and electron energies in the EM calorimeter is affected by several detector-related effects. These include energy leakage outside the reconstructed supercluster due to its finite lateral and longitudinal size, as well as energy losses caused by inactive material located both upstream of the calorimeter (such as the beam pipe, the ID, and the solenoid magnet) and within the calorimeter itself (e.g. the lead absorber plates). Longitudinal energy leakage is negligible over most of the energy range considered and becomes relevant only at very high energies. The amount of material traversed by a particle, expressed in units of radiation lengths X/X_0, as a function of $|\eta|$ in the nominal simulation is shown in Figure 6.1.

As a consequence, the simple sum of the energy deposited in the calorimeter cells, E_{raw}, is biased with respect to the true particle energy, E_{true}. A dedicated calibration procedure is therefore required to correct for these effects and restore an unbiased estimate of the incident electron or photon energy. In addition, the calorimeter response in data and in MC simulation must be equalised to perform accurate precision measurements.

The electron and photon energy calibration procedure developed by the ATLAS Collaboration for Run 2 data is described in the following Sections, closely following the documentation in Ref. [17] and schematised in Figure 6.2. My personal contribution focused on one of the first steps of the calibration chain (step 2 in Figure 6.2): the training, maintenance, and optimisation of the multivariate Monte Carlo-based energy calibration described in Section 6.3. This calibration had not been updated since 2017; I revised and re-optimised it for the full Run 2 data-taking conditions and extended it to the Run 3 detector and simulation configuration.

6.1 Energy reconstruction in the EM Calorimeter

As electrons and photons traverse the EM Calorimeter, they interact with the detector material and initiate electromagnetic showers. The e^+/e^- in the showers ionise the

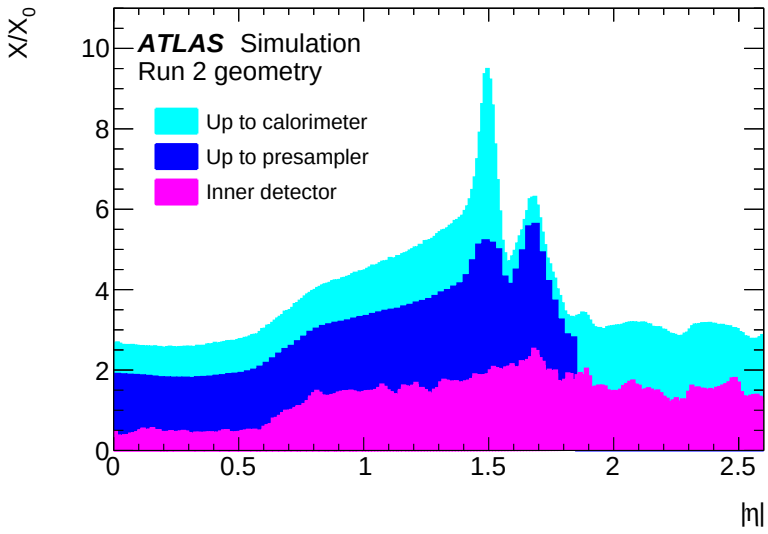

Figure 6.1 – Amount of material traversed by a particle, in units of radiation lengths X/X_0, as a function of $|\eta|$ in the nominal simulation [17].

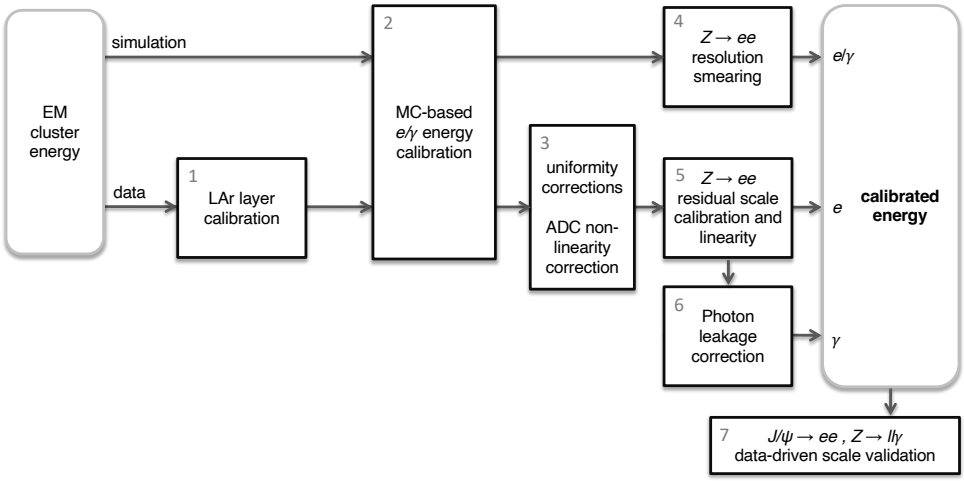

Figure 6.2 – Schematic overview of the electron and photon energy calibration procedure in ATLAS [17].

LAr in the active layers, producing an ionisation current proportional to the deposited energy. The electrons and ions drift under a constant electric field towards the copper electrodes located between the active and absorber layers, as shown in Figure 3.6a. The resulting ionisation pulse has a triangular shape and is read out by the Front End Boards (FEBs) of the LAr Calorimeter, which amplify and shape the signal using a CR-RC^2 fil-

ter. Three overlapping amplification gains (Low, Medium, and High) are implemented to accommodate the large dynamic range of electron and photon energies. Upon an L1 trigger accept, the signal is digitised using the most appropriate gain and transmitted off-detector to the high-level trigger and data-acquisition systems.
The samples of the shaped pulse are converted into the deposited energy in each cell, $E_{\text{raw}}^{\text{cell}}$, using a linear combination of the first four digitised samples after subtraction of the pedestal contribution (measured in dedicated calibration runs). The coefficients of this linear combination are obtained through an optimal filtering algorithm [149, 150], which maximises the energy and timing resolution. The resulting signal is then corrected using a set of calibration constants—derived from calibration runs, simulations, and test-beam measurements—including the cell gain, corrections accounting for the different responses to ionisation and calibration pulses and the conversion factors from digital counts to energy.

6.2 LAr layer calibration

Since the EM Calorimeter is segmented in depth, the scale of each longitudinal layer must be determined separately to provide an accurate description of the Calorimeter response as a function of E_{T}. The raw energy of reconstructed electrons and photons in data is calibrated to ensure that the response of each EM layer to incoming particles matches that observed in the simulation. This procedure involves determining an energy scale for the Presampler, α_{PS}, the relative responses of the first and second accordion layers (L1 and L2), α_{12}, and a global scale factor derived from an *in-situ* measurement using electrons from Z-boson decays, described in Section 6.5.

6.2.1 Presampler energy scale

The presampler energy scale, α_{PS}, is defined as the ratio of the presampler energies between data and simulation. In earlier calibrations [151], it was determined using samples of electrons and photons; however, in the final Run 2 calibration [17] it was measured using muon candidates from $W \to \mu\nu$ and $Z \to \mu\mu$ events selected in a low-pileup data sample ($\langle\mu\rangle \approx 2$). Muon energy deposits are largely insensitive to the amount of material upstream of the presampler and therefore provide a direct measurement of the presampler response, decoupling the uncertainty on α_{PS} from uncertainties in the material description.
The presampler energy scale is extracted in nine $|\eta|$ bins as the ratio of the mean muon energy deposits in data and simulation:

$$\alpha_{\text{PS}}(|\eta|) = \frac{\langle E_{\text{PS}}^{\text{data}}(|\eta|)\rangle}{\langle E_{\text{PS}}^{\text{MC}}(|\eta|)\rangle}. \tag{6.1}$$

The results are shown in Figure 6.3. The statistical uncertainties are at the percent level, while the systematic uncertainties range from approximately 2% to 4%, depending on $|\eta|$.

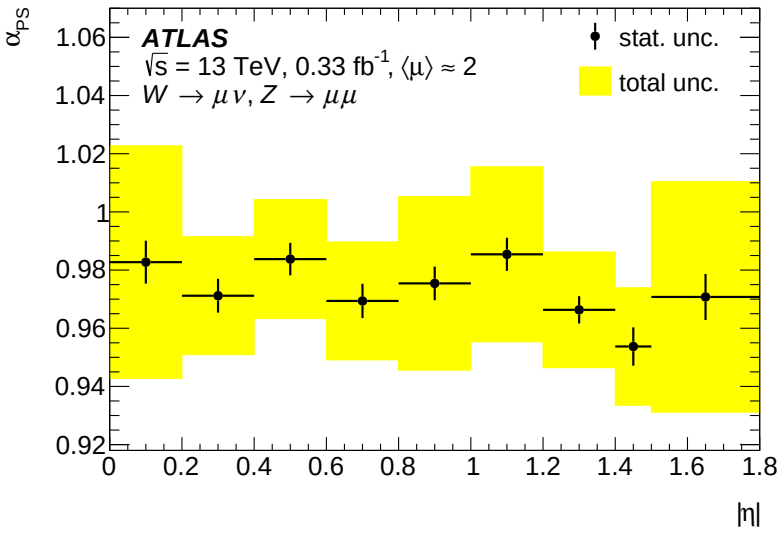

Figure 6.3 – Measured presampler energy scale α_{PS} as a function of $|\eta|$. The error bars represent the statistical uncertainty and the yellow band shows the total uncertainty [17].

6.2.2 Intercalibration of the first and second calorimeter layers

The intercalibration of the EM L1 and L2 layers, represented by the scale factor α_{12}, is determined using Z-boson decays in both the di-muon channel (a method already employed in previous calibrations [151]) and the di-electron channel (introduced in the Run 2 calibration [17]). The results from the two channels are then combined to obtain the final L1-L2 intercalibration scale factors.

Intercalibration using muons

The intercalibration using muons from $Z \to \mu\mu$ decays is based on the ratio of the average energy deposits in L1 and L2 for muon candidates in data and simulation. The corresponding scale factor is defined as

$$\alpha_{12} = \left(\frac{\langle E_1 \rangle}{\langle E_2 \rangle}\right)^{\mathrm{data}} \Big/ \left(\frac{\langle E_1 \rangle}{\langle E_2 \rangle}\right)^{\mathrm{MC}}, \tag{6.2}$$

where $\langle E_i \rangle$ is an estimator of the energy deposited in layer i ($i = 1, 2$). Two approaches are employed to estimate $\langle E_i \rangle$: the *most probable value* method, obtained from a fit to the energy-deposit distributions using a Landau-noise convolution, and the *truncated mean* (TM) method, in which the mean is computed in a restricted window to reduce the impact of distribution tails. In both cases, the measurements are performed in intervals of $\langle \mu \rangle$, and the final α_{12} is obtained by linearly extrapolating to $\langle \mu \rangle = 0$.
In the TM method, the extrapolation was validated by comparing the nominal result with the value obtained using a dedicated low-pileup dataset, where muon candidates

from $W \to \mu\nu$ decays are also included in addition to those from $Z \to \mu\mu$ decays. The evaluation is carried out in $|\eta|$ bins over the range $0 < |\eta| < 2.4$. An example for $0.3 < |\eta| < 0.4$ is shown in Figure 6.4a, and a comparison between the standard and low-pileup samples is presented in Figure 6.4b. The agreement between the two is excellent and well within the total uncertainty of the nominal result. The overall uncertainty of the muon-based measurements ranges from about 0.7% in the barrel to about 2% in the endcap regions.

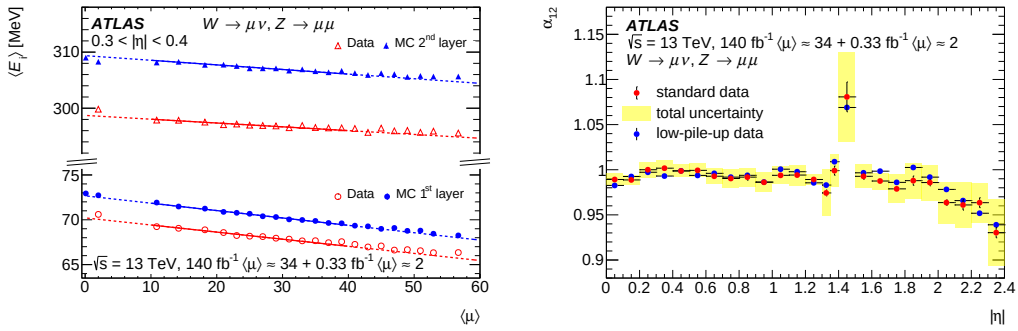

Figure 6.4 – (a) Truncated-mean energy deposits of muons in the first (dots) and second (triangles) calorimeter layers, for $0.3 < |\eta| < 0.4$, shown in data (open symbols), simulation (filled symbols), and in low-pileup and no-pileup samples, as a function of the average number of interactions per bunch crossing $\langle\mu\rangle$. The lines indicate linear fits in the range $\langle\mu\rangle \in [10, 40]$, with dotted extensions showing the extrapolation to $\langle\mu\rangle = 0$. (b) Comparison of α_{12} as a function of $|\eta|$ obtained from the $\mu = 0$ extrapolation in the standard and low-pileup data samples for the TM method. The yellow band represents the total uncertainty of the nominal result, and the error bars show statistical uncertainties only [17].

Intercalibration using electrons

For the $Z \to ee$ channel, α_{12} is derived again in two different ways: one based on the ratio of the measured energy E and momentum p of electron candidates (the E/p method), and another based on the invariant mass of the electron pairs (the m_{ee} method) across bins of the electrons' $|\eta|$ and E_1/E_2 in both data and simulation. Ideally, the ratio of the E/p and m_{ee} estimators between data and simulation should be constant as a function of E_1/E_2, indicating perfect intercalibration between the L1 and L2 layers. Any observed slope in this ratio indicates a miscalibration, and α_{12} is adjusted to minimize the discrepancy of the data-to- MC ratio with respect to a constant. The precision of the α_{12} measurement with electrons ranges from 0.7% to 2% in the barrel, and from 1.5% to 6.2% in the endcap calorimeters.

Combination of muon- and electron-based results

The final value of α_{12} is obtained by combining the results from both the di-muon and di-electron channels. First, the muon and electron results are combined separately for

each of the two methods used in the two channels (E/p and m_{ee} for electrons, TM and most probable value for muons). The results from the two channels are then combined to provide the final measurement, illustrated in Figure 6.5. The total uncertainty varies between 0.6% in the central part of the barrel to 3% at $|\eta| \sim 2.4$. The inclusion of the electron measurement allows the uncertainty to be reduced by a factor of ~ 1.8 in the first half of the barrel. In the endcaps, the combined uncertainties are dominated by the differences between the electron and muon results.

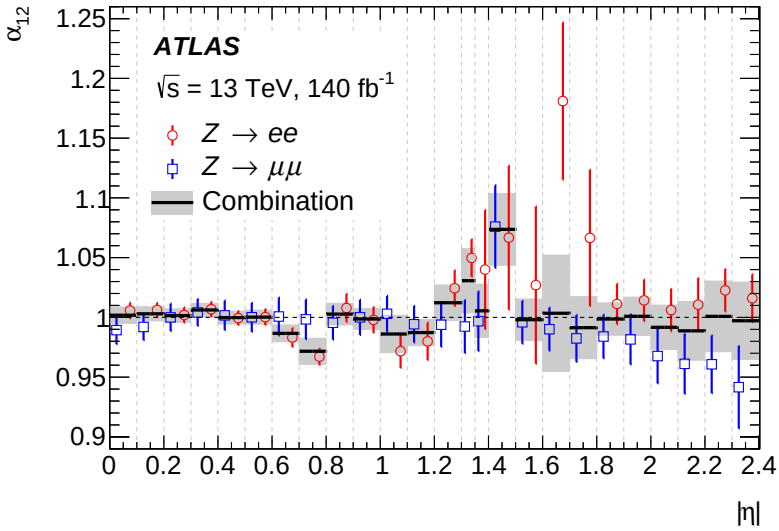

Figure 6.5 – Relative calibration scale factor α_{12} of the first and second EM calorimeter layers as a function of $|\eta|$. Open blue squares correspond to the results obtained from the study of muon energy deposits in $Z \to \mu\mu$ events, combining the truncated mean and most probable value methods. Open red circles show the extracted combined values obtained from the study of the dependence of the dielectron invariant mass m_{ee} and the E/p ratio as a function of E_1/E_2 in $Z \to ee$ events. The final scale factors, combining electron and muon results, are shown as the black solid lines [17].

6.3 Monte Carlo-based energy calibration

One of the key steps in the photon and electron energy calibration procedure in ATLAS is the Monte Carlo-based calibration, which exploits reconstructed shower and cluster variables to convert the raw accordion energy E_{raw} into a calibrated energy E_{calib}, for both data and MC. The quantity E_{raw} does not account for electromagnetic shower energy leaking outside the cluster, nor for losses in inactive material upstream or within the calorimeter; therefore a correction is required to recover the best possible estimate of the true energy E_{true} of the incident particle.

The MC-based calibration relies on a multivariate regression using a Boosted Decision Trees (BDT) with gradient boosting, trained separately for electrons, converted photons, and unconverted photons. The training uses single-particle simulations with

pileup overlaid to match Run 2 (or Run 3) conditions. The method is implemented using the Toolkit for Multivariate Data Analysis (TMVA) framework [152], which provides a ROOT-integrated machine-learning environment for multivariate regression and classification. In this case, the calibration is a regression problem in which the algorithm minimises the deviation between E_{calib} and the target E_{true}. Evaluating the BDT on reconstructed clusters yields a predicted correction factor $E_{\text{true}}/E_{\text{raw}}$, which, when multiplied by E_{raw}, gives the calibrated energy E_{calib}.
Figure 6.6 shows the distribution of the energy response $E_{\text{reco}}/E_{\text{true}}$ before (E_{raw}) and after (E_{calib}) the MC-based calibration, for unconverted photons, converted photons, and electrons.

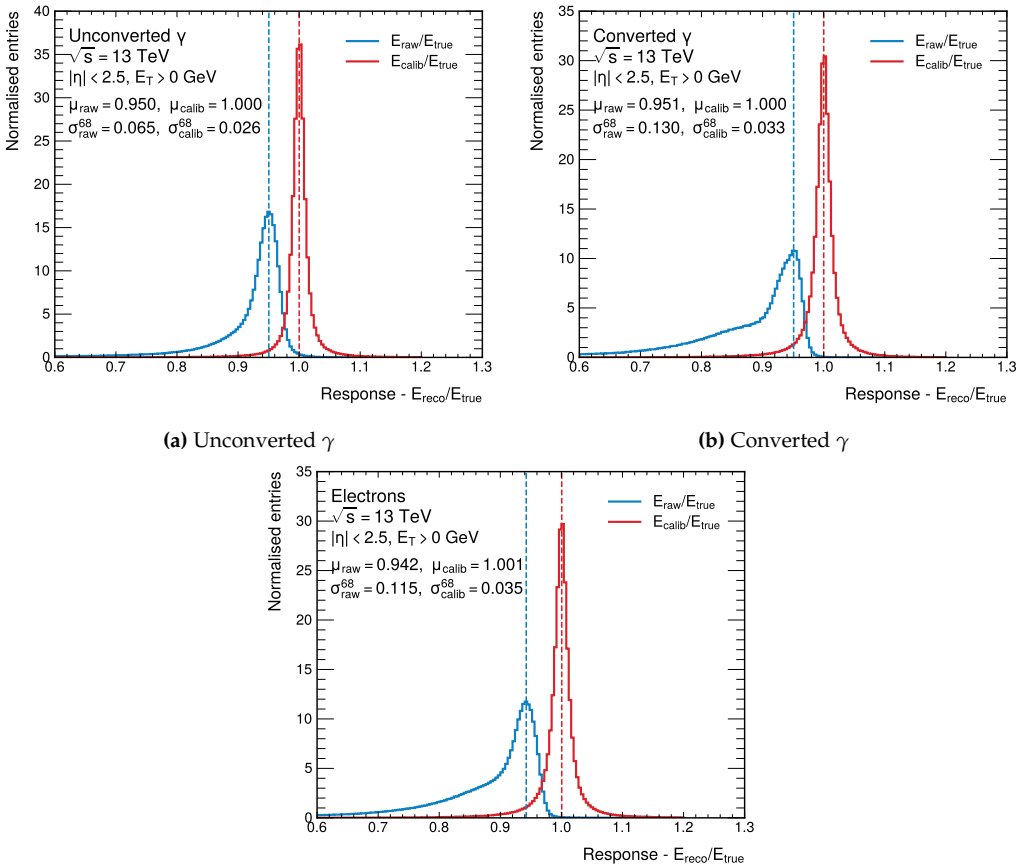

(a) Unconverted γ

(b) Converted γ

(c) Electrons

Figure 6.6 – Comparison of the energy response $E_{\text{reco}}/E_{\text{true}}$ before (blue, E_{raw}) and after (red, E_{calib}) the MC-based calibration for (a) unconverted photons, (b) converted photons, and (c) electrons, inclusive in $|\eta|$ and E_{T}. The calibrated energy show a reduced bias (response closer to 1) and improved resolution, quantified using the truncated mean (evaluated with the 10% core events around the peak) and the 68% smallest interval width.

The calibration leads to a clear improvement in both energy scale (peak position) and

energy resolution (peak width), bringing the mean reconstructed energy to within 0.1% of the true value for all particle types.
Section 6.3.1 details the Monte Carlo-based energy calibration developed for Run 2, including the training samples used, input variables, binning scheme, and BDT architecture, as well as the resulting performance. The improvements and optimisation work performed for Run 3 are then presented in Section 6.3.2.

6.3.1 Run 2 MC-based energy calibration

Training samples and selections

The training of the MC-based energy calibration is performed on simulated samples of single-particle events generated at the ATLAS interaction point. Single electrons and photons are produced using the GEANT PARTICLE GUN generator and propagated through a full GEANT4 simulation [153] of the detector. Before any selection, the samples contain 40 M single-photon events and 40 M single-electron events.
For the first time, the training samples include pileup overlay to match Run 2 conditions, with an average number of interactions per bunch crossing $\langle\mu\rangle$ ranging from 10 to 60, and a mean value of $\langle\mu\rangle = 33.7$, as shown in Figure 2.9a.
The photons and electrons used for the training are required to satisfy a set of selection criteria, which depend on the particle type and the binning (see Section 6.3.1). The selections are summarised in Table 6.1. After applying these requirements, the available statistics correspond to 35.5 M single-electron events, 25.3 M single unconverted-photon events, and 12.4 M single converted-photon events.

Selection cut	Cut	Details
`ENERGY_MATCHED`	`abs(cl_E/truth_E - 1) < 0.5`	Loose matching between previous calibrated cluster energy and truth value
`PDG_ID`	`abs(truth_pdgId) == 22/11`	$22 = \gamma$, $\mp 11 = e^{\pm}$
Identification WP	*Loose*	Not applied in special $\lvert\eta\rvert$ bins 6, 7, 8, 15, 16
`CONVERTED` γ	`0 < ph_Rconv < 800`	Converted γ definition
`UNCONVERTED` γ	`ph_conv_type == 0`	Unconverted γ definition

Table 6.1 – Photons and electrons selection requirements used in the MC-based calibration.

Input variables

The Multivariate Analysis (MVA)-based calibration exploits a set of input variables used to compute the correction to the total raw cluster energy, with configurations defined separately for each particle type and for each ($\lvert\eta\rvert$, E_{T}) bin. The variables are chosen based on their correlation with the target energy response and on how well their distributions are modelled in simulation, since any mismodelling could bias the regression output when applied to real data.

Although shower-shape observables (introduced in Section 5.1.5) are highly sensitive to the shower development and therefore to the energy response, they are not yet used in the calibration due to remaining differences between data and MC.

Input variables for all particle types and bins The following seven variables are used in all ($|\eta|$, E_T) bins and for all particle types (electrons, converted photons, unconverted photons):

- **Total raw cluster energy in the accordion**, defined as the sum of the uncalibrated energies of the three accordion layers, $E^{\text{acc}}_{\text{raw}} = E^{\text{L1}}_{\text{raw}} + E^{\text{L2}}_{\text{raw}} + E^{\text{L3}}_{\text{raw}}$;
- $\boldsymbol{f_0 = E^{\text{PS}}_{\text{raw}}/E^{\text{acc}}_{\text{raw}}}$, the ratio of the energy in the presampler to the energy in the accordion. It is used only in the acceptance of the presampler, $|\eta| < 1.8$;
- $\boldsymbol{E_1/E_2 = E^{\text{L1}}_{\text{raw}}/E^{\text{L2}}_{\text{raw}}}$, the ratio of the energy in the first accordion layer to the second one;
- **Pseudorapidity η in the ATLAS frame** that helps to take into account the misalignment of the detector, in order to correct for the variation of the material in front of the accordion;
- **cell Index**: an integer number between 0 an 99 which identifies the cell in the Layer 2 of the Calorimeter and is defined as the integer part of the division $\eta_{\text{calo}}/\Delta\eta$, where η_{calo} is the pseudorapidity of the cluster in the calorimeter frame and $\Delta\eta = 0.025$ is the size of one cell in the second accordion layer;
- **η with respect to the cell edge**, `etaModCalo`: $\eta_{\text{calo}} \bmod (\Delta\eta = 0.025)$. This variable allows correcting for the variation of the lateral energy leakage due to the finite cluster size, which is larger for particles that hit the cell close to the edges;
- **ϕ position with respect to the lead absorber structure**, `phiModCalo`: defined as $\phi_{\text{calo}} \bmod (\pi/512)$ in the barrel and $\phi_{\text{calo}} \bmod (\pi/384)$ in the endcap, matching the absorber periodicity. This variable compensates for ϕ-dependent variations in the sampling fraction.

Additional inputs in the transition region In the transition region between the barrel and endcap EM calorimeters ($1.4 < |\eta| < 1.6$), the amount of upstream inactive material rises sharply, reaching between 5 and almost 10 radiation lengths X_0, as shown in Figure 6.1. Part of this material corresponds to the TileCal services and support structures, and leads to substantial energy loss before the particle reaches the first active EM layer. To mitigate this effect, dedicated TileCal gap/crack scintillators, instrument the region between the barrel and endcap calorimeters. As illustrated in Figure 6.7, the scintillator modules covering the interval $1.4 < |\eta| < 1.6$ are labelled E3. Electrons and photons in this region deposit energy not only in the EM barrel and endcap calorimeters, but also in these scintillators.
For this reason, additional input variables describing the energy deposited in the E3 scintillators are included in the Monte Carlo-based calibration for the three relevant $|\eta|$ bins (see Section 6.3.1): 1.40-1.46, 1.46-1.52 and 1.52-1.60 (corresponding to bins 7, 8 and 9):

- **fTG3**: the ratio between the energy in three consecutive E3 scintillators in ϕ over the energy in EM accordion: $E_{TileGap3}/E^{acc}_{raw}$. The electron shower width is wider than one E3 scintillator, thus for each electron/photon the sum of the energies from three consecutive E3 scintillators along ϕ ($E_{TileGap3}$) is considered;
- **DeltaPhiTG3**: the difference in ϕ between the angle of the electron cluster barycentre and the position of the E3 scintillator: $\Delta\phi = \phi_{cluster} - \phi_{E3}$.

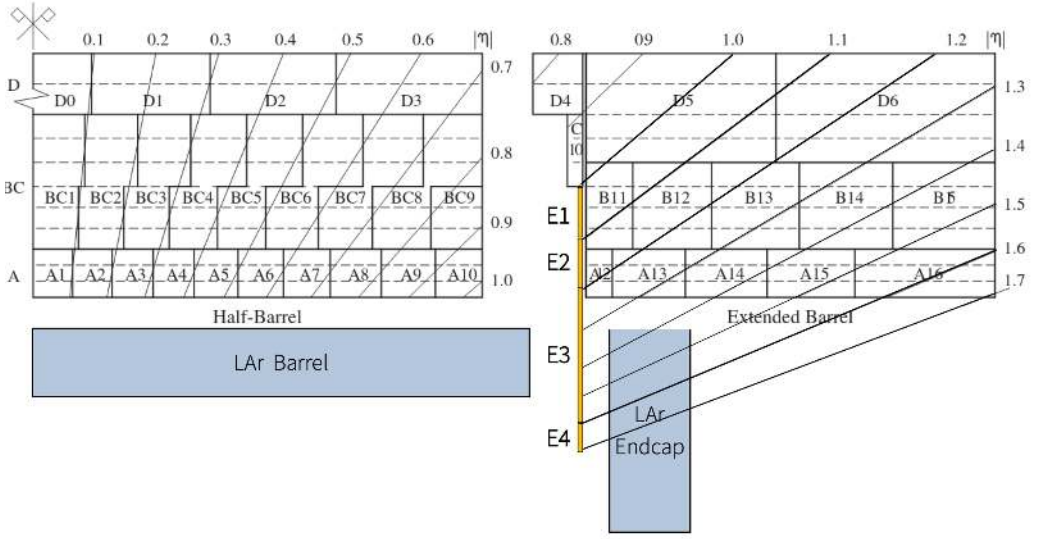

Figure 6.7 – Schematic showing the TileCal cell and scintillator structure, including the so-called "E-cells" (E1-E4) which are highlighted in yellow. The region between $1.4 < |\eta| < 1.6$ is covered by the E3 scintillators.

Additional inputs for converted γ Three additional input variables are included in the energy calibration of photons that convert within the ID volume ($0 < R_{conv} < 800$ mm):

- **Conversion radius of the photon**, R_{conv};
- **convEtOverPt =** $\boldsymbol{E^{acc}_T/p^{conv}_T}$ where $E^{acc}_T = E^{acc}_{raw}/\cosh(\eta)$ and p^{conv}_T is the sum of the transverse momenta of the two tracks associated with the conversion;
- **convPtRatios**: the fraction of the p^{conv}_T carried by the highest-p_T track associated with the conversion.

Target, BDTs structure, binning

Target The goal of the photon and electron energy calibration procedure is to convert the raw accordion energy E_{raw} of the cluster into a calibrated energy estimate, making use of several reconstructed quantities associated with the particle. For this reason, the

MVA target defined for the training is the correction factor to the raw cluster energy,

$$\text{target} \equiv \frac{E_{\text{true}}}{E_{\text{raw}}},$$

from which the calibrated energy can be obtained as:

$$E_{\text{calib}} = E_{\text{raw}} \cdot \text{target}. \tag{6.3}$$

Using the ratio rather than predicting the calibrated energy directly is preferable in a regression context, as normalised target variables are typically easier to handle than absolute quantities spanning several orders of magnitude.

BDTs structure and binning To allow the MVA to learn the energy response across regions of phase space where different input variables exhibit distinct behaviours, the training sample is split into bins of pseudorapidity $|\eta|$ and transverse energy in the accordion, E_{T}, separately for electrons, converted photons, and unconverted photons.
In the current calibration, 117 independent optimisations are defined over the phase-space grid $(|\eta| \times E_{\text{T}}) = ([0, 2.5] \times [0, 50\ \text{TeV}])$ for each particle type, resulting in a total of 351 BDT trainings.
The nominal binning for Run 2 has 17 $|\eta|$ bins, divided by the following bin edges:

$$|\eta| : [0, 0.05, 0.65, 0.80, 1.0, 1.2, 1.37, 1.40, 1.46, 1.52, 1.60, 1.74, 1.82, 2.0, 2.2, 2.37, 2.47, 2.50]$$

The number of bins in E_{T} depends on the considered $|\eta|$ bin. There are three possible cases:

- 9 E_{T} bins for the 10 following $|\eta|$ bins: [0.05, 0.65, 0.80, 1.0, 1.2, 1.37] and [1.60, 1.74, 1.82, 2.0, 2.2, 2.37]. The E_{T} bin edges are:

  $$[0, 10, 20, 40, 60, 80, 120, 500, 1000, 50000]\ \text{GeV};$$

- 6 E_{T} bins for the 4 following $|\eta|$ bins: [0, 0.05], [1.37, 1.4], [2.37, 2.47] and [2.47, 2.50]. The E_{T} bin edges are:

  $$[0, 25, 50, 100, 500, 1000, 50000]\ \text{GeV};$$

- 1 E_{T} bin for the 3 following $|\eta|$ bins: [1.4, 1.46], [1.46, 1.52] and [1.52, 1.6]. The E_{T} bin edges are: [0, 50000] GeV.

The relevant BDT parameters used in the training are summarised in Table 6.2.
Multivariate regression algorithms are trained by minimising an absolute-error–based loss function, which corresponds to estimating the median of the target distribution rather than its mean. Since the target variable $\text{target} = E_{\text{true}}/E_{\text{raw}}$ is not strictly Gaussian—particularly at low E_{T} as can be seen from Figure 6.6—this optimisation does not guarantee that the mean calibrated energy E_{calib} exactly reproduces the true energy E_{true}.

Parameter	Value	Description
`Ntrees`	`800`	Number of trees in the boosted forest.
`MaxDepth`	`2` or `3`	Maximum allowed depth for each tree. Set to `3` only in $\|\eta\|$ bins 6, 7 and 8 due to increased complexity in the transition region.
`nCuts`	`20`	Number of grid points scanned when searching for the optimal node-splitting threshold.
`Loss function`	`MAE`	Regression optimised using the Mean Absolute Error: MAE $= \sum_{i=1}^{n} \|y_i - f(x_i)\|$.
`Statistics`	`95% train`	95% of events used for training, remaining 5% retained as test sample to evaluate performance.

Table 6.2 – Summary of the BDT hyperparameters used for each $(|\eta| \times E_{\mathrm{T}})$ bin in the MC-based calibration.

Instead, it provides a robust calibration of the typical detector response, reducing the sensitivity to asymmetric tails and outliers in the target distribution.
To correct for this, additional shifts are applied on top of the raw MVA output so that the peak of the $E_{\mathrm{calib}}/E_{\mathrm{true}}$ distribution is centred at unity. The peak position is estimated in each $(|\eta|, E_{\mathrm{T}})$ bin using the mean of the smallest interval containing 10% of the events (as discussed in Section 6.3.1).
The single-bin shifts in $(|\eta| \times E_{\mathrm{T}})$ are observed to vary between adjacent transverse-energy intervals, reflecting the evolution of the target distribution with energy. The correction procedure is most relevant at low E_{T}, where non-Gaussian tails are more pronounced, and thus a finer binning than that used in the MVA training is adopted in this region. A linear interpolation was used to produce a continuous energy dependence, connecting the barycentre of adjacent transverse energy bins.

Performance

The performance of the calibration based on the MVA optimization is evaluated in terms of linearity, energy resolution, and dependence of the response on the MVA calibration input quantities, in order to verify that the calibration has been correctly trained and that it is not affected by residual dependencies on the input variables.
The **resolution** is quantified as the smallest interval containing 68% of the $E_{\mathrm{calib}}/E_{\mathrm{true}}$ distribution. This estimator is less sensitive to tails than the standard deviation and therefore more robust against outliers. Figure 6.8 shows the $E_{\mathrm{calib}}/E_{\mathrm{true}}$ resolution as a function of $p_{\mathrm{T}}^{\mathrm{true}}$ and $|\eta|$ for unconverted photons, converted photons, and electrons, in dedicated sub-ranges of pseudorapidity and transverse momentum.
As expected from Equation (3.13), the relative resolution improves with increasing p_{T}, due to the decreasing relative contribution of the sampling term.
The **linearity** is evaluated using the mean inside the smallest interval containing 10% of the events in the $E_{\mathrm{calib}}/E_{\mathrm{true}}$ distribution. This metric is less sensitive to tails than the

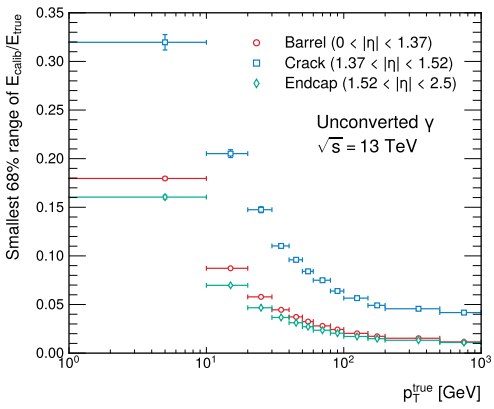

(a) Unconverted γ, vs $p_{\mathrm{T}}^{\mathrm{true}}$

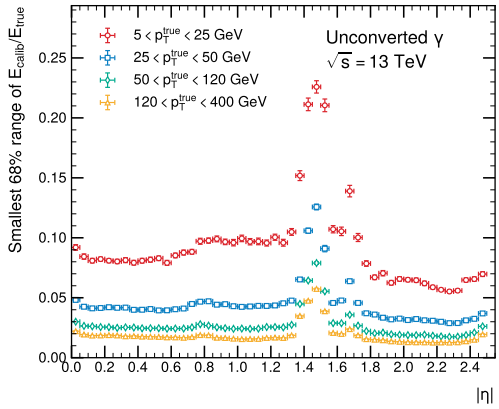

(b) Unconverted γ, vs $|\eta|$

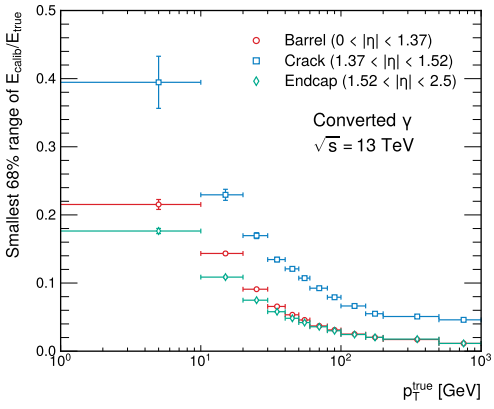

(c) Converted γ, vs $p_{\mathrm{T}}^{\mathrm{true}}$

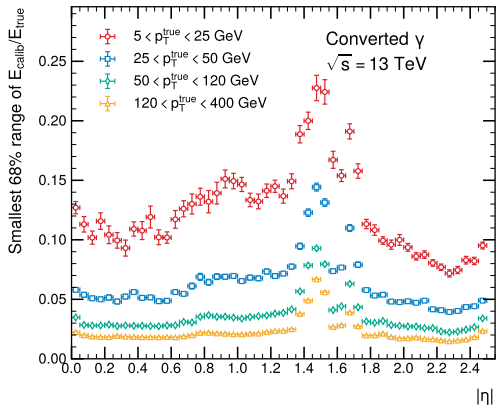

(d) Converted γ, vs $|\eta|$

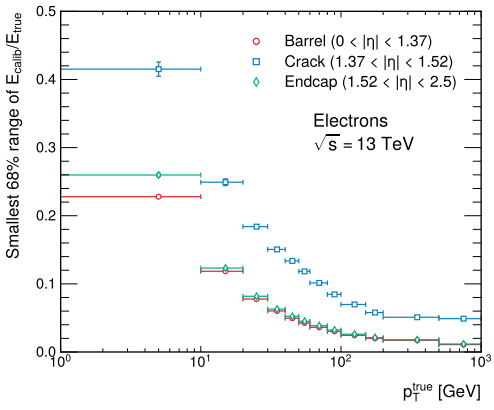

(e) Electrons, vs $p_{\mathrm{T}}^{\mathrm{true}}$

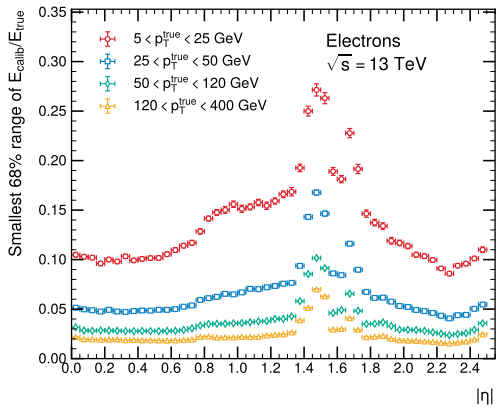

(f) Electrons, vs $|\eta|$

Figure 6.8 – Energy resolution for unconverted photons, converted photons and electrons, expressed as the width of the smallest interval containing 68% of the $E_{\mathrm{calib}}/E_{\mathrm{true}}$ distribution. For each particle type, the resolution is shown as a function of transverse momentum (left column) and pseudorapidity (right column).
Pseudorapidity regions used: barrel $0 < |\eta| < 1.37$, transition $1.37 < |\eta| < 1.52$, endcap $1.52 < |\eta| < 2.5$. p_{T} ranges: 5-25 GeV, 25-50 GeV, 50-120 GeV, 120-400 GeV.

arithmetic mean, and provides a robust estimate of the peak position. Figure 6.9 shows the linearity as a function of $p_{\mathrm{T}}^{\mathrm{true}}$ and $|\eta|$ for unconverted photons, converted photons, and electrons, in dedicated sub-ranges of pseudorapidity and transverse momentum. The linearity is within 1% when considering low-p_{T} objects (< 20 GeV), and improves to the 0.1% level at high-p_{T}, apart from the crack region. The linearity as a function of some input variables used in the MVA training is also studied, confirming that no residual dependencies remain after the calibration is applied. Figure 6.10 shows the linearity as a function of $E_1/E_2 = E_{\mathrm{raw}}^{\mathrm{L1}}/E_{\mathrm{raw}}^{\mathrm{L2}}$, the ratio of the energy in the first accordion layer to the second one. The dependence of $E_{\mathrm{raw}}/E_{\mathrm{true}}$ on E_1/E_2 is effectively corrected by the calibration, resulting in a flat energy response. Additional checks are performed on all other input variables, yielding similar results; these Figures are reported in Appendix A.1.

Pileup dependence

For the first time, the training samples include pileup overlay to match Run 2 conditions, with an average number of interactions per bunch crossing $\langle\mu\rangle$ ranging from 10 to 50, and a mean value of $\langle\mu\rangle = 25$, as shown in Figure 2.9a, since it was using simulates samples to match the 2015-2016 conditions. At an early stage, the inclusion of pileup-related variables among the training inputs was considered, such as the average number of pp interactions per bunch crossing and the actual number of simulated interactions on an event-by-event basis. However, studies indicated that the raw energy already exhibited a negligible dependence on pileup, becoming only marginally visible in the low-energy region ($0 < p_{\mathrm{T}} < 25$ GeV). This is visible in Figure 6.11 for each particle type, where the linearity is shown as a function of μ (average number of pp interactions per bunch crossing). Overall, both the linearity and the resolution were found to remain substantially stable as a function of pileup. Furthermore, the explicit inclusion of these variables in the training did not yield any significant improvement in performance. Consequently, they were not included in the final model. The same Figures are reported in Appendix A.2 for the Run 3 conditions.

6.3.2 Run 3 MC-based energy calibration studies

Training samples and selections

The MVA has been retrained for Run 3 using MC samples produced with the full Run 3 ATLAS detector simulation and reconstruction software. As in Run 2, the training is performed on simulated samples of single-particle events generated at the ATLAS interaction point. Single electrons and photons are produced with the GEANT PARTICLE GUN generator and propagated through a full GEANT4 simulation of the detector. Before any selection, the samples contain 140 M single-photon events and 140 M single-electron events.

The training samples include pileup overlay matching Run 3 conditions, with an average number of interactions per bunch crossing $\langle\mu\rangle$ between 20 and 80, and a mean value of $\langle\mu\rangle = 55$, as shown in Figure 2.9b.

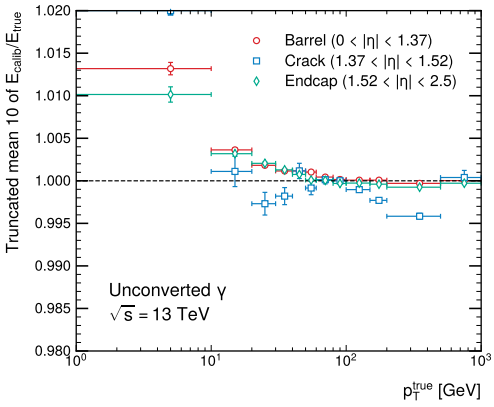

(a) Unconverted γ, vs $p_{\mathrm{T}}^{\mathrm{true}}$

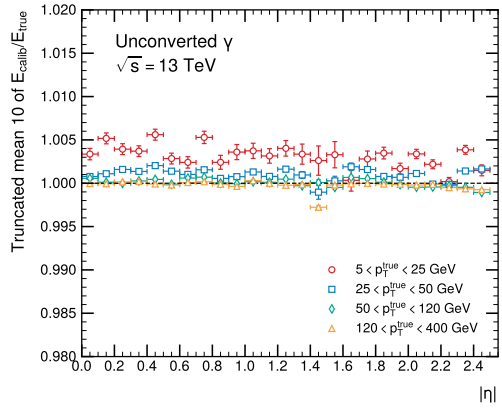

(b) Unconverted γ, vs $|\eta|$

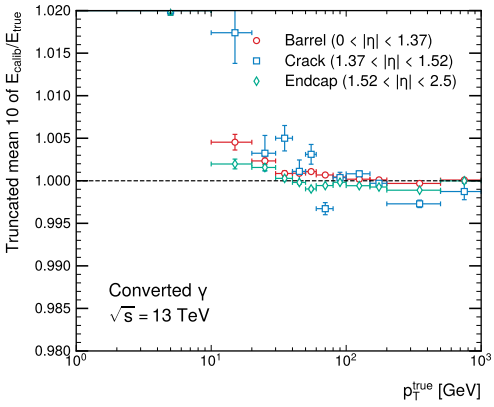

(c) Converted γ, vs $p_{\mathrm{T}}^{\mathrm{true}}$

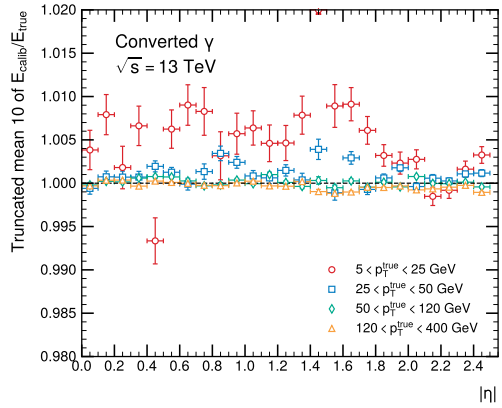

(d) Converted γ, vs $|\eta|$

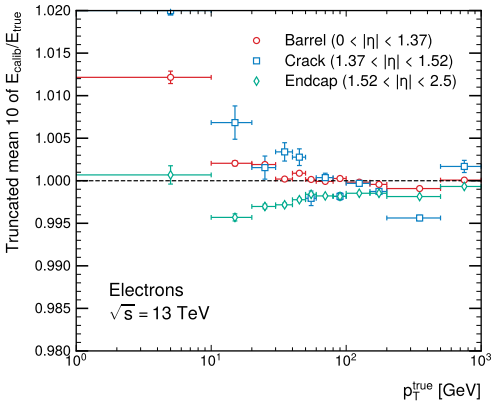

(e) Electrons, vs $p_{\mathrm{T}}^{\mathrm{true}}$

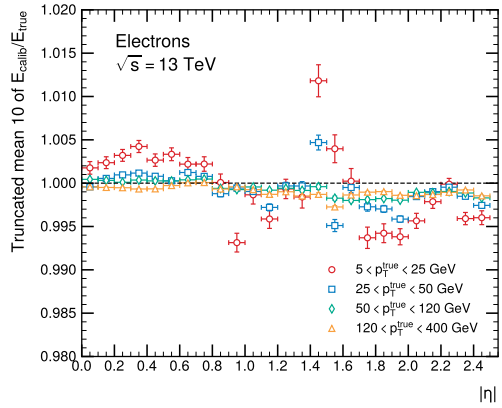

(f) Electrons, vs $|\eta|$

Figure 6.9 – Linearity for unconverted photons, converted photons and electrons, expressed using the mean of the smallest interval containing 10% of the events of the $E_{\mathrm{calib}}/E_{\mathrm{true}}$ distribution. For each particle type, the linearity is shown as a function of transverse momentum (left column) and pseudorapidity (right column).
Pseudorapidity regions used: barrel $0 < |\eta| < 1.37$, transition $1.37 < |\eta| < 1.52$, endcap $1.52 < |\eta| < 2.5$. p_{T} ranges: 5-25 GeV, 25-50 GeV, 50-120 GeV, 120-400 GeV.

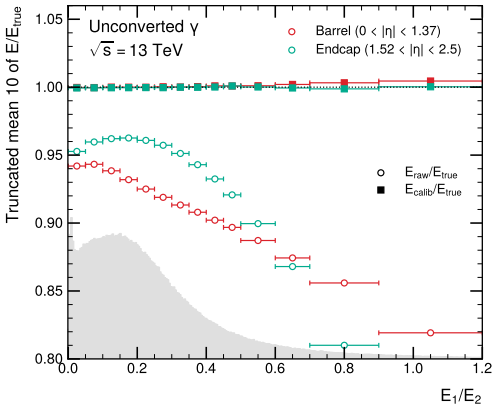

(a) Unconverted γ, vs E_1/E_2

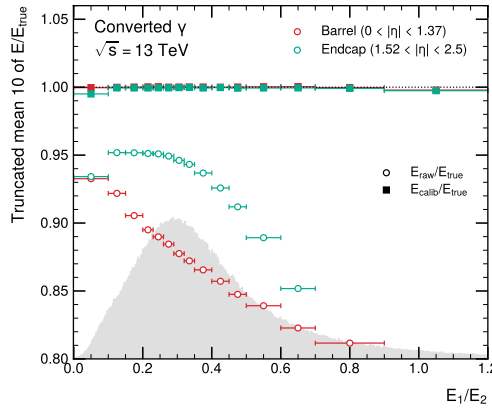

(b) Converted γ, vs E_1/E_2

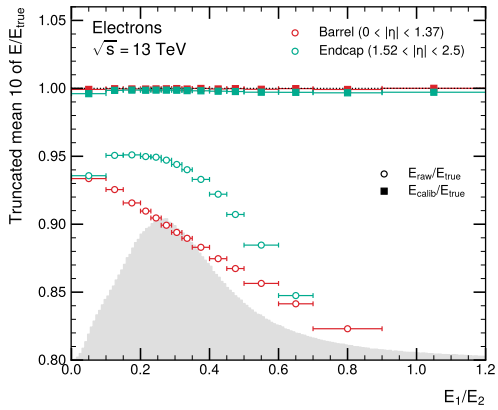

(c) Electrons, vs E_1/E_2

Figure 6.10 – Linearity for unconverted photons (a), converted photons (b) and electrons (c), expressed using the mean of the smallest interval containing 10% of the events of the $E_{\text{calib}}/E_{\text{true}}$ and $E_{\text{raw}}/E_{\text{true}}$ distributions. For each particle type, the linearity is shown as a function of the ratio of the energy in the first accordion layer to the second one. The dependence of $E_{\text{raw}}/E_{\text{true}}$ on E_1/E_2 is effectively corrected by the MVA calibration, recovering linearity across the full range of this variable. Pseudorapidity regions used: barrel $0 < |\eta| < 1.37$ (red), endcap $1.52 < |\eta| < 2.5$ (green).

Photons and electrons used in the training are required to satisfy a set of selection criteria that depend on the particle type and on the binning scheme (see Section 6.3.1). With respect to Table 6.1, the only difference is regarding the definition of converted and unconverted photons. Given the performance and the mismodelling of the TRT conversions in Run 3, it was decided to consider the TRT conversions in the central barrel region ($|\eta| < 0.8$) as unconverted photons. This change affected $\sim$ 0.1% of the unconverted photons in the training. The new definitions of converted and unconverted photons for Run 3 are summarised in Table 6.3.

After applying all selections, the available statistics amount to 124.3 M single-electron events, 88.6 M unconverted-photon events, and 43.4 M converted-photon events.

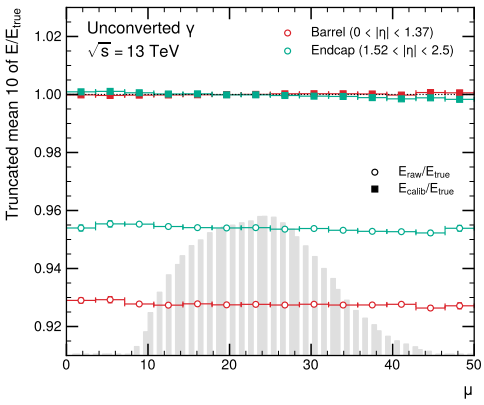

(a) Unconverted γ, vs μ

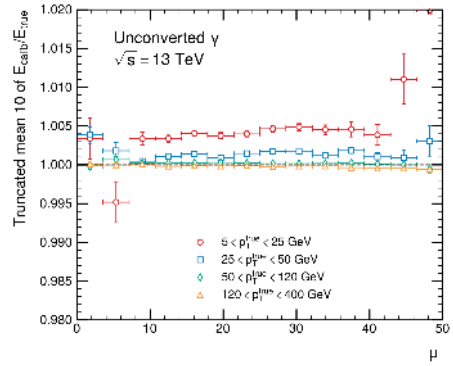

(b) Unconverted γ, vs μ

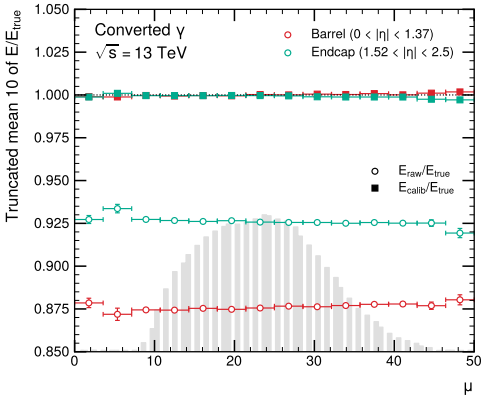

(c) Converted γ, vs μ

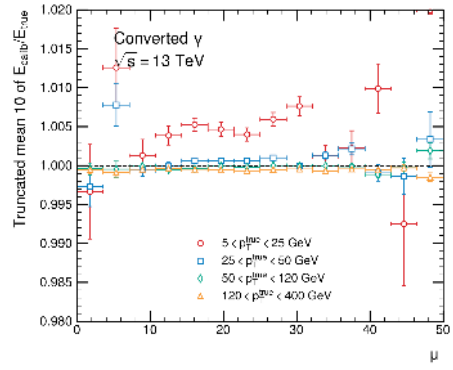

(d) Converted γ, vs μ

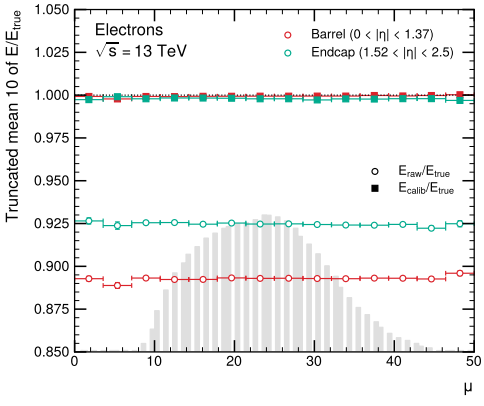

(e) Electrons, vs μ

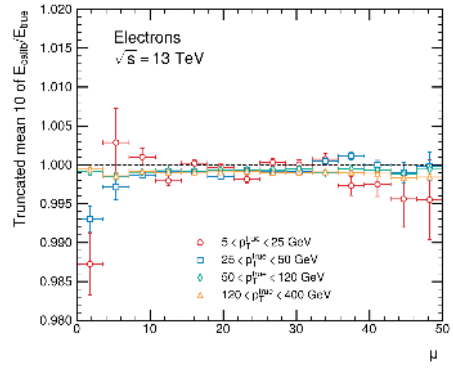

(f) Electrons, vs μ

Figure 6.11 – Linearity for unconverted photons, converted photons and electrons, expressed using the mean of the smallest interval containing 10% of the events of the $E_{\text{calib}}/E_{\text{true}}$ distribution. For each particle type, the linearity is shown as a function of μ (average number of pp interactions per bunch crossing), dividing in barrel and endcap regions (left column) and in transverse momentum (right column). Pseudorapidity regions used: barrel $0 < |\eta| < 1.37$, endcap $1.52 < |\eta| < 2.5$. p_{T} ranges: 5-25 GeV, 25-50 GeV, 50-120 GeV, 120-400 GeV.

Selection name	Selection	Details
CONV. γ Run 2	0 < ph_Rconv < 800	Converted-γ definition used in Run 2
UNCONV. γ Run 2	ph_conv_type == 0	Unconverted-γ definition used in Run 2
isTRTconversion	ph_conv_type == 2 || ph_conv_type == 4	Single or double TRT conversion
CONV. γ Run 3	CONV_Run2 && ($\|\eta\|$ >= 0.8 || !isTRTconversion)	Converted-γ definition used in Run 3
UNCONV. γ Run 3	UNCONV_Run2 || ($\|\eta\|$ < 0.8 && isTRTconversion)	Unconverted-γ definition used in Run 3

Table 6.3 – Run 2 and new Run 3 definitions of converted and unconverted photons used in the nominal MVA training.

ϕ modulation studies

One of the studies carried out for Run 3 concerns the improvement of the ϕ modulation correction in the MVA calibration. This effect had already been accounted for in Run 2 (and in previous calibrations) by including, as an input variable, the ϕ position with respect to the lead-absorber structure (phiModCalo). This variable is defined as ϕ_{calo} mod $(\pi/512)$ in the barrel and as ϕ_{calo} mod $(\pi/384)$ in the endcap, matching the periodicity of the absorber geometry. The phiModCalo observable allows one to correct for the slight variations in the sampling fraction experienced by a particle as a function of ϕ.
Figure A.2 (in Appendix A.1) shows the linearity as a function of ϕ with respect to the lead absorber. The MVA calibration recovers linearity across the full range of these variables, but some residual modulations have been observed.
For Run 3, new variables were studied to improve the correction of this effect. In particular, three new variables were defined, and MVA trainings were performed including them as additional inputs to the nominal set of variables, instead of phiModCalo:

- phiModCalo1: ϕ_{calo} mod $(\pi/512)$ in the barrel and ϕ_{calo} mod $(\pi/384)$ in the endcap, matching the periodicity of the absorber geometry. It has the same periodicity as phiModCalo; however, in the phiModCalo1 definition ϕ_{calo} is explicitly rotated in the positive and negative η regions, separately for the barrel and the endcap. This ensures that a given value of phiModCalo1 corresponds to the same relative position with respect to the absorber structure across all detector regions.
- phiModCalo2: ϕ_{calo} mod $(\pi/128)$, defined with a coarser periodicity than phiModCalo1. As for phiModCalo1, ϕ_{calo} is rotated according to the sign of η so that a given value of phiModCalo2 corresponds to the same relative position within the detector geometry in the $+\eta$ and $-\eta$ regions. This periodicity is chosen to be sensitive to effects related to the calorimeter cell size in the ϕ direction.
- phiModCalo3: ϕ_{calo} mod $(\pi/64)$, defined with an even coarser periodicity. Similarly to phiModCalo1 and phiModCalo2, ϕ_{calo} is rotated in the positive and negative η

regions to preserve a consistent mapping of the variable to the underlying detector structure. This variable is intended to capture residual ϕ-dependent effects at larger geometric scales.

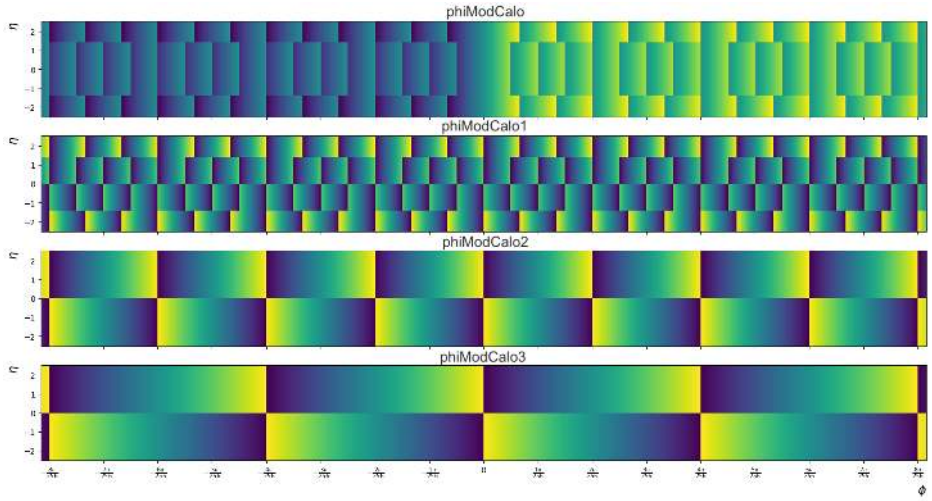

Figure 6.12 – The four `phiModCalo` variables as a function of ϕ (x-axis) and η (y-axis). The different periodicities and the different definitions in positive and negative η regions can be observed.

Figure 6.12 shows the four different variables as a function of ϕ and η, highlighting their different periodicities and definitions in positive and negative η regions.
The different trainings including each of these new variables (or their combinations) were compared with the nominal Run 3 training that used `phiModCalo`. The best performance in terms of linearity and resolution was achieved with `phiModCalo1`, which was therefore chosen as the nominal input variable to correct for the ϕ modulation effect in Run 3. The resolution improvement obtained with this new variable is more visible at high p_{T} (> 100 GeV), where a gain of a few % is observed especially in the barrel and in the endcap regions for all particle types (see Figure 6.13).

TileCal scintillators extensions

As reported in Section 6.3.1, dedicated TileCal gap scintillators are installed in the transition region to correct for energy losses in the inactive material between the barrel and endcap calorimeters. In particular, the used scintillators (E3) covered the $1.4 < |\eta| < 1.6$ region up to Run 2. In Run 3, their coverage in $|\eta|$ was extended from 1.6 to 1.72 with the addition of the E4 scintillators, as can also be seen in Figure 6.7.
For this reason, a new training was performed including the (E3+E4) scintillator variables (`fTG3` and `DeltaPhiTG3`) also in the $1.6 \leq |\eta| < 1.72$ bin (bin number 9). Its performance was compared with that of a training carried out with the nominal input-variable configuration used in Run 2. Since the scintillator extension only reached up to $|\eta| = 1.72$, a small adjustment to the η bin edges was required: from 1.74 in Run 2 to 1.72

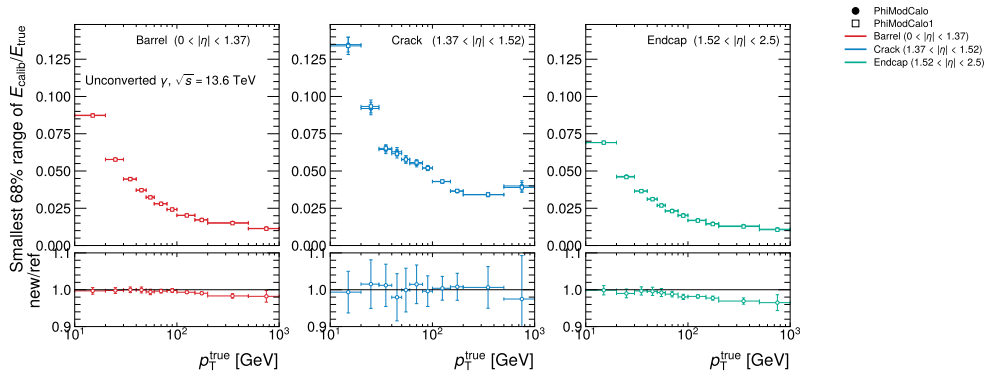

(a) Unconverted photons

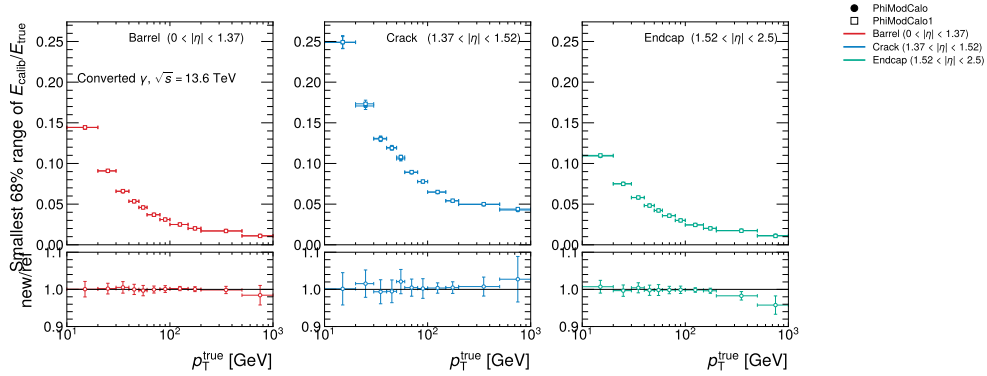

(b) Converted photons

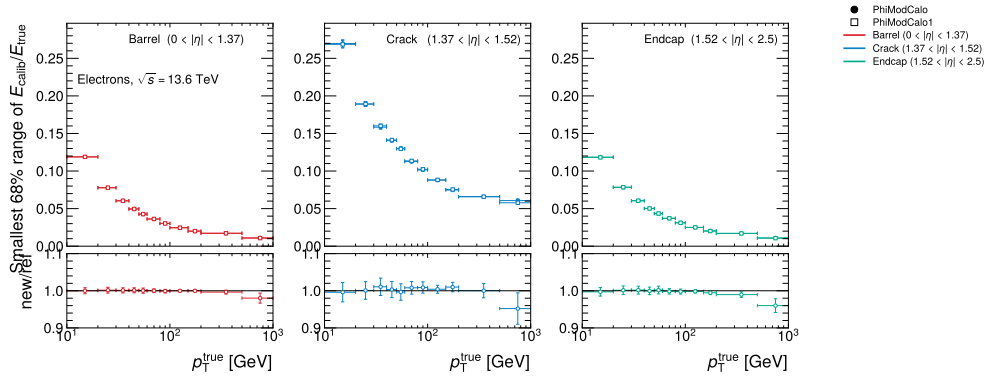

(c) Electrons

Figure 6.13 – Energy resolution expressed as the width of the smallest interval containing 68% of the $E_{\text{calib}}/E_{\text{true}}$ distribution for the trainings using `phiModCalo` and `phiModCalo1` as input variables. The resolution is shown as a function of the transverse momentum p_T^{true}, in three pseudorapidity regions: barrel ($0 < |\eta| < 1.37$), transition ($1.37 < |\eta| < 1.52$), and endcap ($1.52 < |\eta| < 2.5$). Results are shown separately for unconverted photons (a), converted photons (b), and electrons (c).

in Run 3. In the considered $|\eta|$ bin, an improvement of about 5-10% in resolution was observed for all particle types (apart from low-p_{T} unconverted photons) when including the TileGap3 variables in the training (see Figure 6.14).

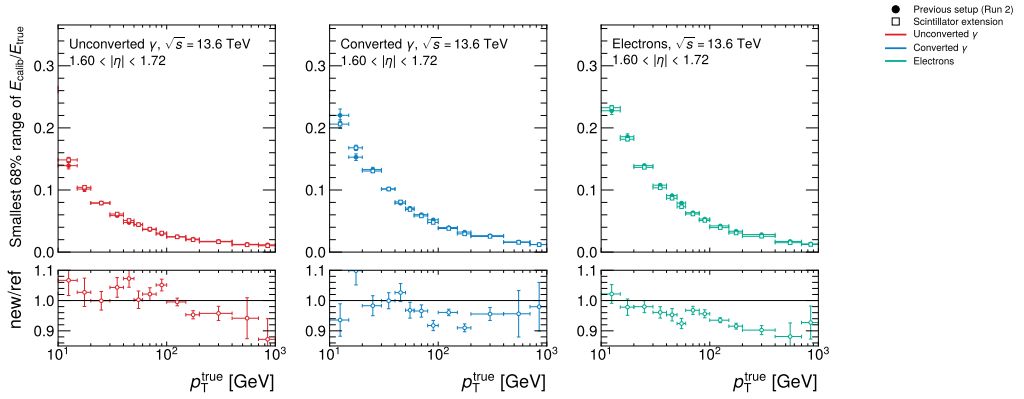

Figure 6.14 – Energy resolution expressed as the width of the smallest interval containing 68% of the $E_{\mathrm{calib}}/E_{\mathrm{true}}$ distribution for the trainings adding `fTG3` and `DeltaPhiTG3` as input variables in the $1.60 < |\eta| < 1.72$ bin. The resolution is shown as a function of the transverse momentum p_T^{true}, for unconverted photons (a), converted photons (b), and electrons (c).

6.4 Uniformity and ADC non-linearity corrections

A set of additional corrections is applied to data to account for response variations not included in the simulation in specific detector regions, e.g. regions with non-optimal high voltage, azimuthal non-uniformities, or biases associated with the LAr calorimeter's electronics calibration. The stability of the calorimeter response as a function of azimuth, time and pileup is also studied.

6.4.1 ADC non-linearity correction

The energy reconstruction in a LAr calorimeter cell relies on a linear conversion from ADC counts to current, followed by a second conversion from current to energy. The ADC-to-current conversion is assumed to be linear and is calibrated during dedicated electronic calibration runs using a known injected current. However, small non-linearities and non-zero residuals may still arise due to intrinsic non-linear behaviour of the readout electronics.

In the Run 2 calibration [17], a new method was introduced to measure and correct these residual non-linearities. For each calorimeter cell, the residuals are fitted with a fifth-order polynomial, and the resulting parametrisation is added as a correction to the reconstructed cell energy. The correction is constructed such that it does not alter the cluster energies of electrons at $E_{\mathrm{T}} = 40\,\mathrm{GeV}$, where the global energy scale is defined (see Section 6.5).

The impact of this procedure for electrons, unconverted photons, and converted photons is shown in Figure 6.15. Cluster energies increase by approximately 0.4% at low E_T, and decrease by about 0.2% at high E_T, with a moderate dependence on particle type and pseudorapidity.

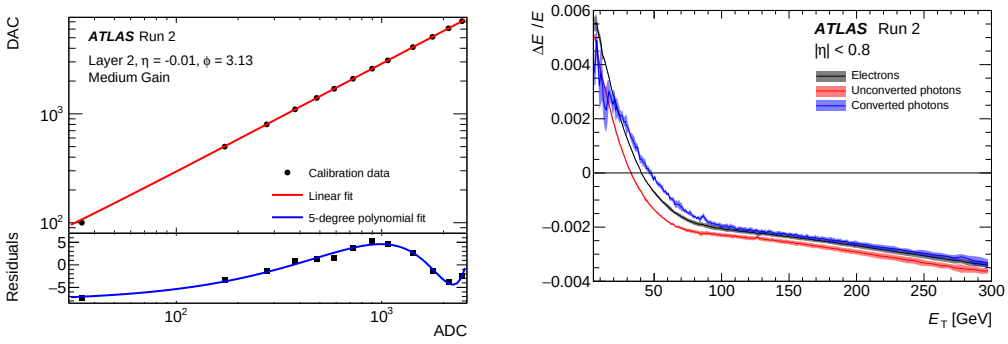

Figure 6.15 – (a) Example of a calibration run in medium gain for a cell in the second layer of the EM calorimeter. The injected-current response (in DAC units) is fitted with a linear function (top), and the residuals with respect to this fit (bottom) are modelled with a fifth-order polynomial used to correct the cell energy. (b) Relative cluster-energy correction as a function of E_T for electrons (black), unconverted photons (red), and converted photons (blue) in the region $|\eta| < 0.8$. The envelope indicates the variation of the correction with η for each particle type [17].

6.4.2 High/Medium gain intercalibration

The linearity of the readout electronics is better than a few per mille in each of the three gains used to digitise the calorimeter signals. While the relative calibration of the High-, Medium- and Low-gain readouts is assumed to be perfect in the simulation, it is less precisely known in data. In standard running conditions, the High Gain (HG) readout is used for most cells in clusters from electrons in $Z \to ee$ decays, whereas in about 30% of $H \to \gamma\gamma$ events at least one photon has a cell reconstructed in Medium Gain (MG). The transition from HG to MG readouts occurs for second-layer (L2) cell energies above 25 GeV, corresponding to electrons of $E_T \sim 50 - 60$ GeV.

The relative calibration of the HG and MG gains is studied using 0.3 fb^{-1} of data collected in 2017-2018 under special conditions in which the threshold for switching from HG to MG in the second calorimeter layer was lowered—typically by a factor of three—so that almost all electrons from Z-boson decays have their highest-energy L2 cell recorded in MG. The dielectron invariant-mass distribution in these special runs is compared with that from 1.5 fb^{-1} of data recorded with the standard gain configuration at similar times. An example comparison for electrons with $|\eta| < 0.8$ is shown in Figure 6.16a.

The relative energy scale α_G between the MG and HG configurations is then extracted using the $Z \to ee$ events from the standard and special runs, as illustrated in Fig-

ure 6.16b.

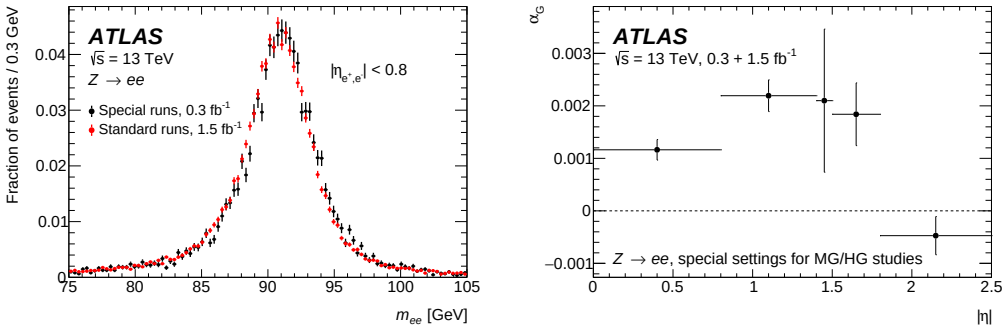

(a) **(b)**

Figure 6.16 – (a) Example dielectron invariant mass distributions, one from events collected in special runs and the other from standard runs, and (b) corresponding energy scale factors and their statistical uncertainties as a function of $|\eta|$ [17].

6.5 In-situ calibration for scale and resolution

A final calibration step, referred to as the *in-situ calibration*, exploits $Z \to ee$ events to correct any remaining mismatch between data and simulation. A global energy-scale factor α is extracted in bins of the electron pseudorapidity and applied to data to align the reconstructed Z-boson mass peak with that observed in the simulation. In the same procedure, resolution-smearing factors are derived to match the slightly worse energy resolution observed in data. These smearing terms are applied to the simulation. Both α and the smearing factor contribute to the total systematic uncertainty on the final electron and photon energy, with a dependence on η and E_{T}.

Accordion scale calibration

After the independent calibration of the Presampler and the L1-L2 relative response, the overall energy scale of the accordion calorimeter (L1, L2, L3) is determined. This scale factor, denoted α_{acc}, accounts for differences between data and simulation that affect the combined response of the three electromagnetic sampling layers. The calibration is performed in bins of electron pseudorapidity.
The determination of α_{acc} relies on the global in-situ scale factors extracted from $Z \to ee$ events (see Section 6.5.1). The accordion scale for each η bin is defined through the relation

$$E_{\mathrm{corr}}^{\mathrm{data}} = \frac{E_{\mathrm{raw}}^{\mathrm{data}}}{1 + \alpha_{\mathrm{acc}}}, \tag{6.4}$$

where $E_{\mathrm{raw}}^{\mathrm{data}}$ is the raw energy reconstructed in the accordion layers. The α_{acc} values derived for the individual Run 2 data-taking periods, together with the residual scale factors from the final closure test, are shown in Figure 6.17. Changes in the α_i^{acc} values

between successive years are mainly due to variations of the LAr temperature and the instantaneous luminosity. The temperature variations induce changes in the charge/energy collection, affecting the energy response by about -2%/K. Increases in luminosity during Run 2 imply that more energy is deposited in the liquid-argon gap, which creates a higher current in the high-voltage lines, effectively reducing the high voltage applied to the gap and changing the response by up to 0.1% in the endcap regions, as visible in Figure 6.17. Given the small size of the observed dependence, dedicated energy scale corrections for each data-taking year provide adequate stability for the energy measurement.

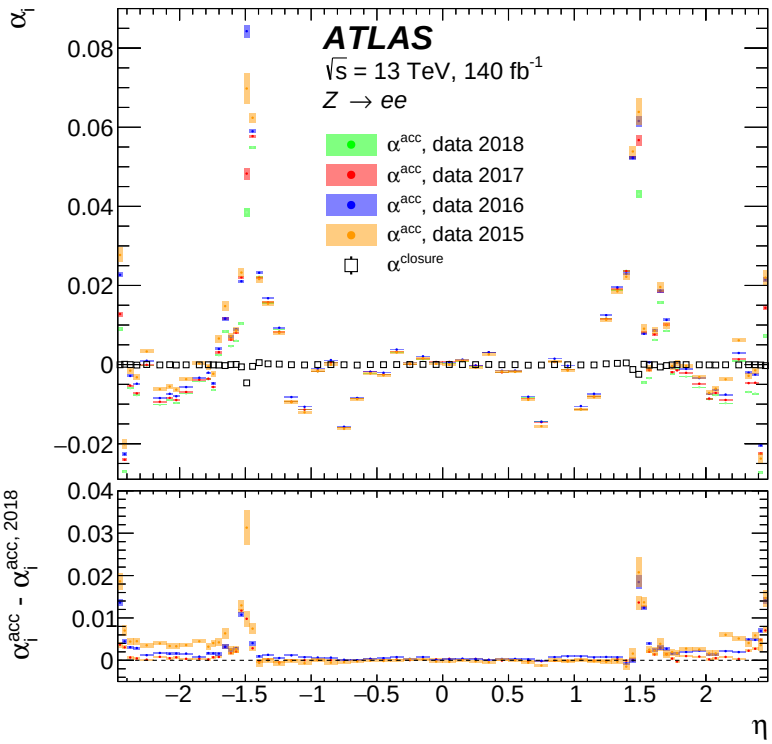

Figure 6.17 – Energy scale calibration factors α_{acc} and α_{closure} as a function of $|\eta|$ for electrons from Z boson decays. The α_{acc} factors are shown separately for each data-taking year in Run 2, while the α_{closure} factors are integrated over the full Run 2 data. The bottom panel shows the difference between α_{acc} measured in a given data-taking period and the measurements using 2018 data [17].

6.5.1 In-situ measurement of the global energy scale and resolution from $Z \to ee$ events

Once all layer-specific calibration factors (Presampler scale, L1-L2 intercalibration, accordion scale) and the simulation-based calibration are applied, any remaining differences

between data and simulation are quantified using $Z \to ee$ decays. For each electron η bin, a global energy-scale factor α_i is obtained by fitting the reconstructed di-electron invariant-mass distribution and aligning the Z peak in data with that in simulation:

$$E_i^{\text{data}} = \frac{E_i^{\text{MC}}}{1+\alpha_i}. \tag{6.5}$$

Accordion energy scale corrections for single electrons, defined as $E_i^{\text{acc,corr}} = E_i^{\text{acc}}/(1+\alpha_i^{\text{acc}})$, are related at first order to the di-electron invariant-mass scale factors α_{ij} according to

$$\alpha_{ij} = \frac{f_i^{\text{acc}}\alpha_i^{\text{acc}} + f_j^{\text{acc}}\alpha_j^{\text{acc}}}{2}, \tag{6.6}$$

where f_i^{acc}, shown in Figure 6.18, is determined from simulation and represents the fractional sensitivity of the total calibrated electron energy to the energy measured in the accordion calorimeter for electrons in the η bin i. Since part of the electron energy is deposited in the presampler (for $|\eta| < 1.8$) and in the scintillators in the barrel–endcap transition regions ($1.4 < |\eta| < 1.6$), f_i^{acc} is expected to be smaller than unity.

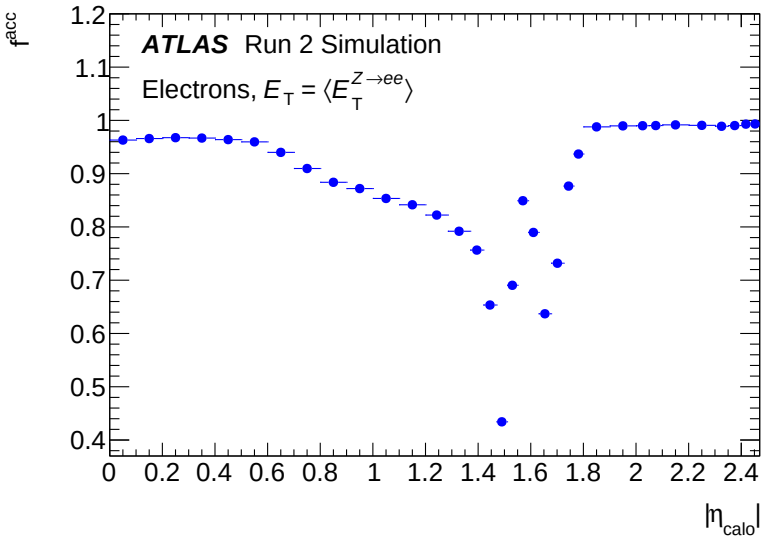

Figure 6.18 – Sensitivity of the calibrated electron energy to the energy measured in the accordion calorimeter, f^{acc}, as a function of $|\eta|$ for electrons from Z-boson decays [17].

The electron energy resolution in the simulation is adjusted with an additional η-dependent term c_i, applied in quadrature:

$$\left(\frac{\sigma(E)}{E}\right)_i^{\text{data}} = \left(\frac{\sigma(E)}{E}\right)_i^{\text{MC}} \oplus c_i. \tag{6.7}$$

For a pair of electrons from Z-boson decays falling into the η bins i and j, the miscalibration of the di-electron invariant mass can be expressed in terms of the global scale factors

α_i and the smearing terms c_i as:

$$\left(m_{ee}^{\text{data}}\right)_{ij} = \left(m_{ee}^{\text{MC}}\right)_{ij} / \left(1 + \alpha_{ij}\right), \qquad \alpha_{ij} \approx \frac{\alpha_i + \alpha_j}{2}, \tag{6.8}$$

$$\left(\frac{\sigma(m_{ee})}{m_{ee}}\right)_{ij}^{\text{data}} = \left(\frac{\sigma(m_{ee})}{m_{ee}}\right)_{ij}^{\text{MC}} \oplus c_{ij}, \qquad c_{ij} \approx \frac{c_i \oplus c_j}{2}. \tag{6.9}$$

The scale factors α_i and smearing terms c_i are extracted simultaneously by comparing the invariant-mass distributions for all (i, j) combinations of electron pseudorapidity bins. The resulting resolution terms are typically below 1% in the barrel and between 1-2% in the endcaps, as shown in Figure 6.19.

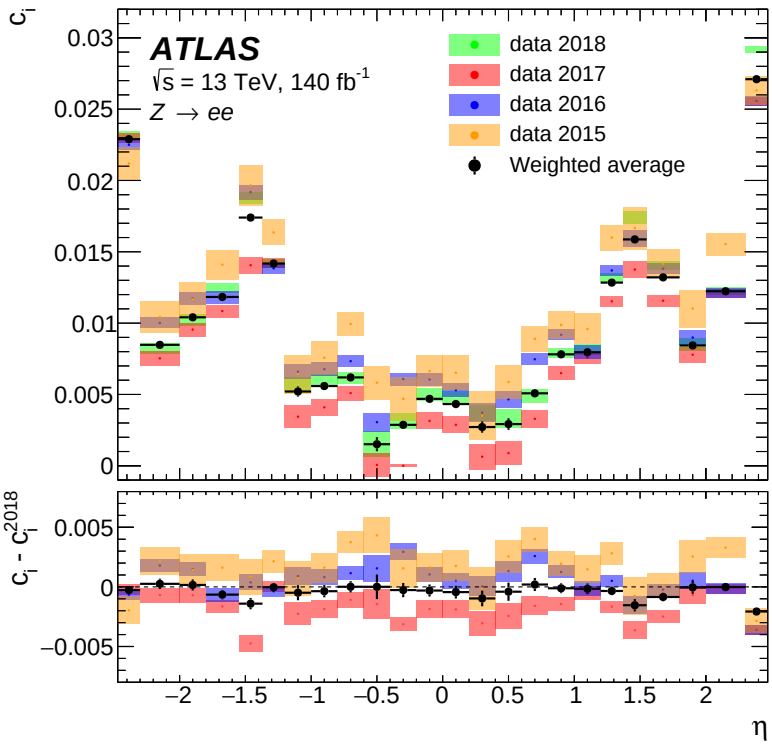

Figure 6.19 – Energy resolution calibration factors c a function of η for electrons from Z boson decays. The bottom panel shows the difference between c measured in a given data-taking period and the measurements using 2018 data [17].

As a final consistency check, the Z-based calibration is repeated after applying all corrections. The resulting residual scale factors $\alpha_{\text{residual},i}$ are found to be smaller than 10^{-4} across most of the calorimeter acceptance, except in the barrel-endcap transition region ($1.37 < |\eta| < 1.52$) where TileCal contributes to the energy measurement. These residual corrections are applied to the reconstructed energy in data.

After the full calibration chain has been applied, a good agreement is observed between the invariant-mass distributions of $Z \to ee$ events in data and simulation, as illustrated in Figure 6.20.

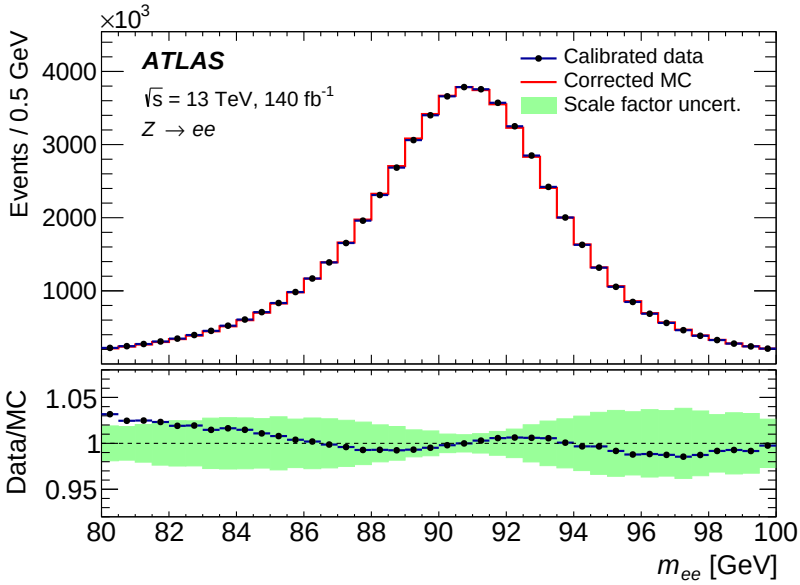

Figure 6.20 – Comparison of the invariant mass distributions of the electron pair in the selected $Z \to ee$ candidates in data and simulation, after the calibration and resolution corrections are applied. The total number of events in the simulation is normalized to that in data. The ratio between data and simulation is shown in the bottom panel, where the uncertainty band represents the impact of the uncertainties in the calibration and resolution correction factors [17].

6.5.2 Photon-specific corrections

Photon conversion reconstruction and classification

The photon energy reconstruction is optimised separately for converted and unconverted photons; therefore, differences between data and simulation in the photon classification rates can induce a bias in the photon energy scale. Misclassifications originate from inefficiencies in the conversion-finding algorithm and from the incorrect association of unconverted photon candidates to pile-up tracks. The classification performance is measured using photons from radiative Z-boson decays as a function of $|\eta|$ and E_{T}. The associated energy-scale uncertainty is evaluated by reweighting the conversion fractions in simulated single-photon samples to match those observed in data and is defined as the relative difference in the energy response. For photons with $E_{\mathrm{T}} = 60$ GeV, the uncertainty for unconverted photons is about 0.02% in the barrel and 0.02%–0.13% in the endcaps, while for converted photons it is approximately 0.12% in the barrel and below 0.01% in the endcaps. At $E_{\mathrm{T}} = 15$ GeV, the uncertainty increases to 0.18% in the barrel and 0.08%–0.67% in the endcaps for unconverted photons, and to 0.69%–1.31%

in the barrel and 0.01%–0.1% in the endcaps for converted photons. This systematic uncertainty is treated as a single source and is assumed to be fully correlated between converted and unconverted photons.

Out-of-cluster energy leakage mis-modelling

Electrons and photons deposit a fraction of their energy outside the reconstruction cluster, leading to a lateral energy leakage that is on average corrected by the simulation-based energy calibration. Residual differences between data and simulation are studied using $Z \to ee$ and $Z \to \ell\ell\gamma$ events by comparing the energy measured in the second calorimeter layer within the nominal supercluster to that collected in a larger window. The leakage observable is evaluated as a function of E_{T} and $|\eta|$ for electrons, converted photons, and unconverted photons.
A double-difference observable, α_l, is defined to quantify the relative discrepancy between electrons and photons in data and simulation and is used to correct the photon energy scale. The effect is largest at low E_{T}, reaching values of order -0.3%, and decreases with increasing energy, becoming smaller than $\sim 0.05\%$ at high E_{T}. The corresponding absolute uncertainties range from 0.01% to 0.07%, depending on the kinematic region and particle type. Contributions from photon conversion reconstruction and classification are included and treated as systematic uncertainties. The increased statistical power of Run 2 data allows an improved modelling of this effect and a significant reduction of the associated calibration uncertainty compared to previous measurements.

6.5.3 Systematic uncertainties

Several sources of systematic uncertainty affect the energy scale and resolution of electrons and photons, with a dependence on their transverse energy and pseudorapidity. The Z-based calibration constrains the electron energy scale around the characteristic transverse momentum of electrons from $Z \to ee$ decays ($p_{\mathrm{T}} \sim 45$ GeV). Photons from $H \to \gamma\gamma$ decays typically have a harder p_{T} spectrum, and therefore their associated uncertainties must be extrapolated beyond the region directly probed by the Z peak, generally resulting in a larger impact.
Most uncertainties are evaluated separately for converted and unconverted photons. Converted photons produce showers that more closely resemble those of electrons and therefore tend to have smaller energy-scale uncertainties. In contrast, unconverted photons rely entirely on the calorimetric measurement and are more sensitive to imperfect modelling of the electromagnetic shower development.
The complete systematic-uncertainty model used in the Run 2 electron and photon energy calibration includes 64 independent variations for electrons and 67 for photons. The main sources of systematic uncertainty are summarised below:

- *In-situ $Z \to ee$ calibration*: The Z-based calibration fit used to extract the energy scale and resolution carries systematic uncertainties associated with the measurement itself, such as the event selection and the choice of the fitting range in the m_{ee} spectrum. The impact is typically below 0.05% across most η regions, but can reach up to 0.5% in the transition region.

- *LAr layer calibration*: The measurements of α_{PS} and α_{12} carry systematic uncertainties arising from the selection of candidate electrons or muons, uncertainties in the material description, and the choice of the estimators used for $\langle E_i \rangle$, $\langle m_{ee} \rangle$, and $\langle E/p \rangle$. The uncertainty associated with α_{12} can affect the energy scale by up to 0.2%, while the impact of the presampler scale α_{PS} is typically below 0.1%.
- *Non-linearity of the LAr readout electronics*: The energy reconstruction in the EM calorimeter cells relies on a linear conversion from ADC counts to deposited energy, using calibration constants obtained from dedicated electronic calibration runs. Since the relation between injected current and ADC response is not perfectly linear, residual non-linearities are evaluated cell by cell and used to correct the raw cell energies. The impact on the reconstructed electron or photon energy is estimated by re-evaluating the non-linearity corrections for all cells in the cluster and computing the relative change in the cluster energy. This variation is reparameterised to be zero for electrons at $E_T = 40$ GeV, where the global scale is anchored. The resulting uncertainty affects the energy scale by up to 0.4% for low-E_T electrons and photons, and remains below 0.2% at higher E_T.
- *Intercalibration of High to Medium Gain*: As described in Section 6.4.2, the relative calibration of the HG and MG readout modes is assumed to be perfect in simulation, and must therefore be measured directly in data. This is achieved using dedicated runs in which the MG threshold in the L1 or L2 layers is lowered, ensuring that the highest-energy cells within electron clusters from $Z \to ee$ decays are read out in MG. By comparing the dielectron invariant-mass distributions in these special runs with those recorded under nominal gain settings, the uncertainty on the High-to-Medium gain intercalibration can be extracted for the L1 and L2 EM layers. Its impact on the energy scale reaches up to 0.1% in the barrel and up to 0.4% in the endcaps. A corresponding, independent, uncertainty is defined for the transition between the Medium and Low Gain (LG) readouts, whose impact is non-negligible only at very high energies ($E_T > 400$ GeV). By isolating the High-to-Medium gain intercalibration uncertainty from the Medium-to-Low gain intercalibration uncertainty, the calibration fit described in the following Section 6.5.4 constrains the former more effectively, since it is more relevant in the E_T range close to the average of $Z \to ee$ electrons.
- *Material modelling*: The electron and photon energy response is influenced by the amount of passive material located upstream of the EM calorimeter. Although the simulation-based calibration accounts for the material description in the detector model, discrepancies between the simulated and actual material distribution lead to differences in the reconstructed energy between data and MC. For electrons with $E_T \approx 40$ GeV, such differences are largely absorbed by the Z-based calibration; however, residual biases remain, depending on the particle type and energy. The uncertainty associated with passive material, parameterised as a function of particle type, E_T and $|\eta|$, predominantly affects low-E_T electrons and unconverted photons, with typical impacts in the range of 0.1–0.2%.
- *Photon conversions mismodelling*: The simulation-based calibration is optimised sep-

arately for unconverted photons and converted photons. Differences between data and simulation in classification rates of converted and unconverted photons generate biases in the photon energy scale. The conversion rates are measured using a sample of photons from radiative Z events. The uncertainty in the photon energy scale is evaluated by reweighting the conversion fractions (corresponding to the fraction of true photon conversions, photon conversions reconstruction efficiency, and fraction of reconstructed fake photon conversions) in simulated photons in single-particle samples to those observed in radiative Z samples in data and MC. The impact of the bias from the photon conversion fractions is assumed correlated among reconstructed converted and unconverted photons, across the full η range. However, the magnitude of the uncertainty varies between converted and unconverted photons and with their $|\eta|$ and E_{T}. For photons with $E_{\mathrm{T}} = 60$ GeV, the uncertainty is about 0.02%-0.13% for unconverted photons and 0.01%-0.12% for converted photons, depending on the region. At lower E_{T}, these uncertainties increase significantly: for unconverted photons, they can be as large as 0.67%, while for converted photons they reach up to 1.31%.

The effects of the most significant uncertainties are shown as a function of electron or photon E_{T} for two different pseudorapidity values in Figure 6.21.

6.5.4 Energy linearity and constraints on the calibration uncertainties

As a first-order approximation, the energy scales extracted from the in-situ $Z \to ee$ calibration (Section 6.5) are assumed to be valid over the full electron transverse-energy spectrum. In this approach, the residual difference between data and simulation is absorbed into η-dependent scale factors, such that

$$E^{\mathrm{data}} = E^{\mathrm{MC}} \left(1 + \alpha(\eta)\right). \tag{6.10}$$

However, possible non-linear effects in the energy response may induce a residual dependence of the energy scale on the electron transverse energy. To investigate this effect, the $Z \to ee$ invariant-mass fit is repeated in bins of $|\eta|$ and E_{T}, and the calibrated energy is written as

$$E^{\mathrm{data}} = E^{\mathrm{MC}}(1 + \alpha_i(\eta))(1 + \alpha'_j(|\eta|, p_{\mathrm{T}})), \tag{6.11}$$

where $\alpha_i(\eta)$ denotes the nominal η-dependent scale factors obtained from the inclusive Z calibration, and $\alpha'_j(|\eta|, p_{\mathrm{T}})$ encodes a residual dependence on the transverse energy. The index j labels bins in the two-dimensional $(|\eta|, E_{\mathrm{T}})$ space, defined by the boundaries $|\eta| \in [0, 0.6, 1.0, 1.37, 1.55, 1.82, 2.47]$ and $E_{\mathrm{T}} \in [27, 33, 38, 44, 50, 62, 100, \sqrt{s}/2]$ GeV. An event is assigned to a given j category if at least one of the two electrons falls into the corresponding bin.

The residual scale factors $\alpha'_j(|\eta|, E_{\mathrm{T}})$ can be interpreted as a probe of non-linear effects in the energy response, which are not fully constrained by the inclusive Z calibration. These effects are modelled by parametrising α' as a linear combination of the energy-

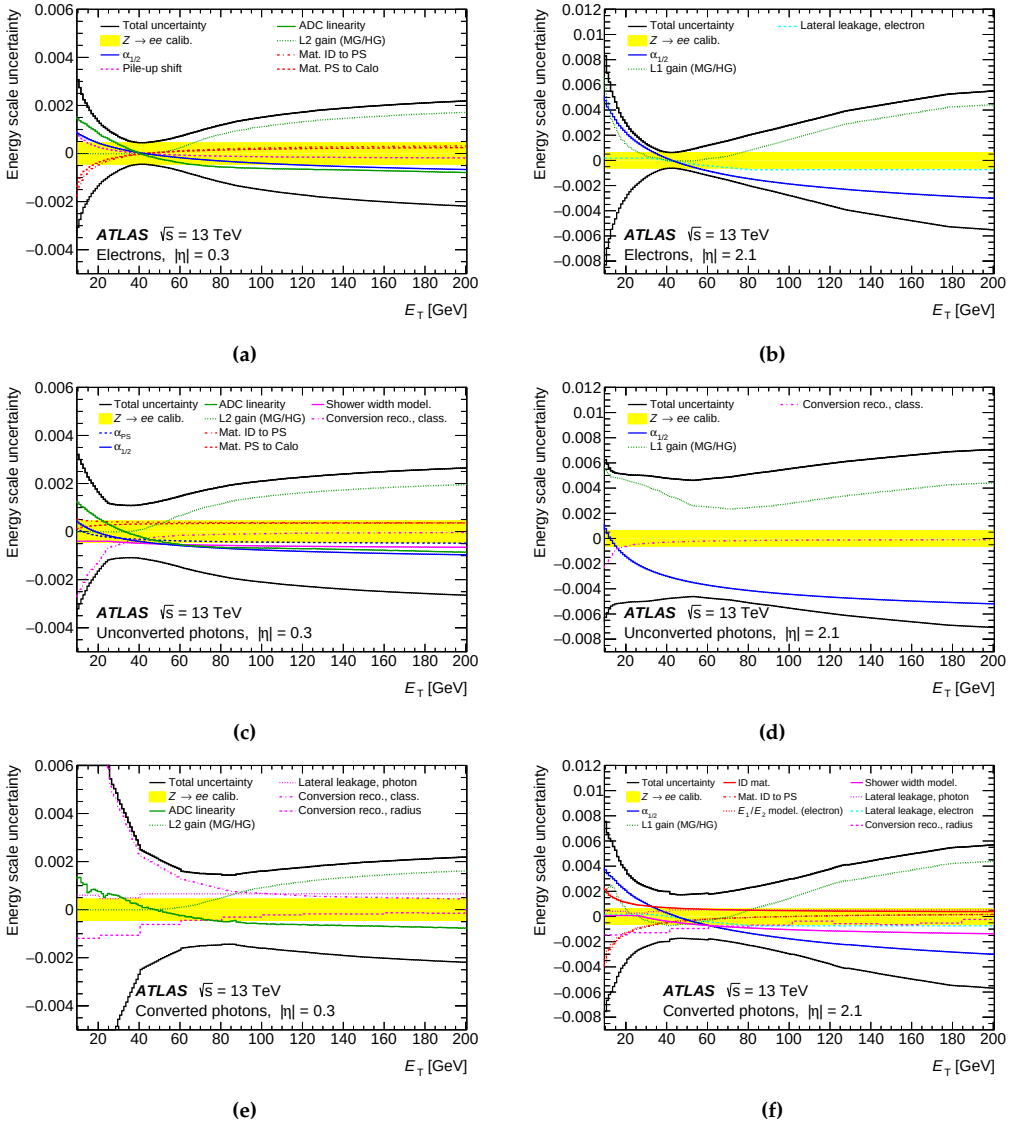

Figure 6.21 – Relative energy scale calibration uncertainty for electrons, unconverted photons, and converted photons, as a function of E_{T} for $|\eta| = 0.3$ (left) and $|\eta| = 2.1$ (right) [17].

scale systematic uncertainties:

$$\alpha'(|\eta|, E_{\mathrm{T}}) = \sum_{k}^{N_{\mathrm{sys}}} \delta_{\alpha k}(|\eta|, E_{\mathrm{T}})\, \theta_k, \tag{6.12}$$

where $\delta_{\alpha k}(|\eta|, E_{\mathrm{T}})$ represents the variation associated with the k-th energy-scale systematic uncertainty as a function of pseudorapidity and transverse energy, and θ_k are nui-

sance parameters constrained by standard Gaussian priors.
The parameters θ_k are determined through a χ^2 minimisation comparing the model prediction to the α' values measured in data:

$$\chi^2(\vec{\alpha}', \vec{\theta}) = \sum_{ij} \left[\alpha'^i(\vec{\theta}) - \alpha'^i\right] V_{ij}^{-1} \left[\alpha'^j(\vec{\theta}) - \alpha'^j\right] + \sum_{k}^{N_{\text{sys}}} \theta_k^2, \tag{6.13}$$

where the indices i and j run over the $(|\eta|, E_{\text{T}})$ bins, and V_{ij} is the covariance matrix of the measured α' values.
This linearity-fit approach provides a data-driven constraint on the energy-scale systematic uncertainties as a function of transverse energy, leading to a significant improvement in the precision of the electron and photon energy calibration and, consequently, of the Higgs boson mass measurement as discussed in the next Chapter 7.
A fit to the di-electron invariant mass distribution is performed to extract the α'_j values that best align data and simulation. The resulting α'_j coefficients are shown in Figure 6.22. These results reveal a clear residual E_{T} dependence of the energy scale, measured with a precision better than 0.03% (rising to about 0.3% in the transition region). The precision on the α'_j parameters is superior to that of the η-dependent scales α_i derived earlier far from 45 GeV. As a consequence, the linearity fit provides an additional and powerful constraint on the systematic uncertainties affecting the energy scale across the full E_{T} spectrum. While the E_{T} behaviour of these uncertainties can be estimated from simulation (by evaluating the sensitivity of the reconstructed energy to each uncertainty source), the linearity fit delivers direct data-driven constraints in several E_{T} regions, rather than only at $E_{\text{T}} \simeq 40$ GeV, characteristic of electrons from Z decays.
The impact of this fit on the total scale uncertainty is illustrated in Figure 6.22, which compares the pre-fit (outer band) and post-fit (inner band) uncertainty envelopes. The linearity fit reduces the systematic uncertainty on the energy scale by up to a factor of two for $E_{\text{T}} < 50$ GeV and by up to a factor of three around $E_{\text{T}} \simeq 150$ GeV. As shown in Figure 6.23, this reduction is mainly driven by the nuisance parameters associated with cell-level non-linearity (ADC corrections and the HG/ MG transition) and shower development (lateral leakage and shower width). Most other nuisance parameters are typically constrained at the level of 5-10%. The output of the fit consists of pulled, constrained, and correlated systematic uncertainties.
The detailed impact on the electron energy scale uncertainty for electrons is shown in Figure 6.24a as a function of E_{T} and $|\eta|$. As expected, the precision for electrons with $E_{\text{T}} \simeq 40$ GeV remains essentially unchanged: these electrons, produced abundantly in on-shell Z decays, are already tightly constrained by the in-situ calibration of the accordion scales and by the η-dependent residual scale factors. In contrast, uncertainties for electrons with $E_{\text{T}} = 10$ GeV or $E_{\text{T}} = 1$ TeV are typically reduced by 30-50%, reaching 0.2-0.3% for $|\eta| < 1$ and $|\eta| > 1.8$, and between 0.5% and 1% in the region $1 < |\eta| < 1.8$.
The corresponding impact on photon calibration uncertainties is shown in Figure 6.24b for converted and unconverted photons at $E_{\text{T}} = 60$ GeV, representative of photons from Higgs boson decays. For converted photons—whose shower development closely resembles that of electrons—the improvement from the linearity fit is modest for this en-

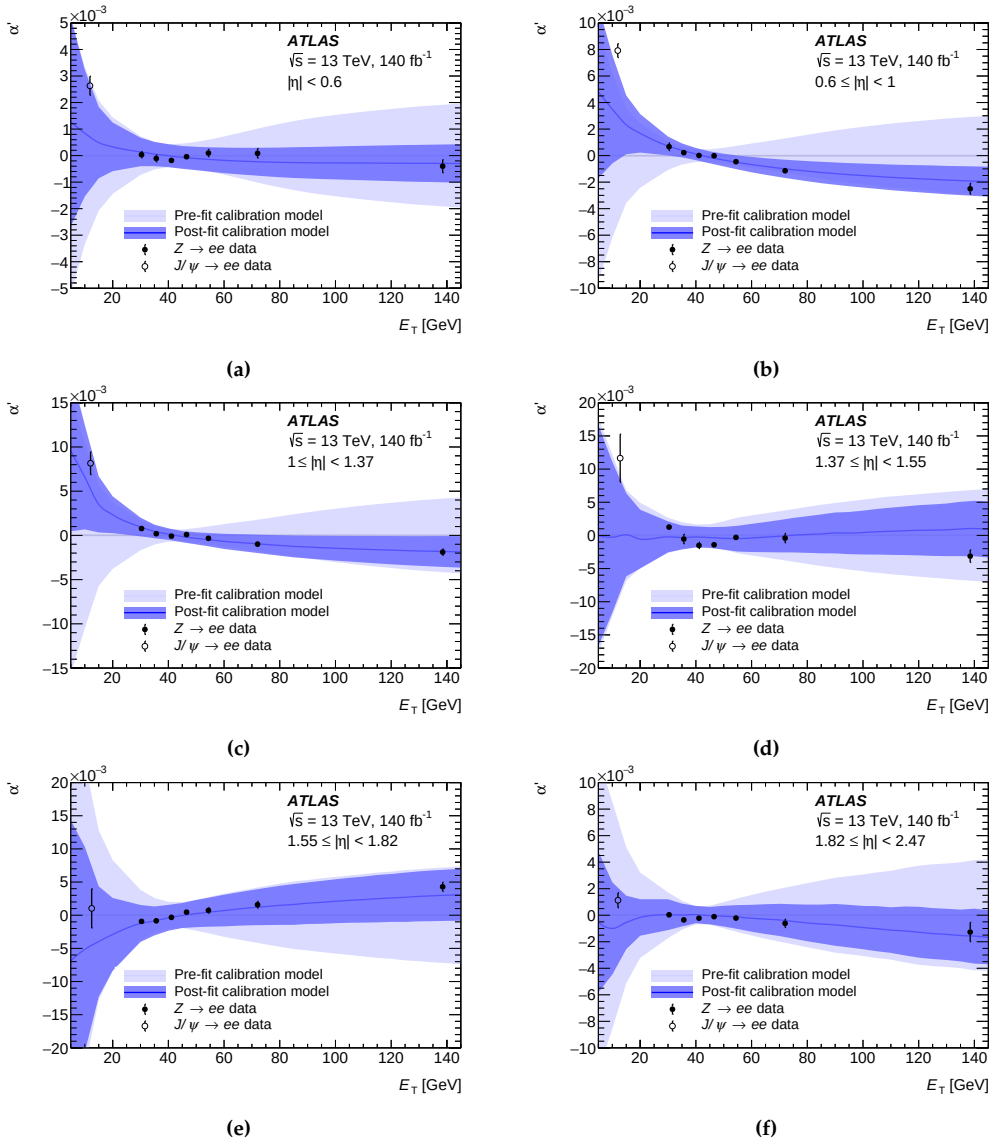

Figure 6.22 – Comparison of the measured values of α'_j from $Z \to ee$ events (black dots) with the results extracted from the linearity fit, including their corresponding uncertainty band. The pre-fit value of α' (namely, $\alpha' = 0$ before the linearity constraint) and its associated uncertainty are also displayed. Additionally, the measured values of α' from $J/\psi \to ee$ events, used as a cross-check for the linearity model in the low-E_T region, are shown (open dots) [17].

ergy. For unconverted photons, however, the total energy-scale uncertainty is typically reduced by about 30% in the barrel and by up to a factor of two in the endcap region.

The auxiliary constraints and the correlations of the systematic uncertainties obtained from the linearity fit are propagated to the Higgs boson mass measurement in the $H \to$

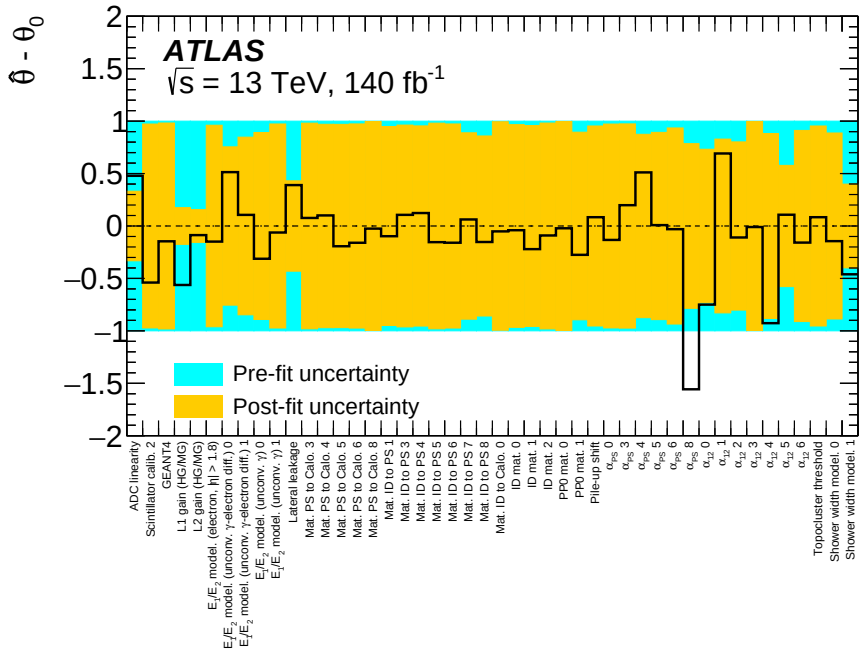

Figure 6.23 – Shifts and constraints on the nuisance parameters of the systematic uncertainty model from the energy linearity fit. A digit after the Nuisance Parameter (NP) name represents a given η range (a priori different for different NP sources) [17].

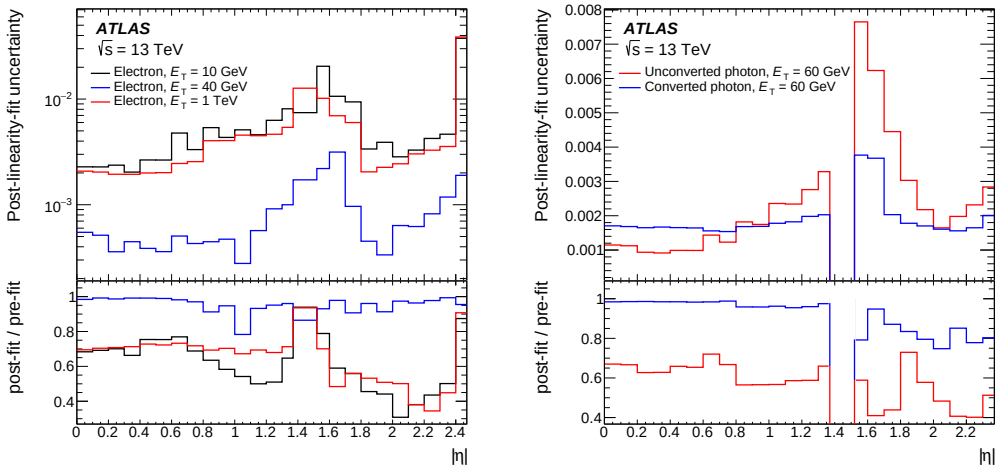

Figure 6.24 – Total relative systematic uncertainty in the energy scale as a function of $|\eta|$ for electrons with $E_{\mathrm{T}} = 10$ GeV, 40 GeV or 1 TeV (left) photons with $E_{\mathrm{T}} = 60$ GeV, after the constraints from the linearity fit. The bottom panels show the ratio of the post-fit to pre-fit uncertainties [17].

$\gamma\gamma$ channel, as described in Chapter 7. This improved modelling of the energy-scale uncertainties is one of the main reasons why the final Higgs boson mass result achieves such a high level of precision.

6.6 Energy calibration validation

The J/Ψ resonance provides an independent check of the energy calibration for electrons with transverse energy in the range from 5 to 30 GeV. The full calibration procedure is applied to a sample of $J/\Psi \to ee$ events and the difference between data and simulation for $J/\Psi \to ee$ events is then quantified using residual energy scale factors extracted from the peak positions of the reconstructed invariant mass. If the energy calibration is correct, the residual energy scale factors should be consistent with zero within the combined uncertainties of the $J/\Psi \to ee$ measurement and the systematic uncertainty of the energy calibration. The evolution of the scale α is shown in Figure 6.25 as a function of (a) η and (b) E_{T}, before and after including the constraints from the linearity fit. The residual post-fit scale factors are below 0.5% and are compatible with zero within the total calibration uncertainty.

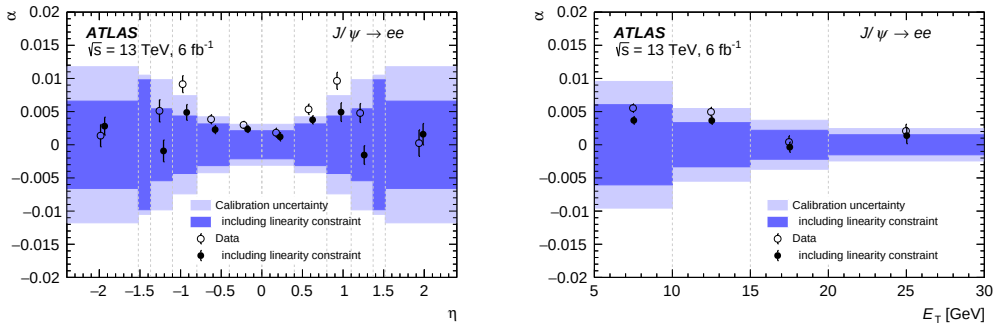

Figure 6.25 – Variation of the residual energy scale as a function of (a) η and (b) E_{T}, as measured with $J/\Psi \to ee$ events. The data points and uncertainty bands are shown for both the pre- and post-linearity-fit energy scale models. The uncertainty bands correspond to the energy calibration uncertainty for the energy range of the $J/\Psi \to ee$ decays [17].

A further validation of the energy calibration is performed using radiative Z boson decays $Z \to \ell\ell\gamma$, with $\ell = e, \mu$ and a photon from the final-state radiation. The photon energy scale is probed by comparing the three-body invariant mass ($m_{\ell\ell\gamma}$) in data and simulation. The inclusive residual photon energy scale factors are measured to be $(3.3 \pm 2.0) \times 10^{-3}$ and $(1.4 \pm 1.1) \times 10^{-3}$ in the $Z \to ee\gamma$ and $Z \to \mu\mu\gamma$ samples, respectively. The residual scales measured in the two channels agree within one standard deviation.

The dependence of α on the energy and pseudorapidity of the photon is illustrated in Figure 6.26, separately for converted photons and unconverted photons. The residual photon energy scales are compared with the total energy calibration uncertainty for pho-

tons from $Z \to \ell\ell\gamma$ decays, before and after including the constraints from the linearity fit.

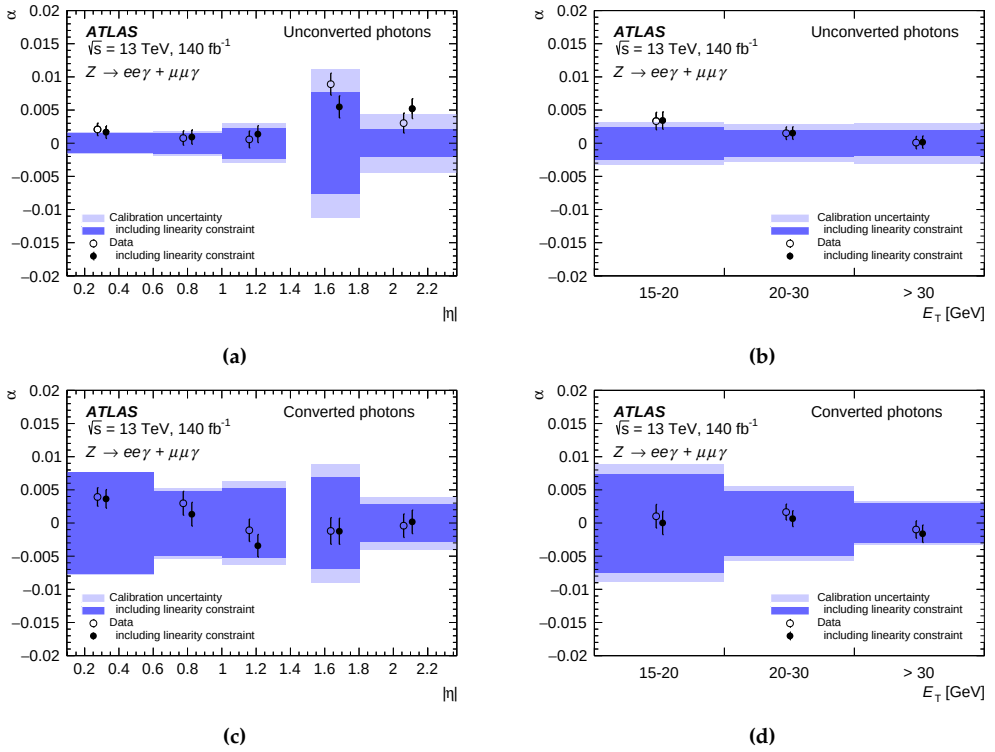

Figure 6.26 – Variation of the residual energy scale for (a, b) unconverted and (c, d) converted photons as a function of (a, c) $|\eta|$ and (b, d) E_{T}, as measured with $Z \to \ell\ell\gamma$ events. The data points and uncertainty bands are shown for both the pre-and post-linearity-fit energy scale models. The uncertainty bands correspond to the energy calibration uncertainty for photons from $Z \to \ell\ell\gamma$ decays [17].

7 | Measurement of the Higgs boson mass in the $H \to \gamma\gamma$ channel in Run 2

This Chapter presents the measurement of the Higgs boson mass in the diphoton decay channel, using pp collision data recorded by the ATLAS detector during the full Run 2 data-taking period at a centre-of-mass energy of $\sqrt{s} = 13$ TeV, corresponding to a total integrated luminosity of 140 fb^{-1} [14].

Following the announcement by the ATLAS [113] and CMS [114] collaborations in 2012 of the observation of a new particle compatible with the SM Higgs boson, the precise determination of its properties—most notably its mass, m_H—has become of primary importance for improving our understanding of the fundamental laws of the Universe.

As already discussed in Section 1.2, the Higgs boson is a massive scalar particle whose existence is implied by the Higgs mechanism, proposed in 1964 by Higgs [6], and by Englert and Brout [7]. The introduction of this mechanism in the SM is essential for generating the mass terms of all massive elementary particles without explicitly breaking the gauge symmetries of the SM Lagrangian. The Higgs mass enters the theory as a free parameter; since the Higgs production cross-sections and decay branching ratios are fully specified only once m_H is fixed (see Figures 4.3 and 4.4), a precise experimental determination of m_H is required to evaluate the consistency of its couplings to all other particles.

Secondly, the measured value of m_H is a key input to global fits of electroweak observables [11]. Its precise determination therefore plays an important role in testing the internal consistency of the SM, especially through the interplay between the masses of the top quark and the W and Higgs bosons.

Finally, the stability of the electroweak vacuum is strongly dependent on the value of the Higgs mass [12]. By measuring m_H, one can infer whether the Universe resides in a global and thus stable minimum of the Higgs potential, or in a local, metastable one from which it could, in principle, tunnel to the true ground state in the future.

Section 4.4 provided an overview of the Higgs boson mass measurements in the two high-resolution decay channels, $H \to \gamma\gamma$ and $H \to ZZ^* \to 4\ell$, performed by both the ATLAS and CMS Collaborations during Run 1. The dataset consisted of 25 fb^{-1} of pp collisions at centre-of-mass energies of $\sqrt{s} = 7$ and 8 TeV. The combined Run 1 measurement in the two channels and across the two experiments yielded the following result [13]:

$$m_H = 125.09 \pm 0.21\ (\text{stat.}) \pm 0.11\ (\text{syst.})\ \text{GeV} = 125.09 \pm 0.24\ \text{GeV}, \tag{7.1}$$

which has since been regarded as the nominal value of m_H within the HEP community. The results obtained from the individual channels and experiments in Run 1, as well as from their combination, are summarised in Figure 4.9.

Updated Run 2 measurements were also performed in both channels by the two experiments, using pp collision data at $\sqrt{s} = 13$ TeV collected between 2015 and 2018. In 2018, using both the $H \to ZZ^* \to 4\ell$ and $H \to \gamma\gamma$ decays selected in a partial Run 2 dataset (36 fb^{-1} of pp collisions recorded before 2017), the ATLAS Collaboration measured $m_H = 124.86 \pm 0.27$ GeV [15]. Using a dataset of equivalent size and the same two final states, the CMS Collaboration obtained $m_H = 125.46 \pm 0.16$ GeV [154], whose combination with the Run 1 yielded the most precise determination of m_H to date (prior to the publication of the analysis summarised in this Chapter [14]), achieving a relative uncertainty of 0.11%: $m_H = 125.38 \pm 0.14$ GeV. CMS measurements in the diphoton [154] and four-lepton [155] final states, and their combination using Run 1 and Run 2 data, are shown in Figure 7.1a. More recently, in 2024, a measurement in the four-lepton channel using the full Run 2 dataset corresponding to an integrated luminosity of 138 fb^{-1} reported $m_H = 125.04 \pm 0.12$ GeV: the various channels, the Run 1, the Run 2 and the combination results are reported in Figure 7.1b.

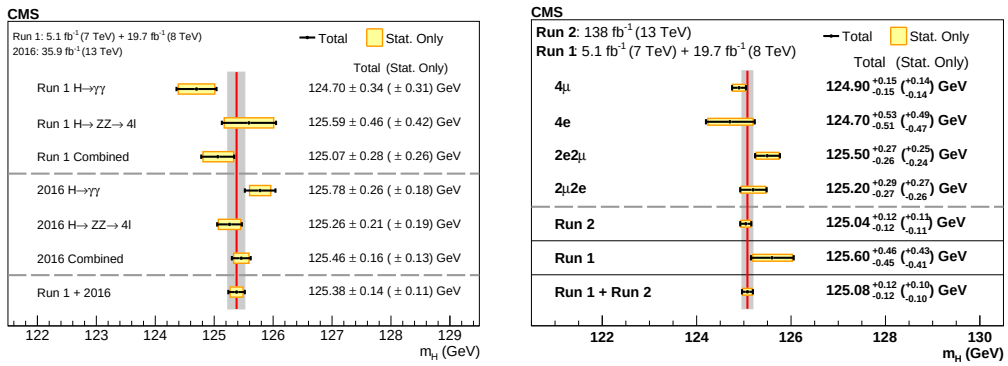

Figure 7.1 – (a) A summary of the measured Higgs boson mass in the $H \to \gamma\gamma$ and $H \to ZZ^* \to 4\ell$ decay channels, and for the combination of the two [154]. The statistical (wider, yellow-shaded bands), and total (black error bars) uncertainties are indicated. The (red) vertical line and corresponding (grey) shaded column indicate the central value and the total uncertainty of the Run 1 + 2016 combined measurement, respectively. (b) Summary of the observed CMS Higgs boson mass measurements using the four-lepton final state [155]. The red vertical line and the grey column represent the best fit value and the total uncertainty respectively as measured from the Run 1 and Run 2 combination.

ATLAS released an updated measurement of m_H using $H \to ZZ^* \to 4\ell$ decays in the full Run 2 dataset [18], consisting of 139 fb^{-1} of pp collisions. The result, $m_H = 124.99 \pm 0.19$ GeV, combined with that of the corresponding Run 1 analysis, yields a single-channel Higgs boson mass measurement with a total uncertainty of 0.14%, $m_H = 124.94 \pm 0.18$ GeV. The Run 2 4ℓ analysis will be briefly described in Section 8.1 in the context of the ATLAS Run 2 legacy mass combination.

The analysis presented in this Chapter benefits from the larger data sample of 140 fb^{-1}, a new photon reconstruction algorithm with improved energy resolution (see Section 5.1 and Ref. [16]), an improved determination of the photon energy scale with reduced uncertainties (see Section 6.5.4 and Ref. [17]), and an optimised event classification strategy. A description of the dataset, as well as all the simulated samples for the signal, background, and interference processes used in the $H \to \gamma\gamma$ analysis, is provided in Section 7.1. The definition of the physics objects and the event selection requirements aimed at selecting events containing a pair of good-quality photons are summarised in Section 7.2. To optimise the analysis sensitivity and the measurement precision, the events are further classified into 14 exclusive categories; the optimisation studies and the final categorisation are presented in Section 7.3. The modelling of the diphoton invariant mass spectrum for the signal and background processes is described in Section 7.4 and Section 7.5, respectively. Section 7.6 details all sources of systematic uncertainties—dominated by those associated with the electromagnetic energy calibration—and explains how they affect the analysis results. All these ingredients are combined to construct the statistical model, described in Section 7.7. The expected and observed results of the Higgs boson mass measurement in the $H \to \gamma\gamma$ channel are presented in Section 7.8. Finally, a combination with the ATLAS Run 1 measurement [13] is performed and presented in Section 7.9.

7.1 Data and simulation samples

7.1.1 Data

The measurement was performed using the full Run 2 pp dataset collected by ATLAS at $\sqrt{s} = 13$ TeV from 2015 to 2018, corresponding to a total integrated luminosity of 140.1 ± 1.2 fb^{-1} [73, 156] after the application of data-quality requirements. A breakdown of the delivered luminosity by year, together with the corresponding uncertainties, is provided in Table 7.1.

Year	Luminosity [fb^{-1}]	Uncertainty	
		Absolute [fb^{-1}]	Relative [%]
2015+2016	36.6	0.3	0.8
2017	44.6	0.5	1.1
2018	58.8	0.6	1.1
Total	140.1	1.2	0.8

Table 7.1 – Breakdown of the integrated luminosities per year with their absolute and relative uncertainties.

Events were recorded using unprescaled diphoton and single-photon triggers [139]. The diphoton triggers had transverse-momentum thresholds of 35 GeV and 25 GeV on the leading and subleading photon candidates, respectively, while the single-photon trigger thresholds were 120 GeV (2015-2016) and 140 GeV (2017-2018). Shower-shape require-

ments looser than those used in the offline analysis were applied to photon candidates at the trigger level.
Data are required to satisfy the Good Run List (GRL) conditions: they must correspond to luminosity blocks in which all subdetectors relevant for the analysis were fully operational. Events exhibiting calorimeter data-integrity errors, as well as incomplete events with missing detector information, are removed.

7.1.2 Simulation samples

Monte Carlo (MC) samples are datasets of simulated events widely used for physics analyses in ATLAS. In this analysis, they are used to optimise the event selection, to model the detector response, to choose an analytic function describing the diphoton mass distribution, and to estimate the reconstruction efficiency in each analysis region. The signal samples, as well as most of the background processes discussed in this section, were processed through the full ATLAS detector simulation software [157], based on GEANT4 [153].
The simulation involves several stages. The first step, performed by an *event generator*, consists of producing the physics event, including the hard-scattering interaction, parton showering (with the underlying event), hadronisation, and the decays of unstable particles. In the next step, the interaction of particles with matter, pileup effects, and the detector response are simulated in detail using GEANT4. A digitization step converts the output in a format identical to that of the real detector data-acquisition system, allowing both real and simulated events to be processed by the same ATLAS trigger and reconstruction chains.
The QCD diphoton background samples were instead produced using fast simulation [158], based on an effective parametrisation of the detector response, enabling a much larger number of events to be generated with reduced computing resources.

Signal samples

Signal samples were produced for the main Higgs boson production modes (described in Section 4.1): gluon-gluon fusion (ggF), vector-boson fusion (VBF), and associated production with a vector boson (VH, $V = W, Z$), a top-quark pair ($t\bar{t}H$), a bottom-quark pair ($b\bar{b}H$) or a single top quark (tH).
Signal event samples were produced with either the POWHEG-BOX [159] or (for tH only) MADGRAPH5_AMC@NLO [160] event generator, using matrix element calculations at the highest available order of accuracy in the strong coupling constant α_s:

- The ggF is generated at next-to-next-to-leading order (NNLO) precision in QCD with the POWHEG-BOX NNLOPS generator [161], which implements soft gluons resummation up to next-to-next-to-logarithmic order (NNLL), using the PDF4LHC15 parton distribution function [162], interfaced to PYTHIA 8 [163] for hadronization and underlying event, tuned with the AZNLO parameter set [164]. This sample is then normalized to the latest N^{3}LO (QCD) + NLO (EW) cross section [165].
- The VBF, VH, $t\bar{t}H$, $b\bar{b}H$ are produced with POWHEG-BOX [159] at NLO precision in QCD and interfaced with PYTHIA 8 [163] tuned with AZNLO parameters set for

hadronization and underlying event. Then the samples are normalized to the latest NNLO (QCD) + NLO (EW) cross sections [106], except the $t\bar{t}H$ production which is normalized at NLO (QCD) + NLO (EW).

- The tH production is generated with MADGRAPH5_AMC@NLO [160] at NLO precision in QCD, interfaced with PYTHIA 8 [163] tuned with the A14 parameter set for hadronization and underlying event.

In the analysis the samples are normalised to the integrated luminosity of the data, using state-of-the-art SM calculations for the Higgs boson production cross-sections and branching ratios at the hypothesised Higgs boson mass [106]. In particular, the nominal signal samples were generated assuming a Higgs boson mass of 125 GeV. The Higgs boson width Γ_H in all signal samples was set to the SM prediction for $m_H = 125$ GeV, $\Gamma_H = 4.07$ MeV [106], which is negligible compared to the experimental resolution on the diphoton invariant mass. The normalisation takes also into account the $H \to \gamma\gamma$ branching ratio of 2.27×10^{-3} [106].

The first part of Table 7.2 summarises the nominal signal samples used in the analysis. The cross-section values at $\sqrt{s} = 13$ TeV for $m_H = 125.0$ GeV are reported in Table 4.1.

Process	Generator	Showering	PDF set	Order (QCD + EW)	Events [M]
ggF	POWHEG NNLOPS	PYTHIA 8	PDF4LHC15	$N^3LO + NLO$	18.3
VBF	POWHEG-BOX	PYTHIA 8	PDF4LHC15	NNLO + NLO	7.00
W^+H	POWHEG-BOX	PYTHIA 8	PDF4LHC15	NNLO + NLO	3.65
W^-H	POWHEG-BOX	PYTHIA 8	PDF4LHC15	NNLO + NLO	3.65
$qq \to ZH$	POWHEG-BOX	PYTHIA 8	PDF4LHC15	NNLO + NLO	7.05
$gg \to ZH$	POWHEG-BOX	PYTHIA 8	PDF4LHC15	NNLO	0.75
$t\bar{t}H$	POWHEG-BOX	PYTHIA 8	PDF4LHC15	NLO + NLO	7.80
$b\bar{b}H$	POWHEG-BOX	PYTHIA 8	PDF4LHC15	NNLO	0.40
tHW	MADGRAPH5_AMC@NLO	PYTHIA 8	NNPDF3.0	NLO	0.21
tHbj	MADGRAPH5_AMC@NLO	PYTHIA 8	NNPDF3.0	NLO	0.40
$\gamma\gamma + 0, 1, 2, 3j$	SHERPA	SHERPA	CT10	0,1 @ NLO; 2,3 @ LO	720
gg interf.	SHERPA	SHERPA	NNPDF3.0	NLO	33.5
qg interf.	SHERPA	SHERPA	NNPDF3.0	LO	34.7

Table 7.2 – Summary of the event generators and PDF sets used to model the signal, background and interference processes in the analysis. The "Events" column indicates the number of generated events (in millions). The order of the cross-section calculation used for normalisation is given in each case, together with the corresponding value; when two orders are listed, the first refers to the QCD calculation and the second to the electroweak corrections. The calculation order is omitted for the main background processes, as their normalisation is determined from fits to data.

Additional signal samples have been generated and fully simulated with m_H values different from 125 GeV, in order to parametrise the variations in the signal shape and yields as functions of m_H (see Section 7.4). For each signal process listed in Table 7.2 (except for $b\bar{b}H$), samples with $m_H = 110, 122, 123, 124, 126, 127, 130$, and 140 GeV were produced using the same generator, PDF set, and tunes, but with reduced MC statistics. These samples are also normalised to the $H \to \gamma\gamma$ branching ratios and cross sections corresponding to their respective m_H values, as reported in Ref. [106].

Background samples

The irreducible non-resonant background $pp \to \gamma\gamma + n$ partons ($n \geq 0$) was also simulated using the SHERPA 2.2.4 event generator [166], which provides matrix-element calculations at NLO accuracy for $\gamma\gamma + 0, 1$ jet and at LO accuracy for $\gamma\gamma + 2, 3$ jets. The generation phase space is restricted so that only events in the Higgs mass region are produced, with $m_{\gamma\gamma} \in [90, 175]$ GeV. Owing to the large size of this sample, the $pp \to \gamma\gamma$ simulation was processed using the fast simulation of the ATLAS detector [158], based on a parametrisation of the calorimeter response. Since the diphoton background is estimated from the sidebands of the diphoton invariant-mass distribution in data, the simulated background is used only to select the background model, to evaluate the associated systematic uncertainty, and for this purpose the fast simulation is sufficiently accurate. This sample is listed in the third-to-last row of Table 7.2.

Interference samples

The effect of interference between the $gg \to H \to \gamma\gamma$ signal and the $gg \to \gamma\gamma$ continuum background and between $qg \to H \to \gamma\gamma$ and $qg \to \gamma\gamma$ is not included in the simulated event samples used to study the nominal signal model. The effect of interference between resonant signal production and non-resonant background diphoton production is studied using samples of simulated diphoton events including contributions from both processes (produced by either the gg or qg partonic channels) and their interference. The accuracy of the calculations is NLO for the gg-interference and LO for the qg-interference samples. The events were generated using SHERPA 2.2.11 and passed through the GEANT4 detector simulation. The interference events are generated with $m_H = 125$ GeV and $\Gamma_H = 4.07$ MeV.

7.2 Event selection

In order to reduce the background contamination from γ-jet and di-jet processes and to increase the significance of the Higgs boson signal, several requirements are applied to find two good-quality photons.

7.2.1 Triggers and photons preselection

Events must pass the HLT triggers `HLT_g35_loose_g25_loose` in 2015-2016 data and `HLT_g35_medium_g25_medium_L12EM20VH` for the 2017-2018 data, respectively. These triggers require the presence of two reconstructed photons with E_{T} greater than 35 GeV (leading) and 25 GeV (subleading), passing the *loose* or *medium* identification criteria at the trigger level. Additionally, events may also be selected by the `HLT_g120_loose` (for 2015-2016 data) and `HLT_g140_loose` (for 2017-2018 data) triggers, which require a single *loose* photon with E_{T} larger than 120 GeV or 140 GeV, respectively. The single-photon triggers recover approximately 3% of the signal efficiency in the very high-p_{T}^{H} phase space (> 300 GeV), where the photons can become collimated.

At least one primary vertex, as described in the next Section 7.2.2, is required to be reconstructed in the event.
Offline photon candidates are reconstructed from dynamic, variable-size clusters ("superclusters"), as described in Section 5.1. The photon energy is determined from the signals arising from energy deposits in the electromagnetic calorimeter, after applying the calibration scheme detailed in Chapter 6.
From the list of photon candidates in events with optimal detector conditions, at least two photons are required to pass the *loose* identification criteria, based on shower shapes variables as defined in Section 5.1.5. The *loose* photons are pre-selected requiring for $p_{\mathrm{T}} > 25$ GeV in the $|\eta_{S2}| < 2.37$ region, vetoing the transition region between $1.37 < |\eta_{S2}| < 1.52$, where η_{S2} is the pseudorapidity of the barycentre of the EM cluster in the second layer of the EM calorimeter. The two *loose* photons in the event with the highest p_{T} define the Higgs boson candidate.

7.2.2 Diphoton primary vertex

The photon direction is calculated from the positions of the supercluster and the pp collision vertex, which is selected from among the reconstructed primary-vertex candidates by a dedicated Neural Network (NN) algorithm [167]. Unlike most other ATLAS physics analyses, which use the vertex with the largest scalar $\sum p_{\mathrm{T}}^2$ of the tracks associated with it, the diphoton analysis uses the so-called "diphoton primary vertex". Since unconverted (and in many cases also converted) photons do not leave tracks in the ID coming from a primary vertex, the hardest-vertex criterion is generally suboptimal for identifying the correct interaction vertex in diphoton events, particularly for Higgs production modes with little additional activity in the final state, such as ggF.
For this reason, a NN is employed to assign a score to each vertex reconstructed by ATLAS during a bunch crossing, and the vertex with the highest score is selected. This choice is crucial, as it ensures that the contribution of the diphoton opening-angle resolution remains subdominant compared with the photon energy resolution in the uncertainty on $m_{\gamma\gamma}$ (see Equation (7.3)). As can be seen in Figure 7.2, the choice of the diphoton primary vertex leads to a 10% gain in the resolution of the reconstructed $m_{\gamma\gamma}$.
The NN is trained on ggF signal samples and combines information from the directions of the preselected photons—exploiting the longitudinal segmentation of the EM Calorimeter—as well as track-related quantities. The following variables are used as inputs to the NN:

- $\sum p_{\mathrm{T}}^2$: the scalar sum of the squared transverse momenta of the tracks associated with the vertex;
- $\sum p_{\mathrm{T}}$: the scalar sum of the transverse momenta of the tracks associated with the vertex;
- Δz: defined as $(z - z_{\mathrm{common}})/z_{\mathrm{error}}$, where z is the position of the candidate primary vertex, z_{common} is the weighted mean of the intersections of the extrapolated photon trajectories with a constraint from the beam-spot position, and z_{error} is the associated uncertainty;

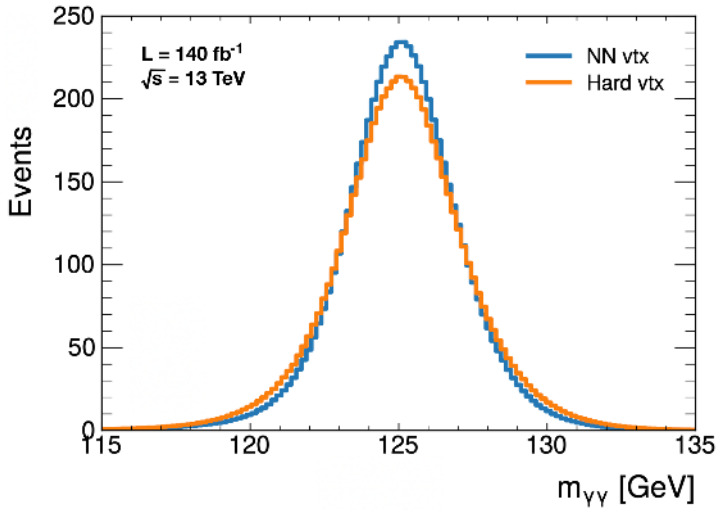

Figure 7.2 – Diphoton invariant mass distributions for the simulated ggF signal events that pass the full analysis selection described in this Section when the selected Primary Vertex (PV) is the nominal ATLAS vertex ("Hard vtx", orange) compared to the diphoton primary vertex (" NN vtx", blue).

- $\Delta\Phi$: the azimuthal angle between the diphoton system and the vector sum of the tracks associated with the vertex.

Two NNs are trained: one for unconverted-photon pairs and one for pairs containing at least one converted photon. The NN generally outperforms the standard "hardest-vertex" requirement: in ggF simulated events, it selects a vertex within 0.3 mm of the true one with an efficiency of 79%, compared with 56% for the hardest-vertex criterion. For the other production modes, this efficiency ranges between 84% and 97%. In $t\bar{t}H$ events, however, the NN efficiency is slightly lower (98% instead of nearly 100%) than that of the hardest-vertex requirement. This difference is negligible for the $H \to \gamma\gamma$ mass measurement.
The extracted vertex is then used to update the diphoton kinematics: a straight line between the PV and the centre of the associated cluster in the first layer of the EM calorimeter is used to recompute η. The p_{T} used for the kinematic selections and for the invariant-mass calculation incorporates this updated η. In addition, the kinematic variables of all other reconstructed objects are re-evaluated, which is particularly important for the particle-flow jets and for the computation of $E_{\mathrm{T}}^{\mathrm{miss}}$.

7.2.3 Diphoton event selection

On top of the trigger and data-quality requirements, and following the diphoton preselections described in Section 7.2.1, the two highest-p_{T} preselected photon candidates are further required to pass the *tight* identification and to satisfy the `FixedCutLoose` isolation criteria, in order to suppress candidates originating from neutral meson decays to photon pairs. The `FixedCutLoose` isolation requirement is based on the calorimeter and

track isolation variables within a cone of $\Delta R = 0.2$, as described in Section 5.1.7:

$$E_{\mathrm{T}}^{\mathrm{cone20}} < 0.065 \times E_{\mathrm{T}} \quad \text{and} \quad p_{\mathrm{T}}^{\mathrm{cone20}} / E_{\mathrm{T}} < 0.05 \tag{7.2}$$

where only tracks associated with the diphoton primary vertex are included in the isolation calculation excluding the γ ones. Events with two photons passing these requirements are selected; events with fewer than two *tight* and isolated photons are rejected. The leading and subleading photons are required to satisfy $p_{\mathrm{T}}/m_{\gamma\gamma} > 0.35$ and $p_{\mathrm{T}}/m_{\gamma\gamma} > 0.25$, respectively, where the diphoton invariant mass $m_{\gamma\gamma}$ is defined as

$$m_{\gamma\gamma} = \sqrt{2E_1E_2\,(1-\cos\theta)}, \tag{7.3}$$

and $m_{\gamma\gamma}$ must lie within the window $105 < m_{\gamma\gamma} < 160$ GeV. Here, E_1 and E_2 are the photon energies, and θ is the opening angle between them. About 1.2 million events in the data pass the selection. The expected efficiency for the signal for $m_H = 125$ GeV is close to 36%, leading to an expected signal yield of about 6200 events. Table 7.3 and Table 7.4 present the cutflow on the data, starting from all recorded events in the `PhysicsMain` data stream. The signal MC cutflow tables in the various production modes at $m_H = 125$ GeV are reported in Tables 7.5 to 7.9.

Data	2015			2016		
Selection cut	Exp. events	Tot. eff [%]	Cut eff [%]	Exp. events	Tot. eff [%]	Cut eff [%]
All events	26684848	100.00	-	221203568	100.00	-
No duplicates	26684804	100.00	100.00	221202752	100.00	100.00
GRL	26074042	97.71	97.71	216177280	97.73	97.73
Pass trigger	25823596	96.77	99.04	208625440	94.31	96.51
Detector DQ	25821060	96.76	99.99	208619504	94.31	100.00
Has PV	25820984	96.76	100.00	208619472	94.31	100.00
2 loose photons	3631912	13.61	14.07	36630884	16.56	17.56
$e-\gamma$ ambiguity	3631912	13.61	100.00	36544356	16.52	99.76
Trigger match	2673716	10.02	73.62	27438996	12.40	75.08
tight ID	377084	1.41	14.10	3688486	1.67	13.44
isolation	151529	0.57	40.18	1465149	0.66	39.72
rel. p_{T} cuts	131470	0.49	86.76	1272148	0.58	86.83
$m_{\gamma\gamma} \in [105, 160]$GeV	28815	0.11	21.92	283574	0.13	22.29

Table 7.3 – Data cutflow in 2015 and 2016.

7.3 Event categorisation

The events passing the selections detailed in Section 7.2 are further classified into reconstructed categories with different signal-to-background ratios, invariant-mass resolutions, and systematic uncertainties. Section 7.3.1 summarises the categorisation strategies used in the diphoton Run 1 [117] and partial Run 2 (36 fb^{-1}) analyses [15]. The studies that led to the development of the new categorisation for the full Run 2 mass analysis described in this Chapter are reported in Section 7.3.2.
The optimal categorisation for the mass analysis is determined from the interplay among

Data	2017			2018		
Selection cut	Exp. events	Tot. eff [%]	Cut eff [%]	Exp. events	Tot. eff [%]	Cut eff [%]
All events	213511216	100.00	-	268678272	100.00	-
No duplicates	213511200	100.00	100.00	268678272	100.00	100.00
GRL	207136448	97.01	97.01	265452832	98.80	98.80
Pass trigger	185083728	86.69	89.35	239147856	89.01	90.09
Detector DQ	185054400	86.67	99.98	239135328	89.00	99.99
Has PV	185054400	86.67	100.00	239135328	89.00	100.00
2 loose photons	21977888	10.29	11.88	28518826	10.61	11.93
$e-\gamma$ ambiguity	21977888	10.29	100.00	28518826	10.61	100.00
Trigger match	13448414	6.30	61.19	18754206	6.98	65.76
tight ID	4624978	2.17	34.39	6411022	2.39	34.18
isolation	1852965	0.87	40.06	2486112	0.93	38.78
rel. p_{T} cuts	1606794	0.75	86.71	2157460	0.80	86.78
$m_{\gamma\gamma} \in [105, 160]$GeV	370862	0.17	23.08	497558	0.19	23.06

Table 7.4 – Data cutflow in 2017 and 2018.

Production mode	ggF			VBF		
Selection cut	Exp. events	Tot. eff [%]	Cut eff [%]	Exp. events	Tot. eff [%]	Cut eff [%]
All events	10476.96	68.45	-	1260.52	100.00	-
No duplicates	15305.66	100.00	146.09	1192.09	94.57	94.57
GRL	15305.66	100.00	100.00	1192.09	94.57	100.00
Pass trigger	9993.18	65.29	65.29	833.10	66.09	69.89
Detector DQ	9993.18	65.29	100.00	833.10	66.09	100.00
Has PV	9993.18	65.29	100.00	833.10	66.09	100.00
2 loose photons	8180.27	53.45	81.86	656.10	52.05	78.75
$e-\gamma$ ambiguity	8175.61	53.42	99.94	655.73	52.02	99.94
Trigger match	7531.01	49.20	92.12	606.44	48.11	92.48
tight ID	6653.69	43.47	88.35	533.02	42.29	87.89
isolation	5856.73	38.27	88.02	475.27	37.70	89.16
rel. p_{T} cuts	5436.53	35.52	92.83	428.05	33.96	90.07
$m_{\gamma\gamma} \in [105, 160]$GeV	5435.20	35.51	99.98	427.51	33.92	99.87

Table 7.5 – Signal cutflow for the $H \to \gamma\gamma$ decay considering the ggF and VBF processes.

Production mode	W^-H			W^+H		
Selection cut	Exp. events	Tot. eff [%]	Cut eff [%]	Exp. events	Tot. eff [%]	Cut eff [%]
All events	177.42	100.00	-	280.90	100.00	-
No duplicates	167.60	94.47	94.47	264.35	94.11	94.11
GRL	167.60	94.47	100.00	264.35	94.11	100.00
Pass trigger	114.00	64.26	68.02	166.65	59.33	63.04
Detector DQ	114.00	64.26	100.00	166.65	59.33	100.00
Has PV	114.00	64.26	100.00	166.65	59.33	100.00
2 loose photons	87.23	49.17	76.52	123.59	44.00	74.16
$e-\gamma$ ambiguity	87.18	49.14	99.95	123.52	43.97	99.95
Trigger match	80.39	45.31	92.21	114.24	40.67	92.48
tight ID	70.46	39.71	87.64	99.90	35.56	87.45
isolation	61.21	34.50	86.87	86.77	30.89	86.86
rel. p_{T} cuts	55.56	31.31	90.77	78.83	28.06	90.85
$m_{\gamma\gamma} \in [105, 160]$GeV	55.28	31.16	99.49	78.37	27.90	99.42

Table 7.6 – Signal cutflow for the $H \to \gamma\gamma$ decay considering the W^-H and W^+H processes.

Production mode	ZH			ggZH		
Selection cut	Exp. events	Tot. eff [%]	Cut eff [%]	Exp. events	Tot. eff [%]	Cut eff [%]
All events	253.62	100.00	-	42.00	100.00	-
No duplicates	239.65	94.49	94.49	38.71	92.16	92.16
GRL	239.65	94.49	100.00	38.71	92.16	100.00
Pass trigger	155.95	61.49	65.07	31.33	74.61	80.95
Detector DQ	155.95	61.49	100.00	31.33	74.61	100.00
Has PV	155.95	61.49	100.00	31.33	74.61	100.00
2 loose photons	119.18	46.99	76.42	23.66	56.34	75.51
$e-\gamma$ ambiguity	119.11	46.96	99.94	23.65	56.31	99.96
Trigger match	110.23	43.46	92.55	22.15	52.75	93.66
tight ID	96.39	38.00	87.44	19.39	46.17	87.54
isolation	83.76	33.02	86.90	17.18	40.90	88.57
rel. p_{T} cuts	75.97	29.95	90.70	15.33	36.51	89.27
$m_{\gamma\gamma} \in [105, 160]$GeV	75.64	29.83	99.57	15.26	36.34	99.52

Table 7.7 – Signal cutflow for the $H \to \gamma\gamma$ decay considering the ZH and ggZH processes.

Production mode	$t\bar{t}H$			$b\bar{b}H$		
Selection cut	Exp. events	Tot. eff [%]	Cut eff [%]	Exp. events	Tot. eff [%]	Cut eff [%]
All events	173.93	100.00	-	63.47	100.00	-
No duplicates	159.78	91.86	91.86	53.40	93.84	93.84
GRL	159.78	91.86	100.00	53.40	93.84	100.00
Pass trigger	133.76	76.91	83.72	06.52	65.16	69.44
Detector DQ	133.76	76.91	100.00	06.52	65.16	100.00
Has PV	133.76	76.91	100.00	06.52	65.16	100.00
2 loose photons	101.79	58.53	76.10	88.31	54.02	82.91
$e-\gamma$ ambiguity	101.75	58.50	99.96	88.27	54.00	99.95
Trigger match	93.69	53.87	92.08	80.94	49.51	91.69
tight ID	79.89	45.93	85.27	71.62	43.81	88.49
isolation	65.14	37.45	81.54	62.92	38.49	87.85
rel. p_{T} cuts	58.71	33.75	90.12	58.64	35.87	93.20
$m_{\gamma\gamma} \in [105, 160]$GeV	58.08	33.39	98.93	58.62	35.86	99.97

Table 7.8 – Signal cutflow for the $H \to \gamma\gamma$ decay considering the $t\bar{t}H$ and $b\bar{b}H$ processes.

Production mode	tHjb			tWH		
Selection cut	Exp. events	Tot. eff [%]	Cut eff [%]	Exp. events	Tot. eff [%]	Cut eff [%]
All events	24.88	100.00	-	5.09	100.00	-
No duplicates	23.43	94.17	94.17	4.79	94.10	94.10
GRL	23.43	94.17	100.00	4.79	94.10	100.00
Pass trigger	16.52	66.40	70.51	4.11	80.89	85.96
Detector DQ	16.52	66.40	100.00	4.11	80.89	100.00
Has PV	16.52	66.40	100.00	4.11	80.89	100.00
2 loose photons	12.03	48.35	72.82	3.13	61.53	76.06
$e-\gamma$ ambiguity	12.02	48.31	99.91	3.13	61.51	99.97
Trigger match	11.18	44.96	93.07	2.90	56.99	92.65
tight ID	9.75	39.20	87.20	2.51	49.27	86.45
isolation	8.50	34.17	87.17	2.12	41.61	84.45
rel. p_{T} cuts	7.67	30.85	90.28	1.91	37.60	90.38
$m_{\gamma\gamma} \in [105, 160]$GeV	7.64	30.69	99.49	1.88	37.04	98.50

Table 7.9 – Signal cutflow for the $H \to \gamma\gamma$ decay considering the tH processes.

three key quantities:

- the category **significance**[1] Z, quantifying the Higgs signal relative to the continuum background;
- the $m_{\gamma\gamma}$ peak **resolution** ($\sigma_{\gamma\gamma}$), which depends only on the p_{T}, pseudorapidity, and conversion type of the two photons selected in a given category;
- the impact of photon **energy-scale uncertainties**, which affect the $m_{\gamma\gamma}$ peak position and depend only on the p_{T}, pseudorapidity, and conversion type of the two photons.

7.3.1 Past categorisations

The Run 1 and partial Run 2 analyses followed different strategies to minimise the expected uncertainty on the mass measurement. The Run 1 analysis employed a categorisation based solely on photon kinematic variables, whereas the partial Run 2 categorisation sought to enhance the signal significance by isolating events associated with specific Higgs production modes.

Run 1 The Run 1 categorisation [117] was based solely on photon kinematics, without attempting to tag specific Higgs production processes. The kinematic quantities considered were:

- $|\eta_{S2}|$, the pseudorapidity of the barycentre of the photon cluster in the second layer of the EM calorimeter;
- the conversion status of the photons (converted or unconverted);
- $p_{\mathrm{Tt}}^{\gamma\gamma}$, the component of the diphoton transverse momentum $p_{\mathrm{T}}^{\gamma\gamma}$ orthogonal to the thrust axis $\hat{t}$:

$$p_{\mathrm{Tt}}^{\gamma\gamma} = \left| \, p_{\mathrm{T}}^{\gamma\gamma} \times \hat{t} \, \right|, \qquad \hat{t} = \frac{p_{\mathrm{T}}^{\gamma 1} - p_{\mathrm{T}}^{\gamma 2}}{\left| p_{\mathrm{T}}^{\gamma 1} + p_{\mathrm{T}}^{\gamma 2} \right|}. \tag{7.4}$$

Regarding the dependence on $|\eta_{S2}|$, the best energy resolution is achieved for photons in the central barrel region ($|\eta_{S2}| < 0.75$), while the worst resolution occurs near the barrel-endcap transition ($1.3 < |\eta_{S2}| < 1.75$). The resolution is also generally better for unconverted photons, as converted photons typically undergo more energy loss before reaching the calorimeter.
Categorising events by conversion status and photon pseudorapidity is also advantageous for controlling systematic uncertainties: the largest energy-scale uncertainties arise for unconverted photons—primarily due to the electron-to-photon scale extrapolation—and for photons in the transition region, due to uncertainties in the material description. Introducing an additional split in $p_{\mathrm{Tt}}^{\gamma\gamma}$ further improves the separation of events by signal-to-background ratio and mass resolution, since a harder $p_{\mathrm{T}}^{\gamma\gamma}$ spectrum

[1] $Z_c = S_c/\sqrt{B_c}$, where S_c is the number of Higgs signal events and B_c is the number of continuum background events in category c within a window of approximately 3 times the expected resolution around the nominal Higgs boson mass.

is expected for certain Higgs production modes, whereas this is not typical for the background.
Based on these considerations, the Run 1 reconstructed categories were defined by first separating events in which both photons were unconverted ("UU") from those with at least one converted photon ("Conv"). Each of these two groups was then divided into three sub-regions according to the $|\eta_{S2}|$ of the photons:

- **Cen**: both photons satisfy $|\eta_{S2}| < 0.75$;
- **Trans**: at least one photon lies in the range $1.3 < |\eta_{S2}| < 1.75$, excluding the crack region $1.37 < |\eta_{S2}| < 1.52$;
- **Rest**: all remaining events.

For the "Cen" and "Rest" regions, two $p_{\mathrm{Tt}}^{\gamma\gamma}$ bins were introduced using a threshold of 70 GeV, defining Low and High $p_{\mathrm{Tt}}^{\gamma\gamma}$ subcategories.
In total, the Run 1 categorisation comprised ten categories:

UU Cen High, UU Cen Low, UU Rest High, UU Rest Low, UU Trans,
Conv Cen High, Conv Cen Low, Conv Rest High, Conv Rest Low, Conv Trans.

Partial Run 2 The partial Run 2 categorisation, for the analysis based on 36 fb^{-1} of pp collision data [15], was instead designed primarily for the measurement of Higgs boson production cross sections (in the Simplified Template Cross Sections (STXS) framework [106]) and later adapted for the mass analysis. The events were divided into 31 categories: ten categories optimised to measure gluon-fusion properties, four targeting vector-boson fusion production, eight designed to study associated production with a vector boson, and nine optimised for associated production with a top-antitop pair or a single top quark.
Among these categories, most of the sensitivity to m_H was provided by the "ggF 0-jet" category, a gluon-fusion category with zero reconstructed jets. For the mass analysis, this category was further split into a central region (both photons with $|\eta_{S2}| < 0.95$) and a forward region (at least one photon with $|\eta_{S2}| > 0.95$). Additional sensitivity was contributed by the "ggF 1-jet" and VBF categories, owing to their higher signal-to-background ratios.

7.3.2 Categorisation studies

Relying on the physically well-motivated results of the Run 1 and partial Run 2 categorisations, the strategy for the full Run 2 analysis was designed to follow a similar approach. All categorisation schemes discussed in this section are compared using a simple yet complete full-shape analysis. For each categorisation, the signal and background analytical functions are fitted to the signal MC samples and to the data sidebands, respectively, as described in Sections 7.4 and 7.5.
The impact of systematic uncertainties is evaluated by considering only the photon energy-scale uncertainties—those with the largest effect—for each category. These uncertainties are propagated to the diphoton invariant mass, and their impact is computed

using Equation (7.9), as detailed in Section 7.6. All systematic errors are then incorporated into a statistical model (see Section 7.8) and applied on the peak-position parameter. An Asimov[2] dataset is produced with m_H fixed to 125.09 GeV, and the expected results are extracted.
The attempts discussed in this section represent possible variations and/or combinations of the Run 1 and Run 2 categorisations, obtained using the previous Run 2 calibration model (named `es2018_R21_v0`), not yet the final of Ref. [17]. After a brief description of each categorisation, the corresponding results are reported in Table 7.10, where each categorisation is assigned an identification number. The **Test 14** categorisation was ultimately selected for the final results, as it provides an improvement over the Run 1 categorisation, which was reimplemented as a benchmark under **Test 1**.

- **Test 2** variation divides the Run 1 "Conv" categories in the two sub-categories where exactly one photon is converted (UC) or both are converted (CC), so five more categories are created in the end.
- **Tests 3 to 7** explore categorisations based on combinations of the Run 1 and Run 2 schemes. As discussed in Section 7.3.1, the mass analysis using $36\,\text{fb}^{-1}$ included four VBF categories, two of which ("tight") were defined using a BDT trained to separate VBF from ggF and background. The idea behind these tests is to isolate these four VBF categories from the rest of the events in order to obtain regions with higher signal-to-background ratios, and then apply the Run 1 categorisation on top of the remaining events (Test 3). Variants of this approach include isolating only the two "tight" VBF categories rather than all four (Test 4), applying the additional conversion split introduced in Test 2 on top of the Run 1 categories (Test 5), or isolating both the ggF and VBF categories from all other events (Tests 6 and 7).
- **Tests 8 and 9** further subdivide the Run 1 categories into three or four regions based on the average pileup. These tests were carried out because the photon energy resolution exhibits a mild dependence on pileup, degrading as the pileup increases.
- **Tests 10 to 21** explore variations of the Run 1 categorisation or of the Test 3 categorisation in which different p_{Tt} selections are applied. These include: removing the p_{Tt} requirement altogether (Tests 10 and 11); increasing the p_{Tt} threshold from 70 GeV to 100 GeV (Tests 12 and 13); and introducing three p_{Tt} regions (Tests 14 and 15). These tests are then repeated with p_{T} thresholds replacing the p_{Tt} thresholds (Tests 16-21).

As can be seen from Table 7.10, all tests yield very similar results, with a total expected uncertainty on m_H of around 290 MeV. The best-performing categorisations are **Test 14** and **Test 15**, in which the additional p_{Tt} split reduces the statistical uncertainty by about 8 MeV compared with the Run 1 categorisation, while also improving the separation of events with large photon energy scale systematics uncertainties into the high-p_{Tt} categories. **Test 14** was considered the most favourable option and was chosen over **Test 15**, as it provides nearly identical performance while using only half as many categories.

[2]The Asimov dataset is a toy dataset constructed to follow exactly a given probability density function, without statistical fluctuations. By construction, evaluating the estimator for a parameter on the Asimov dataset returns the true value of that parameter; in this case, $m_H = 125.09$ GeV.

Test	Categorisation	N_{cat}	Uncertainty [MeV] Total	Stat	Syst
1	Plain Run 1	10	292	133	260
2	Run 1 with splitting in conversion (UU/UC/CC)	15	292	132	260
3	VBF and (rest+ggH), then Run 1	20	291	130	260
4	VBF_{tight} and (rest+ggH), then Run 1	20	291	130	260
5	VBF and (rest+ggH), then Run 1 with (UU/UC/CC)	30	291	130	261
6	ggF, VBF, rest and then plain Run 1 on ggF,VBF	21	293	133	261
7	ggF, VBF, rest, then Run 1 with (UU/UC/CC) on ggF,VBF	31	293	132	262
8	Run 1 with 3 $<\mu>$ regions (μ=15,30)	30	291	132	259
9	Run 1 with 4 $<\mu>$ regions (μ=15,25,42)	40	291	132	259
10	Run 1 without $p_{\text{Tt}}^{\gamma\gamma}$ cut	6	293	149	252
11	Test 3 without $p_{\text{Tt}}^{\gamma\gamma}$ cut	12	292	144	254
12	Run 1 with $p_{\text{Tt}}^{\gamma\gamma}$ cut at 100 GeV	10	290	129	260
13	Test 3 with $p_{\text{Tt}}^{\gamma\gamma}$ cut at 100 GeV	20	289	128	259
14	**Run 1 with 3 $p_{\text{Tt}}^{\gamma\gamma}$ regions (70, 130) GeV**	**14**	**287**	**125**	**258**
15	Test 3 with 3 $p_{\text{Tt}}^{\gamma\gamma}$ regions (70, 130) GeV	28	286	122	259
16	Run 1 with $p_{\text{T}}^{\gamma\gamma}$ cut at 100 GeV	10	292	134	259
17	Test 3 with $p_{\text{T}}^{\gamma\gamma}$ cut at 100 GeV	20	291	131	260
18	Run 1 with $p_{\text{T}}^{\gamma\gamma}$ cut at 130 GeV	10	291	132	259
19	Test 3 with $p_{\text{T}}^{\gamma\gamma}$ cut at 130 GeV	20	289	129	259
20	Run 1 with 3 $p_{\text{T}}^{\gamma\gamma}$ regions (130, 190) GeV	14	287	128	257
21	Test 3 with 3 $p_{\text{T}}^{\gamma\gamma}$ regions (130, 190) GeV	28	295	129	265

Table 7.10 – Expected uncertainties on the Higgs mass of the various categorisation tests based on Run 1 and Run 2 approaches, using the previous Run 2 precision recommendations (named `es2018_R21_v0`).

The **Test 14** categorisation was then optimised using the latest Run 2 precision recommendations, `es2022_R21_Precision`. In particular, the $|\eta|$ boundaries were slightly shifted, moving the "Cen" selection from 0.75 to 0.8. The final categorisation for the Run 2 mass analysis therefore consists of 14 categories, all untagged with respect to specific Higgs production processes. As in the Run 1 analysis, categories are defined according to whether both photons are unconverted ("UU") or whether at least one photon is converted ("Conv"). Each of these is then subdivided into three $|\eta|$ regions: a "Central-barrel" region, where both photons satisfy $|\eta_{S2}| < 0.8$; an "Outer-barrel" region, where at least one photon lies within $0.8 < |\eta_{S2}| < 1.37$; and an "Endcap" region, where at least one photon lies within $1.52 < |\eta_{S2}| < 2.37$. These three regions are shown in Figure 7.3a. On top of these selections, three $p_{\text{Tt}}^{\gamma\gamma}$ regions are defined for the "Central" and "Outer-barrel" categories, using boundaries at 70 GeV and 130 GeV. These two $p_{\text{Tt}}^{\gamma\gamma}$ thresholds were chosen to ensure sufficient signal yield in the highest-$p_{\text{Tt}}^{\gamma\gamma}$ region, as the 70 GeV and 130 GeV boundaries correspond to the 30% and 10% quantiles of the signal $p_{\text{Tt}}^{\gamma\gamma}$ distribution. Low ($p_{\text{Tt}}^{\gamma\gamma} < 70$ GeV), medium ($70\,\text{GeV} < p_{\text{Tt}}^{\gamma\gamma} < 130$ GeV), and high ($p_{\text{Tt}}^{\gamma\gamma} > 130$ GeV) categories are defined from the "Central" and "Outer-barrel" regions, while no $p_{\text{Tt}}^{\gamma\gamma}$ split is applied to the "Endcap" categories. A schematic representation of this

categorisation is shown in Figure 7.3b.

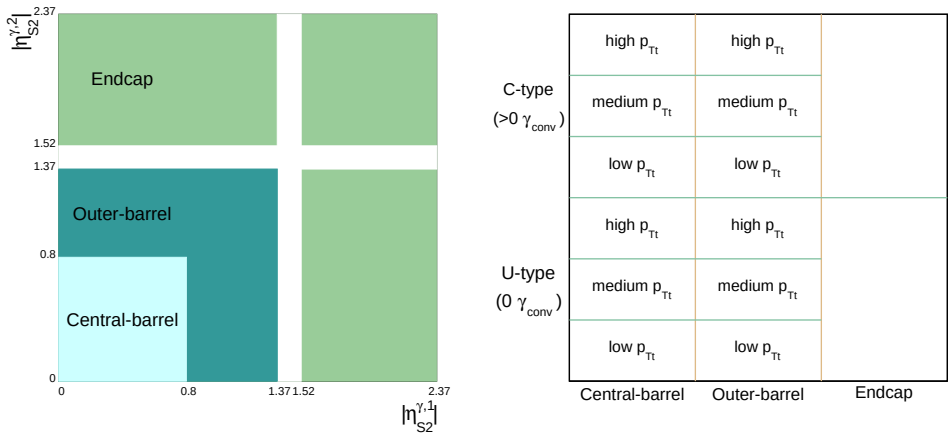

(a) (b)

Figure 7.3 – Definition of the three photon pseudorapidity regions used to define the event categories: Central-barrel (light-blue), Outer-barrel (blue) and Endcap (light green). (b) Illustration of the event categories used for the Higgs boson mass measurement with $H \to \gamma\gamma$ decays.

The final Run 2 categorisation comprises fourteen categories, which will be referred to throughout this Chapter as:

UU Central-barrel high p_{Tt}, UU Central-barrel medium p_{Tt}, UU Central-barrel low p_{Tt}, UU Outer-barrel high p_{Tt}, UU Outer-barrel medium p_{Tt}, UU Outer-barrel low p_{Tt}, UU Endcap, Conv Central-barrel high p_{Tt}, Conv Central-barrel medium p_{Tt}, Conv Central-barrel low p_{Tt}, Conv Outer-barrel high p_{Tt}, Conv Outer-barrel medium p_{Tt}, Conv Outer-barrel low p_{Tt}, Conv Endcap.

The results obtained with this categorisation are reported in Table 7.11, together with those from the Run 1 and partial Run 2 categorisations updated to the latest precision-calibration recommendations. The expected total uncertainty on m_H is approximately 196 MeV, with a systematic component of about 155 MeV arising solely from photon energy-scale uncertainties. Comparing the results of **Test 14** in Table 7.10 with those of the final Run 2 categorisation in Table 7.11—which are nearly identical aside from updated precision corrections and minor adjustments to the $|\eta|$ boundaries—highlights the substantial impact of the improved precision corrections, which reduce the systematic uncertainty from 258 MeV to 155 MeV.

The SM yields at 140 fb^{-1} and the performance of the designed categories will be described in the next Sections and are summarised in Table 7.12.

Categorisation	N_{cat}	Uncertainty [MeV] Total	Stat	Syst
Inclusive	1	236	159	175
Partial Run 2 [15]	31	209	127	167
Run 1 [117]	10	202	141	144
Run 2 (this analysis)	14	196	119	155

Table 7.11 – Results obtained with a full shape workspace including energy scale systematic uncertainties for the mass analysis. The Run 2 categorisation described in this section is compared to three other categorisations built with samples updated to the latest precision recommendations: "Inclusive" where only the standard diphoton selection is applied, the Run 2 (2016) partial mass analysis categorisation and the Run 1 categorisation. It can be observed that the categorisation detailed in this chapter represents the best result among the other reported.

Category	$\sigma_{90}^{\gamma\gamma}$ [GeV]	S_{90}	B_{90}	f_{90} [%]	Z_{90}
UU, Central-barrel, high $p_{\mathrm{Tt}}^{\gamma\gamma}$	1.88	42	65	39.1	4.7
UU, Central-barrel, medium $p_{\mathrm{Tt}}^{\gamma\gamma}$	2.34	102	559	15.4	4.2
UU, Central-barrel, low $p_{\mathrm{Tt}}^{\gamma\gamma}$	2.63	837	13226	6.0	7.2
UU, Outer-barrel, high $p_{\mathrm{Tt}}^{\gamma\gamma}$	2.16	31	83	27.4	3.3
UU, Outer-barrel, medium $p_{\mathrm{Tt}}^{\gamma\gamma}$	2.63	108	981	9.9	3.4
UU, Outer-barrel, low $p_{\mathrm{Tt}}^{\gamma\gamma}$	3.00	869	22919	3.7	5.7
UU, Endcap	3.33	759	29383	2.5	4.4
Conv, Central-barrel, high $p_{\mathrm{Tt}}^{\gamma\gamma}$	2.10	26	44	37.3	3.6
Conv, Central-barrel, medium $p_{\mathrm{Tt}}^{\gamma\gamma}$	2.62	62	389	13.8	3.1
Conv, Central-barrel, low $p_{\mathrm{Tt}}^{\gamma\gamma}$	3.00	508	9726	5.0	5.1
Conv, Outer-barrel, high $p_{\mathrm{Tt}}^{\gamma\gamma}$	2.56	34	103	25.0	3.2
Conv, Outer-barrel, medium $p_{\mathrm{Tt}}^{\gamma\gamma}$	3.20	114	1353	7.8	3.1
Conv, Outer-barrel, low $p_{\mathrm{Tt}}^{\gamma\gamma}$	3.71	914	30121	2.9	5.2
Conv, Endcap	4.04	1249	52160	2.3	5.5
Inclusive	3.32	5653	128774	4.2	15.6

Table 7.12 – The expected signal (S_{90}) and background (B_{90}) yields, the signal yield as a percentage of the total (f_{90}), and the signal significance (Z_{90}) in a diphoton invariant mass window whose half-width $\sigma_{90}^{\gamma\gamma}$ is chosen in such a way that it is the narrowest interval containing 90% of signal events. All quantities are given for each analysis category and for the inclusive case.

7.4 Signal modelling

7.4.1 Yields and efficiencies

The number of expected signal events (yield) for each category N_c is defined as the following product summed over the different Higgs boson production modes i (ggF, VBF,

WH, ZH, ggZH, $t\bar{t}H$, $b\bar{b}H$, tHbj and tWH):

$$N_c(m_H) = \sum_i N_{ci}(m_H) = \sum_i L \cdot (\sigma_i(m_H) \cdot \mathcal{BR}(m_H) \cdot \epsilon_{ci}(m_H)) \tag{7.5}$$

where

- L is the total integrated luminosity, $L = 140$ fb^{-1} as described in Section 7.1.1;
- $\sigma_i(m_H)$ is the Higgs production cross section of the considered process i, as a function of m_H;
- $\mathcal{BR}(m_H)$ is the $H \to \gamma\gamma$ branching ratio, $\mathcal{BR}(m_H) \sim 0.227\%$ at $m_H = 125.09$ GeV, as a function of m_H;
- $\epsilon_{ci}(m_H)$ is the signal efficiency. It measures the probabilities for a truth-level Higgs event to end up in a given reconstructed category c for a certain production process i, as a function of m_H. The evaluate efficiencies ϵ_{ci} are reported in Appendix B.1.

Table 7.13 show the values of the yields N_{ci} for each category c and for the different Higgs boson production modes i evaluated using the MC sample generated at $m_H = 125$ GeV.

Category	ggF	VBF	WH	ZH	ggZH	$t\bar{t}H$	$b\bar{b}H$	tHbj	tWH	Total
UU, Central-barrel, high p_{Tt}	26.72	10.16	2.95	1.70	0.89	3.14	0.14	0.28	0.13	46.11
UU, Central-barrel, med p_{Tt}	76.33	21.45	5.62	3.30	1.25	4.05	0.46	0.39	0.14	112.99
UU, Central-barrel, low p_{Tt}	846.35	45.30	13.13	7.47	0.96	5.43	10.20	0.55	0.16	929.55
UU, Outer-barrel, high p_{Tt}	20.32	7.71	2.38	1.35	0.63	2.03	0.10	0.20	0.08	34.80
UU, Outer-barrel, med p_{Tt}	81.15	22.50	6.19	3.59	1.24	3.84	0.49	0.44	0.12	119.56
UU, Outer-barrel, low p_{Tt}	878.47	46.80	14.25	8.06	1.04	5.37	10.36	0.63	0.17	965.15
UU, Endcap	739.27	56.43	19.85	11.05	1.72	5.81	7.55	1.14	0.17	842.99
Conv, Central-barrel, high p_{Tt}	16.69	6.31	1.83	1.05	0.54	1.95	0.08	0.17	0.08	28.70
Conv, Central-barrel, med p_{Tt}	46.67	13.11	3.48	2.03	0.77	2.51	0.29	0.26	0.09	69.21
Conv, Central-barrel, low p_{Tt}	513.55	27.47	7.98	4.53	0.57	3.31	6.19	0.34	0.10	564.04
Conv, Outer-barrel, high p_{Tt}	22.19	8.33	2.63	1.49	0.68	2.23	0.12	0.23	0.09	37.99
Conv, Outer-barrel, med p_{Tt}	86.13	23.84	6.63	3.84	1.27	4.06	0.47	0.47	0.14	126.85
Conv, Outer-barrel, low p_{Tt}	924.52	49.18	15.02	8.52	1.06	5.59	10.74	0.70	0.16	1015.49
Conv, Endcap	1214.77	93.86	33.73	18.68	2.85	9.54	12.16	1.94	0.28	1387.81
Total	5493.13	432.45	135.67	76.66	15.47	58.86	59.35	7.74	1.91	6281.24

Table 7.13 – Expected SM signal yields N_{ci} for each production mode i and for each category c, at $\sqrt{s} = 13$ TeV, $m_H = 125$ GeV and $L = 140$ fb^{-1}. The last column shows the total yields per category summed over all the production processes.

Since the terms in Equation (7.5) depend on m_H, the variation of the yield N_c with m_H is evaluated using the MC samples generated at different Higgs boson masses, as described in Section 7.1.2. The efficiencies and yields for each category and production mode are therefore recomputed for every MC sample. The resulting yields are then fitted with a second-degree polynomial as a function of m_H:

$$N_{ci}(m_H) = p_0 + p_1 (m_H - 125\,\mathrm{GeV}) + p_2 (m_H - 125\,\mathrm{GeV})^2. \tag{7.6}$$

As an illustrative example, Figure 7.4 shows the fitted yield parametrisation for the UU, Central-barrel, low-p_{Tt} category in the ggF production mode. The corresponding fits for the remaining production modes in the same category, are reported in Appendix B.2.

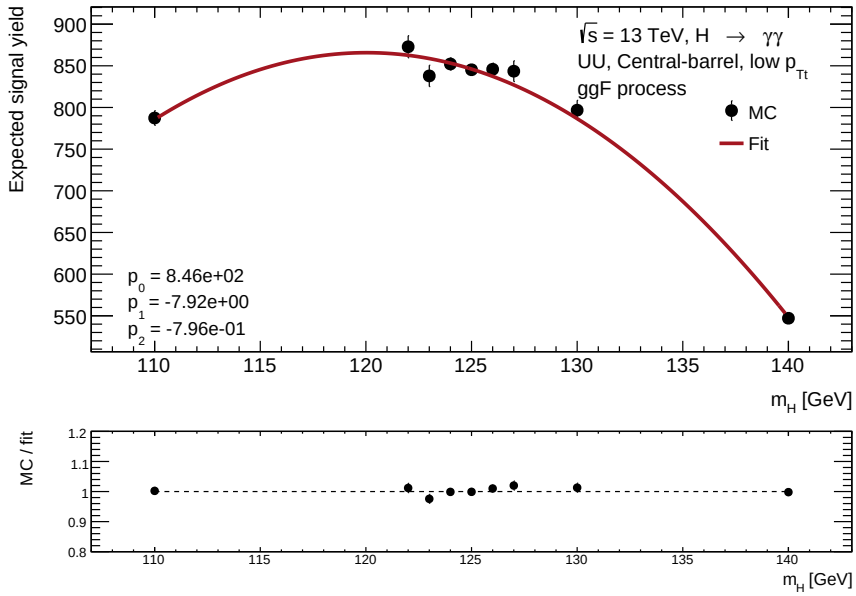

Figure 7.4 – Yield parametrisation as a function of m_H for the UU, Central-barrel, low-p_{Tt} category in the ggF production mode. The black points represent the expected signal yields extracted from the nine MC samples generated at different Higgs-boson masses, while the red curve shows the fitted second-degree polynomial. The fitted values of the polynomial parameters are listed in the bottom-left corner of the plot.

7.4.2 Signal model

The $m_{\gamma\gamma}$ invariant-mass distribution of the resonant signal process is modelled with a DSCB. The DSCB consists of a Gaussian core in the peak region and two asymmetric power-law tails. Ignoring the normalisation factor, the DSCB is described by:

$$f_{\mathrm{DSCB}}(m_{\gamma\gamma}) = \begin{cases} e^{-t^2/2}, & -\alpha_{\mathrm{Low}} \leq t \leq \alpha_{\mathrm{High}}, \\ \dfrac{e^{-\alpha_{\mathrm{Low}}^2/2}}{\left[\frac{1}{R_{\mathrm{Low}}}\left(R_{\mathrm{Low}} - \alpha_{\mathrm{Low}} - t\right)\right]^{n_{\mathrm{Low}}}}, & t < -\alpha_{\mathrm{Low}}, \\ \dfrac{e^{-\alpha_{\mathrm{High}}^2/2}}{\left[\frac{1}{R_{\mathrm{High}}}\left(R_{\mathrm{High}} - \alpha_{\mathrm{High}} + t\right)\right]^{n_{\mathrm{High}}}}, & t > \alpha_{\mathrm{High}}, \end{cases} \tag{7.7}$$

where $t = \frac{m_{\gamma\gamma} - \mu_{\mathrm{CB}}}{\sigma_{\mathrm{CB}}}$, $R_{\mathrm{Low}} = \frac{n_{\mathrm{Low}}}{\alpha_{\mathrm{Low}}}$, and $R_{\mathrm{High}} = \frac{n_{\mathrm{High}}}{\alpha_{\mathrm{High}}}$.
Here, μ_{CB} and σ_{CB} are the mean and standard deviation of the Gaussian core, n_{Low} and n_{High} define the powers of the power-law tails on the low- and high-mass sides, and α_{Low} and α_{High} determine the transition points between the Gaussian core and the tails. In particular, the tails begin at deviations of $\alpha\,\sigma_{\mathrm{CB}}$ from the peak. The DSCB shape is therefore fully described by six parameters: μ_{CB}, σ_{CB}, α_{Low}, α_{High}, n_{Low}, and n_{High}.

The input mass distributions for each category and each m_H value are obtained by summing all Higgs boson production processes (ggF, VBF, WH, ZH, ggZH, $t\bar{t}H$, $b\bar{b}H$, tHbj, tWH), taking their SM cross sections into account. A signal fit using the DSCB is performed on the invariant-mass distribution derived from the MC templates at $m_H = 110, 122, 123, 124, 125, 126, 127, 130$, and 140 GeV, separately for each category, within the mass range

$$m_{\gamma\gamma} \in [m_H - 15\,\text{GeV},\, m_H + 15\,\text{GeV}].$$

All six parameters of the DSCB are fitted in this first step. A second fit is then performed in which n_{Low} and n_{High} are fixed to the values extracted from the first fit, in order to improve the stability and convergence of the remaining four DSCB parameters.
A fit performed on a single mass point for one category at a time will be referred to as a *single fit*. The result of the single fit to the invariant-mass distribution $m_{\gamma\gamma}$ for the UU, Central-barrel, low-p_{Tt} category at $m_H = 125$ GeV is shown in Figure 7.5. Two comparisons between some of the signal probability density functions (pdfs) obtained from the fit at $m_H = 125$ GeV, highlighting the variation of the $m_{\gamma\gamma}$ resolution with p_{Tt} across different categories, are shown in Figure 7.6. The same trend is also observed in Table 7.12, as reflected by the values of the half-width $\sigma_{90}^{\gamma\gamma}$ across the different categories. Additional examples of *single fits* for all the other categories at $m_H = 125$ GeV and for the UU, Central-barrel, low-p_{Tt} category at all the other generated m_H values are reported in Appendix B.3.

7.4.3 Signal parametrisation

In order to perform the mass measurement, the signal shape must be described by a parametric function of m_H. This is achieved by including, in addition to the MC sample at 125 GeV, the signal MC samples generated at different Higgs boson masses. These samples allow the dependence of the signal-model parameters (such as the peak position and width) on m_H to be extracted.
To this end, the parameters of the DSCB defined in Equation (7.7) are parametrised as functions of m_H for each category as:

$$\begin{aligned}
\mu_{\text{CB}}(m_H) &= m_H + B_{\mu_{\text{CB}}} + A_{\mu_{\text{CB}}}(m_H - 125\,\text{GeV}) \\
\sigma_{\text{CB}}(m_H) &= B_{\sigma_{\text{CB}}} + A_{\sigma_{\text{CB}}}(m_H - 125\,\text{GeV}) \\
\alpha_{\text{Low}}(m_H) &= \alpha_{\text{Low}} \\
\alpha_{\text{High}}(m_H) &= \alpha_{\text{High}} \\
n_{\text{Low}}(m_H) &= n_{\text{Low}}|_{125\,\text{GeV}} \\
n_{\text{High}}(m_H) &= n_{\text{High}}|_{125\,\text{GeV}}
\end{aligned} \tag{7.8}$$

where $n_{\text{Low}}|_{125\,\text{GeV}}$ and $n_{\text{High}}|_{125\,\text{GeV}}$ are the values obtained from the *single fit* to the MC sample at $m_H = 125$ GeV.
The parametrisation described in Equation (7.8) is used in a *simultaneous fit* to all the signal MC templates for different m_H values. The fitted parameters for each category are therefore $B_{\mu_{\text{CB}}}$, $A_{\mu_{\text{CB}}}$, $B_{\sigma_{\text{CB}}}$, $A_{\sigma_{\text{CB}}}$, α_{Low}, and α_{High}. Since the parameters n_{Low} and

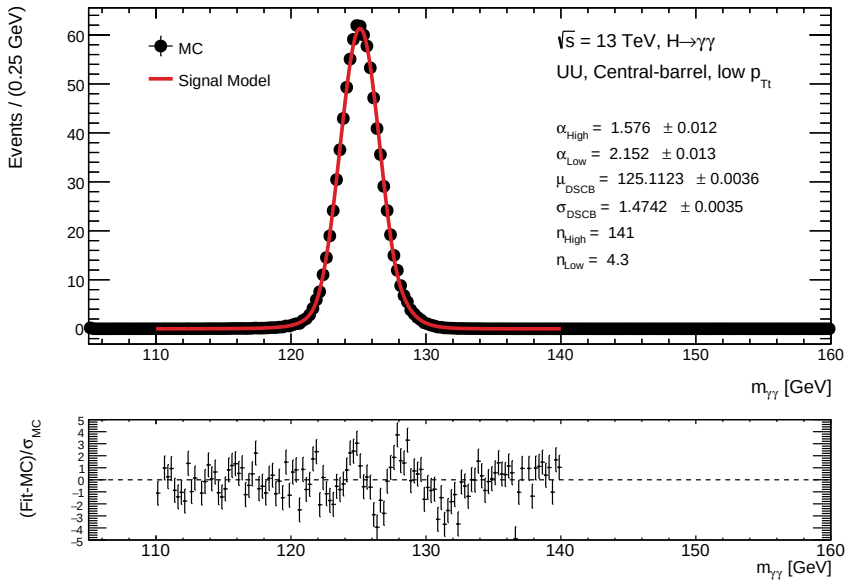

Figure 7.5 – Result of the *single fit* for the category UU, Central-barrel, low-p_{Tt} for the MC sample with $m_H = 125$ GeV: the fitted signal pdf is shown by the red line, the black dots correspond to the MC sample. The values of the fitted parameters of the DSCB are shown in the legend on the right side of the plot. The residuals are shown in the lower part of the plot.

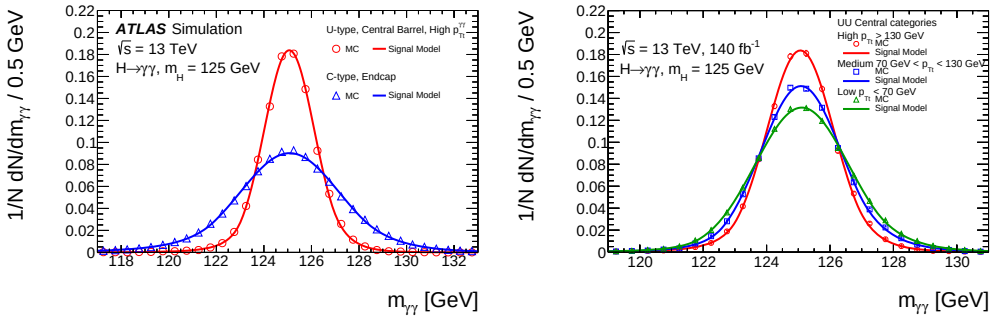

Figure 7.6 – (a) Invariant-mass distributions of simulated $H \to \gamma\gamma$ events reconstructed in the categories with the best (U-type, Central-barrel, High p_{Tt}; open circles) and worst (C-type, Endcap; open squares) experimental resolutions [14]. (b) Comparison of invariant-mass distributions for the UU, Central-barrel categories, illustrating the variation of the signal $m_{\gamma\gamma}$ resolution with p_{Tt}. The signal model obtained from the fit to the simulated events is superimposed (solid lines) on the corresponding $m_{\gamma\gamma}$ distributions of the signal MC samples at $m_H = 125$ GeV.

n_{High} do not exhibit a clear dependence on m_H, they are kept constant in the simultaneous fit, fixed to the values obtained from the *single fit* performed on the MC sample at $m_H = 125$ GeV, which is the mass point closest to the region of interest. Moreover,

these parameters affect only the behaviour of the tails and have a negligible impact on the peak position of the DSCB, and therefore do not influence the mass measurement. After determining the signal model from the simultaneous fits for each category, the resulting parameters are treated as constants in the analysis when fitting the observed data. As an example, the outcome of the simultaneous fit across the MC samples for the UU, Central-barrel, low p_{Tt} category is shown in Figure 7.7. The shape parameters that parametrise the dependence on the mass, as obtained from the simultaneous fit, are reported in Table 7.14 for each category.

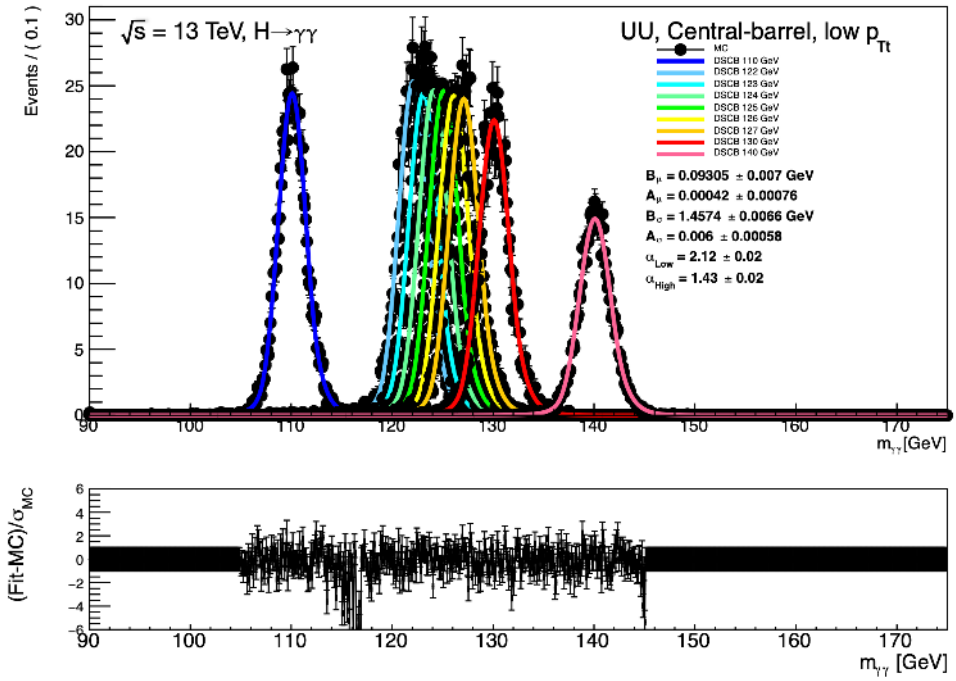

Figure 7.7 – Result of the simultaneous fit for the category UU, Central-barrel, low-p_{Tt}: the black dots correspond to the various MC samples, whereas each signal pdf (each one for a different m_H value) is shown in a different colour. The values of the simultaneously fitted parameters are shown in the legend on the right side of the plot. The residuals are shown in the lower part of the plot.

The signal model has been extensively validated through a series of tests:

- For each parameter, Figure 7.8 shows a comparison for the first category UU, Central-barrel, high p_{Tt} between the result of the *simultaneous fit* and the result of a linear fit performed on the black points which are the results of the separate *single fits*, each one done considering only one MC sample at a time. As can be seen in Figure 7.8, the simultaneous fit is able to catch the trend of the parameters as a function of m_H.
- **Closure test**: as a cross-check, the fit is repeated after removing the $m_H = 125$ GeV distribution from the input and new values of the $B_{\mu_{\mathrm{CB}}}$, $A_{\mu_{\mathrm{CB}}}$, $B_{\sigma_{\mathrm{CB}}}$, $A_{\sigma_{\mathrm{CB}}}$, α_{Low}, and α_{High} parameters are obtained. The signal model for $m_H = 125$ GeV predicted by

Category	$B_{\mu_{CB}}$ [GeV]	$A_{\mu_{CB}}$	$B_{\sigma_{CB}}$ [GeV]	$A_{\sigma_{CB}}$	α_{Low}	$n_{Low}\|_{125\,GeV}$	α_{High}	$n_{High}\|_{125\,GeV}$
UU, Central-barrel, high p_{Tt}	0.080	0.000 33	1.06	0.006 63	2.01	4.7	1.61	21
UU, Central-barrel, med p_{Tt}	0.060	0.000 37	1.26	0.009 47	1.86	4.9	1.28	390
UU, Central-barrel, low p_{Tt}	0.093	0.000 42	1.46	0.006 02	2.12	4.3	1.43	3200
UU, Outer-barrel, high p_{Tt}	0.10	−0.0021	1.18	0.008 94	1.65	7.0	1.54	28
UU, Outer-barrel, med p_{Tt}	0.093	0.0027	1.43	0.008 65	1.90	6.0	1.40	79
UU, Outer-barrel, low p_{Tt}	0.094	0.000 070	1.66	0.007 16	1.89	5.4	1.51	4300
UU, Endcap	−0.14	−0.0011	1.76	0.008 75	1.66	9.5	1.38	5600
Conv, Central-barrel, high p_{Tt}	0.15	0.0011	1.09	0.006 10	1.78	4.8	1.45	22
Conv, Central-barrel, med p_{Tt}	0.17	0.0017	1.34	0.007 87	1.86	3.5	1.30	100
Conv, Central-barrel, low p_{Tt}	0.17	−0.0014	1.60	0.005 91	1.92	3.2	1.38	5800
Conv, Outer-barrel, high p_{Tt}	0.15	0.000 91	1.30	0.0105	1.67	5.5	1.51	16
Conv, Outer-barrel, med p_{Tt}	0.22	−0.000 59	1.64	0.009 45	1.64	4.7	1.25	2300
Conv, Outer-barrel, low p_{Tt}	0.25	0.000 79	1.97	0.006 79	1.66	4.5	1.47	6800
Conv, Endcap	0.053	0.000 34	2.02	0.009 55	1.48	6.7	1.28	7600

Table 7.14 – Parameters describing the signal shape for each category according to the parametrisation of Equation (7.8).

this parameterisation is then compared with the model determined from a single fit, with a Crystal-Ball lineshape with floating μ_{CB}, σ_{CB}, α_{Low}, and α_{High} parameters, to the $m_H = 125$ GeV simulated signal events. Good agreement is observed.

- **Goodness-of-fit**: the quality of the single fits and simultaneous fit procedure was evaluated using a χ^2 test.

7.5 Background modelling

The dominant and irreducible background in the invariant-mass spectrum arises from SM continuum $\gamma\gamma$ production via QCD processes. In addition, since a large number of photons originate from neutral-meson decays within jets, photon-jet and di-jet events in which jets are misidentified as photons constitute a non-negligible background component. The background-shape parameters and normalisation factors are determined directly from the observed data. Nevertheless, an analytical function must be chosen to model the background in each reconstructed category, and a systematic uncertainty associated with this choice must be assigned. The steps of the background-modelling strategy are summarised in the following paragraphs.

7.5.1 Background templates

The composition of the continuum background in terms of the $\gamma\gamma$, γj, and jj components is estimated using data-driven techniques for each category entering the measurement. These background fractions are then used to construct $m_{\gamma\gamma}$ background templates for each category. The $\gamma\gamma$ component is taken from MC, while the γj and jj components are measured in data control regions.

The number of $\gamma\gamma$, γj and jj events entering each category after the final selection is estimated using a double two-dimensional sideband ABCD method [168]. This data-driven technique extrapolates the fraction of fake photons in the signal region from the composition of the sideband control regions, defined by inverting the photon identification and isolation requirements. The full method involves sixteen input equations, whose solution returns the fractions of the three background components.

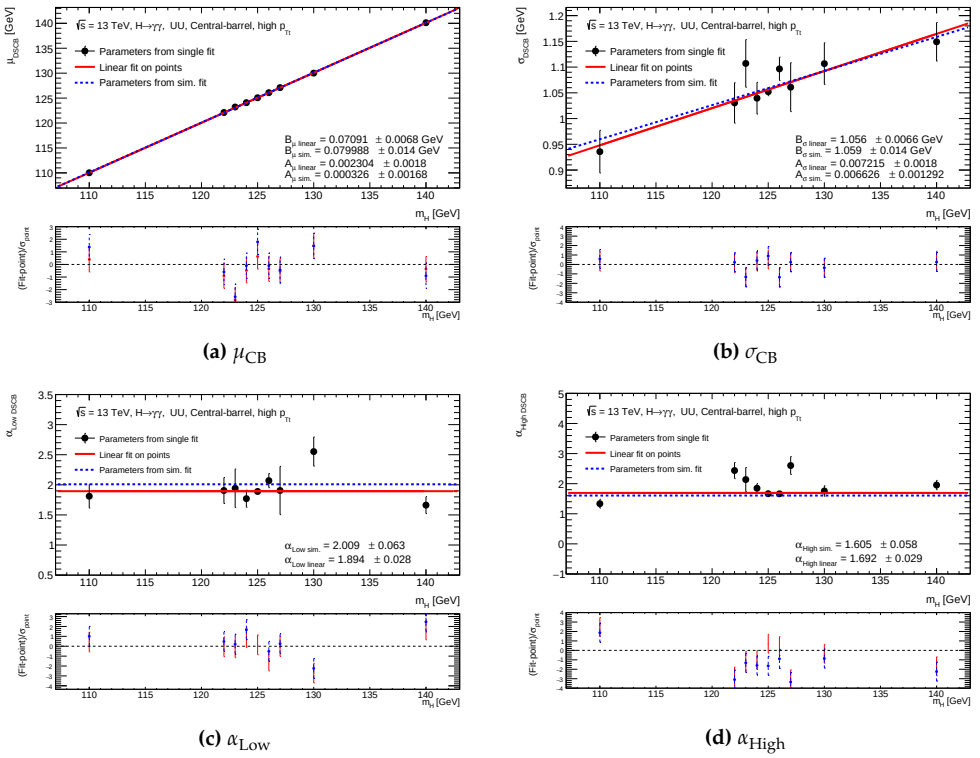

(a) μ_{CB} **(b)** σ_{CB}

(c) α_{Low} **(d)** α_{High}

Figure 7.8 – Comparison between the results of the *simultaneous fit* (dashed blue line) and of the linear fit (solid red line) for the category UU, Central-barrel, high p_{Tt} for each parameter((a): μ_{CB}, (b): σ_{CB}, (c): α_{Low}, (d): α_{High}) as a function of m_H, superimposed on the value obtained from the *single fits* for each available MC sample.

Once the background fractions have been determined, the simulated $\gamma\gamma$ shape is compared with that observed in a γj-enriched data control region in which the identification criteria of exactly one of the two photons are inverted. The small $\gamma\gamma$ contamination in this region, estimated from simulated samples, is subtracted, and a linear weighting is derived to make the MC $\gamma\gamma$ shape reproduce the shape observed in data. The procedure is repeated in a control region where the identification criteria of both photons are inverted, in order to derive a shape weighting for jj events. These weighted shapes are then combined with the measured event fractions to obtain the final background template for each category.
An example of the comparison between the constructed background template and the data sidebands is shown in Figure 7.9 for the UU, Central-barrel, low p_{Tt} category.

7.5.2 Spurious signal test

The *spurious signal* approach is used to select the functional form employed to describe each background template, as well as to determine the associated bias that enters the measurement as a systematic uncertainty (see Section 7.6 and Section 7.7 for their imple-

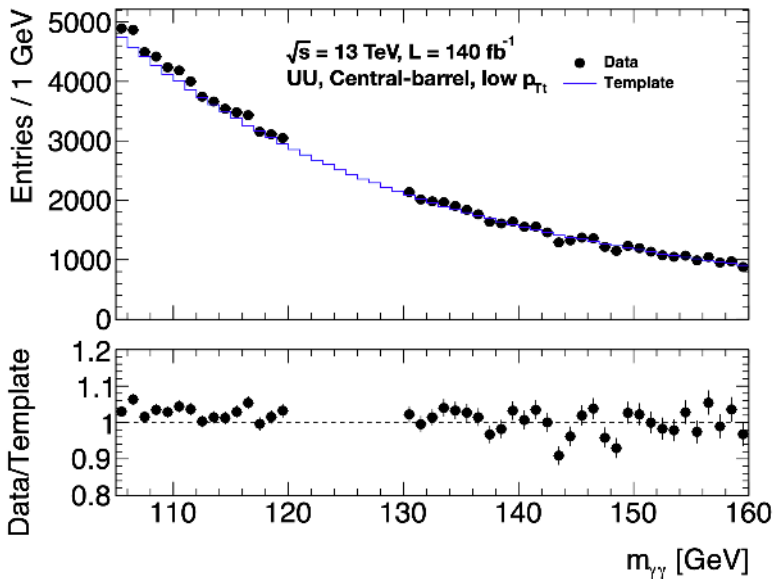

Figure 7.9 – Comparison of the background template (blue histogram) with the data sidebands (black points) for the reconstructed category UU, Central-barrel, low p_{Tt}. The bottom panel shows the ratio of data to the background template.

mentation in the statistical model). The background $m_{\gamma\gamma}$ shape in each analysis category is modelled using an analytic function whose parameters and normalisation are fitted directly to data. The candidate analytic functions considered are:

- Exponential function:
$$f(m_{\gamma\gamma}) = e^{p_0 m_{\gamma\gamma}}$$
- Exponential of a second-order polynomial (ExpPoly2):
$$f(m_{\gamma\gamma}) = e^{\left(p_0\, m_{\gamma\gamma} + p_1\, m_{\gamma\gamma}^2\right)}$$
- Exponential of a third-order polynomial:
$$f(m_{\gamma\gamma}) = e^{\left(p_0\, m_{\gamma\gamma} + p_1\, m_{\gamma\gamma}^2 + p_2\, m_{\gamma\gamma}^3\right)}$$
- Bernstein polynomial of order N:
$$B_N(m_{\gamma\gamma}) = \sum_{i=0}^{N} p_i\, b_{i,N}, \qquad b_{i,N} = \binom{N}{i} m_{\gamma\gamma}^i \left(1 - m_{\gamma\gamma}\right)^{N-i}$$
- First-order power-law function:
$$f(m_{\gamma\gamma}) = m_{\gamma\gamma}^{p_0}$$

To perform the spurious signal test, the full analytic signal-plus-background model is fitted to the background-only template, constructed as described in Section 7.5.1, separately for each category. The fit is carried out in the nominal diphoton mass range $105 \leq m_{\gamma\gamma} \leq 160$ GeV. A scan is then performed by varying m_H in steps of 0.50 GeV within the interval $123 \leq m_{\gamma\gamma} \leq 127$ GeV, and at each step a signal-plus-background fit is executed. For every scan point, the fitted number of signal events is recorded, allowing for negative fitted yields. The spurious signal N_{sp} is defined as the maximum absolute value of the fitted signal yield within the signal mass window when fitting the background-only template.
A candidate analytic function is considered to pass the spurious signal test if at least one of the following criteria is satisfied:

- $|N_{\text{sp}}| < 10\%\, N_{s,\text{exp}}$, where $N_{s,\text{exp}}$ is the expected number of signal events in the category under the SM assumption;
- $|N_{\text{sp}}| < 20\%\, \delta N_{\text{sp}}$, where δN_{sp} is the statistical uncertainty on the fitted number of signal events obtained by fitting the signal-plus-background model to a background-only Asimov dataset.

In addition, the fit of the analytic function to the background template must yield a χ^2 probability of at least 1%. If multiple functions satisfy all requirements, the one with the smallest number of degrees of freedom is selected. If two functions have the same number of degrees of freedom, the one with the smaller maximum spurious signal N_{sp} is chosen.
The determined analytical functions modelling the background in each category entering the measurement are found in Table 7.15, as well as the corresponding spurious signal systematic uncertainty.

Category	m_H	N_{sp}	Function	$p(\chi^2)$ [%]	$N_{\text{sp}}/\delta N_{\text{sp}}$ [%]	$N_{\text{sp}}/N_{\text{s,exp}}$ [%]
UU, Central-barrel, high p_{Tt}	127.0	0.235	Exponential	27.1	-2.66	-0.57
UU, Central-barrel, med p_{Tt}	123.0	5.31	Exponential	20.8	21.0	4.77
UU, Central-barrel, low p_{Tt}	123.0	25.0	ExpPoly2	81.8	-17.8	-2.80
UU, Outer-barrel, high p_{Tt}	125.5	0.766	Power law	4.13	-8.13	-2.10
UU, Outer-barrel, med p_{Tt}	126.0	4.92	ExpPoly2	53.1	-13.7	-3.92
UU, Outer-barrel, low p_{Tt}	123.5	34.9	ExpPoly2	26.4	-18.9	-3.35
UU, Endcap	123.0	63.0	ExpPoly2	15.6	-30.4	-7.34
Conv, Central-barrel, high p_{Tt}	126.5	-0.529	Power law	21.3	-7.81	-1.81
Conv, Central-barrel, med p_{Tt}	123.5	6.99	Exponential	8.27	32.8	9.83
Conv, Central-barrel, low p_{Tt}	124.5	21.2	ExpPoly2	40.5	-18.2	-3.78
Conv, Outer-barrel, high p_{Tt}	126.5	2.35	Exponential	12.8	21.5	5.54
Conv, Outer-barrel, med p_{Tt}	126.5	6.97	ExpPoly2	69.1	-16.5	-5.47
Conv, Outer-barrel, low p_{Tt}	125.5	28.7	ExpPoly2	59.4	-14.2	-2.83
Conv, Endcap	126.5	137	ExpPoly2	1.53	-51.1	-9.89

Table 7.15 – Final background-modelling choices and associated spurious-signal uncertainties. The scan is performed in the range 123-127 GeV in steps of 0.5 GeV. Here N_{sp} is the maximum fitted spurious signal, δN_{sp} is the statistical uncertainty on the fitted signal from a signal+background fit to the background template, and $N_{\text{s,exp}}$ is the expected signal yield under the SM assumption. The quoted m_H is the scan point at which the maximum spurious signal is observed. The χ^2 probability is computed from the fit to the background template.

7.5.3 Data sidebands fit for Asimov dataset construction

The selected functions are used in a background only fit on the observed data sidebands, blinding the range $m_{\gamma\gamma} \in [120\text{ GeV}, 130\text{ GeV}]$, to determine the background shape parameters and normalisation factors. The result of the background fit on the invariant mass distribution $m_{\gamma\gamma}$ for the category UU, Central-barrel, low p_{Tt} is shown in Figure 7.10. The fitted shape parameters and yields obtained from this background fit are shown in Table 7.16 for each category. These values are employed to build the Asimov datasets used in Section 7.8 to evaluate the expected results. However, in the maximum likelihood fits the parameters are left free to float.

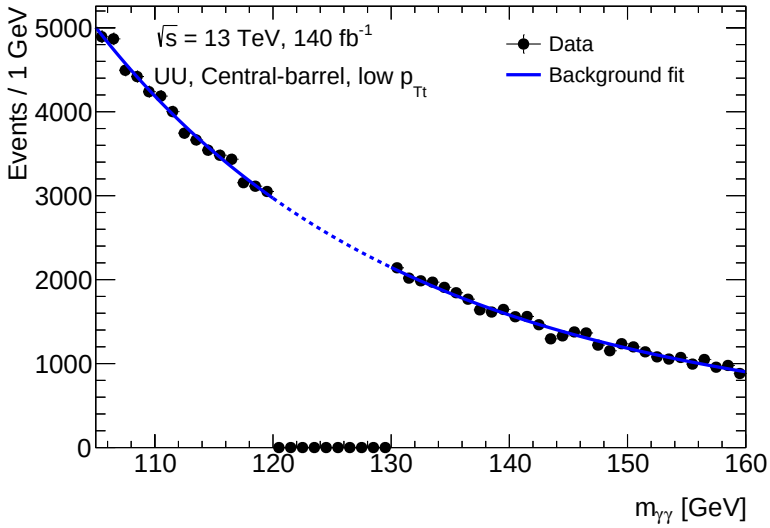

Figure 7.10 – Result of the background fit on data sidebands for the category UU, Central-barrel, low p_{Tt}. The fitted background pdf, in this case an exponential function of a 2nd order polynomial (ExpPoly2), is shown by the blue line; the black dots correspond to the data, blinding the $m_{\gamma\gamma} \in [120, 130]$ GeV range.

7.6 Systematic uncertainties

7.6.1 Scale and resolution systematic uncertainties

Experimental uncertainties affecting the $m_{\gamma\gamma}$ shape arise mainly from the photon energy scale (photon energy scale (PES)) and photon energy resolution (photon energy resolution (PER)) uncertainties. Photon energy scale uncertainties induce a shift in the position of the $m_{\gamma\gamma}$ peak (and therefore in μ_{CB}), while photon energy resolution uncertainties affect the width of the $m_{\gamma\gamma}$ signal distribution (σ_{CB}). Since the mass measurement is primarily driven by an accurate determination of the peak position, the dominant contribution to the total systematic uncertainty on m_H originates from the PES uncertainties. For this reason, in the categorisation studies described in Section 7.3.2, only the impact

Category	Function	p_0	p_1	N
UU, Central-barrel, high p_{Tt}	Exponential	-0.0058		900
UU, Central-barrel, med p_{Tt}	Exponential	-0.0178		5616
UU, Central-barrel, low p_{Tt}	ExpPoly2	-3.72	0.930	126 089
UU, Outer-barrel, high p_{Tt}	Power law	-0.556		963
UU, Outer-barrel, med p_{Tt}	ExpPoly2	-0.883	-1.04	9234
UU, Outer-barrel, low p_{Tt}	ExpPoly2	-4.02	1.30	191 895
UU, Endcap	ExpPoly2	-3.77	1.09	218 654
Conv, Central-barrel, high p_{Tt}	Power law	-0.677		574
Conv, Central-barrel, med p_{Tt}	Exponential	-0.0191		3629
Conv, Central-barrel, low p_{Tt}	ExpPoly2	-3.76	1.03	81 867
Conv, Outer-barrel, high p_{Tt}	Exponential	0		1076
Conv, Outer-barrel, med p_{Tt}	ExpPoly2	-0.456	-1.49	10 437
Conv, Outer-barrel, low p_{Tt}	ExpPoly2	-3.77	0.976	204 216
Conv, Endcap	ExpPoly2	-3.58	0.912	319 182

Table 7.16 – Values of the parameters (p_0 and p_1) describing the background shape for each category, extracted from fits to the data sidebands. The last column reports the fitted background yield N.

of the PES uncertainties was considered for each category.

Each contribution is evaluated using dedicated auxiliary MC samples (all generated at $m_H = 125$ GeV) in which the corresponding systematic variations are applied to the reconstructed photons energies. The resulting impact on the $m_{\gamma\gamma}$ shape is then assessed as described below.

To evaluate the **scale** systematic uncertainties arising from the photon energy scale, the ratio-of-mean technique is used. The means of the $m_{\gamma\gamma}$ distributions, $\left\langle m_{\gamma\gamma} \right\rangle$, are computed for the nominal sample and for the two variations corresponding to $\pm 1\sigma$ shifts of each independent energy-scale systematic uncertainty (see Section 6.5.3) applied to the reconstructed photons. The systematic uncertainty for each category c and for each scale variation is then defined as

$$\delta^{c}_{\mathrm{PES}}(\pm 1\sigma) = \frac{\left\langle m^{\pm 1\sigma}_{\gamma\gamma} \right\rangle}{\left\langle m^{\mathrm{nom}}_{\gamma\gamma} \right\rangle} - 1. \tag{7.9}$$

Figure 7.11 shows the scale uncertainty breakdown for the UU, Central-barrel, low-p_{Tt} category. Uncertainties labelled with the prefix "EG" affect both electrons and photons, while those labelled "PH" are photon-specific. The "PS" uncertainties arise from the Presampler energy scale (Section 6.2.1), "ADCLIN" from the ADC non-linearity correction (Section 6.4.1), and "E4SCINTILLATOR" from the additional TileCal gap/crack scintillators shown in Figure 6.7. The "G4" uncertainty accounts for the modelling of electromagnetic showers in GEANT4, while "L1" and "L2 GAIN" correspond to the High/Medium and Medium/Low gain intercalibration of the calorimeter readout (Section 6.4.2). Uncertainties labelled "LARELEC" refer to the calibration of the LAr calorimeter electron-

ics, while "LARUNCONVCALIB" denotes the energy calibration uncertainty for unconverted photons. The "S12" uncertainty is associated with the intercalibration of the first two layers of the electromagnetic calorimeter (Section 6.2.2). Material-related uncertainties include "MATCALO" for the calorimeter material, "MATID" for the inner detector material, "MATPP0" for passive material at the ID, and "MATCRYO" for the cryostat material. The "ZEE" uncertainties correspond to the statistical and systematic components of the energy scale calibration derived from $Z \to ee$ events (Section 6.5). The "WTOTS1" uncertainty accounts for the modelling of the lateral shower shape in the first calorimeter layer, while "LEAKAGE" refers to uncertainties related to longitudinal energy leakage. Finally, "PH_CONVRADIUS" describes uncertainties in the modelling of the photon conversion radius in the ID, and "PH_CONVRECO" corresponds to uncertainties in the reconstruction efficiency of photon conversion (Section 6.5.2).

Figure 7.12 displays the squared sum of all upward photon energy scale systematic variations for each category. The total impact on the measured mass ranges from ± 1.12‰ in the Conv, Central-barrel, low p_{Tt} category to ± 3.76‰ in the UU Endcap category. As anticipated in Section 7.3.1, the largest photon energy scale uncertainties occur for unconverted photons, mainly due to the electron-to-photon scale extrapolation; this trend is visible in Figure 7.12, where UU categories exhibit a larger squared sum of scale-related uncertainties than the corresponding Conv categories. In addition, a decrease in the squared-sum impact is observed when moving from high- to low-p_{Tt} categories.

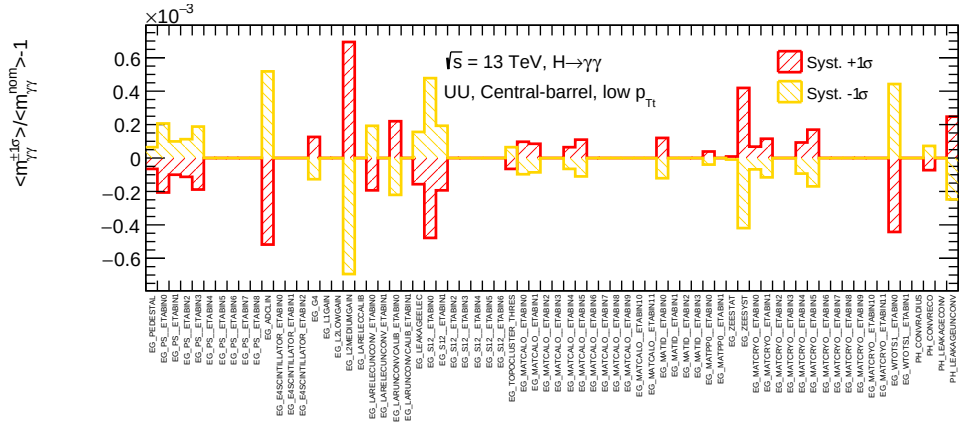

Figure 7.11 – Impact of the photon scale systematic uncertainties (PES) for the category UU, Central-barrel, low p_{Tt}. The up and down systematics (evaluated using respectively the $+1\sigma$ and -1σ varied distributions) are shown in red and in yellow. The naming of each uncertainty on the x-axis reflect its origin.

To estimate the **resolution** systematic uncertainties, the relative difference of inter-quartile ranges is used. The inter-quartile range is computed as $\mathrm{IQR} = \mathrm{CDF}^{-1}(75\%) - \mathrm{CDF}^{-1}(25\%)$, where the CDF is the cumulative distribution function of the $m_{\gamma\gamma}$ nominal and varied distributions. Then, the systematic uncertainty is evaluated for each category c and for each one of the 9 resolution uncertainties as

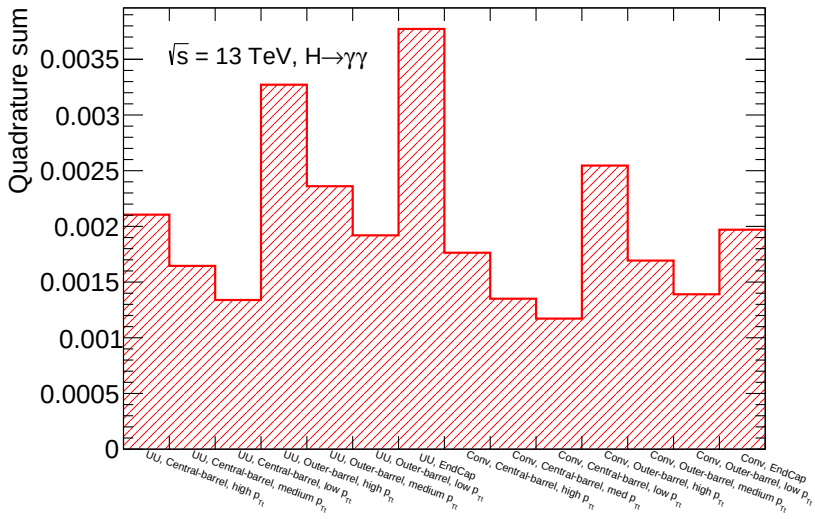

Figure 7.12 – Squared sum of all the photon energy scale systematic impacts of the up contributions on the mass m_H for each category. The total impact ranges from $\pm 0.11\%$ in the Conv, Central-barrel, low p_{Tt} category to $\pm 0.38\%$ in the UU Endcap category.

$$\delta^{c}_{\mathrm{PER}}(\pm 1\sigma) = \frac{\mathrm{IQR}^{\pm 1\sigma}}{\mathrm{IQR}^{\mathrm{nom}}} - 1. \tag{7.10}$$

This procedure was repeated for the nine resolution systematic uncertainties. These were subsequently grouped into five combined uncertainties, by summing in quadrature some of the individual components, in order to match the grouping scheme adopted in the Run 1 analysis. The grouping scheme is reported in Table 7.17. Figure 7.13 shows the five grouped resolution uncertainties for the UU, Central-barrel, low p_{Tt} category. Figure 7.14 presents the squared sum of all upward energy-resolution variations for each category. The overall impact on the mass resolution ranges from $\pm 4.5\%$ in the Conv, Outer-barrel, low p_{Tt} category to $\pm 17\%$ in the UU, Central-barrel, high p_{Tt} category.

Final 5 uncertainties	Grouping
MATERIAL_RUN1_RUN2	MATERIALCALO, MATERIALCRYO, MATERIALGAP, MATERIALID
MATERIAL_RUN2	MATERIALIBL, MATERIALPP0
PILEUP	PILEUP
SAMPLINGTERM	SAMPLINGTERM
ZSMEARING	ZSMEARING

Table 7.17 – Grouping of the 9 resolution systematics in 5 final uncertainties: the uncertainties on the same line on the right column are summed in quadrature to obtain the systematic on the left column.

In principle all the scale and resolution systematics have a dependence on the m_H value, since they depend on the photon p_{T}. To assess the impact of this dependence, the proce-

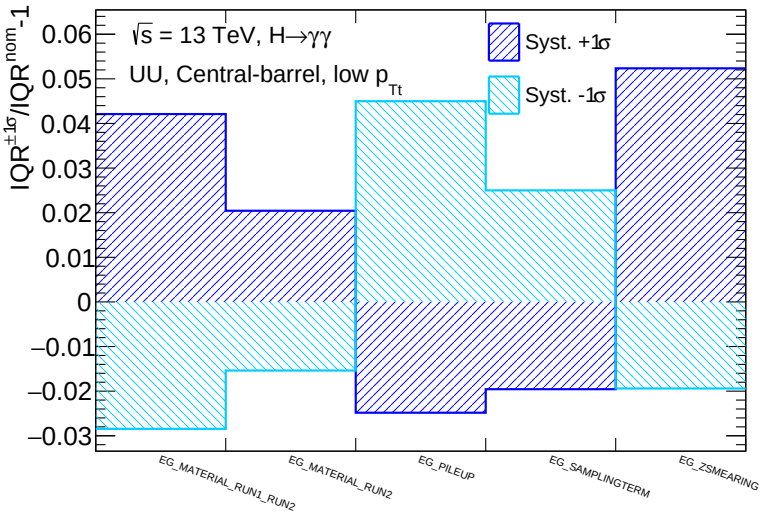

Figure 7.13 – Evaluation of the 5 resolution systematic uncertainties (PER) for the category UU, Central-barrel, low p_{Tt}. The up and down systematics (evaluated using respectively the $+1\sigma$ and -1σ varied distributions) are shown in blue and in light-blue.

dure to evaluate the scale and resolution systematic uncertainties described in the previous pararagraph was repeated using varied mass systematic MC samples generated at different values of m_H besides the MC sample at 125 GeV: $m_H = 110, 124, 126, 140$ GeV. Since the evaluated percentual variations (at $m_H = 124$ and 126 GeV with respect to 125 GeV) is practically always less than 1% (the maximum value is 2.5%) for the three main scale systematics and less than 2% (the maximum value is 3.4%) for the three main resolution systematics for each category, it was decided not to include this dependence on m_H of the systematics in the analysis and therefore to consider these uncertainties as constants.

7.6.2 Modelling biases on m_H

Signal modelling uncertainty

Since the parameters of the signal model are fixed to the values obtained in Section 7.4.3, an inaccurate signal modelling could induce a bias in the mass measurement, which must therefore be evaluated. To assess this potential bias, a *signal injection test* is performed. A dataset composed of a background Asimov sample and the signal MC sample at $m_H = 125$ GeV is fitted with the nominal signal-plus-background model.
The shape parameters and yields of the background-only Asimov dataset for each category are derived from fits to the data sidebands (see Section 7.5.3), using as background models the functional forms selected by the spurious signal test (Section 7.5.2). The signal MC sample generated at $m_H = 125$ GeV is then injected on top of the background Asimov. The resulting signal-plus-background sample is fitted with the nominal

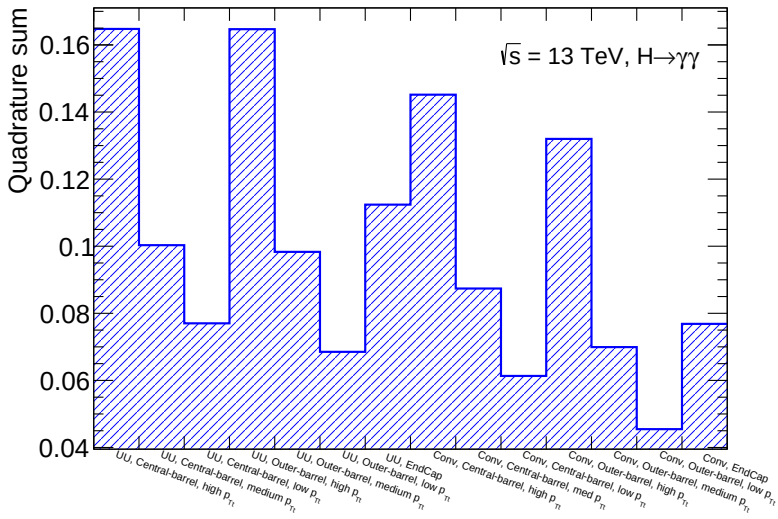

Figure 7.14 – Squared sum of all the energy resolution systematic up contributions for each category. The overall impact on the mass resolution ranges from ±4.5% in the Conv, Outer-barrel, low p_{Tt} category to ±17% in the UU, Central-barrel, high p_{Tt} category.

signal-plus-background model, where the signal component is the parametrised model obtained in Section 7.4.3 and the background component follows the functions listed in Table 7.15. In this fit, the only free parameters are m_H, the background-shape parameters, and the normalisation factors N_{sig} and N_{bkg}.

The signal bias for each category is evaluated as the relative shift between the fitted mass and the injected value ($m_H = 125$ GeV). The results for all categories are reported in the first four columns of Table 7.18.

To assess whether the signal bias is statistically significant, a bootstrap[3] of the signal MC sample at $m_H = 125$ GeV is performed, producing $N_{\mathrm{bootstrap}} = 1000$ replicas for each category. Each bootstrap replica is added on top of the same background Asimov sample, and the resulting $N_{\mathrm{bootstrap}}$ composite datasets are fitted using the same signal-plus-background model employed in the nominal bias evaluation. For each replica, the signal bias is computed as before from the relative shift between the fitted and injected Higgs boson mass. The mean and standard deviation of the bootstrap bias distribution are then calculated; these results are shown in Table 7.18 in the "Bootstrap" columns.

In particular, the last column of the "Bootstrap" section gives the uncertainty on the signal bias, which provides an indication of its statistical significance. For most categories, the bias is found to be statistically significant ($\mu/\sigma > 1$).

Moreover, the last two columns of the table provide a comparison between the evaluated

[3]The bootstrap is a resampling technique used to estimate statistical properties of a distribution by sampling with replacement. To construct one bootstrap sample, events (defined as pairs of the observable $m_{\gamma\gamma}$ and their MC weight) are drawn at random from the original MC sample, with replacement, until the bootstrap sample reaches the same size as the original MC. This procedure is repeated $N_{\mathrm{bootstrap}}$ times to produce $N_{\mathrm{bootstrap}}$ replicas.

signal bias and the total systematic uncertainty arising from the PES, as evaluated in Section 7.6.1. The second-to-last column reports the quadrature sum of the scale systematics for each category (the same information displayed in Figure 7.12), while the final column shows the ratio between the nominal signal bias and the total scale systematic uncertainty, expressed as a percentage. As can be seen, for most categories the size of the signal-modelling uncertainty is less than 10% of the total scale systematic uncertainty.

Category	Nominal fit			Bootstrap			Comparison with PES	
	m_H^{fitted} [GeV]	bias [GeV]	bias [‰]	μ [‰]	σ [‰]	$\lvert\frac{\mu}{\sigma}\rvert$	$\sum \delta^2_{PES}$ [‰]	Bias size [%]
UU, Central-barrel, high p_{Tt}	124.975	-0.025	-0.20	-0.17	0.07	2.6	2.10	9.5
UU, Central-barrel, med p_{Tt}	125.009	0.009	0.07	0.07	0.06	1.2	1.64	4.3
UU, Central-barrel, low p_{Tt}	125.005	0.005	0.04	0.03	0.03	1.1	1.34	3.0
UU, Outer-barrel, high p_{Tt}	124.971	-0.029	-0.23	-0.14	0.09	1.7	3.27	7.0
UU, Outer-barrel, med p_{Tt}	125.035	0.035	0.28	0.28	0.07	4.0	2.36	12
UU, Outer-barrel, low p_{Tt}	125.008	0.008	0.06	0.05	0.04	1.3	1.92	3.1
UU, Endcap	125.016	0.016	0.13	0.10	0.04	2.6	3.86	3.4
Conv, Central-barrel, high p_{Tt}	125.000	0.000	0.00	0.04	0.09	0.49	1.76	0.0
Conv, Central-barrel, med p_{Tt}	124.997	-0.003	-0.02	-0.02	0.09	0.24	1.34	1.5
Conv, Central-barrel, low p_{Tt}	125.012	0.012	0.10	0.09	0.05	2.0	1.15	8.7
Conv, Outer-barrel, high p_{Tt}	125.030	0.030	0.24	0.24	0.10	2.5	2.53	9.5
Conv, Outer-barrel, med p_{Tt}	124.986	-0.014	-0.12	-0.11	0.08	1.3	1.69	7.1
Conv, Outer-barrel, low p_{Tt}	125.016	0.016	0.13	0.12	0.05	2.4	1.37	9.5
Conv, Endcap	125.018	0.018	0.14	0.11	0.04	3.1	1.94	7.2

Table 7.18 – Signal bias computed as difference between the fitted and injected (125 GeV) Higgs boson mass. Mean and standard deviation obtained from a bootstrap procedure with 1000 replicas is reported as well. The significance μ/σ of the bias for each category is reported. In addition, a comparison of the signal bias with the quadrature sum of the PES systematic uncertainties is reported, with "Bias size" computed as the ratio between the nominal signal bias and the quadrature sum of the scale systematics.

Background modelling uncertainty

An inaccurate modelling of the background can also introduce a bias in the mass measurement. To quantify it, a *background injection test* is performed following the same strategy used for the signal bias. A sample consisting of a signal Asimov dataset generated at $m_H = 125$ GeV and a background MC sample is fitted with the nominal signal-plus-background model, using the signal shape parameters extracted in Section 7.4.3. The signal Asimov is then injected on top of the background MC (the $\gamma\gamma$ SHERPA sample reweighted to the background templates described in Section 7.5.1), and the resulting composite dataset is fitted again with the nominal model, where the background component is described by the functional form selected through the spurious signal test. The only free parameters in the fit are m_H, the background-shape parameters, and the normalisation factors N_{sig} and N_{bkg}.

The background bias for each category is defined as the relative shift between the fitted and injected Higgs boson mass. The results are reported in the "Nominal fit" columns of Table 7.19.

To assess the statistical significance of this bias, a bootstrap procedure—analogous to that used for the signal bias—is applied to the background MC sample, generating $N_{\text{bootstrap}} = 1000$ replicas for each category. Each replica is added to the same signal

Category	Nominal fit			Bootstrap			Comparison with PES	
	m_H^{fitted} [GeV]	bias [GeV]	bias [‰]	μ [‰]	σ [‰]	$\frac{\mu}{\sigma}$	$\sum \delta^2_{PES}$ [‰]	Bias size [%]
UU, Central-barrel, high p_{Tt}	124.990	-0.010	-0.08	-0.13	0.25	0.55	2.10	3.8
UU, Central-barrel, med p_{Tt}	124.975	-0.025	-0.20	-0.22	0.25	0.88	1.64	12
UU, Central-barrel, low p_{Tt}	125.013	0.013	0.10	0.10	0.17	0.58	1.34	7.5
UU, Outer-barrel, high p_{Tt}	125.030	0.030	0.24	0.16	0.52	0.30	3.27	7.3
UU, Outer-barrel, med p_{Tt}	125.017	0.017	0.14	0.15	0.05	3.0	2.36	5.9
UU, Outer-barrel, low p_{Tt}	125.051	0.051	0.41	0.37	0.27	1.4	1.92	21
UU, Endcap	125.194	0.194	1.6	1.6	0.33	4.8	3.86	41
Conv, Central-barrel, high p_{Tt}	125.024	0.024	0.19	0.24	0.34	0.71	1.76	11
Conv, Central-barrel, med p_{Tt}	124.945	-0.055	-0.44	-0.44	0.42	1.1	1.34	33
Conv, Central-barrel, low p_{Tt}	125.118	0.118	0.94	0.88	0.32	2.8	1.15	82
Conv, Outer-barrel, high p_{Tt}	125.209	0.209	1.7	1.7	0.47	3.6	2.53	67
Conv, Outer-barrel, med p_{Tt}	124.858	-0.142	-1.1	-1.0	0.62	1.6	1.69	65
Conv, Outer-barrel, low p_{Tt}	125.035	0.035	0.28	0.25	0.40	0.64	1.37	12
Conv, Endcap	125.283	0.283	2.3	2.3	0.4	5.4	1.94	119

Table 7.19 – Background bias as relative shift between the fitted and injected (125 GeV) Higgs boson mass. Mean and standard deviation obtained from a bootstrap procedure with 1000 replicas is reported as well. The significance μ/σ of the bias for each category is reported. In addition, a comparison of the signal bias with the quadrature sum of the PES systematic uncertainties is reported, with "Bias size" computed as the ratio between the nominal background bias and the quadrature sum of the scale systematics.

Asimov sample and fitted with the nominal model. The mean and standard deviation of the resulting bias distribution are shown in the "Bootstrap" columns of Table 7.19; the latter quantifies the uncertainty on the bias. For most categories, the bias is statistically significant ($\mu/\sigma > 1$).

Finally, the last two columns compare the size of the background-modelling bias with the total photon energy scale systematic uncertainty discussed in Section 7.6.1. The second-to-last column lists the quadrature sum of the scale uncertainties for each category (also shown in Figure 7.12), while the final column provides the ratio between the nominal background bias and this total scale uncertainty, expressed as a percentage. The background modelling bias is normally small (< 10% PES) for the UU Central-barrel and Outer-barrel categories, but becomes significant for the UU Endcap and the Conv categories, reaching values between 10%-100% of the PES. In particular, for the Conv Endcap category the background modelling bias is found to be 119% of the total scale systematic uncertainty.

Interference uncertainty

The effect of interference between the $gg \to H \to \gamma\gamma$ signal and the $gg \to \gamma\gamma$ continuum background and between $qg \to H \to \gamma\gamma$ and $qg \to \gamma\gamma$ is not included in the simulated event samples used to study the nominal signal model. In the SM, this interference is expected to change the signal cross-section by 1%-2% [169] and to shift the position of the peak in the diphoton invariant mass distribution by a few tens of MeV [170]. Figure 7.15 illustrates the inclusive mass distributions with and without the gg interference contribution. Its impact on the mass measurement is not corrected and therefore treated as a systematic uncertainty, evaluated following the same strategy adopted for the signal modelling uncertainties.

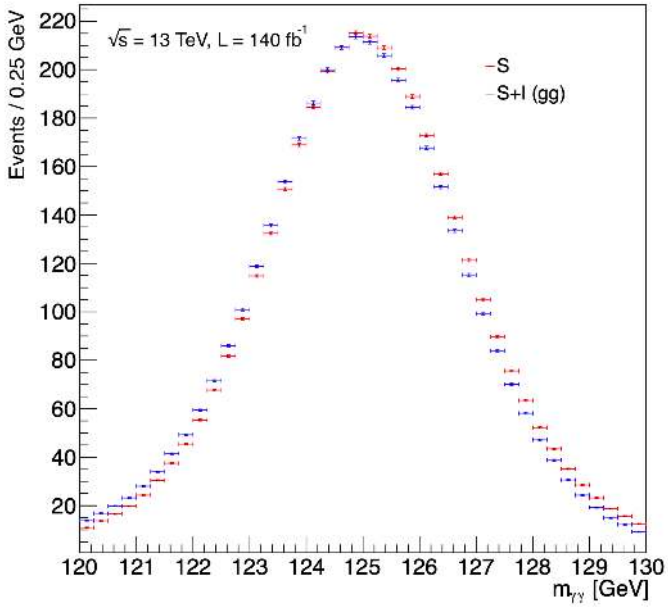

Figure 7.15 – Inclusive invariant mass distributions with (red) and without (blue) the gg interference contribution.

A dataset composed of a signal-plus-background Asimov sample generated at $m_H = 125$ GeV and the interference MC sample (with $\Gamma_H = \Gamma_H^{\text{SM}}$ and including both the gg and qg contributions, see Section 7.1.2) is fitted with the nominal signal-plus-background model. The signal shape parameters and yields entering the Asimov are taken from the global simultaneous fit described in Section 7.4.3, while the background component is constrained using the functions selected through the spurious-signal test (Section 7.5.2). In this fit, the only free parameters are m_H, the background-shape parameters, and the normalisation factors N_{sig} and N_{bkg}. The resulting shift in m_H defines the systematic uncertainty associated with the interference modelling.

The interference bias for each category is evaluated as the relative shift between the fitted and injected Higgs boson mass ($m_H = 125$ GeV). The results are reported in Table 7.20. Two noteworthy features emerge: the bias is negative in almost all categories (i.e. $m_H^{\text{fit}} < m_H^{\text{inj}} = 125.0$ GeV), and its magnitude generally grows as the transverse momentum decreases (from high- to low-p_{Tt} categories). Both behaviours arise from the characteristic shape of the interference term [171].

To assess the statistical significance of the interference bias, a bootstrap of the MC interference sample at $m_H = 125$ GeV is performed, generating $N_{\text{bootstrap}} = 1000$ replicas for each category. Each bootstrapped interference sample is added to the same signal-plus-background Asimov dataset, and the resulting ensembles are fitted using the same signal-plus-background model adopted for the nominal bias determination. For every replica, the interference bias is computed as the relative shift between the fitted and injected Higgs boson mass. The mean and standard deviation of these bias distributions

Category	Nominal fit			Bootstrap			Comparison with PES	
	m_H^{fitted} [GeV]	bias [GeV]	bias [‰]	μ [‰]	σ [‰]	$\lvert\frac{\mu}{\sigma}\rvert$	$\sum\delta^2_{PES}$ [‰]	Bias size [%]
UU, Central-barrel, high p_{Tt}	125.003	0.003	0.02	0.02	0.006	3.9	2.10	0.95
UU, Central-barrel, med p_{Tt}	124.995	-0.005	-0.04	-0.04	0.023	1.6	1.64	2.4
UU, Central-barrel, low p_{Tt}	124.956	-0.044	-0.36	-0.35	0.030	12	1.34	27
UU, Outer-barrel, high p_{Tt}	124.993	-0.007	-0.05	0.00	0.024	0.17	3.27	1.5
UU, Outer-barrel, med p_{Tt}	124.985	-0.015	-0.12	-0.13	0.03	4.4	2.36	5.1
UU, Outer-barrel, low p_{Tt}	124.956	-0.044	-0.35	-0.37	0.03	12	1.92	18
UU, Endcap	124.955	-0.045	-0.36	-0.39	0.03	14	3.86	9.3
Conv, Central-barrel, high p_{Tt}	124.998	-0.002	-0.02	0.02	0.04	0.63	1.76	1.1
Conv, Central-barrel, med p_{Tt}	124.997	-0.003	-0.02	-0.02	0.03	0.65	1.34	1.5
Conv, Central-barrel, low p_{Tt}	124.951	-0.049	-0.39	-0.38	0.05	8.2	1.15	34
Conv, Outer-barrel, high p_{Tt}	125.001	0.001	0.01	0.00	0.04	0.02	2.53	0.40
Conv, Outer-barrel, med p_{Tt}	124.993	-0.007	-0.05	-0.05	0.04	1.4	1.69	3.0
Conv, Outer-barrel, low p_{Tt}	124.943	-0.057	-0.46	-0.46	0.05	9.0	1.37	34
Conv, Endcap	124.953	-0.047	-0.38	-0.42	0.02	18	1.94	20

Table 7.20 – Interference bias as relative shift between the fitted and injected (125 GeV) Higgs boson mass. Mean and standard deviation obtained from a bootstrap procedure with 1000 replicas is reported as well. The significance μ/σ of the bias for each category is reported.

are quoted in Table 7.20 under the "Bootstrap" columns, where the quoted uncertainty provides a measure of the statistical significance. For most categories, the interference bias is statistically significant ($\mu/\sigma > 1$).
The last two columns of Table 7.20 compare the nominal interference bias with the total photon energy scale (PES) systematic uncertainty evaluated in Section 7.6.1. The second-to-last column reports the quadrature sum of the PES contributions for each category (also shown in Figure 7.12), while the final column gives the ratio between the nominal interference bias and the total PES uncertainty expressed as a percentage. The interference bias is normally small (< 5% PES), but its magnitude generally grows as the transverse momentum decreases (from high- to low-p_{Tt} categories and in the Conv Endcap category) where it reaches values between 18%-34% of the PES.

7.6.3 Signal yield uncertainties

Yield uncertainties affect the signal yield in a given reconstructed category by causing migrations of events among categories or by modifying the efficiency of the diphoton selection. Several experimental systematic sources are taken into account: photon *isolation* and *identification* efficiency uncertainties, uncertainties on the diphoton *trigger* efficiency, and uncertainties arising from the modelling of *pileup* in simulation.
Concerning the impact of PER and PES on the category yields, this effect is typically smaller than that of the other systematic sources. Therefore, instead of evaluating separately the impact of each of the 67 energy-scale and 5 energy-resolution systematics on the yield, a simplified model is adopted in which a single global variation is used for the scale and one for the resolution. In this model, the individual systematic contributions are treated as uncorrelated (except for correlations across η) and added in quadrature to obtain one effective uncertainty for the energy scale and one for the energy resolution.
The yields for each category c are computed for the nominal sample and for the two varied samples corresponding to $\pm1\sigma$ shifts, where the systematic variations are applied upstream and their effect propagated to the $m_{\gamma\gamma}$ shape using the signal MC samples.

The impact on the yield is then evaluated as the relative difference between the varied and nominal yields:

$$\delta N_c(\pm 1\sigma) = \frac{N_c^{\pm 1\sigma}}{N_c^{\text{nom}}} - 1. \tag{7.11}$$

The PES and PER yield uncertainties are below 0.1% in all categories, while the signal yield uncertainties related to identification, isolation, trigger efficiencies, and pileup modelling are typically below 1–2%. Since these effects impact the event yield rather than the position of the reconstructed mass peak, their contribution to the Higgs boson mass systematic uncertainty is expected to be negligible.

7.6.4 Theoretical systematic uncertainties

Theoretical uncertainties affecting the cross section of the SM Higgs production modes arising from missing higher-order terms in perturbative QCD calculations (the "Scale" uncertainties) are evaluated by varying the factorization and normalization scales used for theoretical calculations and taking the largest relative difference between the varied and nominal cross sections. The relative impact of the Scale uncertainty ranges from 0.3% (VBF) up to 25% (ggZH); the impact for the ggH production mode is found to be $\sim$ 5%.

The uncertainty on parton distribution functions and on the value of the strong coupling constant ("PDF + α_S" uncertainty) ranges instead from $\sim$ 1% (WH) to 6% (tWH), with an impact of 2-3% for the ggH and VBF production modes.

Finally a 2.9% uncertainty on the branching ratio $\mathcal{BR}(H \to \gamma\gamma)$ is included for all the resonant processes.

7.6.5 Additional systematic uncertainties

Diphoton production vertex As discussed in Section 7.2.2, the primary-vertex selection in the $H \to \gamma\gamma$ analysis relies on a NN to rank the reconstructed vertices in an event and identify the most probable hard-scattering vertex. This vertex is then used to recompute the photon kinematics. Since the photon pseudorapidity and the pointing information used by the NN are derived from the cluster barycentre and its position relative to the tracking system, any misalignment between the ID and the electromagnetic calorimeter could introduce a systematic bias in the $m_{\gamma\gamma}$ reconstruction. In addition, the NN algorithm itself may contain an intrinsic preference in the z direction.

To assess whether these effects are properly modelled in the simulation, a data/ MC comparison is performed using a $Z \to e^+e^-$ control sample.

The directions of the selected electrons and positrons, and therefore their invariant mass, are computed using either (i) the vertex candidate with the largest scalar sum of track p_{T}^2 (including the $e^{\pm}$ tracks), or (ii) the NN-selected vertex, for which the electron and positron tracks are deliberately excluded. The separation between the peak positions of the two resulting e^+e^- invariant-mass distributions is measured independently in data and in simulation. The maximal observed difference between data and MC—found to be 5 MeV—is taken as an additional systematic uncertainty on m_H.

Migration from photon conversion mis-modelling Given that the analysis categorisation relies on requirements on η, $p_{\mathrm{Tt}}^{\gamma\gamma}$ and photon conversion status, events may migrate between categories if the modelling of the photon p_{T} spectrum or the photon-conversion reconstruction differs between data and simulation. The former effect is already covered by the photon energy scale and resolution uncertainties, as well as parton-shower systematics, whereas the latter requires a dedicated study.

Mis-modelling of the photon-conversion rate can bias the photon energy response, since the MC MVA calibration is trained separately for converted and unconverted photons, as explained in Section 6.3. This effect is parameterised in the calibration by the PH_SCALE_CONVRECO systematic uncertainty, which is correlated across the two photon types. When propagated to the mass analysis, it accounts for a possible bias in the peak position but does not describe the relative migration of events between the UU and Conv categories.

To quantify this migration, the same method used in the photon calibration is adopted. The number of converted and unconverted photons entering the analysis is expressed in terms of three probabilities: the true-photon conversion probability f_{conv}, the conversion-reconstruction efficiency f_{reco}, and the fake-conversion rate f_{fake}. These quantities are measured in radiative Z decays in both data and simulation.

The impact on the mass categories is obtained by reweighting a ggH MC sample so that it reproduces the f_{conv}, f_{reco} and f_{fake} values observed in data, while keeping the total number of selected photons constant. The relative yield variations between the nominal and reweighted configurations provide the category-by-category systematic uncertainty associated with conversion mis-modelling, as reported in Table 7.21.

Category	Relative yield variation [%]
UU, Central-barrel, high p_{Tt}	−0.81
UU, Central-barrel, med p_{Tt}	−0.93
UU, Central-barrel, low p_{Tt}	−1.13
UU, Outer-barrel, high p_{Tt}	1.87
UU, Outer-barrel, med p_{Tt}	1.61
UU, Outer-barrel, low p_{Tt}	1.56
UU, Endcap	10.97
Conv, Central-barrel, high p_{Tt}	2.25
Conv, Central-barrel, med p_{Tt}	2.98
Conv, Central-barrel, low p_{Tt}	3.57
Conv, Outer-barrel, high p_{Tt}	−2.79
Conv, Outer-barrel, high p_{Tt}	−2.41
Conv, Outer-barrel, low p_{Tt}	−2.27
Conv, Endcap	−7.68

Table 7.21 – Category yield variation due to the mis-modelling of the photon conversion between data and MC.

7.6.6 Main sistematic uncertainties summary

Table 7.22 summarises the main source of systematic uncertainties for the m_H measurement in the diphoton channel and their expected pre-fit and pre-linearity impacts for category and for systematic group.

Category	LAr cell non-linearity	$Z \to ee$ calibration	Layer calibration	Other material (not ID)	Lateral shower shape	Conversion reconstruction	ID material	Interference bias	Background modelling bias	Signal modelling bias	Vertex bias
UU, Central-barrel, high p_{Tt}	0.171	0.042	0.083	0.046	0.065	0.003	0.014	0.002	0.008	0.020	0.004
UU, Central-barrel, med p_{Tt}	0.122	0.042	0.070	0.046	0.057	0.005	0.013	0.004	0.020	0.007	0.004
UU, Central-barrel, low p_{Tt}	0.087	0.042	0.061	0.044	0.053	0.007	0.013	0.035	0.010	0.004	0.004
UU, Outer-barrel, high p_{Tt}	0.264	0.047	0.130	0.119	0.050	0.006	0.039	0.005	0.024	0.023	0.004
UU, Outer-barrel, med p_{Tt}	0.161	0.048	0.110	0.110	0.042	0.010	0.038	0.012	0.014	0.028	0.004
UU, Outer-barrel, low p_{Tt}	0.101	0.048	0.100	0.106	0.039	0.012	0.038	0.035	0.041	0.006	0.004
UU, Endcap	0.099	0.090	0.196	0.106	0.183	0.040	0.074	0.036	0.160	0.013	0.004
Conv, Central-barrel, high p_{Tt}	0.144	0.042	0.055	0.032	0.057	0.037	0.011	0.002	0.019	0.000	0.004
Conv, Central-barrel, med p_{Tt}	0.092	0.042	0.039	0.024	0.050	0.058	0.008	0.002	0.044	0.002	0.004
Conv, Central-barrel, low p_{Tt}	0.056	0.042	0.028	0.018	0.045	0.075	0.006	0.039	0.094	0.010	0.004
Conv, Outer-barrel, high p_{Tt}	0.208	0.048	0.084	0.080	0.048	0.044	0.036	0.001	0.170	0.024	0.004
Conv, Outer-barrel, med p_{Tt}	0.112	0.049	0.056	0.052	0.044	0.069	0.034	0.005	0.110	0.012	0.004
Conv, Outer-barrel, low p_{Tt}	0.061	0.049	0.043	0.036	0.041	0.086	0.033	0.046	0.028	0.013	0.004
Conv, Endcap	0.053	0.094	0.100	0.036	0.068	0.053	0.063	0.038	0.230	0.014	0.004

Table 7.22 – Pre-fit and pre-linearity impacts (in %) of the main systematic uncertainty groups. The quadrature sum of the first seven columns corresponds to the total photon energy scale uncertainty.

7.7 Statistical model

The Higgs boson mass is extracted from a maximum-likelihood fit to the diphoton invariant mass distributions in the range $105 < m_{\gamma\gamma} < 160$ GeV, performed simultaneously across all analysis categories. An *extended likelihood function* is constructed for the $N_{\mathrm{cat}} = 14$ categories, incorporating the signal and background models described in Sections 7.4 and 7.5, together with the nuisance-parameter constraints associated with the systematic uncertainties discussed in Section 7.6.

The number of expected events for each category c and for each production mode i (ggH, VBF, WH, ZH, ggZH, $t\bar{t}H$, $b\bar{b}H$, tHbj and tWH) is modelled as in Equation (7.5), introducing the signal strength μ as an overall multiplicative factor. The parameter μ quantifies the agreement between the yields predicted by the SM and the value measured in data. The expected yield in category c is therefore:

$$N_c(m_H,\mu,\boldsymbol{\theta}) = \sum_i \mu \cdot L(\theta_{\text{lumi}}) \cdot \sigma_i(m_H,\boldsymbol{\theta}_{\text{theo}}) \cdot \mathcal{BR}_{\gamma\gamma}(m_H,\theta_{\mathcal{BR}}) \cdot (\mathcal{A}\cdot\epsilon)_{ic}(m_H,\boldsymbol{\theta}_{\text{sig}})$$
$$= \sum_i \mu \cdot N_{ci}(m_H,\boldsymbol{\theta}), \tag{7.12}$$

where:

- L is the total integrated luminosity, $L = 140\ \text{fb}^{-1}$;
- $\boldsymbol{\theta}$ denotes the Nuisance Parameters (NPs), i.e. all parameters entering the fit except for the Parameters of Interest (POIs) (m_H and μ);
- $\sigma_i(m_H,\boldsymbol{\theta}_{\text{theo}})$ is the Higgs production cross section for process i;
- $\mathcal{BR}_{\gamma\gamma}(m_H,\theta_{\mathcal{BR}})$ is the diphoton branching ratio ($\mathcal{BR}_{\gamma\gamma} \simeq 0.227\%$ at $m_H = 125.09\,\text{GeV}$);
- $\mathcal{A}_{ic}$ is the geometric/kinematic acceptance and ϵ_{ic} the reconstruction and selection efficiency for a Higgs event of production mode i to be reconstructed in category c;
- N_{ci} denotes the yield in category c from production mode i, given by the product $L\cdot\sigma_i\cdot\mathcal{BR}_{\gamma\gamma}\cdot(\mathcal{A}\epsilon)_{ic}$.

The dependence of the yield N_{ci} on m_H was studied for each category and production mode in Section 7.4.1 and it is included in the model. The *likelihood function* $\mathcal{L}$ is

$$\mathcal{L}\left(m_H,\mu,\boldsymbol{\theta};m_{\gamma\gamma}\right) = \prod_{c=1}^{N_{\text{cat}}}\left(\text{Pois}\left(N_c|\nu_c\left(m_H,\mu,\boldsymbol{\theta}\right)\right)\prod_{i=1}^{N_c} f_c\left(m^i_{\gamma\gamma};m_H,\boldsymbol{\theta}\right)\right)\prod_j G\left(\theta_j\right). \tag{7.13}$$

The first product is the likelihood extended term and it spans the analysis categories: the number of observed events for each category N_c is modelled with a Poisson distribution with mean

$$\nu_c\left(m_H,\mu,\boldsymbol{\theta}\right) = N_c(m_H,\mu,\boldsymbol{\theta}) + N_c^{bkg} + N_{sp}^c\cdot\theta_{sp}^c \tag{7.14}$$

where N_c is the number of expected Higgs signal events for the c-th category, N_c^{bkg} the number of background events fitted on data and N_{sp}^c is the spurious signal with its associated nuisance parameter θ_{sp}^c.
For each category, the diphoton mass probability density function is built from the signal and background functions as

$$f_c\left(m^i_{\gamma\gamma};m_H,\boldsymbol{\theta}\right) = \frac{1}{\nu_c}\left\{\left(N_c(m_H,\mu,\boldsymbol{\theta}) + N_{sp}^c\theta_{sp}^c\right)\cdot f_{sig}^c\left(m^i_{\gamma\gamma};m_H,\boldsymbol{\theta}_{SS}\right) + \right.$$
$$\left. + N_c^{bkg}\cdot f_{bkg}^c\left(m^i_{\gamma\gamma},\boldsymbol{\theta}_{BS}\right)\right\} \tag{7.15}$$

where f_{sig}^c and f_{bkg}^c are the analytical functions for signal and background respectively evaluated in Section 7.4.3 and 7.5, $\boldsymbol{\theta}_{SS}$ are the shape uncertainties on the peak position and width of the signal shape (Section 7.6.1, Section 7.6.2) and $\boldsymbol{\theta}_{BS}$ are the background shape parameters which are free to float in the fit. The Higgs boson mass m_H represents the main Parameter of Interest (POI) of the fit.

The last term in the likelihood function (Eq. 7.13) is the product of constraint terms on the NPs. Systematic uncertainties enter the likelihood by multiplying the affected quantity with a response function which may differ according to the considered systematic; the possible choices are

$$\begin{aligned} F_{\mathrm{G}}(\delta,\theta) &= (1+\delta\,\theta) && \text{gaussian response,} \\ F_{\mathrm{LN}}(\delta,\theta) &= e^{\sqrt{\ln\left(1+\delta^2\right)}\,\theta} && \text{log-normal response,} \\ F_{\mathrm{AS}}(\delta^{\pm},\theta) &= \begin{cases} P_6(\theta;\,\delta^-,0,\delta^+), & \theta \in [\delta^-,\delta^+], \\ F_{\mathrm{LN}}(\delta,\theta), & \text{otherwise,} \end{cases} && \text{asymmetric response,} \end{aligned} \tag{7.16}$$

where δ is the relative uncertainty amplitude estimated as explained in Section 7.6, $\delta^{\pm}$ in the case of asymmetric $\pm 1\sigma$ variations. Asymmetric uncertainties are implemented with two log-normal response functions, one for the up and one for the down variation, linked by a six-degree polynomial P_6. In general, log-normal constraints are used whenever a negative model parameter has no physical sense, as in the case of luminosity. The nuisance parameter θ is constrained by probability density function which is an unitary Gaussian $G(\theta)$ of mean 0 and width 1. Some details on the systematics implementation are listed below:

- The 67 photon energy **scale** systematics (PES) of Section 7.6.1 are included in the fit to data as response functions $F_{\mathrm{G}}^{\mathrm{PES}}$ on μ_{CB} of the signal DSCB:

$$\mu'_{\mathrm{CB}} = \mu_{\mathrm{CB}}(m_H) F_{\mathrm{G}}^{\mathrm{PES}}(\delta^{\pm},\theta) \tag{7.17}$$

  where $\mu_{\mathrm{CB}}(m_H)$ comes from the parametrization of Equation (7.8). The constrained nuisance parameters $\boldsymbol{\theta}$ are implemented in the fit to data as Gaussian response using the $+1\sigma$ variation, because of the high symmetry observed. The constraint is applied to μ_{CB} as a response function of the type $F_{\mathrm{G}}^{\mathrm{PES}}(\delta^{\pm},\theta) = (1+\delta^{\pm}_{\mathrm{PES}}\cdot\theta_{\mathrm{PES}})$. The other parameters of the analytic function used to model the signal are not affected. These 67 $\delta^{\pm}$ systematic variations are extracted for each analysis category using the techniques described in the corresponding Section 7.6.1 and are then considered fully correlated[4] across the categories;

- The 5 **resolution** uncertainties (PER) are applied to σ_{CB} as a response function $F_{\mathrm{AS}}^{\mathrm{PER}}(\delta^{\pm},\theta)$ and they are implemented in the fit to data with an asymmetric constraint, to take into account differences in the $+1\sigma$ and -1σ variations:

$$\sigma'_{\mathrm{CB}} = \sigma_{CB}(m_H) F_{\mathrm{AS}}^{\mathrm{PER}}(\delta^{\pm},\theta) \tag{7.18}$$

  where $\sigma_{\mathrm{CB}}(m_H)$ comes from the parametrization of Equation (7.8). All the energy

[4] Correlation among a systematic source is imposed by using the same nuisance parameter θ with different values of δ: in this case for each one of the 67 scale systematics 14 values of δ are implemented (one for each category) but with the same name.

resolution effects are then considered fully correlated across the categories;

- The **signal** and **background** biases evaluated in Section 7.6.2 are both assumed uncorrelated among the categories, thus leading to 14 additional NPs each, one for each category. Each bias is considered as uncorrelated because it might depend on the kinematic selections applied to obtain the categories and these effects are not clearly correlated between the categories. They are included in the fit as response functions with a Gaussian response on μ_{CB} of the signal DSCB, in the same way of the scale systematics;
- The **interference** biases of Section 7.6.2 are assumed correlated among the categories, thus leading to only 1 additional NP. Also this bias is included in the fit with a Gaussian response on μ_{CB};
- The **spurious signal** is different from all the other uncertainty implemented, since the response function is just $F_{\text{sp}} = \theta_{sp}$, as shown in Equation (7.14)
- The **yield** uncertainties related to photon isolation, photon identification, trigger, and pileup, described in Section 7.6.3, are assumed to be fully correlated across categories and therefore introduce a single additional NP per systematic source. These uncertainties are implemented in the fit as response functions acting on the expected yield N_c, using an asymmetric response, with the exception of the trigger uncertainty, which is modelled with a log-normal response. The effects of energy scale and resolution uncertainties on the yield are also assumed to be correlated across categories and are implemented using 67 and 5 NPs, respectively, following the same strategy adopted for the corresponding shape systematics. Scale-induced yield uncertainties are modelled with gaussian responses, while resolution-induced yield uncertainties are implemented using asymmetric responses.

A summary of the number of nuisance parameter and the relative constraint is reported in Table 7.23.

Likelihood ratio and scan

As defined in Equation (7.13), the *likelihood function* quantifies the compatibility of a model, depending on the parameters $(m_H, \mu, \boldsymbol{\theta})$, with the observed dataset $(m_{\gamma\gamma})$. In the framework of *maximum likelihood estimation* [172], the parameter values that maximise the likelihood are the *maximum-likelihood estimators*; in this analysis, the principal estimator is $\hat{m}_H$. For sufficiently large datasets, maximum-likelihood estimators are consistent, asymptotically unbiased, and efficient.
Maximising $\mathcal{L}$ is equivalent to maximising the log-likelihood $\ln \mathcal{L}$, or, equivalently, to minimising the negative log-likelihood $-2\ln\mathcal{L}$. From the latter, the *profile likelihood ratio* is defined as

$$-2\ln\Lambda(m_H) = -2\ln\frac{\mathcal{L}(m_H;\,\hat{\hat{\boldsymbol{\theta}}}(m_H))}{\mathcal{L}(\hat{m}_H;\,\hat{\boldsymbol{\theta}})} = -2\left[\ln\mathcal{L}(m_H;\,\hat{\hat{\boldsymbol{\theta}}}(m_H)) - \ln\mathcal{L}(\hat{m}_H;\,\hat{\boldsymbol{\theta}})\right], \quad (7.19)$$

where $\hat{m}_H$ and $\hat{\boldsymbol{\theta}}$ are the values of the POI and NPs that maximize the likelihood

		Systematic source	NP	Implementation
Yield	Theo	Branching ratio	1	$N_{\text{tot}}\, F_{\text{LN}}(\delta_i, \theta_i)$
		PDF	9	$N_p\, F_{\text{AS}}(\delta_i, \theta_i)$
		α_S	1	$N_p\, F_{\text{AS}}(\delta_i, \theta_i)$
	Exp	Luminosity	1	$N_{\text{tot}}\, F_{\text{LN}}(\delta_i, \theta_i)$
	Exp	Trigger	1	$N_c\, F_{\text{LN}}(\delta_i, \theta_i)$
		Photon Isolation	1	$N_c\, F_{\text{AS}}(\delta_i, \theta_i)$
		Photon Identification	1	$N_c\, F_{\text{AS}}(\delta_i, \theta_i)$
		Photon Scale	1	$N_c\, F_{\text{G}}(\delta_i, \theta_i)$
		Photon Resolution	1	$N_c\, F_{\text{AS}}(\delta_i, \theta_i)$
		Pileup	1	$N_c\, F_{\text{AS}}(\delta_i, \theta_i)$
Shape		Photon Scale	67	$\mu_{\text{CB}}\, F_{\text{G}}(\delta_i, \theta_i)$
		Photon Resolution	5	$\sigma_{\text{CB}}\, F_{\text{AS}}(\delta_i, \theta_i)$
		Signal Bias	14	$\mu_{\text{CB}}\, F_{\text{G}}(\delta_i, \theta_i)$
		Background Bias	14	$\mu_{\text{CB}}\, F_{\text{G}}(\delta_i, \theta_i)$
		Interference Bias	1	$\mu_{\text{CB}}\, F_{\text{G}}(\delta_i, \theta_i)$
Bkg		Spurious signal	14	$N_{\text{spur},c}\, \theta_{\text{spur},c}$

Table 7.23 – Summary of sources of systematic uncertainty θ_i along with their implementation in the likelihood function, impacting on signal yields, mass scale/resolution and the spurious signals resulting from the background parametrization. When acting on N_{tot} the uncertainty value is the same for all the categories, whereas the uncertainty has a different value for each category on the case denoted by N_c and a different value for each production mode when denoted by N_p.

$\mathcal{L}(\hat{m}_H; \hat{\boldsymbol{\theta}})$, while $\hat{\hat{\boldsymbol{\theta}}}(m_H)$ corresponds to the values of the NPs that maximize the likelihood for a given value of m_H. By construction, $\mathcal{L}(\hat{m}_H; \hat{\boldsymbol{\theta}}) \geq \mathcal{L}(m_H; \hat{\hat{\boldsymbol{\theta}}}(m_H))$.
In the asymptotic regime, which is valid for all results presented here, the test statistic $-2\ln\Lambda(m_H)$ follows a χ^2 distribution with a number of degrees of freedom equal to the number of parameters of interest. This allows confidence intervals on m_H to be constructed. The endpoints of the 68% confidence interval for $\hat{m}_H$ are obtained by solving

$$-2\ln\Lambda(m_H) = 1. \tag{7.20}$$

7.8 Results

7.8.1 Expected results without linearity

In order to estimate the expected values of the uncertainties on the m_H value, a fit is performed on an Asimov dataset corresponding to the SM expectations (i.e. signal strength set to 1.0, $m_H = 125.00$ GeV, all systematic nuisance parameters set to 0, and background normalisation and shape fitted in the $m_{\gamma\gamma}$ data sidebands). The fitted POIs in the nom-

inal fit are the Higgs boson mass and the 14 signal strenghts μ_{cat}, one for each category. The best value obtained for m_H from the fit is:

$$m_H = 125.00 \pm 0.12\,(\text{stat.}) \pm 0.18\,(\text{syst.})\,\text{GeV} = 125.00 \pm 0.21\,\text{GeV} \tag{7.21}$$

where the first error is the statistical uncertainty while the second is the total systematic uncertainty evaluated as the quadratic difference between the total error and the statistical-only error. The statistical-only error is evaluated by repeating the fit after fixing all the systematic nuisance parameters to their best values (which is by defition ~ 0 on a prefit Asimov dataset). The total uncertainty corresponds to a relative error of 0.17%, while the systematic uncertainty corresponds to a relative uncertainty of 0.14%; as expected the measurement would therefore still be dominated by systematic uncertainty, and in particular by the uncertainties arising from the photon energy calibration (as detailed in Section 7.6). The total systematic is decomposed in the main components, grouping several systematics in common set of uncertainty. The contribution of a particular set of systematic uncertainties is computed as a quadratic difference between the total uncertainty, obtained floating all the nuisance parameters, and a fit with all the nuisance parameters free to float except for the ones under study. This is done always using the same Asimov input dataset, with $m_H = 125.00$ GeV and the signal strengths fixed to 1. The errors on the m_H are obtained from a scan of the likelihood ratio. The results are shown in Table 7.24.

	Impact on m_H [MeV]	
Systematic group	Down	Up
LAr cell non-linearity	126	127
$Z \to ee$ calibration	61	61
Layer calibration	61	61
Other material (not ID)	51	51
Lateral shower shape	51	51
Interference bias	34	34
Conversion reconstruction	29	30
Background model bias	28	28
ID material	21	21
Vertex bias	5	5
Signal model bias	4	4
Resolution	3	3
Spurious Signal	3	3
Theory	0	0
Yield	0	0
Luminosity	0	0

Table 7.24 – Systematic decomposition on the Asimov dataset.

The main POI is the Higgs boson mass m_H but in the maximum likelihood fit it is possible to constrain also the global signal strength μ. The global μ however can be parametrised by the product of the signal strengths for each production mode μ_i or

considering the 14 signal strenghts μ_{cat}, one for each category. The main features and expected results of these fit schemes are listed below. The main result, i.e. the expected Higgs boson mass and its uncertainties, is not affected by the choice of the signal yields fit strategy.

- **global μ**: The expected result considering the global signal strength μ is

$$\begin{aligned} m_H &= 125.00 \pm 0.22 \text{ GeV} &&= 125.00 \pm 0.12 \text{ (stat.)} \pm 0.18 \text{ (syst.) GeV} \\ \mu &= 1.00 \,^{+0.10}_{-0.09} &&= 1.00 \pm 0.06 \text{ (stat.)} \,^{+0.08}_{-0.07} \text{ (syst.)} \end{aligned} \tag{7.22}$$

- **14 $\mu_{category}$**: the baseline configuration considers a different μ for each analysis category to be as model independent as possible. The expected result is

$$\begin{aligned} m_H &= 125.00 \pm 0.21 \text{ GeV} &&= 125.00 \pm 0.12 \text{ (stat.)} \pm 0.18 \text{ (syst.) GeV} \\ \mu_{\text{UU,Central}-\text{barrel,high}-p_{Tt}} &= 1.00 \,^{+0.27}_{-0.24} &&= 1.00 \,^{+0.25}_{-0.24} \text{ (stat.)} \,^{+0.10}_{-0.06} \text{ (syst.)} \\ \mu_{\text{UU,Central}-\text{barrel,med}-p_{Tt}} &= 1.00 \,^{+0.26}_{-0.25} &&= 1.00 \pm 0.24 \text{ (stat.)} \,^{+0.10}_{-0.07} \text{ (syst.)} \\ \mu_{\text{UU,Central}-\text{barrel,low}-p_{Tt}} &= 1.00 \,^{+0.18}_{-0.16} &&= 1.00 \pm 0.15 \text{ (stat.)} \,^{+0.10}_{-0.06} \text{ (syst.)} \\ \mu_{\text{UU,Outer}-\text{barrel,high}-p_{Tt}} &= 1.00 \,^{+0.36}_{-0.33} &&= 1.00 \,^{+0.34}_{-0.32} \text{ (stat.)} \,^{+0.12}_{-0.08} \text{ (syst.)} \\ \mu_{\text{UU,Outer}-\text{barrel,med}-p_{Tt}} &= 1.00 \,^{+0.34}_{-0.32} &&= 1.00 \,^{+0.32}_{-0.31} \text{ (stat.)} \,^{+0.11}_{-0.08} \text{ (syst.)} \\ \mu_{\text{UU,Outer}-\text{barrel,low}-p_{Tt}} &= 1.00 \,^{+0.21}_{-0.20} &&= 1.00 \pm 0.19 \text{ (stat.)} \,^{+0.09}_{-0.06} \text{ (syst.)} \\ \mu_{\text{UU,Endcap}} &= 1.00 \,^{+0.31}_{-0.27} &&= 1.00 \pm 0.24 \text{ (stat.)} \,^{+0.20}_{-0.12} \text{ (syst.)} \\ \mu_{\text{Conv,Central}-\text{barrel,high}-p_{Tt}} &= 1.00 \,^{+0.34}_{-0.31} &&= 1.00 \,^{+0.33}_{-0.30} \text{ (stat.)} \,^{+0.08}_{-0.08} \text{ (syst.)} \\ \mu_{\text{Conv,Central}-\text{barrel,med}-p_{Tt}} &= 1.00 \,^{+0.36}_{-0.34} &&= 1.00 \,^{+0.33}_{-0.32} \text{ (stat.)} \,^{+0.14}_{-0.11} \text{ (syst.)} \\ \mu_{\text{Conv,Central}-\text{barrel,low}-p_{Tt}} &= 1.00 \,^{+0.24}_{-0.22} &&= 1.00 \pm 0.21 \text{ (stat.)} \,^{+0.12}_{-0.07} \text{ (syst.)} \\ \mu_{\text{Conv,Outer}-\text{barrel,high}-p_{Tt}} &= 1.00 \,^{+0.36}_{-0.33} &&= 1.00 \,^{+0.33}_{-0.32} \text{ (stat.)} \,^{+0.14}_{-0.08} \text{ (syst.)} \\ \mu_{\text{Conv,Outer}-\text{barrel,med}-p_{Tt}} &= 1.00 \,^{+0.38}_{-0.36} &&= 1.00 \,^{+0.36}_{-0.35} \text{ (stat.)} \,^{+0.12}_{-0.08} \text{ (syst.)} \\ \mu_{\text{Conv,Outer}-\text{barrel,low}-p_{Tt}} &= 1.00 \,^{+0.23}_{-0.22} &&= 1.00 \pm 0.21 \text{ (stat.)} \,^{+0.09}_{-0.07} \text{ (syst.)} \\ \mu_{\text{Conv,Endcap}} &= 1.00 \,^{+0.26}_{-0.24} &&= 1.00 \pm 0.20 \text{ (stat.)} \,^{+0.17}_{-0.13} \text{ (syst.)} \end{aligned} \tag{7.23}$$

7.8.2 Expected results with linearity fit

A significant improvement on the precision of the Higgs boson mass measurement is coming from a innovative method to evaluate the electron and photon energy scale, the *linearity fit*, as explained in Section 6.5.4.

The output of the fit returns a set of new additional scales $\hat{\alpha}'$ which evolve according to the post-fit pulled, constrained and correlated systematic uncertainties described by the best fitted $\hat{\theta}_k$ and the covariance matrix $\Sigma_{n_{NP} \times n_{NP}}$. The new scales are applied to data on top of the inclusive in-situ scales. The additional constraint and correlation of the

systematic uncertainties is propagated to Higgs boson mass measurement by modifying the auxiliary measurements in the likelihood described in Section 7.7. In particular, the product of the Gaussian constraint terms (one for each systematic uncertainty when the systematic uncertainties are uncorrelated) is substituted by a unique multivariate Gaussian defined from the covariance matrix obtained from the fit:

$$\prod_j G\left(0|\theta_j, 1\right) \qquad \rightarrow \qquad G\left(0|\vec{\theta}, \Sigma_{n_{NP}\times n_{NP}}\right). \tag{7.24}$$

After including the new constraints and correlation of the scale systematic uncertainties in the statistical model, as shown in Equation (7.24), the expected value of the Higgs boson mass becomes:

$$m_H = 125.00 \pm 0.12\ (\text{stat.}) \pm 0.09\ (\text{syst.})\,\text{GeV} = 125.00 \pm\ 0.15\,\text{GeV}. \tag{7.25}$$

The additional linearity measurement reduces the systematic uncertainties by 50%, and the total uncertainty by 30%. After including the linearity constraints in the fit, the dominant source of uncertainty of the mass measurement in the diphoton channel becomes the statistical uncertainty.

The reduction of the total energy scale uncertainty per category is reported in Figure 7.16, which shows the quadrature sum of energy scale impacts with and without the linearity constraints. It also compares the same quantity on the same categorisation but obtained from MC samples with the reconstruction algorithm (Rel. 20.7) and energy calibration used for the partial Run 2 $H \rightarrow \gamma\gamma$ mass publication [15]. With respect to the previous calibration, the new precision recommendations reduce the energy scaled impact per category by a factor of 2, while the constraint induced by the linearity fit reduces the impact by another factor of 2, with a larger reduction observed for "high" p_{Tt} categories. The observed mass measurement with and without the linearity constraints are expected to be different not only for the precision level, but also for the central value for the mass, as new additional energy scales are included in the calibration procedure. The additional energy scale will be applied to data, therefore no difference in the central value is propagated to the expected results, but only on the observed. However, it is important to understand what the shift might be on m_H with and without linearity correction, to check that the two measurement result in two compatible values of the mass.

As a first test, the expected shift of the $m_{\gamma\gamma}$ peak induced by the additional energy scale due to the linearity correction was computed in each category. The additional energy correction $E'_{\text{MC}} = (1+\hat{\alpha}')E_{\text{MC}}$[5] is applied to each selected photon in the signal MC, to obtain the corrected $m'_{\gamma\gamma}$ values. In each category the expected shift of the average value $m_{\gamma\gamma}$ (which is a proxy for the signal peak) is smaller than the $\pm 1\sigma$ uncertainty variations coming from the energy scales systematics evaluated before including the linearity constraint. In every category we can expect a compatible value of m_H before and after the linearity constraint.

As second test, in order to evaluate the expected total shift on m_H, the likelihood which

[5] The standard calibration procedure requires that the energy scale is applied to data as: $E'_{data} = E_{data}/(1+\hat{\alpha}')$

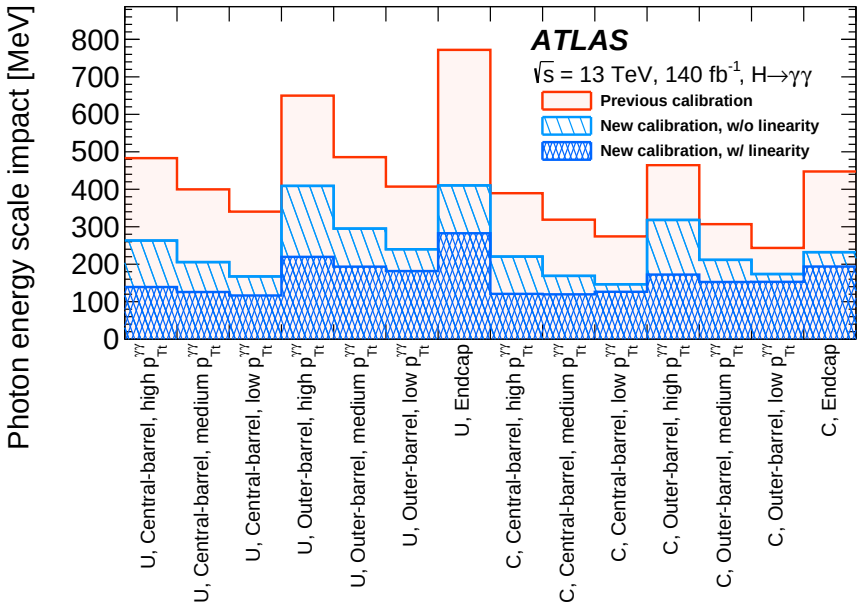

Figure 7.16 – Total systematic uncertainty in the Higgs boson mass from the photon energy scale calibration using the analysis strategy of this analysis [14] and, respectively, the previous calibration model [151] (light red histogram) or the new calibration model [17] with (light-blue hatched histogram) or without (dark-blue hatched histogram) the linearity fit to constrain the E_{T}-dependence of the energy scale corrections.

includes the multivariate linearity constraints and correlation (as in Eq. 7.24) is modified to account also for the additional energy scale, by shifting the global observables from zero to the observed pulls $\hat{\theta}_k$ in the linearity fit[6], see Equation (6.13). The modified likelihood is then fitted on an Asimov dataset generated from the likelihood with global observables and pulls equal to zero (*i.e.* un-shifted) and with an expected value of $m_H = 125$ GeV. The fit returns a best-fit value of $m_H = 125.085$ GeV. The corresponding shift of 85 MeV away from the Asimov dataset hypothesis 125 GeV is significantly smaller than the inclusive 1σ systematic uncertainty expected for the m_H measurement without linearity correction, equal to 180 MeV.

Once the linearity fit constraint is included in the likelihood, the total systematic uncertainty is decomposed in different groups in order to provide meaningful comparisons with the previous case without linearity fit. In particular, in Table 7.25, the "E_{T} dependent electron energy scale" group is composed by all uncertainties constrained by the linearity fit, such as the LAr Cell non-linearity, the Layer Calibration, Other Material (not ID), ID Material groups plus the EG_SCALE_WTOTS and EG_SCALE_LEAKAGEELEC nuisance parameters. The two latter NPs are therefore removed from the "Lateral shower

[6]When the energy scale correction (from linearity) are applied to data the global observables are fixed to zero because we assume no additional scale. Setting the global observables of each NP to the corresponding $\hat{\theta}$ results in a shift on the signal model of the same magnitude but in the opposite direction with respect to the one would be applied to data: energy in data is corrected for $(1 - \hat{\alpha}')$ while MC is corrected for $(1 + \hat{\alpha}')$.

shape" group. The change in impact for NPs groups not affected by the linearity fit is due to the different weight that each reconstructed category has in the fit: in fact, with the linearity fit applied, the "high" p_{Tt} categories present a reduced energy scale systematic uncertainty therefore they become more important in the likelihood fit; on the other hand, for example, these categories are less affected by the interference and background biases, therefore the total impacts from these groups decrease as well.

Systematic group	Impact on m_H [MeV] Without Linearity	With Linearity
E_{T} dependent electron energy scale	163	43
$Z \to ee$ calibration	61	60
Interference bias	34	24
Lateral shower shape	31	30
Conversion reconstruction	30	23
Background model bias	28	18
Vertex bias	5	5
Signal model bias	4	5
Resolution	3	3
Spurious Signal	3	3
Yield	0	0
Theory	0	0
Luminosity	0	0

Table 7.25 – Systematic decomposition on the Asimov dataset.

7.8.3 Observed results

The $m_{\gamma\gamma}$ distribution of the data, overlaid with the sum of the signal and background models corresponding to the maximum-likelihood estimates of the parameters of the likelihood function, is shown in Figure 7.17. All event categories are included. For illustration purposes, events in each category are weighted by a factor $\ln(1 + S_{90}^{\mathrm{obs}}/B_{90}^{\mathrm{obs}})$, where S_{90}^{obs} and B_{90}^{obs} are the fitted signal and background yields in the smallest $m_{\gamma\gamma}$ interval containing 90% of the signal. Figures 7.18 to 7.20 show the $m_{\gamma\gamma}$ data distributions for each of the 14 categories separately with the corresponding fitted signal-plus-background models.
The profile likelihood ratio as a function of m_H is shown in Figure 7.21. The value of the Higgs boson mass determined by fitting the profile likelihood ratio in Equation (7.19) to the diphoton invariant mass distribution in data is:

$$m_H = 125.17 \pm 0.11\ (\mathrm{stat.}) \pm 0.09\ (\mathrm{syst.})\ \mathrm{GeV} = 125.17 \pm 0.14\ \mathrm{GeV}. \tag{7.26}$$

The statistical and systematic uncertainties are in good agreement with the values of 120 MeV and 90 MeV expected for a SM Higgs boson with the observed mass. The main sources of systematic uncertainty and their impact on the measurement are summarised in Table 7.26 and well agree with their expectations reported in Table 7.25.

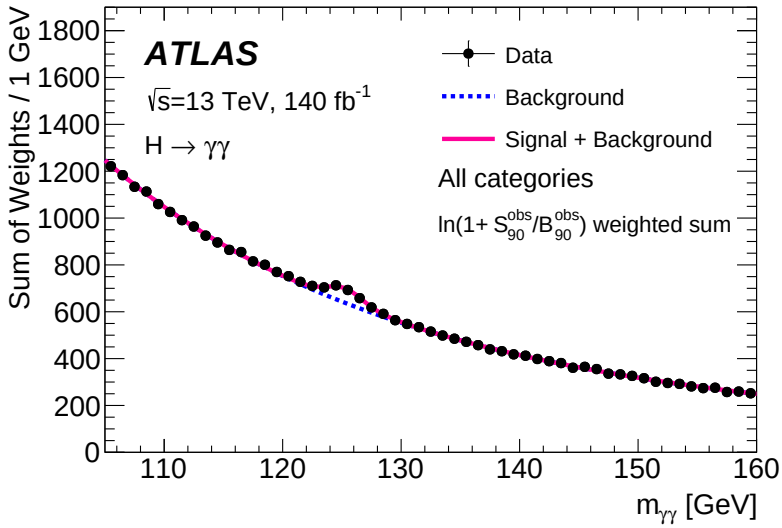

Figure 7.17 – Diphoton invariant mass distribution of all selected data events (black dots with error bars), overlaid with the result of the fit (solid red line). For both the data and the fit, each category is weighted by a factor $\ln(1 + S_{90}^{\text{obs}}/B_{90}^{\text{obs}})$, where S_{90}^{obs} and B_{90}^{obs} are the fitted signal and background yields in the smallest $m_{\gamma\gamma}$ interval containing 90% of the expected signal. The dotted line describes the background component of the model [14].

Source	Impact [MeV]
Photon energy scale	83
$Z \to e^+e^-$ calibration	59
E_{T}-dependent electron energy scale	44
$e^{\pm} \to \gamma$ extrapolation	30
Conversion modelling	24
Signal–background interference	26
Energy resolution	15
Background model	14
Diphoton vertex selection	5
Signal model	1
Total	90

Table 7.26 – Impact of the main sources of systematic uncertainties on the Higgs boson mass measurement.

The signal strength μ_c in each category c is compatible with the SM prediction $\mu_c = 1$, with the largest difference being 2.2 standard deviations (σ) for the Conv, Central-barrel, medium-p_{Tt} category. The measured signal strengths for each category are reported in Figure 7.22. The global significance of this difference, taking into account a trial factor of 14, is less than 1σ. The best-fit m_H values for the individual categories are in good agreement with each other, with a global p-value of 8%.

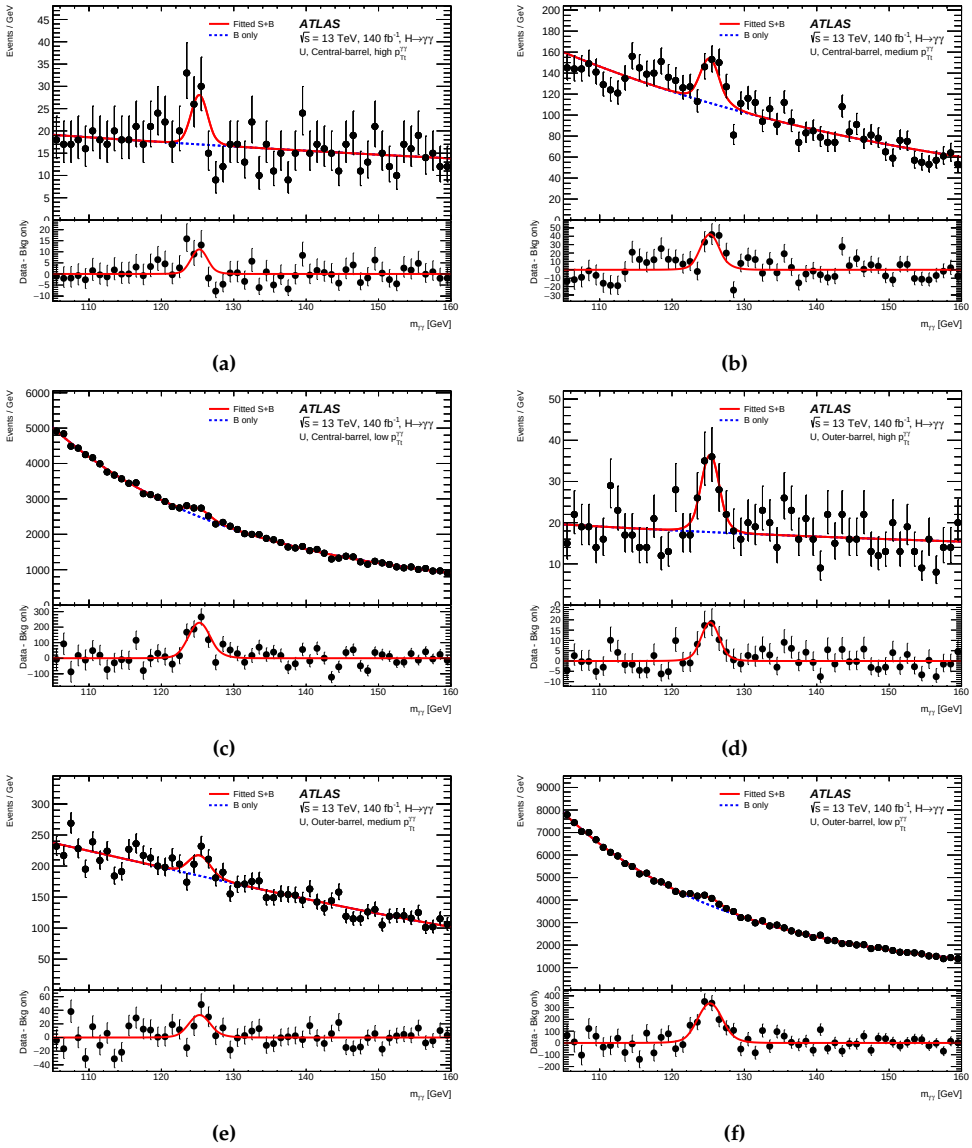

Figure 7.18 – Projections of the final fit to the diphoton invariant mass distribution in each category: the diphoton invariant mass distribution of all selected data events (black dots with error bars), overlaid with the result of the fit (solid red line) for the categories UU, Central-barrel, high p_{Tt} (a), medium p_{Tt} (b), low p_{Tt} (c), UU, Outer-barrel, high p_{Tt} (d), medium p_{Tt} (e), low p_{Tt} (f). The dotted line describes the background component of the model. In addition, the lower panels show the residuals between the data and the fitted background-only model [14].

If the same signal strength μ is used for each category, the central value of m_H is shifted by -35 MeV, and the fitted value of μ is in agreement with the SM prediction within 1.4 standard deviations. If the signal $m_{\gamma\gamma}$ model is modified to account for the expected

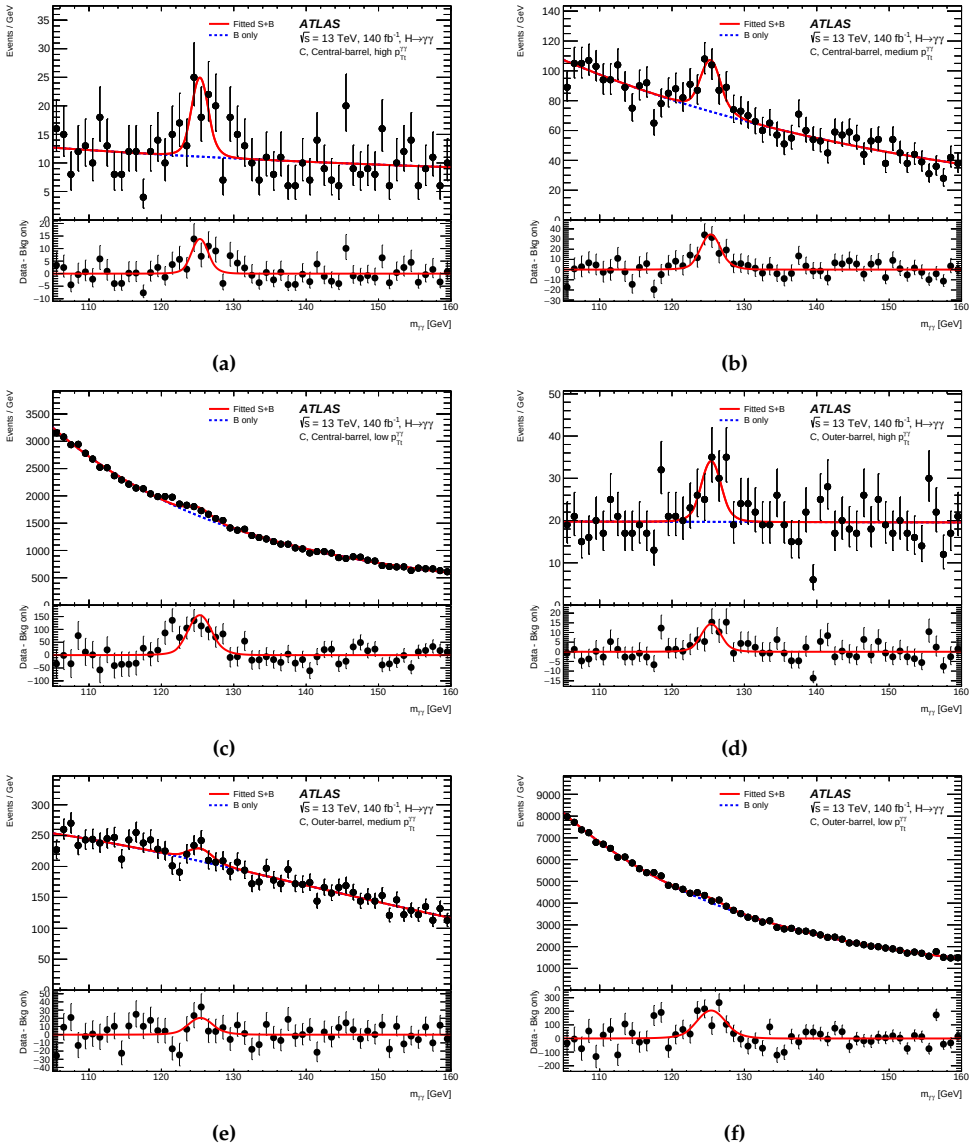

Figure 7.19 – Projections of the final fit to the diphoton invariant mass distribution in each category: the diphoton invariant mass distribution of all selected data events (black dots with error bars), overlaid with the result of the fit (solid red line) for the categories Conv, Central-barrel, high p_{Tt} (a), medium p_{Tt} (b), low p_{Tt} (c), Conv, Outer-barrel, high p_{Tt} (d), medium p_{Tt} (e), low p_{Tt} (f). The dotted line describes the background component of the model. In addition, the lower panels show the residuals between the data and the fitted background-only model [14].

shift induced by interference with non-resonant background diphoton production, the measured value of the Higgs boson mass is increased by approximately 26 MeV.

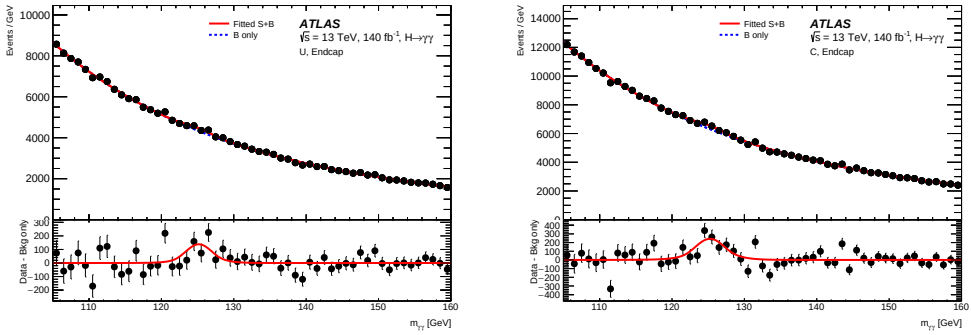

(a) (b)

Figure 7.20 – Projections of the final fit to the diphoton invariant mass distribution in each category: the diphoton invariant mass distribution of all selected data events (black dots with error bars), overlaid with the result of the fit (solid red line) for the categories UU Endcap (a), Conv Endcap (b). The dotted line describes the background component of the model. In addition, the lower panels show the residuals between the data and the fitted background-only model [14].

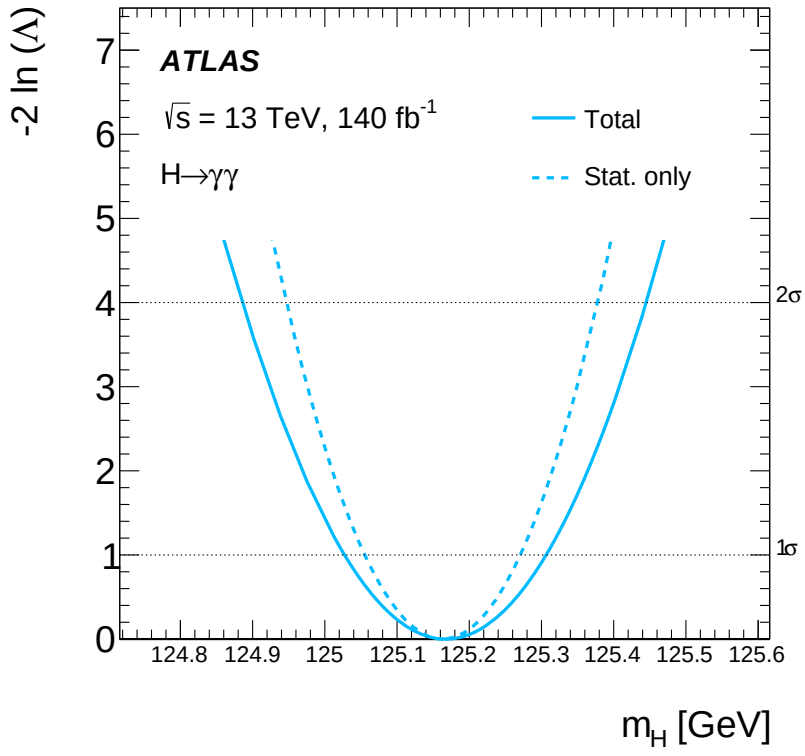

Figure 7.21 – Value of $-2\ln\Lambda$ as a function of m_H for the combined fit to all $H \to \gamma\gamma$ categories. The intersections of the $-2\ln\Lambda$ curve with the horizontal lines labelled 1σ and 2σ provide the 68.3% and 95.5% confidence intervals [14].

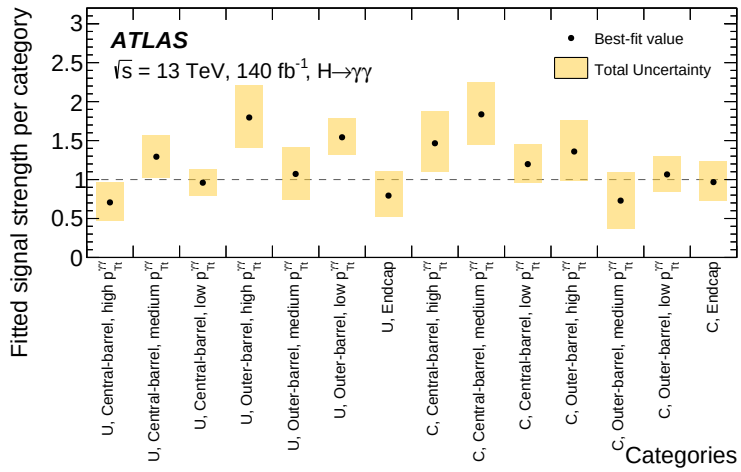

Figure 7.22 – Best-fit values of the signal strength μ for each reconstructed category, with their total uncertainties. The dashed line indicates the SM prediction $\mu = 1$ [14].

7.8.4 Cross-checks

In order to assess the robustness of the mass measurement and to probe potential biases in the photon energy calibration, the analysis is repeated using four additional, mostly detector-oriented, categorisation schemes:

- **Category-by-category mass compatibility.** Instead of extracting a single common value of m_H, the fit is repeated allowing an independent Higgs boson mass parameter in each category. For a given category i, the mass is parametrised as

  $$m_H^i = \hat{\hat{m}}_H + \Delta m_H^i,$$

  where $\hat{\hat{m}}_H$ is the global best-fit Higgs boson mass and Δm_H^i represents the deviation of category i from the global value. The compatibility of the set of Δm_H^i values with zero is then evaluated using the asymptotic χ^2 distribution with $N_{\text{cat}} - 1$ degrees of freedom.

- **Compatibility across detector-oriented category groups.** A similar study is performed by grouping categories according to detector-related properties and assigning a common mass shift Δm_H to each group:

  - *Photon conversion status*: one common Δm_H is assigned to all "UU" categories and one to all "Conv" categories, to test for possible biases between the calibrations of unconverted and converted photons;
  - *Photon pseudorapidity*: three independent Δm_H parameters are assigned to the "Central-barrel", "Outer-barrel", and "Endcap" categories, respectively, to probe potential η-dependent calibration biases;
  - *Photon transverse momentum*: three independent Δm_H parameters are assigned to the "high", "medium", and "low" $p_{\text{Tt}}^{\gamma\gamma}$ categories, respectively, to test for possible energy-dependent calibration biases.

For all the above cases, the null hypothesis to be excluded is "m_H is the same in all the categories". This can be checked assuming as alternative one of two kind of hypotheses, i.e.,"only m_H in category i is different" or "the values of m_H in all the categories are different". The test based on the second alternative hypothesis is less powerful, but more general. The test is done implementing a workspace where the value of the mass of the Higgs boson is $m_H + \Delta m_H^i$, where i is the index of the categories or a group of categories, depending on the test. Under the first alternative hypothesis, the following likelihood ratio test is used for the first category:

$$q_0^{(1)} = -2 \log \frac{L\left(\Delta_1 = 0, \Delta_2 = 0, \ldots, \Delta_n = 0, \hat{\hat{m}}_H\right)}{L\left(\hat{\Delta}_1, \Delta_2 = 0, \ldots, \Delta_n = 0, \hat{m}_H\right)}.$$

All other parameters, including m_H, the 14 signal strengths and all the pulls are profiled. The asymptotic approximation is assumed, so $q_0^{(1)}$ is assumed to be distributed as χ^2

with 1 degree of freedom. For the second kind of alternative hypothesis the statistic

$$q_0^{(1)} = -2 \log \frac{L\left(\Delta_1 = 0, \Delta_2 = 0, \ldots, \Delta_n = 0, \hat{\hat{m}}_H\right)}{L\left(\hat{\Delta}_1, \hat{\Delta}_2, \ldots, \hat{\Delta}_n, \hat{m}_H\right)}$$

is used and it is assumed to be distributed as a χ^2 with $n-1$ degrees of freedom. In the special case where the number n is equal to the number of categories, the m_H value is fixed to the best fit value of Equation (7.26) in order to have a non-degenerate fit.
The best-fit values and uncertainties of the differences Δm_H^i are shown in Figure 7.23a for the different categories and in Figure 7.23b for the detector oriented groups of categories.

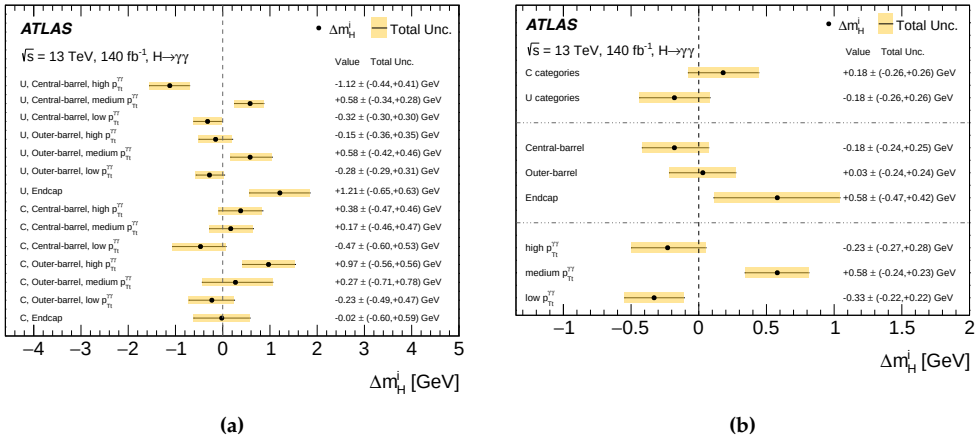

Figure 7.23 – Best-fit values and uncertainties of the differences Δm_H^i between the mass measured in the analysis category i with respect to the mass measured simultaneously (under the first alternative hypothesis) in all other analysis categories. For this measurement, the mass in the analysis category under test is parametrised as $m_H^i = \hat{\hat{m}}_H + \Delta m_H^i$. The results are obtained from the scan of the modified profile likelihood ratio as a function of Δm_H^i. (a) Results for each of the 14 analysis categories. (b) Results for groups of categories defined according to detector-related properties: photon conversion status ("UU" and "Conv"), photon pseudorapidity ("Central-barrel", "Outer-barrel", and "Endcap"), and photon transverse momentum ("high", "medium", and "low" $p_{\mathrm{Tt}}^{\gamma\gamma}$ categories) [14].

The global p-value under the first alternative hypothesis for the compatibility of the 14 individual categories is 8%. The p-value for the conversion based categorization is 48%, the one for the barrel/endcap categorization is 43% and the one for the high/medium/low p_{Tt} is 6%. All the results indicate good compatibility among the categories, with no significant sign of potential biases in the photon energy calibration.

7.9 Combination with Run 1 measurement

To improve on the precision of the mass measurement in the $\gamma\gamma$ channel, the presented measurement is combined with the previous one, obtained by ATLAS in the diphoton

channel using 25 fb^{-1} of proton-proton collisions recorded at $\sqrt{s}$ = 7 and 8 TeV during Run 1 of the LHC in 2011-2012 [13], $m_H = 126.02 \pm 0.43(\text{stat.}) \pm 0.27(\text{syst.})$GeV.
The Run 1 $H \to \gamma\gamma$ workspace was re-created and the Run 1 expected and observed results obtained in the ATLAS and CMS Run 1 combination [13] were reproduced. The expected results are obtained fitting an Asimov dataset built with $m_H = 125$ GeV, while the observed results are obtained fitting the Run 1 dataset. The results are obtained fitting simultaneously m_H and two signal strengths, one for the coupling to fermions and one to vector bosons: μ_F and μ_V. The results are reported in Table 7.27: the total and statistical uncertainties are obtained from a profile likelihood ratio Λ scan.

	Expected [GeV]				Observed [GeV]			
Workspace	Fitted m_H	Total Unc.	Stat. Unc.	Syst. Unc.	Fitted m_H	Total Unc.	Stat. Unc.	Syst. Unc.
Run 1 $H \to \gamma\gamma$	125.00	$\pm$ 0.52	$\pm$ 0.44	$\pm$ 0.27	126.02	$\pm$ 0.51	$\pm$ 0.43	$\pm$ 0.27

Table 7.27 – Expected and observed Run 1 $H \to \gamma\gamma$ results.

The combination of ATLAS Run 1 and Run 2 results is performed by simultaneously fitting a single m_H parameter to the two datasets. The nominal model including the 14 signal strengths μ_c of the reconstructed categories is used for the Run 2 dataset, while two separate signal strengths, one each for production processes involving Higgs boson couplings to either fermions or vector bosons, are used for the Run 1 dataset. All 16 signal-strength parameters are profiled in the combined fit for m_H.
Almost all the nuisance parameters, especially the E_{T}-dependent photon energy scale parameters affected by the linearity measurement and the parameters describing the extrapolation of the energy scale from electrons to photons, are assumed to be uncorrelated between the two measurements because of differences in the reconstruction algorithms and in the calibration procedures and control samples. The $Z \to e^+e^-$ scale uncertainties and some of the resolution uncertainties, estimated in the same way for the two measurements, are treated as being fully correlated between the two data-taking periods. The combination with the Run 1 ATLAS measurement in the diphoton channel produces a small shift (+50 MeV) of the central value and a slight reduction (<10 MeV) of the statistical uncertainty, leading to:

$$m_H = 125.22 \pm 0.11\ (\text{stat.}) \pm 0.09\ (\text{syst.})\,\text{GeV} = 125.22 \pm 0.14\,\text{GeV}. \tag{7.27}$$

The individual profile likelihood ratios as a function of m_H of the ATLAS Run 1 and Run 2 measurements in the diphoton channel and their combination are shown in Figure 7.24a; all the results are summarised in Figure 7.24b together with the ATLAS+ CMS Run 1 measurement [13] using $H \to \gamma\gamma$ and $H \to 4\ell$ decays.

7.10 Conclusions

The Run 2 $H \to \gamma\gamma$ result represents a significant improvement over the previous ATLAS measurement in this channel. This gain is driven both by the use of the full LHC Run 2 dataset—which reduces the statistical uncertainty by approximately a factor

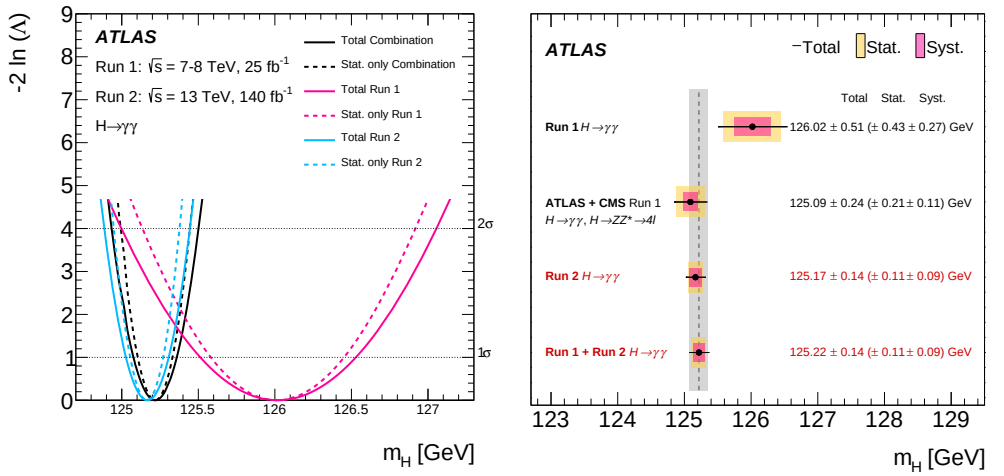

Figure 7.24 – (a) Value of $-2\ln\Lambda$ as a function of m_H for the Run 1 (magenta) and Run 2 (cyan) data and their combination (black), taking into account all uncertainties (solid lines) or only the statistical component (dashed lines). The intersections of the $-2\ln\Lambda$ curve with the horizontal lines labelled 1σ and 2σ provide the 68.3% and 95.5% confidence intervals [14]. (b) Summary of the Higgs boson mass measurements from the analysis of $H \to \gamma\gamma$ decays in ATLAS Run 2 data and combined Run 1 + Run 2 data presented in the [14] paper, compared with the combined Run 1 ATLAS result in the diphoton channel and with the Run 1 measurement by ATLAS and CMS [13] combining the diphoton and four-lepton channels. The statistical, systematic and total uncertainties are indicated with horizontal yellow-shaded bands, pink-shaded bands and black error bars, respectively. The vertical dashed line and grey shaded band around it indicate the central value and total uncertainty of the $H \to \gamma\gamma$ ATLAS Run 1 + Run 2 measurement.

of two—and by substantial improvements in the calibration of the photon energy response, which lower the systematic uncertainty by nearly a factor of four with respect to the earlier publication based on 36 fb^{-1} of Run 2 data [15]. After the inclusion of the linearity corrections, the precision of the Higgs boson mass measurement in the diphoton channel is primarily limited by the statistical uncertainty.

The Higgs boson mass measured in the $H \to \gamma\gamma$ decay channel, using pp collision data recorded by the ATLAS detector during the full Run 2 data-taking period at a centre-of-mass energy of $\sqrt{s} = 13$ TeV, corresponding to a total integrated luminosity of 140 fb^{-1}, is:

$$m_H = 125.17 \pm 0.11\ (\text{stat.}) \pm 0.09\ (\text{syst.})\ \text{GeV} = 125.17 \pm 0.14\ \text{GeV}. \tag{7.28}$$

The combination with the Run 1 ATLAS measurement in the diphoton channel (25 fb^{-1} of proton-proton collisions data recorded at $\sqrt{s} = 7$ and 8 TeV) produces a small shift (+50 MeV) of the central value and a slight reduction (<10 MeV) of the statistical uncertainty, leading to:

$$m_H = 125.22 \pm 0.11\ (\text{stat.}) \pm 0.09\ (\text{syst.})\ \text{GeV} = 125.22 \pm 0.14\ \text{GeV}. \tag{7.29}$$

8 | Combined measurement of the Higgs mass from $H \to ZZ^* \to 4\ell$ and $H \to \gamma\gamma$ channels

This Chapter presents the measurement of the Higgs boson mass combining the results from the $H \to ZZ^* \to 4\ell$ [18] and $H \to \gamma\gamma$ [14] decay channels. The result [19] is based on 140 fb^{-1} of pp collision data collected by the ATLAS detector during the LHC Run 2 data-taking period at a centre-of-mass energy of $\sqrt{s} = 13$ TeV, then combined with the previous ATLAS measurement using Run 1 data at centre-of-mass energies of $\sqrt{s} = 7$ and 8 TeV. The full Run 2 combined measurement updates and supersedes that based on the same final states and a partial Run 2 dataset corresponding to an integrated luminosity of 36.1 fb^{-1} [15]. It profits from the increased dataset, and from significantly improved calibrations of the electron and photon energy (Chapter 6) and of the muon momentum (Section 5.2.1).

8.1 The $H \to ZZ^* \to 4\ell$ decay channel

As mentioned in Section 4.4, the $H \to ZZ^* \to 4\ell$ decay channel is one of the two golden channels for the Higgs boson mass measurement due to its excellent mass resolution, which produce a clear peak above a continuum background. The Run 2 mass measurement in this channel is fully described in Ref. [18] and will be briefly described in this Section.

The $H \to ZZ^* \to 4\ell$ decay is reconstructed by requiring two pairs of same-flavour opposite-sign isolated leptons ($\ell = e, \mu$) in the final state. The pair with the invariant mass closer to that of the Z boson mass is defined as the leading dilepton pair, while the remaining one is referred to as the subleading dilepton pair. The selected quadruplets are separated into four sub-channels according to the flavour of the leading and subleading dilepton pairs (4μ, $2e2\mu$, $2\mu2e$, $4e$).

A Neural Network (NN)-based classifier is employed to discriminate between the Higgs boson signal and the dominant $ZZ^* \to 4\ell$ background. The m_H measurement is performed with a simultaneous unbinned maximum likelihood fit of the reconstructed invariant mass of the four leptons system, m_{4l}, in the four sub-channels.

The event-level m_{4l} resolution, σ_i, is estimated using a Quantile Regression Neural Network (QRNN), with inputs the p_{T}, η and ϕ of the individual leptons as well as the four-lepton momentum, constrained by the Z-boson mass constraint, and its uncertainty. The

output of the QRNN for each final state is the predicted quantile of the difference between the reconstructed mass and the true mass of the four-lepton system. The m_{4l} resolution ranges from about 1.5 GeV (4μ and $2e2\mu$ sub-channels) to about 2.1 GeV ($2\mu2e$ and $4e$ sub-channels).
The signal model consists of a Double-Sided Crystal Ball (DSCB) probability density function, with the mean of its Gaussian core parameterized as a function of m_H and the standard deviation expressed as a function of the predicted event-level resolution. The signal and background normalization for each of the four sub-channels are free parameters in the fit. The m_{4l} distribution is shown in Figure 8.2a for the inclusive final state for the mass range of 105-160 GeV; the signal-plus-background fit on the inclusive data distribution from all sub-channels combined is shown in Figure 8.2b.
The measured mass of the Higgs boson in the $H \to ZZ^* \to 4\ell$ final state using the full Run 2 dataset is [18]

$$m_H = 124.99 \pm 0.18\,(\text{stat.}) \pm 0.04\,(\text{syst.})\ \text{GeV} = 124.99 \pm 0.19\ \text{GeV}. \tag{8.1}$$

The dominant sources of systematic uncertainty on the measurement are the uncertainties in the muon momentum scale, resolution and sagitta bias correction (28 MeV) and the electron energy scale (19 MeV). With respect to the di-photon channel, the measurement of m_H in the four lepton channel is characterized by a smaller systematic uncertainty, due to the smaller calibration uncertainties for muons compared to electrons and photons. The profile likelihood ratios as a function of m_H for each channel (4μ, $2e2\mu$, $2\mu2e$, $4e$) and for their combination, giving the result of Equation (8.1), are shown in Figure 8.1.
A combination with the measurement of m_H using the Run 1 dataset [13], $m_H = 124.51 \pm 0.52(\text{stat.}) \pm 0.04(\text{syst.}) = 124.51 \pm 0.52$ GeV has been performed. In this combination, only the uncertainties on the electron calibration were considered correlated, while the muon calibration systematic uncertainty is uncorrelated between the two measurements due to improved and independent techniques in the muon momentum scale calibration. The combined measurement of m_H performed with Run 1 and Run 2 datasets in the $H \to ZZ^* \to 4\ell$ channel is

$$m_H = 124.94 \pm 0.17\,(\text{stat.}) \pm 0.03\,(\text{syst.})\ \text{GeV} = 124.94 \pm 0.18\ \text{GeV}. \tag{8.2}$$

8.2 Combination

As for the Run 2 $H \to \gamma\gamma$ mass measurement described in Chapter 7, the combination is performed using a profile likelihood ratio [172], defined as in Equation (7.19). Systematic uncertainties are modelled by constrained NP, while the signal and background normalizations in the various channels entering the fit are treated as free parameters. The confidence intervals are obtained assuming the asymptotic distribution of the $2\ln\Lambda(m_H)$ test statistic. The statistical uncertainty on m_H is estimated by fixing all the NPs that are associated with systematic uncertainties to their best-fit values and leaving all the remaining parameters unconstrained. The total systematic uncertainty, whose squared

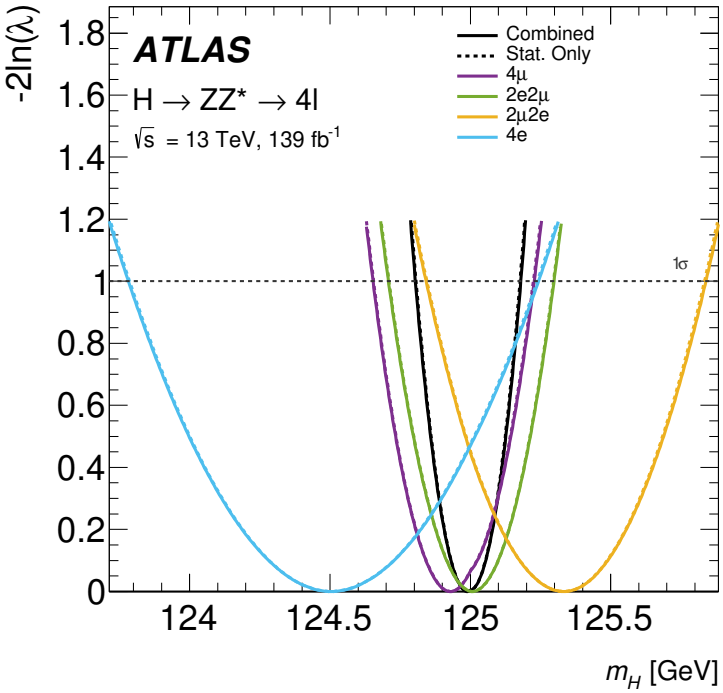

Figure 8.1 – Values of the test statistic $-2\ln(\lambda)$ as a function of m_H for the fit in each of the final states 4μ (purple), $2e2\mu$ (green), $2\mu2e$ (orange), and $4e$ (blue), and for the combined fit (black), both with (solid lines) and without (dashed lines) systematic uncertainties. The horizontal dashed line indicates the location of the 1σ uncertainty [18].

value is evaluated as the difference between the squares of the total uncertainty and the statistical uncertainty, can be decomposed into categories representing distinct sources of uncertainty by setting all relevant subsets of NP to their best-fit values.

8.2.1 Systematics correlation scheme

In the combination, the correlations between systematic uncertainties in the two measurements are accounted for in the profile likelihood function by using the same constraint for each of the correlated NP. Due to substantial variations in the calibration of electrons, photons, and muons, most correlations are small. The choice of correlation model between the Run 2 $H \to \gamma\gamma$ and $H \to ZZ^* \to 4\ell$ measurements reflects the improvements in the photon calibration adopted by the $H \to \gamma\gamma$ analysis described in Section 6.5.4 not being mirrored in the calibration of the electrons used in the $H \to ZZ^* \to 4\ell$ analysis; only the electron and photon resolution systematic uncertainties and those associated with the E_{T}-independent component of the electron and photon in-situ energy scale are considered as correlated.
Other sources of systematic uncertainty considered as correlated between the two measurements are: theoretical uncertainties on the prediction of the various Higgs produc-

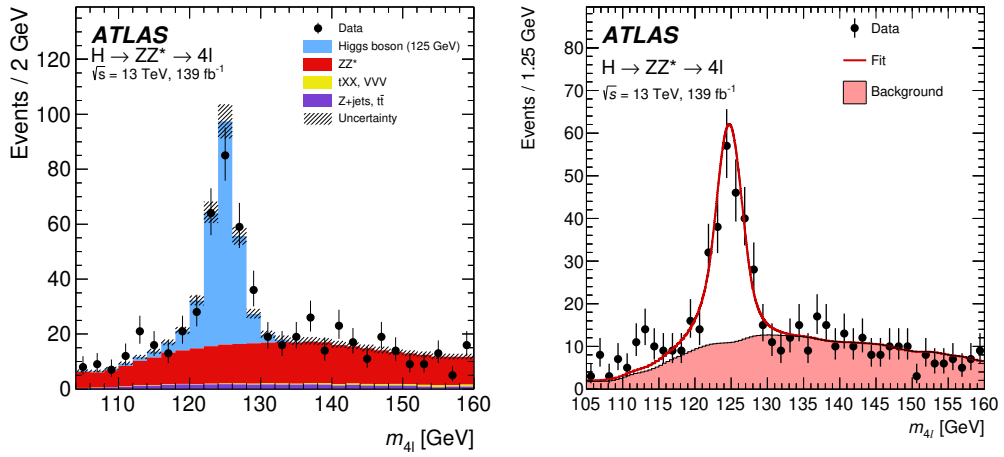

(a) (b)

Figure 8.2 – (a) The observed and expected (pre-fit) m_{4l} distributions for the selected Higgs boson candidates. The predicted number of events for these distributions is taken from simulation for the signal, ZZ^*, tXX, and VVV processes, while it is taken from the data-driven estimate for the Z+jets and $t\bar{t}$ backgrounds. The total uncertainty in the prediction is shown by the hatched band, which also includes the theoretical uncertainties of the SM cross-section for the signal and the ZZ^* background. Higgs boson events in this plot are simulated with $m_H = 125$ GeV. (b) The m_{4l} data distribution from all sub-channels combined (black points) is shown along with the signal-plus-background post-fit probability density function (red line) [18].

tion modes, uncertainties on the modelling of additional pileup pp collisions and uncertainties on the integrated luminosity.

8.2.2 Combination results

The combined measurement of the Higgs boson mass using the $H \to ZZ^* \to 4\ell$ and $H \to \gamma\gamma$ decay channels with the full Run 2 dataset collected by ATLAS at a centre-of-mass energy of $\sqrt{s} = 13$ TeV is [19]

$$m_H = 125.10 \pm 0.09\,(\text{stat.}) \pm 0.07\,(\text{syst.})\ \text{GeV} = 125.10 \pm 0.11\ \text{GeV}. \tag{8.3}$$

The corresponding profile likelihood, for the two channels and for their combination, is shown in Figure 8.3a as a function of m_H. If the small interference predicted by the SM between the Higgs boson and the non-resonant diphoton background was considered for the $H \to \gamma\gamma$ signal parameterization, the m_H value measured by the combination would increase by 15 MeV. This result is in good agreement with the ATLAS + CMS Run 1 measurement [13], $m_H = 125.09 \pm 0.24$ GeV.

The contributions of the main sources of systematic uncertainty to the combined measurement, using ATLAS Run 2 data, are summarised in Table 8.1. The values differ from those reported in Refs. [18] and [14] because of the relative impact of the $H \to \gamma\gamma$

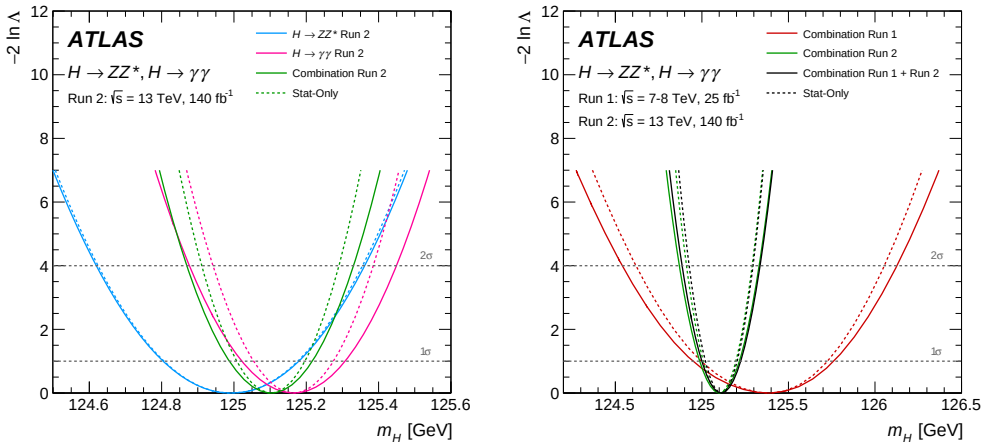

(a) **(b)**

Figure 8.3 – Value of $-2\ln\Lambda$ as a function of m_H for (a) $H \to \gamma\gamma$, $H \to ZZ^* \to 4\ell$ channels and their combination (magenta, cyan and green, respectively) using Run 2 data only and for (b) Run 1, Run 2 and their combination (red, green and black, respectively). The dashed lines show the statistical component of the uncertainty. The 1σ (2σ) confidence interval is indicated by the intersections of the horizontal line at 1 (4) with the log-likelihood curves [19].

and $H \to ZZ^* \to 4\ell$ results in the combination. The E_{T}-independent component of the electron and photon in-situ energy scale ("e/γ E_{T}-independent $Z \to ee$ calibration" in Table 8.1) is among the few uncertainties correlated between the $H \to \gamma\gamma$ and $H \to ZZ^* \to 4\ell$ measurements, and impacts the former measurement by 59 MeV [14] (see Table 7.26), and the latter by 19 MeV [18].

Source	Systematic uncertainty on m_H [MeV]
e/γ E_T-independent $Z \to ee$ calibration	44
e/γ E_T-dependent electron energy scale	28
$H \to \gamma\gamma$ interference bias	17
e/γ photon lateral shower shape	16
e/γ photon conversion reconstruction	15
e/γ energy resolution	11
$H \to \gamma\gamma$ background modelling	10
Muon momentum scale	8
All other systematic uncertainties	7

Table 8.1 – Impact of the main sources of systematic uncertainty on the m_H measurement from the combination of the $H \to ZZ^* \to 4\ell$ and $H \to \gamma\gamma$ final states using Run 2 data. The systematic uncertainties associated with the combination of Run 1 and Run 2 data are nearly identical. The sum in quadrature of the individual contributions is not expected to reproduce the total systematic uncertainty due to the different methodologies employed to derive them.

The combination of the Run 2 result with the previous ATLAS measurement using Run 1

data at centre-of-mass energies of $\sqrt{s} = 7$ and 8 TeV [13] yields the final ATLAS measurement of the Higgs boson mass:

$$m_H = 125.11 \pm 0.09\,(\text{stat.}) \pm 0.06\,(\text{syst.})\ \text{GeV} = 125.11 \pm 0.11\ \text{GeV}. \tag{8.4}$$

Figure 8.3b shows the corresponding profile likelihoods, separately for the ATLAS Run 1 and Run 2 datasets, as well as for their combination, as a function of m_H. The four combined measurements are compatible with a p-value of 18%.
Figure 8.4 presents a summary of the all the ATLAS m_H measurements from the individual $H \to \gamma\gamma$ and $H \to ZZ^* \to 4\ell$ channels and their Run 1 and Run 2 combinations.

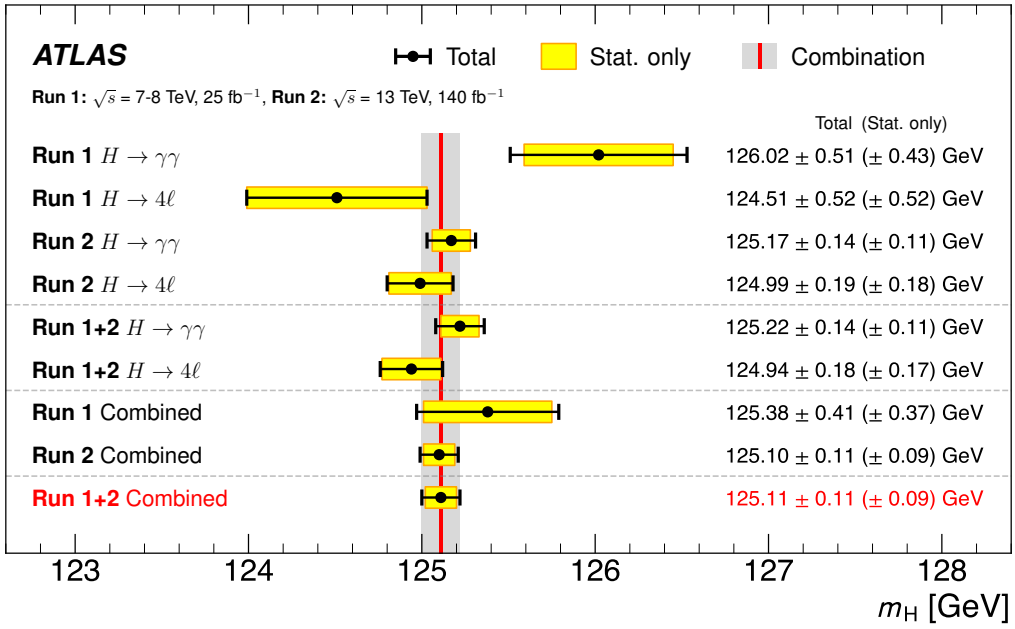

Figure 8.4 – Summary of m_H measurements from the individual $H \to \gamma\gamma$ and $H \to ZZ^* \to 4\ell$ channels and their combination presented in this Chapter. The uncertainty bar on each point corresponds to the total uncertainty; the horizontal shaded bands represent the statistical component of the uncertainties; the vertical red line and gray band represent the combined result with its total uncertainty [19].

The combined Run 1 and Run 2 ATLAS Higgs boson mass measurement in the $H \to \gamma\gamma$ and $H \to ZZ^* \to 4\ell$ decay channels, reported in Equation (8.4), achieves a precision of 0.09% on this fundamental parameter of the SM of particle physics. At present, this result represents the most precise determination of the Higgs boson mass.

9 Search for the Higgs boson decaying to a low-mass dilepton pair and a photon in Run 3

Note for the referees. This Chapter is based on an ongoing ATLAS analysis. As such, some details may be subject to change before the final publication. However, the overall analysis strategy and the expected results presented here are not expected to change significantly.

As discussed in Chapter 4, the Higgs boson exhibits a rich phenomenology. A number of rare Higgs boson decay modes are predicted by the SM but have not yet been observed, owing to their small branching ratios and the presence of large backgrounds. Among these, the $H \to \mu\mu$ decay provides the most direct probe of the Higgs boson Yukawa coupling to second-generation fermions, while the $H \to Z\gamma$ decay is sensitive to potential BSM effects, as the SM contribution to this process is loop-induced.

The ATLAS Collaboration has recently published improved analyses of both decay channels, based on the large partial Run 3 dataset collected between 2022 and 2024 and on their combination with Run 2 results [21]. For the $H \to \mu\mu$ decay [22], an excess of events over the background is observed with a significance of 3.4σ (2.5σ expected), providing evidence for this decay mode. For the $H \to Z\gamma$ decay [23], the analysis yields an observed (expected) significance of 2.5σ (1.9σ). In the previous round of Run 2 analyses, the ATLAS and CMS Collaborations combined their results and reported the first evidence for the Higgs boson decay into a Z boson and a photon, with a statistical significance of 3.4σ [24].

In this context, this Chapter presents the Run 3 search for the rare SM Higgs boson decay into a photon (γ) and an off-shell photon (γ^*), $H \to \gamma\gamma^*$, where the γ^* internally converts into a dilepton pair, $\gamma^* \to \ell\ell$ ($\ell = e, \mu$). Several processes lead to the same $\ell\ell\gamma$ final state, including Dalitz decays involving a Z boson or a virtual photon γ^* (see the Feynman diagrams in Figure 9.1(a–c)), as well as Higgs boson decays into two leptons accompanied by a photon radiated via FSR (Figure 9.1(d)).

Such $\ell\ell\gamma$ final states provide sensitivity to modifications of the Higgs boson couplings induced by possible extensions of the SM [25]. In addition, three-body Higgs boson decays offer a unique probe of CP-violation in the Higgs sector through the study of angular and kinematic observables, such as the forward–backward asymmetry [26, 27].

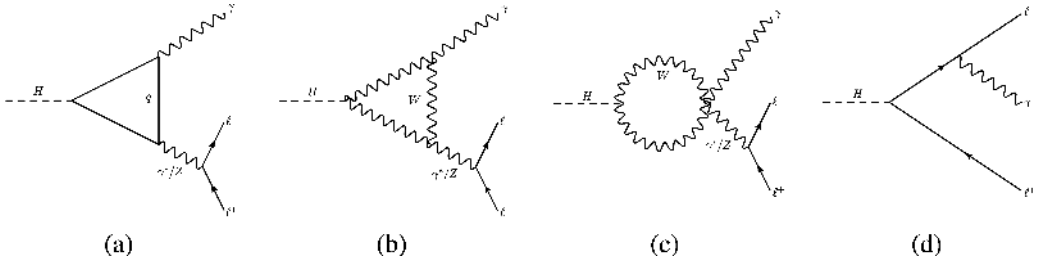

Figure 9.1 – Feynman diagrams for the $H \to \ell\ell\gamma$ process, (a-c) Dalitz decays involving a Z boson or a virtual photon γ^*, (d) decay of the Higgs boson to two leptons and a photon from FSR [29].

The relative contributions of these processes depend on the invariant mass of the dilepton pair, $m_{\ell\ell}$. The decay mediated by a virtual photon, γ^*, dominates the low dilepton mass region, $m_{\ell\ell} < 30$ GeV. By applying this requirement, the analysis remains statistically independent of the $H \to Z\gamma$ search, which targets events with an on-shell Z boson and requires $|m_{\ell\ell} - m_Z| < 10$ GeV, where $m_Z = 91.2$ GeV.

The CMS Collaboration published a result in the $\mu\mu\gamma$ channel using 35.9 fb^{-1} of Run 2 data collected at $\sqrt{s} = 13$ TeV, setting a 95% CL upper limit on the Higgs boson production cross section times branching ratio of 4.0 times the SM prediction [28]. The ATLAS Collaboration subsequently reported about this search using the full Run 2 dataset, corresponding to a total integrated luminosity of 139 fb^{-1} [29]. That analysis provided evidence for the $H \to \ell\ell\gamma$ process with a significance of 3.2σ over the background-only hypothesis, compared with an expected significance of 2.1σ for the SM prediction. The best-fit value of the signal-strength parameter was found to be $\mu = 1.5 \pm 0.5$.

The analysis presented in this Chapter is based on pp collision data recorded at $\sqrt{s} = 13.6$ TeV during the 2022–2024 data-taking period, corresponding to an integrated luminosity of 165 fb^{-1}. It benefits from both the larger dataset and the higher centre-of-mass energy, which result in an increase in the Higgs boson production cross sections with respect to Run 2. In particular, the total Higgs boson production cross section increases from approximately 55.83 pb at 13 TeV to approximately 59.98 pb at 13.6 TeV, as can be seen from Table 4.1 when summing over all production modes at the two energies. This corresponds to a relative increase of about 7.4%.

The analysis follows the strategy developed for the Run 2 search [29]. A description of the dataset, as well as all the simulated samples used in the $H \to \gamma\gamma^*$ analysis, is provided in Section 9.1. The analysis proceeds by selecting events with two electrons or muons and a photon in the final state. Events are categorised into mutually exclusive categories to optimise the signal significance. Because of the event kinematics of the signal process, it is common for the energy deposits of the two electrons in the electromagnetic calorimeter to be reconstructed as a single cluster. Therefore, two types of electron candidates are defined, each with its own selection criteria: one in which a cluster of energy deposits is associated with one selected track from the inner detector (*resolved electron*), representing a single electron, and one in which a cluster is associated with two selected tracks (*merged ee*), representing a merged electron pair. For this reason, the events are

categorised in three channels: $\mu\mu$, ee resolved (selecting two resolved electrons) and ee merged (selecting a single merged electron). The three channels are then divided in three categories based on kinematic topologies: vector-boson-fusion-like (VBF), high-$p_{\mathrm{Tt}}^{ll\gamma}$ and all the remaining events, for a total of 9 categories. The object definition, the event selection and categorisation is described in Section 9.2. Special care is needed for the merged electrons channel, where a special electron identification is employed to reconstruct two electrons that merge into one electromagnetic cluster. Dedicated identification scale factors are derived for these merged electrons. The energy calibration of merged electrons is taken from the calibration derived for converted photons: from a reconstruction point of view, merged electrons closely resemble photons that have undergone an early conversion (low conversion radius) in the tracker. The calibration and identification of merged electrons is described in Section 9.3. The three-body invariant-mass spectrum is fitted independently in each category using a Double-Sided Crystal Ball (DSCB) function to model the signal (Section 9.4) and a background function (Section 9.5) selected with the spurious signal method. This procedure, already employed in the previous $H \to \gamma\gamma$ analysis (Chapter 7), chooses the background model among a set of simple functional forms in order to reduce the statistical uncertainty and minimise potential fit biases. Section 9.6 summarises the sources of experimental and theoretical systematic uncertainties. The significance of a possible excess is evaluated, and limits are set on the production cross section times branching ratio of the $H \to ll\gamma$ process: the expected results are presented in Section 9.8, based on the statistic model described in Section 9.7.

9.1 Data and simulation samples

9.1.1 Data

The analysis is performed using a partial Run 3 pp dataset collected by ATLAS at $\sqrt{s} = 13.6$ TeV from 2022 to 2024, amounting to a total integrated luminosity of 165.4 fb^{-1} after the application of data quality requirements, with an estimated uncertainty of 1.9% using the LUCID-2 detector [73, 173]. A breakdown of the luminosity per-year together with the corresponding uncertainties, is provided in Table 9.1.

Year	Luminosity [fb^{-1}]	Uncertainty	
		Absolute [fb^{-1}]	Relative [%]
2022	29	0.60	1.9
2023	27	0.50	1.9
2024	110	2.1	1.9
Total	170	3.1	1.9

Table 9.1 – Breakdown of the integrated luminosities per year with their absolute and relative uncertainties.

The average number of inelastic pp interactions per bunch crossing (pileup) increased from 42 in 2022 to 57 in 2024, as visible from Figure 2.9b. The maximum average number

of interaction per bunch crossing was up to 80, with the peak instantaneous luminosity reaching 2.3×10^{34} cm^{-2}s^{-1} (Figure 2.5). Events used in this analysis were recorded using a combination of single lepton, dilepton, single photon, diphoton, and lepton + photon triggers that are detailed in Section 9.2.1.

9.1.2 Simulation samples

Samples of simulated MC events are used to optimise the selection, to model the signal processes, to choose an analytic function modelling the background and to estimate the selection efficiency. The signal samples, as discussed in the following Section 9.1.2, were processed through the full ATLAS detector simulation [157] based on GEANT4 [153]. For the background samples, a mix of full simulation samples and high-statistics fast simulation [158] samples were used, as discussed below in Section 9.1.2. The hadronization, parton showering, and the modelling of the underlying event were simulated using PYTHIA 8 [163].

Signal samples

The signal samples used for this SM Higgs boson search include the six main production modes: ggF, VBF, WH, ZH, ggZH and $t\bar{t}H$. The corresponding production cross sections at $\sqrt{s} = 13.6$ TeV are summarised in Table 4.1. In the simulation, the Higgs boson mass is set to $m_H = 125$ GeV, with a SM width of $\Gamma_H = 4.07$ MeV.

The ggZH and $t\bar{t}H$ production modes were not included in the previous Run 2 analysis [29]. In addition, the $b\bar{b}H$ production mode ($\sigma = 0.5257$ pb) is not explicitly simulated in this analysis. Its contribution is therefore estimated assuming an acceptance similar to that of the ggF production mode. For each analysis category, as defined in Section 9.2, the expected ggF yield in the signal region is scaled by the ratio $\sigma_{b\bar{b}H}/\sigma_{\text{ggF}} \simeq 0.01$, which is taken as an estimate of the corresponding $b\bar{b}H$ yield. With this procedure, the additional contribution from $b\bar{b}H$ is found to be below 1% in all analysis categories.

The matrix elements for the signal samples are generated using POWHEG [159], with different perturbative accuracies depending on the Higgs boson production mode. The Higgs boson decays $H \to \gamma^*\gamma \to ee\gamma$ and $H \to \gamma^*\gamma \to \mu\mu\gamma$, as well as the parton shower, hadronisation and underlying event, are modelled using PYTHIA 8.

An overview of the signal samples, including the generators, PDF sets, tunes and theoretical accuracies, is given in Table 9.2.

The cross sections and branching ratios used for the signal are calculated by the LHC Higgs Cross-section working Group [105] for the SM Higgs 125.09 GeV. The cross sections at $\sqrt{s} = 13.6$ TeV with their relative theoretical uncertainties on QCD scale and PDF + α_S are reported in Table 4.1.

The branching ratios for the processes $H \to \gamma^*\gamma \to ee\gamma$ and $H \to \gamma^*\gamma \to \mu\mu\gamma$ in the dilepton invariant mass range $2m_\ell < m_{\ell\ell} < m_H$ are taken from Ref. [174] and were used in the previous Run 2 publication [29]. Their values are $\mathcal{BR}(H \to ee\gamma) = 7.20 \times 10^{-5}$ and $\mathcal{BR}(H \to \mu\mu\gamma) = 3.42 \times 10^{-5}$. Their sum corresponds to approximately $\sim 5\%$ of the total $H \to \gamma\gamma$ branching ratio. Due to their very small branching ratios, the

Production mode	Matrix-element + Showering	PDF / Tune	Accuracy	Events [10^6]
ggF	POWHEG + PYTHIA 8	NNPDF23LO / A14	N3LO + NLO	2.16
VBF	POWHEG + PYTHIA 8	NNPDF23LO / A14	NNLO + NLO	1.35
W^-H	POWHEG + PYTHIA 8	NNPDF23LO / A14	NNLO + NLO	0.17
W^+H	POWHEG + PYTHIA 8	NNPDF23LO / A14	NNLO + NLO	0.17
ZH	POWHEG + PYTHIA 8	NNPDF23LO / A14	NNLO + NLO	0.35
$t\bar{t}H$	POWHEG + PYTHIA 8	NNPDF23LO / A14	NLO + NLO	0.32
$ggZH$	POWHEG + PYTHIA 8	NNPDF23LO / A14	NNLO + –	0.18

Table 9.2 – Summary of the signal samples used in the analysis. The reported accuracies refer to the perturbative order of the matrix-element calculation in QCD and electroweak corrections, respectively. The number of generated events is given in millions.

$H \to \gamma^* \gamma \to \ell\ell\gamma$ decays are not visible in standard summaries of Higgs boson branching ratios and lie well below the scale shown in Figure 4.4.

Interference effects with the processes $H \to Z\gamma \to \ell\ell\gamma$ and $H \to \ell\ell \to \ell\ell\gamma$ are neglected in this analysis. Such interference contributions are expected to be small [175] and have been shown to be negligible in the signal region considered here, defined by $m_{\ell\ell} < 30$ GeV [176].

Background samples

In order to select the background model and to estimate the systematic uncertainty associated with this choice, simulated background samples are required.

Dedicated low-mass $ll\gamma$ background samples were produced using SHERPA 2.2.14 with the NNPDF3.0 NNLO generator tune, at leading order in QCD for final states with up to three additional jets. To improve the generation efficiency, the phase space was restricted to a region close to the analysis pre-selection. The resulting production cross sections are 2.02 pb for the $ee\gamma$ final state and 1.30 pb for the $\mu\mu\gamma$ final state.

Two types of low-mass $ll\gamma$ background samples were generated:

- high-statistics samples produced with fast detector simulation, corresponding to a total of 221 million events for the dielectron channel and 149 million events for the dimuon channel;
- fully simulated samples used for validation of generator-level kinematic shapes and for the derivation of possible efficiency corrections, comprising 3 million events in total, equally split between the two channels.

Other minor background processes were also simulated. The $H \to \gamma\gamma$ ggF and VBF samples are used to estimate the resonant background, as discussed in Section 9.5.1. Di-Jet Filtered (JF) samples, labelled JF17, JF35 and JF50 according to the generator-level transverse energy threshold applied to pseudo-jets (in GeV), are used for the merged-electron calibration and identification studies described in Section 9.3. These samples provide enhanced statistics in jet-rich topologies, which are particularly relevant for the study of merged electron signatures.

9.2 Event selection and categorisation

9.2.1 Triggers

This analysis employs a combination of single lepton, dilepton, lepton-photon, single photon and diphoton triggers to maximise the signal efficiency. Table 9.3 summarises the triggers used divided by trigger type and year. The trigger menu evolved during Run 3 following updates of the Level-1 trigger system; therefore, different but functionally equivalent triggers were employed in different data-taking years.

Trigger type	Trigger name	2022	2023	2024
Single- and di-muon	HLT_mu24_ivarmedium_L1MU14FCH	✓	✓	✓
	HLT_mu50_L1MU14FCH	✓	✓	✓
	HLT_mu60_0eta105_msonly_L1MU14FCH	✓	✓	✓
	HLT_2mu14_L12MU8F	✓	✓	✓
	HLT_mu22_mu8noL1_L1MU14FCH	✗	✓	✓
Single- and di-electron	HLT_e26_lhtight_ivarloose_L1EM22VHI	✓	✗	✗
	HLT_e60_lhmedium_L1EM22VHI	✓	✗	✗
	HLT_e140_lhloose_L1EM22VHI	✓	✗	✗
	HLT_2e17_lhvloose_L12EM15VHI	✓	✗	✗
	HLT_2e24_lhvloose_L12EM20VH	✓	✗	✗
	HLT_e26_lhtight_ivarloose_L1eEM26M	✗	✓	✓
	HLT_e60_lhmedium_L1eEM26M	✗	✓	✓
	HLT_e140_lhloose_L1eEM26M	✗	✓	✓
	HLT_2e17_lhvloose_L12eEM18M	✗	✓	✓
	HLT_2e24_lhvloose_L12eEM24L	✗	✓	✓
(Di)Lepton-Photon	HLT_g25_medium_mu24_L1MU14FCH	✓	✗	✗
	HLT_g35_loose_mu18_L1EM24VHI	✓	✗	✗
	HLT_g25_medium_L1eEM18L_mu24_L1MU14FCH	✗	✓	✓
	HLT_g35_loose_mu18_L1eEM28M	✗	✓	✓
	HLT_g35_loose_mu15_mu2noL1_L1eEM28M	✗	✓	✓
	HLT_e24_lhmedium_g25_medium_02dRAB_L12EM20VH	✓	✗	✗
	HLT_e25_mergedtight_g35_medium_90invmAB_02dRAB_L12EM20VH	✓	✗	✗
	HLT_e24_lhmedium_g25_medium_02dRAB_L12eEM24L	✗	✓	✓
	HLT_e25_mergedtight_g35_medium_90invmAB_02dRAB_L12eEM24L	✗	✓	✓
Single- and di-photon	HLT_g140_loose_L1EM22VHI	✓	✗	✗
	HLT_g300_etcut_L1EM22VHI	✓	✗	✗
	HLT_g35_medium_g25_medium_L12EM20VH	✓	✗	✗
	HLT_2g50_loose_L12EM20VH	✓	✗	✗
	HLT_g140_loose_L1eEM26M	✗	✓	✓
	HLT_g300_etcut_L1eEM26M	✗	✓	✓
	HLT_g35_medium_g25_medium_L12eEM24L	✗	✓	✓
	HLT_2g50_loose_L12eEM24L	✗	✓	✓

Table 9.3 – Triggers used in this analysis, divided by data-taking year (2022–2024). The symbol ✓ indicates that the trigger was used in a given year, while ✗ indicates that it was not present. Triggers with similar physics selections but different names correspond to updates of the trigger menu across Run 3.

A dedicated cut-based electron identification working point, **mergedtight**, was introduced in Run 2 to allow events with two highly collimated electrons to pass the trigger, addressing the atypical topology of Higgs boson Dalitz decays. This trigger recovers a significant fraction of signal events, particularly in the regime $\Delta R(ee) < 0.1$. In addition, a requirement on the invariant mass of the photon-dielectron system, $m_{ee\gamma} > 90$ GeV, is applied at trigger level to suppress the dominant $Z \to ee$ background, with negligible impact on the signal efficiency.

The "mergedtight" working point differs significantly from standard electron identification working points. In particular, it places stronger emphasis on rejecting clusters with significant energy leakage in the hadronic calorimeter, while removing requirements on the lateral shower width. Variables related to the shower width, which provide strong discrimination for isolated electrons, are not well suited to merged-electron topologies and would otherwise lead to a substantial loss of signal efficiency and a relatively increased trigger rate. Their removal is therefore essential to retain efficiency for highly collimated electron pairs.

9.2.2 Object preselection and selection

In this analysis, photon, electron, muon, and jet candidates are selected. Preselections are applied to define objects used as input to the overlap removal procedure, and final selection criteria are further applied to define the signal region.

Muon reconstruction and identification

As described in Section 5.2, muons are reconstructed by matching tracks in the MS with tracks in the ID. In addition, MS-only tracks compatible with the IP and without a matching ID track are also considered. Preselected muon candidates are required to satisfy $p_{\mathrm{T}} > 5$ GeV, $|\eta| < 2.7$, and to pass the *medium* identification criteria [177]. The highest-p_{T} muon candidate in each event is required to be isolated from additional activity in the tracking detector and in the calorimeters. Muon candidates with an associated ID track must be matched to the primary vertex by having a longitudinal impact parameter Δz_0 that satisfies $|\Delta z_0 \sin\theta| < 0.5$ mm, where θ is the polar angle of the track. The significance of the transverse impact parameter d_0 calculated relative to the measured beam-line position is required to be $|d_0|/\sigma_{d_0} < 3$, where σ_{d_0} is the uncertainty on d_0.
After the preselection, the leading muon is required to satisfy $p_{\mathrm{T}} > 15$ GeV in order to match the lowest dimuon trigger requirements. The p_{T} spectrum of the leading and subleading muons after the event selection is shown in Figure 9.2. A summary of the muon object preselection and selection criteria is provided in Table 9.4. The isolation working point `PflowTight_VarRad`[1] combines track-based and neutral particle-flow isolation components, following the ATLAS combined performance (CP) recommendations. To account for the presence of nearby objects, as can occur in collimated topologies, a close-by correction is applied. In this procedure, contributions from nearby reconstructed objects that enter the isolation cones are identified and subtracted, and the isolation requirement is re-evaluated for the muon after this correction.

Electron reconstruction and identification

As described in Section 5.1, electrons are reconstructed by matching tracks in the ID to topological calorimeter clusters formed using a dynamic cell-clustering algorithm [16]. Owing to the event kinematics of the $H \to \ell\ell\gamma$ signal, the two electrons originating from the Higgs boson decay can be highly collimated and may deposit their energy

[1] Defined as $(\texttt{ptvarcone30\_Nonprompt\_All\_MaxWeightTTVA\_pt500} + 0.4 \times \texttt{neflowiso120})/p_{\mathrm{T}} < 0.045$.

Muon Preselections	
p_T [GeV]	> 5
$\|\eta\|$	< 2.7
Identification WP	*Medium*
Muon Selections	
$\|\Delta z_0 \sin\theta\|$ [mm]	< 0.5
$\|d_0\|/\sigma_{d_0}$	< 3
Leading muon p_T [GeV]	> 15
Leading muon Isolation WP	`CloseByCorrected PflowTight_VarRad`
CP recommendations	`250418_Preliminary_r24run3`

Table 9.4 – Summary of muon preselections and selections.

within the same region of the EM calorimeter. In such cases, the clustering algorithm is unable to resolve the two electrons into separate clusters. This configuration occurs for approximately 60% of signal $ee\gamma$ events, corresponding to electron pairs with an angular separation $\Delta R_{ee} < 0.1$.

For this reason, two categories of electron candidates are defined in this analysis, each with dedicated reconstruction and selection criteria. *Resolved* electrons correspond to the standard case in which a topological cluster is matched to a single ID track. *Merged* electrons instead arise when a single calorimeter cluster is matched to two distinct ID tracks, reflecting the presence of two spatially close electrons. Each ID track considered must satisfy $|\Delta z_0 \sin\theta| < 0.5$ mm and $|d_0|/\sigma_{d_0} < 5$. The reconstruction and selection criteria for both resolved and merged electrons are described in the following paragraphs.

Resolved electrons are preselected by requiring $p_T > 4.5$ GeV, $|\eta| < 2.47$ (excluding the crack region $1.37 < |\eta| < 1.52$), and requiring the *VeryLoose* selection criteria, based on a likelihood discriminant made from calorimeter shower shapes and track parameters (Section 5.1.6). After the overlap removal procedure (described in Section 9.2.2) and requirements on *same flavour, opposite sign* leptons, the resolved electrons are required to pass the *Medium* likelihood selection criteria. The highest p_T candidate in each event is then required to satisfy $p_T > 18$ GeV to match the lowest dielectron triggers requirements and to be isolated.

Merged electron candidates are built starting from objects in the electron container and are preselected by requiring $p_T > 20$ GeV and $|\eta| < 2.37$, excluding the crack region $1.37 < |\eta| < 1.52$. In addition, the ratio of transverse energy deposited in the hadronic calorimeter (R_{had} or R_{had1}) to that in the associated EM cluster is required to be smaller than 0.1. To suppress backgrounds from converted photons, candidates identified as ambiguous by the reconstruction algorithm and compatible with photon-conversion topologies are rejected at the preselection stage. In particular, merged-electron candidates are discarded if they match a reconstructed conversion vertex with a radius larger than 20 mm whose momentum is more consistent with the calorimeter cluster energy than that of the track geometrically best matched to the cluster. A preselected merged-electron cluster is then required to be matched to two tracks with opposite charge. Tracks considered for merged electrons must satisfy $p_T > 5$ GeV, $|\eta| < 2.5$, and quality require-

ments including at least seven hits in the silicon detector and a hit in the innermost pixel layer, in order to further suppress converted-photon backgrounds. The selected track candidates are ranked following the procedure described in Ref. [16], and the highest-ranked track together with the highest-ranked opposite-charge track are chosen. These two tracks define the electron-track candidates associated with the merged-electron object and are used in all subsequent reconstruction and event selection steps. Finally, the two electron-track candidates are fitted to a common vertex to reconstruct the direction of the merged electron candidate.

For the final selection, merged electrons must also satisfy the custom identification requirements described in Section 9.3. To suppress SM backgrounds arising from a single real electron accompanied by an additional track, a requirement is imposed on the azimuthal separation $\Delta\phi$ between the two electron-track candidates. This requirement depends on the transverse momentum of the subleading track and is designed to retain efficiency for signal-like topologies while rejecting background configurations. The scalar sum of the track transverse momentum within a variable-size cone around the merged electron must be less than 4% of the electron p_{T}, excluding tracks associated with the merged object itself.

A summary of the resolved and merged electron preselection and selection criteria is provided in Table 9.5. The p_{T} spectrum of the leading and subleading resolved electrons and for the merged electrons after the event selection is shown in Figure 9.2. The isolation working points listed follow the ATLAS CP recommendations, while the `CloseByCorrected` correction accounts for the presence of nearby objects, as can occur in collimated topologies. Electron isolation is defined using the `Loose_VarRad`[2] and `Tight_VarRad`[3] working points, which rely on the same track-based and calorimeter-based isolation variables but differ in the applied thresholds.

	Resolved electrons	**Merged electrons**
	Preselections	
p_{T} [GeV]	> 4.5	> 4.5
$\lvert\eta\rvert$	< 2.47	< 2.47
Identification WP	*VeryLoose*	/
	Selections	
$\lvert\Delta z_0 \sin\theta\rvert$ [mm]	< 0.5	< 0.5
$\lvert d_0\rvert/\sigma_{d_0}$	< 5	< 5
p_{T} [GeV]	> 18 (leading only)	> 20
Identification WP	*Medium*	Custom
Isolation WP	CloseByCorrected `Loose_VarRad`	`Tight_VarRad`
CP recommendations	`es2024_Run3_v0`	

Table 9.5 – Summary of resolved and merged electron preselections and selections.

[2] The `Loose_VarRad` working point is defined as `ptvarcone30_Nonprompt_All_MaxWeightTTVALooseCone_pt1000`$/p_{\mathrm{T}} < 0.15$ and `topoetcone20`$/p_{\mathrm{T}} < 0.2$.

[3] The `Tight_VarRad` working point is defined as `ptvarcone30_Nonprompt_All_MaxWeightTTVALooseCone_pt1000`$/p_{\mathrm{T}} < 0.06$ and `topoetcone20`$/p_{\mathrm{T}} < 0.06$.

Z/γ^* pair selection

The selection of the Z/γ^* lepton pair is performed after the preselection of muon, resolved electron and merged electron candidates, but before the overlap removal procedure.

For opposite-charge muon pairs, the leading muon is required to satisfy $p_{\mathrm{T}} > 15$ GeV. Among all preselected muons passing this requirement, the pair with the highest vector-sum transverse momentum is chosen. Muon pairs are given priority over electron pairs when forming the Z/γ^* candidate; once a muon pair is selected, all remaining preselected muons are discarded.

If no opposite-charge muon pair satisfies these criteria, electron candidates are considered. For resolved electrons, the leading candidate must satisfy $p_{\mathrm{T}} > 18$ GeV and be unambiguous, in order to suppress backgrounds from converted photons. To avoid biasing the selection toward either merged or resolved electron topologies, electron-track candidates are used to compute the vector-sum transverse momentum of the Z/γ^* candidate. The Z/γ^* candidate is formed from same-flavour opposite-sign electron pairs, using the electron-track candidates for merged electrons and the best-matched track for resolved electrons. The resolved electron pair or merged electron candidate with the highest vector-sum transverse momentum is selected. In cases where the same two tracks can be interpreted either as a resolved electron pair or as a merged electron candidate, the resolved interpretation is retained and its kinematics are used. After the Z/γ^* candidate is selected, any remaining preselected resolved or merged electrons are discarded.

Photon reconstruction and identification

Photons are reconstructed from calorimeter clusters formed using the same dynamic, topological cell-clustering algorithm employed for electron reconstruction, as described in Section 5.1. A photon candidate can be either converted or unconverted. The photon energy is calibrated following the procedure described in Chapter 6.

Reconstructed photons are preselected by requiring $p_{\mathrm{T}} > 20$ GeV and $|\eta| < 2.37$, excluding the calorimeter transition region $1.37 < |\eta| < 1.52$. A *Loose* identification working point based on calorimeter shower-shape variables is applied to suppress backgrounds from jets. Among the surviving candidates, the highest-p_{T} photon is selected for the Higgs boson system.

To avoid double-counting, if the selected photon overlaps with one of the electromagnetic clusters used to form the Z/γ^* candidate within $\Delta R < 0.02$, it is discarded and the next highest-p_{T} preselected photon is considered, in order to avoid double-counting electromagnetic cluster objects. This procedure is repeated until no overlap remains or no further photon candidates are available. Once a photon candidate is selected, all remaining preselected photons are discarded.

The selected photon is then required to pass the *Tight* identification working point (see Section 5.1.5) and both calorimeter- and track-based isolation requirements (see Section 5.1.7). The isolation is defined using the `FixedCutLoose` working point, and photons failing either identification or isolation criteria are rejected.

A summary of the photon preselection and selection requirements is provided in Table 9.6.

Photon Preselections	
p_{T} [GeV]	> 20
$\lvert\eta\rvert$	< 2.37, exlcuding $1.37 < \lvert\eta\rvert < 1.52$
Identification WP	*Loose*
Photon Selections	
Identification WP	*Tight*
Isolation WP	`FixedCutLoose`
CP recommendations	`es2024_Run3_v0`

Table 9.6 – Summary of photon preselections and selections.

Jet reconstruction and identification

Jets are reconstructed using the particle-flow (PFlow) algorithm, as described in Section 5.3.1, and clustered with the anti-k_t algorithm [147] using a distance parameter of $R = 0.4$. The resulting jet candidates are required to satisfy $p_{\mathrm{T}} > 20$ GeV and $|\eta| < 4.4$. Jets originating from pileup interactions are suppressed using dedicated vertex-based tagging techniques. In the central region ($|\eta| < 2.5$), jets with $p_{\mathrm{T}} < 60$ GeV are required to pass the jet vertex tagger (JVT) selection, which exploits the association of tracks within the jet to the primary vertex [178]. In the forward region ($2.5 < |\eta| < 4.4$), where tracking information is limited, pileup suppression is achieved using the forward jet vertex tagger (fJVT); the *loose* fJVT working point is applied to jets with $p_{\mathrm{T}} < 60$ GeV [179]. In events containing more than two jets passing the selection criteria, only the two highest-p_{T} jets are retained for the subsequent analysis steps.

Overlap removal

After object preselection and the Z/γ^* candidate selection, each event contains exactly one photon candidate, two lepton candidates (either two muons, two resolved electrons, or one merged electron corresponding to two leptons), and a set of jet candidates. An overlap removal procedure is applied to avoid double counting of reconstructed objects. The procedure follows the sequence listed below:

1. if an electron (resolved or merged) overlaps with the photon within $\Delta R < 0.4$[4], the event is discarded;
2. if a jet overlaps with the photon within $\Delta R < 0.4$, the jet is discarded;
3. if a remaining jet overlaps with an electron (resolved or merged) within $\Delta R < 0.2$, the jet is discarded;

[4]The electron-photon overlap removal procedure (with $\Delta R < 0.4$) is distinct from the "double-counting" step described earlier (with $\Delta R < 0.02$). The double-counting step is meant to address the issue of a single EM cluster showing up in both the electron and photon containers; the overlap removal step is meant to remove events where an electron and a photon are nearby (e.g. a near- FSR photon radiated from an electron).

4. if a remaining jet overlaps with an electron (resolved or merged) within $0.2 < \Delta R < 0.4$, the event is discarded;
5. if a muon overlaps with the photon within $\Delta R < 0.4$, the event is discarded;
6. if a remaining jet overlaps with a muon within $\Delta R < 0.4$, the jet is discarded.

Events containing overlapping preselected objects are removed rather than resolved by selecting subleading object candidates. This choice serves two purposes. First, it suppresses backgrounds with multiple preselected objects that would otherwise have several opportunities to satisfy the final event selection. Second, it allows the definition of clean and well-controlled background control regions based on preselected leptons and photons, in which identification, isolation, and impact-parameter requirements can be inverted without altering the object definitions or their multiplicities, including jets.
The overlap removal is applied immediately after the Z/γ^* candidate selection and corresponds to Cut 13 in the signal cutflow shown in Tables 9.7, 9.8 and 9.10.

9.2.3 Event selection

An event selection is applied after the object preselection, the Z/γ^* candidate selection, and the overlap removal. To select the Higgs boson system, each event is required to contain two opposite-charge, same-flavour leptons and one tight photon. The dilepton invariant mass requirement $m_{\ell\ell} < 30$ GeV allows control of the non-resonant background shape and enables the use of background functions with a reduced number of degrees of freedom. Events in which the dilepton invariant mass is compatible with J/ψ or Y resonances are rejected. In particular, contributions from $J/\psi \to \ell\ell$ decays are suppressed by excluding the muon mass window $2.9 < m_{\mu\mu} < 3.3$ GeV and the electron mass window $2.5 < m_{ee} < 3.5$ GeV. Similarly, events consistent with $\Upsilon \to \ell\ell$ decays are removed by excluding the muon mass window $9.1 < m_{\mu\mu} < 10.6$ GeV and the electron mass window $8.0 < m_{ee} < 11.0$ GeV.
The signal events are further defined by a three-body system invariant mass requirement of $m_{\ell\ell\gamma} \in [105, 160]$ GeV for fitting the signal and background components. Events also need to satisfy relative photon and di-lepton p_{T} requirements as $p_T^{\ell\ell}/m_{\ell\ell\gamma} > 0.3$ and $p_T^{\gamma}/m_{\ell\ell\gamma} > 0.3$. Tables 9.7, 9.8 and 9.10 list the event yields and selection efficiencies (before categorization) for the inclusive, di-muon, and di-electron final states in $H \to \gamma^*\gamma$ process including all production modes. Table 9.10 splits event into reconstructed resolved and merged electron categories after assignment of the Z/γ^* candidate. The overall signal selection efficiency is 12.5%.
The p_{T} spectra after the event selection, considering all production modes and all MC campaigns for the partial Run 3 dataset for the leading and subleading muons (a,b), for the leading and subleading resolved electrons (c,d), for the merged electrons (e) and for the photons (f) are shown in Figure 9.2.

9.2.4 Event categorisation

The surviving events are first divided into three final-state channels: dimuon, resolved-electron, and merged-electron. These channels exhibit different background composi-

Cut	Surviving events	Cut efficiency [%]	Total efficiency [%]
3. All $H \to \gamma\gamma^*$	1158.32 ± 1.31	100.0	100.0
4. No duplicates	1158.32 ± 1.31	100.0	100.0
5. GRL	1158.32 ± 1.31	100.0	100.0
6. Pass trigger	760.56 ± 0.68	65.7	65.7
7. Detector DQ	760.56 ± 0.68	100.0	65.7
8. Has PV	760.56 ± 0.68	100.0	65.7
9. ≥ 2 same-flavor leptons	696.72 ± 0.65	91.6	60.1
10. 1 loose photon	580.04 ± 0.58	83.3	50.1
11. $e-\gamma$ ambiguity / dead HV cell	579.56 ± 0.58	99.9	50.0
12. Z/γ^* pair selection	411.30 ± 0.49	71.0	35.5
13. Overlap Removal and 2 same-flavor leptons	402.77 ± 0.49	97.9	34.8
14. 1 loose photon (post-OR)	402.77 ± 0.49	100.0	34.8
15. Trigger match	388.55 ± 0.48	96.5	33.5
16. lepton ID	264.05 ± 0.39	68.0	22.8
17. lepton impact parameter	255.66 ± 0.38	96.8	22.1
18. lepton isolation	238.33 ± 0.37	93.2	20.6
19. photon tight ID	214.21 ± 0.35	89.9	18.5
20. photon isolation	201.42 ± 0.34	94.0	17.4
21. $m_{\ell\ell} < 30$ GeV	179.11 ± 0.32	88.9	15.5
22. $m_{\ell\ell\gamma} \in [105, 160]$GeV	178.61 ± 0.32	99.7	15.4
23. $m_{\ell\ell}$ veto J/Ψ and Υ window	167.75 ± 0.31	93.9	14.5
24. $p_{\mathrm{T}}^{\ell\ell}/m_{\ell\ell\gamma} > 0.3$	158.88 ± 0.30	94.7	13.7
25. $p_{\mathrm{T}}^{\gamma}/m_{\ell\ell\gamma} > 0.3$	144.31 ± 0.29	90.8	12.5

Table 9.7 – Signal cutflow for the $H \to \gamma\gamma^*$ process, including all the production modes (ggF, VBF, WH, ZH, ggZH and $t\bar{t}H$) and all the MC campaigns for the partial Run 3 dataset.

tions and are therefore treated independently in the signal and background extraction. To further enhance the signal-to-background ratio, each channel is subsequently subdivided into three exclusive kinematic categories.

- **VBF category**: events are required to satisfy a set of selections targeting the vector-boson fusion topology, as summarised in Table 9.9. In this topology, the Higgs boson (or the $\ell\ell\gamma$ system in this analysis) is typically produced centrally between two forward jets with large invariant mass and pseudorapidity separation. The selections exploit these features by requiring at least two high-p_{T} jets, large dijet invariant mass and pseudorapidity gap, as well as a central $\ell\ell\gamma$ system with respect to the dijet system, quantified using the Zeppenfeld variable, defined as

$$\eta_{\text{Zeppenfeld}} = \left| \eta_{\ell\ell\gamma} - \frac{1}{2}\left(\eta_{j1} + \eta_{j2}\right) \right|,$$

  where $\eta_{\ell\ell\gamma}$ denotes the pseudorapidity of the $\ell\ell\gamma$ system and η_{j1} (η_{j2}) that of the leading (subleading) jet. Additional angular requirements are imposed to suppress background processes. Events passing all these selections are assigned to the VBF category;
- **High-$p_{\mathrm{Tt}}^{\ell\ell\gamma}$ category**: events failing the VBF selection but with $p_{\mathrm{Tt}}^{\ell\ell\gamma} > 100$ GeV. The variable $p_{\mathrm{Tt}}^{\ell\ell\gamma}$ is defined as the transverse momentum of the $\ell\ell\gamma$ system projected onto its thrust axis, as defined in Equation (7.4);
- **Low-$p_{\mathrm{Tt}}^{\ell\ell\gamma}$ category**: all remaining events failing both the VBF and the high-$p_{\mathrm{Tt}}^{\ell\ell\gamma}$

Cut	Surviving events	Cut efficiency [%]	Total efficiency [%]
3. All $H \to \mu\mu\gamma$	388.22 ± 0.49	100.0	100.0
4. No duplicates	388.22 ± 0.49	100.0	100.0
5. GRL	388.22 ± 0.49	100.0	100.0
6. Pass trigger	257.06 ± 0.39	66.2	66.2
7. Detector DQ	257.06 ± 0.39	100.0	66.2
8. Has PV	257.06 ± 0.39	100.0	66.2
9. ≥ 2 same-flavor leptons	232.36 ± 0.37	90.4	59.9
10. 1 loose photon	184.85 ± 0.33	79.6	47.6
11. $e-\gamma$ ambiguity / dead HV cell	184.68 ± 0.33	99.9	47.6
12. Z/γ^* pair selection	149.56 ± 0.30	81.0	38.5
13. Overlap Removal and 2 same-flavor leptons	147.67 ± 0.29	98.7	38.0
15. 1 loose photon (post-OR)	147.67 ± 0.29	100.0	38.0
15. Trigger match	144.10 ± 0.29	97.6	37.1
16. lepton ID	140.09 ± 0.28	97.2	36.1
17. lepton impact parameter	135.98 ± 0.28	97.1	35.0
18. lepton isolation	123.18 ± 0.27	90.6	31.7
19. photon tight ID	110.21 ± 0.25	89.5	28.4
20. photon isolation	103.42 ± 0.24	93.8	26.6
21. $m_{\ell\ell} < 30$ GeV	89.46 ± 0.23	86.5	23.0
22. $m_{\ell\ell\gamma} \in [105, 160]$GeV	89.10 ± 0.23	99.6	23.0
23. $m_{\ell\ell}$ veto J/Ψ and Υ window	83.57 ± 0.22	93.8	21.5
24. $p_{\mathrm{T}}^{\ell\ell}/m_{\ell\ell\gamma} > 0.3$	77.75 ± 0.21	93.0	20.0
25. $p_{\mathrm{T}}^{\gamma}/m_{\ell\ell\gamma} > 0.3$	70.71 ± 0.20	90.9	18.2

Table 9.8 – Signal cutflow for the $H \to \gamma\gamma^*$ process, including all the production modes (ggF, VBF, WH, ZH, ggZH and $t\bar{t}H$) and all the MC campaigns for the partial Run 3 dataset, but considering only the $H \to \mu\mu\gamma$ decay.

selections.

Category	Selections
VBF	Jet multiplicity ≥ 2, with $p_{\mathrm{T}} > 25$ GeV $p_{\mathrm{T}} > 30$ GeV if $\lvert\eta\rvert > 2.5$ $m_{jj} > 500$ GeV $\lvert\Delta\eta_{jj}\rvert > 2.7$ $\lvert\eta_{\ell\ell\gamma} - 0.5(\eta_{j1} + \eta_{j2})\rvert < 2.0$ $\Delta R(jj, \ell) > 1.5$, $\Delta R(jj, \gamma) > 1.5$ $\lvert\Delta\phi(\ell\ell\gamma, jj)\rvert > 2.8$

Table 9.9 – VBF selections used in the analysis to define VBF category in each final state channel.

The Run 3 categorisation, identical to the Run 2 one [29], comprises nine categories, which will be referred to throughout this Chapter as:

$\mu\mu$ low-p_{Tt}, ee resolved low-p_{Tt}, ee merged low-p_{Tt}, $\mu\mu$ VBF, ee resolved VBF, ee merged VBF, $\mu\mu$ high-p_{Tt}, ee resolved high-p_{Tt}, ee merged high-p_{Tt}.

	All $H \to ee\gamma$			Merged events (@Reco)			Resolved events (@Reco)		
Cut	Surviving events	Cut ϵ [%]	Total ϵ [%]	Surviving events	Cut ϵ [%]	Total ϵ [%]	Surviving events	Cut ϵ [%]	Total ϵ [%]
3. All $H \to ee\gamma$	769.84 ± 0.69	100.0	100.0						
4. No duplicates	769.84 ± 0.69	100.0	100.0						
5. GRL	769.84 ± 0.69	100.0	100.0						
6. Pass trigger	503.68 ± 0.55	65.4	65.4						
7. Detector DQ	503.68 ± 0.55	100.0	65.4						
8. Has PV	503.68 ± 0.55	100.0	65.4						
9. ≥ 2 same-flavor leptons	464.55 ± 0.53	92.2	60.3						
10. 1 loose photon	395.33 ± 0.48	85.1	51.4						
11. $e-\gamma$ ambiguity / dead HV cell	395.02 ± 0.48	99.9	51.3						
12. Z/γ^* pair selection	261.79 ± 0.39	66.3	34.0	167.66 ± 0.31	100.0	100.0	93.50 ± 0.23	100.0	100.0
13. OR and 2 same-flavor leptons	255.15 ± 0.39	97.5	33.1	163.19 ± 0.31	97.3	97.3	91.35 ± 0.23	97.7	97.7
14. 1 loose photon (post-OR)	255.15 ± 0.39	100.0	33.1	163.19 ± 0.31	100.0	97.3	91.35 ± 0.23	100.0	97.7
15. Trigger match	244.49 ± 0.38	95.8	31.8	155.16 ± 0.30	95.1	92.5	88.77 ± 0.23	97.2	94.9
16. lepton ID	123.97 ± 0.27	50.7	16.1	68.43 ± 0.20	44.1	40.8	55.01 ± 0.17	62.0	58.8
17. lepton impact parameter	119.68 ± 0.26	96.5	15.5	66.58 ± 0.20	97.3	39.7	52.77 ± 0.17	95.9	56.4
18. lepton isolation	115.16 ± 0.26	96.2	15.0	62.85 ± 0.19	94.4	37.5	52.01 ± 0.17	98.6	55.6
19. photon tight ID	104.00 ± 0.25	90.3	13.5	56.76 ± 0.18	90.3	33.9	46.97 ± 0.16	90.3	50.2
20. photon isolation	98.00 ± 0.24	94.2	12.7	53.45 ± 0.18	94.2	31.9	44.29 ± 0.16	94.3	47.4
21. $m_{\ell\ell} < 30$ GeV	89.65 ± 0.23	91.5	11.6	53.45 ± 0.18	100.0	31.9	36.19 ± 0.14	81.7	38.7
22. $m_{\ell\ell\gamma} \in [105, 160]$GeV	89.51 ± 0.23	99.8	11.6	53.39 ± 0.18	99.9	31.8	36.11 ± 0.14	99.8	38.6
23. $m_{\ell\ell}$ veto J/Ψ and Υ window	84.19 ± 0.22	94.1	10.9	53.38 ± 0.18	100.0	31.8	30.81 ± 0.13	85.3	32.9
24. $p_{\mathrm{T}}^{\ell\ell}/m_{\ell\ell\gamma} > 0.3$	81.13 ± 0.22	96.4	10.5	51.78 ± 0.18	97.0	30.9	29.35 ± 0.13	95.3	31.4
25. $p_{\mathrm{T}}^{\gamma}/m_{\ell\ell\gamma} > 0.3$	73.60 ± 0.21	90.7	9.6	46.70 ± 0.17	90.2	27.9	26.89 ± 0.12	91.6	28.8

Table 9.10 – Signal cutflow for the $H \to \gamma\gamma^*$ process, including all the production modes (ggF, VBF, WH, ZH, ggZH and $t\bar{t}H$) and all the MC campaigns for the partial Run 3 dataset, but considering only the $H \to ee\gamma$ decay. Events are split into merged and resolved reconstruction categories after Z/γ^* pair selection.

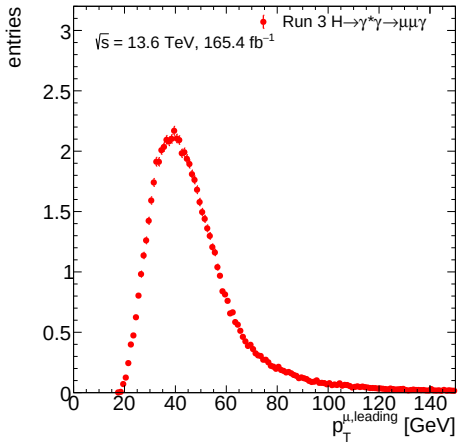

(a) Leading μ p_{T}

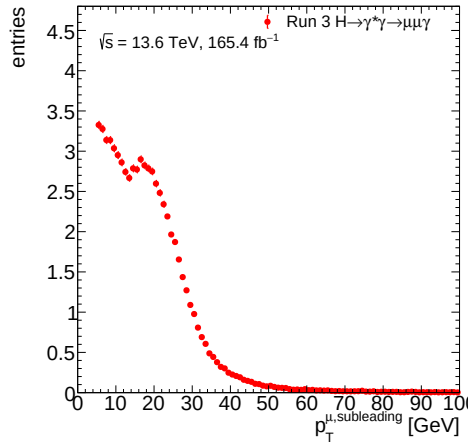

(b) Subleading μ p_{T}

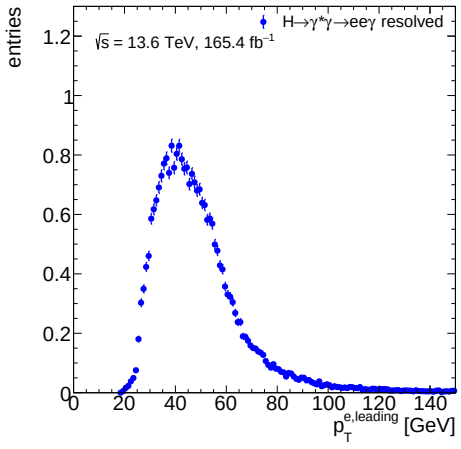

(c) Leading resolved e p_{T}

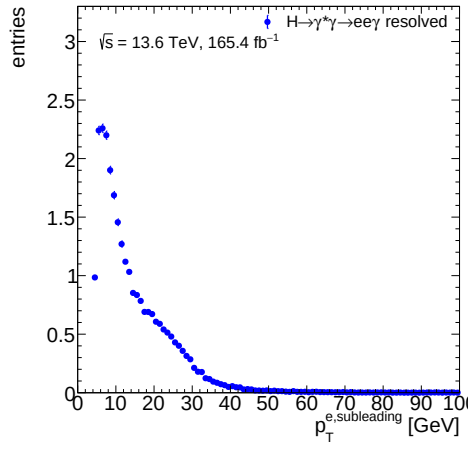

(d) Subleading resolved e p_{T}

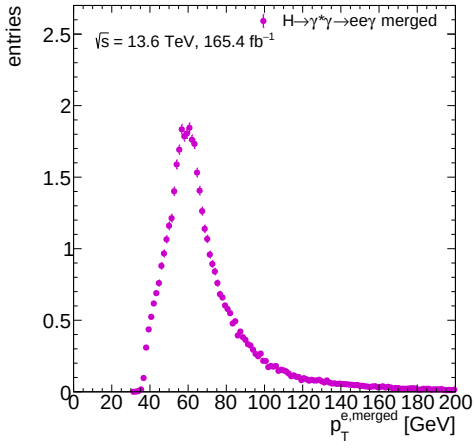

(e) Merged e p_{T}

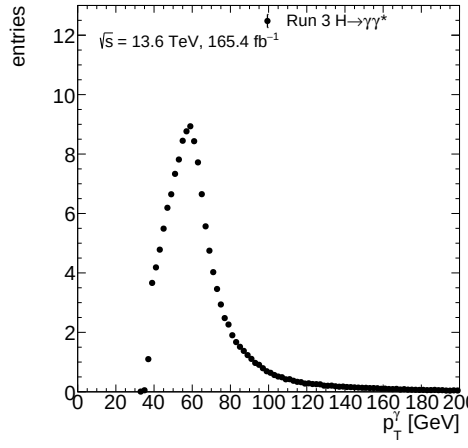

(f) Photon γ p_{T}

Figure 9.2 – The p_{T} spectra after event selection, considering all production modes and all MC campaigns for the partial Run 3 dataset: leading and subleading muons (a,b), leading and subleading resolved electrons (c,d), merged electron (e) and on-shell photon (f).

9.3 Calibration and identification of merged electrons

Because the calorimeter response for merged electrons closely resembles that of photons converting in the detector material near the interaction point, the energy of merged-*ee* objects is calibrated using the converted-photon energy calibration. In this procedure, the conversion radius is fixed to $r_{\text{conv}} = 30$ mm, defined with respect to the measured beam-line position. As shown in Figure 9.3, the previous Run 2 analysis [29] demonstrated that this approach minimises the energy bias, particularly in the mean reconstructed dielectron energy, compared to alternative calibration schemes such as treating merged electrons as standard electron objects.

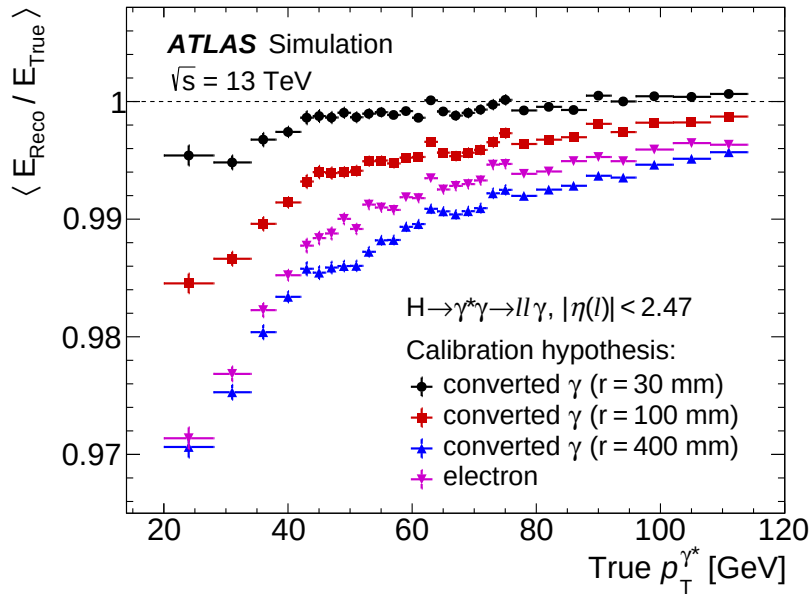

Figure 9.3 – Ratio of reconstructed to true merged-*ee* energy in simulated $H \to \gamma^*\gamma \to ee\gamma$ events as a function of the true merged-*ee* p_{T} for several energy calibration techniques. The merged-*ee* object is calibrated as a photon with a conversion radius of 30 mm (black circles, analysis choice), 100 mm (red squares), and 400 mm (blue upward triangles) or as an electron (purple downward triangles) [29].

Converted photons used for this comparison are required to be Silicon–Silicon conversions, i.e. both conversion tracks must be reconstructed in the silicon detector, in order to ensure a topology most similar to that of merged electrons. To account for residual differences between the simulated detector response to converted photons and merged-*ee* objects, an additional energy resolution uncertainty is introduced. This uncertainty is defined as the difference between the squares of the energy resolutions of merged-*ee* objects and converted photons in simulation. The resulting term is treated as an extra contribution to the merged-*ee* energy resolution uncertainty.

9.3.1 Identification of merged electrons

The following section describes the optimisation of the custom merged-electron identification. A dedicated identification is required because the standard electron criteria have a low efficiency for objects characterised by closely spaced energy deposits leading to broader EM showers. The optimisation is performed using MC samples. Since calorimeter shower-shape variables are known to be mismodelled in simulation, corrections are applied to improve the agreement between data and MC. In standard ATLAS analyses, these corrections (so-called *fudge factors*) are provided by the e/γ CP group for electrons and photons. In this analysis, merged-electron shower-shape variables are corrected by treating merged electrons as converted photons.
The custom merged-electron identification developed during Run 2, briefly described in the next Section, is applied to merged electrons and used as a comparison while awaiting the completion of the dedicated Run 3 merged-electron identification studies, which are described below.

Run 2 merged electron identification

In the Run 2 merged-electron dedicated identification [29], a multivariate discriminator was trained to separate the $\gamma^* \to ee$ signal objects from jets or single electrons. The input variables for the training included:

- Shower-shape variables: $R_{\text{had}}, R_\eta, R_\phi, E_{\text{ratio}}, f_3, w_{\eta 2}, w_{\text{tot,s1}}$ defined in Table 5.1;
- Track-to-calorimeter pointing variables:
  - $\Delta\eta_1(\text{trk1}) = \Delta\eta$ between the cluster and the leading track η in the first layer of the EM calorimeter;
  - E/p_{vtx} = ratio between the cluster energy and the absolute value of the vectorial sum of the transverse momentum of the two tracks (that have been selected to run the vertex fit);
  - $\Delta\phi(\text{vtx}) = \Delta\phi$ between: vertex (sum of the tracks) extrapolated at calorimeter as NeutralParameter and the cluster ϕ in the EM layer 2;
  - $\Delta\eta(\text{vtx}) = \Delta\eta$ between: vertex (sum of the tracks) extrapolated at calorimeter as NeutralParameter and the cluster η in the EM layer 2;
  - $|z_0^{\text{trk1}} - z_0^{\text{trk2}}|$ = difference in z_0 impact parameter between the two tracks;
- TRT probabilities for both electrons tracks.

To find the optimal selection requirements for other variables, the TMVA package [152] was used with simple cut-based approach. The optimization was done using simulated signal events, and simulated background JF events for the Run 2 conditions. A combined efficiency of $\sim$ 50% for the merged-ee identification and isolation was achieved for $H \to \gamma^*\gamma \to ee\gamma$ events.

Run 3 merged electron identification studies

This Section describes the development and the expected performance improvements of a new Run 3 dedicated merged-electron identification based on a multivariate approach.

The identification is obtained through the training of a BDT classifier. A single BDT model, without explicit binning in η or p_{T}, is trained using the Light Gradient Boosting Machine (LightGBM) framework [180].

Training samples The optimisation is performed using simulated signal and background events from the following MC samples, described in Section 9.1.2:

- **Signal**: reconstructed merged electrons from all available $H \to \gamma\gamma^*$ samples;
- **JF background**: reconstructed merged electrons from the JF17, JF35 and JF50 samples;
- $\boldsymbol{H \to \gamma\gamma}$ **background**: reconstructed merged electrons from $H \to \gamma\gamma$ events (ggF and VBF production), included to enrich the training sample with real photon candidates, given their similarity to merged electrons.

A series of selections, summarised in Table 9.11, are applied to both signal and background samples in order to closely match the selections used in the analysis.
For the JF samples, potential signal-like contamination is suppressed by rejecting reconstructed merged electrons matched to true electrons (`pdgId` $= \pm 11$) originating from photons (`parentPdgId` $= 22$). For the $H \to \gamma\gamma$ background samples, only photons originating directly from the Higgs boson decay (`pdgId` $= 22$ and `parentPdgId` $= 25$) are retained, in order to remove contributions from Dalitz decays, which constitute signal in this analysis.

	Selections		
	$\boldsymbol{H \to \gamma\gamma^*}$ **Signal**	**JF bkg**	$\boldsymbol{H \to \gamma\gamma}$ **bkg**
reco merged electron	✓	✓	✓
p_{T} [GeV]	> 10	> 10	> 10
$\lvert\eta\rvert$	< 2.5	< 2.5	< 2.5
Identification WP	*Loose*	*Loose*	*Loose*
Match a γ^* from H decay	✓	✗ (not required)	✗ (not required)
Remove possible signal-like contamination	✗ (not required)	✓	✓

Table 9.11 – Summary of the selections applied to the signal and background samples used in the BDT training.

After the selection, the signal $H \to \gamma\gamma^*$ sample contains approximately 870 k events, while the background sample consists of about 400 k events from JF samples and 70 k events from $H \to \gamma\gamma$ production.
In addition, for the $H \to \gamma\gamma^*$ signal, a statistically independent sub-sample is defined using the `eventNumber`. This sub-sample is excluded from the signal modelling performed later in the analysis, ensuring statistical independence and avoiding potential biases.

Input variables The training is performed using the following input variables, most of them already employed in the Run 2 optimization:

- p_{T} and η: a kinematic 1D $\times$ 1D reweighting has been applied so that the signal and background p_{T} and η distributions are matched. The goal is to train a model that

distinguishes prompt merged electrons from background events, exploiting differences between signal and background in a set of discriminating features. However, since the purpose is to develop a procedure that is not strictly limited to our specific analysis, differences in the p_{T} and η distributions can lead the model to learn spurious correlations, reducing its generalization power. To mitigate this effect, kinematic weights are applied such that the p_{T} and η distributions of each background component match those of the signal, ensuring that the model does not rely on these variables for discrimination. The p_{T} and η distributions before and after the reweighting are shown in Figure 9.4 and Figure 9.5.

- Standard shower-shape variables employed in the electron identification are used, namely R_{had}, R_{had1}, R_{η}, R_{ϕ}, E_{ratio}, ΔE, $w_{\eta 1}$, $w_{\eta 2}$, and $w_{\mathrm{tot,s1}}$, as defined in Table 5.1. All variables are reweighted with weights defined above depending on p_{T} and η to account for their kinematic dependence. Representative distributions are shown in Figure 9.6 for R_{had} and R_{η}, comparing signal and background contributions; distributions for the remaining variables are provided in Appendix C.1. In general, the discriminating power of a given variable increases with the degree to which its distribution differs between signal and background.
- Track-to-calorimeter pointing variables already used in the previous Run 2 optimization: $\Delta\phi(\mathrm{vtx})$, E/p_{vtx}, $\Delta\eta_1(\mathrm{trk1})$, $|\Delta\eta_1(\mathrm{trk1})|$, $\Delta\eta(\mathrm{vtx})$, $|z_0^{\mathrm{trk1}} - z_0^{\mathrm{trk2}}|$. E/p_{vtx} and $|z_0^{\mathrm{trk1}} - z_0^{\mathrm{trk2}}|$ are shown in Figure 9.7 while the remaining variables are reported in Appendix C.1.
- TRT variables for both electron tracks have not been included because of mismodelling issues observed in Run 3 MC samples.

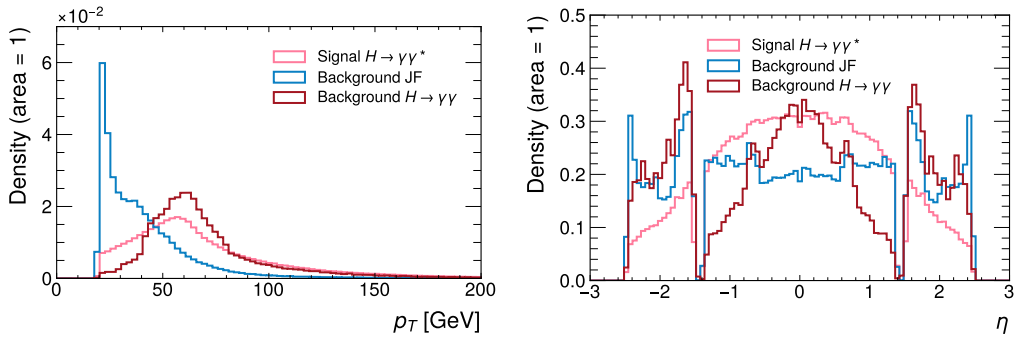

(a) p_T **(b)** η

Figure 9.4 – Comparison between the normalised p_{T} (a) and η (b) distributions before the reweighting procedure for the signal and background samples used in the BDT training.

Training and results A single BDT classifier, without explicit binning in η or p_{T}, is trained using the LightGBM framework. No dedicated hyperparameter optimisation is performed, as satisfactory performance is achieved with a simple configuration. The main hyperparameter values used in the training are reported in Table 9.12; all other

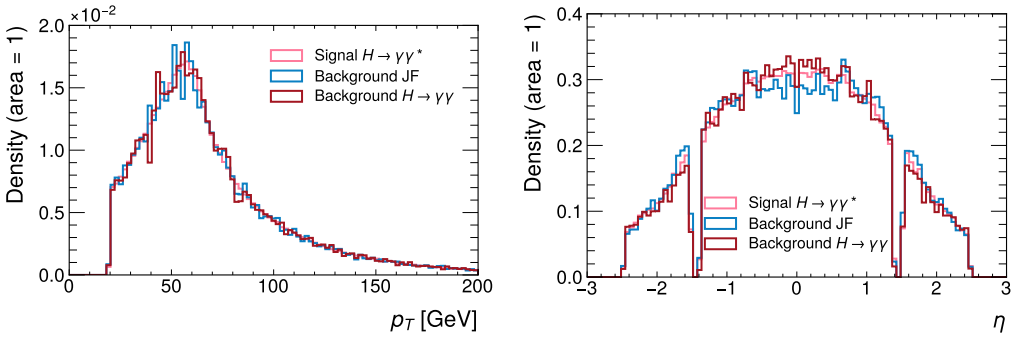

(a) p_T **(b)** η

Figure 9.5 – Comparison between the normalised p_{T} (a) and η (b) distributions after the reweighting procedure for the signal and background samples used in the BDT training.

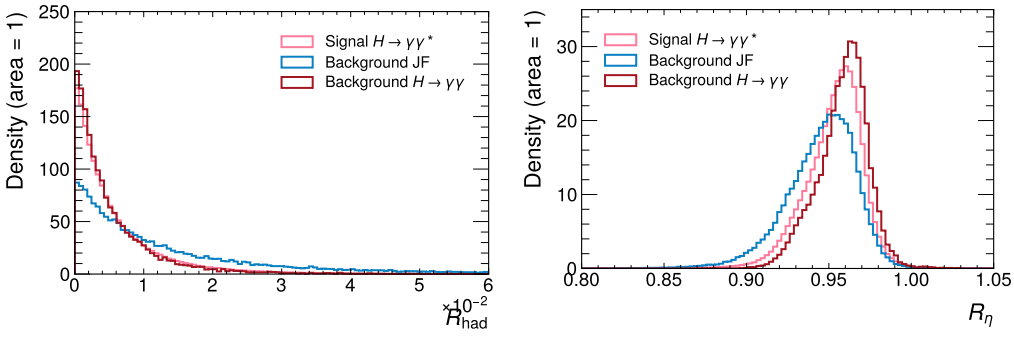

(a) R_{had} **(b)** R_η

Figure 9.6 – Comparison between the normalised shower-shape variables R_{had} (a) and R_η (b) distributions after the reweighting procedure for the signal and background samples used in the BDT training.

parameters are set to their default values in the LightGBM classifier. Early stopping is applied to prevent overfitting. The dataset is split evenly, with 50% of the events used for training and the remaining 50% reserved for testing. As discussed previously, the training is performed using kinematic weights in η and p_{T} to account for differences between signal and background distributions.

Hyperparameter	**Value**
Learning rate	0.09
Number of leaves	100
Objective	`xentropy`
Early stopping rounds	10

Table 9.12 – Summary of the main hyperparameters used in the training.

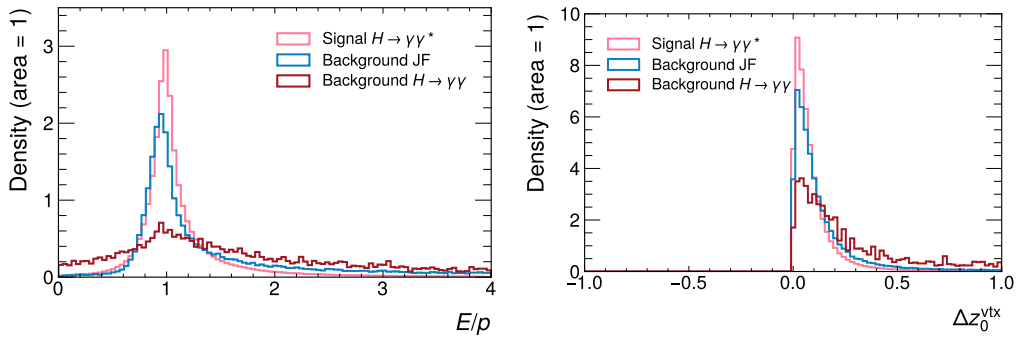

(a) E/p_{vtx} **(b)** $|z_0^{\text{trk1}} - z_0^{\text{trk2}}|$

Figure 9.7 – Comparison between the track-to-calorimeter pointing variables variables E/p_{vtx} (a) and $|z_0^{\text{trk1}} - z_0^{\text{trk2}}|$ (b) distributions after the reweighting procedure for the signal and background samples used in the BDT training.

The trained BDT assigns a score in the range $[0, 1]$, where values close to 1 indicate signal-like behaviour and values close to 0 indicate background-like behaviour. The distribution of the BDT score for the test sample is shown in Figure 9.8, while the corresponding Receiver Operating Characteristic (Receiver Operating Characteristic (ROC)) curve is presented in Figure 9.9. The marker in Figure 9.9 indicates the signal and background efficiencies (s_{eff}, b_{eff}) obtained using the `pass ID Run 2` working point, corresponding to the merged-electron identification employed in Run 2.
Since the primary goal of this analysis is to increase the signal efficiency for merged-electron identification, a natural comparison strategy is to select a BDT threshold yielding roughly the same background efficiency as the `pass ID Run 2` working point. At fixed background efficiency, the BDT-based identification achieves a higher signal efficiency on the test sample, as can be clearly inferred from Figure 9.9.

Expected analysis significance To obtain a quantitative estimate of the impact of the new BDT model on the expected analysis significance, a dedicated study was performed comparing its performance to that of the Run 2 identification. Up to this point, the performance metrics of the identification strategies have been evaluated on a test sample drawn from the same dataset used for the BDT training. As a result, the background composition of this sample does not reflect that expected in data, motivating the need for an alternative evaluation strategy.
Focusing on the three merged-electron categories, the impact on the expected significance is evaluated through the following procedure:

1– The full analysis event selection is applied to the MC $H \to \gamma\gamma^*$ signal sample and to the data sidebands (2022+2023+2024), with the exception of the merged-electron identification requirement. The data are blinded in the invariant-mass window $m_{\ell\ell\gamma} \in [120, 130]$ GeV.

2– Two identification working points are considered: the Run 2 photon identification and the Run 3 BDT-based identification. For the latter, no dedicated optimiza-

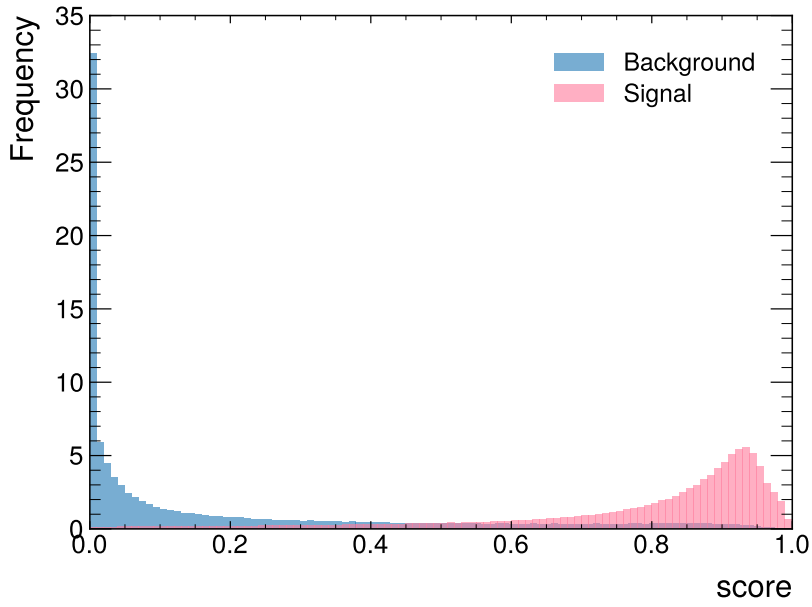

Figure 9.8 – Distribution of the BDT output score for signal and background events on the test sample.

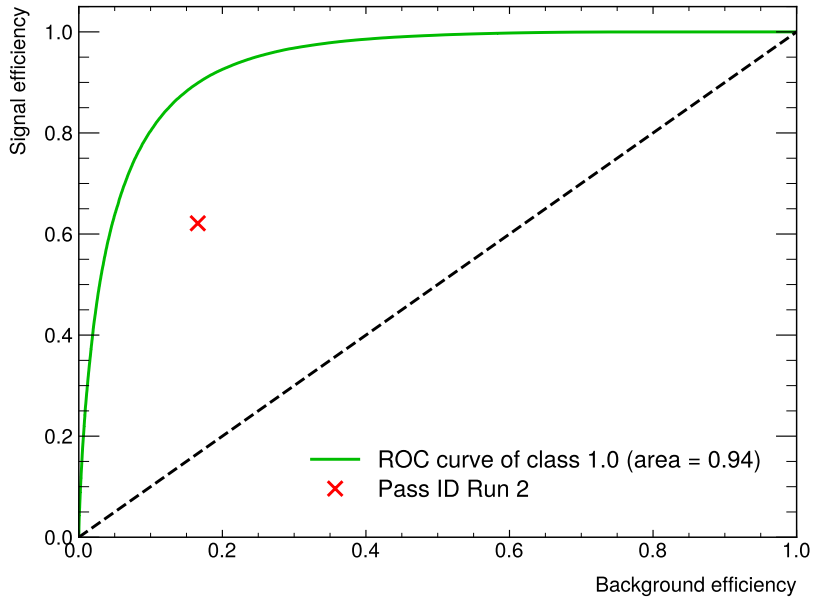

Figure 9.9 – ROC curve of the BDT model. The red mark (pass ID Run 2) indicates the signal and background efficiencies of the Run 2 dedicated merged identification.

tion of the BDT score is performed at this stage. Instead, a common threshold on the BDT output is chosen to match the background efficiency of the Run 2 identi-

fication. This corresponds to requiring a score larger than 0.80, applied uniformly across the three categories. This choice simply guarantees that the same amount of background is retained in the three merged electron categories.

3– A fit to the signal MC samples is used to determine σ_{90}, defined as the smallest $m_{\ell\ell\gamma}$ interval containing 90% of the signal events, S_{90}.

4– The background yield B_{90} is estimated by fitting the data sidebands with the background functions selected by the spurious signal test (see Section 9.5.2) and integrating the resulting probability density function over the previously defined σ_{90} interval.

5– The expected significance is computed for each category and identification working point as $Z_{90} = S_{90}/\sqrt{B_{90}}$.

Table 9.13 reports all the evaluated values for S_{90}, B_{90} for the three merged categories and for the two different identification points. The Z_{90} is the expected Run 3 significance evaluated with the two different ID. The last column reports instead the improvement [%] with respect to when using the Run 2 ID.

Run 2 ID				
Category	B_{90}	S_{90}	Z_{90}	
ee merged low-p_{Tt}	1359.89	30.67	0.83	
ee merged VBF	3.63	1.03	0.54	
ee merged high-p_{Tt}	34.86	3.71	0.63	
BDT Run 3 ID				
Category	B_{90}	S_{90}	Z_{90}	Improvement
ee merged low-p_{Tt}	1379.43	36.67	0.98	18.1%
ee merged VBF	3.91	1.19	0.59	9.3%
ee merged high-p_{Tt}	31.28	4.55	0.81	28.6%

Table 9.13 – Summary of the S_{90}, B_{90} and expected significance in Run 3 Z_{90} evaluated with the two different ID (Run 2 and Run 3 BDT).

Table 9.14 summarises the expected significance Z_{90} in each category for the two identification strategies, anticipating the expected results of Section 9.8. The sizeable impact of the updated merged-*ee* identification on the affected categories is partially mitigated when considering the overall expected sensitivity of the analysis, as the improvement is confined to the merged-electron categories and is therefore diluted by the remaining six categories, for which no changes are applied. The total expected significance is here computed as the quadratic sum of the individual category contributions, providing an approximate estimate of the overall sensitivity: a value of $Z_{90} = 2.27$ is obtained using the Run 2 identification, while $Z_{90} = 2.39$ is achieved with the Run 3 BDT-based approach. In the final results, the expected significance is instead extracted from a simultaneous likelihood fit using the full statistical model implemented in the analysis workspace. This corresponds to an overall increase in the expected analysis sensitivity of approximately 5% when adopting the new merged-electron identification.
Since photons converting at small radii produce signatures that closely resemble those of merged-*ee* objects, the merged-*ee* identification efficiency is measured directly in data

Category	Z_{90} Run 2 ID	Z_{90} BDT Run 3 ID
$\mu\mu$ low $-$ p_{Tt}	1.37	1.37
ee resolved low $-$ p_{Tt}	0.68	0.68
ee merged low $-$ p_{Tt}	0.83	0.98
$\mu\mu$ VBF	0.62	0.62
ee resolved VBF	0.31	0.31
ee merged VBF	0.54	0.59
$\mu\mu$ high $-$ p_{Tt}	0.88	0.88
ee resolved high $-$ p_{Tt}	0.41	0.41
ee merged high $-$ p_{Tt}	0.63	0.81
Total	2.27	2.39

Table 9.14 – Expected significance Z_{90} in the 90% signal window for each category. The total significance is computed as the quadrature sum of the individual categories.

using a tag-and-probe technique applied to FSR photons from radiative Z boson decays ($Z \to \ell\ell\gamma$). Only converted photons reconstructed with exactly two tracks and with a conversion radius $r_{\text{conv}} < 160$ mm—corresponding to conversions within the silicon pixel detector—are considered. The efficiencies are extracted from a simultaneous fit performed in a signal region and in a background-enriched control region. The resulting data-to- MC scale factors are found to be consistent with unity within uncertainties.

9.4 Signal modelling

The signal modelling is based on the signal MC samples described in Section 9.1 and follows the same strategy adopted in the Run 2 $H \to \gamma\gamma$ analysis, detailed in Section 7.4. Unlike the previous case, no parametric dependence on the Higgs boson mass is required (Section 7.4.3), as only a single mass hypothesis (only one MC at $m_H = 125$ GeV) is considered. The Higgs boson mass is fixed at $m_H = 125.09$ GeV $\pm$ 0.24 GeV from the ATLAS and CMS Run 1 combination [13] in the statistical model of the analysis, including the corresponding 0.19% uncertainty as a nuisance parameter affecting the signal peak position.

The expected signal yield for each category N_c can be evaluated from Equation (7.5), now considering $L = 165.4$ fb^{-1} for the integrated luminosity of the partial Run 3 dataset, $\mathcal{BR}(H \to ee\gamma) = 7.20 \times 10^{-5}$ and $\mathcal{BR}(H \to \mu\mu\gamma) = 3.42 \times 10^{-5}$ for the branching ratios.

Table 9.15 and Table 9.16 show the values of the efficiencies ϵ_{ci} and of the yields N_{ci} for each category c and for the different Higgs boson production modes i evaluated using the MC sample generated at $m_H = 125$ GeV. As anticipated in Section 9.1, the $b\bar{b}H$ sample is not explicitly simulated. Its contribution is estimated assuming an acceptance similar to that of the ggF production mode. For each analysis category, as defined in Section 9.2, the expected ggF yield in the signal region is scaled by the ratio $\sigma_{b\bar{b}H}/\sigma_{\text{ggF}} \simeq 0.01$ (see Table 4.1), which is taken as an estimate of the corresponding $b\bar{b}H$ yield. With this procedure, the additional contribution from $b\bar{b}H$ is found to be below 1% in all

analysis categories.

Category	ggF	ggZH	$t\bar{t}H$	VBF	WH	ZH
$\mu\mu$ low $-$ p_{Tt}	5.63	3.52	3.59	3.73	4.06	4.00
ee resolved low $-$ p_{Tt}	2.22	1.25	1.19	1.38	1.44	1.42
ee merged low $-$ p_{Tt}	3.62	2.42	2.44	2.42	2.61	2.56
$\mu\mu$ VBF	0.06	0.16	0.08	1.43	0.02	0.03
ee resolved VBF	0.02	0.04	0.02	0.47	0.01	0.01
ee merged VBF	0.04	0.15	0.07	1.09	0.02	0.02
$\mu\mu$ high $-$ p_{Tt}	0.45	3.47	2.39	0.89	1.26	1.30
ee resolved high $-$ p_{Tt}	0.13	1.03	0.60	0.26	0.36	0.36
ee merged high $-$ p_{Tt}	0.37	2.68	1.94	0.67	0.95	0.96
Total eff. prod. mode	12.54	14.72	12.32	12.34	10.73	10.66

Table 9.15 – Expected reconstruction and selection efficiencies ϵ_{ci} in % for each considered Higgs production mode i and for each category c, at $\sqrt{s} = 13.6$ TeV and $m_H = 125$ GeV. The last row shows the total efficiency per production process summed over all the categories.

Category	ggF	ggZH	$t\bar{t}H$	VBF	WH	ZH	$b\bar{b}H$	Total yield category
$\mu\mu$ low $-$ p_{Tt}	57.3689	0.0935	0.3981	2.9671	1.1361	0.7355	0.5781	63.2772
ee resolved low $-$ p_{Tt}	22.5552	0.0331	0.1322	1.0987	0.4014	0.2603	0.2273	24.7082
ee merged low $-$ p_{Tt}	36.9124	0.0642	0.2708	1.9261	0.7238	0.4717	0.3720	40.7409
$\mu\mu$ VBF	0.5828	0.0042	0.0089	1.1374	0.0063	0.0051	0.0059	1.7505
ee resolved VBF	0.2076	0.0011	0.0024	0.3701	0.0023	0.0019	0.0021	0.5873
ee merged VBF	0.4345	0.0039	0.0077	0.8651	0.0060	0.0045	0.0044	1.3259
$\mu\mu$ high $-$ p_{Tt}	4.6034	0.0919	0.2657	0.7107	0.3549	0.2384	0.0464	6.3114
ee resolved high $-$ p_{Tt}	1.3589	0.0273	0.0667	0.2038	0.1022	0.0661	0.0137	1.8387
ee merged high $-$ p_{Tt}	3.7501	0.0710	0.2155	0.5321	0.2684	0.1772	0.0378	5.0520
Total yield prod. mode	127.7738	0.3901	1.3679	9.8110	3.0013	1.9605	1.2875	145.5922

Table 9.16 – Expected SM signal yields N_{ci} for each production mode i and for each category c, at $\sqrt{s} = 13.6$ TeV, $m_H = 125$ GeV and $L = 165.4$ fb^{-1}. The last column shows the total yields per category summed over all the considered production processes.

The $m_{ll\gamma}$ invariant-mass distribution of the resonant signal process is modelled with a DSCB, as described in Section 7.4.2 in Equation (7.7). The input mass distributions for each category is obtained by summing all Higgs boson production processes (ggF, ggZH, $t\bar{t}H$, VBF, WH, ZH, $b\bar{b}H$), taking their SM cross sections into account. A signal fit using the DSCB is performed on the invariant-mass distribution derived from each MC sample at $m_H = 125$ GeV, separately for each category, within the mass range $m_{ll\gamma} \in [110\text{ GeV}, 140\text{ GeV}]$. All the six parameters of the DSCB are fitted in this first step. A second fit is then performed in which n_{Low} and n_{High} are fixed to the values extracted from the first fit, in order to improve the stability and convergence of the remaining four DSCB parameters.

The fit result to the invariant-mass distribution $m_{ll\gamma}$ for the first category $\mu\mu$ low $-$ p_{Tt} is shown in Figure 9.10. The signal model fits for all the other categories are reported in Appendix C.2. Only the statistically independent sub-sample defined using the `eventNumber` is used to derive the signal model, in order to ensure statistical independence and avoid potential biases; the other sub-sample was used for the merged electron Run 3 BDT

training as described in Section 9.3.1. As a consequence, the number of events shown in the signal-model fit plots corresponds to approximately half of the available simulated sample. For ease of comparison, the normalisation of the fitted distributions is rescaled to the full-sample expectation; however, small differences with respect to the yields reported in Table 9.16 are expected due to the finite size of the samples and the fact that the `eventNumber`-based split does not guarantee an exact 50/50 partition once event weights and filtering effects are taken into account. The DSCB shape parameters evaluated from the fit for each category are also summarised in Table 9.17. The effective signal mass resolutions obtained from the signal modelling are summarised in Table 9.18 for each event category. The table reports the width of the fitted DSCB signal model, σ_{CB}, together with the effective mass resolutions σ_{68} and σ_{90}, defined as half of the smallest invariant-mass interval containing 68% and 90% of the signal events, respectively. The corresponding mass windows centred on the fitted peak position μ_{CB}, used in the evaluation of S_{90} and B_{90}, are also reported. The values of σ_{90} and S_{90} are reported in the summary Table 9.22 to compute the expected significance of the analysis.

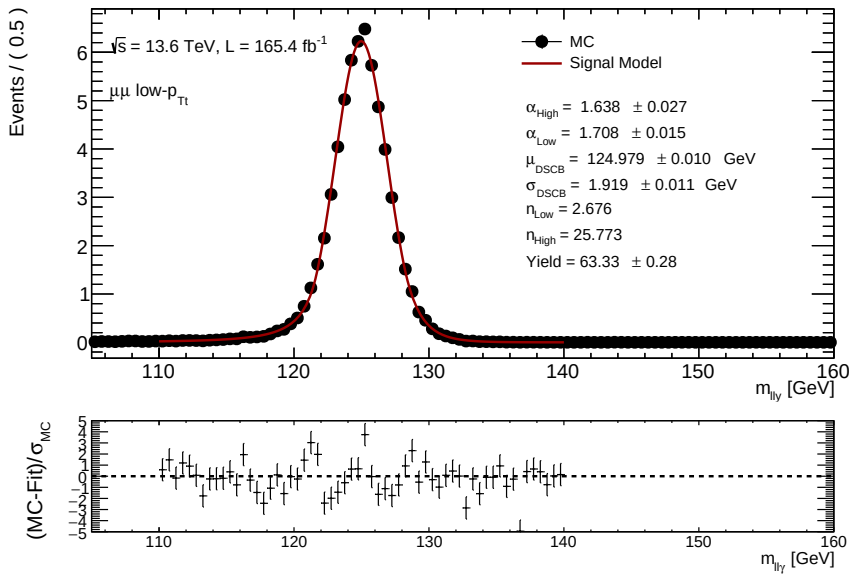

Figure 9.10 – Result of the signal fit for the category $\mu\mu$ low $-$ $\mathrm{p_{Tt}}$ for the MC sample with $\mathrm{m_H} = 125$ GeV: the fitted signal pdf is shown by the red line, the black dots correspond to the MC sample. The values of the fitted parameters of the DSCB are shown in the legend on the right side of the plot. The residuals are shown in the lower part of the plot.

Category	μ_{CB} [GeV]	σ_{CB} [GeV]	α_{Low}	α_{High}	n_{Low}	n_{High}
$\mu\mu$ low $-$ p_{Tt}	124.979±0.010	1.919±0.011	1.71±0.02	1.64±0.03	2.68	25.77
ee resolved low $-$ p_{Tt}	125.168±0.019	2.138±0.021	1.38±0.02	1.66±0.05	5.00	108.89
ee merged low $-$ p_{Tt}	124.920±0.014	2.051±0.015	1.40±0.02	1.85±0.04	7.86	18.06
$\mu\mu$ VBF	124.960±0.042	1.879±0.050	1.47±0.06	1.56±0.09	3.17	9.98
ee resolved VBF	125.109±0.068	1.915±0.071	1.64±0.09	1.86±0.17	4.84	8.49
ee merged VBF	124.961±0.042	1.589±0.034	1.42±0.07	1.54±0.06	5.94	12.19
$\mu\mu$ high $-$ p_{Tt}	125.010±0.032	1.911±0.040	1.57±0.05	1.37±0.06	3.59	20.56
ee resolved high $-$ p_{Tt}	125.037±0.047	1.636±0.049	1.71±0.08	1.53±0.11	3.56	13.09
ee merged high $-$ p_{Tt}	125.121±0.028	1.531±0.030	1.40±0.05	1.82±0.10	6.52	11.68

Table 9.17 – Parameters of the fitted DSCB for the nine analysis categories.

Category	σ_{CB} [GeV]	σ_{68} [GeV]	σ_{90} [GeV]	$[\mu_{CB}-\sigma_{90}, \mu_{CB}+\sigma_{90}]$ [GeV]
$\mu\mu$ low $-$ p_{Tt}	1.92	2.05	3.72	[121.26, 128.70]
ee resolved low $-$ p_{Tt}	2.14	2.34	4.26	[120.91, 129.43]
ee merged low $-$ p_{Tt}	2.05	2.19	3.90	[121.02, 128.82]
$\mu\mu$ VBF	1.88	2.10	3.99	[120.97, 128.95]
ee resolved VBF	1.91	2.02	3.55	[121.55, 128.66]
ee merged VBF	1.59	1.75	3.22	[121.74, 128.19]
$\mu\mu$ high $-$ p_{Tt}	1.91	2.11	3.96	[121.05, 128.97]
ee resolved high $-$ p_{Tt}	1.64	1.77	3.19	[121.84, 128.23]
ee merged high $-$ p_{Tt}	1.53	1.65	2.98	[122.14, 128.11]

Table 9.18 – Effective signal mass resolutions σ_{68} and σ_{90} in each event category, σ_{68} (and σ_{90}) is defined as half of the smallest interval expected to contain 68% (90%) of the signal events for a mass m_H = 125 GeV. They are compared with σ_{CB} obtained from the DSCB fit. In the last column the σ_{90} bin ends around the μ_{CB} peak (necessary for the evaluation of S_{90} and B_{90}) are shown.

9.5 Background modelling

9.5.1 Resonant $H \to \gamma\gamma$ background

In the merged and resolved electron channels, $H \to \gamma\gamma$ events in which one photon converts and is misidentified as either a merged electron or two resolved electrons give rise to a resonant background. Only contributions from the ggF and VBF production modes (accounting for approximately 94% of the total Higgs boson cross section, see Table 4.1) are considered. Other production modes are neglected, as their contributions are negligible. As in the Run 2 analysis, the $H \to \gamma\gamma$ background is parameterised using the same DSCB function and parameters as the signal in each category (see Section 9.4), and is normalised to the $H \to \gamma\gamma$ yields obtained.

In most categories, the $H \to \gamma\gamma$ background sample contains too few events to allow a meaningful parameterisation of its shape after the full event selection. For this reason, the $H \to \gamma\gamma$ background is modelled using the same DSCB function and parameters as the signal in each category (see Section 9.4), and is normalised to the $H \to \gamma\gamma$ yields obtained. The agreement between the signal shape and the $H \to \gamma\gamma$ background shape is verified in each category, as shown in Figure 9.11 for the resolved *ee* categories and in Figure 9.12 for the merged *ee* categories. In the merged channel, the $H \to \gamma\gamma$ background

is predicted to be 17.8% of the signal yield, while in the resolved channel it is only 3.3% of the signal yield.

Category	$H \to \gamma\gamma$ yield	Size w.r.t. to signal [%]
$\mu\mu$ low $-$ p_{Tt}	/	/
ee resolved low $-$ p_{Tt}	0.873	3.5
ee merged low $-$ p_{Tt}	7.556	18.5
$\mu\mu$ VBF	/	/
ee resolved VBF	0.015	2.6
ee merged VBF	0.230	17.3
$\mu\mu$ high $-$ p_{Tt}	/	/
ee resolved high $-$ p_{Tt}	0.018	1.0
ee merged high $-$ p_{Tt}	0.606	12.0

Table 9.19 – Expected yields for each category c, at $\sqrt{s} = 13.6$ TeV, $m_H = 125$ GeV and $L = 165.4$ fb^{-1} for the resonant background $H \to \gamma\gamma$ (ggF+VBF). It does not impact the $\mu\mu$ categories. The last column represents the size of the $H \to \gamma\gamma$ background with respect to the expected signal yield.

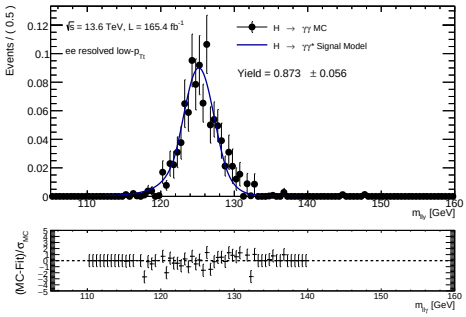

(a) ee resolved low $-$ p_{Tt} category

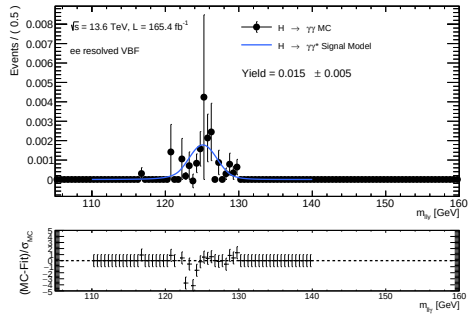

(b) ee resolved VBF

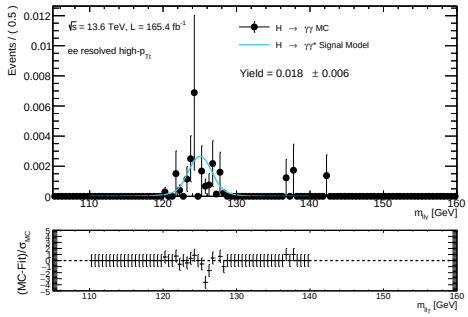

(c) ee resolved high $-$ p_{Tt} category

Figure 9.11 – Comparison of the $H \to \gamma\gamma$ (ggF+VBF) MC events and the signal $H \to \gamma\gamma^*$ DSCB in the ee resolved categories: (a) low $-$ p_{Tt}, (b) VBF, (c) high $-$ p_{Tt}.

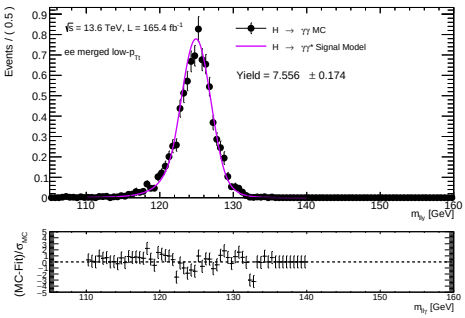

(a) *ee* merged low $-$ p_{Tt} category

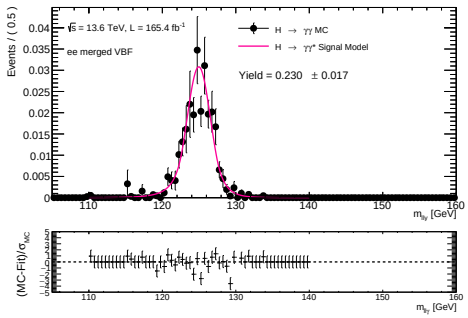

(b) *ee* merged VBF

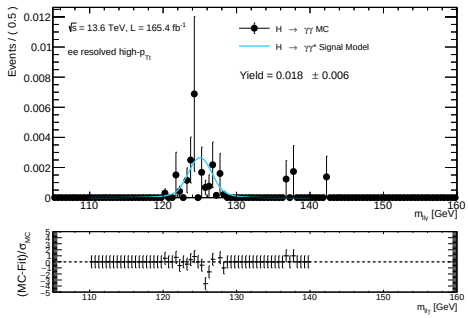

(c) *ee* merged high $-$ p_{Tt} category

Figure 9.12 – Comparison of the $H \to \gamma\gamma$ (ggF+VBF) MC events and the signal $H \to \gamma\gamma^*$ DSCB in the *ee* merged categories: (a) low $-$ p_{Tt}, (b) VBF, (c) high $-$ p_{Tt}.

9.5.2 Non-resonant background

The dominant background in all categories arises from the non-resonant contribution, originating from SM processes that produce a $\gamma^*\gamma$ final state, where the virtual photon converts into a lepton pair. As in the $H \to \gamma\gamma$ analysis described in Section 7.5, this background is modelled using analytic functions chosen independently for each category to minimise potential bias in the fitted signal yields. Preference is given to functions with a smaller number of degrees of freedom that pass the spurious signal test (see Section 7.5.2), thereby reducing statistical uncertainty. The spurious signal test requires a high-statistics template that accurately represents the non-resonant background in the signal region. This template is based on a generator-level SM $\ell\ell\gamma$ high-statistics background sample, described in Section 9.1.2, which is subsequently modified to account for contributions from background sources involving misidentified objects. The steps of the background-modelling strategy are summarised in the following paragraphs.

Background templates

The low-mass $\ell\ell\gamma$ sample (Section 9.1.2) is used to construct the background templates and to determine the analytic description of the non-resonant background through the

spurious signal test. To achieve sufficient statistical precision, a high-statistics fast-simulation MC sample is employed. The full event selection is then applied to produce the $\ell\ell\gamma$ mass distributions in each of the nine categories, which are normalised to the data sidebands (105 GeV $< m_{\ell\ell\gamma} <$ 160 GeV, excluding 120 GeV $< m_{\ell\ell\gamma} <$ 130 GeV).
Before performing the spurious signal tests used to determine the analytic background functions, the agreement between the MC-based templates and the data sidebands is verified in all categories. An example of this validation is shown in Figure 9.13 for the first category $\mu\mu$ low-p_{Tt}.

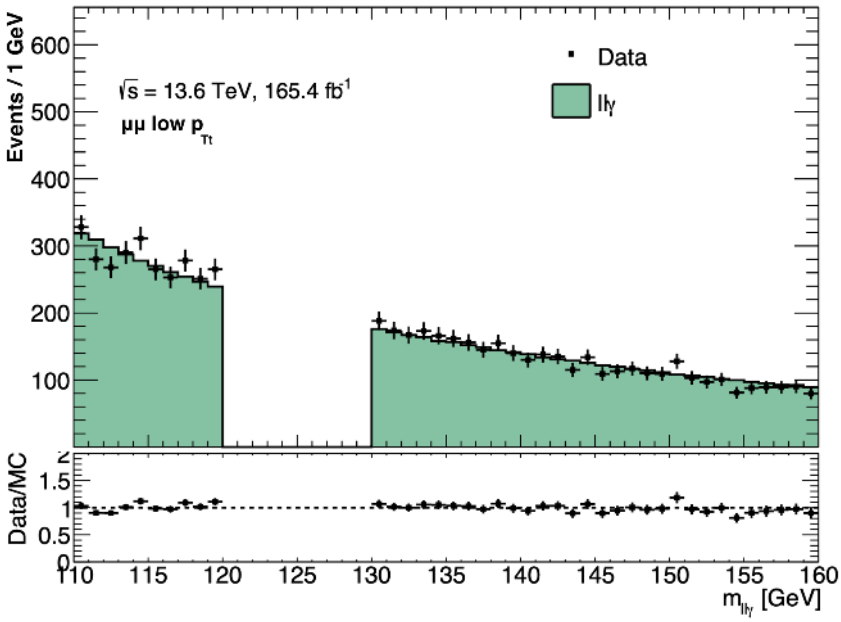

Figure 9.13 – Comparison of the $\ell\ell\gamma$ invariant-mass distribution from data sidebands (black points) and from the MC-based background template (green histogram) in the $\mu\mu$ low $-$ $\mathrm{p_{Tt}}$ category. The lower panel shows the ratio between data and the MC background template.

The background templates are expected to include contributions from processes involving misidentified objects. Studies of backgrounds with non-prompt photons and non-prompt leptons are currently being finalised. A general description of these background sources is therefore provided, and this section will be updated once the studies are completed.

Non-prompt photon background In $\gamma\gamma^*$ events, the photon candidate is a prompt photon, producing a narrow energy cluster in the EM calorimeter and typically being isolated from hadronic activity. In contrast, in $\gamma^* +$ jet events the photon candidate predominantly originates from the decay of a neutral meson, most commonly a π^0, carrying a large fraction of the initiating parton energy. Such candidates generally produce

a broader energy cluster in the EM calorimeter, with non-negligible leakage into the hadronic calorimeter, and are not isolated due to additional energy deposits from nearby particles in the jet.

As a result, photon identification and isolation variables can be exploited to estimate the contribution of $\gamma^* +$ jet events in data using a method equivalent to the standard ABCD technique [181]. Control regions are defined by inverting the photon identification and isolation requirements, allowing the contribution of non-prompt (fake) photon backgrounds in the signal region to be estimated under the assumption of a weak correlation between the two variables.

Non-prompt leptons background The fraction of events containing non-prompt leptons in data is estimated using template fits to the distribution of the subleading lepton isolation variable `topoetcone20`$/E_T$, defined in Section 5.1.7. Templates for prompt leptons are derived from simulated SHERPA $\ell\ell\gamma$ samples, while templates for non-prompt leptons are constructed from events in data that fail the subleading lepton identification requirements.

The non-prompt lepton template contains a residual contamination from prompt leptons failing the identification criteria. This contribution is subtracted using simulated SHERPA $\ell\ell\gamma$ events through an iterative procedure. In the first iteration, the fractions of prompt and non-prompt leptons in the data sidebands are extracted without applying any subtraction. In the second iteration, the prompt lepton contribution failing the identification requirements is subtracted from the non-prompt template using the normalisation factor obtained in the first step, and the template fit is repeated.

Spurious signal test

As described in Section 7.5.2, the spurious signal approach is used to select the functional form employed to model each background template and to evaluate the associated bias, which is assigned as a systematic uncertainty. The $m_{\ell\ell\gamma}$ background shape in each analysis category is modelled using an analytic function whose parameters and normalisation are fitted directly to data. The set of candidate analytic functions includes an exponential function, exponentials of second- and third-order polynomials, Bernstein polynomials of order N, and a power-law function.

For each candidate function, a signal-plus-background fit is performed to the corresponding background template in each category, using the signal model described in Section 9.4. The fit is carried out over the mass range $110 \leq m_{\ell\ell\gamma} \leq 160$ GeV. A scan is then performed by varying the Higgs boson mass hypothesis, m_H, in steps of 1.0 GeV within the interval $120 \leq m_{\ell\ell\gamma} \leq 130$ GeV.

The candidate function that satisfies the spurious signal criteria defined in Section 7.5.2 with the lowest number of degrees of freedom is selected as the background model for the given category. The results of the spurious signal tests are summarised in Table 9.20, which reports the chosen background functions and the corresponding spurious signal yields for all analysis categories.

Category	m_H	N_{sp}	Function	$p(\chi^2)$ [%]	$N_{sp}/\delta N_{sp}$[%]	$N_{sp}/N_{s,exp}$ [%]
$\mu\mu$ low-p_{Tt}	125.0	-5.91	ExpPoly3	91.3	-11.5	-8.6
ee resolved low-p_{Tt}	130.0	-2.26	Power Law	57.3	-7.82	-9.3
ee merged low-p_{Tt}	124.0	3.49	Exponential	32.3	12.6	9.5
$\mu\mu$ VBF	130.0	-0.12	Power Law	45.7	-4.15	-6.4
ee resolved VBF	124.0	-0.11	Power Law	1.72	-9.11	-19.0
ee merged VBF	121.0	-0.07	Power Law	5.19	-5.65	-6.1
$\mu\mu$ high-p_{Tt}	130.0	-1.51	Power Law	65.7	-18.3	-24.1
ee resolved high-p_{Tt}	127.0	-0.43	Power Law	84.5	-10.9	-22.5
ee merged high-p_{Tt}	130.0	0.39	Exponential	76.6	9.48	8.4

Table 9.20 – Spurious signal test results in each category and associated uncertainties. The scan is performed in the range 120-130 GeV in steps of 1.0 GeV. Here N_{sp} is the maximum fitted spurious signal, δN_{sp} is the statistical uncertainty on the fitted signal from a signal+background fit to the background template, and $N_{s,exp}$ is the expected signal yield under the SM assumption. The quoted m_H is the scan point at which the maximum spurious signal is observed. The χ^2 probability is computed from the fit to the background template.

Data sidebands fit for Asimov dataset construction

The selected functions are used in a background only fit on the observed data sidebands, blinding the range $m_{\ell\ell\gamma} \in$ [120 GeV, 130 GeV], to determine the background shape parameters and normalisation factors in order to create an Asimov dataset to estimate the expected results in Section 9.8. The result of the background fit on the invariant mass distribution $m_{\ell\ell\gamma}$ for the first category $\mu\mu$ low-p_{Tt}, is shown in Figure 9.14. The data sideband fits for all the other categories are reported in Appendix C.3. The fitted shape parameters and yields obtained from this background fit are shown in Table 9.21 for each category.

Category	Function	p_0	p_1	p_2	N	B_{90}
$\mu\mu$ low-$\mathrm{p_{Tt}}$	ExpPoly3	-3.79 ± 0.35	3.34 ± 0.59	-3 ± 8	9248 ± 111	1724.1
ee resolved low-$\mathrm{p_{Tt}}$	PowerLaw	-4.63 ± 0.12	/	/	5079 ± 80	1061.3
ee merged low-$\mathrm{p_{Tt}}$	Exponential	-0.022 ± 0.001	/	/	6961 ± 93	1379.4
$\mu\mu$ VBF	PowerLaw	-1.5 ± 1.4	/	/	33.5 ± 6.5	6.4
ee resolved VBF	PowerLaw	-1.3 ± 1.9	/	/	17.4 ± 4.7	2.9
ee merged VBF	PowerLaw	-0.9 ± 1.6	/	/	25.9 ± 5.7	3.9
$\mu\mu$ high-$\mathrm{p_{Tt}}$	PowerLaw	-1.46 ± 0.56	/	/	218 ± 16	41.3
ee resolved high-$\mathrm{p_{Tt}}$	PowerLaw	-2.95 ± 0.82	/	/	104 ± 11	16.4
ee merged high-$\mathrm{p_{Tt}}$	Exponential	-0.010 ± 0.004	/	/	219 ± 17	31.4

Table 9.21 – Values of the parameters describing the background shape for each category, extracted from fits to the data sidebands. The parameter N corresponds to the fitted background yield, while B_{90} is the expected number of background events in the 90% signal window around the peak, σ_{90}, defined in Table 9.18.

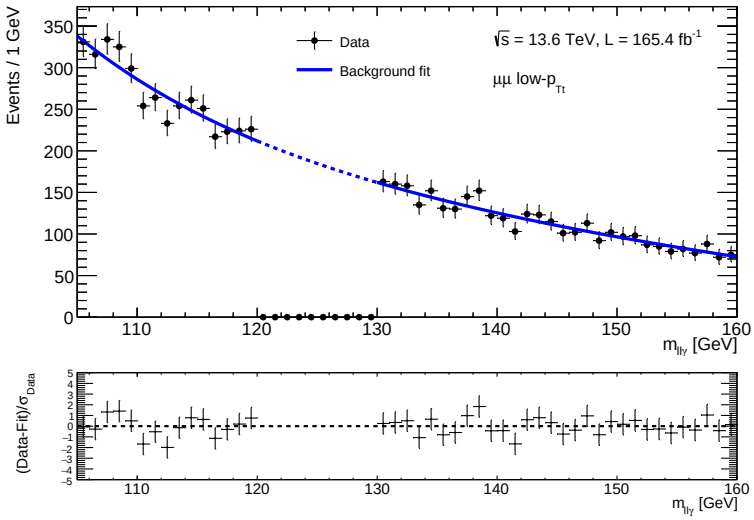

Figure 9.14 – Result of the background fit on data sidebands for the category $\mu\mu$ low-p_{Tt}. The fitted background pdf, in this case an exponential function of a 3rd order polynomial (ExpPoly3), is shown by the blue line; the black dots correspond to the data, blinding the $m_{\ell\ell\gamma} \in [120, 130]$ GeV range. The bottom panels shows the residuals.

9.6 Systematic uncertainties

Systematic uncertainties are being finalized and are not yet included in the workspace and in the expected results.

The previous Run 2 analysis [29] was statistically limited, with a total observed systematic uncertainty on the signal strength measurement of about 11%, corresponding to roughly 35% of the statistical uncertainty. Systematic uncertainties therefore did not play a dominant role in that analysis, and a similar situation is expected for the present Run 3 analysis.

9.7 Statistical model

The signal and background functional forms, together with their corresponding parameters determined in Section 9.4 and Section 9.5, are used to construct the background-only and signal-plus-background likelihood models.
Systematic uncertainties, that will be described in Section 9.6, will be implemented as response terms in the likelihood function (see Section 9.7.1). Uncertainties affecting the signal or background yields and resolutions are modelled with log-normal constraints, while uncertainties affecting the energy scale are modelled with Gaussian constraints. In cases where uncertainties are asymmetric, which is the most common scenario, a single Gaussian-distributed nuisance parameter is employed together with a polynomial

interpolation around $NP = 0$. The response functions used in the analysis are defined as follows:

$$\begin{aligned} F_{\mathrm{G}}(\delta,\theta) &= (1+\delta\,\theta) && \text{gaussian response,} \\ F_{\mathrm{LN}}(\delta,\theta) &= e^{\sqrt{\ln\left(1+\delta^2\right)}\,\theta} && \text{log-normal response,} \\ F_{\mathrm{AS}}(\delta^{\pm},\theta) &= \begin{cases} P_6(\theta;\,\delta^-,0,\delta^+), & \theta \in [\delta^-,\delta^+], \\ F_{\mathrm{LN}}(\delta,\theta), & \text{otherwise,} \end{cases} && \text{asymmetric response.} \end{aligned} \tag{9.1}$$

The best-fit signal strenght μ (the ratio between the observed event yield and the SM expected yield) maximizing the signal-plus-background likelihood is then calculated. Both statistical Δ_{stat} and systematic Δ_{syst} uncertainties are translated into the total uncertainty Δ_{tot} on resulting signal strength. The systematic and statistical components are quantifies by employing likelihood models with statistical uncertainties only, thereby evaluating the statistical uncertainty Δ_{stat}. The systematic uncertainty Δ_{syst} is then calculated as $\Delta_{\mathrm{syst}} = \sqrt{\Delta^2_{\mathrm{tot}} - \Delta^2_{\mathrm{stat}}}$.
The sensitivity is quantified using the profile likelihood ratio method [182] to derive 95% CL_s upper limits on the signal strength under the background-only hypothesis. The *observed* limit is obtained by constraining the parameters of the likelihood model using data, while the *expected* limit is derived from a background-only Asimov dataset ($\mu = 0$) constructed using data sidebands and MC simulation. In addition, a signal-plus-background Asimov dataset ($\mu = 1$) is used to evaluate the expected limit under the assumption of the presence of a SM Higgs boson.
The probability (p-value) of observing data with an equal or greater level of incompatibility with the background-only hypothesis is computed from the test statistic of the profile likelihood method using the asymptotic formulae [182]. The p-value is then converted into an equivalent significance Z, defined such that a Gaussian-distributed variable fluctuating Z standard deviations above its mean corresponds to the same probability p.
In all of the calculations presented above, the Higgs boson mass is fixed to 125.09 GeV. No limits or significances are derived as a function of the Higgs boson mass, since its value has already been precisely measured in other decay channels (for examples the $H \to \gamma\gamma$ analysis presented in Chapter 7) and the sensitivity of the present data set is insufficient to provide additional constraints on the mass in this channel.

9.7.1 Likelihood definition

To construct the likelihood function, the event counts in different invariant-mass bins of $m_{\gamma\gamma^*}$ are assumed to follow Poisson statistics. The Poisson term in the likelihood is combined with the probability density function $f_{\mathrm{c}}(m^i_{\gamma\gamma^*}, \mu, \vec{\theta})$ describing the invariant-mass distribution for each candidate event i. The mass probability density functions are built from the signal and background functional forms introduced in Sections 9.4 and 9.5. The likelihood is extended by the inclusion of constraint terms $G(\theta)$, which encode the

effect of nuisance parameters θ. These nuisance parameters are modelled with Gaussian or log-normal constraints, depending on their role, as described in Section 9.6. Both systematic uncertainties and background-shape parameters are treated as nuisance parameters and are constrained in the likelihood.

The resulting extended likelihood is written as:

$$\mathcal{L}\left(\mu, \vec{\theta} \mid \{m^i_{\gamma\gamma^*}\}_{i=1}^n\right) = \prod_c \left[\frac{e^{-N_c(\mu,\vec{\theta})} N_c^{n_c}(\mu,\vec{\theta})}{n_c!} \prod_{i=1}^{n_c} f_c(m^i_{\gamma\gamma^*}, \mu, \vec{\theta})\right] G(\vec{\theta}). \tag{9.2}$$

Here, μ denotes the signal strength, $\vec{\theta}$ the nuisance parameters, and n_c the observed number of events. The expected event yield N_c is given by the sum of the following contributions:

- the expected number of signal events,

  $$N_c = L \times \mu \times \sigma(pp \to H) \times \mathcal{BR}(H \to \gamma\gamma^*) \times \mathcal{BR}(\gamma^* \to \ell\ell\gamma) \times \epsilon_c,$$

  as described in Section 9.4;
- the number of resonant background events from $H \to \gamma\gamma$, $N_{H\to\gamma\gamma}$;
- the number of non-resonant background events, N_{bkg};
- the spurious signal yield, $N_{\text{spur}}(\theta_{\text{spur}})$, which depends on the spurious signal uncertainty σ_{spur} and is constrained by the corresponding nuisance parameter θ_{spur}.

The probability density function $f_c(m^i_{\gamma\gamma^*}, \mu, \theta)$ is constructed from the component probability density functions f_{sig}, $f_{H\to\gamma\gamma}$, and f_{bkg}, weighted by their corresponding expected event yields $N^{(c)}_{\text{sig}}$, $N^{(c)}_{\text{spur}}$, $N^{(c)}_{H\to\gamma\gamma}$, and $N^{(c)}_{\text{bkg}}$ in each category c:

$$\begin{aligned} f_c(m^i_{\gamma\gamma^*}, \mu, \theta) = \frac{1}{N^{(c)}} \Big[&\left(N^{(c)}_{\text{sig}}(\mu, \theta_{\text{sig}}) + N^{(c)}_{\text{spur}}(\theta_{\text{spur}})\right) \times f^{(c)}_{\text{sig}}(m^i_{\gamma\gamma^*}, \theta_{\text{sig}}) \\ &+ N^{(c)}_{H\to\gamma\gamma}(\theta_{H\to\gamma\gamma}) \times f^{(c)}_{H\to\gamma\gamma}(m^i_{\gamma\gamma^*}) + N^{(c)}_{\text{bkg}} \times f^{(c)}_{\text{bkg}}(m^i_{\gamma\gamma^*}, \theta_{\text{bkg}})\Big]. \end{aligned} \tag{9.3}$$

Here, $N^{(c)}$ denotes the total expected event yield in category c. The yields $N^{(c)}_{\text{sig}}$ correspond to the sum of contributions from all considered Higgs boson production modes (ggF, VBF, WH, ZH, $t\bar{t}H$, and ggZH). The nuisance parameters associated with the signal yields, θ_{sig}, and with the resonant background, $\theta_{H\to\gamma\gamma}$, encode the impact of systematic uncertainties and are treated as fully correlated across categories. In contrast, the nuisance parameters describing the spurious signal, $\theta^{(c)}_{\text{spur}}$, and the background-shape parameters, $\theta^{(c)}_{\text{bkg}}$, are defined independently for each category.

9.7.2 Significance calculation and CL_s limits

To compute the p-value for the background-only hypothesis, the following test statistic is used:

$$q_0 = \begin{cases} -2\ln\dfrac{\mathcal{L}(0,\hat{\hat{\theta}}(0))}{\mathcal{L}(\hat{\mu},\hat{\theta})}, & \hat{\mu} \geq 0, \\ 0, & \hat{\mu} < 0, \end{cases} \tag{9.4}$$

where $\mathcal{L}$ is the likelihood defined in Section 9.7.1, $(\hat{\mu},\hat{\theta})$ are the unconditional maximum-likelihood estimators, and $\hat{\hat{\theta}}(0)$ is the conditional maximum-likelihood estimator of θ for $\mu = 0$. By construction, this one-sided test statistic is sensitive only to upward fluctuations ($\hat{\mu} \geq 0$), while downward fluctuations do not contribute to rejecting the background-only hypothesis.

The p-value is defined as

$$p_0 = \int_{q_{0,\text{obs}}}^{+\infty} f(q_0 \mid 0)\,\mathrm{d}q_0, \tag{9.5}$$

where $f(q_0 \mid 0)$ denotes the probability density of q_0 under the background-only hypothesis. In the asymptotic regime, the distribution of q_0 can be obtained using the Wald approximation [183], which yields

$$-2\ln\frac{\mathcal{L}(0,\hat{\hat{\theta}}(0))}{\mathcal{L}(\hat{\mu},\hat{\theta})} = \frac{\hat{\mu}^2}{\sigma^2} + \mathcal{O}\left(\frac{1}{\sqrt{N}}\right), \tag{9.6}$$

where $\hat{\mu}$ is asymptotically Gaussian distributed with mean zero under the background-only hypothesis, σ is its standard deviation, and N is the sample size. Using this result, the p-value can be expressed as [182]

$$p_0 = 1 - \Phi(\sqrt{q_0}), \tag{9.7}$$

where Φ is the cumulative distribution function of the standard normal distribution. The corresponding significance is defined as

$$Z = \Phi^{-1}(1 - p_0), \tag{9.8}$$

with Φ^{-1} the inverse of the standard normal cumulative distribution function.

To set an upper limit on the signal strength, the following test statistic is employed:

$$\tilde{q}_\mu = \begin{cases} -2\ln\tilde{\lambda}(\mu), & \hat{\mu} \leq \mu, \\ 0, & \hat{\mu} > \mu, \end{cases} \tag{9.9}$$

where the modified profile likelihood ratio $\tilde{\lambda}(\mu)$ is defined as

$$\tilde{\lambda}(\mu) = \begin{cases} \dfrac{\mathcal{L}(\mu, \hat{\hat{\theta}}(\mu))}{\mathcal{L}(\hat{\mu}, \hat{\theta})}, & \hat{\mu} \geq 0, \\ \dfrac{\mathcal{L}(\mu, \hat{\hat{\theta}}(\mu))}{\mathcal{L}(0, \hat{\theta}(0))}, & \hat{\mu} < 0. \end{cases} \tag{9.10}$$

By construction, the test statistic vanishes for $\hat{\mu} > \mu$, such that upward fluctuations of the signal estimator beyond the tested value μ do not constitute evidence against the signal hypothesis. In addition, the signal strength is constrained to be non-negative, which is reflected in the use of the background-only hypothesis ($\mu = 0$) in the denominator when $\hat{\mu} < 0$.

Based on this test statistic, the local p_μ-value is defined as

$$p_\mu = \int_{\tilde{q}_{\mu,\mathrm{obs}}}^{+\infty} f(\tilde{q}_\mu \mid \mu)\, \mathrm{d}\tilde{q}_\mu \equiv CL_{s+b}. \tag{9.11}$$

To avoid overly aggressive exclusion in the presence of limited sensitivity, the modified frequentist CL_s prescription is adopted:

$$CL_s = \frac{CL_{s+b}}{CL_b}, \tag{9.12}$$

where

$$CL_b = \int_{\tilde{q}_{\mu,\mathrm{obs}}}^{+\infty} f(\tilde{q}_\mu \mid 0)\, \mathrm{d}\tilde{q}_\mu \tag{9.13}$$

is the p-value for the background-only hypothesis.

In the asymptotic regime, the Wald approximation [183] can be used to derive a closed-form expression for CL_s [182]:

$$CL_s = \frac{1 - F(\tilde{q}_\mu \mid \mu)}{1 - F(\tilde{q}_\mu \mid 0)}, \tag{9.14}$$

where the cumulative distribution function F is given by

$$F(\tilde{q}_\mu \mid \mu) = \begin{cases} \Phi\left(\sqrt{\tilde{q}_\mu}\right), & 0 < \tilde{q}_\mu \leq \mu^2/\sigma^2, \\ \Phi\left(\dfrac{\tilde{q}_\mu + \mu^2/\sigma^2}{2\mu/\sigma}\right), & \tilde{q}_\mu > \mu^2/\sigma^2, \end{cases} \tag{9.15}$$

As discussed above, the result depends on the determination of σ, the standard deviation of the estimator $\hat{\mu}$. While σ can in principle be obtained from ensembles of pseudo-experiments, this approach is computationally expensive. Instead, an alternative method based on the properties of the Asimov dataset is employed, following the prescription derived in [182].

A hypothesised signal strength μ is excluded at the 95% confidence level when $CL_s < 0.05$. Accordingly, different values of μ are tested by constructing an Asimov dataset for each assumed signal strength, and the largest value of μ that cannot be excluded by the data is taken as the 95% confidence level upper limit.

9.8 Results

9.8.1 Expected results

A summary of the expected signal and background yields (S_{90}, B_{90} and $H \to \gamma\gamma_{90}$ for the resonant background) in the smallest window containing 90% of signal events $\sigma_{90}^{ll\gamma}$ obtained in Sections 9.4 and 9.5, are shown in Table 9.22 for each category. The B_{90} and $H \to \gamma\gamma_{90}$ are summed up to obtain the total background B_{90}^{tot} for the calculation of the expected purity $f_{90} = S_{90}/(S_{90} + B_{90}^{\text{tot}})$ and of the expected significance $Z_{90} = S_{90}/\sqrt{B_{90}^{\text{tot}}}$.

Category	$\sigma_{90}^{ll\gamma}$[GeV]	$[\mu_{CB} - \sigma_{90}, \mu_{CB} + \sigma_{90}]$	S_{90}	B_{90}	$H \to \gamma\gamma_{90}$	f_{90}[%]	Z_{90}
$\mu\mu$ low $-$ p_{Tt}	3.72	[121.26, 128.70]	56.95	1724.15	/	3.2	1.37
ee resolved low $-$ p_{Tt}	4.26	[120.91, 129.43]	22.24	1061.31	0.79	2.1	0.68
ee merged low $-$ p_{Tt}	3.90	[121.02, 128.82]	36.67	1379.43	6.80	2.6	0.98
$\mu\mu$ VBF	3.99	[120.97, 128.95]	1.58	6.40	/	19.8	0.62
ee resolved VBF	3.55	[121.55, 128.66]	0.53	2.93	0.01	15.3	0.31
ee merged VBF	3.22	[121.74, 128.19]	1.19	3.91	0.21	22.4	0.59
$\mu\mu$ high $-$ p_{Tt}	3.96	[121.05, 128.97]	5.68	41.27	/	12.1	0.88
ee resolved high $-$ p_{Tt}	3.19	[121.84, 128.23]	1.65	16.39	0.02	9.1	0.41
ee merged high $-$ p_{Tt}	2.98	[122.14, 128.11]	4.55	31.28	0.54	12.5	0.81

Table 9.22 – Summary of the categorisation performance evaluated in the smallest $m_{\ell\ell\gamma}$ window containing 90% of the signal events. The window width is denoted by $\sigma_{90}^{\ell\ell\gamma}$, while S_{90}, B_{90} and $H \to \gamma\gamma_{90}$ represent the expected numbers of signal events, non-resonant background events, and resonant $H \to \gamma\gamma$ background events within this window, respectively. The signal fraction $f_{90} = S_{90}/(S_{90} + B_{90} + H \to \gamma\gamma_{90})$ and the expected significance Z_{90} are also reported.

Information from all analysis categories, including the signal model, the resonant background, and the non-resonant background, is combined into a single statistical model to evaluate the expected significance and the expected upper limit on the signal strength. For the merged electrons categories, the new Run 3 BDT identification working point is employed. The signal model parameters are fixed in the fit to the values determined in Section 9.4, while the non-resonant background parameters are left free to float, with initial values taken from the data sideband fits described in Section 9.5.

An example of the invariant mass distribution $m_{\ell\ell\gamma}$ for the $\mu\mu$ low-p_{Tt} category is shown in Figure 9.15. The signal-plus-background model constructed under the SM hypothesis ($\mu = 1$) and fitted to the data sidebands is overlaid, with the signal region $m_{\ell\ell\gamma} \in [120, 130]$ GeV blinded.

The expected 95% confidence level upper limit on the Higgs boson production cross-

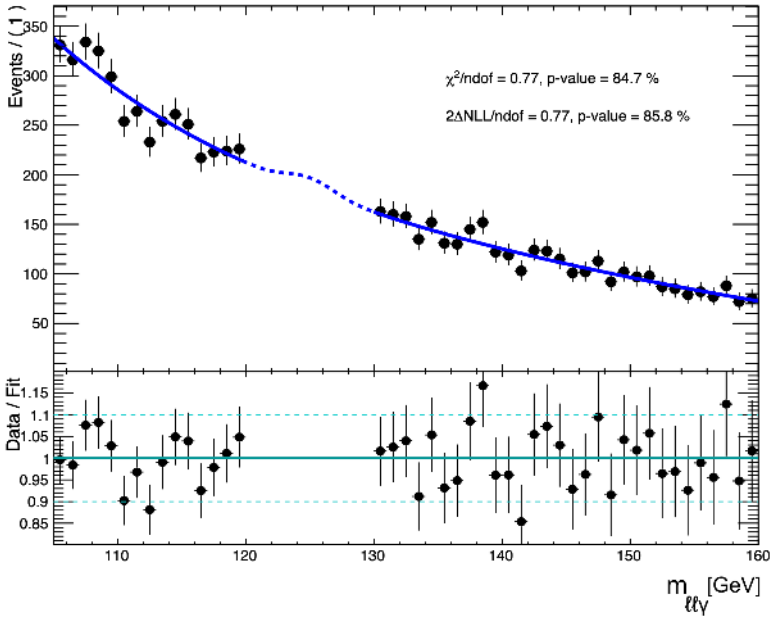

Figure 9.15 – Invariant mass distribution $m_{\ell\ell\gamma}$ for the $\mu\mu$ low-p_{Tt} category. The signal-plus-background model (blue line) from the signal-plus-background workspace constructed under the SM hypothesis ($\mu = 1$) and fitted to the data sidebands is overlaid, with the signal region $m_{\ell\ell\gamma} \in [120, 130]$ GeV blinded.

section times the $H \to \ell\ell\gamma$ branching ratio in the $m_{\ell\ell} < 30$ GeV region is found to be 1.65 times the SM prediction when evaluated using a signal-plus-background Asimov dataset ($\mu = 1$), considering statistical uncertainties only. In the absence of a SM Higgs boson signal, the expected upper limit derived from a background-only Asimov dataset ($\mu = 0$) is 0.70 times the SM prediction, again considering statistical uncertainties only. The expected signal strength is extracted by fitting a signal-plus-background Asimov dataset constructed under the SM hypothesis ($\mu = 1$). The best-fit value obtained from this procedure, considering statistical uncertainties only, is:

$$\mu_{\mathrm{exp}} = 1.00^{+0.41}_{-0.40}\,(\mathrm{stat.}) \tag{9.16}$$

The combined expected significance derived from the likelihood fit is $Z = 2.53\,\sigma$, accounting for statistical uncertainties only. A combination with the corresponding Run 2 search performed by ATLAS is foreseen and is expected to further enhance the sensitivity of the analysis. For reference, the full Run 2 search, based on an integrated luminosity of 139 fb^{-1} [29], provided evidence for the $H \to \ell\ell\gamma$ process with an observed (expected) significance of 3.2σ (2.1σ).

10 | Conclusions

This thesis presents three analyses based on proton–proton collision data recorded by the ATLAS detector, exploiting the full Run 2 dataset collected between 2015 and 2018 at a centre-of-mass energy of $\sqrt{s} = 13$ TeV, corresponding to an integrated luminosity of 140 fb^{-1}, as well as data recorded during the first part of Run 3 between 2022 and 2024 at an increased centre-of-mass energy of $\sqrt{s} = 13.6$ TeV, amounting to an integrated luminosity of about 165 fb^{-1}. The analyses focus on a detailed investigation of the Higgs boson within the SM, through the precision measurement of one of its fundamental parameters, the Higgs boson mass m_H, and the search for a rare decay mode not yet observed, namely the decay into a low-mass dilepton system accompanied by a photon.
The first analysis focuses on the precision measurement of the Higgs boson mass in the diphoton decay channel, $H \to \gamma\gamma$, using the full Run 2 dataset. The measured m_H, extracted from a fit to the diphoton invariant mass distribution in data, is [14]:

$$m_H^{\gamma\gamma,\text{Run 2}} = 125.17 \pm 0.11\ (\text{stat.}) \pm 0.09\ (\text{syst.})\,\text{GeV} = 125.17 \pm 0.14\,\text{GeV}.$$

This result represents a significant improvement over the previous ATLAS measurement in this channel. The increased precision is driven by both the use of the full Run 2 dataset, which reduces the statistical uncertainty by approximately a factor of two, and by major advances in the calibration of the photon energy response, which lower the dominant systematic uncertainty by nearly a factor of four with respect to the earlier publication based on 36 fb^{-1} of Run 2 data [15], $m_H^{36\,\text{fb}^{-1}} = 124.93 \pm 0.21\ (\text{stat.}) \pm 0.34\ (\text{syst.})\,\text{GeV}$. As a result of the improved electron and photon energy scale determination, the measurement of the Higgs boson mass in the diphoton channel is now statistically limited.
In the same analysis, a combination with the corresponding measurement by ATLAS using 7 and 8 TeV pp collision data results in a Higgs boson mass measurement of [14]:

$$m_H^{\gamma\gamma,\text{Run 1+2}} = 125.22 \pm 0.11\ (\text{stat.}) \pm 0.09\ (\text{syst.})\,\text{GeV} = 125.22 \pm 0.14\,\text{GeV}.$$

With a relative uncertainty of approximately 1.1 per mille, this result represented, at the time of its publication, the most precise determination of the Higgs boson mass from a single decay channel and remains a benchmark for precision measurements in the diphoton final state.
The second analysis consists of the combination of the Higgs boson mass measurements obtained by ATLAS in the $H \to ZZ^* \to 4\ell$ [18] and $H \to \gamma\gamma$ [14] decay channels, the two highest-resolution final states used for Higgs boson mass measurements. The

result is based on 140 fb^{-1} of proton-proton collision data collected by the ATLAS detector during LHC Run 2 at a centre-of-mass energy of 13 TeV combined with the Run 1 ATLAS mass measurement, performed at centre-of-mass energies of 7 and 8 TeV, yielding a Higgs boson mass of [19]

$$m_H^{\gamma\gamma+4\ell,\text{Run 1+2}} = 125.11 \pm 0.09\ (\text{stat.}) \pm 0.06\ (\text{syst.})\,\text{GeV} = 125.11 \pm 0.11\,\text{GeV}.$$

This combined ATLAS measurement achieves a precision of 0.9 per mille on this fundamental parameter of the SM of particle physics. At present, this result represents the most precise determination of the Higgs boson mass. All these measurements are in excellent agreement with each other and with the combined ATLAS and CMS Higgs boson mass determination from Run 1 data, $m_H^{\text{Run 1, ATLAS+CMS}} = 125.09 \pm 0.24$ GeV [13].
The third analysis consists of a search for the rare SM Higgs boson decay into a low-mass dilepton system accompanied by a photon, $H \to \ell\ell\gamma$, with $\ell = e, \mu$, using 165 fb^{-1} of pp collision data collected by the ATLAS detector during the first part of Run 3 at a centre-of-mass energy of $\sqrt{s} = 13.6$ TeV. The search targets the low-mass dilepton region, $m_{\ell\ell} < 30$ GeV, where the decay is dominated by contributions mediated by an off-shell photon, $H \to \gamma^*\gamma$, where the γ^* subsequently converts into the dilepton pair.
The analysis is currently under ATLAS internal review. While the finalisation of the systematic uncertainties evaluation is still ongoing, they are expected to have a limited impact on the overall sensitivity. For this reason, the preliminary expected results based on statistical uncertainties only are presented in this thesis.
The expected 95% confidence level upper limit on the Higgs boson production cross section times the $H \to \ell\ell\gamma$ branching ratio in the $m_{\ell\ell} < 30$ GeV region is found to be 1.65 times the SM prediction when evaluated using a signal-plus-background Asimov dataset ($\mu = 1$), considering statistical uncertainties only. In the absence of a SM Higgs boson signal, the corresponding expected upper limit derived from a background-only Asimov dataset ($\mu = 0$) is 0.70 times the SM prediction.
The expected signal strength is extracted by fitting a signal-plus-background Asimov dataset constructed under the SM hypothesis ($\mu = 1$). The best-fit value obtained from this procedure, considering statistical uncertainties only, is:

$$\mu_{\text{exp}} = 1.00^{+0.41}_{-0.40}\,(\text{stat.}).$$

The corresponding expected significance is $2.53\,\sigma$. A combination with the corresponding Run 2 search performed by ATLAS is foreseen and is expected to further enhance the sensitivity of the analysis. For reference, the full Run 2 search, based on an integrated luminosity of 139 fb^{-1} [29], provided evidence for the $H \to \ell\ell\gamma$ process with an observed (expected) significance of 3.2σ (2.1σ).
Studies of the ATLAS detector performance are also presented, including the training, maintenance, and optimisation of the multivariate Monte Carlo–based energy calibration for electrons and photons in Run 2 and Run 3, as well as dedicated studies of the identification of merged electrons from low-mass dilepton systems, which are crucial for the $H \to \ell\ell\gamma$ search.

Appendices

A Additional material for Monte Carlo-based energy calibration

A.1 Linearity as a function of input variables for Run 2 MVA

This section contains additional plots showing the linearity of the Run 2 MVA calibration as a function of various input variables. Figure A.1 shows the linearity as a function of E_{raw}, the total energy deposited in the accordion calorimeter, and f_0, the ratio of the energy deposited in the presampler to that in the accordion. Figure A.2 shows the linearity as a function of η with respect to the cell edge and ϕ with respect to the lead absorber. In all cases, the MVA calibration recovers linearity across the full range of these variables.

A.2 Linearity as a function of pileup for Run 3 MVA

Figure A.3 shows the linearity as a function of μ (average number of pp interactions per bunch crossing) for each particle type, dividing in barrel and endcap regions (left column) and in transverse momentum (right column). The linearity is expressed using the mean of the smallest interval containing 10% of the events of the $E_{\text{calib}}/E_{\text{true}}$ distribution. The MVA calibration recovers linearity across the full range of μ for all particle types, pseudorapidity regions and transverse momentum ranges.

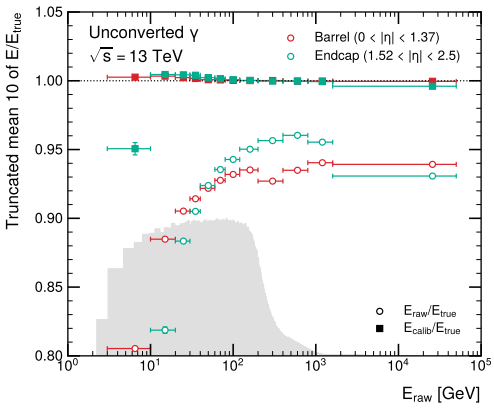

(a) Unconverted γ, vs E_{raw}

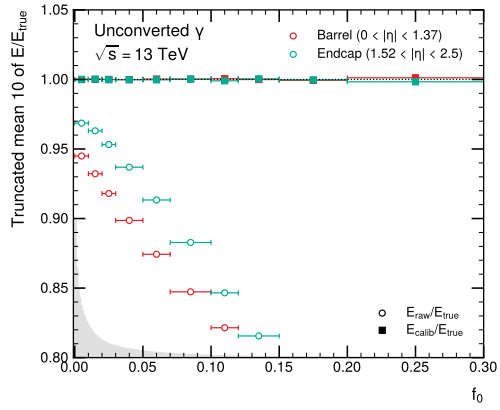

(b) Unconverted γ, vs f_0

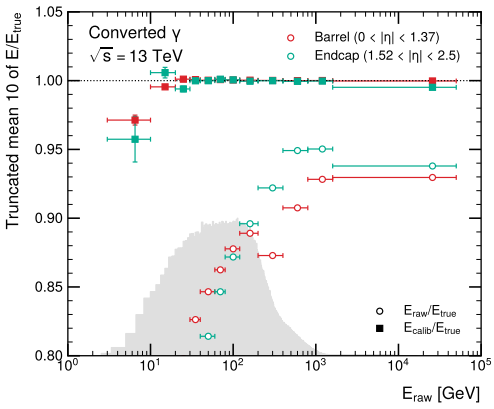

(c) Converted γ, vs E_{raw}

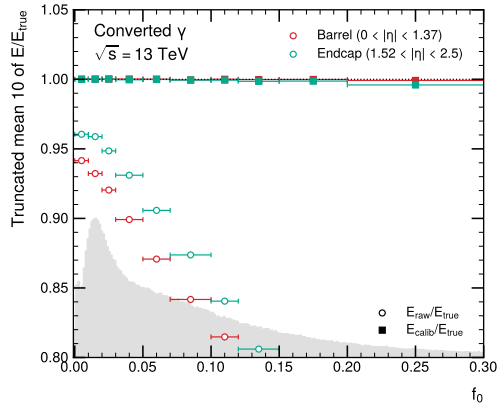

(d) Converted γ, vs f_0

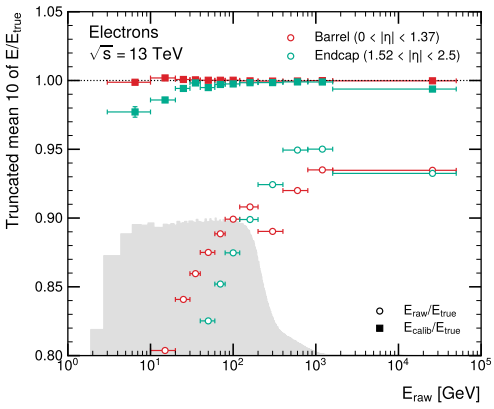

(e) Electrons, vs E_{raw}

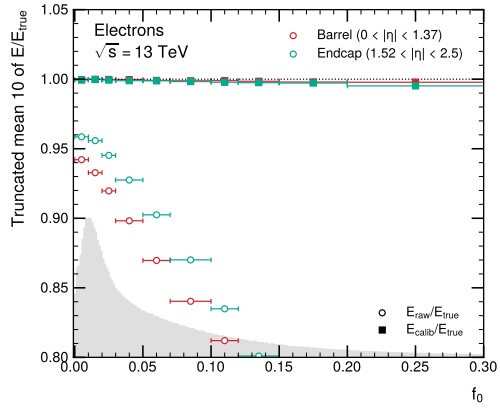

(f) Electrons, vs f_0

Figure A.1 – Linearity for unconverted photons (a,b), converted photons (c,d) and electrons (e,f), expressed using the mean of the smallest interval containing 10% of the events of the $E_{\text{calib}}/E_{\text{true}}$ and $E_{\text{raw}}/E_{\text{true}}$ distributions. For each particle type, the linearity is shown as a function of the total raw cluster energy in the accordion E_{raw} (left) and f_0 (right), the ratio of the energy in the presampler to the energy in the accordion. The MVA calibration recovers linearity across the full range of these variables. Pseudorapidity regions used: barrel $0 < |\eta| < 1.37$ (red), endcap $1.52 < |\eta| < 2.5$ (green).

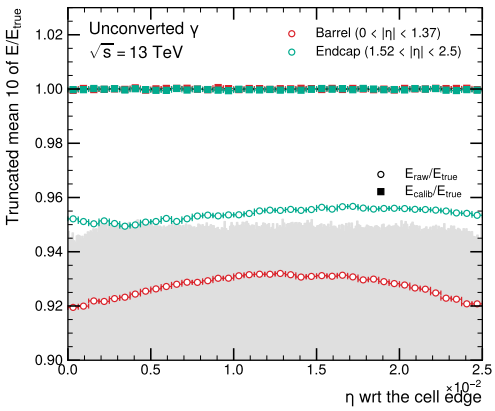

(a) Unconverted γ, vs η wrt the cell edge

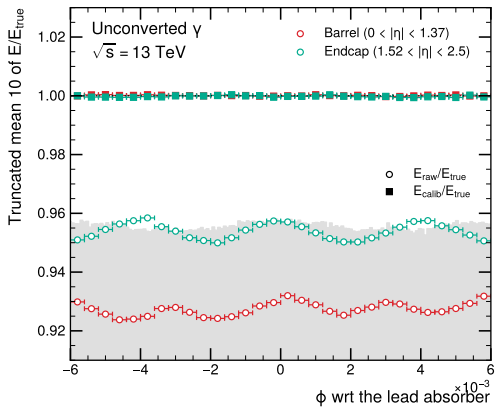

(b) Unconverted γ, vs ϕ wrt the lead absorber

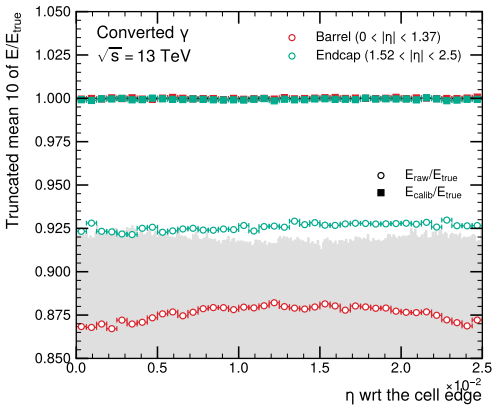

(c) Converted γ, vs η wrt the cell edge

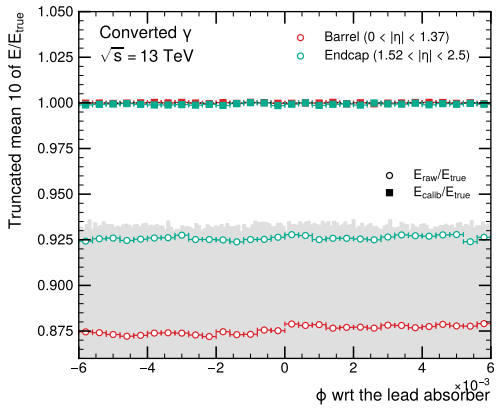

(d) Converted γ, vs ϕ wrt the lead absorber

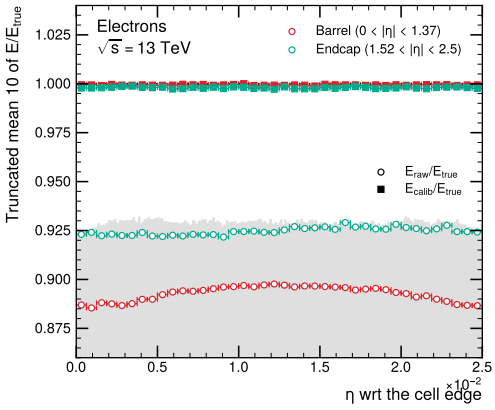

(e) Electrons, vs η wrt the cell edge

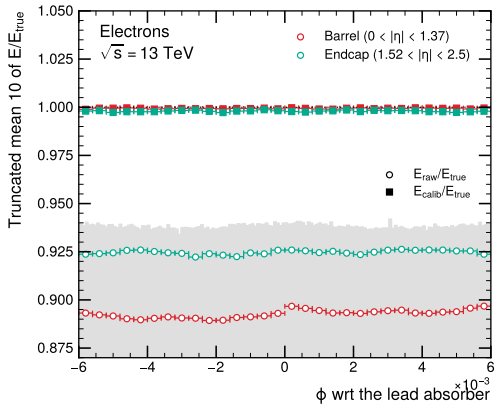

(f) Electrons, vs ϕ wrt the lead absorber

Figure A.2 – Linearity for unconverted photons (a,b), converted photons (c,d) and electrons (e,f), expressed using the mean of the smallest interval containing 10% of the events of the $E_{\text{calib}}/E_{\text{true}}$ and $E_{\text{raw}}/E_{\text{true}}$ distributions. For each particle type, the linearity is shown as a function of the η with respect to the cell edge (left) and ϕ with respect to the lead absorber (right). The MVA calibration recovers linearity across the full range of these variables. Pseudorapidity regions used: barrel $0 < |\eta| < 1.37$ (red), endcap $1.52 < |\eta| < 2.5$ (green).

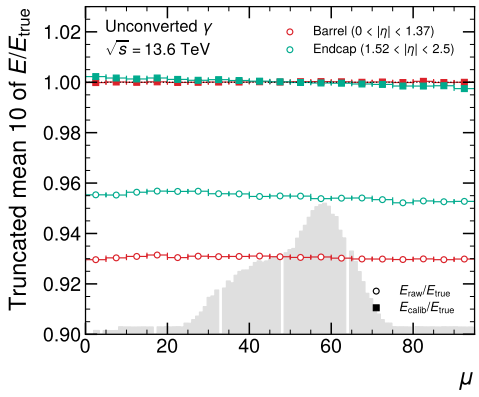

(a) Unconverted γ, vs μ

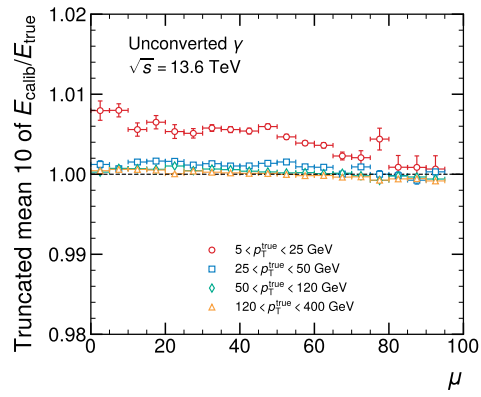

(b) Unconverted γ, vs μ

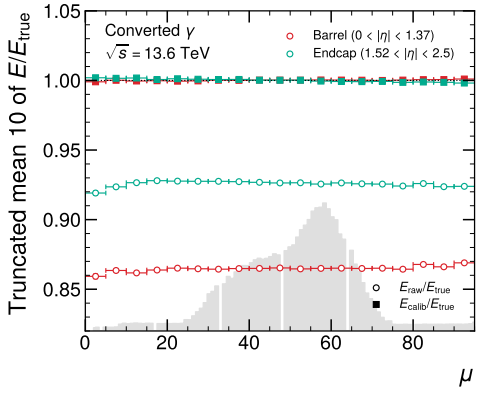

(c) Converted γ, vs μ

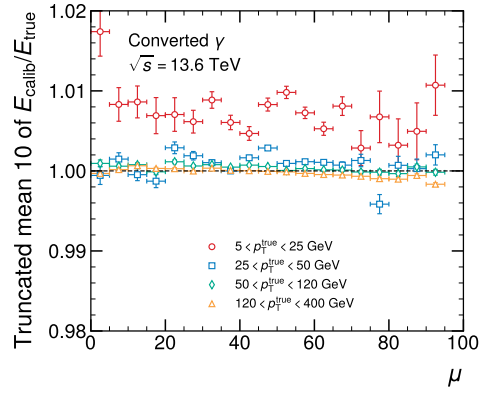

(d) Converted γ, vs μ

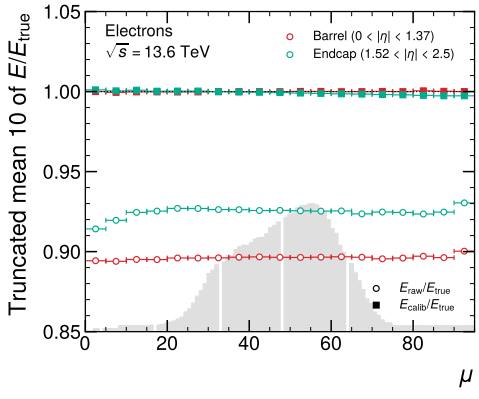

(e) Electrons, vs μ

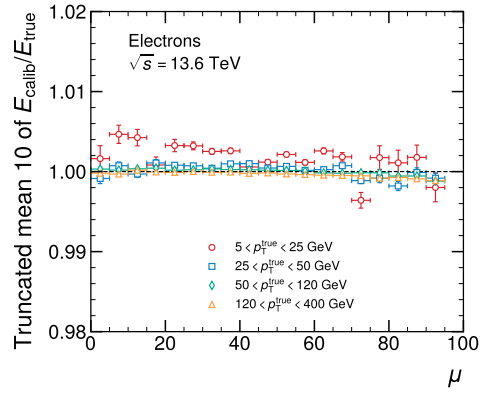

(f) Electrons, vs μ

Figure A.3 – Linearity for unconverted photons, converted photons and electrons, expressed using the mean of the smallest interval containing 10% of the events of the $E_{\text{calib}}/E_{\text{true}}$ distribution. For each particle type, the linearity is shown as a function of μ (average number of pp interactions per bunch crossing), dividing in barrel and endcap regions (left column) and in transverse momentum (right column). Pseudorapidity regions used: barrel $0 < |\eta| < 1.37$, endcap $1.52 < |\eta| < 2.5$. p_{T} ranges: 5-25 GeV, 25-50 GeV, 50-120 GeV, 120-400 GeV.

B Additional material for the Higgs boson mass analysis in the $H \to \gamma\gamma$ channel

B.1 Signal efficiencies

Table B.1 show the values of the efficiencies ϵ_{ci} for each category c and for the different Higgs boson production modes i evaluated using the MC sample generated at $m_H = 125$ GeV.

Category	ggF	VBF	WH	ZH	ggZH	$t\bar{t}H$	$b\bar{b}H$	tHbj	tWH
UU, Central-barrel, high p_{Tt}	0.0017	0.0085	0.014	0.0069	0.023	0.020	0.000 90	0.011	0.025
UU, Central-barrel, medium p_{Tt}	0.0050	0.018	0.026	0.014	0.032	0.025	0.0033	0.016	0.030
UU, Central-barrel, low p_{Tt}	0.055	0.038	0.062	0.031	0.025	0.034	0.066	0.023	0.035
UU, Outer-barrel, high p_{Tt}	0.0013	0.0064	0.011	0.0056	0.016	0.013	0.000 70	0.0069	0.017
UU, Outer-barrel, medium p_{Tt}	0.0053	0.019	0.029	0.015	0.032	0.024	0.0030	0.021	0.026
UU, Outer-barrel, low p_{Tt}	0.057	0.039	0.067	0.033	0.027	0.034	0.067	0.028	0.036
UU, Endcap	0.048	0.047	0.092	0.046	0.044	0.036	0.049	0.047	0.036
Conv, Central-barrel, high p_{Tt}	0.0011	0.0054	0.0084	0.0043	0.014	0.012	0.000 40	0.0080	0.014
Conv, Central-barrel, med p_{Tt}	0.0031	0.011	0.016	0.0084	0.020	0.016	0.0022	0.011	0.020
Conv, Central-barrel, low p_{Tt}	0.033	0.023	0.038	0.019	0.015	0.021	0.040	0.014	0.022
Conv, Outer-barrel, high p_{Tt}	0.0014	0.0070	0.012	0.0062	0.017	0.014	0.000 80	0.011	0.021
Conv, Outer-barrel, med p_{Tt}	0.0056	0.020	0.031	0.016	0.033	0.026	0.0030	0.019	0.028
Conv, Outer-barrel, low p_{Tt}	0.060	0.041	0.071	0.036	0.028	0.035	0.070	0.032	0.034
Conv, Endcap	0.079	0.078	0.16	0.078	0.073	0.060	0.077	0.082	0.058
Total	0.36	0.36	0.32	0.32	0.40	0.37	0.38	0.33	0.40

Table B.1 – Expected reconstruction and selection efficiencies ϵ_{ci} for each Higgs production mode i and category c, at $\sqrt{s} = 13$ TeV and $m_H = 125$ GeV. The last row shows the total efficiency per production process summed over all categories.

B.2 Yield parametrisation

This section contains additional plots showing the signal-yield parametrisation as a function of the Higgs boson mass for the UU, Central-barrel, low-p_{Tt} category for all production modes considered in the analysis: ggF, VBF, WH, ZH, ggZH and $t\bar{t}H$ (in Figure B.1), tHbj and tWH (in Figure B.2). The $b\bar{b}H$ production mode is not shown, as no MC samples were available for this process at Higgs boson masses different from the nominal value of 125 GeV.

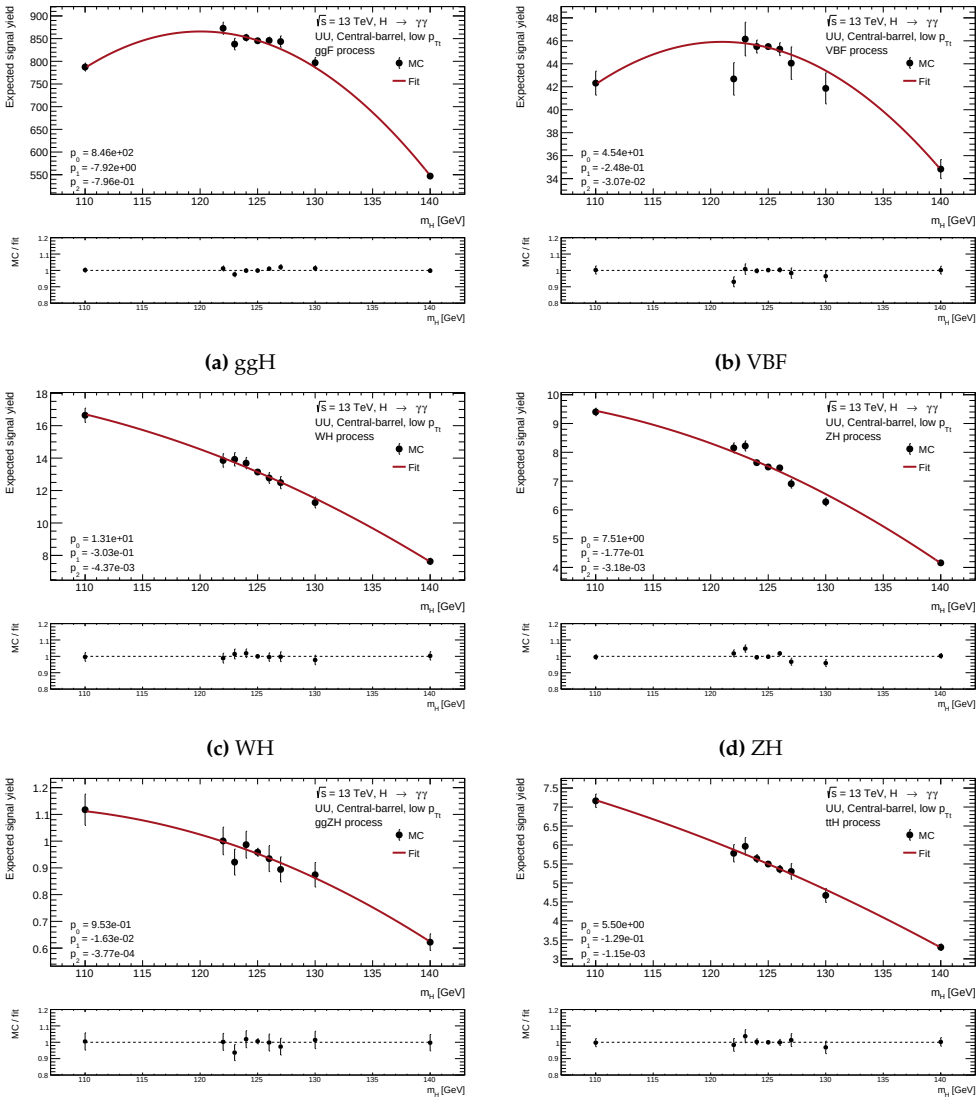

(a) ggH **(b)** VBF

(c) WH **(d)** ZH

(e) ggZH **(f)** $t\bar{t}H$

Figure B.1 – Yield parametrisation as a function of m_H for the UU, Central-barrel, low-p_{Tt} category in the ggF (a), VBF (b), WH (c), ZH (d), ggZH (e), $t\bar{t}H$ (f) production modes. The black points represent the expected signal yields extracted from the nine MC samples generated at different Higgs-boson masses, while the red curve shows the fitted second-degree polynomial. The fitted values of the polynomial parameters are listed in the bottom-left corner of the plot.

B.3 Signal model fits

This section contains additional plots with respect to Section 7.4.2, showing the signal model fits for the 14 categories used in the Higgs boson mass analysis in the $H \to \gamma\gamma$

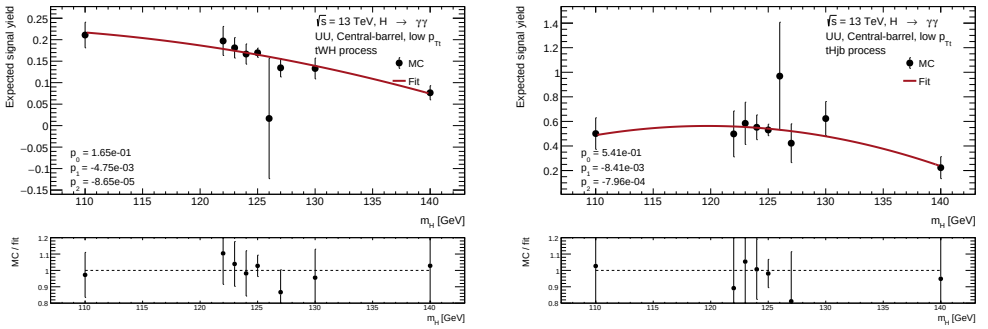

(a) tWH **(b)** tHbj

Figure B.2 – Yield parametrisation as a function of m_H for the UU, Central-barrel, low-p_{Tt} category in the tWH (a), tHbj (b) production modes. The black points represent the expected signal yields extracted from the nine MC samples generated at different Higgs-boson masses, while the red curve shows the fitted second-degree polynomial. The fitted values of the polynomial parameters are listed in the bottom-left corner of the plot.

channel. The fits are shown for the nominal Higgs boson mass of 125 GeV in Figures B.3 to B.5. For the UU, Central-barrel, low-p_{Tt} category the fits are also shown for all the other generated m_H samples in Figures B.6 and B.7.

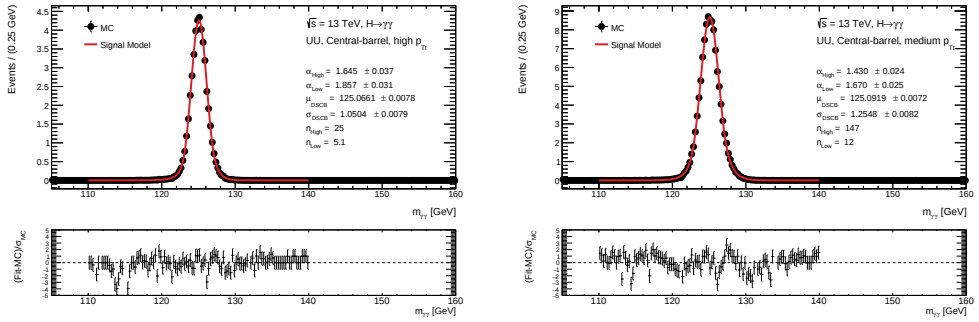

(a) **(b)**

Figure B.3 – Result of the *single fit* for the categories UU, Central-barrel, high p_{Tt} (a), medium p_{Tt} (b): the fitted signal pdf is shown by the red line, the black dots correspond to the MC sample at $m_H = 125$ GeV. The values of the fitted parameters of the DSCB are shown in the legend on the right side of the plot. The residuals are shown in the lower part of the plot.

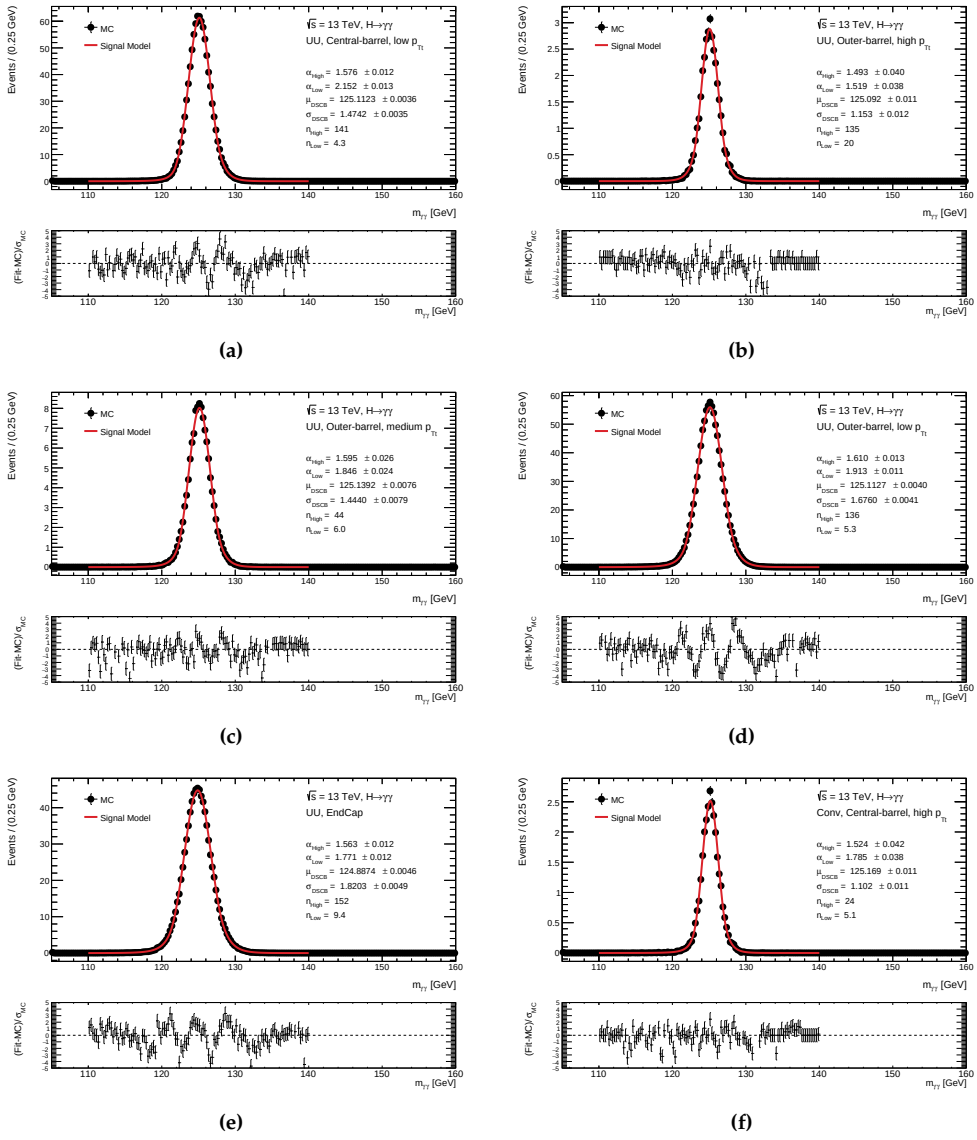

Figure B.4 – Result of the *single fit* for the categories UU, Central-barrel, low p_{Tt} (a), UU, Outer-barrel, high p_{Tt} (b), medium p_{Tt} (c), low p_{Tt} (d), UU Endcap (e), Conv, Central-barrel, high p_{Tt} (f): the fitted signal pdf is shown by the red line, the black dots correspond to the MC sample at $m_H = 125$ GeV. The values of the fitted parameters of the DSCB are shown in the legend on the right side of the plot. The residuals are shown in the lower part of the plot.

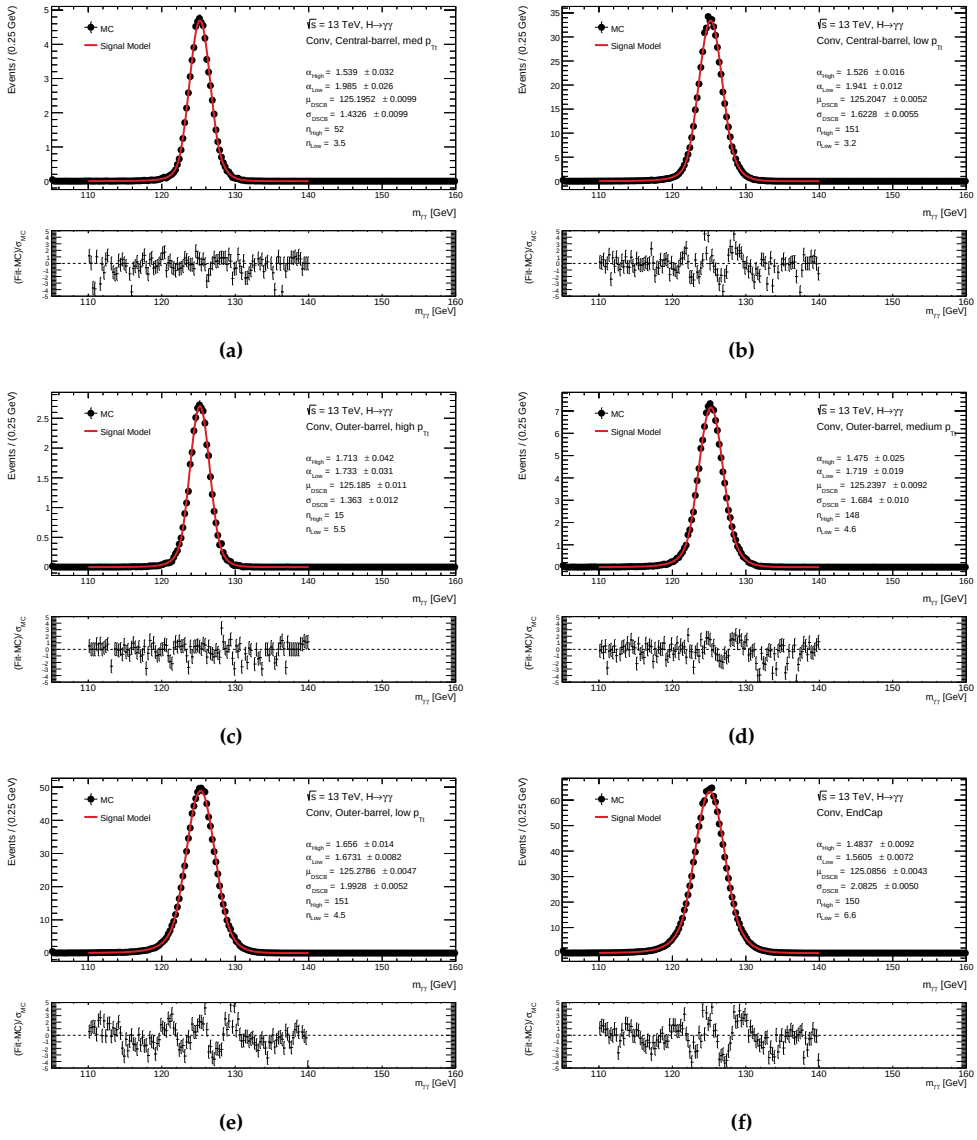

Figure B.5 – Result of the *single fit* for the categories Conv, Central-barrel, medium p_{Tt} (a), low p_{Tt} (b), Conv, Outer-barrel, high p_{Tt} (c), medium p_{Tt} (d), low p_{Tt} (e) and Conv Endcap (f): the fitted signal pdf is shown by the red line, the black dots correspond to the MC sample at $m_H = 125$ GeV. The values of the fitted parameters of the DSCB are shown in the legend on the right side of the plot. The residuals are shown in the lower part of the plot.

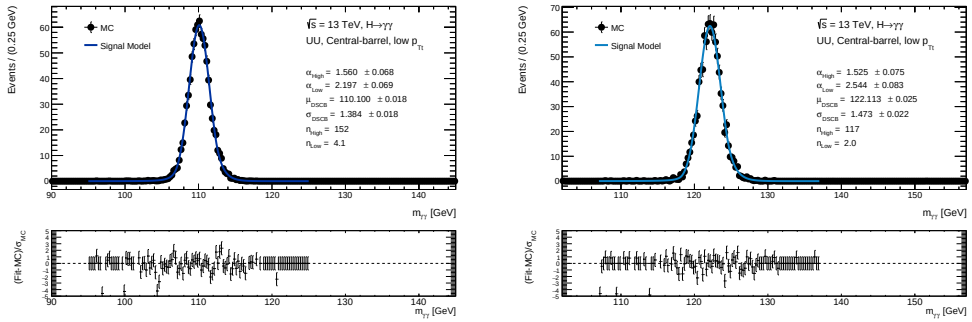

(a) 110 GeV

(b) 122 GeV

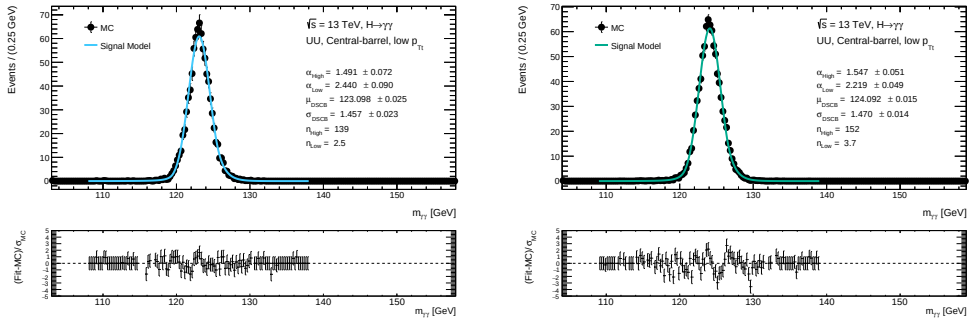

(c) 123 GeV

(d) 124 GeV

Figure B.6 – Result of the *single fit* for the category UU, Central-barrel, low p_{Tt} for the various MC sample at 110 GeV (a), 122 GeV (b), 123 GeV (c), 124 GeV (d): the fitted signal pdf is shown by the coloured line, the black dots correspond to the MC sample. The values of the fitted parameters of the DSCB are shown in the legend on the right side of the plot. The residuals used are shown in the lower part of the plot.

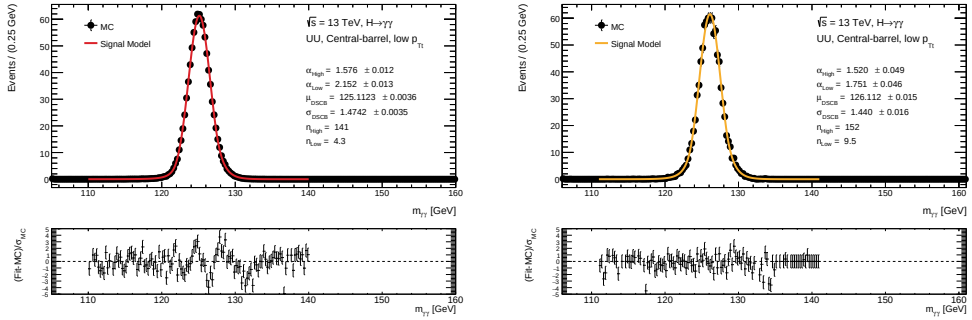

(a) 125 GeV **(b)** 126 GeV

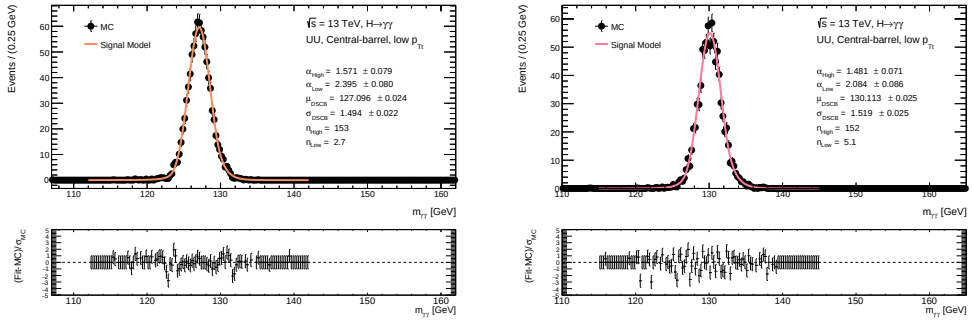

(c) 127 GeV **(d)** 130 GeV

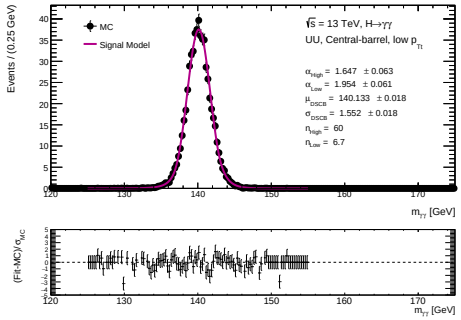

(e) 140 GeV

Figure B.7 – Result of the *single fit* for the category UU, Central-barrel, low p_{Tt} for the various MC sample at 125 GeV (a), 126 GeV (b), 127 GeV (c), 130 GeV (d) and 140 GeV (e): the fitted signal pdf is shown by the coloured line, the black dots correspond to the MC sample. The values of the fitted parameters of the DSCB are shown in the legend on the right side of the plot. The residuals are shown in the lower part of the plot.

C Additional material for the Higgs boson search in the $H \to \gamma\gamma*$ channel

C.1 Merged electron identification

This section contains additional plots with respect to Section 9.3.1, showing the distributions of the shower-shape and track-to-calorimeter pointing variables used in the merged electron identification BDT, after the reweighting procedure. The distributions are shown in Figures C.1 and C.2 for the signal and background samples.

C.2 Signal model fits

This section contains additional plots with respect to Section 9.4, showing the signal model fits for the 9 categories used in the Higgs boson search in the $H \to \gamma\gamma^*$ channel. The fits are shown for the nominal Higgs boson mass of 125 GeV in Figures C.3 to C.5.

C.3 Data sidebands fits

This section contains additional plots with respect to Section 9.5.2, showing the background fits on data sidebands for the 9 categories used in the Higgs boson search in the $H \to \gamma\gamma^*$ channel. The fits are shown in Figures C.6 and C.7.

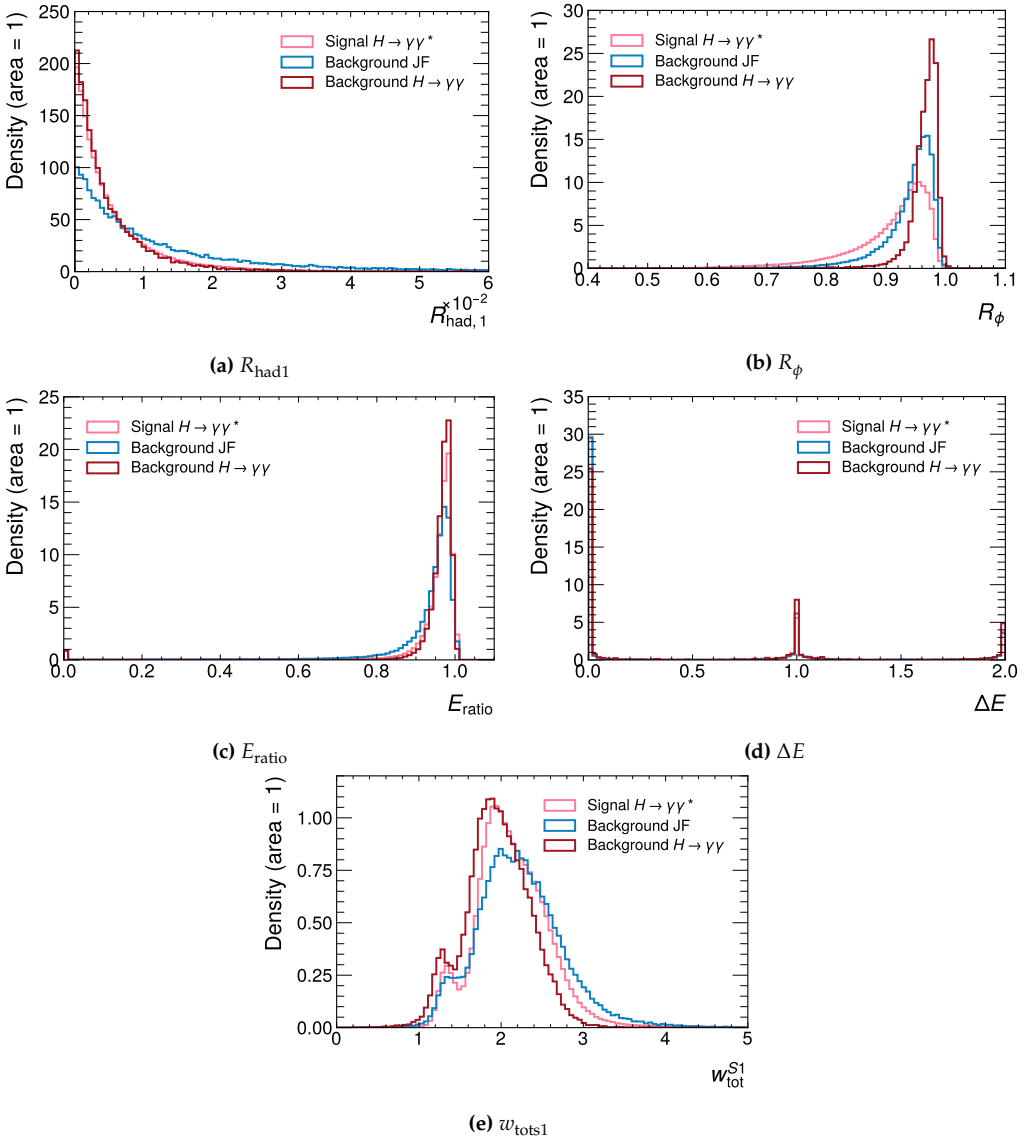

(a) R_{had1} **(b)** R_ϕ

(c) E_{ratio} **(d)** ΔE

(e) w_{tots1}

Figure C.1 – Comparison between the normalised shower-shape variables distributions after the reweighting procedure for the signal and background samples used in the BDT training.

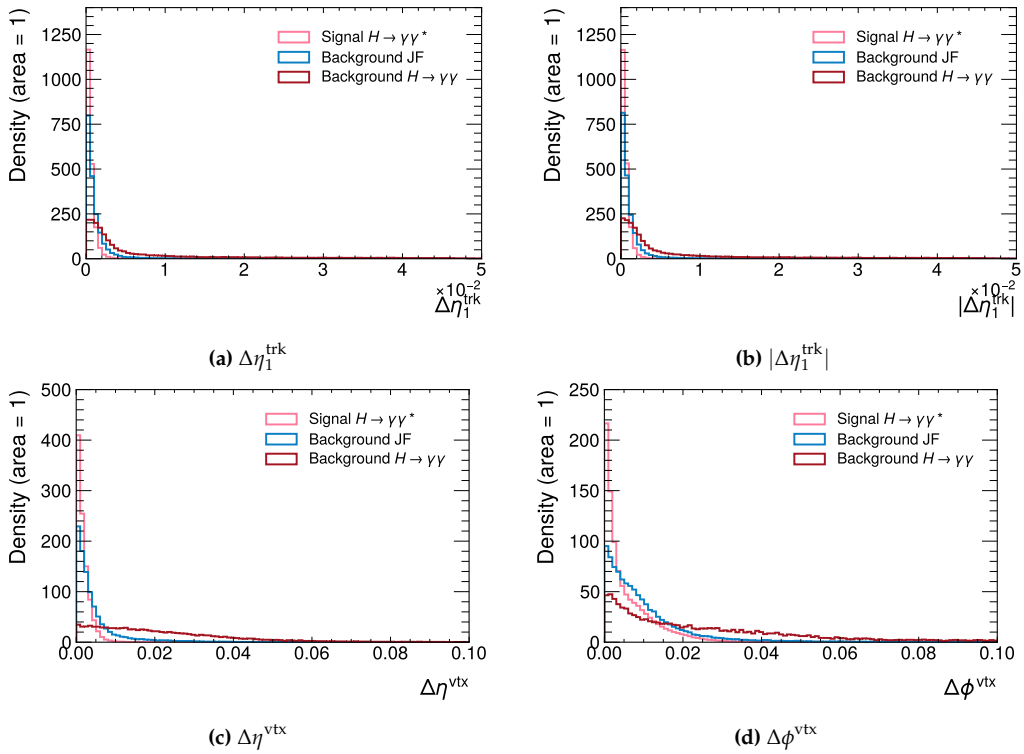

(a) $\Delta\eta_1^{\text{trk}}$ **(b)** $|\Delta\eta_1^{\text{trk}}|$

(c) $\Delta\eta^{\text{vtx}}$ **(d)** $\Delta\phi^{\text{vtx}}$

Figure C.2 – Comparison between the normalised track-to-calorimeter pointing variables distributions after the reweighting procedure for the signal and background samples used in the BDT training.

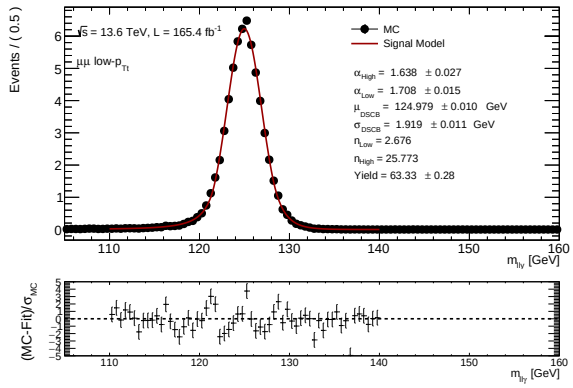

(a) $\mu\mu$ low $-$ p_{Tt} category

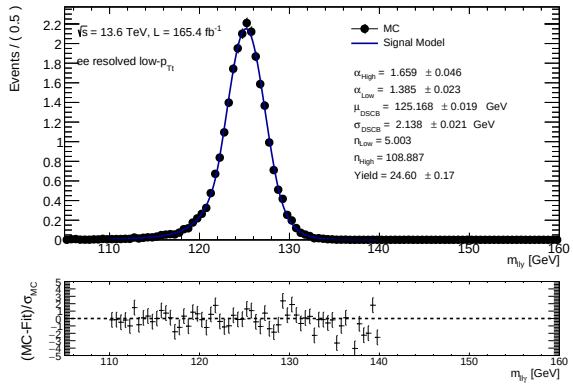

(b) ee resolved low $-$ p_{Tt} category

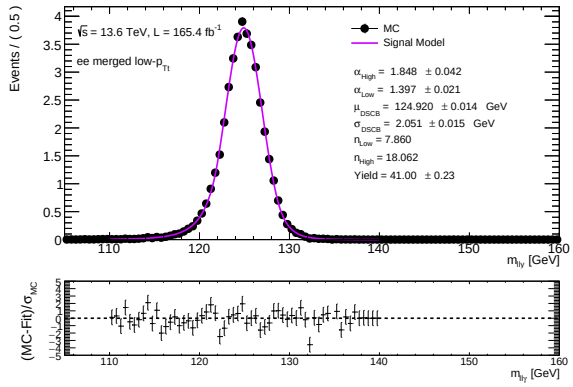

(c) ee merged low $-$ p_{Tt} category

Figure C.3 – Result of the signal fit for the low $-$ p_{Tt} categories: $\mu\mu$ (a), ee resolved (b), ee merged (c): the fitted signal pdf is shown by the coloured line, the black dots correspond to the MC sample at $m_H = 125$ GeV. The values of the fitted parameters of the DSCB are shown in the legend on the right side of the plot. In the lower part of the plot the residuals are shown.

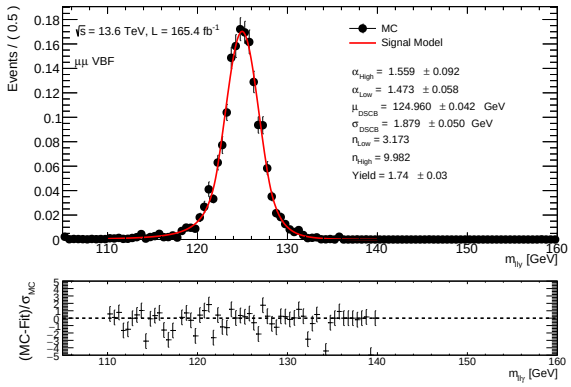

(a) $\mu\mu$ VBF category

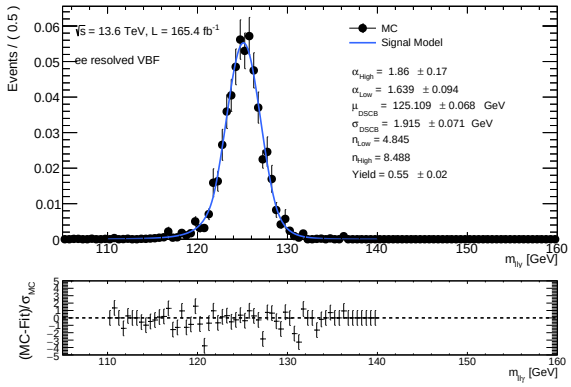

(b) ee resolved VBF category

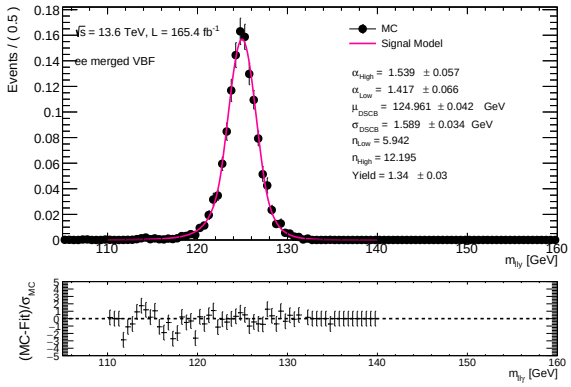

(c) ee merged VBF category

Figure C.4 – Result of the signal fit for the VBF categories: $\mu\mu$ (a), ee resolved (b), ee merged (c): the fitted signal pdf is shown by the coloured line, the black dots correspond to the MC sample at $m_H = 125$ GeV. The values of the fitted parameters of the DSCB are shown in the legend on the right side of the plot. In the lower part of the plot the residuals are shown.

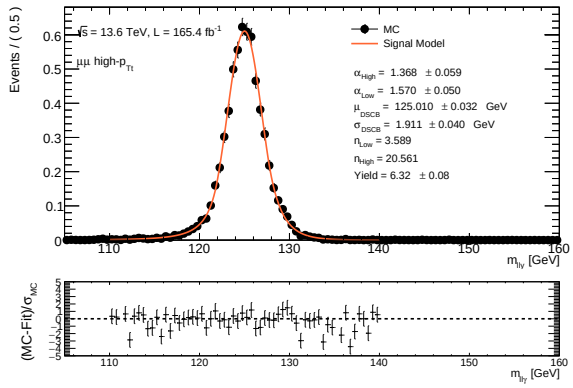

(a) $\mu\mu$ high $-$ p_{Tt} category

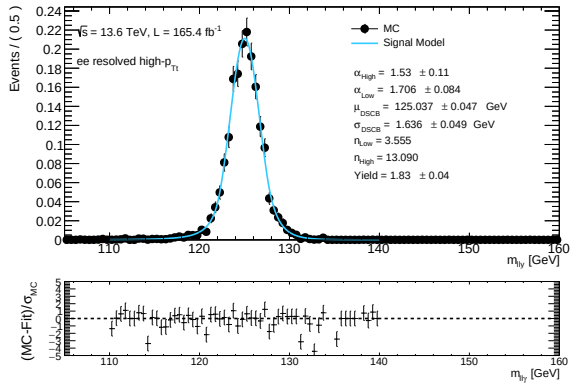

(b) ee resolved high $-$ p_{Tt} category

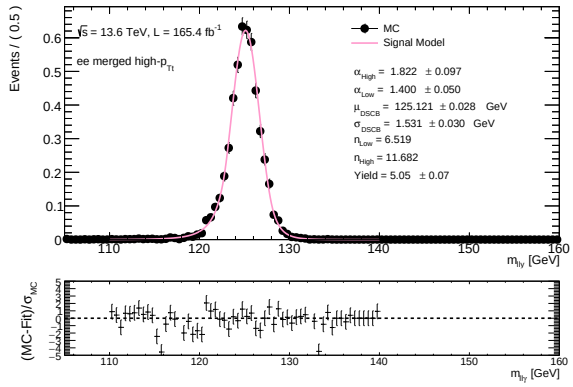

(c) ee merged high $-$ p_{Tt} category

Figure C.5 – Result of the signal fit for the high $-$ p_{Tt} categories: $\mu\mu$ (a), ee resolved (b), ee merged (c): the fitted signal pdf is shown by the coloured line, the black dots correspond to the MC sample at $m_H = 125$ GeV. The values of the fitted parameters of the DSCB are shown in the legend on the right side of the plot. In the lower part of the plot the residuals are shown.

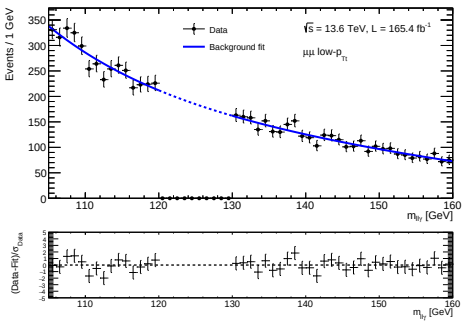

(a) $\mu\mu$ low $-$ p_{Tt} category

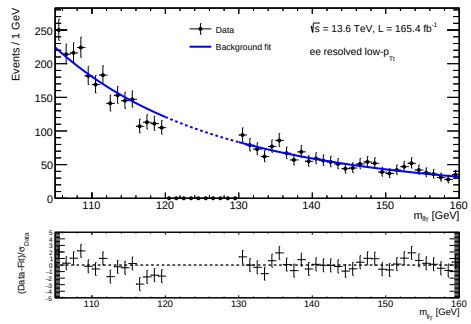

(b) ee resolved low $-$ p_{Tt} category

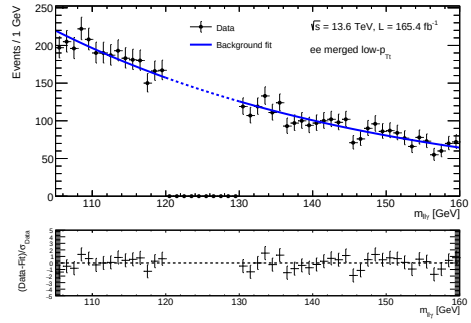

(c) ee merged low $-$ p_{Tt} category

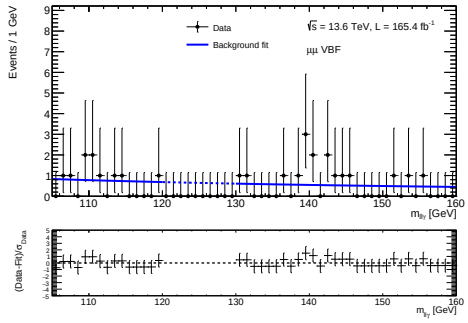

(d) $\mu\mu$ VBF category

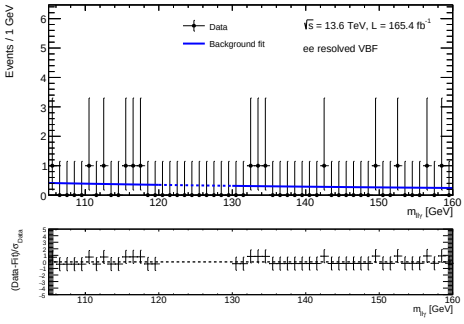

(e) ee resolved VBF category

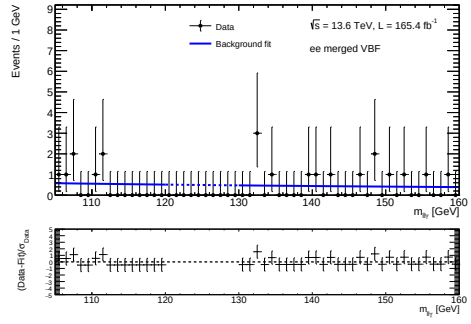

(f) ee merged VBF category

Figure C.6 – Result of the background fit on data sidebands for the low-p_{Tt} categories: $\mu\mu$ (a), ee resolved (b), ee merged (c) and for the VBF categories: $\mu\mu$ (d), ee resolved (e), ee merged (f). The fitted background pdf is shown by the coloured blue line, the black dots correspond to the data. In the lower part of the plot the residuals are shown.

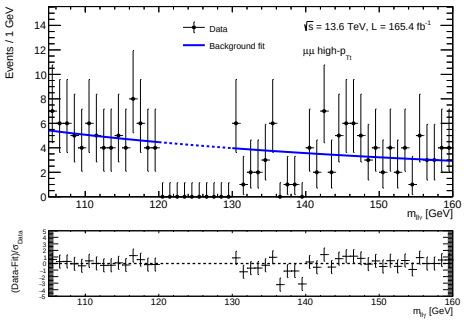

(a) $\mu\mu$ high $-$ p_{Tt} category

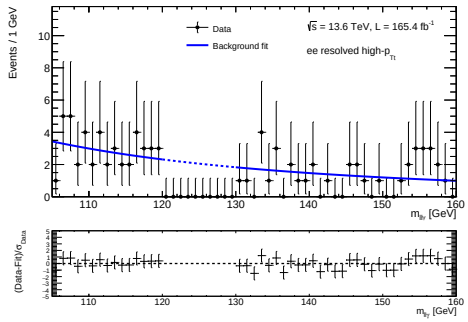

(b) ee resolved high $-$ p_{Tt} category

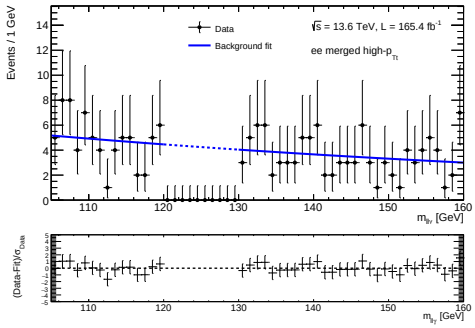

(c) ee merged high $-$ p_{Tt} category

Figure C.7 – Result of the background fit on data sidebands for the high-p_{Tt} categories: $\mu\mu$ (a), ee resolved (b), ee merged (c): the fitted background pdf is shown by the coloured blue line, the black dots correspond to the data. In the lower part of the plot the residuals are shown.

Bibliography

[1] ATLAS Collaboration, *The ATLAS Experiment at the CERN Large Hadron Collider*, JINST **3** (2008) S08003, URL: https://cds.cern.ch/record/1129811 (cited on pages xi, 23, 31).

[2] L. Evans and P. Bryant, *LHC Machine*, Journal of Instrumentation **3** (2008) S08001, URL: http://stacks.iop.org/1748-0221/3/i=08/a=S08001 (cited on pages xi, 17, 20, 24).

[3] CMS Collaboration, *The CMS experiment at the CERN LHC. The Compact Muon Solenoid experiment*, JINST **3** (2008) S08004, URL: https://cds.cern.ch/record/1129810 (cited on pages xi, 23, 31).

[4] S. Weinberg, *The Quantum Theory of Fields. Vol. 1: Foundations*, Cambridge University Press, 1995, ISBN: 9780521337837 (cited on pages xi, 1).

[5] S. Weinberg, *The Quantum Theory of Fields. Vol. 2: Modern Applications*, Cambridge University Press, 1996, ISBN: 9780521550024, 9780521550024 (cited on pages xi, 1).

[6] P. W. Higgs, *Broken symmetries and the masses of gauge bosons*, Phys. Rev. Lett. **13** (1964) p. 508, ed. by J. C. Taylor (cited on pages xi, 1, 2, 11, 129).

[7] F. Englert and R. Brout, *Broken symmetry and the mass of gauge vector mesons*, Phys. Rev. Lett. **13** (1964) p. 321, ed. by J. C. Taylor (cited on pages xi, 1, 2, 11, 129).

[8] G. S. Guralnik et al., *Global conservation laws and massless particles*, Phys. Rev. Lett. **13** (1964) p. 585, ed. by J. C. Taylor (cited on pages xi, 1, 2).

[9] ATLAS Collaboration, *Observation of a new particle in the search for the Standard Model Higgs boson with the ATLAS detector at the LHC*, Physics Letters B **716** (2012) p. 1, ISSN: 0370-2693, arXiv: 1207.7214 [hep-ex], URL: http://www.sciencedirect.com/science/article/pii/S037026931200857X (cited on pages xi, 1).

[10] CMS Collaboration, *Observation of a new boson at a mass of 125 GeV with the CMS experiment at the LHC*, Physics Letters B **716** (2012) p. 30, ISSN: 0370-2693, URL: http://www.sciencedirect.com/science/article/pii/S0370269312008581 (cited on pages xi, 1).

[11] J. Haller et al., *Update of the global electroweak fit and constraints on two-Higgs-doublet models*, The European Physical Journal C **78** (2018), ISSN: 1434-6052, URL: http://dx.doi.org/10.1140/epjc/s10052-018-6131-3 (cited on pages xi, 61, 129).

[12] G. Degrassi et al., *Higgs mass and vacuum stability in the Standard Model at NNLO*, Journal of High Energy Physics **2012** (2012), ISSN: 1029-8479, URL: http://dx.doi.org/10.1007/JHEP08(2012)098 (cited on pages xii, 61, 129).

[13] ATLAS and CMS Collaborations, *Combined Measurement of the Higgs Boson Mass in pp Collisions at $\sqrt{s} = 7$ and 8 TeV with the ATLAS and CMS Experiments*, Phys. Rev. Lett. **114** (2015) p. 191803, arXiv: 1503.07589 [hep-ex] (cited on pages xii, 62, 63, 129, 131, 184, 185, 188, 190, 192, 217, 234).

[14] ATLAS Collaboration, *Measurement of the Higgs boson mass with $H \to \gamma\gamma$ decays in 140 fb^{-1} of $\sqrt{s} = 13$ TeV pp collisions with the ATLAS detector*, Physics Letters B **847** (2023), ISSN: 0370-2693, URL: http://dx.doi.org/10.1016/j.physletb.2023.138315 (cited on pages xii, xv, 61, 129, 130, 149, 175, 177–181, 183, 185, 187, 190, 191, 233).

[15] ATLAS Collaboration, *Measurement of the Higgs boson mass in the $H \to ZZ^* \to 4\ell$ and $H \to \gamma\gamma$ channels with $\sqrt{s} = 13$ TeV pp collisions using the ATLAS detector*, Phys. Lett. B **784** (2018) p. 345, arXiv: 1806.00242 [hep-ex] (cited on pages xii, 130, 137, 141, 145, 174, 185, 187, 233).

[16] ATLAS Collaboration, *Electron and photon performance measurements with the ATLAS detector using the 2015–2017 LHC proton-proton collision data*, JINST **14** (2019) P12006, arXiv: 1908.00005 [hep-ex] (cited on pages xii, 71, 75, 77, 78, 80, 84–86, 131, 199, 201).

[17] ATLAS Collaboration, *Electron and photon energy calibration with the ATLAS detector using LHC Run 2 data*, JINST **19** (2024) P02009, arXiv: 2309.05471 [hep-ex] (cited on pages xii, xiii, 93–98, 113–119, 123, 125–128, 131, 142, 175).

[18] ATLAS Collaboration, *Measurement of the Higgs boson mass in the $H \to ZZ^* \to 4\ell$ decay channel using 139 fb^{-1} of $\sqrt{s} = 13$ TeV pp collisions recorded by the ATLAS detector at the LHC*, Physics Letters B **843** (2023) p. 137880, ISSN: 0370-2693, URL: http://dx.doi.org/10.1016/j.physletb.2023.137880 (cited on pages xii, xv, 62, 130, 187–191, 233).

[19] ATLAS Collaboration, *Combined measurement of the Higgs boson mass from the $H \to \gamma\gamma$ and $H \to ZZ^* \to 4\ell$ decay channels with the ATLAS detector using $\sqrt{s} = 7, 8$, and 13 TeV pp collision data*, Phys. Rev. Lett. **131** (2023) p. 251802, arXiv: 2308.04775 [hep-ex] (cited on pages xii, xv, 61, 187, 190–192, 234).

[20] ATLAS Collaboration, *Studies of the muon momentum calibration and performance of the ATLAS detector with pp collisions at $\sqrt{s} = 13$ TeV*, The European Physical Journal C **83** (2023), ISSN: 1434-6052, URL: http://dx.doi.org/10.1140/epjc/s10052-023-11584-x (cited on pages xiii, 87–89).

[21] ATLAS Collaboration, *ATLAS closes in on rare Higgs decays*, 2025, URL: https://atlas.cern/Updates/Briefing/Rare-Higgs-Run3 (cited on pages xiii, 193).

[22] ATLAS Collaboration, *Evidence for the dimuon decay of the Higgs boson in pp collisions with the ATLAS detector*, 2025, arXiv: 2507.03595 [hep-ex], URL: https://arxiv.org/abs/2507.03595 (cited on pages xiii, 58, 193).

[23] ATLAS Collaboration, *Search for the Higgs boson decay to a Z boson and a photon in pp collisions at $\sqrt{s} = 13$ TeV and 13.6 TeV with the ATLAS detector*, 2025, arXiv: 2507.12598 [hep-ex], URL: https://arxiv.org/abs/2507.12598 (cited on pages xiii, 193).

[24] ATLAS and CMS Collaboration, *Evidence for the Higgs Boson Decay to a Z Boson and a Photon at the LHC*, Physical Review Letters **132** (2024), ISSN: 1079-7114, URL: http://dx.doi.org/10.1103/PhysRevLett.132.021803 (cited on pages xiii, 59, 193).

[25] A. Kachanovich et al., *Higgs boson decay into a lepton pair and a photon revisited*, Physical Review D **101** (2020), ISSN: 2470-0029, URL: http://dx.doi.org/10.1103/PhysRevD.101.073003 (cited on pages xiii, 193).

[26] A. Y. Korchin and V. A. Kovalchuk, *Angular distribution and forward-backward asymmetry of the Higgs-boson decay to photon and lepton pair*, The European Physical Journal C **74** (2014), ISSN: 1434-6052, URL: http://dx.doi.org/10.1140/epjc/s10052-014-3141-7 (cited on pages xiii, 193).

[27] Y. Chen et al., *New observables for CP violation in Higgs decays*, Physical Review D **90** (2014), ISSN: 1550-2368, URL: http://dx.doi.org/10.1103/PhysRevD.90.113006 (cited on pages xiii, 193).

[28] CMS Collaboration, *Search for the decay of a Higgs boson in the $ll\gamma$ channel in proton-proton collisions at $\sqrt{s} = 13$ TeV*, J. High Energ. Phys. (2018) (cited on pages xiii, 194).

[29] ATLAS Collaboration, *Evidence for Higgs boson decays to a low-mass dilepton system and a photon in pp collisions at $\sqrt{s} = 13$ TeV with the ATLAS detector*, Physics Letters B **819** (2021) p. 136412, ISSN: 0370-2693, URL: https://www.sciencedirect.com/science/article/pii/S037026932100352X (cited on pages xiii, 194, 196, 206, 209, 210, 226, 232, 234).

[30] S. Weinberg, *The making of the Standard Model*, The European Physical Journal C - Particles and Fields **34** (2004) p. 5, URL: https://doi.org/10.1140/epjc/s2004-01761-1 (cited on page 1).

[31] S. L. Glashow, *Partial-symmetries of weak interactions*, Nuclear Physics **22** (1961) p. 579, ISSN: 0029-5582, URL: https://www.sciencedirect.com/science/article/pii/0029558261904692 (cited on page 1).

[32] S. Weinberg, *A Model of Leptons*, Phys. Rev. Lett. **19** (21 1967) p. 1264, URL: https://link.aps.org/doi/10.1103/PhysRevLett.19.1264 (cited on page 1).

[33] A. Salam and J. Ward, *Electromagnetic and weak interactions*, Physics Letters **13** (1964) p. 168, ISSN: 0031-9163, URL: https://www.sciencedirect.com/science/article/pii/0031916364907115 (cited on page 1).

[34] A. Salam, "Weak and electromagnetic interactions", *Selected Papers of Abdus Salam* p. 244, eprint: https://www.worldscientific.com/doi/pdf/10.1142/9789812795915_0034, URL: https://www.worldscientific.com/doi/abs/10.1142/9789812795915_0034 (cited on page 1).

[35] Y. Fukuda et al., *Evidence for oscillation of atmospheric neutrinos*, Phys. Rev. Lett. **81** (8 1998) p. 1562, URL: https://link.aps.org/doi/10.1103/PhysRevLett.81.1562 (cited on page 2).

[36] Q. R. Ahmad et al., *Direct Evidence for Neutrino Flavor Transformation from Neutral-Current Interactions in the Sudbury Neutrino Observatory*, Phys. Rev. Lett. **89** (2002) p. 011301 (cited on page 2).

[37] M. E. Peskin and D. V. Schroeder, *An Introduction to Quantum Field Theory*, CRC Press, 2019, ISBN: 9780367406786 (cited on page 3).

[38] F. Mandl and G. Shaw, *Quantum Field Theory*, 2nd ed., Wiley, 2010, ISBN: 9780471496847 (cited on page 3).

[39] M. Gell-Mann, *A Schematic Model of Baryons and Mesons*, Phys. Lett. **8** (1964) p. 214 (cited on page 5).

[40] R. Hofstadter, *Nobel Lecture*, NobelPrize.org. Nobel Prize Outreach AB 2022, 1961, URL: https://www.nobelprize.org/prizes/physics/1961/hofstadter/lecture/ (cited on page 5).

[41] W. Bartel et al., *Observation of planar three-jet events in e^+e^- annihilation and evidence for gluon bremsstrahlung*, Physics Letters B **91** (1980) p. 142, URL: https://www.sciencedirect.com/science/article/abs/pii/0370269380906802?via%3Dihub (cited on page 6).

[42] W. Pauli, *Letter to the Physical Society of Tübingen on the neutrino hypothesis*, 1930 (cited on page 7).

[43] E. Fermi, *Tentativo di una teoria dell'emissione dei raggi beta*, Il Nuovo Cimento **11** (1934) p. 1 (cited on page 8).

[44] S. L. Glashow, *Partial-symmetries of weak interactions*, Nuclear Physics **22** (1961) p. 579, ISSN: 0029-5582, URL: http://www.sciencedirect.com/science/article/pii/0029558261904692 (cited on page 8).

[45] CMS Collaboration, *High-precision measurement of the W boson mass with the CMS experiment at the LHC*, arXiv preprint arXiv:2412.13872 (2024), URL: https://arxiv.org/abs/2412.13872 (cited on pages 11, 15).

[46] P. D. Group, *PDG Live: Review of Particle Physics*, https://pdglive.lbl.gov/Viewer.action (cited on pages 11, 15, 18, 37, 39, 40, 46).

[47] J. Goldstone et al., *Broken Symmetries*, Phys. Rev. **127** (3 1962) p. 965, URL: https://link.aps.org/doi/10.1103/PhysRev.127.965 (cited on page 13).

[48] R. L. Workman et al., *Review of Particle Physics*, PTEP **2022** (2022) p. 083C01 (cited on page 15).

[49] J. D. Jackson, *Classical Electrodynamics*, 3rd, New York: Wiley, 1999 (cited on page 18).

[50] G. Arduini et al., *Electron-positron collisions at 209 GeV in LEP*, Proceedings of the Particle Accelerator Conference (PAC 2001) **1** (2001) p. 65 (cited on page 18).

[51] Y. L. Dokshitzer, *Calculation of the Structure Functions for Deep Inelastic Scattering and e+e- Annihilation by Perturbation Theory in Quantum Chromodynamics*, Soviet Physics JETP **46** (1977) p. 641 (cited on page 19).

[52] V. N. Gribov and L. N. Lipatov, *Deep inelastic e+ p scattering in perturbation theory*, Soviet Journal of Nuclear Physics **15** (1972) p. 438 (cited on page 19).

[53] G. Altarelli and G. Parisi, *Asymptotic freedom in parton language*, Nuclear Physics B **126** (1977) p. 298 (cited on page 19).

[54] R. D. Ball et al., *Parton distributions from high-precision collider data. Parton distributions from high-precision collider data*, Eur. Phys. J. C **77** (2017) p. 663, arXiv: 1706.00428, URL: http://cds.cern.ch/record/2267455 (cited on pages 19, 20).

[55] CERN, *The Large Hadron Collider*, 2025, URL: https://home.cern/science/accelerators/large-hadron-collider (cited on pages 20, 21).

[56] AC Team, "Diagram of an LHC dipole magnet. Schéma d'un aimant dipôle du LHC", 1999, URL: https://cds.cern.ch/record/40524 (cited on page 21).

[57] CERN, *The accelerators complex at Large Hadron Collider*, 2025, URL: https://home.cern/science/accelerators (cited on page 21).

[58] E. Lopienska, *The CERN accelerator complex, layout in 2022. Complexe des accélérateurs du CERN en janvier 2022*, (2022), URL: https://cds.cern.ch/record/2800984 (cited on page 22).

[59] LHCb Collaboration, *The LHCb Detector at the LHC*, JINST **3** (2008) S08005, URL: https://cds.cern.ch/record/1129809 (cited on page 23).

[60] ALICE Collaboration, *The ALICE experiment at the CERN LHC*, JINST **3** (2008) S08002 (cited on page 23).

[61] The TOTEM Collaboration, *The TOTEM Experiment at the CERN Large Hadron Collider*, Journal of Instrumentation **3** (Anno) S08007, URL: https://doi.org/10.1088/1748-0221/3/08/S08007 (cited on page 23).

[62] The LHCf Collaboration, *The LHCf detector at the CERN Large Hadron Collider*, Journal of Instrumentation **3** (Anno) S08007, URL: https://doi.org/10.1088/1748-0221/3/08/S08007 (cited on page 23).

[63] J. L. Pinfold, "The MoEDAL experiment at the LHC: Searching beyond the Standard Model", *Proceedings of the International Conference on New Frontiers in Physics (ICNFP 2016)*, vol. 126, EPJ Web of Conferences, EDP Sciences, 2016 p. 02024, URL: https://doi.org/10.1051/epjconf/201612602024 (cited on page 23).

[64] The FASER Collaboration, *FASER: ForwArd Search ExpeRiment at the LHC*, arXiv:1901.04468 [hep-ex] (2019), URL: https://arxiv.org/abs/1901.04468 (cited on page 23).

[65] C. Ahdida et al., *SND@LHC: Scattering and Neutrino Detector at the LHC*, arXiv:2002.08722 [physics.ins-det] (2020), URL: https://arxiv.org/abs/2002.08722 (cited on page 23).

[66] *9th LHC Operations Evian Workshop, Proceedings*, CERN, Geneva, 2019, URL: https://cds.cern.ch/record/2706427 (cited on page 24).

[67] R. Bruce et al., *Review of LHC Run 2 Machine Configurations*, (2019) p. 187, URL: https://cds.cern.ch/record/2750415 (cited on page 24).

[68] B. Salvachua, *Overview of Proton-Proton Physics during Run 2*, (2019) p. 7, URL: https://cds.cern.ch/record/2750272 (cited on page 24).

[69] Particle Data Group, *High-Energy Collider Parameters*, https://pdg.lbl.gov/2025/web/viewer.html?file=../reviews/rpp2024-rev-hep-collider-params.pdf (cited on page 25).

[70] G. Rumolo et al., *High intensity beam dynamics assessment and challenges for HL-LHC*, JINST **19** (2024) T05016, URL: https://cds.cern.ch/record/2901253 (cited on page 25).

[71] ATLAS Collaboration, *Website of ATLAS Luminosity Public Results in Run 2*, URL: https://twiki.cern.ch/twiki/bin/view/AtlasPublic/LuminosityPublicResultsRun2 (cited on pages 25, 27, 29, 30).

[72] ATLAS Collaboration, *Website of ATLAS Luminosity Public Results in Run 3*, URL: https://twiki.cern.ch/twiki/bin/view/AtlasPublic/LuminosityPublicResultsRun3 (cited on pages 26, 28–30).

[73] G. Avoni et al., *The new LUCID-2 detector for luminosity measurement and monitoring in ATLAS*, JINST **13** (2018) P07017, URL: https://cds.cern.ch/record/2633501 (cited on pages 26, 131, 195).

[74] M. Hostettler et al., *Operational β^* levelling at the LHC in 2022 and beyond*, JACoW **IPAC2023** (2023) MOPL045 (cited on page 28).

[75] ATLAS Collaboration, *The ATLAS experiment at the CERN Large Hadron Collider: a description of the detector configuration for Run 3*, Journal of Instrumentation **19** (2024) P05063 (cited on pages 31, 32, 35, 38, 47).

[76] ATLAS Collaboration, *ATLAS central solenoid: Technical design report*, (1997) (cited on page 33).

[77] ATLAS Collaboration, *ATLAS barrel toroid: Technical design report*, (1997) (cited on page 34).

[78] ATLAS Collaboration, *ATLAS end-cap toroids: Technical design report*, (1997) (cited on page 34).

[79] ATLAS Collaboration, *The ATLAS Experiment at the CERN Large Hadron Collider*, URL: https://atlas.web.cern.ch/Atlas/GROUPS/PHYSICS/PAPERS/PERF-2007-01/ (cited on page 34).

[80] ATLAS Collaboration, *ATLAS inner detector: Technical Design Report, 1*, Technical design report. ATLAS, Geneva: CERN, 1997, URL: https://cds.cern.ch/record/331063 (cited on page 34).

[81] ATLAS Collaboration, *The ATLAS Inner Detector commissioning and calibration*, Eur. Phys. J. C **70** (2010) p. 787, arXiv: 1004.5293 [physics.ins-det] (cited on pages 34, 37).

[82] N. Wermes and G. Hallewel, *ATLAS pixel detector: Technical Design Report*, Technical design report. ATLAS, Geneva: CERN, 1998, URL: https://cds.cern.ch/record/381263 (cited on page 35).

[83] M. Capeans et al., *ATLAS Insertable B-Layer Technical Design Report*, (2010) (cited on page 35).

[84] J. N. Jackson, *The ATLAS semiconductor tracker (SCT)*, Nucl. Instrum. Meth. A **541** (2005) p. 89, ed. by T. Ohsugi et al. (cited on page 36).

[85] A. Vogel, *ATLAS Transition Radiation Tracker (TRT): Straw Tube Gaseous Detectors at High Rates*, tech. rep., CERN, 2013, URL: https://cds.cern.ch/record/1537991 (cited on page 36).

[86] C. W. Fabjan and F. Gianotti, *Calorimetry for particle physics*, Rev. Mod. Phys. **75** (2003) p. 1243 (cited on page 37).

[87] CMS Collaboration, *Performance and operation of the CMS electromagnetic calorimeter*, JINST **5** (2010) T03010, URL: https://doi.org/10.1088/1748-0221/5/03/T03010 (cited on page 37).

[88] ATLAS Collaboration, *ATLAS liquid argon calorimeter: Technical design report*, (1996) (cited on pages 42, 43, 45).

[89] ATLAS Collaboration, *Readiness of the ATLAS Liquid Argon Calorimeter for LHC Collisions*, Eur. Phys. J. C **70** (2010) p. 723, arXiv: 0912.2642 [physics.ins-det] (cited on page 42).

[90] M. Aleksa et al., *ATLAS Liquid Argon Calorimeter Phase-I Upgrade Technical Design Report*, (2013), URL: https://cds.cern.ch/record/1602230/ (cited on page 42).

[91] G. Aad et al., *The Phase-I trigger readout electronics upgrade of the ATLAS Liquid Argon calorimeters*, Journal of Instrumentation **17** (2022) P05024, URL: https://doi.org/10.1088/1748-0221/17/05/P05024 (cited on page 44).

[92] ATLAS Collaboration, *The ATLAS trigger system for LHC Run 3 and trigger performance in 2022*, JINST **19** (2024) P06029, arXiv: 2401.06630 [hep-ex] (cited on pages 45, 49).

[93] ATLAS Collaboration, *ATLAS tile calorimeter: Technical Design Report*, Technical design report. ATLAS, Geneva: CERN, 1996, URL: https://cds.cern.ch/record/331062 (cited on page 44).

[94] ATLAS Collaboration, *Readiness of the ATLAS Tile Calorimeter for LHC collisions*, Eur. Phys. J. C **70** (2010) p. 1193, arXiv: 1007.5423 [physics.ins-det] (cited on page 44).

[95] ATLAS Collaboration, *Performance of the ATLAS Hadronic Endcap Calorimeter in beam tests: Selected results*, tech. rep., CERN, 2022, URL: https://cds.cern.ch/record/2811731 (cited on page 45).

[96] T. Barillari, *The ATLAS liquid argon hadronic end-cap calorimeter: Construction and selected beam test results*, Nucl. Phys. B Proc. Suppl. **150** (2006) p. 102, ed. by C. Bosio et al., arXiv: physics/0407026 (cited on page 45).

[97] A. Artamonov et al., *The ATLAS Forward Calorimeter*, JINST **3** (2008) P02010, URL: https://cds.cern.ch/record/1094547 (cited on page 46).

[98] ATLAS Collaboration, *ATLAS muon spectrometer: Technical design report*, (1997) (cited on page 46).

[99] ATLAS Collaboration, *Performance of the ATLAS Trigger System in 2015*, Eur. Phys. J. C **77** (2017) p. 317, arXiv: 1611.09661 [hep-ex] (cited on page 48).

[100] ATLAS Collaboration, *ATLAS level-1 trigger: Technical Design Report*, (1998) (cited on page 48).

[101] ATLAS Collaboration, *ATLAS high-level trigger, data acquisition and controls: Technical design report*, (2003) (cited on page 48).

[102] ATLAS Collaboration, *Operation of the ATLAS trigger system in Run 2*, JINST **15** (2020) P10004, arXiv: 2007.12539 [physics.ins-det] (cited on page 49).

[103] ATLAS Collaboration, *Website of ATLAS Trigger Operation Public Results in Run 2*, URL: https://twiki.cern.ch/twiki/bin/view/AtlasPublic/TriggerOperationPublicResults (cited on page 50).

[104] ATLAS Collaboration, *ATLAS images gallery*, URL: https://home.cern/resources/image/experiments/atlas-images-gallerys (cited on page 51).

[105] A. Karlberg et al., *Ad interim recommendations for the Higgs boson production cross sections at* $\sqrt{s} = 13.6$ *TeV*, 2024, arXiv: 2402.09955 [hep-ph], URL: https://arxiv.org/abs/2402.09955 (cited on pages 53, 55, 196).

[106] D. de Florian et al., *Handbook of LHC Higgs Cross Sections: 4. Deciphering the Nature of the Higgs Sector*, CERN Yellow Reports: Monographs, Geneva: CERN, 2017, URL: https://cds.cern.ch/record/2227475 (cited on pages 55, 56, 58, 59, 62, 133, 141).

[107] M. Aaboud et al., *Observation of* $H \to b\bar{b}$ *decays and* VH *production with the ATLAS detector*, (2018), arXiv: 1808.08238 [hep-ex] (cited on page 56).

[108] ATLAS Collaboration, *Identification of boosted Higgs bosons decaying into b-quark pairs with the ATLAS detector at 13 TeV*, The European Physical Journal C **79** (2019), ISSN: 1434-6052, URL: http://dx.doi.org/10.1140/epjc/s10052-019-7335-x (cited on page 56).

[109] ATLAS Collaboration, *Search for* $H \to c\bar{c}$ *and measurement of* $H \to b\bar{b}$ *in vector-boson fusion production with the ATLAS Detector*, 2025, arXiv: 2511.21911 [hep-ex], URL: https://arxiv.org/abs/2511.21911 (cited on page 58).

[110] S. Wuchterl, *Search for Higgs boson decay to a charm quark-antiquark pair via* $tt\bar{H}$ *production*, 2025, arXiv: 2506.02163 [hep-ex], URL: https://arxiv.org/abs/2506.02163 (cited on page 58).

[111] CMS Collaboration, *Evidence for Higgs boson decay to a pair of muons*, JHEP **01** (2021) p. 148, arXiv: 2009.04363 [hep-ex] (cited on page 58).

[112] ATLAS Collaboration, *Search for the Higgs boson decay to a Z boson and a photon in pp collisions at $\sqrt{s}$ = 13 TeV and 13.6 TeV with the ATLAS detector*, 2025, arXiv: 2507.12598 [hep-ex], URL: https://arxiv.org/abs/2507.12598 (cited on page 59).

[113] ATLAS Collaboration, *Observation of a new particle in the search for the Standard Model Higgs boson with the ATLAS detector at the LHC*, Phys. Lett. B **716** (2012) p. 1, arXiv: 1207.7214 [hep-ex] (cited on pages 60, 129).

[114] CMS Collaboration, *Observation of a new boson at a mass of 125 GeV with the CMS experiment at the LHC*, Phys. Lett. B **716** (2012) p. 30, arXiv: 1207.7235 [hep-ex] (cited on pages 60, 129).

[115] ATLAS Collaboration, *Measurements of Higgs boson production and couplings in the four-lepton channel in pp collisions at center-of-mass energies of 7 and 8 TeV with the ATLAS detector*, Physical Review D **91** (2015), ISSN: 1550-2368, URL: http://dx.doi.org/10.1103/PhysRevD.91.012006 (cited on pages 62, 63).

[116] CMS Collaboration, *Measurement of the properties of a Higgs boson in the four-lepton final state*, Physical Review D **89** (2014), ISSN: 1550-2368, URL: http://dx.doi.org/10.1103/PhysRevD.89.092007 (cited on page 62).

[117] ATLAS Collaboration, *Measurement of the Higgs boson mass from the $H \to \gamma\gamma$ and $H \to ZZ^* \to 4\ell$ channels with the ATLAS detector using 25 fb^{-1} of pp collision data*, Phys. Rev. **D90** (2014) p. 052004, arXiv: 1406.3827 [hep-ex] (cited on pages 62, 63, 137, 140, 145).

[118] CMS Collaboration, *Observation of the diphoton decay of the Higgs boson and measurement of its properties*, The European Physical Journal C **74** (2014), ISSN: 1434-6052, URL: http://dx.doi.org/10.1140/epjc/s10052-014-3076-z (cited on page 62).

[119] ATLAS Collaboration, *Evidence of off-shell Higgs boson production from ZZ leptonic decay channels and constraints on its total width with the ATLAS detector*, Phys. Lett. B **846** (2023) p. 138223, arXiv: 2304.01532 [hep-ex] (cited on page 64).

[120] CMS Collaboration, *Measurement of the Higgs boson width and evidence of its off-shell contributions to ZZ production. First evidence for off-shell production of the Higgs boson and measurement of its width*, Nature Phys. (2022), arXiv: 2202.06923, URL: https://cds.cern.ch/record/2801541 (cited on page 64).

[121] ATLAS Collaboration, *Constraining off-shell Higgs boson production and the Higgs boson total width using $WW \to \ell\nu\ell\nu$ final states with the ATLAS detector*, Physics Letters B **870** (2025) p. 139898, ISSN: 0370-2693, URL: http://dx.doi.org/10.1016/j.physletb.2025.139898 (cited on page 64).

[122] CMS Collaboration, *Measurement of the Higgs boson total decay width using the $H \to WW \to e\nu\mu\nu$ decay channel in proton-proton collisions at $\sqrt{s}$ = 13 TeV*, 2026, arXiv: 2601.05168 [hep-ex], URL: https://arxiv.org/abs/2601.05168 (cited on page 64).

[123] ATLAS Collaboration, *Measurement of off-shell Higgs boson production in the $H \to ZZ^* \to 4\ell$ decay channel using a neural simulation-based inference technique in 13 TeV pp collisions with the ATLAS detector*, Reports on Progress in Physics **88** (2025) p. 057803, ISSN: 1361-6633, URL: http://dx.doi.org/10.1088/1361-6633/adcd9a (cited on page 64).

[124] ATLAS Collaboration, *Constraint on the total width of the Higgs boson from Higgs boson and four-top-quark measurements in pp collisions at $\sqrt{s} = 13$ TeV with the ATLAS detector*, Physics Letters B **861** (2025) p. 139277, ISSN: 0370-2693, URL: http://dx.doi.org/10.1016/j.physletb.2025.139277 (cited on page 64).

[125] L. Landau, "On the Angular Momentum of a System of two Photons", *Collected Papers of L.D. Landau*, ed. by D. T. HAAR, Pergamon, 1965 p. 471, ISBN: 978-0-08-010586-4, URL: http://www.sciencedirect.com/science/article/pii/B9780080105864500705 (cited on page 64).

[126] ATLAS Collaboration, *Study of the spin and parity of the Higgs boson in diboson decays with the ATLAS detector*, Eur. Phys. J. C **75** (2015) p. 476, arXiv: 1506.05669 [hep-ex] (cited on page 64).

[127] ATLAS Collaboration, *Determination of spin and parity of the Higgs boson in the $WW^* \to e\nu\mu\nu$ decay channel with the ATLAS detector*, The European Physical Journal C **75** (2015), ISSN: 1434-6052, URL: http://dx.doi.org/10.1140/epjc/s10052-015-3436-3 (cited on page 64).

[128] CMS Collaboration, *Constraints on the spin-parity and anomalous HVV couplings of the Higgs boson in proton collisions at 7 and 8 TeV*, Phys. Rev. D **92** (2015) p. 012004, arXiv: 1411.3441 [hep-ex] (cited on page 64).

[129] ATLAS Collaboration, *A detailed map of Higgs boson interactions by the ATLAS experiment ten years after the discovery*, Nature **607** (2022) p. 52, arXiv: 2207.00092 [hep-ex] (cited on pages 65, 67).

[130] CMS Collaboration, *A portrait of the Higgs boson by the CMS experiment ten years after the discovery.*, Nature **607** (2022) p. 60, arXiv: 2207.00043 [hep-ex] (cited on pages 66, 67).

[131] J. Pequenao and P. Schaffner, "How ATLAS detects particles: diagram of particle paths in the detector", 2013, URL: https://cds.cern.ch/record/1505342 (cited on page 70).

[132] ATLAS Collaboration, *Topological cell clustering in the ATLAS calorimeters and its performance in LHC Run 1*, Eur. Phys. J. C **77** (2017) p. 490, arXiv: 1603.02934, URL: https://cds.cern.ch/record/2138166 (cited on page 71).

[133] ATLAS Collaboration, *Performance of the ATLAS Track Reconstruction Algorithms in Dense Environments in LHC Run 2*, Eur. Phys. J. **C77** (2017) p. 673, arXiv: 1704.07983 [hep-ex] (cited on page 72).

[134] T. Cornelissen et al., *Concepts, Design and Implementation of the ATLAS New Tracking (NEWT)*, tech. rep., CERN, 2007, URL: https://cds.cern.ch/record/1020106 (cited on pages 72, 86).

[135] R. Frühwirth, *Application of Kalman filtering to track and vertex fitting*, Nuclear Instruments and Methods in Physics Research Section A: Accelerators, Spectrometers, Detectors and Associated Equipment **262** (1987) p. 444, ISSN: 0168-9002, URL: https://www.sciencedirect.com/science/article/pii/0168900287908874 (cited on page 72).

[136] W. Waltenberger et al., *Adaptive vertex fitting*, Journal of Physics G: Nuclear and Particle Physics **34** (2007) N343, URL: https://doi.org/10.1088/0954-3899/34/12/n01 (cited on page 73).

[137] ATLAS Collaboration, *Improved electron reconstruction in ATLAS using the Gaussian Sum Filter-based model for bremsstrahlung*, tech. rep., CERN, 2012, URL: https://cds.cern.ch/record/1449796 (cited on page 73).

[138] ATLAS Collaboration, *Electron and photon reconstruction and performance in ATLAS using a dynamical, topological cell clustering-based approach*, tech. rep., CERN, 2017, URL: https://cds.cern.ch/record/2298955 (cited on page 75).

[139] ATLAS Collaboration, *Performance of electron and photon triggers in ATLAS during LHC Run 2*, Eur. Phys. J. C **80** (2020) p. 47, arXiv: 1909.00761 [hep-ex] (cited on pages 79, 131).

[140] ATLAS Collaboration, *Measurement of the photon identification efficiencies with the ATLAS detector using LHC Run-1 data*, Eur. Phys. J. C **76** (2016) p. 666, arXiv: 1606.01813 [hep-ex] (cited on page 80).

[141] *Expected photon performance in the ATLAS experiment*, tech. rep., CERN, 2011, URL: https://cds.cern.ch/record/1345329 (cited on page 80).

[142] ATLAS Collaboration, *Electron and photon efficiencies in LHC Run 2 with the ATLAS experiment*, JHEP **05** (2024) p. 162, arXiv: 2308.13362 [hep-ex] (cited on pages 80–83, 86).

[143] ATLAS Collaboration, *Measurement of Electron Identification efficiency using* $\sqrt{s} = 13.6$ *TeV collisions recorded in 2023 at the ATLAS experiment*, URL: https://atlas.web.cern.ch/Atlas/GROUPS/PHYSICS/PLOTS/EGAM-2025-04/ (cited on page 83).

[144] ATLAS Collaboration, *Muon reconstruction and identification efficiency in ATLAS using the full Run 2 pp collision data set at* $\sqrt{s} = 13$ *TeV*, Eur. Phys. J. C **81** (2021) p. 578, arXiv: 2012.00578 [hep-ex] (cited on page 86).

[145] ATLAS Collaboration, *Jet reconstruction and performance using particle flow with the ATLAS Detector*, Eur. Phys. J. C **77** (2017) p. 466, arXiv: 1703.10485 [hep-ex] (cited on pages 88, 90).

[146] ATLAS Collaboration, *Jet energy scale and resolution measured in proton–proton collisions at* $\sqrt{s} = 13$ *TeV with the ATLAS detector*, Eur. Phys. J. C **81** (2021) p. 689, arXiv: 2007.02645 [hep-ex] (cited on page 88).

[147] M. Cacciari et al., *The anti-k_t jet clustering algorithm*, JHEP **04** (2008) p. 063, arXiv: 0802.1189 [hep-ph] (cited on pages 91, 203).

[148] ATLAS Collaboration, *The performance of missing transverse momentum reconstruction and its significance with the ATLAS detector using 140 fb^{-1} of $\sqrt{s} = 13$ TeV pp collisions*, The European Physical Journal C **85** (2025), ISSN: 1434-6052, URL: http://dx.doi.org/10.1140/epjc/s10052-025-14062-8 (cited on page 92).

[149] W. E. Cleland and E. G. Stern, *Signal processing considerations for liquid ionization calorimeters in a high rate environment*, Nucl. Instrum. Meth. A **338** (1994) p. 467 (cited on page 95).

[150] D. Oliveira Damazio, *Signal Processing for the ATLAS Liquid Argon Calorimeter : studies and implementation*, tech. rep., CERN, 2013, URL: https://cds.cern.ch/record/1630826 (cited on page 95).

[151] ATLAS Collaboration, *Electron and photon energy calibration with the ATLAS detector using 2015–2016 LHC proton-proton collision data*, Journal of Instrumentation **14** (2019) P03017, ISSN: 1748-0221, URL: http://dx.doi.org/10.1088/1748-0221/14/03/P03017 (cited on pages 95, 96, 175).

[152] A. Hoecker et al., *TMVA - Toolkit for Multivariate Data Analysis*, 2009, arXiv: physics/0703039 [physics.data-an] (cited on pages 99, 210).

[153] S. Agostinelli et al., *GEANT4–a simulation toolkit*, Nucl. Instrum. Meth. A **506** (2003) p. 250 (cited on pages 100, 132, 196).

[154] CMS Collaboration, *A measurement of the Higgs boson mass in the diphoton decay channel*, Phys. Lett. B **805** (2020) p. 135425, arXiv: 2002.06398 [hep-ex] (cited on page 130).

[155] CMS Collaboration, *Measurement of the Higgs boson mass and width using the four-lepton final state in proton-proton collisions at $\sqrt{s} = 13$ TeV*, Physical Review D **111** (2025), ISSN: 2470-0029, URL: http://dx.doi.org/10.1103/PhysRevD.111.092014 (cited on page 130).

[156] ATLAS Collaboration, *Luminosity determination in pp collisions at $\sqrt{s} = 13$ TeV using the ATLAS detector at the LHC*, Eur. Phys. J. C **83** (2023) p. 982, arXiv: 2212.09379 [hep-ex] (cited on page 131).

[157] ATLAS Collaboration, *The ATLAS Simulation Infrastructure*, Eur. Phys. J. **C70** (2010) p. 823, arXiv: 1005.4568 [physics.ins-det] (cited on pages 132, 196).

[158] ATLAS Collaboration, *The simulation principle and performance of the ATLAS fast calorimeter simulation FastCaloSim*, tech. rep., CERN, 2010, URL: https://cds.cern.ch/record/1300517 (cited on pages 132, 134, 196).

[159] S. Alioli et al., *A general framework for implementing NLO calculations in shower Monte Carlo programs: the POWHEG BOX*, JHEP **06** (2010) p. 043, arXiv: 1002.2581 [hep-ph] (cited on pages 132, 196).

[160] J. Alwall et al., *The automated computation of tree-level and next-to-leading order differential cross sections, and their matching to parton shower simulations*, JHEP **07** (2014) p. 079, arXiv: 1405.0301 [hep-ph] (cited on pages 132, 133).

[161] K. Hamilton et al., *NNLOPS simulation of Higgs boson production*, JHEP **10** (2013) p. 222, arXiv: 1309.0017 [hep-ph] (cited on page 132).

[162] J. Butterworth et al., *PDF4LHC recommendations for LHC Run II*, J. Phys. G **43** (2016) p. 023001, arXiv: 1510.03865 [hep-ph] (cited on page 132).

[163] T. Sjöstrand et al., *A brief introduction to PYTHIA 8.1*, Comput. Phys. Commun. **178** (2008) p. 852, arXiv: 0710.3820 [hep-ph] (cited on pages 132, 133, 196).

[164] ATLAS Collaboration, *Measurement of the Z/γ^* boson transverse momentum distribution in pp collisions at $\sqrt{s} = 7$ TeV with the ATLAS detector*, JHEP **09** (2014) p. 145, arXiv: 1406.3660 [hep-ex] (cited on page 132).

[165] C. Anastasiou et al., *High precision determination of the gluon fusion Higgs boson cross-section at the LHC*, Journal of High Energy Physics **2016** (2016) p. 58, ISSN: 1029-8479, URL: https://doi.org/10.1007/JHEP05(2016)058 (cited on page 132).

[166] E. Bothmann et al., *Event Generation with Sherpa 2.2*, SciPost Phys. **7** (2019) p. 034, arXiv: 1905.09127 [hep-ph] (cited on page 134).

[167] ATLAS Collaboration, *Measurement of Higgs boson production in the diphoton decay channel in pp collisions at center-of-mass energies of 7 and 8 TeV with the ATLAS detector*, Phys. Rev. D **90** (2014) p. 112015, arXiv: 1408.7084 [hep-ex] (cited on page 135).

[168] ATLAS Collaboration, *Measurement of the production cross section of pairs of isolated photons in pp collisions at 13 TeV with the ATLAS detector*, JHEP **11** (2021) p. 169, arXiv: 2107.09330 [hep-ex] (cited on page 151).

[169] L. Dixon and M. S. Siu, *Resonance-Continuum Interference in the Diphoton Higgs Signal at the LHC*, Physical Review Letters **90** (2003), ISSN: 1079-7114, URL: http://dx.doi.org/10.1103/PhysRevLett.90.252001 (cited on page 162).

[170] *Estimate of the m_H shift due to interference between signal and background processes in the $H \to \gamma\gamma$ channel, for the $\sqrt{s} = 8$ TeV dataset recorded by ATLAS*, tech. rep., CERN, 2016, URL: https://cds.cern.ch/record/2146386 (cited on page 162).

[171] L. J. Dixon and Y. Li, *Bounding the Higgs Boson Width through Interferometry*, Physical Review Letters **111** (2013), ISSN: 1079-7114, URL: http://dx.doi.org/10.1103/PhysRevLett.111.111802 (cited on page 163).

[172] G. Cowan et al., *Asymptotic formulae for likelihood-based tests of new physics*, The European Physical Journal C **71** (2011) p. 1554, ISSN: 1434-6052, URL: https://doi.org/10.1140/epjc/s10052-011-1554-0 (cited on pages 170, 188).

[173] *Preliminary analysis of the luminosity calibration for the ATLAS 13.6 TeV data recorded in 2023*, tech. rep., CERN, 2024, URL: https://cds.cern.ch/record/2900949 (cited on page 195).

[174] A. Firan and R. Stroynowski, *Internal conversions in Higgs decays to two photons*, Physical Review D **76** (2007), ISSN: 1550-2368, URL: http://dx.doi.org/10.1103/PhysRevD.76.057301 (cited on page 196).

[175] A. Abbasabadi and W. W. Repko, *Higgs boson decay to $\mu\mu\gamma$*, Phys. Rev. D **62** (5 2000) p. 054025, URL: https://link.aps.org/doi/10.1103/PhysRevD.62.054025 (cited on page 197).

[176] Y. Sun et al., *Higgs decays to $\gamma l^+ l^-$ in the standard model*, Journal of High Energy Physics **5** (2012) p. 61 (cited on page 197).

[177] ATLAS Collaboration, *Muon reconstruction performance of the ATLAS detector in proton-proton collision data at $\sqrt{s}$=13 TeV*, The European Physical Journal C **76** (2016), ISSN: 1434-6052, URL: http://dx.doi.org/10.1140/epjc/s10052-016-4120-y (cited on page 199).

[178] ATLAS Collaboration, *Performance of pile-up mitigation techniques for jets in pp collisions at $\sqrt{s}$=8 TeV using the ATLAS detector*, The European Physical Journal C **76** (2016), ISSN: 1434-6052, URL: http://dx.doi.org/10.1140/epjc/s10052-016-4395-z (cited on page 203).

[179] ATLAS Collaboration, *Identification and rejection of pile-up jets at high pseudorapidity with the ATLAS detector*, The European Physical Journal C **77** (2017), ISSN: 1434-6052, URL: http://dx.doi.org/10.1140/epjc/s10052-017-5081-5 (cited on page 203).

[180] Microsoft Corporation, *LightGBM: A Highly Efficient Gradient Boosting Decision Tree*, https://lightgbm.readthedocs.io/en/stable/, 2017 (cited on page 211).

[181] M. Ablikim et al., *Study of χ_{cJ} radiative decays into a vector meson*, Physical Review D **83** (2011), ISSN: 1550-2368, URL: http://dx.doi.org/10.1103/PhysRevD.83.112005 (cited on page 224).

[182] G. Cowan et al., *Asymptotic formulae for likelihood-based tests of new physics*, Eur. Phys. J. C **71** (2011) p. 1554, arXiv: 1007.1727 [physics.data-an] (cited on pages 227, 229, 230).

[183] A. Wald, *Tests of statistical hypotheses concerning several parameters when the number of observations is large*, Trans. Amer. Math. Soc. **54** (1943) p. 426 (cited on pages 229, 230).

Acknowledgements

This work marks the conclusion of a long and intense journey, which would not have been possible without the support, guidance, and patience of many people whom I would like to thank.

First of all, I would like to thank my supervisor, Leonardo Carminati, for guiding me continuously since as far back as 2019, when I was still an undergraduate student. Your precise and expert mentorship is undoubtedly the main reason this thesis exists today. Thank you for always giving me countless opportunities and for everything you have taught me.

I would also like to thank my supervisors, Stefano and Ruggero, for their constant presence, for all their valuable advice, and for correcting my endless mistakes. In particular, Stefano, thank you for your unlimited willingness to stop by the office to explain things to me or simply to check on the progress of the work: every piece of advice was deeply appreciated. A huge thank you as well to Davide, who over these years has taken on the role of a shadow supervisor, gaining nothing from it except trouble from me. Thank you for your endless availability and patience.

My thanks go to the ATLAS group at the University of Milan for allowing me to have this experience: to Tommaso Lari, Silvia Resconi, and especially Francesco Tartarelli, for all his advice on the LAr HV system. Thank you for giving me the opportunity to spend all this time at CERN, and thanks as well to the Liquid Argon group for all the support provided over the years.

Thank you to Elena, Federica, and Sofia for all the days shared in the office, the lunch breaks, and the coffee breaks. Thank you for listening with infinite patience to my most naïve questions and occasional breakdowns. I am so happy that you are my friends outside the doors of CERN as well.

Thank you to Mattia and Emanuele for all the time spent together over these years — for the dinners, the outings, the laughter. You always make me feel at ease. Thanks also to all the other people I met through the PhD whom I now have the fortune to call friends: Sara, Chiara, Claudia, Alberto, Simone, and Alessandro.

A heartfelt thank you to my lifelong friends — Alessia, Sara, Liliana, Giulia, Laura, Niccolò, Giulia, and Denise. Our friendship has overcome distance throughout all these years; every time we manage to meet, you make me feel as if I had never left and nothing had changed. I am also deeply grateful to Andrea, Giovanni, Irene, Rebecca, and Rosa: I know I can always count on you.

An enormous thank you to my parents, Luciano and Nadia, and to my brother Andrea. Thank you for being understanding and for always allowing me the freedom to pursue

the path I preferred, even if it meant that we had to live far apart in recent years. Despite that, you have always welcomed me back with open arms.
Finally, thank you to the most unexpected and precious gift this PhD could have given me: Mathis. Since the day we met, we have not let go of each other. Thank you for the unconditional support you showed me every single day during the most intense months of writing this thesis. I am ready to offer you the same — your turn is coming soon. I am grateful for you, and I cannot wait to see what life has in store for us together.

Italian version:
Questo lavoro rappresenta la conclusione di un percorso lungo e intenso, che non sarebbe stato possibile senza il supporto, la guida e la pazienza di molte persone, che desidero ringraziare.
Vorrei innanzitutto ringraziare il mio relatore Leonardo Carminati per avermi seguito ininterrottamente dall'ormai lontano 2019 in triennale. La tua guida precisa ed esperta è stata sicuramente la principale ragione per cui oggi può esistere questa tesi. Grazie per avermi sempre dato mille opportunità e per tutto ciò che mi hai insegnato.
Grazie ai miei supervisori Stefano e Ruggero per la loro presenza costante, per tutti i preziosi consigli e correzioni ai miei infiniti errori. In particolare per Stefano, grazie per l'illimitata disponibilità a passare in ufficio a spiegarmi cose o anche a semplicemente informarti sul procedere del lavoro: ogni consiglio è stato enormemente apprezzato. Un enorme grazie anche a Davide che ha svolto in questi anni il ruolo di shadow-supervisor, senza ricavarne nulla a parte rotture da parte mia. Grazie per l'infinita disponibilità e pazienza.
Grazie al gruppo ATLAS dell'Università di Milano che mi ha permesso di fare questa esperienza: a Tommaso Lari, Silvia Resconi e in particolare a Francesco Tartarelli, per tutti i suoi consigli sul sistema HV del LAr. Grazie per avermi permesso di fare tutta questa esperienza al CERN, e grazie anche al gruppo del Liquid Argon, per tutto il supporto che mi ha dato in questi anni.
Grazie a Elena, Federica e Sofia per tutte le giornate condivise in ufficio, le pause pranzo e i caffè. Vi ringrazio per aver ascoltato le mie domande più stupide e scleri con pazienza infinita. Son contenta che siate mie amiche anche fuori dalle porte del CERN.
Grazie a Mattia ed Emanuele per tutto il tempo passato insieme in questi anni. Grazie per tutte le cene, le uscite, le risate. Mi fate sempre stare bene. Grazie anche a tutte le altre persone che ho conosciuto tramite il dottorato e che ormai ho la fortuna di considerare amici, Sara, Chiara, Claudia, Alberto, Simone e Alessandro.
Un grazie di cuore ai miei grandi amici di sempre, Alessia, Sara, Liliana, Giulia, Laura, Niccolò, Giulia e Denise. La nostra amicizia ha superato la lontananza tutti questi anni, ogni volta che riusciamo a vederci mi fate sentire come se non me ne fossi mai andata e nulla fosse cambiato. Ringrazio tanto Andrea, Giovanni, Irene, Rebecca, Rosa: so di poter sempre contare su di voi.
Un enorme grazie ai miei genitori Luciano e Nadia e a mio fratello Andrea: grazie per essere stati comprensivi e per avermi lasciata sempre libera di intraprendere la strada che preferivo, anche se magari ci ha portati a stare lontani negli ultimi anni. Nonostante

ciò, mi avete sempre riaccolta a braccia aperte.
Grazie al regalo più inaspettato e prezioso che questo dottorato potesse farmi, Mathis. Da quando ci siamo conosciuti non ci siamo più lasciati. Ti ringrazio per il supporto incondizionato che mi hai dimostrato ogni giorno durante i mesi più intensi della tesi, e sono pronta a offrirti lo stesso (tra poco tocca a te eheh). Ti ringrazio e non vedo l'ora di vedere cosa questa vita avrà da offrirci insieme.

List of Acronyms

ALICE A Large Ion Collider Experiment. 23

ATLAS A Toroidal LHC ApparatuS. 1, 23, 26–35, 37–39, 41, 44, 46–49, 51, 58–70, 72, 88, 91–94, 98, 100, 101, 106, 129–132, 134–136, 183–185, 187, 190–196, 199, 201, 210, 217, 232–234

BDT Boosted Decision Trees. 98–100, 103, 104, 211–216, 218, 231, 249–251

BSM Beyond the Standard Model. xi, xiii, 49, 59, 91, 193

CERN European Organization for Nuclear Research. 17, 22

CL Confidence Level. xiii, 194

CMS Compact Muon Solenoid. 1, 23, 28, 31, 37, 58–60, 62–64, 66, 67, 129, 130, 184, 185, 190, 193, 194, 217, 234

CP combined performance. 199, 201, 210

CSC Cathode Strip Chambers. 47

CTP Central Trigger Processor. 48

DESY Deutsches Elektronen-Synchrotron. 6

DIS deep inelastic scattering. 5

DSCB Double-Sided Crystal Ball. xiv, 147–150, 169, 170, 188, 195, 218–222, 243–247, 252–254

DT Digital Trigger. 44

eFEX electromagnetic Feature Extraction. 49

EM Electromagnetic. 31, 33, 34, 38, 42–45, 49, 69–74, 76, 77, 93, 95, 96, 98, 101, 102, 114, 121, 135, 136, 140, 200, 203, 210, 223, 224

EMB Electromagnetic Barrel. 42–44

EMEC ElectroMagnetic EndCap. 26, 42–44

FASER ForwArd Search ExpeRiment. 23

FCal Forward Calorimeter. 26, 45, 46

FEBs Front End Boards. 94

FEX Feature Extraction. 49

fJVT forward jet vertex tagger. 203

FSR final-state radiation. xiii, 193, 194, 203, 217

gFEX global Feature Extraction. 49

GRL Good Run List. 132

GSC Global Sequential Calibration. 91

GSF Gaussian Sum Filter. 73

HEC Hadronic EndCap. 45

HEP High Energy Physics. xii, 2, 62, 130

HG High Gain. 114, 121, 124

HL-LHC High Luminosity Large Hadron Collider. xiv, 31, 47

HLT High-Level Trigger. 48–50, 134

IBL Insertable B-Layer. 35–37

ID Inner Detector. 26, 31, 33–37, 42, 46, 69, 70, 72–75, 80, 84, 86–88, 90, 93, 102, 135, 157, 165, 199, 200

IP interaction point. 23, 24, 31, 32, 34, 35, 42, 48, 86, 87, 157, 199

JADE Japan Deutschland England. 6

JF Di-Jet Filtered. 197, 210, 211

jFEX jet Feature Extraction. 49

JVT jet vertex tagger. 203

L1 Level-1. 48–50

LAr Liquid Argon. 38–46, 49, 94, 113, 116, 156

LEP Large Electron-Positron Collider. 17, 18

LG Low Gain. 121

LHC Large Hadron Collider. xi, xiv, xv, 17, 18, 20–29, 31, 32, 43, 48, 49, 51, 53–57, 60, 61, 64, 88, 184, 187, 196, 234

LHCb Large Hadron Collider beauty. 23

LHCf Large Hadron Collider forward. 23

LightGBM Light Gradient Boosting Machine. 211–213

Linac2 Liner accelerator 2. 22

Linac4 Liner accelerator 4. 21, 22

LS1 Long Shutdown 1. 17

LS2 Long Shutdown 2. 17, 22, 49

LUCID-2 LUminosity Cherenkov Integrating Detector 2. 26

LVPS Low Voltage Power Supply. xiv

MC Monte Carlo. 79– 84, 87, 89, 93, 97– 101, 104, 106, 121, 122, 132, 133, 137, 141, 146– 152, 156, 159– 161, 163– 166, 174, 175, 196, 204– 208, 210– 212, 214, 216– 219, 221– 223, 227, 241– 247, 252– 254

MDT Monitored Drift Tubes. 46, 47

MG Medium Gain. 114, 121, 124

MicroMegas Micro-Mesh Gaseous Structure. 47, 51

MoEDAL-MAPP Monopole and Exotics Detector at the LHC - MoEDAL Apparatus for Penetrating Particles. 23

MS Muon Spectrometer. 31, 33, 34, 46, 69, 86, 87, 199

MVA Multivariate Analysis. 100, 103, 104, 106, 108, 110, 166, 237– 239

NN Neural Network. 135, 136, 165, 187

NP Nuisance Parameter. 126, 170, 175, 188, 189, 227

NPs Nuisance Parameters. 168– 171, 175, 176, 188

NSW New Small Wheels. 47, 49, 51

PDF Parton Distribution Function. 19, 20

PER photon energy resolution. 155, 159, 164, 165, 169

PES photon energy scale. 155– 157, 161, 162, 164, 165, 169

POI Parameter of Interest. 168, 170, 172

POIs Parameters of Interest. 168, 171

PS Proton Synchrotron. 22

PSB Proton Synchrotron Booster. 22

PV Primary Vertex. 136

QCD Quantum Chromodynamics. xii, 1, 2, 5– 7, 9, 14, 17, 19, 53, 55, 56, 58, 62, 132, 133, 151, 165, 196, 197

QED Quantum Electrodynamics. 1, 3– 6, 8– 11, 14

QRNN Quantile Regression Neural Network. 187, 188

RF radio-frequency. 20, 21

ROC Receiver Operating Characteristic. 214, 215

RoI Regions-of-Interest. 49

RPC Resistive Plate Chambers. 47

SCT SemiConductor Tracker. 35, 36, 72, 80

SLAC Stanford Linear Accelerator Center. 5

SM Standard Model. xi, xiii– xv, 1– 3, 7, 8, 11, 23, 53– 56, 58– 68, 129, 133, 144, 146, 148, 151, 154, 162, 165, 167, 171, 176– 178, 181, 190, 192– 194, 196, 201, 218, 222, 225, 227, 231– 234

SND@LHC Scattering and Neutrino Detector at the LHC. 23

SPS Super Proton Synchrotron. 22

STXS Simplified Template Cross Sections. 141

SW Small Wheels. 47

TDAQ Trigger and Data Acquisition. 31, 48

TGC Thin Gap Chambers. 47, 48, 51

TLA trigger-level analysis. 50

TMVA Toolkit for Multivariate Data Analysis. 99

TOB Trigger OBjects. 48

TOTEM TOTal cross section, Elastic scattering and diffraction dissociation Measurement. 23

TRT Transition Radiation Tracker. 35, 36, 73, 74, 76, 80, 108, 210, 212

TT Trigger Towers. 44, 45, 49

VEV Vacuum Expectation Value. 12, 14– 16

WP Working Points. 77, 79, 82, 84